THÈSE

Pour obtenir le grade de

DOCTEUR DE L'UNIVERSITÉ GRENOBLE ALPES

École doctorale : I-MEP² - Ingénierie - Matériaux, Mécanique, Environnement, Energétique, Procédés, Production
Spécialité : 2MGE - Matériaux, Mécanique, Génie civil, Electrochimie
Unité de recherche : CEA Grenoble - LITEN

Variation de la structure de l'encre catalytique en fonction de la composition grâce à la diffusion de neutrons aux petits angles à variation de contraste et effet sur les propriétés électrochimiques des couches catalytiques résultantes

Catalyst Ink Structure Variation as Function of Ink Composition using Contrast-Variation Small Angle Neutron Scattering and Effect on Electrochemical Properties of Resulting Catalyst Layers

Présentée par :

Martha Yael STANDO

Direction de thèse :

Gérard GEBEL DIRECTEUR DE RECHERCHE, CEA - Centre de Grenoble	Directeur de thèse
Arnaud MORIN DIRECTEUR DE RECHERCHE, CEA - Centre de Grenoble	Co-encadrant de thèse
Lionel PORCAR Institut Laue Langevin (ILL)	Co-encadrant de thèse
Jakub DRNEC ESRF	Co-encadrant de thèse

Rapporteurs :

Julian OBERDISSE
DIRECTEUR DE RECHERCHE, CNRS délégation Occitanie Est
Cécile ZAKRI
PROFESSEURE DES UNIVERSITES, Université de Bordeaux

Thèse soutenue publiquement le **5 décembre 2024**, devant le jury composé de :

Pierre-Antoine BONNEFONT, PROFESSEUR DES UNIVERSITES, Grenoble INP - UGA	Président
Gérard GEBEL, DIRECTEUR DE RECHERCHE, CEA centre de Grenoble	Directeur de thèse
Julian OBERDISSE, DIRECTEUR DE RECHERCHE, CNRS délégation Occitanie Est	Rapporteur
Cécile ZAKRI, PROFESSEURE DES UNIVERSITES, Université de Bordeaux	Rapporteure
Emmanuelle DUBOIS, DIRECTRICE DE RECHERCHE, CNRS délégation Paris Centre	Examinatrice
Olivier LOTTIN, PROFESSEUR DES UNIVERSITES, Université de Lorraine	Examinateur

Invités :

Stéphane Cotte
SENIOR SCIENTIST, Toyota Motor Europe

Acknowledgements

To begin, I would like to acknowledge the thesis committee for taking part in the assessment of my work throughout the PhD project - Pierre-Antoine Bonnefont, Emmanuelle Dubois, Olivier Lottin, Julian Oberdisse, and Cécile Zakri. Thank you for all your time and effort spent not only during the PhD defense itself, but also when going over the manuscript, particularly when its first iteration ended up being long and rather dense. An additional thank you to Prof. Zakri and Dr. Oberdisse for their job as reviewers – the feedback from the reports greatly aided me in preparation for the defense itself, and to target areas where corrections had to be made. On the day of the defense, I enjoyed the fruitful discussions, which gave me a lot of new ideas going forward. Thank you Prof. Bonnefont for acting as the committee chair.

Thank you to Gérard Gebel, Arnaud Morin, and Lionel Porcar, without whom this project would not be possible. Your expertise on the PFSA ionomers, PEMFC electrodes and system, as well as SANS guided me towards achieving the best results possible. Although at the beginning my knowledge could only be described as lacking, your keenness to answer my questions and patience when corrections had to be applied helped me to grow into a capable researcher. I will always be grateful for all your engagement and unwavering support throughout this project, working with you has been a pleasure.

Thank you to Jakub Drnec and Stéphane Cotte for their input into the project, as well as productive discussions. Moreover, I am very thankful for the knowledge I gained during my secondment at Toyota Motor Europe, giving me an enhanced understanding of the relation between academia and industry, in line with the intended outcome of the InnovaXN doctoral training programme.

Throughout the PhD project I was able to travel to several facilities to perform various experiments. I would like to thank the ANSTO and ISIS institutes, for providing neutron beamtimes that allowed this project to continue moving forward in light of the long shutdown at the ILL taking place over the first year of my PhD. Aside from the valuable data obtained, I was able to learn much about the operation of different neutron facilities across the world. Thank you to Dr. Anna Sokolova and Dr. Najet Mahmoudi for their help during the experiments at these two institutions. Thank you to Prof. Wolfgang Peukert and Dr. Cornelia Damm of the Institute of Particle Technology of the Friedrich-Alexander University Erlangen-Nürnberg, for a rewarding collaboration, allowing me to perform isothermal titration calorimetry experiments at their institute.

Thank you to all my many colleagues from the ILL and CEA-Liten for their continuous support and many helpful discussions throughout the last three years. Clémence Marty and Armelle Fabulet, who introduced me to the CEA-Liten fuel cell laboratory and helped me to prepare samples. Laure Guetaz, who performed electron microscopy measurements on several samples. Pierre Toudret and Benoit Gouze for their help with SANS experiments measuring catalyst layer powders. Martina Sandroni, who was always available to help with any laboratory related question or issue. Leonardo Chiappisi and Pierre Lloria for the access and many tutorials using various equipment of the Partnership for Soft Condensed Matter.

Lastly, a big thank you to my family and friends, for their unwavering support over the last few years, which could at times prove challenging. I am very grateful that I could always turn to you for words of encouragement, or if simply I had to vent some frustrations, and you were always there for me. It made the whole difference. In particular, during the last few months, when I was writing the manuscript, thank you to my mother for always being there to talk, and Maciej, who supported and took care of me night and day. I couldn't have done it without you.

Table of Contents

List of acronyms **10**

Introduction **12**

1. Basic principles and state of the art **17**

1.1 Proton exchange membrane fuel cell (PEMFC) 17

1.1.1 Gas flow plates 17

1.1.2 Gas diffusion layer (GDL) 18

1.1.3 Proton exchange membrane (PEM) 20

1.1.4 Catalyst layer (CL) 21

1.2 Catalyst ink and preparation of the catalyst layer 23

1.2.1 Carbon support 23

1.2.2 Ionomer 25

1.2.3 Platinum 26

1.2.4 Solvent 26

1.3 State of the art 28

1.3.1 Carbon support 28

1.3.2 Ionomer 32

1.3.3 Platinum 37

1.3.4 Dispersion Solvent 39

1.3.5 Summary of observations from state of the art research on component variation effect 43

1.4 **Application of small-angle scattering towards an enhanced understanding of the PEMFC electrode** 44

1.4.1 SAS of catalyst layers 44

1.4.2 SAS of catalyst inks 48

1.5 **Conclusions** 50

2. Small-Angle Neutron Scattering **52**

2.1 SANS theory 54

2.1.1 Experimental Considerations – Setting up the Measurement Configuration 57

2.1.2 Experimental Considerations – Data Processing 57

2.1.3 Advantages of SANS for catalyst ink/layer structural investigations 59

2.2 Contrast variation and partial scattering functions 61

2.2.1 Contrast variation 61

2.2.2 Partial scattering functions 62

2.2.3 Contrast matching determination of component SLD 64
2.2.4 Component SLD input for PSF extraction – an experimental queary. 66
2.2.5 CV-SANS simulations 67
2.2.6 Investigation of PSF input effect 74
2.2.6.1 component SLD variation 74
2.2.6.2 Solvent SLD range & number of input data 79
2.2.6.3 Comparison to experimental data 80
2.2.6.4 Direct scattering subtraction 83
2.3 CV-SANS experimental results – investigation of catalyst ink structure variation as function of ink composition 86
2.3.1 Methodology 86
2.3.1.1 Sample preparation 86
2.3.1.2 Instrumental set-up and data processing 89
2.3.2 SANS on component dispersions 89
2.3.2.1 Ionomer dispersions 89
2.3.2.2 Carbon dispersions 95
2.3.3 CV-SANS measurements of catalyst inks – results and discussion 98
2.3.3.1 Effect of carbon support 98
2.3.3.2 Effect of ionomer-to-carbon (I/C) ratio 111
2.3.3.3 Effect of solvent 114
2.2.3.4 Effect of ionomer type 120
2.3.3.5 Concentration effect 124
2.3.3.6 Effect of Pt 128
2.3.3.6.1 Introduction of Pt 128
2.3.3.6.2 Effect of Pt + I/C ratio 132
2.3.3.6.3 Effect of Pt + solvent system 135
2.3.4 Conclusions 141
2.4 Catalyst Layer SANS 146
2.4.1 Sample preparation and methodology 147
2.4.1.1 TEM/EDS characterization 148
2.4.1.2 SANS measurements 149
2.4.2 Results 150
2.4.2.1 TEM/EDS characterization 150

2.4.2.2 SANS results 152
2.4.3 Conclusions 157
3. Ultra Small Angle X-ray Scattering 159
3.1 Theory 160
3.2 Methodology 163
3.3 USAXS results 164
3.3.1 Comparison of scattering functions obtained from USAXS and CV-SANS 164
3.3.2 Effect of Pt on aggregate size 165
3.3.3 Effect of increasing ionomer content on aggregate size 167
3.3.3.1 High surface area carbon (HSAC) 167
3.3.3.2 High surface area carbon and platinum (Pt/HSAC) 173
3.3.3.3 Graphitized carbon (GC) 174
3.3.3.4 Graphitized carbon and platinum (Pt/GC) 178
3.3.5 Comparison of carbon supports, with and without Pt 180
3.4 Conclusions 181
4 Isothermal Titration Calorimetry (ITC) 183
4.1 Theory 184
4.2 Methodology 186
4.3 Results 188
4.3.1 Adsorption of ionomer to carbon support only 188
4.3.2 Adsorption of ionomer to Pt/C complexes 191
4.4 Conclusions 193
5 Electrochemical Characterization 195
5.1 Theory 196
5.1.1 Polarization curves 196
5.1.2 Electrochemical Impedance spectroscopy (EIS) 199
5.1.3 Cyclic voltammetry (CV) 201
5.2 Sample preparation and methodology 203
5.2.1 Measuring protocols 205
5.3 Results 208
5.3.1 Pt/HSAC based CCMs 208
5.3.2 Pt/GC based CCMs 218
5.3.3 Comparison of MEAs based on different Pt/C complexes 223
5.4 Conclusions 225

6 Conclusions 227
References 235
Appendix 240

List of acronyms

1-PrOH	**1-Pr**opanol
AST	**A**ccelerated **S**tress **T**est
ATR-FTIR	**A**ttenuated **T**otal **R**eflectance **F**ourier **T**ransform **I**nfrared **S**pectroscopy
CCL	**C**athode **C**atalyst **L**ayer
CCM	**C**atalyst **C**oated **M**embrane
CL	**C**atalyst **L**ayer
CryoSTEM	**S**canning **T**ransmission **E**lectron **C**ryo**M**icroscopy
CryoTEM	**T**ransmission **E**lectron **C**ryo**M**icroscopy
CV-SANS	**C**ontrast **V**ariation **S**mall-**A**ngle **N**eutron **S**cattering
DAA	**D**i**A**cetone **A**lcohol
DLS	**D**ynamic **L**ight **S**cattering
ECSA	**E**lectro**C**hemical **S**urface **A**rea
EDS	**E**nergy **D**ispersive **S**pectroscopy
ELS	**E**lastic **L**ight **S**cattering
EtOH	**Et**hanol
EW	**E**ffective **W**eight
FCEV	**F**uel **C**ell **E**lectric **V**ehicle
GC	**G**raphitized **C**arbon
GDL	**G**as **D**iffusion **L**ayer
HAADF-STEM	**H**igh **A**nnular **A**ngle **D**ark **F**ield **S**canning **T**ransmission **E**lectron **M**icroscopy
HRTEM	**H**igh **R**esolution **T**ransmission **E**lectron **M**icroscopy
HSAC	**H**igh **S**urface **A**rea **C**arbon
HOR	**H**ydrogen **O**xidation **R**eaction
I/C ratio	**I**onomer-to-**C**arbon ratio
iPrOH	**i**so**Pr**opanol
ITC	**I**sothermal **T**itration **C**alorimetry
LSC	**L**ong **S**ide**C**hain
MD	**M**olecular **D**ynamics
MEA	**M**embrane **E**lectrode **A**ssembly
MeOH	**Me**thanol

MPL	**M**icro**P**orous **L**ayer
NMR	**N**uclear **M**agnetic **R**esonance
OCV	**O**pen **C**urrent **V**oltage
ORR	**O**xygen **R**eduction **R**eaction
PEM	**P**roton **E**xchange **M**embrane
PEMFC	**P**roton **E**xchange **M**embrane **F**uel **C**ell
PFSA	**P**er**F**luoro**S**ulfonic **A**cid
PG	**P**ropylene **G**lycol
PSF	**P**artial **S**cattering **F**unction
Pt/C ratio	**P**latinum-to-**C**arbon ratio
PTFE	**P**oly**T**etra**F**luoro**E**thylene
RH	**R**elative **H**umidity
SAS	**S**mall-**A**ngle **S**cattering
SANS	**S**mall-**A**ngle **N**eutron **S**cattering
SAXS	**S**mall-**A**ngle **X**-ray **S**cattering
SEM	**S**canning **E**lectron **M**icroscopy
SLD	**S**cattering **L**ength **D**ensity
SSC	**S**hort **S**ide**C**hain
STEM	**S**canning **T**ransmission **E**lectron **M**icroscopy
SVD	**S**ingular **V**alue **D**ecomposition
TEM	**T**ransmission **E**lectron **M**icroscopy
TGA	**T**hermo**G**ravimetric **A**nalysis
USANS	**U**ltra-**S**mall-**A**ngle **N**eutron **S**cattering
USAXS	**U**ltra-**S**mall-**A**ngle **X**-ray **S**cattering
WAXS	**W**ide **A**ngle **X**-ray **S**cattering
XRD	**X**-**R**ay **D**iffraction

Introduction

In light of both the climate change and fossil fuel sustainability concerns faced globally today, hydrogen fuel has been recognized as a promising alternative. With water and heat composing the only reaction by-products, application of hydrogen fuel in transportation, a sector responsible for 14% of global,[1] as well as 30% of EU,[2] greenhouse gas emissions, has garnered significant research attention.

Proton exchange membrane fuel cells (PEMFCs) which can be used to power fuel-cell electric vehicles (FCEVs) by converting chemical energy stored in hydrogen fuel to electrical energy. FCEVs present multiple advantages including fuelling times as short as 3 minutes and long driving ranges of over 500 km, making them particularly appealing for heavy duty vehicles.[3]

Although FCEVs have been commercially available for several years, large-scale commercialization requires progress in performance, cost and durability of the PEMFC, for which the electrode is one the most limiting components. Also known as the catalyst layer, the electrode is composed of Pt nanoparticles (catalyst) supported on a carbon composite (electron collector), embedded in a proton conductive polymer, referred to as an ionomer. The electrode is obtained from a slurry after evaporating solvent consisting of a mixture of water and alcohol.

The performance and durability of the electrode are strongly influenced by its final structure, namely the ionomer dispersion, catalyst aggregation and ionomer coverage onto the Pt/C complex. The nano- and micro-structures of the electrode depend on the quality of the dispersion of the materials in the ink throughout the drying process. Currently little is known on these structures, including that of the initial slurry or the final electrode. This is particularly true with regards to the dispersion of the ionomer component, despite the fact it is now established that it plays a crucial role in the operation of the PEMFC.[4]

The lack of information leaves research and development to be heavily reliant on a trial and error basis. Developing the understanding of the individual structures the components undertake during the preparation stages, their evolution throughout manufacturing, as well as their correlation to the final electrode and fuel cell performance, are all key steps in advancing our understanding of the PEMFC technologies. This in turn will allow for a more targeted synthesis approach and production of highly optimized fuel cells, resulting in further commercialization capabilities. A detailed study of both inter- and intramolecular behaviours in the multi-component ink dispersion is a credible strategy for gaining a comprehensive understanding of the reaction environment.

Nevertheless, this is not a straightforward task. Both the catalyst layer and catalyst ink are complex, multi-component, highly heterogeneous systems. The Pt/C complex forms polydisperse aggregates and agglomerates, whose sizes range from a couple of hundred nanometres all the way to the micrometre scale. In the ink the ionomer adsorbs to the Pt/C surface, but also exists as an ‘unadsorbed’ ionomer dispersion in the slurry. In the catalyst layer the ionomer forms a thin film on the Pt/C surface and the aggregates/agglomerates mentioned above are separated by ionomer clusters formed during the drying process. It is known the ionomer does not form a layer of uniform thickness on the Pt/C, and coverage can be ‘patchy’ – areas with no ionomer coverage on Pt/C can also be present.[5] It can be assumed this is most likely also the case in the inks, considering the non-uniform distribution of Pt on the carbon surface as well as the complex geometric shape and number of defects found in the latter.

In addition to this, a plethora of variations can be introduced into the catalyst ink composition, which may alter the mechanism of interactions between components, as well as result in complex inter-component dependencies. For example, porous and non-porous carbon supports not only present very different surfaces for ionomer to interact with, but also result in very different distribution of Pt, which in the case of porous carbons may be found inside the pores themselves. It remains unclear whether ionomer interacts preferentially with carbon or Pt, yet this interaction may be dependent on the solvent system, where varying

the concentration or type of alcohol chosen in the mixture may result in conformation changes of the ionomer that alter the interaction mechanism. Moreover, the choice of the ionomer itself, with popular options including both short- and long-side chain perfluorinated polymers, will affect the degree of adsorption of the ionomer on the Pt/C. These ink compositional variations themselves can be expected to have a significant impact on the catalyst layer structure, and that is not to mention the manufacturing process, where choice of ink coating method, drying temperature and humidity can all affect additionally alter the final electrode structure.

Nevertheless, due to the complexity of the system, a fundamental understanding of component interactions, commencing with the catalyst ink, is required. **The aim of this PhD project is to progress such knowledge through investigation of the variation in catalyst ink structure as a function of a systematic composition variation.** The prospect is that introducing small changes in between each ink sample will allow to pin-point structural variation to one component in particular, or to an alteration in behaviour that arises in specific compositions.

Aside from the complexity of the ink system itself, finding a suitable method for its investigation is not an easy task. Optical methods, such as light or laser scattering, often used to study distribution of components in a dispersion, are incompatible with the ink system due to the opacity of samples arising from the nature of carbon. In samples where concentration is comparable to industrially applicable catalyst inks, no light permeation is possible, therefore the samples must be heavily diluted and are no longer representative of the system in question. Microscopy methods such as transmission electron cryomicroscopy (cryoTEM) can be useful to obtaining information on the Pt/C dispersion in the system, however it only probes a small area of a highly heterogeneous sample, which may not be representative of the system overall. Moreover, the observation of the ionomer component proves near impossible due to damage sustained from the electron beam.

Small-angle scattering (SAS) is a suitable technique as it allows for bulk characterization of the catalyst ink system in the size range of one to several hundred nm, which is particularly suitable for investigation of the ionomer structure, where both the adsorbed layer and unabsorbed aggregates in the dispersion exist on the nanometre size scale. In particular, small-angle neutron scattering (SANS) is highly promising, where facile alteration of contrast between a specific component and a dispersion medium allows for extraction of component specific structural information, even for a complex, multi-component system. Reducing contrast of one component renders it effectively ‘invisible’ to neutrons, resulting in a scattering function which contains less convoluted structural information. This method of contrast variation (CV) allows for direct interpretation of the structure of the ionomer inside the catalyst ink, a feature not attainable in any other bulk-probing techniques.

In this work, CV-SANS will be employed to investigate the effect of composition on the catalyst ink structure, with specific regard to the structure of the ionomer component. Compositional variations will include altering the carbon support and ionomer types, concentration of alcohol in the solvent, ionomer-to-carbon (I/C) ratio, as well as solid content (component concentration). Additionally, alongside conventional inks containing the Pt/C complex, the same variations will be introduced to carbon support-only containing pseudo inks, allowing for an in-depth study of the effect of Pt in the system. In particular, it is of interest to deduce whether ionomer interacts preferentially with the carbon or Pt component, and gain insight into the ionomer layer formation mechanism.

In addition to CV-SANS, isothermal titration calorimetry (ITC) will be employed to obtain supporting insights into the thermodynamics of ionomer adsorption to different carbon supports and Pt/C complexes in the ink. Furthermore, ultra-small-angle X-ray scattering (USAXS) will be used to probe a size scale >100 nm, yielding information on the alteration of carbon aggregate structure with increasing ionomer content and in the presence of Pt.

As achieving a better understanding of ink structure is only the first step in developing a more targeted electrode optimization approach, the effect of one compositional variable will be studied further – on the final catalyst layer structure using SANS, as well as on the final electrochemical performance of the resulting membrane-electrode-assembly (MEA). **In a first study to date, a full correlation between the structures of the catalyst ink and the final catalyst layer, as well as the resulting electrochemical performance, will be performed.**

Chapter 1 will introduce basic principles that will enhance the understanding of the topic of this PhD project. The operation mechanism as well as components found inside the PEMFC overall will be discussed. Next, an introduction on the catalyst ink will follow, including the conventional process used to manufacture catalyst layers. Each ink component will be discussed in detail, and subsequently a literature review will be undertaken, presenting state of the art research on the impact of component variation on the catalyst ink and catalyst layer structures, with a specific section dedicated to the use of SANS and SAXS techniques in this field.

Many of the subsections will contain summaries of results, written in bold. Additionally, a more general conclusion section will be present at the end of each chapter, containing main results, as well as a broader discussion and future perspectives. For a general overview of key findings, please refer to such fragments of the work.

En raison des préoccupations liées au changement climatique et à la durabilité des combustibles fossiles auxquelles le monde est confronté aujourd'hui, l'hydrogène a été reconnu comme une alternative prometteuse. Avec *l'eau et la chaleur étant les seuls sous-produits de la réaction, l'application de l'hydrogène comme carburant dans les transports, un secteur responsable de 14 % des émissions de gaz à effet de serre dans le monde[1] et de 30 % dans l'UE,[2] a suscité une attention particulière de la part des chercheurs.*

Piles à combustible à membrane échangeuse de protons (PEMFC) qui peuvent être utilisées pour alimenter les véhicules électriques à pile à combustible (FCEV) en convertissant l'énergie chimique stockée dans l'hydrogène en énergie électrique. Les FCEV présentent de nombreux avantages, notamment des temps de ravitaillement aussi courts que 3 minutes et une longue autonomie de plus de 500 km, ce qui les rend particulièrement attrayants pour les véhicules lourds.[3]

Bien que les FCEV soient disponibles dans le commerce depuis plusieurs années, une commercialisation à grande échelle nécessite des progrès en termes de performances, de coût et de durabilité des PEMFC, pour lesquelles l'électrode est l'un des composants les plus limitants. Également connue sous le nom de couche catalytique, l'électrode est composée de nanoparticules de Pt (catalyseur) supportées sur un composite de carbone (collecteur d'électrons), noyées dans un polymère conducteur de protons, appelé ionomère. L'électrode est obtenue à partir d'une suspension après évaporation d'un solvant constitué d'un mélange d'eau et d'alcool.

Les performances et la durabilité de l'électrode sont fortement influencées par sa structure finale, à savoir la dispersion de l'ionomère, l'agrégation du catalyseur et la couverture de l'ionomère sur le complexe Pt/C. Les nano- et micro-structures de l'électrode dépendent de la qualité de la dispersion des matériaux dans l'encre tout au long du processus de séchage. Actuellement, on sait peu de choses sur ces structures, y compris sur celle de la suspension initiale ou de l'électrode finale. Cela est particulièrement vrai en ce qui concerne la dispersion du composant ionomère, même s'il est désormais établi qu'il joue un rôle crucial dans le fonctionnement de la PEMFC.[4]

Le manque d'informations fait que la recherche et le développement dépendent fortement d'une approche basée sur les essais et les erreurs. Développer la compréhension des structures individuelles que les composants adoptent au cours des étapes de préparation, leur évolution tout au long de la fabrication, ainsi

que leur corrélation avec l'électrode finale et les performances de la pile à combustible, sont autant d'étapes importantes pour faire progresser notre compréhension des technologies PEMFC. Cela permettra à son tour une approche de synthèse plus ciblée et la production de piles à combustible hautement optimisées, se traduisant par de nouvelles capacités de commercialisation. Une étude détaillée des comportements intermoléculaires et intramoléculaires dans la dispersion d'encre multi-composants constitue une stratégie crédible pour acquérir une compréhension globale de l'environnement réactionnel.

Néanmoins, ce n'est pas une tâche simple. La couche catalytique et l'encre catalytique sont des systèmes complexes, multi-composants et hautement hétérogènes. Le complexe Pt/C forme des agrégats et des agglomérats polydispersés, dont les tailles varient de quelques centaines de nanomètres jusqu'à l'échelle micrométrique. Dans l'encre, l'ionomère s'adsorbe sur la surface Pt/C, mais existe également sous forme de dispersion d'ionomère « non adsorbée » dans la suspension. Dans la couche de catalyseur, l'ionomère forme un film mince sur la surface Pt/C et les agrégats/agglomérats mentionnés ci-dessus sont séparés par des grappes d'ionomères formées pendant le processus de séchage. Il est connu que l'ionomère ne forme pas une couche d'épaisseur uniforme sur le Pt/C, et la couverture peut être « inégale » – des zones sans couverture d'ionomère sur le Pt/C peuvent également être présentes.[5] On peut supposer que c'est probablement aussi le cas dans les encres, compte tenu de la distribution non uniforme du Pt sur la surface du carbone ainsi que de la forme géométrique complexe et du nombre de défauts trouvés dans cette dernière.

En plus de cela, une multitude de variations peuvent être introduites dans la composition de l'encre catalytique, ce qui peut modifier le mécanisme d'interactions entre les composants et entraîner des dépendances inter-composants complexes. Par exemple, les supports de carbone poreux et non poreux présentent non seulement des surfaces très différentes avec lesquelles l'ionomère peut interagir, mais entraînent également une distribution très différente du Pt, qui, dans le cas des carbones poreux, peut se trouver à l'intérieur des pores eux-mêmes. Il n'est pas encore clair si l'ionomère interagit préférentiellement avec le carbone ou le Pt, mais cette interaction peut dépendre du système solvant, où la variation de la concentration ou du type d'alcool choisi dans le mélange peut entraîner des changements de conformation de l'ionomère qui modifient le mécanisme d'interaction. De plus, le choix de l'ionomère lui-même, avec des options populaires incluant des polymères perfluorés à chaîne courte et longue, affectera le degré d'adsorption de l'ionomère sur le Pt/C. On peut s'attendre à ce que ces variations de composition de l'encre elles-mêmes aient un impact significatif sur la structure de la couche de catalyseur, sans parler du processus de fabrication, où le choix de la méthode de revêtement de l'encre, la température de séchage et l'humidité peuvent tous affecter et modifier en outre la structure finale de l'électrode.

Néanmoins, en raison de la complexité du système, une compréhension fondamentale des interactions entre les composants, en commençant par l'encre catalytique, est nécessaire. ***L'objectif de ce projet est de faire progresser ces connaissances en étudiant l'idée est qu'une introduction de catalytique en fonction d'une variation*** *petits changements entre chaque échantillon d'encre permettra d'identifier une variation structurelle d'un composant en particulier ou une altération du comportement qui survient dans des compositions spécifiques.*

Outre la complexité du système d'encre lui-même, trouver une méthode appropriée pour son étude n'est pas une tâche facile. Les méthodes optiques, telles que la diffusion de la lumière ou du laser, souvent utilisées pour étudier la distribution des composants dans une dispersion, sont incompatibles avec le système d'encre en raison de l'opacité des échantillons résultant de la nature du carbone. Dans les échantillons où la concentration est comparable à celle des encres catalytiques applicables industriellement, aucune perméation de la lumière n'est possible, les échantillons doivent donc être fortement dilués et ne sont plus représentatifs du système en question. Les méthodes de microscopie telles que la cryomicroscopie électronique à transmission (cryoTEM) peuvent être utiles pour obtenir des informations sur la dispersion Pt/C dans le système, mais elles ne sondent qu'une petite zone d'un échantillon très hétérogène, qui peut ne pas

être représentatif du système dans son ensemble. De plus, l'observation du composant ionomère s'avère presque impossible en raison des dommages causés par le faisceau d'électrons.

La diffusion aux petits angles (SAS) est une technique appropriée car elle permet une caractérisation en masse du système d'encre catalyseur dans la gamme de tailles d'une à plusieurs centaines de nm, ce qui est particulièrement adapté à l'étude de la structure ionomère, où la couche adsorbée et les agrégats non absorbés dans la dispersion existent à l'échelle nanométrique. En particulier, la diffusion de neutrons aux petits angles (SANS) est très prometteuse, où la modification facile du contraste entre un composant spécifique et un milieu de dispersion permet l'extraction d'informations structurelles spécifiques au composant, même pour un système complexe à plusieurs composants. La réduction du contraste d'un composant le rend effectivement « invisible » aux neutrons, ce qui donne lieu à une fonction de diffusion qui contient des informations structurelles moins alambiquées. Cette méthode de variation de contraste (CV) permet une interprétation directe de la structure de l'ionomère à l'intérieur de l'encre catalytique, une caractéristique qui n'est réalisable dans aucune autre technique de sondage en vrac.

Dans ce travail, CV-SANS sera utilisé pour étudier l'effet de la composition sur la structure de l'encre catalytique, en particulier en ce qui concerne la structure du composant ionomère. *Les variations de composition comprendront la modification du support de carbone et des types d'ionomères, la concentration d'alcool dans le solvant, le rapport ionomère/carbone (I/C), ainsi que la teneur en solides (concentration du composant). De plus, parallèlement aux encres conventionnelles contenant le complexe Pt/C, les mêmes variations seront introduites dans les pseudo-encres contenant uniquement un support en carbone, permettant une étude approfondie de l'effet du Pt dans le système. En particulier, il est intéressant de déduire si l'ionomère interagit préférentiellement avec le composant carbone ou Pt, et de mieux comprendre le mécanisme de formation de la couche ionomère.*

En plus du CV-SANS, la calorimétrie de titration isotherme (ITC) sera utilisée pour obtenir des informations complémentaires sur la thermodynamique de l'adsorption d'ionomères sur différents supports de carbone et complexes Pt/C dans l'encre. De plus, la diffusion des rayons X aux ultra-petits angles (USAXS) sera utilisée pour sonder une échelle de taille > 100 nm, fournissant des informations sur l'altération de la structure des agrégats de carbone avec l'augmentation de la teneur en ionomères et en présence de Pt.

Comme une meilleure compréhension de la structure de l'encre n'est que la première étape dans le développement d'une approche d'optimisation des électrodes plus ciblée, l'effet d'une variable de composition sera étudié plus en détail – sur la structure finale de la couche de catalyseur à l'aide de SANS, ainsi que sur les performances électrochimiques finales de l'assemblage membrane-électrode (AME) résultant.

Dans une première étude à ce jour, une corrélation complète entre les structures et la couche catalytique finale, ainsi que les performances électrochimiques résultantes, seront réalisées.

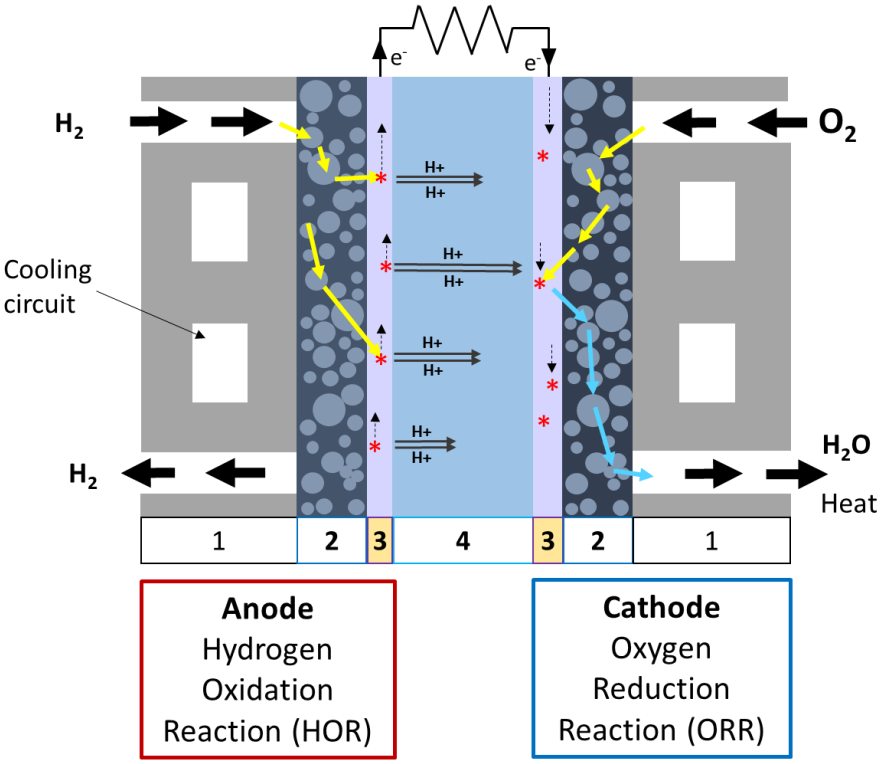
Le chapitre 1 présentera les principes de base qui permettront de mieux comprendre le sujet de ce projet de doctorat. Le mécanisme de fonctionnement ainsi que les composants présents à l'intérieur de la PEMFC dans son ensemble seront abordés. Ensuite, une introduction sur l'encre catalytique suivra, y compris le processus conventionnel utilisé pour fabriquer des couches catalytiques. Chaque composant de l'encre sera discuté en détail, puis une revue de la littérature sera entreprise, présentant l'état de l'art des recherches sur l'impact de la variation des composants sur les structures de l'encre catalytique et de la couche catalytique, avec une section spécifique dédiée à l'utilisation des techniques SANS et SAXS dans ce domaine.

De nombreuses sous-sections contiendront des résumés des résultats, écrits en gras. De plus, une section de conclusion plus générale sera présente à la fin de chaque chapitre, contenant les principaux résultats, ainsi qu'une discussion plus large et des perspectives d'avenir. Pour un aperçu général des principales conclusions, veuillez-vous référer à ces fragments de l'ouvrage.

1. Basic principles and state of the art

1.1 Proton exchange membrane fuel cell (PEMFC)

PEM fuel cells are devices used to convert hydrogen fuel into electrical energy.



1. Bipolar Plate
2. Gas Diffusion Layer (GDL)
3. **Catalyst Layer (CL)**
4. Proton permeable membrane

HOR: $2H_2 \rightarrow 4H^+ + 4e^-$

ORR: $4H^+ + O_2 + 4e^- \rightarrow 2H_2O + heat$

Overall: $\mathbf{2H_2 + O_2 \rightarrow 2H_2O + heat}$

Figure 1. *Schematic of PEMFC operation*

Humidified hydrogen gas is introduced to the anode through the bipolar flow field plate, and diffuses through the gas diffusion layer (GDL), consisting of carbon with gradient porosity, towards the catalyst layer (CL). The Pt catalyst in the CL aids with the hydrogen oxidation reaction (HOR), resulting in protons which cross through the ionomer membrane towards the cathode, and electrons which travel through an external circuit. Oxygen gas diffuses towards the cathode through the opposite flow field plate and GDL, to the catalyst layer where Pt facilitates the oxygen reduction reaction (ORR) with the above-mentioned protons and electrons to yield water and heat by-products. Such cells can be joined together through connection in an electrical series via the bipolar plates, to form a PEMFC stack, where the voltage and power generated are proportional to the number of cells in the stack. A stack may contain hundreds of individual cells.[6]

1.1.1 Gas flow plates

In PEMFCs bipolar plates are used, which manage the gas migration through both the anode and cathode, heat removal from active areas, as well as current flow of adjoining cells in the stack.[7] Moreover, the use of bipolar plates allows for facile electrical connectivity in series from one cell to the other, amplifying the voltage and power output of the overall stack. The bipolar plate consists of conductive and fluid channels etched or stamped into its inner and outer layers.[8]

Figure 2 presents a schematic of a bipolar plate with some common channel geometries.

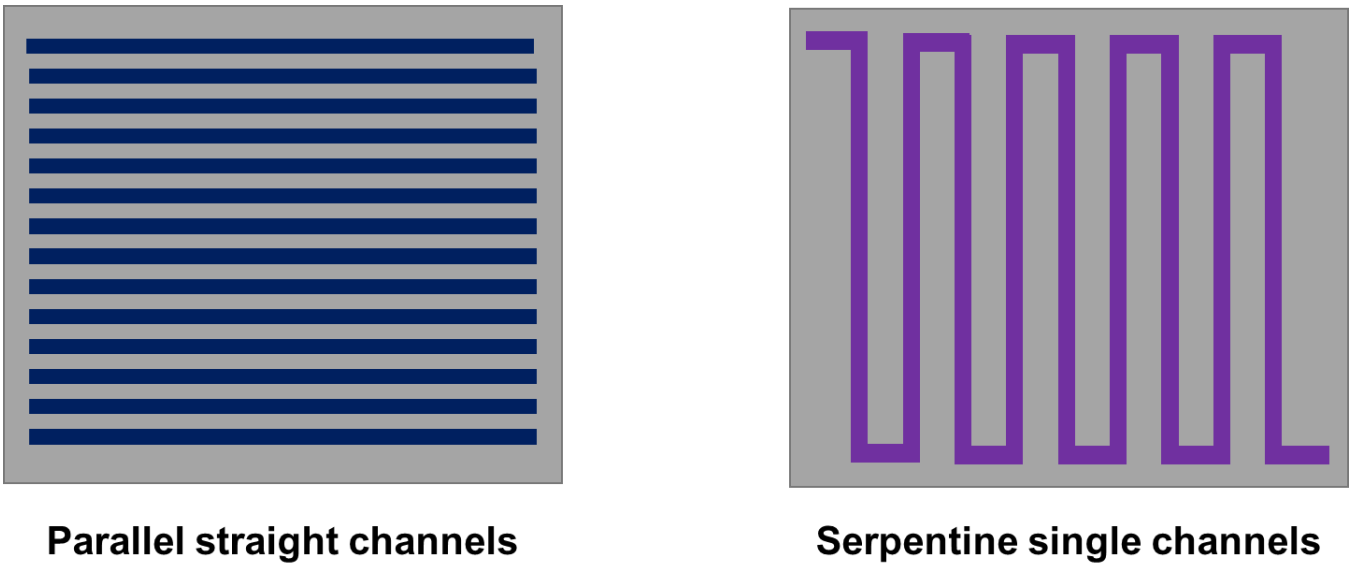


Figure 2. *Common geometries utilized in bipolar plates.*

The bipolar plates are the main mechanical support for MEAs, but also have a major influence on the performance of the fuel cell through managing both reactant and product migration through the catalyst layer, which is achieved through the design of the geometrical flow channels. As additionally they are responsible for electronic conductivity between cells, the bipolar plate material must display high thermal and electrical conductivity, be chemically stable, have low gas permeability and good mechanical strength. Furthermore, for electrical vehicle applications low mass and volume plates are desired.[7] The most common materials used in bipolar plate manufacture are graphitic-based, consisting of approximately 70% of graphite and a polymeric binder, or metallic, most commonly stainless steel or titanium alloys. Graphitic bipolar plates allow for a much more complex design of flow channels, resulting in optimized gas flows, and are superior in terms of chemical stability. However, the moulding process commonly used for their manufacture results in a formation of a layer with significantly reduced graphite content on the surface which hinders electrical contact between the cells in the stack. On the other hand, metallic bipolar plates are able to operate at much higher power densities, yielding improved performance, yet corrosion is a major issue throughout the stack operation. The latter can be somewhat mitigated by the use of corrosion resistant coatings.[9]

Overall, the choice of channel geometry and material of the bipolar plate will relate to the specific application of the fuel cell. The second-generation Toyota Mirai, a commercially available FCEV, utilizes titanium bipolar plates with wavy flow fields on the anode side and partially narrow straight flow fields on the cathode side.[10]

1.1.2 Gas diffusion layer (GDL)

The GDL is responsible for homogenous reactant/product transport between the catalyst layer and the bipolar plate, as well as electron and heat conductivity between the components. Additionally, the GDL provides physical support to the catalyst layer. It generally consists of two layers – a macroporous carbon substrate facing towards the bipolar plate and a thin microporous carbon layer (MPL) facing towards the catalyst layer. Most commonly the GDL is wet-proofed through addition of a hydrophobic agent, for example PTFE, to facilitate liquid water removal from the cell, averting water clogging.[11] Carbon cloth or non-woven carbon materials are most commonly employed as the macroporous layer, providing good mechanical

support.[12] The large pores allow for efficient water evacuation from the cell. The MPL commonly consists of fine carbon powders[11] and provides an intermediary layer between the macroporous GDL component and the catalyst layer, minimizing contact resistance and loss of catalyst to the macroporous carbon layer.[13] The porosity of the MPL is lower in comparison to the macroporous GDL (approximately 35-50% and 75% respectively), and contains finer pores, which are comparable in size to those of the catalyst layer, improve the distribution of reactive gases throughout the catalyst layer.[14] Moreover, the nature of the pores allows for an improved water management throughout the catalyst layer, aiding in the migration of water vapour towards the membrane, improving its hydration (which results in improved proton transport).[11] However, note the net water flow in the cell can be either from the anode to cathode side, or vice-versa, depending on the operating conditions and position on the surface of the active area, corresponding to the gas inlet/outlet.

Figure 3 presents a schematic of the GDL[11]:

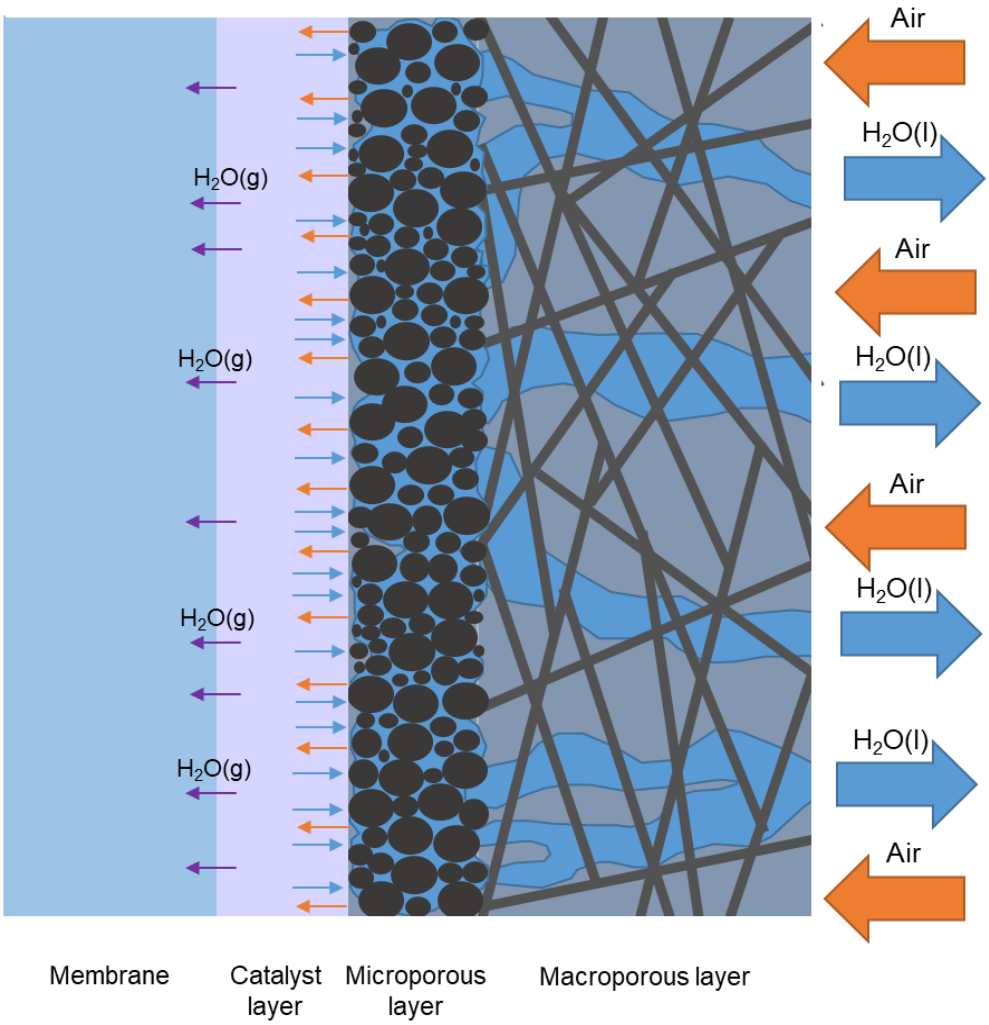


Figure 3. *Schematic of the gas diffusion layer and reactant/product migration. Air enters from the macroporous layer, through the microporous layer, and diffuses towards the catalyst layer (orange arrows). Conversely, liquid water is transferred from the catalyst layer, through the GDL, towards the bipolar plate (blue arrows). Water vapour moves from the catalyst layer towards the membrane, aiding in its hydration (purple arrows). Note some migration of water vapour also occurs through the GDL towards the bipolar plate and gas outlet. The presence of a microporous layer allows for a finer reactant gas distribution in the catalyst layer.*

1.1.3 Proton exchange membrane (PEM)

The proton exchange membrane, which this fuel cell type is named after, is an important component separating the anode and cathode. The membrane acts as a barrier between the two electrodes, preventing flow of electrons directly through the cell as well as by limiting diffusion of reactive gases towards the electrodes, which would result in a direct combustion reaction and a decrease of the fuel cell performance.[14] Instead, as the name suggests, the membrane allows for proton migration from the anode to the cathode, where the ORR occurs. Nafion, a perfluorinated co-polymer first manufactured by DuPont in the 1960s, remains a popular material choice for the PEM due to its high proton conductivity as well as superior chemical and mechanical properties.[15]

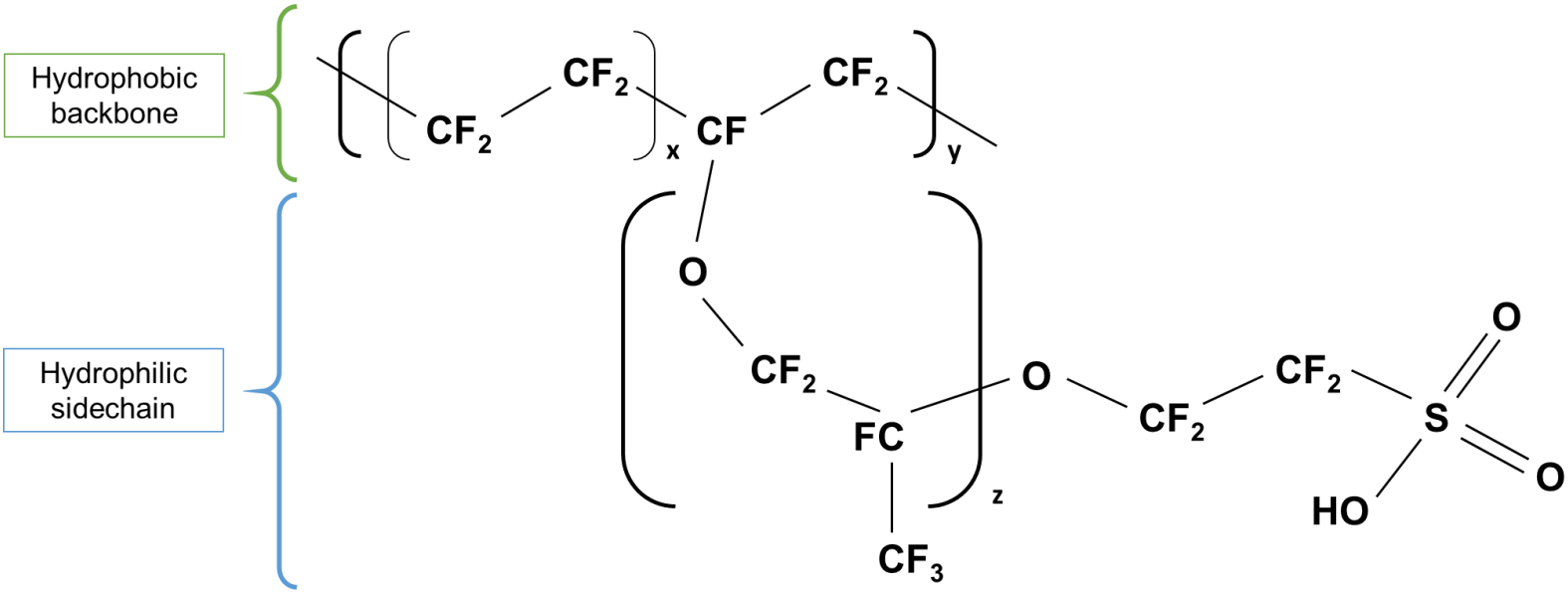


Figure 4. *Schematic showing the chemical formula of Nafion.*

Nafion is a perfluorosulfonic acid, containing a hydrophobic polytetrafluoroethylene (PTFE) backbone and a hydrophilic sidechain, terminated by a sulfonate group. The length of the hydrophobic backbone may differ based on the effective weight (EW) of the polymer (altered by the length of the backbone, **x**), which describes its weight per mole of SO_3^- groups. For an efficient proton conduction, the PEM membrane needs to be hydrated, with water molecules found in the vicinity of the hydrophilic SO_3^- groups in the sidechain increasing proton conductivity of the membrane. For the PEMFC, which operates at low temperatures of 80^{o}C, relative humidity (RH) in the cell is high, and this condition is satisfied. Note an ionic conducting polymer, such as Nafion, is often referred to as an ionomer, which will also be the case throughout this work.

1.1.4 Catalyst layer (CL)

Figure 5 presents a generalized schematic of the catalyst layer structure.

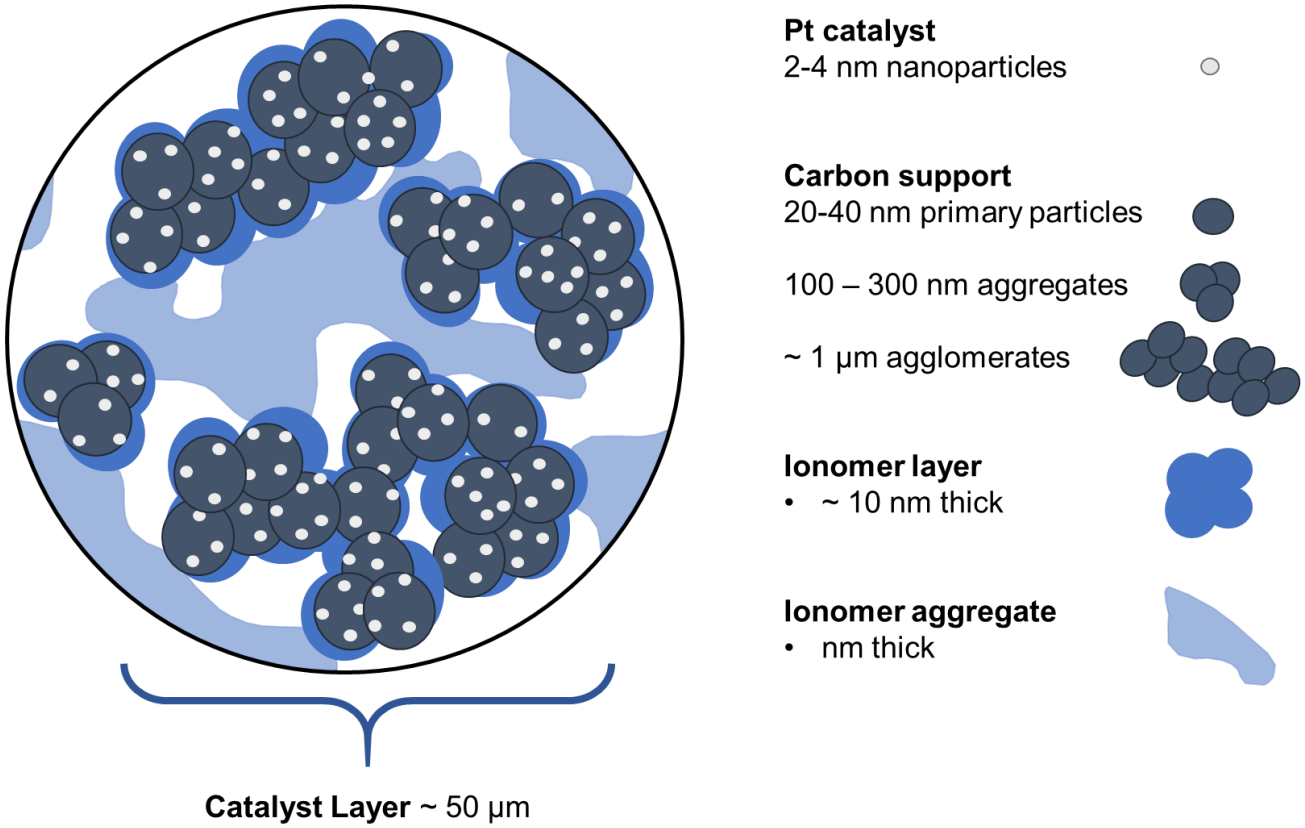


Figure 5. *Generalized schematic of the catalyst layer structure.*

2-4 nm Pt nanoparticles act as the catalyst for both the HOR and ORR. These are deposited on carbon nanospheres, which act both as the catalyst support and electron conductor. The deposition is achieved chemically, most commonly utilizing a Pt inorganic complex, through methods such as wet impregnation, microwave irradiation, the polyol process, or electrodeposition, yielding the Pt/carbon (Pt/C) complex. The carbon primary particle size is in the tens of nanometres,[16] which then form aggregates of hundreds of nm in size and further agglomerates which are on the µm scale. A thin film of ionomer is adsorbed to the carbon, creating a proton conducting shell. In addition, separation of the carbon particles occurs due to the presence of ionomer aggregates in between them.

The cathode and anode both consist of the same materials but have different Pt loadings. Most commonly this is correlated with varying catalyst layer thickness in order to achieve a different mass of Pt per surface area, however the Pt loading can also be varied on the carbon support itself through adjusting the Pt-to-carbon (Pt/C) ratio. In the anode, where the HOR occurs rather dynamically, a Pt loading of 0.1 mg/cm^2 is sufficient. On the other hand, the sluggish kinetics of the ORR which make cathode the limiting electrode require higher Pt loadings between 0.2 and 0.3 mg/cm^2.

For a successful reaction in the PEMFC electrode, a two-way boundary between the catalyst and ion conducting electrolyte (ionomer or water) is required, where the reactant gases, protons and electrons are all able to meet at the catalyst active site.

In the ideal case, a thin layer of the ionomer is homogenously adsorbed onto the Pt/C complex, which can conduct protons and allow reactant gases to easily pass. However, if the ionomer layer is too thick or dense the reactant gases will pass through to the reaction site too slowly, impeding reaction rates and also potentially leading to flooding of the catalyst layer, where the water by-product is unable to diffuse out efficiently. Additionally, too much ionomer may lead to disconnection of carbon aggregates and reduced electron transport. In the case where the ionomer layer is not homogenously distributed, regions where no ionomer coverage is present may occur. Consequently, protons are not able to reach the Pt active site (particularly in low RH conditions). In order to optimize performance, and potentially to reduce costs (by reducing the Pt loading), the number of usable active sites has to be maximized through ensuring the ideal two-way boundary case.

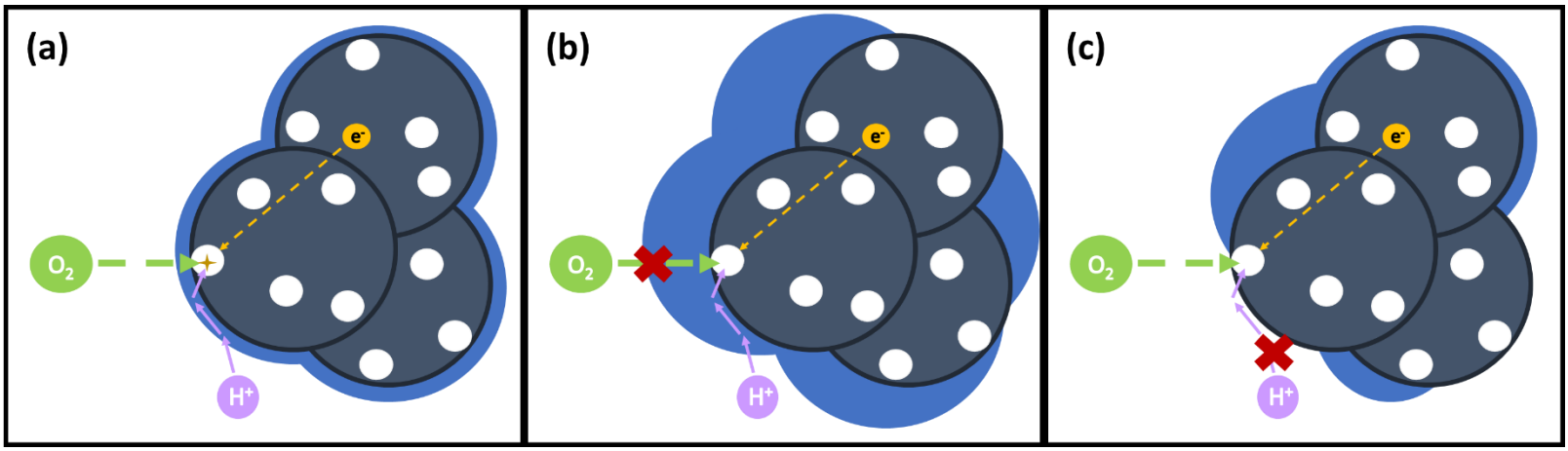


Figure 6. *Schematic of two-way boundaries:* ***(a)*** *ideal case - thin homogenous ionomer layer permeable to gases,* ***(b)*** *thick ionomer layer - reactant gases are unable to reach the active site efficiently,* ***(c)*** *non-homogenous ionomer distribution, protons are unable to reach certain active sites due to lack of coverage.*

1.2 Catalyst ink and preparation of the catalyst layer

The final structure of the catalyst layer is directly linked to its manufacture– the components chosen and dispersion method of the catalyst ink, followed by coating of the ink onto a substrate, drying, and finally transferring the finished CL onto the PEM.

The catalyst ink is a dispersion of the electrode components in an alcohol/water mixture solvent. The ink is deposited onto a substrate, such as PTFE, or the PEM directly, and dried at temperatures of approximately 80°C to yield the catalyst layer. Deposition techniques can include coating, jet ink spray, laser deposition and more. In the instance when the ink is coated onto a substrate, the resulting catalyst layer must be later transferred to the membrane through processes such as hot pressing or decal transfer. The anode-membrane-cathode complex is known as the catalyst coated membrane (CCM).

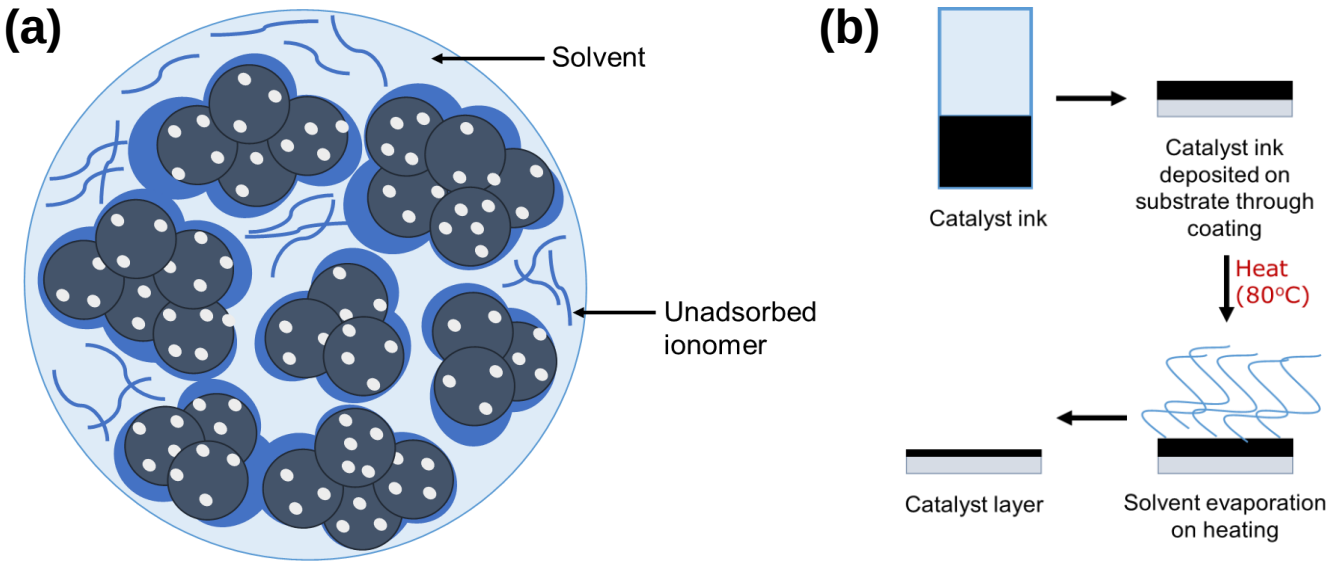


Figure 7. (a) *Generalized catalyst ink schematic,* ***(b)*** *example of processing of the catalyst ink into a catalyst layer*

It is known the ionomer structure has a big impact on electrode performance, however, it is yet unclear to what extent the ionomer interacts with the Pt/C complex in the ink already. Where in the catalyst layer large ionomer aggregates can be observed separating the carbon particles, in the catalyst ink ionomer may exist in the adsorbed form, on the Pt/C complex, or as unadsorbed ionomer, which forms long, rod-like aggregates when dispersed in solvent.[17] Compositional variations can be introduced to the ink with regards to each component, altering the dispersion structure.

1.2.1 Carbon support

Carbon black nanospheres commonly act as a support to the Pt catalyst, offering good electronic conductivity, high surface areas, high stability and low material cost.[18] Many variations of carbon black can be employed, including materials which are porous or non-porous, graphitized or amorphous, functionalized, and more. The most industrially relevant carbon supports are high surface area carbon (HSAC), Vulcan, and graphitized carbon (GC).

HSAC is a highly porous carbon, consisting of a graphitized exterior and a large proportion of amorphous carbon forming a porous network inside the particle. Approximately 70% of Pt particles are located in the interior of the pores.[18] Due to this unique distribution, Pt particle coalescence is highly reduced, increasing the active surface area, leading to superior ORR rates.[16] Moreover, a proportion of the pores is only accessible via bottleneck channels, a few nm in diameter, too small for ionomer penetration, which reduces

Pt poisoning by SO_3^- groups of the ionomer sidechains. Nevertheless, despite the reduced Pt contact with the ionomer, water can additionally act as an electrolyte, conducting protons to the active site. On the other hand, the high surface area of such porous carbons results in faster mass loss occurring due to carbon corrosion, which may result in encapsulation of Pt particles.[18] Moreover, performance significantly drops in low RH conditions, due to a reduced presence of water electrolyte in the carbon pores.

Vulcan is the research standard of carbon supports. Contrary to HSAC, Vulcan contains a low degree of porosity, however, it still displays high surface areas, as well as high conductivity due to its turbostratic structure, where graphitic layers are arranged in a 'haphazardly folded or crumbled manner'[19,20] The majority of Pt is distributed on the Vulcan surface. This carbon black can be considered a compromise between the high surface area necessary for the ORR, as well as improved material conductivity.[21]

Graphitized carbon, also known as low surface area carbon (LSAC), as the name suggests exhibits comparably the lowest carbon surface areas. The particles consist of a graphitic shell which fully encapsulates a hollow space inside, which is inaccessible to Pt or any other molecules. For this reason, all of Pt is distributed on the carbon particle surface. Moreover, the high hydrophobicity of the graphitized carbon surfaces means Pt preferentially packs into crevices in between carbon particles as well as defect rich graphitic edge sites, which promotes Pt nucleation.[18] Nevertheless, graphitized carbon shows a remarkable tolerance to oxidation, which improves the materials resistance to corrosion and the overall durability of the catalyst layer. [22-24]

The choice of carbon support has a great impact on both the durability and performance of the electrode. With regards to structural considerations, the Pt nanoparticle distribution on the support is key, altering the availability of active sites towards the ORR. However, different hydrophobicity of the carbon support surface may also impact the quality of dispersion of the Pt/C in the ink, as well as alter interactions between the ionomer and the Pt/C itself. This may not only have a significant impact on the nature of the catalyst-ionomer interface obtained in resulting catalyst layers, but also on the degree of Pt/C aggregation observed, as the ionomer aids in stabilization of Pt/C particles through mechanical and electronic repulsions.[25]

In order to deconvoluted the nature of ionomer interaction with both the carbon and Pt components, it is of interest to investigate the ionomer adsorption to carbon black surfaces only in inks – whether the different

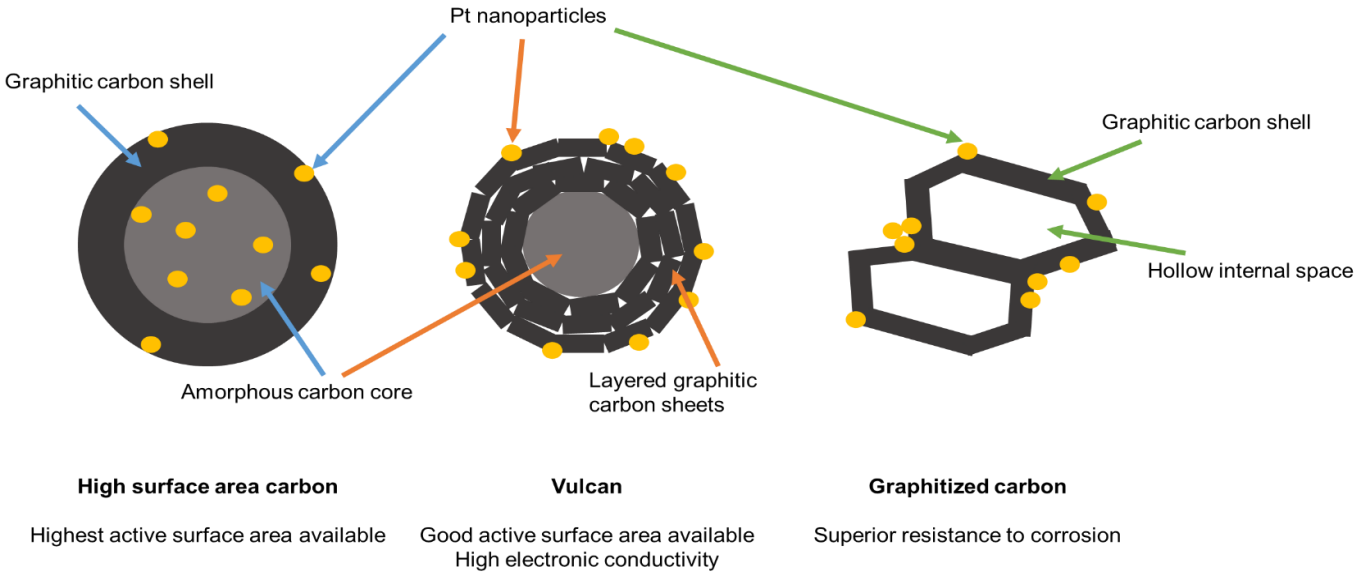


Figure 8. *General schematic of the structure of the three industrially relevant carbon supports – HSAC, Vulcan, and graphitized carbon.[18]*

support morphologies impact the adsorption behaviour and if differences in the carbon dispersion quality can be observed.

1.2.2 Ionomer

In the catalyst layer the ionomer acts as a proton conductor towards the reaction active site. In an ideal scenario a thin, uniform layer would be present on top of the Pt/C complex, allowing from proton transport to all active sites and in tandem a good gas permeation. In reality, a fine balance must be achieved between attaining sufficient coverage on the Pt/C surface and creating layers which are not too thick, poisoning the catalyst and impeding gas transport towards the active site. Another important role of the ionomer in the ink is the stabilization of the Pt/C dispersion by providing additional repulsive forces, resulting in improved surface areas in the final catalyst layer.

The most common example of the ionomer component is the same material as used in the PEM, Nafion (figure 4), a long side chain (LSC) perfluorosulfonic acid (PFSA) polymer. In addition, Aquivion, a short side chain (SSC) PFSA polymer first synthesized by DOW, has garnered significant attention for PEMFC applications due to its improved stability in extreme conditions such as low RH and increased temperatures that may be present throughout PEMFC operation in transport applications.[26]

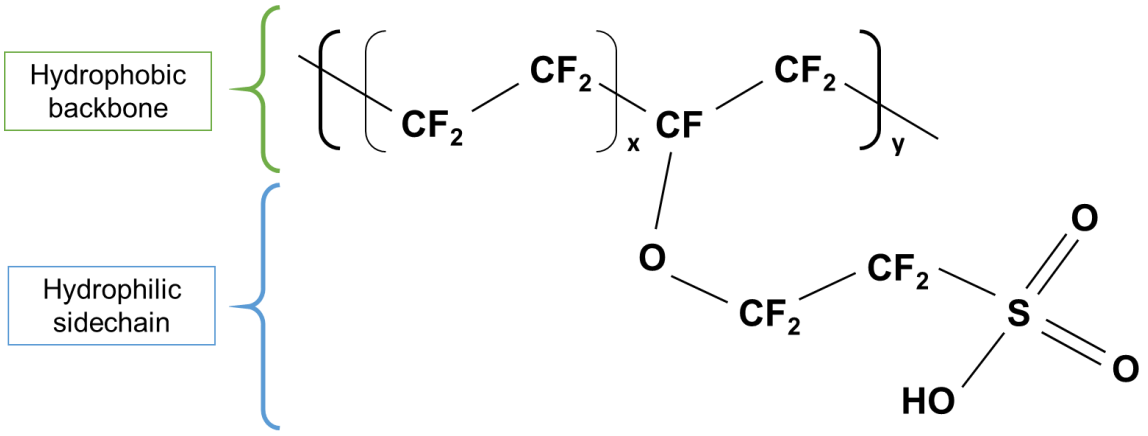


Figure 9. *Schematic showing the chemical formula of Nafion*

Considering the structure of Nafion presented in figure 4, which contains additional atoms in the side chain, labelled with a **z** subscript, the difference in Aquivion is that **z** = 0.

In addition to the length of the side chain, both LSC and SSC ionomers may contain different distance between the sidechain, characterized by the effective weight (EW) per mole of the SO^{3-} group found in the sidechain. Therefore, with increasing EW the distance between the sidechain groups will increase, and concurrently their density in the ionomer molecule will decrease. Generally, low EW ionomers are found to perform better in low RH conditions, with more SO_3^- groups present for proton transfer. However, as low EW ionomers show higher volumetric swelling in the presence of water, their performance is generally worse than for high EW ionomers in high RH conditions.[27] Moreover, adsorption of SO^{3-} groups to Pt is known to poison its catalytic performance, and this effect becomes more pronounced in low EW ionomers.[28, 29] With regards to the effect of EW on the ionomer adsorption behaviour to Pt/C, it seems to be heavily correlated with the dispersing medium of choice. Molecular dynamics simulations performed by Mashio et al.[30] suggest low EW ionomers, with an increased number of hydrophilic domains, show preferential adsorption in water-rich solvents, while high EW ionomer, where the distance between sidechain groups in the ionomer molecule is longer, show increased adsorption in alcohol-rich solvents.

Aside from the nature of the ionomer used, the ionomer-to-carbon (I/C) ratio is an important parameter to control, allowing for sufficient ionomer concentration to achieve a good coverage on the Pt/C surface as well as good component dispersion, however, preventing suffocation of the Pt by ionomer. With regards to the Pt/C dispersion quality, it has been found maximum stabilization is already achieved with Nafion present at lower I/C ratios of 0.25 or 0.5 [25,31] (the variation highlighting the differences in the ink nature as composition is altered). However, optimum electrode performance has been found for Nafion at higher concentrations, generally with I/C ratio between 0.7 and 1.1.[32-35]

Although it has been shown the ionomer is an important parameter that introduces a lot of variables into the catalyst layer system, its effects prove difficult to investigate. Experimentally, characterization of the effect of I/C, ionomer EW and type occurs with regards to the Pt/C structure and overall performance, quantifying the active surface area available as well as potential obtained from the catalyst layer when variation to the ionomer component is introduced.[27] However, the actual structure of the ionomer in the catalyst layer remains a challenge to investigate experimentally, with theoretical modelling studies proving more prominent.[28,30,35] Indeed, developing the ability to characterize the structure of the ionomer in experimental conditions would also increase the understanding of the mechanism of ionomer interaction with the Pt/C surface.

1.2.3 Platinum

Pt nanoparticles are likely the most important component in the PEMFC electrodes, responsible for both the anodic and cathodic reactions taking place. Concurrently, Pt is also one of the costliest components in the PEMFC, and large efforts are taking place in order to reduce the Pt loading in catalyst layers.

Although on the laboratory scale alloys of Pt and other metals, such as Pt/Co, Pt/Ru or Pt/Ni, along with noble metal-free catalysts are being developed, industrially optimizing the utilization of the Pt is a more prominent approach. This is particularly considered with regards to reducing mass transport limitations, arising from the nature of the ionomer layer, which become more prominent at lower Pt loadings.[36]

Nevertheless, as highlighted in the section above, the mechanism of ionomer layer formation is not understood, and optimization is mainly undertaken by comparison of the overall performance of varying catalyst layers in different conditions. To what extent the ionomer interacts with the carbon support (where variation may be introduced by the surface porosity and functionalization), and with the Pt is a point of discussion.[25,37-39] It has been also suggested by Guo et al.[40] through the use of molecular dynamics simulations that the nature of the ionomer adsorption mechanism varies with the Pt loading itself. Initially Ionomer-Pt interactions dominate, however a preferential shift to carbon-ionomer interactions is present if enough carbon surface is available between Pt particles when the Pt loading is reduced.

Although this is not an easy parameter to investigate, in particular since introduction of Pt may introduce some variation to the carbon surface itself, understanding the effect of Pt on formation of the ionomer layer is an important question to tackle.

1.2.4 Solvent

Despite the fact the solvent component evaporates during catalyst layer manufacturing, it remains one of the most significant factors in the catalyst ink composition. This is because the nature of the solvent, characterized by its dielectric constant, boiling point, viscosity, and more,[41] directly impacts the dispersion of the other components in the ink, and therefore their interactions.

Most notably, the ionomer, which contains both hydrophobic and hydrophilic domains, will rearrange to different conformations depending on the solvent's solubility parameters, a numerical value used to understand ionomer behaviour in a particular solvent. A higher solubility parameter for the ionomer side chains indicates it is the hydrophilic domain that preferentially interacts with the solvent, and therefore the

ionomer aggregate can be expected to conform in such a manner so that the sidechains are pointing towards the solvent. Conversely, if the solubility parameter is higher for the hydrophobic backbone, the ionomer may for coil-like aggregates, with the hydrophobic backbone arranged towards the solvent interface.[41] Such conformational changes could have a direct impact on the adsorption of the ionomer to the Pt/C complex, where the SO_3^- groups bind to Pt, while the hydrophobic backbone preferentially interacts with the carbon particles.

Additionally, the dielectric constant of the solvent will impact the aggregation of the Pt/C complex, with solvents of lower dielectric constant resulting in improved component dispersion.[41] However, note the ionomer is an important component in improving Pt/C dispersion also, therefore, the dispersion quality may be a convoluted effect between the inherent stability of the Pt/C in the solvent as well as the ionomer conformation.

In addition to the major structural effect on the catalyst ink, the solvent choice also affects the manufacturing process of catalyst layers, and therefore their final structure. The viscosity of the ink is a significant parameter towards the coating process, which dictates the homogeneity of the catalyst layer. In blade coating, the industrial standard, high viscosity inks are desired, however, methods such as inkjet printing deposition, where the ink can be directly applied to the PEM, are compatible with lower viscosity inks.[42,43] Therefore, for different deposition processes, different solvent compositions in the ink may be suitable, and a balance between the effect of solvent on the ink dispersion structure and the deposition method of choice may be required.

Moreover, the drying procedure is affected by the boiling points of the individual solvents in the mixture, as well as the proportion of alcohol and water. Since the dispersion medium is a mixture of different solvents, their individual boiling points, as well as the difference between them will dictate which evaporates first and how rapidly. Usually this is the alcohol component, which means a water-rich phase remains during the drying process. If the proportion of water in the solvent is high, the formation of such a phase may alter the conformation of components in the drying ink dramatically. On the other hand, it is known that aspects such as aggregation of Pt/C terminate fairly quickly into the drying processes,[44] therefore utilization of high alcohol proportions may mitigate the structural rearrangement associated with the formation of water rich phases on alcohol evaporation. Nevertheless, in such cases correct drying temperatures must be chosen, ensuring the majority of the solvent does not evaporate too suddenly, which would result in the formation of cracks, detrimental to the performance of the catalyst layer.[41]

The solvent is most commonly a mixture of alcohol and water, however the choice of alcohol type and concentration can lead to broad variations. Propanol (PrOH) and ethanol (EtOH) remain the most common choices for the alcohol component of the solvent, however, high boiling point organic solvents have also been garnering research attention due to the resulting improved ink coating as well as lower crack formation throughout the ink drying process.[44-46] However, where low boiling point solvents can directly evaporate upon drying, removing high boiling point solvents proves more challenging.

In industrial applications, as well as many research studies, high alcohol content inks remain the standard in compositions, however, use of water-rich solvents has been investigated for several years due to their improved environment friendliness.[47] Nevertheless, challenges associated with increased carbon agglomeration as well as thicker ionomer layers post drying remain.[48]

The choice of solvent is crucial towards optimizing the structure of the catalyst layer, arising both from the initial component conformations and interactions in the catalyst ink, as well as from the structural alterations throughout the drying process. In the case of the former, the discussion suggests the choice of solvent is heavily convoluted with other parameters such as the carbon support utilized, Pt loading or the nature of the ionomer. For example, different carbon supports, where the hydrophobicity of the surface is known to

vary, may be more or less sensitive to aggregation based on the dielectric constant of the solvent. Moreover, the ionomer type used, LSC or SSC, or the EW chosen, will most likely show different conformation behaviours depending on the alcohol solubility parameters.

The enormous number of variations induced by solvent composition alteration require a development in fundamental understanding of the solvent effect on each component, as well as the system overall, along with cross-correlation to the impact on the final catalyst layer during the manufacturing process, making it a big area of study.

1.3 State of the art

Section 1.2 presented catalyst inks as well as the manufacturing process for catalyst layer formation, and focused on a general overview of how the variation of each component may affect the ink and resulting catalyst layer structures. In the case of each component it was shown small changes, with regards to the alcohol type or concentration chosen, ionomer type and EW, carbon support, Pt loading, and more, can have a severe impact on the overall structure, and many of these parameters are cross-correlated between each other. Indeed, with the complexity surrounding the generation of the catalyst layer structure, a lot of research must be undertaken on a system that is by its multi-component, heterogeneous nature not easy to study. Where section 1.2 focused on generalized effects of component variation, figure 1.3 will delve into the state of the art research undertaken with regards to each component. Following, as the method of choice in this work is small-angle scattering (SAS), a discussion focusing on studies using such techniques will follow.

1.3.1 Carbon support

In section 1.2.1.1 three industrially relevant carbon supports have been discussed – HSAC, Vulcan and graphitized carbon (GC), along with their general advantages and drawbacks.

With the carbon support playing a big role in the active Pt surface area available, the Pt/C nanostructure in general is of interest. This includes the initial effect of the carbon support and Pt distribution on mass transport losses at the Pt/C surface, as well as its structural evolution, and inevitable degradation throughout PEMFC operation.

Padgett et al.[16] utilized high resolution TEM (HRTEM) as well as cryo-STEM tomography to obtain a detailed 3D characterization of the carbon support surface of HSAC and Vulcan, along with their respective Pt distribution as a function of increasing Pt loading. HRTEM images show that for both carbon supports the primary particles can be separated into two distinct atomic structures based on the particle size. In the case of Vulcan, a clear size segregation could be observed, with the smaller primary particles (10-20 nm in diameter) consisting of thinner graphitic shells with bigger proportions of the amorphous carbon core, while bigger particles (25-40 nm in diameter) displayed denser graphitic shells and smaller amorphous cores. HSAC primary particles also showed structural differences related to particle size, although the size distribution was not as drastic. Smaller particles (15-35 nm) consisted of a graphitic shell and a ‘hollow’ core of relatively lower density. Bigger particles (20 – 40 nm diameter) proved to be denser, with a significantly lower degree of porosity. Additionally, STEM tomography of HSAC revealed that for both primary particle types the porous interior is accessible. In the case of the ‘hollow’, smaller primary particles, the small opening (2-5 nm) are present in the graphitic shell itself, while in the denser, bigger particles, 2-8 nm wide channels allow access to the porous surface.

With regards to the Pt distribution, as expected, cryo-STEM tomography revealed on the Vulcan support the majority of Pt is found on the surface of the support (although some Pt is also present in the support interior), while approximately 60-70% of Pt supported on HSAC is found within the porous interior of primary particles. Note increasing Pt loading on the carbon (Pt/C ratio) resulted in increased volume fraction of Pt on the support surface (although this effect was less pronounced in the case of HSAC). Correlation to the

electrochemical surface area (ECSA) revealed that all of the Pt surface area is available to protons in liquid. However, HSAC in low RH conditions displayed lower Pt utilization, suggesting the ionomer cannot penetrate the HSAC surface, and the proton transport mechanism may be different towards the Pt found in interior pores, utilizing water as the proton conducting electrolyte.[16]

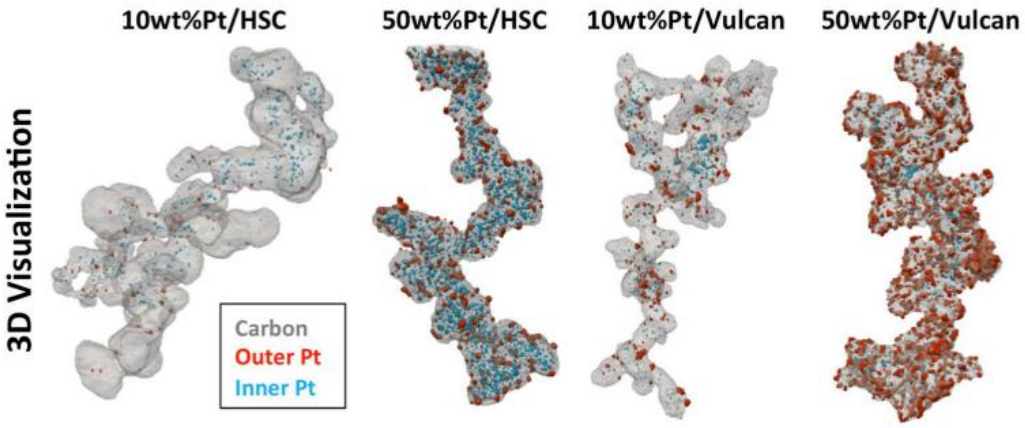


Figure 10. *3D visualizations of segmented tomograms of high surface area carbon (HSC) and Vulcan based Pt/C complexes. Pt particles on the carbon support surface are shown in red, while Pt particles inside the carbon support pores are shown in blue. All content of the figure falls under the copyright of the authors, as part of the work published by Padgett et al.[16]*

This work very clearly shows the significant variation in between the carbon support structure itself, as well as the effect on Pt distribution. Sneed et al.[18] also utilized 3D electron tomography, however focusing on the change in Pt structure on different carbon supports before and after operation – namely the degradation of the Pt/C structure.

Firstly, Pt/C complexes based on HSAC, Vulcan and GC with different Pt loading were characterized using electron tomography. For each carbon support it was observed Pt aggregation was reduced with low Pt loadings of 5 wt%, however it was noted such low concentrations are not suitable for the use in commercial PEMFC at this stage. In the case of HSAC, increasing Pt loading resulted in higher proportions of Pt present on the surface, concurrent with the observations made by Padgett et al.[16] For both Vulcan and GC, increasing Pt loading revealed preferential nucleation of Pt particles on the external surface defects (domain boundaries) of the former and particle intersections/corners of the latter. For Pt/C complexes with 40 wt% Pt loading, accelerated stress-tests (ASTs) were performed over 30 000 cycles between 0.6 and 1.0 V, after which the Pt/C was again characterized by 3D electron tomography. Note the AST protocol focused on triggering changes in the Pt size distribution, rather than the carbon corrosion related degradation. In all instances after ASTs, increases in Pt nanoparticle size and inter-particle distances were observed, coherent with Pt particle coarsening through the coalescence and dissolution/redeposition mechanisms. However, it was noted both of these effects were more pronounced in the case of Vulcan and GC, which was attributed to the initially increased Pt aggregation observed, facilitating further nucleation during operation. Indeed, for the HSAC support, the Pt inter-particle distance was only found to increase slightly, suggesting the internal pores act as a barrier against increased particle nucleation. Nevertheless, although the least pronounced, Pt/HSAC still showed an electrochemical surface area (ECSA) loss of 34%. Interestingly, a similar loss was observed in the case of GC (34%), although the ECSA initially available was significantly lower. The highest loss was observed in the case of Vulcan, of 55%. This trend was explained by the different degradation mechanism occurring in the case of each support. Pt dissolution is more pronounced in the presence of smaller particles (roughly 2 nm), and may explain the losses observed in the case of the HSAC support, where aggregation is suppressed by the physical presence of the pores. The reverse is true in the case of GC, where larger particles are initially observed, and therefore the aggregation mechanism

is dominant over the dissolution scenario. In the case of Vulcan, the intermediate case, both the aggregation and dissolution mechanisms seem to have a significant effect, resulting in the highest ECSA loss. These trends are very insightful into the Pt degradation behaviour on different carbon supports, however, it is worth noting that although HSAC and GC showed similar ECSA loss, the final ECSA of HSAC (45.8 m^2/g) was very similar to the initial ECSA of GC (46.9 m^2/g), presenting the reason why porous supports are garnering such research interest.

Carbon corrosion occurs during the start-up and shutdown of fuel cell operation due to high potentials present at the cathode generated as a result of a hydrogen/air interface at the anode.[24,49,50] It is a detrimental process to the catalyst layer durability, occurring through oxidation of carbon to CO_2 in the presence of water, directly due to the high potentials, or with the aid of the Pt catalyst. Qi et al.[50] compared the effect of carbon corrosion in catalyst layers containing Pt/C complexes based on HSAC and GC using accelerated stress tests (ASTs) as well as electrochemical characterization methods such as measurements of the ECSA. To commence, 1000 and 10000 AST cycles were opted for in the case of Pt/HSAC and Pt/GC based catalyst layers respectively, due to the different carbon corrosion rates. This already shows how significant the difference in durability of the two supports is. After 1000 AST cycles both catalyst layers showed more disordered carbon contacts, however, the Pt/GC based catalyst layer showed 2 times less ECSA reduction and 2.5 times less reduction in ionic conductivity in comparison to the Pt/HSAC based composition. The great reduction of ECSA in Pt/HSAC can be associated with the collapse of the pore network, encapsulating Pt particles and also breaking the physical barrier that was previously hindering Pt aggregation, an effect that was not considered by the ASTs performed by Sneed et al.[18]

In light of these findings the benefits and downfalls of both the HSAC and GC supports are clear. With regards to the effect of the carbon support choice on performance and durability, a solution which would satisfy both the requirements remains to be found.

With respect to the carbon corrosion, certain operation protocols have been proposed in order to mitigate this effect present at the beginning and end of PEMFC operation. Gas purges, involving flushing either the anode or cathode with N_2, air, or H_2 aim at reducing the duration of the hydrogen/air interface and therefore the high potentials at the cathode. Moreover, use of auxiliary loads, which consume the residual reactant gases from corresponding electrodes were reported to mitigate their effect in the GDL or catalyst layers that contribute to the interface generation.[49] Oyarce et al.[51] compared several shut-down strategies and suggested an H_2 purge or an O_2 auxiliary load at the cathode proved the most promising.

With regards to the catalyst ink, choice of carbon support may affect the Pt/C aggregation behaviour as well as the adsorption of the ionomer to the complex, altering the ink dispersion quality and physical properties. Khandavalli et al.[25] used rheology to systematically build a picture of the effect of increasing ionomer content and Pt presence on the carbon aggregation structure of HSAC and Vulcan supports. Firstly, carbon support dispersions of varying concentrations were investigated using steady-shear rheology measurement, showing HSAC-only dispersions inherently displayed higher viscosities due to the porous structure of the support, resulting in higher effective volume fractions for the same mass concentration of carbon. Introducing progressively larger concentrations of ionomer into the system showed gradually decreasing viscosities of both the systems based on HSAC and Vulcan, suggesting in both instances the ionomer aids with the stabilization of the carbon dispersion. For the Vulcan based dispersion, a critical ionomer concentration was found when I/C = 0.5, where maximum stabilization of the carbon aggregates by ionomer was achieved, after which no significant alteration in the low shear rate viscosity of the measured dispersion was observed. On the other hand, the low shear rate viscosity of HSAC based dispersion continually decreased with the addition of ionomer up until I/C = 1.4, the maximum concentration used in this study. A potential explanation was offered that HSAC forms a larger degree of agglomerates which require more ionomer for complete stabilization. Investigation of Pt/C-only dispersions showed lower

viscosities at low shear rates in comparison to the carbon only dispersion of same concentration investigated, as well as reduced magnitude behaviour of shear thinning, suggesting Pt presence decreases the carbon aggregate sizes for both Vulcan and HSAC through electrostatic repulsion. This observation was confirmed by USAXS measurements, where comparison of scattering functions at high magnitudes of Q ($1x10^{-4}$ $\dot{}^{-1}$) showed decreased aggregate size for both carbon supports in the presence of Pt. On the other hand, investigation of effect of increasing ionomer content on Pt/C aggregation showed very contrasting effects for HSAC and Vulcan based compositions. Increasing ionomer content in Pt/Vulcan based ink resulted in decreasing low shear rate viscosity until a critical ionomer concentration was achieved, similarly to the effect observed when ionomer content was increased in Vulcan only dispersions. However, for Pt/HSAC based compositions, viscosity was observed to increase with increasing ionomer content, along with a strong shear-thinning behaviour present, a highly contrasting behaviour to dispersions based on the HSAC support only. This increasing viscosity was attributed to flocculation of aggregates, suggesting a strong interaction mechanism between Pt and the ionomer.

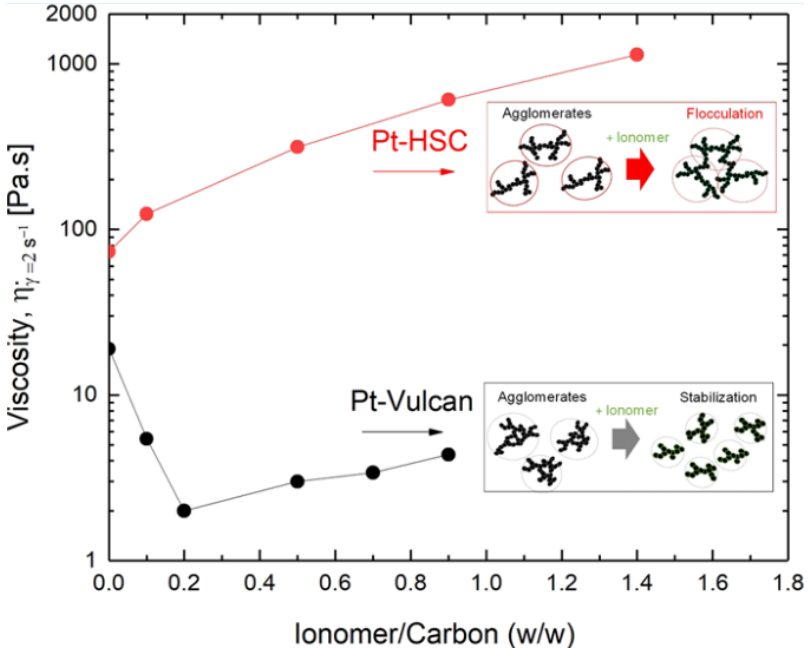


Figure 11. *Schematic representing change in Pt/C carbon aggregate structure with increasing ionomer content in catalyst inks based on different carbon supports: high surface area carbon (red) and Vulcan (black), as found through rheological studies performed by Khandavalli et al.[25]* *All content of the figure falls under the copyright of the authors, as part of the work published by Khandavalli et al.[25]*

Moreover, Du et al.[52] reported variations in Pt/HSAC aggregate size when the sonication and ball-milling dispersion methods were used, with the former showing significantly larger aggregates. Such an observation was not made for Pt/Vulcan based compositions. The contrasting behaviour of the two Pt/C complexes is consistent with the rheological observations made by Khandavalli et al.[25], whose hypothesis may explain such a phenomenon.

Li et al.[53] investigated the effect of solvent dielectric constant and increasing ionomer content on aggregation of Pt/GC complex using rheology, elastic light scattering (ELS) and dynamic light scattering (DLS). Their results show decreasing ink viscosities and increasing zeta potentials, suggesting decreasing Pt/GC aggregate size with increasing ionomer content. Such behaviour indicates the Pt/GC support may be more similar to Pt/Vulcan based compositions rather than Pt/HSAC ones, considering observations presented by Khandavalli et al.[25]

These findings suggest that along with the varied performance and durability considerations associated with the carbon black support chosen, the choice of carbon support may result in different aggregation behaviours in the presence of ionomer and Pt that should be taken into account when formulating ink compositions. In addition, the contrasting behaviours observed for the porous HSAC support and Vulcan or GC may suggest a different ionomer interaction mechanism, most likely with Pt particles, as their presence was crucial for the contrasting viscosity trends to emerge. This effect would be of interest for further investigation.

1.3.2 Ionomer

In section 1.2.1.2 ionomer related variations were presented with regards to the ionomer type (i.e. side chain length), its effective weight (EW), as well as the I/C ratio utilized in the compositions.

The ionomer influences proton transport towards the active site, however dense layers on the Pt/C interface are known to hinder reactant gas transport, reducing the rate of the ORR reaction. In addition, SO^{3-} groups of the ionomer side chain are known to bind to the Pt catalyst, poisoning it towards the ORR. With the performance of the catalyst layer heavily impacted by gas transport properties, a finely tailored structure of the ionomer layer must be achieved.

Xue et al.[32] utilized molecular dynamics (MD) simulations combined with single-cell experiments to evaluate the effect of ionomer content on performance of the cathode catalyst layer. The Pt/C complex is simulated using graphite sheets and Pt nanoparticles, based on a commercial Pt/C complex with 60 wt% loading as a reference. Nafion was adopted as the ionomer component in the simulation. Corresponding materials are employed in the cathode catalyst layers (CCLs) used for single cell tests. MD simulations reveal the ECSA of Pt is directly linked to the ionomer coverage on the Pt/C surface, with full coverage obtained with Nafion concentrations of 29.6 wt% (I/C ≈ 1.1 considering the 60 wt% Pt loading on carbon support). Increasing Nafion content from 20 to 30 wt% resulted in a 15.1 wt% increase in ECSA. Single cell experiments agreed with the simulation results, where ohmic and charge transfer resistances extracted showed a U-shaped dependence as a function of ionomer content, with both minima located at Nafion content of 30 wt%. Concurrently, the CCL utilizing 30 wt% of Nafion showed the lowest voltage loss at both low and high current densities.

Ishikawa et al.[35] used a similar approach based on numerical simulations to model the effect of Pt loading and ionomer content on the catalyst layer structure. The model assumed a catalyst layer consisting of Ketjenblack porous carbon, pure Pt nanoparticles and Nafion. The structural model was characterized with regards to the Pt inter-particle distance, ionomer coating thickness, pore size distribution, tortuosity and ionomer coverage on Pt. The model showed a significant dependence of the catalyst layer structure on the Pt loading and ionomer content. Parameters related to the ionomer show again that increasing I/C ratio reduces pore connectivity, with larger pores becoming isolated, which could hinder O_2 transport. On the other hand, increasing I/C up until 1.0 significantly improved proton conductivity, and this was found to be the optimum I/C ratio based on performance.

Yakovlev et al.[54] investigated the effect of Nafion ionomer content on the local transport properties inside the catalyst layer. Oxygen transport was studied using the limiting current technique, while proton and electron transport resistance was investigated using impedance spectroscopy and polarization curve measurements. Note the catalyst layers were based on Pt/Vulcan with 40 wt% Pt loading, and the ink was deposited directly onto a Nafion membrane using an ultrasonic spraying technique, suggesting inks of low solid content. Results show proton transport resistance significantly decreased with increasing I/C ratio from 0.1 to 1.0, however, at ratios higher than 0.3 no increase in ECSA was observed, suggesting sufficient proton transport pathways. Limiting current tests showed increasing resistances to oxygen transport with increasing ionomer content from I/C = 0.1 to 1.0, as expected. The $R_{Kundsen}$ resistance contributions,

correlated to the porosity in the catalyst layer, increased along with the I/C ratio, however the $R_{Ionomer}$ contribution, characterizing resistance associated with permeation of the ionomer, was minimized at I/C ratio of 0.6. Coherently, the best performance of 595 mW cm^{-2} was achieved for the catalyst layer with I/C = 0.6, showing an optimal balance between proton and oxygen transport was achieved. Nevertheless, the catalyst layer with I/C = 0.3 also achieved a significantly good performance of 560 mW cm^{-2}, suggesting perhaps an optimal I/C range could be established.

In every instance an agreement is reached that an optimal ionomer content is found when ease of proton transport and a reduction of O_2 transport resistance are balanced. The results obtained using modelling approaches performed by Xue et al.[32] and Ishikawa et al.[35] are fairly consistent, showing optimal catalyst layer structure when I/C with Nafion is approximately 1. Moreover, these observations were confirmed through experimental methods. On the other hand, Yakovlev et al.[54], who investigated several catalyst layers with varying ionomer content suggest optimal performance is obtained when I/C with Nafion is lower, reaching optimum at 0.6. Indeed, the variation may arise due to different catalyst layer compositions used in between the works, as well as different preparation methods.

Liu et al.[29] investigated the effect of electrode thickness and ionomer EW on proton resistivity in cathode catalyst layers, suggesting that for uniform electrodes the ionomer loading and EW had a significantly dominant effect on the proton resistivity. Especially for I/C ratios lower than 0.8, it was found proton transport resistance was directly linked to the density of SO_3^- groups and RH, where low RH conditions favoured ionomers with lower EW, and therefore higher density of SO_3^-. Concurrently under high RH conditions high EW ionomers were found to show superior performance.

On the other hand, Ren et al.[55] looked at both the impact of the use of SSC and LSC ionomers (Aquivion and Nafion), as well as the effect of EW (720 and 790 g/mol SO_3^- for Aquivion) on the resulting catalyst layer performance. The Pt/C catalyst used was obtained commercially and contained a 40 wt% Pt loading, however, the carbon support type was not specified. The I/C was fixed at 0.65 and the CCL was prepared by spray coating the ink directly onto the PEM. Measurements of voltage as a function of current density at varying RH conditions, and subsequently obtained plots of maximum power density revealed a direct link of the SO_3^- density to the RH. At RH = 30 and 53% catalyst layers based on Aquivion with EW = 720 g/mol SO_3^- showed the best performance, followed by compositions based on Aquivion with EW = 790 g/mol SO_3^- and Nafion with EW = 1000 g/mol SO_3^-. At RH = 75% the three compositions showed very similar power density outputs, while at high RH conditions of 100% catalyst layers based on Nafion dominated. The good performance of the SSC ionomer was attributed to a formation of a continuous and uniform ionomer network, where a higher side chain density but relatively lower adsorption of the ionomer on Pt/C complex resulted in an ionomer structure allowing for optimized proton as well as gas transport in the catalyst layer.

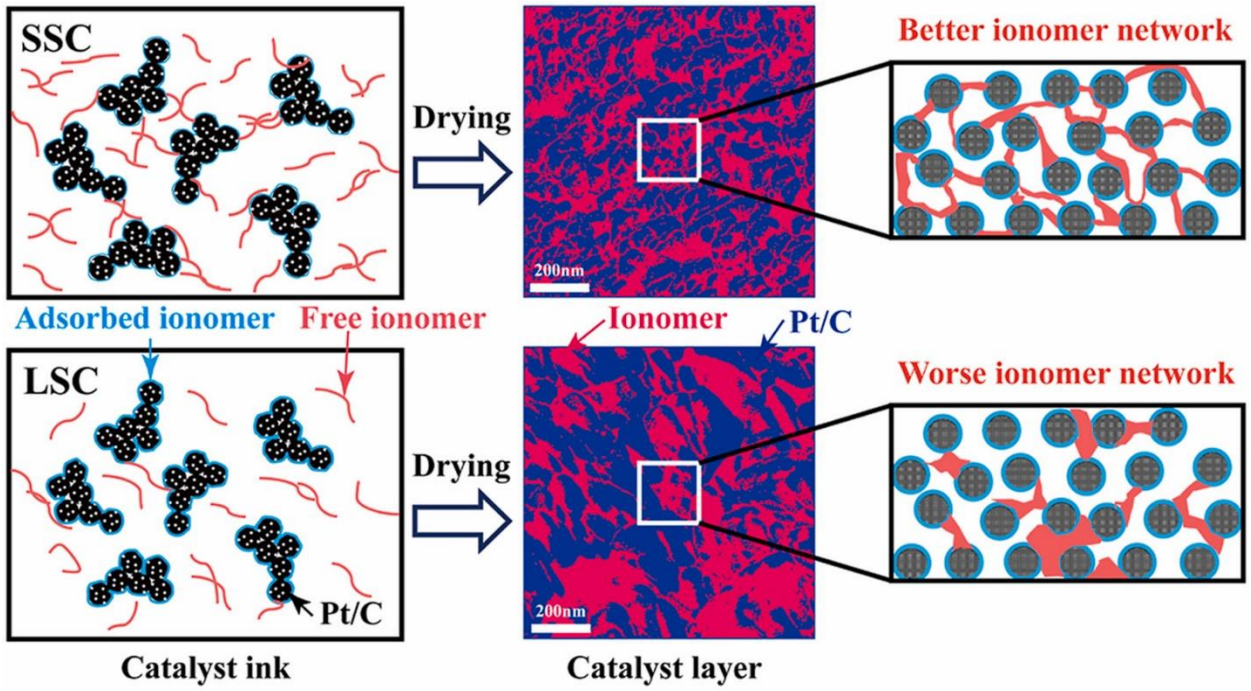


Figure 12. *Summary of results presented by Ren et al.[55], with schematics of ionomer distribution in catalyst layers manufactured from catalyst inks based on short side-chain Aquivion and long side-chain Nafion ionomers.*
All content of the figure falls under the copyright of the authors, as part of the work published by Ren et al.[25]

In addition, Kodama et al.[56] used surface-enhanced infrared absorption spectroscopy (SEIRAS) to show that the ether group found in LSC ionomers (labelled as **z** in figure 4) also interacts with Pt active sites at the interface, leading to stronger adsorption of LSC ionomers and a detrimental effect on the ORR through the poisoning of active sites.

It can be observed both SSC and LSC, as well as their inherently different equivalent weights, prove optimal in different operating conditions. In addition, the LSC ionomers containing longer sidechains may lead to increased poisoning of the Pt active site. Nevertheless, the increased distance between hydrophobic and hydrophilic domains in LSC ionomers aids in management of the water by-product, reducing its agglomeration in the CL, which is key, especially with increased ORR rates.[57]

Some studies are trying to achieve the best of both worlds by design of gradient catalyst layers containing both the SSC and LSC ionomers. By increasing proton transport associated with increased SO_3^- sidechain group densities of SSC ionomers near the PEM, and increased mass transport resulting from the use of LSC ionomers, providing increased porosity, the proton as well as mass transport through the catalyst layer can be optimized. Lyu et al.[58] designed a catalyst layer containing an ionomer gradient consisting of Aquivion (EW = 790 g/mol SO_3^-) near the PEM side and Nafion D2020 (EW = 1000 g/mol SO_3^-) near the GDL, which outperformed its singular counter parts both in terms of proton and reactant gas transport. Huang et al.[57] further optimized this idea, by tailoring proportions of the gradient, with a 3:1 SSC/LSC ratio showing optimal performance. Furthermore, cyclic voltammetry additionally indicated higher Pt ECSA under such a set-up. Both studies noted the catalyst layer remained fairly uniform, however, more research is required into the novel ionomer gradient design.

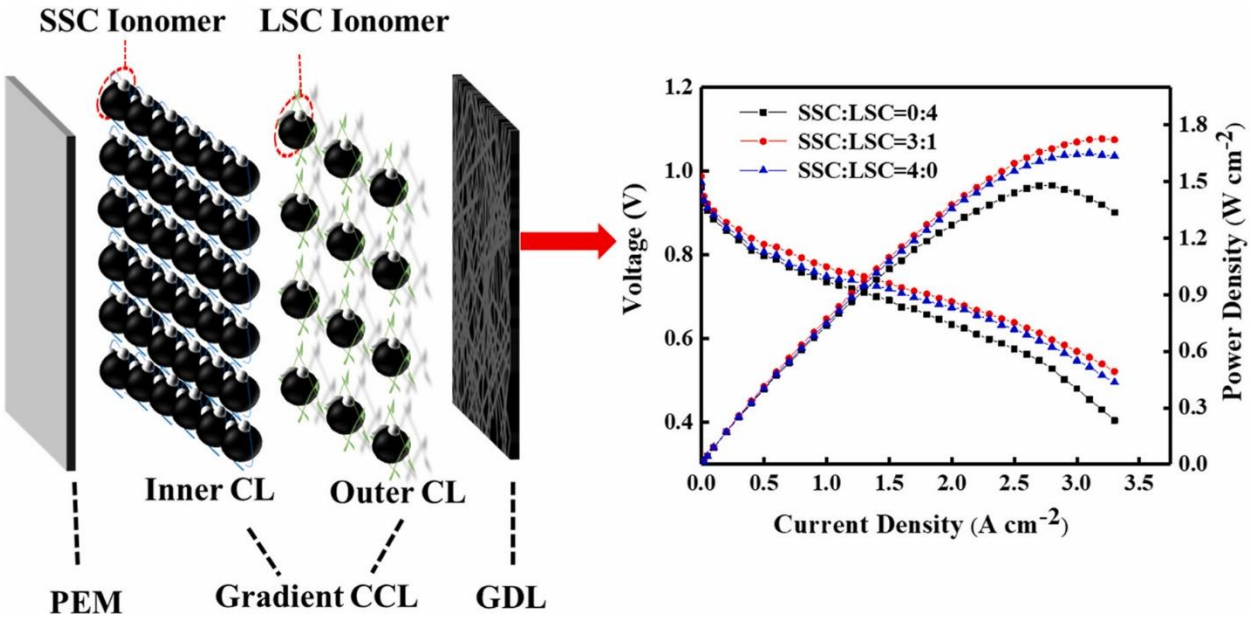


Figure 13. *Schematic of a gradient cathode catalyst layer, utilizing both short and long side-chain ionomers, as designed by Huang et al.[57], together with resulting polarization curve and power density results for combinations of different ratios of the two ionomer types. All content of the figure falls under the copyright of the authors, as part of the work published by Huang et al.[57]*

With regards to the catalyst ink itself, in section 1.3.1 the effect of increasing ionomer content in the ink, mainly focusing on rheological studies, was discussed in combination with use of different carbon supports (note many of the parameters are correlated together, and therefore hard to discuss on a completely separate basis). For carbon only dispersions, increasing ionomer content resulted in stabilization of the aggregates, until a critical I/C value was reached, resulting in no further changes in viscosity observed. For Pt/C based compositions, addition of ionomer had a contrasting effect depending on the carbon type. For compositions based on Vulcan or GC, again progressive increase of ionomer concentration resulted in stabilization of the Pt/C, up until a critical I/C value, but for HSAC based compositions, addition of ionomer was found to increase ink viscosity which was attributed to an aggregate flocculation effect.[25, 53]

Yoshimune et al.[31] employed the CV-SANS method also utilized throughout this project to investigate the impact of increasing ionomer content on the degree of ionomer adsorption to carbon as well as on the overall ionomer structure on the nanometre size scale. The ink formulation utilized Pt/Vulcan with 30 wt% Pt loading, Nafion ionomer, and a solvent based on approximately 30:70 wt% EtOH/water, with some 1-propanol contamination noted due to the nature of the commercial Nafion dispersion used. The CV-SANS

results show increasing I/C from 0.25 to 1.00 did not alter the thickness of the shell of adsorbed ionomer observed on the carbon surface, however its density increased from 0.12 to 0.21. Moreover, increasing the I/C ratio resulted in monotonically increasing unadsorbed ionomer amount found in the dispersion. Rheology measurements were performed, linking the concentration of unadsorbed ionomer in the ink to its high shear rate viscosity, showing the behaviour can be described by the Huggins equation, and is consistent with that observed for typical ionomer dispersions. Furthermore, as the degree of ionomer adsorption was found to remain fairly constant with varying I/C ratio, the stabilization behaviour of aggregates discussed above can be attributed to increased ionomer content in the dispersion overall, rather than an increased amount of adsorption.

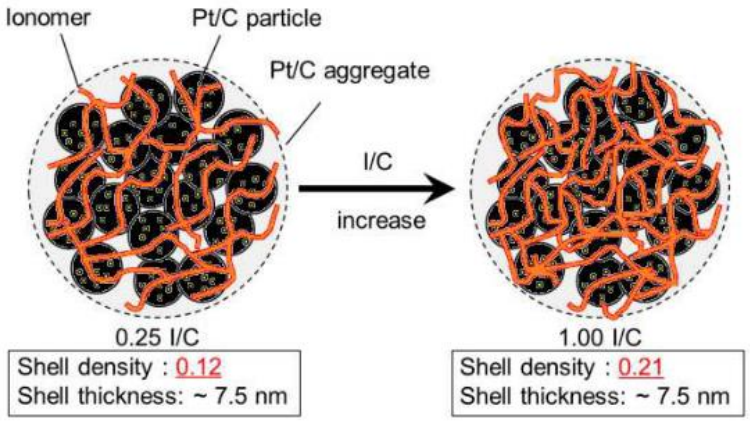


Figure 14. *Schematic of variation in catalyst ink structure with increasing ionomer content in the ink composition, as reported by Yoshimune et al.[31] using CV-SANS results. All content of the figure falls under the copyright of the authors, as part of the work published by Yoshimune et al.[31]*

Mashio et al.[30] used molecular dynamics simulations to investigate the degree of ionomer adsorption with varying EW to a graphite sheet as a function of varying solvent composition. The ionomer simulated was Nafion, with EW of 760 (x = 3), 1140 (x = 7) and 1560 (x = 11) g/mol SO_3^-. The solvent used in this study was based on MeOH/water with different MeOH concentrations. Differences in the ionomer conformation were observed. In water-rich solvent increased aggregation was noted, with sidechains containing the sulfonic acid groups pointing outwards. In alcohol-rich solvent, the ionomer molecule dispersion was generally improved. It was found the ionomer interacts with the graphite sheet through the hydrophobic backbone, and functionalization of the graphite sheet resulted in increased repulsive interactions between the graphite and ionomer sidechains, resulting in a lower degree of adsorption. The degree of ionomer adsorption with different EW was found to vary significantly depending on the solvent system. In pure water, lower EW ionomer showed the most adsorption, with a conclusion reached that the presence of hydrophilic sidechains aids in reducing the interfacial energy between the graphite sheet and the solvent. For low EW ionomer, the adsorption decreased with increasing alcohol content in the solvent. This was attributed to several effects, including reduction of interfacial energy at the graphite surface by the solvent itself, improved dispersion of the ionomer, as well as an increase in electrostatic repulsive forces among the dense sulfonic acid groups. In the case of high EW ionomer the trend observed was somewhat different. Addition of MeOH into the system first boosted adsorption of ionomer to the graphite, however when MeOH concentration reached 80 wt% some desorption could be observed. The increasing adsorption was explained by high adsorption energies of high EW ionomer, which arise as a result of increasing proportions of the hydrophobic backbone domain, boosting adsorption in increasing alcohol content. Moreover, the sidechain groups are not densely packed so the electrostatic repulsion between them when on the graphite

surface is not as significant. The decreasing adsorption with high alcohol content was explain by dissolution of the ionomer into the solvent.

Thoma et al.[59] studied the adsorption of Aquivion ionomer with different EW to Vulcan carbon in water using densitometry, isothermal titration calorimetry (ITC) and thermogravimetric analysis (TGA). The EW of Aquivion in this work varied between 650 and 980 g/mol SO_3^-. All methods showed consistent results, where obtained adsorption isotherms suggested an increase in EW resulted in higher maximum coverage, however the number of ionic groups deposited on the carbon surface remained constant. Considering the ionomer is assumed to interact with the carbon via the hydrophobic backbone, an increase in maximum coverage with increasing EW is a consistent observation. However, the lack of change in the sulfonate groups calculated on the surface suggests no major alteration in the degree of ionomer adsorption with varying EW. In addition, it was found the EW had very little effect on calculated free energy of adsorption. Where in the study by Mashio et al.[30] very drastic alterations in EW were considered, it is possible small variations, at least in the case of the water solvent, do not have such a pronounced impact on the degree of ionomer adsorption.

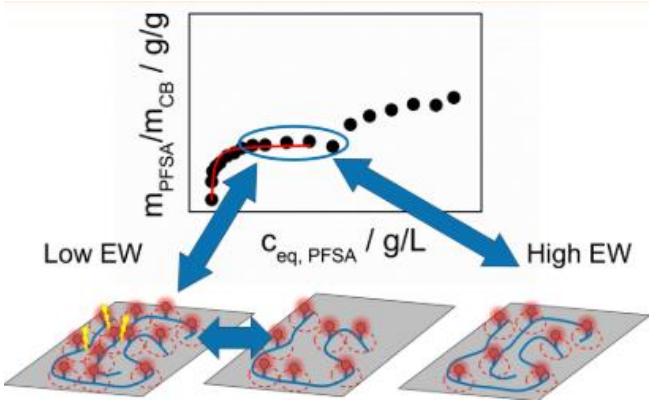


Figure 15. *Schematic of ionomer coverage as function of EW results as presented by Thoma et al.[59], who used densitometry, thermogravimetric analysis, and isothermal titration calorimetry. All content of the figure falls under the copyright of the authors, as part of the work published by Thoma et al.[59]*

In summary, both LSC and SSC ionomers show improved performance in specific operating conditions, and therefore the choice of ionomer type will be dependent on the PEMFC application. Furthermore, both the ionomer type and EW chosen can be broadly characterized by the density of sulfonic acid groups, which seems to be highly correlated to the nature of the ink solvent system (hydrophobic/hydrophilic) with regards to the ionomer conformation and its subsequent interaction with Pt/C. This dependence should be noted in future studies, and investigated thoroughly. In particular, development of experimental methods which could contribute to understanding this relation further is required.

1.3.3 Platinum

With regards to the aim of reducing overall fuel cell cost, many studies focus on characterizing novel catalyst layers with reduced geometrical Pt loading. However, before reduction of Pt loading can be tackled, performance has to be optimized with regards to the Pt active site availability and mass transport limitations associated with the ionomer presence in the catalyst layer. In order to achieve this, understanding of the mechanism of ionomer layer formation must be improved. This is a difficult endeavour, as the ionomer includes both hydrophobic and hydrophilic domains, which interact with both the carbon and Pt particles. In addition, the degree of interactions is likely to change based on the nature of the ionomer – its equivalent weight and the length of the side chains. Moreover, to this day an agreement has not been reached on

whether the ionomer interacts preferentially with the carbon or the Pt component, and again this preference may vary depending on the overall ink system.

Takahashi et al.[60] used cryo-TEM to visualize the ionomer/catalyst interface, noti ng the ionomer coverage is denser near Pt particles, which suggested enhanced interactions between the ionomer sidechains and the Pt nanoparticles. Note the catalyst layers were manufactured from 40/60 wt% iPrOH/water solvent.

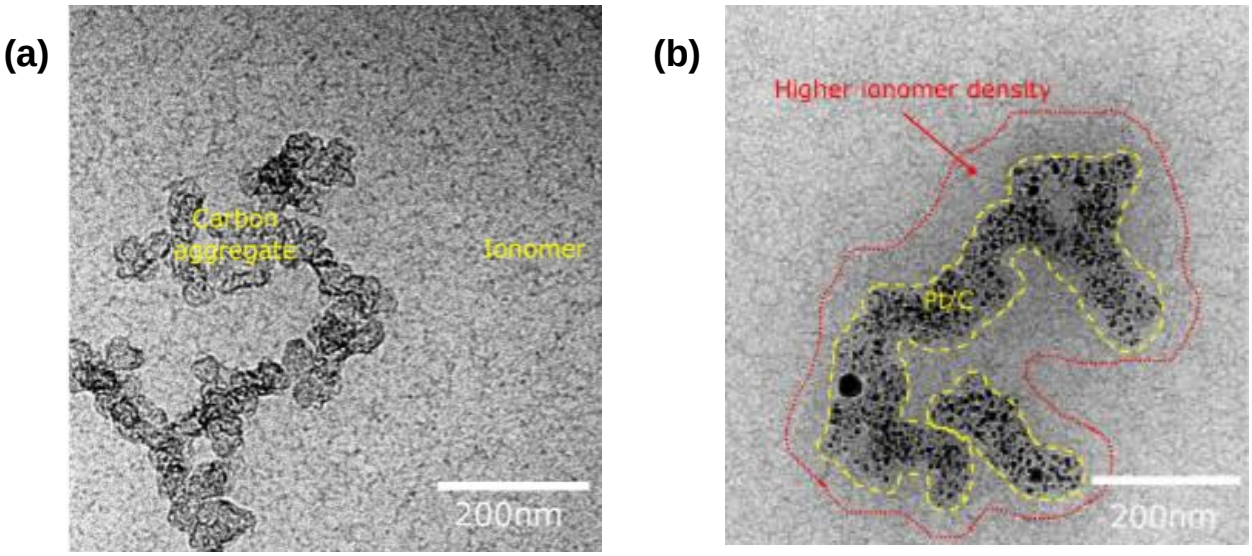


Figure 16. *Cryo-TEM images obtained by Takahashi et al.[60]:* ***(a)*** *reference ink containing carbon and ionomer only,* ***(b)*** *catalyst ink containing Pt/C complex and ionomer. All content of the figure falls under the copyright of the authors, as part of the work published by Takahashi et al.[60]*

Ren et al.[55] noted improved ionomer networks when the SO_3^- group density was increased through the use of lower EW SSC ionomers, which suggested a high structural dependence on the ionomer sidechain-Pt interaction.

Rheological measurements performed by Khandavalli et al.[25] showed contrasting behaviours with increasing ionomer content in HSAC-only and Pt/HSAC based compositions, suggesting a strong shift in the ionomer interaction mechanism in the presence of Pt.

Mashio et al.[30] used simulations to show the interaction of ionomer with Pt/C in an ink dispersion is highly dependent on the nature of the solvent, with preferential sidechain-Pt interactions in water-rich compositions and backbone-carbon interactions in alcohol rich compositions.

On the other hand, Berlinger et al.[39] investigated the ionomer adsorption behaviour in inks with varying solvent, EW, side-chain length and surface type parameters, using isothermal titration calorimetry (ITC) to study adsorption thermodynamics and quartz crystal microbalance for adsorption parameter screening. In particular, ITC results suggested that ionomer adsorption to both Pt and carbon nanoparticles separately is an entropic process driven by hydrophobic interactions in each case. An explanation is provided that the surface charge states of Pt are different in solutions, and therefore the interaction mechanism between catalyst inks and catalyst layers may differ.

Moreover, Yoshimune et al.[38] investigated the effect of Pt loading (Pt/C ratio) on the ionomer adsorption in catalyst inks using CV-SANS, noting the ionomer layers were thinner, but denser at lower Pt loadings of 30 wt%, and conversely thicker, but less dense when Pt loading was increased to 50 wt%. Calculation of free energy of adsorption suggested the ionomer interactions with carbon are slightly stronger, and an adsorption mechanism was proposed where in the instance Pt is more dispersed on the surface, adsorption

of the backbone to the carbon becomes more facile, and thinner layer, where the ionomer is more spread out over the carbon surface, are obtained. On the other hand, when the Pt-Pt distance shrinks, adsorption of ionomer to carbon is inhibited and a proportion of the ionomer chain is left extending over the interface into the dispersion medium, creating thicker, but less dense layers. Nevertheless, note that the carbon support used in this study was HSAC, where it is known the majority of the Pt is located inside the porous core. Therefore, the surface Pt distribution would be sparse to begin with when compared to other supports such as Vulcan or GC , and this study may not be widely representative of all catalyst ink systems.

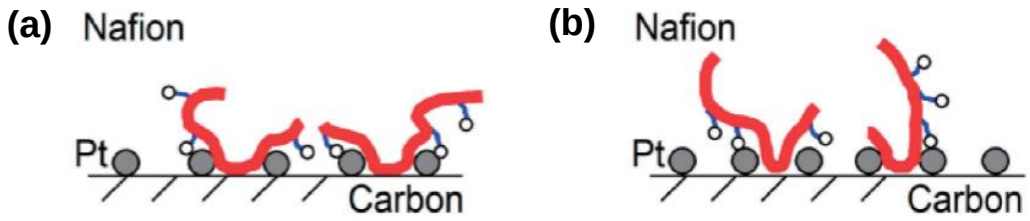


Figure 17. *Illustration depicting Nafion adsorption to* ***(a)*** *high surface area carbon with 30 wt% Pt loading,* ***(b)*** *high surface area carbon with 50 wt% Pt loading, as proposed by Yoshimune et al.[38] through their work using CV-SANS. All content of the figure falls under the copyright of the authors, as part of the work published by Yoshimune et al.[38]*

In a review on the understanding of the catalyst/ionomer interfacial structure, Woo et al.[61] note interaction of sidechains with the Pt can result in bigger separation between the hydrophilic and hydrophobic domains of the ionomer, trapping water molecules at the interface which facilitates proton transport. However, it was also distinguished that poor interaction between the ionomer backbone and the carbon at the interface results in an insufficient coverage of the catalyst layer overall, motivating research into carbon surface functionalization for increased ionomer backbone-carbon interactions. On the other hand, several studies of ionomer adsorption mechanism to Pt/C in catalyst ink based samples suggest preferential interactions of ionomer and carbon. Such deviation in observations between the interactions in catalyst inks and catalyst layers may suggest the ionomer adsorption mechanism changes upon drying, and consequently indicate an ionomer rearrangement on the Pt/C surface.

It is estimated that in current-day PEMFCs only 20% of the available Pt sites are utilized.[61] In order to optimize this critical parameter, it is of great importance to correlate ionomer adsorption observed in catalyst inks, to the subsequent distribution present in the catalyst layer, achieving a conclusion on the mechanism of ionomer-catalyst interface formation.

1.3.4 Dispersion Solvent

The solvent composition used in the catalyst ink is a crucial parameter, dictating the inter-component interactions in the system, as well as structural alterations during drying, and therefore having a significant impact on the final catalyst layer structure.

Li et al.[53] used rheology, zeta potential measurements, as well as dynamic light scattering (DLS) to investigate the effect of solvent dielectric constant, altered by variation of iPrOH concentration, on the catalyst ink viscosity. Solvents of higher dielectric constant, namely water-rich compositions, were found to reduce Pt/GC aggregation, as indicated by increasing zeta potentials. Moreover, higher viscosities at low shear rates for inks based on solvents with high dielectric constants were attributed to increased repulsions between Pt/GC aggregates with adsorbed ionomer. In addition, SEM images linked the increased dielectric constant to reduced crack formation in processed catalyst layers.

Balu et al.[47] used CV-USANS (ultra-small-angle neutron scattering) to characterize the entire ink system, investigating the effect of iPrOH concentration on both the thickness of the adsorbed ionomer layer and size of Pt/C aggregates. The ionomer could be observed to exist both on the surface of Pt/Vulcan, forming a shell of a mass fractal nature, as well as in the dispersion medium, as unadsorbed cylindrical aggregates. Again it was noted using zeta potential measurements that inks with water-rich solvents, and therefore higher dielectric constants, result in greater repulsion between ionomer coated Pt/Vulcan aggregates, improving the dispersion quality. Furthermore, fitting of CV-SANS data using the Guinier-Porod and cylinder models revealed the thickness of the adsorbed ionomer layer changes with the solvent. For an ink composition containing 10 wt% iPrOH a 10 nm thick layer was extracted, while the thickness of the adsorbed ionomer was quantified as 13 nm for an ink composition with 70 wt% iPrOH.

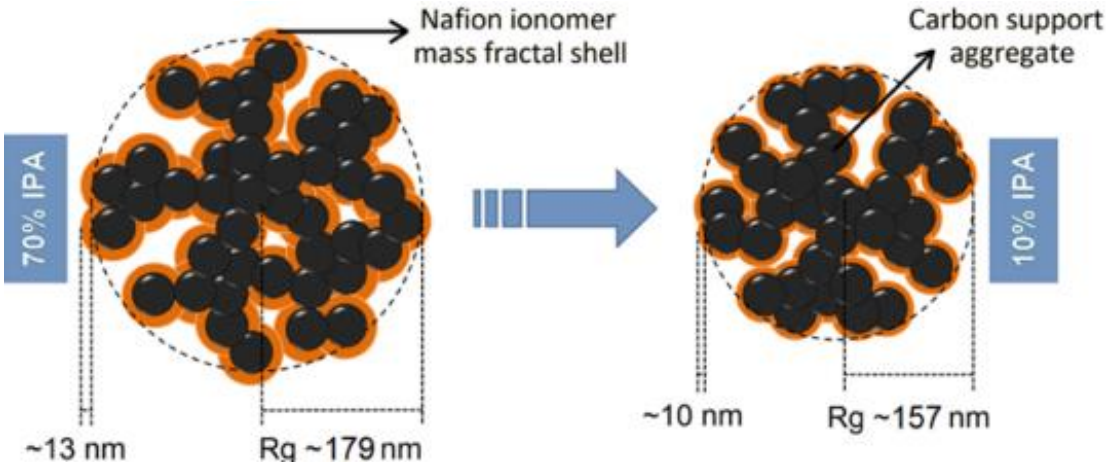


Figure 18. *Schematic of variation in catalyst ink structure as function of isopropanol (IPA) concentration in the solvent system, as presented by Balu et al.[47] through their work using CV-SANS. All content of the figure falls under the copyright of the authors, as part of the work published by Balu et al.[47]*

Orfanidi et al.[62] linked the solvent ink composition to the ionomer distribution in resulting catalyst layers as well as observed electrochemical performance. In this work both iPrOH and 1-PrOH were used as the alcohol solvent component. The H_2O concentration was varied between 16 and 65 wt%. The Pt/C used was based on HSAC, with 50 wt% Pt loading, and a low EW (700 g/mol SO_3^-) PFSA ionomer was used. Interestingly, a correlation between ECSA and alcohol type used was found, with formulations based on 1-propanol showing higher ECSA, irrelevant of the water content. This increase was linked to an improved dispersion of the ionomer. The best performance under both dry and wet operating conditions was observed for the catalyst layer manufactured from ink based on 1-propanol and a low water content of 16 wt%. This improvement in both conditions was linked to a more uniform distribution of the ionomer layer, which was further suggested by SEM images, where no significant ionomer patches could be observed for this composition, contrary to other catalyst layers. Conversely to previous works discussed, DLS measurements revealed the smallest secondary aggregates were present for the ink formulation with the lowest water content. This may perhaps be related to the differences in Pt/C complexes utilized throughout the works, or the low EW ionomer utilized.

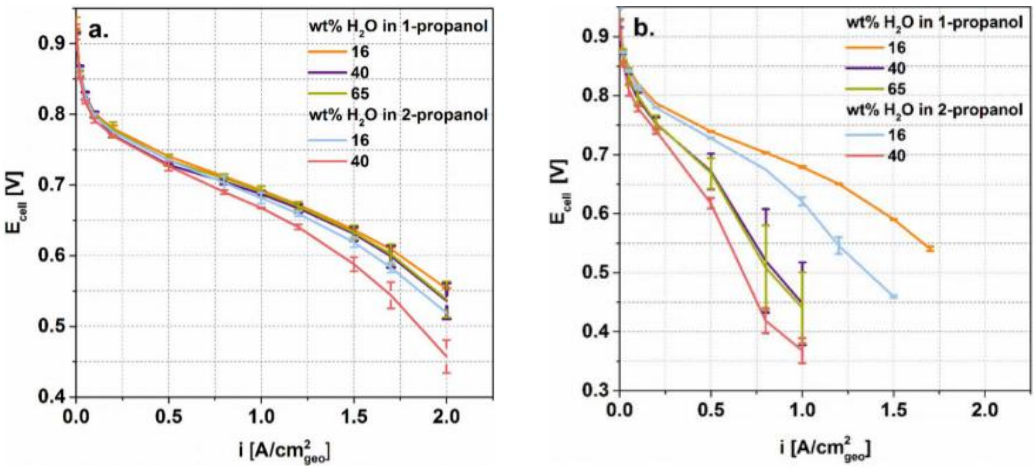


Figure 19. *H_2/Air performance results obtained by Orfanidi et al.[62] of MEAs containing cathode catalyst layers manufactured from inks with solvent systems based on different alcohol types and concentrations, measured at* ***(a)*** *80°C, 30% RH – dry conditions,* ***(b)*** *60°C, 100% RH – wet conditions. All content of the figure falls under the copyright of the authors, as part of the work published by Orfanidi et al.[62]*

Ren et al.[63] investigated inks based on the iPrOH alcohol with different concentrations, corresponding catalyst layers, and their electrochemical performance using a plethora of methods. The carbon support used in the Pt/C complex is not specified (but the Pt loading was 40 wt%), and the ionomer used was Nafion with I/C = 0.65. Their findings suggest water-rich solvents result in formation of discrete Nafion aggregates, which provide insufficient proton transport. On the other hand, ink compositions with alcohol-rich solvents resulted in catalyst layers where the ionomer was well dispersed in a network, however, the rapid evaporation of the iPrOH led to a denser pore structure, blocking oxygen transport. It was suggested a 50 wt% alcohol formulation would aid in creating a balance between the two phenomena.

Aside from the conventional alcohols used in the ink dispersion medium, high boiling point solvents have been garnering some research attention due to their enhanced mechanical properties. Lei et al.[45] compared the use of conventional aqueous solvents based on 1-PrOH or iPrOH and water (3:1 wt%) to non-aqueous, high boiling point solvents, ethylene glycol and 1,2-butanediol in ink compositions. The quality of resulting catalyst layers was investigated using SEM, HAADF-STEM, and EDS elemental mapping, and their performance was characterized using electrochemical testing. The remainder of the ink compositions was kept constant, using Pt/Vulcan with 50 wt% Pt loading and Nafion ionomer with I/C = 0.6. SEM revealed severe cracking in the catalyst layer prepared using iPrOH/water solvent, however, it was noted this is not uncommon for formulations based on this alcohol type. This phenomenon was linked to bigger Pt/C agglomerates in the ink composition using rheological measurements, where shear thinning and elastic dominant behaviour was observed. Like in previous works, the appearance of larger agglomerates was linked to a poorer ionomer distribution. On the other hand, such observations were not made for the CCL manufactured from 1-PrOH based solvent, and it was found to display the best electrochemical performance, achieving 0.663V at 1 A/cm^2 current density. Nevertheless, CCLs manufactured from the non-aqueous solvents proved to be the most durable, showing voltage losses of approximately 35 mV after 30000 cycles. In comparison, the CCLs manufactured from aqueous solvents showed approximately 80 mV loss after the same number of cycles. The improved durability of CCLs manufactured from non-aqueous solvents was attributed to the smallest changes in both the ionomer and Pt nanoparticle distribution observed after accelerated stress tests using STEM-EDS mapping before and after the ASTs.

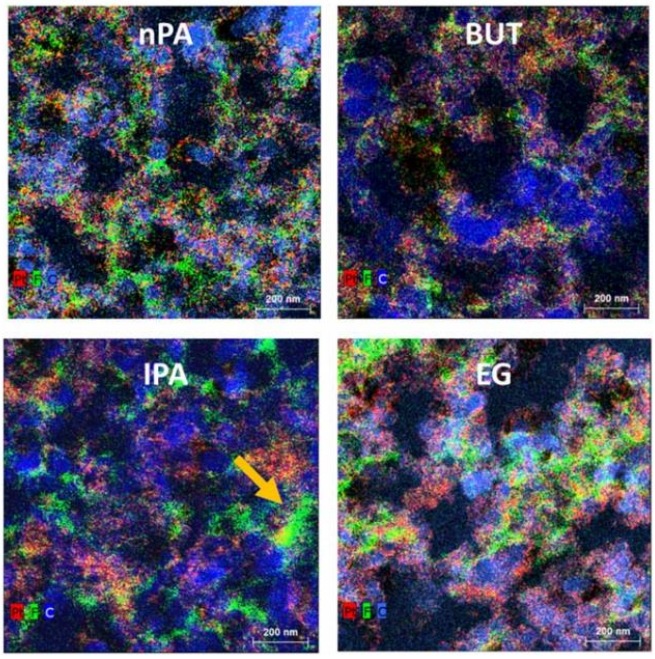


Figure 20. *HAADF-STEM images, with EDS elemental maps, of electrodes fabricated by Lei et al.[45] using ionomer dispersions in various solvents: nPA (1-propanol), BUT (1,2-butanediol), IPA (isopropanol), EG (ethylene glycol). Pt is shown in red, F is shown in green, and C is shown in blue. All content of the figure falls under the copyright of the authors, as part of the work published by Lei et al.[45]*

Hasegawa et al.[44] also noted the benefits of using high boiling point solvents, however relating directly to the ink drying process. The effect of introducing a small amount of propylene glycol (PG) to a catalyst ink on the crack formation and aggregate size of resulting catalyst layers was investigated, approximately 0.1 wt% of PG was added to a more conventional 50:50 wt% EtOH/water based ink composition. H^1 NMR was used to monitor the solvent composition throughout the drying process, and time-resolved USAXS allowed for real time monitoring of the change in Pt/C aggregate size during the drying process. Finally, the quality

of resulting catalyst layers was evaluated using laser microscopy with regards to the observed crack formation. The remainder of the ink formulation consisted of Pt/Vulcan with 30 wt% Pt loading and Nafion with I/C = 1.0. An increase in Pt/C aggregate size with drying time could be observed for both compositions, however in the PG containing ink the aggregate size shift was not only reduced, but also much more constant with drying time. On the other hand, in the composition containing the conventional EtOH/water solvent only, a dramatic shift in aggregate size could be observed between 6 and 14 minutes into the drying process. This shift could be directly correlated to the complete evaporation of EtOH using H^1 NMR, and the point in time where crack formation could be seen to commence in laser microscopy. Although EtOH was found to evaporate in a similar time frame in both compositions, PG was found to remain in the ink throughout the drying process (up to 60 min), and no crack formation was observed in laser microscopy throughout the drying time. Therefore, it was shown even a small proportion of a high boiling point solvent can aid in reducing the water rich domain created on evaporation of low boiling point alcohols in the early stages of the drying process.

Throughout several sections, the dispersion solvent was shown to be strongly correlated with other parameters. Most notably, conclusions seemed to differ with regards to what alcohol concentration in the solvent yielded the best component dispersion. This may be directly related to variation in Pt/C complexes and ionomers used throughout the different works. Use of high boiling point solvent proved promising with regards to reducing Pt/C aggregation throughout the drying process and improving durability of resulting catalyst layers. It is likely these two effects are also somewhat related. The use of such solvents would open many new possibilities for ink compositions, nevertheless, the effect of solvent in the dispersion overall remains to be fully comprehended.

1.3.5 Summary of observations from state of the art research on component variation effect

Section 1.3 built on section 1.2 by presenting state of the art research focusing on the effect of each component on the structure of catalyst inks and catalyst layers. Some work provided a more fundamental understanding of the components, such as the characterization of Pt distribution on different carbon supports, investigation of ionomer interaction mechanism with Pt/C, or molecular simulations of the effect of EW on ionomer hydrophobic/hydrophilic domain interactions with carbon in varying solvent compositions. Others correlated compositional variation directly to catalyst ink/layer structure and best electrochemical performance.

In general, it could be observed that complete deconvolution of structural effects induced by variation of certain parameters is impossible – for example conformation of the ionomer will vary based on solvent composition, which in turn will affect the adsorption to Pt/C and the degree of aggregation. On the other hand, choice of ionomer type and EW might dictate the solvent composition and adsorption mechanism. Different carbon supports may display inherently different aggregation behaviours in the presence of ionomer or varying solvent systems, which affect conclusions drawn on the effect of the former or the latter.

Furthermore, with overall compositional variation observed in between each study, it is difficult to make comparisons between the findings of separate studies – the optimal I/C ratio and iPrOH concentration parameters proposed were found to vary, and this most likely is a result of differences in the overall system compositions, for example in Pt/C complex chosen or type of ionomer used. For this reason, it is key to perform a systematic study, where only one parameter is varied in order to advance a fundamental understanding of how the catalyst ink and subsequently catalyst layer structure arise, as well as develop a method for structural optimization.

With regards to the methods used, imaging techniques such as SEM and TEM along with porosimetry techniques proved to be popular with regards to structural characterization of the catalyst layers, in tandem

with electrochemical characterization for additional insight into the structure and overall performance. In the case of inks, rheology was often employed, with supporting information obtained from zeta potential measurements and DLS.

However, note in the majority of these techniques contributions from specific components in the system cannot be decoupled – the aggregation degree of carbon and adsorption behaviour of the ionomer cannot be evaluated as separate entities. Microscopy can definitely yield useful insights into the structure of the catalyst layer, however it has to be kept in mind the bulk system is not visualized, and the electron beam causes damage to the ionomer. In the case of inks, as mentioned before, light scattering techniques require a serious system dilution, which make it no longer representative of the original ink system, and drawing definite conclusions from zeta potential measurements or DLS can be misleading.

In the case of the study of the ionomer structure, as well as the adsorption mechanism to Pt/C, it was observed molecular dynamics simulations were often employed, which arises from the extreme difficulty to study the ionomer structure alone in the catalyst ink/catalyst layer system. The conclusions made using such simulations were very insightful, shedding light on the behaviour of arguably the most important component in the system. As the next step, the proposed ionomer structures and behaviours must be confirmed in an experimental manner.

Indeed, the only method that proved capable of visualizing the ionomer structure individually in the ink system was CV-SANS, where the thickness and density of the adsorbed ionomer can be fully extracted, and degree of adsorption evaluated. Moreover, use of USAS (ultra-small-angle scattering) allowed for direct visualization of the change in Pt/C agglomeration, also during the ink drying process, providing key insights into how small additions of high boiling point solvents could dramatically improve the quality of the resulting catalyst layer. This demonstrates small-angle scattering techniques can result in novel understandings into the behaviours of individual components in the catalyst ink system, and show great potential for increasing fundamental understanding of the complex system through detailed analysis of each component separately.

In section 1.4 a review will be performed, focusing on the small-angle scattering (SAS) techniques applied to the structural study of both catalyst inks and layers. It addition to the benefits of general structural characterization discussed above, the ability to perform in-situ and operando studies for comprehension of the changes arising in the system on operation will also be demonstrated.

1.4 Application of small-angle scattering towards an enhanced understanding of the PEMFC electrode

1.4.1 SAS of catalyst layers

Contrast variation small-angle neutron scattering (CV-SANS) allows for structural interpretation of complex, multi-component systems. The contrast between neutrons and a specific component in the system can be easily tailored through isotopic substitution of H^1 by H^2, in order to highlight scattering contributions from a desired component only, allowing for its characterization.

Harada et al.[64] used the CV-SANS method to distinguish adsorbed and unabsorbed ionomer on the surface of Pt/C in catalyst layers. Scattering functions contain information on the entirety of the system, however, CV-SANS data can be deconvoluted into several partial scattering functions (PSFs), which contain information on the individual structure of the Pt/C and the ionomer. In addition, a cross-correlation function (cross-term) is obtained which contains information on the Pt/C-ionomer interface, and the interactions between the two components. By fitting of the cross-correlation and ionomer related scattering functions, the ionomer adsorbed to the carbon (i.e interacting with it), and the ionomer deposited on top of the adsorbed thin film could be discerned respectively. The adsorbed ionomer was extracted using a model for fractal aggregates of polydisperse core-shell spheres, while the deposited ionomer was fitted with the

Teubner - Strey model. Results indicate approximately 50% of the ionomer was adsorbed to the Pt/C, forming a 5.1 nm thick shell, while the deposited ionomer thickness was 7.8 nm. Note the composition included Pt/Vulcan with 30 wt% Pt loading and Nafion (EW = 1000 g/mol SO_3^-) with I/C= 0.75. The ink was based on a 30:70 wt% EtOH/water solvent.

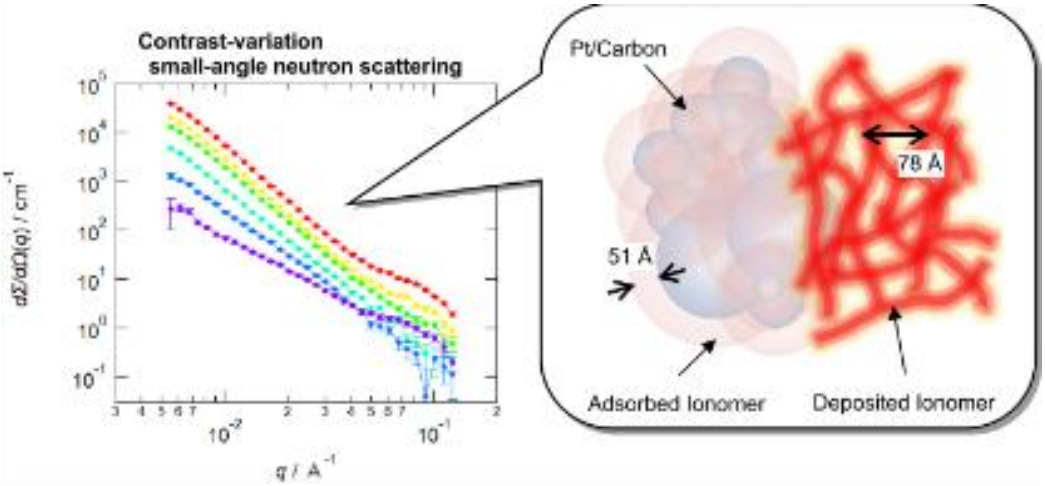


Figure 21. *CV-SANS data of a catalyst layer sample, along with a schematic of extracted structural information. All content of the figure falls under the copyright of the authors, as part of the work published by Harada et al.*[64]

Chabot et al.[46] used CV-SANS, along with measurements at controlled RH values to elucidate differences in the ionomer layer on varying Pt/C complexes, using Vulcan and HSAC as the carbon supports. Pt loading was kept constant at 50 wt%. Nafion (EW = 1000 g/mol SO_3^-) was used as the ionomer with I/C = 0.67 and 0.80 for the Vulcan and HSAC based compositions respectively. The solvent used in corresponding ink compositions was DAA/water with a 60:40 volume ratio. Scattering functions visualized using the Porod plot and fitted using the core-shell model revealed adsorbed ionomer layers of 2-3 nm in both instances. The lack of swelling behaviour of ionomer observed with varying RH suggested the ionomer is well dispersed in the catalyst layer, which was attributed to the dispersion process utilized, involving planetary mixing and ball milling. In addition to the ionomer layer, CV-SANS revealed changes in scattering intensity recorded on substitution of H_2O and D_2O, indicating a presence of a water layer at the Pt/C interface. It was noted the extracted thickness of 1 nm is greater than previously reported water layers at the Pt/ionomer interface, which suggested the water layer must be present at the ionomer/carbon interface also. This was further confirmed by the observation of a water layer in CV-SANS scattering functions of catalyst layers containing no Pt. It was revealed the volume of the condensed water particles was greater for the HSAC support than Vulcan, which was attributed to the ability of water to penetrate the porous structure through capillary action, supporting the idea that water acts as a proton conducting electrolyte for Pt located inside the porous structure.

These studies show the impressive amount of detail that can be extracted with regards to the Pt/C-ionomer interface using catalyst layers, and the variation that can be observed when the composition is adjusted.

SANS also proved to be an appealing technique in monitoring water distribution throughout the catalyst layer. Lee et al.[65] performed an operando study using high-resolution SANS to monitor liquid water saturation and ionomer swelling in the anode, cathode and proton-exchange membrane with varying current densities at ambient temperature. In each region, it was found ionomer hydration increased when the fuel cell was operated at relatively low current densities of 150 mA/cm^2, however the greatest increase in water uptake by the ionomer was observed in the cathode, which could be directly linked to increased water volume fraction in the cathode due to its generation by the ORR.

Martinez et al.[66] performed combined operando high resolution SANS and neutron imaging in order to correlate water movement on the millimetre scale, at the rib-channel level, and water distribution in the membrane at the sub-millimetre scale. Results show no direct correlation, with water accumulation observed at the channel/rib interface, however a smooth hydration of the membrane throughout operation. Such behaviour was attributed to the complex water distribution, reliant on both the evaporation and condensation processes through operation, along with large in-plane and through-plane relative humidity gradients.

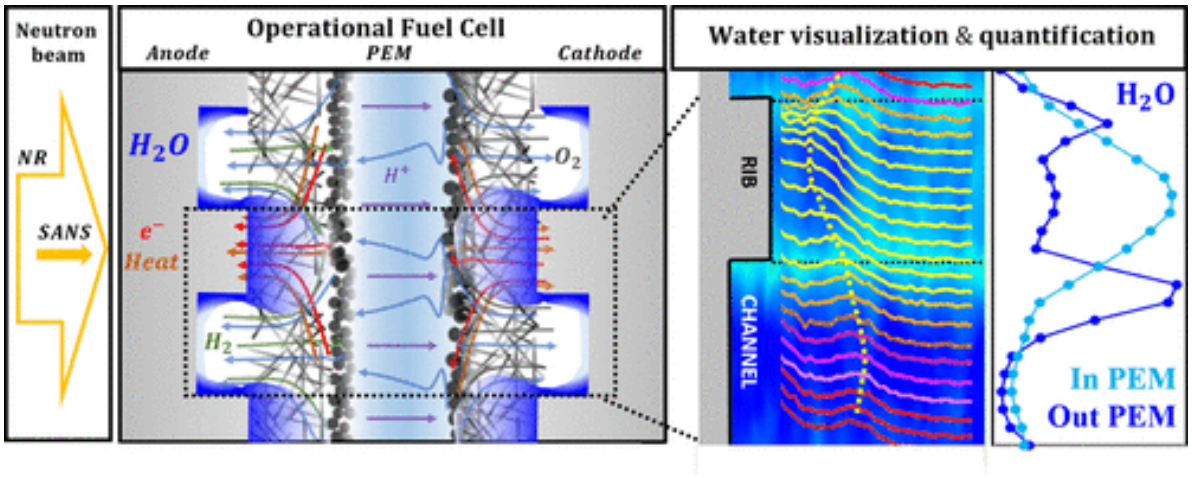


Figure 22. *Schematic of a PEM fuel cell cross-section, showing reactant movement throughout the cell, along with quantification of water content, and corresponding SANS data. All content of the figure falls under the copyright of the authors, as part of the work published by Martinez et al.[66]*

SANS is a very useful technique for the study of fuel cells. Initial catalyst layer structure can be characterized, along with its alteration with parameters such as hydration. Additionally, water distribution throughout the cell operation can be directly visualized, both with regards to the swelling of the ionomer component and liquid water presence. However, beamtime at neutron facilities is hard to come by, and acquiring each scattering function can take between few and tens of minutes. With measuring of samples at different contrasts and RH values, the number of scattering functions that has to be obtained per composition can become rather significant. In SAXS (small-angle X-ray scattering) high flux and beam energies mean the acquisition of data is a lot faster and beamtime at a synchrotron can be utilized much more efficiently. Nevertheless, the presence of Pt in the catalyst layer, which scatters very strongly in comparison to light elements that make up the carbon support and ionomer, means obtaining information on the latter components can be impeded. This is particularly the case for the ionomer, which shows scattering in a similar region to Pt.

Recently Toudret et al.[67] proposed a technique where scattering contributions related to the Pt can be modelled according to the known particle structure and polydispersity (from manufacturer and previous data), and directly removed from the overall scattering function of the catalyst layer. The successful application of this technique was confirmed by comparing resulting SAXS scattering functions of Pt/C based catalyst layers to those obtained for catalyst layers that contained a noble-metal free, transition metal based catalyst. Subsequently, water content of the catalyst layer was quantified at different RH conditions and with current density applied. It was noted the ionomer showed swelling behaviour comparable to that of the bulk membrane in both Pt/C and PGM based catalyst layers, suggesting aggregation and poor ionomer distribution. This may be related to the increased thickness of the catalyst layer and Pt loading that was required for the operando SAXS measurement. Swelling of the ionomer was noted with increasing RH, and current generation resulted in higher water content than observed at OCV in the 100% RH condition, suggesting generation of liquid water through the ORR. It was noted further work must be performed with

regards to quantification of water content in the catalyst layer and performing operando SAXS in real-life fuel cell operating conditions, however, the proposed method of negating Pt scattering opens doors for catalyst layer characterization using SAXS.

On the other hand, because of the strong scattering from Pt, SAXS remains a very useful method for the study of real time evolution of the catalyst nanoparticle structure during fuel cell operation. Martens et al.[68] coupled in-situ SAXS and X-ray diffraction (XRD) measurements to evaluate Pt structural changes during accelerated stress testing. XRD revealed information on the size of the Pt crystallite itself, while SAXS allowed for evaluation of the inter-particle interaction. The study performed on a commercial MEA, containing Pt/C with 60 wt% Pt loading and Nafion, shows progressively different processes occur with increasing number of cycles. Firstly, Pt aggregation was observed within 100 cycles, where the individual Pt crystallite size could be determined by XRD and the size of the aggregate by SAXS. Next, after 900 cycles, coalescence of aggregates was observed through an increasing crystallite size. Lastly, after 5000 cycles, Ostwald ripening was determined, where the crystallite size observed via XRD was equivalent to the particle size measured in SAXS.

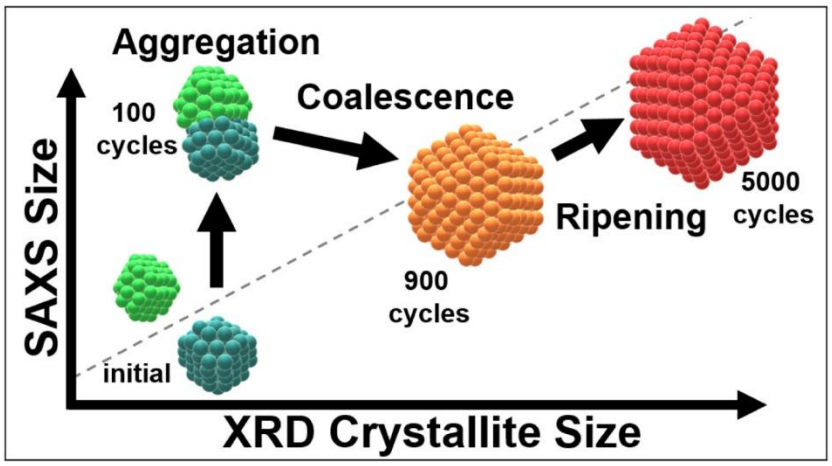


Figure 23. *Schematic showing Pt nanoparticle structural changes throughout MEA operation, as reported by Martens et al.[68] using coupled in-situ SAXS and XRD methods. All content of the figure falls under the copyright of the authors, as part of the work published by Martens et al.[68]*

Schröder et al.[69] combined operando small- and wide-angle X-ray scattering (SAXS/WAXS) in grazing-incidence configuration to study a bimodal catalyst degradation during accelerated stress tests. The bimodal catalyst was composed of a mixture of Pt/HSAC with 20 wt% and 50 wt% Pt loading, in order to investigate the Ostwald ripening degradation mechanism in bigger and smaller particle size populations. It was found that instead of the expected electrochemical Ostwald ripening, where larger Pt particles grow at the expense of smaller ones through formation of ionic metal species, Ostwald ripening occurred via local diffusion of Pt atoms. Moreover, the grazing incidence mode applied allowed for depth dependent degradation evaluation. Contrasting behaviours were observed at the electrolyte-catalyst layer interface, where the fraction of the smaller particle population decreases, suggesting preferential dissolution of smaller Pt particles, and deeper in the catalyst layer, where the fraction of the smaller particle population was seen to increase, suggesting greater degradation of bigger particles.

The research presented above demonstrates the power of the SAS techniques, for initial structural characterization as well as structural alteration with time. Nevertheless, characterization of catalyst inks remains crucial for developing improved protocols for optimization of the catalyst layer structure to begin with.

1.4.2 SAS of catalyst inks

Because of the solvent based nature of catalyst inks, CV-SANS is the only viable experimental method for direct characterization of the ionomer structure in the ink. Over the years, a handful of CV-SANS studies on the catalyst inks have been performed, with the Pt/C and ionomer structure evaluated using extraction of partial scattering functions (as described in section 1.4.1).

Shibayama et al.[70] used CV-SANS along with CV-FSANS (focusing SANS) to extended the size scale probed up to several hundred nm, allowing extraction of a full catalyst ink structural model. The ink composition was based on commercial Vulcan carbon (no Pt), that was synthesized into Pt/Vulcan with approximately 50 wt% loading using a chloroplatinic precursor, and ionomer-A, which was noted to have a similar structure to Nafion with EW = 1000 g/mol SO_3^-. The I/C ratio was approximately 0.5. The solvent used in the ink composition consisted of water only. Analysis of the PSF related to the carbon structure, fitted with a sphere model, revealed carbon aggregates of 57 nm radius. The cross-term, characterizing the carbon-ionomer interface, was fitted with a model based on the core-shell scattering amplitude, revealing an 8 nm thick ionomer layer on the Pt/C aggregates. The PSF related to the ionomer structure consisted of contributions from the adsorbed ionomer in the shell, as well as unadsorbed ionomer in the dispersion. The unadsorbed ionomer contribution was fitted using a scattering function for weakly charged polyelectrolyte solutions proposed by Borue-Erkhimovich, from which a percolated ionomer network was extracted, including ionic clusters of approximately 0.2-1 nm in diameter, separated by a distance of 15.7 nm.

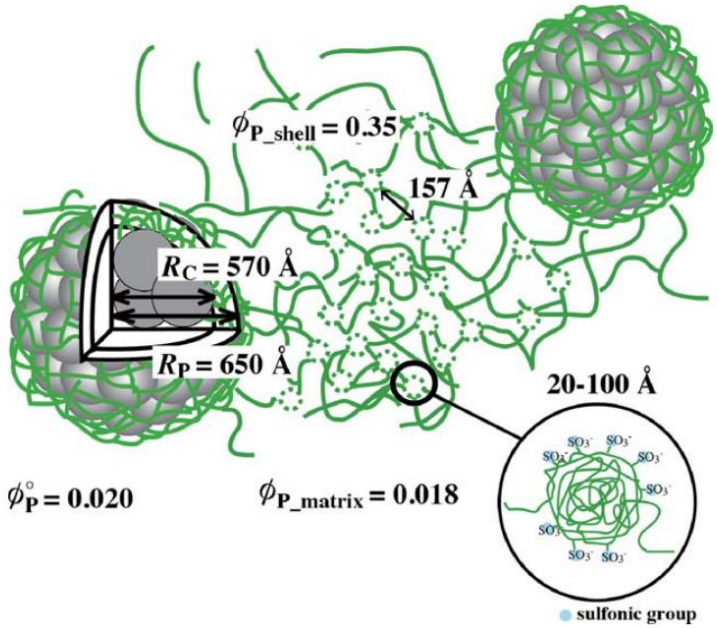


Figure 24. *Schematic of a catalyst ink structure, as proposed by Shibayama et al.[70], who used the CV-SANS method in their work. All content of the figure falls under the copyright of the authors, as part of the work published by Shibayama et al.[70]*

Yoshimune et al. investigated both the effects of I/C ratio[31] and Pt loading[38] on the catalyst ink structure using CV-SANS. The studies are discussed in detail in sections 1.3.2 and 1.3.3. In summary, it was shown the thickness of the ionomer shell does not change with increasing I/C, however it becomes denser. Moreover, with increasing I/C a significant increase in the amount of unadsorbed ionomer in the dispersion was observed, suggesting this parameter does not impact greatly the degree of ionomer adsorption. Lower Pt loadings of 30 wt% resulted in thinner and denser ionomer layers, and conversely, thicker and less dense ionomer layers were extracted for higher Pt loading of 50 wt%. Calculation of Gibbs free energy of adsorption suggested the ionomer has a slightly preferential interaction to the carbon via the hydrophobic

backbone, therefore when the Pt-Pt inter-particle distance increases, more carbon surface is present for the ionomer backbone to interact with.

Balu et al.[47] used CV-SANS in tandem with CV-USANS (ultra-small angle neutron scattering), to again extend the size scale that can be probed by the technique. The effect of alcohol concentration on the catalyst ink structure was investigated, and it was found water-rich solvents yield smaller aggregates and thinner ionomer layers. Note in this study partial scattering functions were not extracted, but instead several scattering functions were fitted with the Guinier-Porod and cylinder models.

Just like in the case of catalyst layers, the presence of Pt makes X-ray scattering difficult to apply to the study of the structure of catalyst inks, predominantly with regards to the evaluation of the ionomer component. Nevertheless, the quick data acquisition time arising from the nature of the X-ray beam makes USAXS (ultra-small-angle X-ray scattering) ideal for time resolved monitoring of the ink drying process, particularly with regards to the change in Pt/C aggregation structure.

Koga et al.[71] utilized time resolved Grazing-Incidence X-ray Scattering (GISAXS) to probe a 100 µm thick catalyst ink coated on a silicon wafer. The ink was composed of Pt/HSAC with 50 wt% Pt loading, Nafion ionomer with I/C = 1.0 and a 50:50 wt% 1-PrOH/water solvent. The time taken for the drying process to finish was first investigated by time-resolved ATR-FT-IR, noting the time taken for peaks associated with H_2O and 1-PrOH to disappear. Furthermore, gravimetric analysis was employed, evaluating the time taken for the entire mass associated with the solvent to be removed from the ink. The two methods showed the ink was completely dry after 1600s. On the other hand, evaluation of the GI-SAXS scattering functions obtained every 1 second showed no further change in the scattering intensity at low Q magnitudes associated with increasing Pt/C aggregate size after 250s. These results suggested the Pt/C aggregation process terminates very quickly into the drying process.

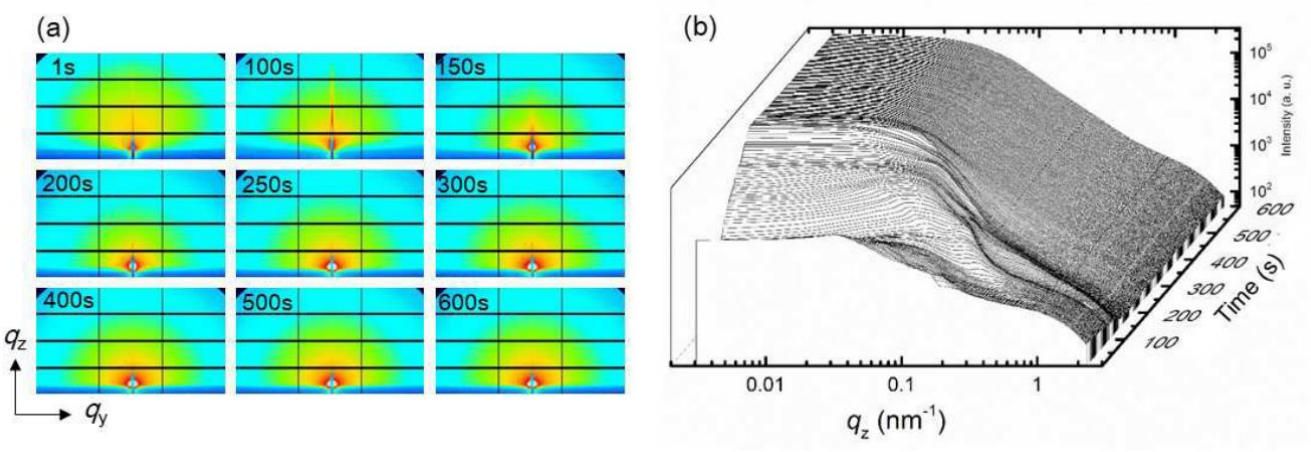


Figure 25. (a) *selected 2D GISAXS patterns,* ***(b)*** *Vertical off-centre line cuts of 2D patterns obtained for a coated catalyst ink sample during drying, plotted in a 3D format as a function of time. All content of the figure falls under the copyright of the authors, as part of the work published by Koga et al.[71]*

Hasegawa et al.[44] used time-resolved USAXS to evaluate the effect of including a small concentration of a high boiling point solvent in the ink composition on the Pt/C aggregation during the drying process (refer to section 1.3.4 for in depth discussion of the results). It was shown this variation resulted in a more gradual Pt/C aggregation process, in comparison to a conventional ink composition based on EtOH/water only. Note for the latter, the aggregation process seemed to also terminate fairly fast into the drying process – after 14 min the scattering functions acquired showed no further change in aggregate size, although the

drying process lasted 60 minutes. Note the variation in ink drying speeds between the two studies may be dependent on the layer thickness as well as drying conditions utilized.

Overall, SAS has been shown to hold great potential in acquiring precise structural information with regards to each component found in the catalyst layer and catalyst ink. CV-SANS can be used to interpret the ionomer structure, both as an adsorbed ionomer shell and unadsorbed ionomer, in catalyst ink and layer systems. SAXS and WAXS can be utilized to study the structure of the Pt specifically. Time resolved USAXS yields information on the Pt/C aggregation process during ink drying. Nevertheless, the use of SAS to study PEMFC electrodes can be considered a niche, with comparably little amount of studies performed in comparison to other techniques. This is particularly the case with regards to the catalyst ink system, where only a handful of published work can be found, performed by a few groups across the world. Indeed, beamtime at large scale facilities is hard to come by, however, the information gained from such experiments is priceless.

1.5 Conclusions

Chapter 1 gave an introduction to the motivation of the PhD project communicated in this manuscript. Large scale commercialization of FCEVs, a zero-emission transportation alternative, requires progress in performance, cost and durability of the cathode catalyst layer. In particular, this involves reducing proton and oxygen transport by tailoring a thin, uniform catalyst layer, optimizing access to Pt active sites by reducing Pt/C aggregation, maximizing the ORR rate.

However, the catalyst layer is a very complex, heterogeneous structure, with a large number of parameters that can be altered including choice of carbon support, ionomer type or Pt loading. The inter-play between these components is not well understood, or how they are affected by the component variation. To add to this, the same problem is present in the case of catalyst inks used to manufacture the catalyst layer – it is not well understood to what extent the structure of the ink itself affects that of the final layer obtained, nor how compositional variations alter said structures.

Many methods including electrochemical characterization, molecular dynamics simulations, rheology, microscopy, SAS, DLS, ITC and others have been employed in the study of both catalyst layer and catalyst ink structures. In particular, CV-SANS shows great promise due to its unique contrast properties, allowing for simplification of bulk scattering from complex systems. In the case of the catalyst ink/layer this means the ionomer structure, which is known to have a great effect on the ORR rate, can be directly characterized.

Nevertheless, although many studies have been performed investigating the impact of ionomer EW, carbon support, dispersion solvent, and more, each investigation has a different fixed composition, which has a direct impact on the variable investigated due to the complex nature of inter-component interactions. Because of this, building a fundamental understanding of the inter-component interactions that would aid in developing an optimization procedure for the electrode is impossible. As an example, table 1 presents some ink compositions used throughout the studies presented in this chapter.

Authors	Variable	Pt/C	Ionomer	Solvent
Balu et al.[47]	Alcohol concentration	Pt/Vulcan, 40 wt% Pt loading	Nafion (EW = 1100) I/C = 0.7	iPrOH/water
Li et al.[53]	Alcohol concentration	Pt/GC, 60 wt% Pt loading	Nafion (EW = 1000) I/C = 0.1	iPrOH/water
Orfanidi et al.[62]	Alcohol concentration/type	Pt/HSAC, 50 wt% Pt loading	PFSA (EW = 700) I/C = 0.65	iPrOH/water 1-PrOH/water
Ren et al.[63]	Alcohol concentration	Pt/C (Johnson Matthey), 40 wt% Pt loading	Nafion (EW = 1000) I/C = 0.65	iPrOH/water
Chabot et al.[46]	Carbon support	Pt/HSAC, Pt/Vulcan, 50 wt% Pt loading	Nafion (EW = 1000) I/C = 0.67-0.8	DAA/water 60:40 vol%
Khandavalli et al.[25]	Carbon support + I/C ratio	HSAC, Vulcan, Pt/HSAC, Pt/Vulcan, 50 wt% Pt loading	Nafion (EW = 1000)	1-PrOH/water 75:25 wt%
Yakovlev et al.[54]	I/C ratio	Pt/Vulcan, 40 wt% Pt loading	Nafion (EW = 1000)	iPrOH/acetone 50:50 wt%
Yoshimune et al.[31]	I/C ratio	Pt/Vulcan, 30 wt% Pt loading	Nafion (EW = 1000)	EtOH/water 35:65 wt%
Thoma et al.[59]	Ionomer EW	Vulcan	Aquivion,	water
Yoshimune et al.[38]	Pt loading	Pt/HSAC	Nafion (EW = 1000) I/C = 0.75	EtOH/water 30:70 wt%

Table 1. *List of ink compositions used in various studies discussed in chapter 1. Note EW units are g/mol SO_3^-.*

The comparison suggests Nafion with EW = 1000 g/mol SO_3^- is the most common ionomer chosen, found in the majority of compositions. Interestingly, the I/C ratio used is also fairly consistent. On the other hand, the solvent choices are quite varied. iPrOH remains the most common alcohol of choice, yet the concentration used varies throughout. Vulcan and HSAC are supports mostly noted, however the Pt loading is different throughout. Most worryingly, the solvent composition and carbon support variation may lead to great discrepancies between results obtained. Indeed, this was observed in studies investigating the alcohol concentration in the ink solvent, where some works suggested improved performance when alcohol concentration was low,[62, 63] while others when it was high.[47, 53] This could perhaps be linked to the specific choice of carbon support, and most definitely to the ionomer and I/C.

Such compositional variations highlight the need for a methodical study, where the effect of each component is investigated, and inter-component correlation effects can be distinguished. Therefore, the objective of this work is to undertake such an endeavour with regards to the catalyst ink structure, which is the first step towards electrode manufacturing, and therefore must be the commencement in building a full picture of composition-structure-performance relation. The variables investigated in this work will be many, including effect of carbon support, ionomer type, solvent system, I/C ratio, and effect of Pt, all altered systematically. The method of choice is CV-SANS due to its unique ability to obtain direct characterization of the ionomer – one of the least understood ink components so far. In addition, the variable that is shown to have the biggest impact on the ink structure will also be investigated with regards to catalyst layer structure using the SANS method. Moreover, for the same variable, structural alteration observed will be correlated to electrochemical performance, allowing for a full composition-structure-performance impact overview.

2. Small-Angle Neutron Scattering

This chapter focuses on the technique of small-angle neutron scattering (SANS), and its use in tandem with the contrast variation (CV) method to study the structural variation of the catalyst ink system as a function of ink composition, as well as investigation of catalyst layer structure using SANS measurements in an environment with controlled relative humidity (RH).

In **section 2.1** an overview of SANS theory is presented – how neutrons interact with matter to begin with, what a typical SANS experiment looks like, and what advantages do neutrons pose for the study of the catalyst ink/catalyst layer systems. An insight will be also given into data processing after the data has been acquired.

The aim of this section is to provide a sufficient background in neutron scattering theory to allow for a comprehensive evaluation of results presented further in this work. For this reason, the theory given will be specific to SANS, particularly when the method is applied to study soft-matter, liquid based samples. For a more general, but also detailed overview of neutron scattering theory, please refer to the variety of literature published on the subject matter.

Section 2.2 will delve into the more specialized contrast variation approach that can be applied to SANS. The theory of contrast variation will be explained, along with the principle of contrast matching, after which the concept of partial scattering functions (PSFs) will be introduced. An in-depth study of the PSF method has been performed, detailing the effects of various method inputs on extracted PSF outputs. This investigation mainly considers simulated datasets, but some comparison to experimental data is also made.

Section 2.3 presents experimental results acquired for catalyst inks using CV-SANS, and corresponding PSF outputs extracted. Sample preparation methodology is presented, followed by discussion of contrast match measurements acquired for the carbon and ionomer components. In the case of the ionomer component, a brief analysis of the aggregate structure as function of iPrOH concentration in the solvent system is also performed. Results acquired for catalyst inks follow, with a detailed discussion of structural variation as a function of ink composition.

Section 2.4 focuses on SANS measurements of several catalyst layer powder samples at different RH values. The catalyst layers are manufactured from inks based on two Pt/C complexes, as well as with varying iPrOH concentration in the ink solvent composition. Results are discussed, with emphasis placed on the ionomer hydration with increasing water content. Comparisons of catalyst layers based on the same Pt/C complex, but manufactured from inks with varying solvent systems, and vice-versa, are performed.

Ce chapitre se concentre sur la technique de diffusion de neutrons aux petits angles (SANS) et son utilisation en tandem avec la méthode de variation de contraste (CV) pour étudier la variation structurelle du système d'encre catalytique en fonction de la composition de l'encre, ainsi que l'étude de la structure de la couche catalytique à l'aide de mesures SANS dans un environnement à humidité relative (HR) contrôlée.

*La **section 2.1** présente un aperçu de la théorie SANS : comment les neutrons interagissent avec la matière, à quoi ressemble une expérience SANS typique et quels avantages les neutrons présentent pour l'étude des systèmes encre catalytique/couche catalytique. Un aperçu du traitement des données après leur acquisition sera également donné.*

L'objectif de cette section est de fournir un contexte suffisant en matière de théorie de la diffusion des neutrons pour permettre une évaluation complète des résultats présentés plus loin dans ce travail. Pour cette raison, la théorie donnée sera spécifique au SANS, en particulier lorsque la méthode est appliquée à l'étude d'échantillons de matière molle à base liquide. Pour un aperçu plus général, mais également détaillé de la théorie de la diffusion des neutrons, veuillez-vous référer à la variété de la littérature publiée sur le sujet.

*La **section 2.2** traitera de l'approche de variation de contraste plus spécialisée qui peut être appliquée au SANS. La théorie de la variation de contraste sera expliquée, ainsi que le principe de l'appariement de contraste, après quoi le concept de fonctions de diffusion partielle (PSF) sera introduit. Une étude approfondie de la méthode PSF a été réalisée, détaillant les effets de diverses entrées de méthode sur les sorties PSF extraites. Cette étude porte principalement sur des ensembles de données simulées, mais certaines comparaisons avec des données expérimentales sont également effectuées.*

*La **section 2.3** présente les résultats expérimentaux obtenus pour les encres catalytiques à l'aide de CV-SANS et les sorties PSF correspondantes extraites. La méthodologie de préparation des échantillons est présentée, suivie d'une discussion des mesures de contraste acquises pour les composants carbone et ionomère. Dans le cas du composant ionomère, une brève analyse de la structure agrégée en fonction de la concentration en iPrOH dans le système solvant est également effectuée. Les résultats acquis pour les encres catalytiques suivent, avec une discussion détaillée de la variation structurelle en fonction de la composition de l'encre.*

*La **section 2.4** se concentre sur les mesures SANS de plusieurs échantillons de poudre de couche de catalyseur à différentes valeurs d'humidité relative. Les couches de catalyseur sont fabriquées à partir d'encres à base de deux complexes Pt/C, ainsi qu'avec une concentration variable d'iPrOH dans la composition du solvant de l'encre. Les résultats sont discutés, en mettant l'accent sur l'hydratation de l'ionomère avec l'augmentation de la teneur en eau. Des comparaisons de couches de catalyseur basées sur le même complexe Pt/C, mais fabriquées à partir d'encres avec différents systèmes de solvants, et vice-versa, sont effectuées.*

2.1 SANS theory

Neutrons are uncharged subatomic particles that are found inside every atomic nucleus. With a mass comparable to protons, however almost 2000 times bigger than that of an electron, neutrons, along with protons, make up almost the whole mass of the atomic nuclei.[72, 73] The discovery of the neutron is attributed to James Chadwick in 1932,[74] after which further research demonstrated that the particle-wave properties of the neutron, which follows the laws of quantum physics, can be exploited for the structural study of materials on a wide scale of size domains.

Because of their particle-wave duality, neutrons are able to interact with nuclei of matter, and yield coherent wave scattering that can be utilized to obtain structural information on a large variety of materials and length scales, from atomic sizes to objects on the micrometre scale.[74] In a typical scattering experiment at a reactor-based facility, a sample is placed in the way of an incident neutron beam, that is a planar monochromatic wave of wavelength λ,[76] generated with the aid of mechanical wavelength selector and collimation set-up.

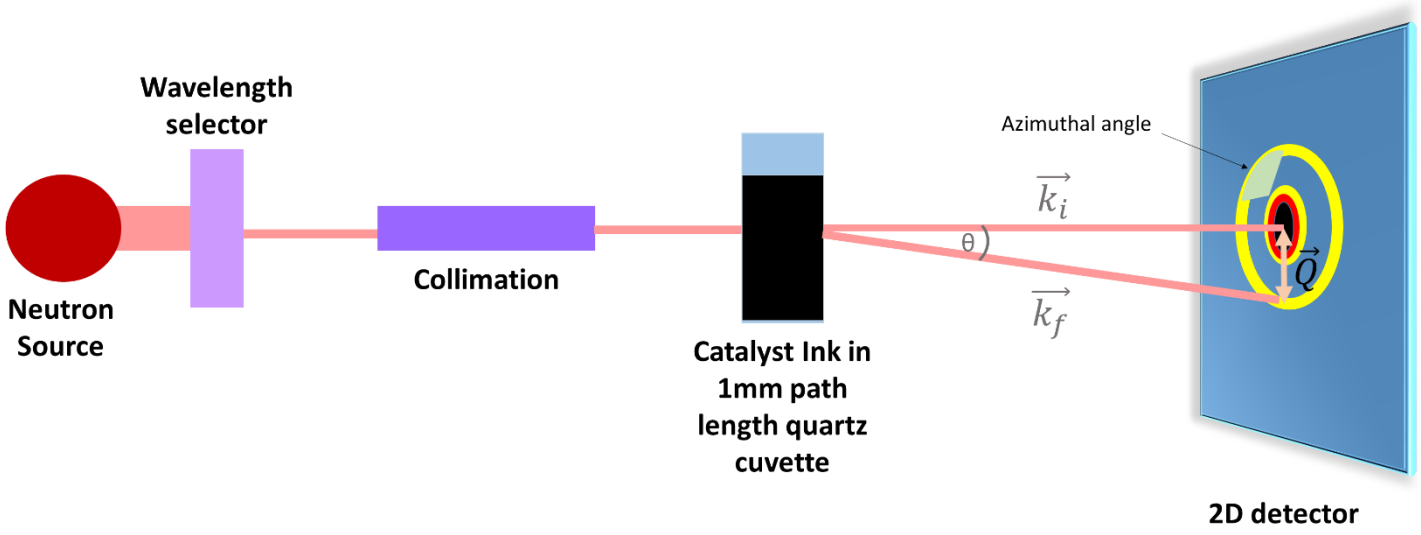


Figure 26. *A schematic of a small-angle neutron scattering experiment.*

The beam penetrates through a sample, where neutrons may interact with the nuclei of atoms, and in this instance are scattered away from their original trajectory through an angle *θ*. Both scattered neutrons, and those which didn't participate in scattering events (and therefore retain their original trajectory) are recorded on a 2D detector, which is located inside a vacuum chamber at a certain distance from the sample. When looking to the atomic scale of a crystalline material, the angle of scattering can be related to the atomic spacing in a lattice, *d*, by Bragg's law:

$$= 2 \quad ( ) \qquad (2.1.1)$$

Scattering from objects with the same *d* spacing will be coherent. Namely, the neutron beam waves will be in-phase with one another, resulting in constructive interference, and increased intensities recorded on the 2D detector due to increased wave amplitude. On the other hand, if the *d* spacing of objects is not consistent (i.e. if the scattteres are not alike), the neutron beam waves will be out of phase, yielding destructive interference and diminished wave amplitudes.

Outside of the atomic scale however, lattices are not generally considered, but rather alike scatterers separated by an equal distance from each other, from which coherent scattering can again be recorded.

In small angle neutron scattering (SANS) objects in the size range of one to few hundred nm are investigated, the name arising from the fact that larger objects cause neutron scattering through smaller angles θ. However, in SANS rather than using θ to describe the scattering event, a property known as the wavevector transfer, Q, is used instead.

Consider a scattering event where a neutron with an initial wavevector k_i and energy E_i is scattered through the angle 2θ into a final wavevector k_f (figure 26) and energy E_f[77]:

$$= \quad - \tag{2.1.2}$$

$$\omega = \quad - \tag{2.1.3}$$

Where ω = energy transfer

Most commonly in small angle neutron scattering it is assumed that there is no energy transfer between the neutrons and nuclei, making it an elastic process, and therefore:

$$| \quad | = | \quad | = \tag{2.1.4}$$

Nevertheless, note inelastic neutron scattering ($| \quad | \neq | \quad |$) can also be utilized to obtain information on particle movement. However, as this method is not relevant to the work in question, it will not be discussed further.

With the elastic scattering assumption, the scattering triangle (figure 26) can now be considered an isosceles[77] and the wavevector transfer related to the angle of scattering:

$$= 2 \qquad (\frac{}{2}) \; = \frac{4}{} \sin (\frac{}{2}) \tag{2.1.5}$$

allowing to link the wavevector transfer to the scattering angle and neutron wavelength. Unlike θ, Q relates to distance in a reciprocal, or Fourier space.[78] The larger the size of the object that the neutrons are scattered from, the lower the magnitude of Q that needs to be achieved to probed the size of such object.

SANS can be used for the study of soft matter such as dispersions, colloids, proteins etc., where molecules in a sample have different orientations. In such cases the scattering from the material is isotropic, observed as a ring of coherent scattering of equivalent intensity recorded on the detector for a given magnitude of Q. In such a case, integration over the azimuthal angle is possible (figure 26), yielding scattering intensity for a specific Q value.

Scattering events, and arising scattering intensity measured on a 2D detector, can be described in terms of the scattering cross-section, σ. The total scattering cross-section, σ_s, describes the probability of a neutron to be scattered by a scatterer per second[79,80]:

$$= \quad \text{———————————————} \tag{2.1.6}$$

The higher the scattering cross-section the more likely a scattering event is to occur. This ‘size’ of the cross-section is dependent on an inherent property of nuclei, known as the scattering length, b, which describes

the effective range of the nuclear potential, and also depends on the spin-state of the neutron-nucleus system.[77] Note that the scattering length can be both a positive or a negative number, and is different for every elemental isotope. In SANS, as the size scale probed is much bigger than that of a single atom, a 'small angle approximation' must be made. Therefore, bearing in mind molecules that can be probed on the corresponding Q scale, instead of atoms, the scattering length density (SLD) must be considered[81]:

$$= \frac{\sum_{=1}}{} = \frac{\sum_{=1}}{\sum_{=1}} \quad (2.1.7)$$

$\sum_{=1}$ represents the summation of all scattering length contributions for all atoms in the molecule (units of fm), V_m is the molecular volume (cm^3) which can be expressed in terms of bulk density, ρ (g/cm^3), the Avogadro number (N_a) and a summation of the molecular masses, M_i (g/mol^{-1}), of all the atoms in the molecule.

As mentioned above, the scattering events are recorded in a reciprocal, or Fourier space. The scattering intensity measured can be linked to the differential scattering cross section[76]:

$$( ) = \frac{\sum}{}( ) = \sum \sum \quad (\cdot(-) \quad (2.1.8)$$

The differential scattering cross section, $\frac{\sum}{}( )$, described the probability of finding atoms with coherent lengths b_i and b_i separated by a vector $-$.

Subsequently, for particles dispersed in a matrix (e.g. solvent), scattering intensity can be described as[82]:

$$\frac{\sum}{}( ) = (—) \ ^2\Delta \ ^2 \ ( ) \ ( ) + \quad (2.1.9)$$

where $\frac{\sum}{}( )$ is the scattering intensity at a specific magnitude of Q (cm^{-1}), which will also be noted as I(Q) throughout this work, (–) is the particle number density (cm^{-3}), V_p is the particle volume (cm^3), $\Delta\rho$ is the contrast factor (cm^{-2}), P(Q) is the particle form factor (cm^{-1}), and S(Q) is the particle structure factor (cm^{-1}).

I_{inc} is the incoherent scattering, which mainly arises from hydrogen scattering in the sample. It is independent of Q, and can be thought of as a constant 'noise' background. Total elastic scattering contains both of the coherent and incoherent contributions, however, in typical SANS experiments it is the coherent part that contains the information of interest:

The form factor, P(Q), contains structural information, such as the shape and size of the scatterer. Different form factor models exist, such as for a sphere, a cylinder or an ellipsoid, which can be fitted to the data in order to extract quantitative structural information on the molecule in question.

The structure factor, S(Q), describes the average inter-particle distances, and therefore is present in the case of concentrated systems. For dilute system, where particles are assumed to not interact with each other, S(Q) = 1.

The contrast factor, $\Delta\rho$ is the difference between the SLD of the scatterer and the SLD of the dispersing medium (solvent, buffer, etc.). A more detailed discussion on the contrast term can be found in section 2.2.

2.1.1 Experimental Considerations – Setting up the Measurement Configuration

SANS theoretically allows for measurement of a Q range that probes object sizes between one and a few hundred nm. The Q range measured can be altered by adjusting the detector distance from the sample as well as neutron beam wavelength. The further the detector is placed from the sample, the lower the magnitude of Q probed. Increasing the Q range is also a trade-off between resolution of the measurement, therefore in certain cases, such as weakly scattering samples, improving the signal to noise ratio (measurement statistics) may be preferable. This is achieved by increasing neutron flux, and subsequently decreasing the detector distance from sample.

2.1.2 Experimental Considerations – Data Processing

The most common way to visualize SANS data is in a 1D profile of scattering intensity as a function of Q. In order to obtain such a format, the measurement collected on a 2D detector undergoes a process known as reduction. In this step several corrections, for example the solid angle correction that accounts for geometrical differences between the spherical scattering and the flat detector, are introduced.[82] Another part of the reduction process involves rescaling the measured scattering intensity to an absolute scale, allowing for a comparison of measurements performed during different experiments and/or at different facilities.

Such corrections yield a scaled scattering intensity corresponding to the sample. However, scattering from the cell that the sample is present in (e.g. quartz cuvette) is also taken into consideration. Therefore, by obtaining a SANS measurement of the empty cell, a step can be applied into the reduction process to account for the transmission as well as to remove scattering arising from the cell itself, leaving a scattering function that corresponds to the sample only.[83]

In this instance the reduction process can be described by:

$$( ) = \frac{1}{}[-] - \frac{1}{}[-] \tag{2.1.10}$$

$$\frac{\sum}{}( ) = \frac{( )}{_0( )} \tag{2.1.11}$$

Where $I_s(Q)$ = scattering intensity arising from the sample only, T_s = sample transmission, T_e = empty cell transmission, I_e = scattering intensity arising from the empty cell, I_{cd} = 'electronic' background

$\frac{\sum}{}( )$ = scattering intensity on absolute scale, $I_0(\lambda)$ = empty beam transmission measurement, d = sample thickness, Ω = solid angle that subtends a detector cell.[82]

After all the corrections have been applied, azimuthal radial integration of the isotropic, scaled, scattering intensity can be performed to convert the 2D signal into a 1D profile of scattering intensity as a function of Q.

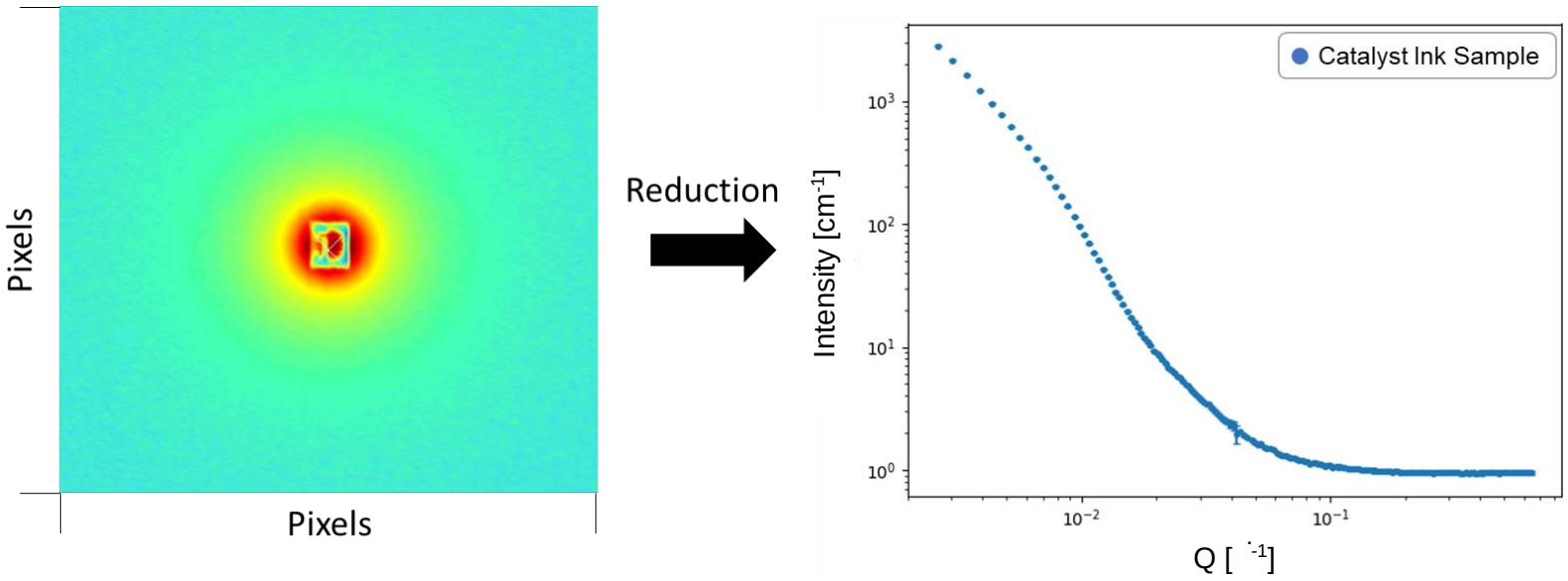


Figure 27. *Visual representation of the reduction process - converting data recorded on a 2D detector into a 1D profile of scattering intensity as a function of wavevector transfer, Q.*

Before data analysis, a data processing step must be applied, which involves removal of incoherent scattering, arising from hydrogen present in the samples as well as the dispersion medium.

Incoherent scattering is a flat, Q-independent background (equation 2.1.9).[82] If a plot of $I(Q)Q^4$ vs Q^4 shows linear behaviour in the asymptotic region ($Q>0.2$ $^{-1}$), a linear fit can be performed to $IQ^4 = A + BQ^4$ where B is the magnitude of incoherent scattering intensity.[84,85] In the case of dilute samples, another approach for removal of incoherent scattering is to measure reference data of the dispersion medium (i.e. solvent), which will contain the incoherent scattering contributions, and subtract it directly from the data scattering signal. A benefit of this approach is that, if any artefacts in the scattering arising from instrumentation are present, they will also be negated.

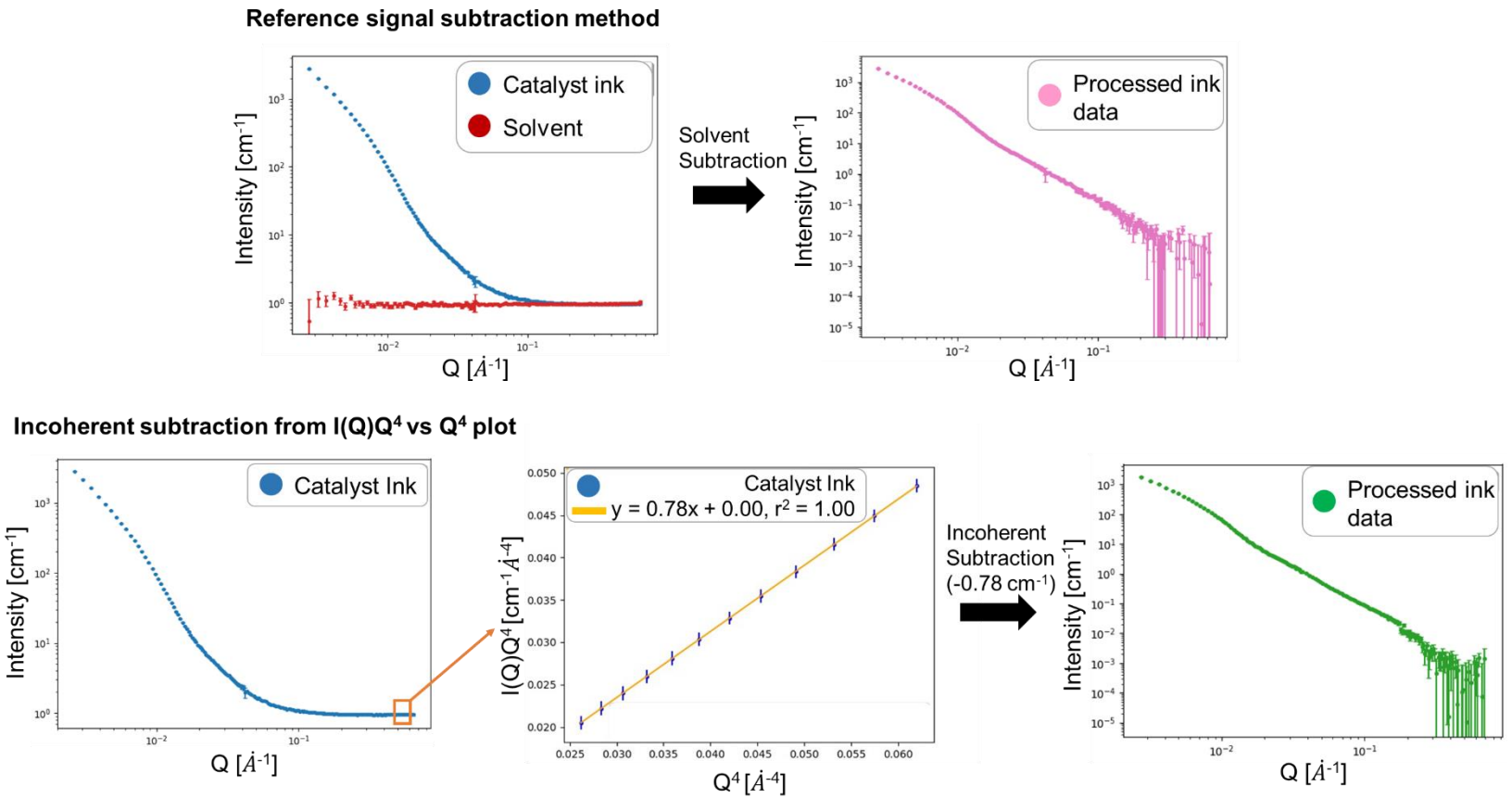


Figure 28. *Example of processing methods used to remove incoherent scattering from SANS 1D scattering function. Ink sample composition included 1 wt% high surface area carbon (HSAC), nafion D2020 with I/C = 0.8, 25:75 wt% iPrOH/water solvent (20 wt% deuterated).*

2.1.3 Advantages of SANS for catalyst ink/layer structural investigations

There are several features of neutron scattering as a technique which make it appealing for the study of catalyst ink/layer systems that must be highlighted.

Firstly, because the neutron-nuclei interactions happen on a very short range of the order 10^{-15} m (1 fm), the probability of scattering is quite low, meaning the neutron has to penetrate fairly deep into the sample before scattering occurs. For this reason, neutron scattering is a technique which probes the bulk of the sample, sampling a large volume and ignoring surface effects. Catalyst inks (and even more so catalyst layers) are highly heterogeneous systems, and therefore obtaining information on the bulk system is necessary. As an addition, it is worth noting that since neutron scattering is an elastic process with no energy transfer between neutrons and nuclei, the technique is non-destructive to the samples. On the other hand, the lower probability of neutron-nuclei interaction, as well as the inherently lower neutron flux, (compared to x-ray scattering for example) means that longer counting times are necessary in order to obtain a good signal-to-noise ratio.[75,77] However, as catalyst inks scatter quite strongly, the counting times in this specific case are very manageable, ranging from 5 to 10 minutes per sample. On the other hand, in the case of catalyst layers, longer counting times, of approximately 30 minutes per sample may be required.

Secondly, SANS specifically probes size ranges that are applicable to the catalyst ink/layer systems, and particularly to the ionomer component, both in terms of the molecule itself and the layer that it forms on the surface of the Pt/C complex, which fall in the few nm-tens of nm size domain. Therefore, in the case of the catalyst ink, information extractable from SANS will include the degree of adsorption of ionomer to carbon

as well as the layer thickness, the size of ionomer aggregates in solution, and the size distribution of carbon primary particles.

Lastly, but most importantly, the large variation in scattering length between different atoms and elements can be exploited. Unlike in x-ray scattering, where the strength of interaction is dependent on the atomic number, and therefore rises across the periodic table, scattering length does not follow a specific trend. For example, in x-ray scattering light elements such as carbon scatter quite weakly in comparison to elements such as Pt. As a result, Pt/C containing inks would be rather difficult to study with x-rays, as the scattering form Pt would heavily mask scattering arising from the ionomer, which also consists of light elements and shows scattering in a similar Q range, due to comparable size domains. However, in neutron scattering carbon and Pt have quite similar theoretical scattering lengths, 6.67 and 6.36 $x10^{10}$ cm^{-2} respectively, despite the large variation in atomic number. As Pt has a very small volume fraction in comparison to carbon in the catalyst ink system, scattering from Pt can be regarded as obsolete and scattering from carbon will dominate. In theory, this means that without the hindering from Pt in a similar size domain, the structure of the ionomer can be well defined, however, in practice this is not necessarily the case. Section 2.2 will delve deeper into this issue.

Additionally, scattering length variation in between isotopes means the contrast of the molecules in the system can be easily adjusted without altering the system properties by isotopic substitution. Most commonly this involves the replacement of protium (hydrogen-1), which has a scattering length of -3.74 fm, by deuterium, which has a contrastingly different scattering length of 6.67 fm. The substitution can occur either in the molecule itself, for example to highlight a specific part of a protein which one wishes to study, or by substitution in the background medium (partial or full deuteration of solvent). In both cases the contrast term, which relies on the difference between the SLD of the particle and background, is altered.

Above all, for a multi-component system such as the catalyst ink, this feature can be exploited to favour scattering from an individual component in the total scattering function, **making SANS the only experimental technique where the structure of the ionomer can be characterized directly.**

This method is known as contrast variation.

2.2 Contrast variation and partial scattering functions

2.2.1 Contrast variation

The scattering length differences between isotopes can be exploited to alter the contrast term, increasing or minimizing scattering from a desired system feature. The case of feature minimization, or even full exclusion from the scattering function (when the contrast term = 0), is known as contrast matching, and is achieved by adjusting the SLD of the dispersion medium (solvent, buffer etc.) to that of a desired component. In other words, the matched out component becomes effectively 'invisible' to neutrons. The SLD of the background can be adjusted by either partial or full deuteration, depending on the desired SLD. If one wishes to investigate several features of a complex, multi-component system, the contrast matching can be performed several times, a method known as contrast variation (CV).

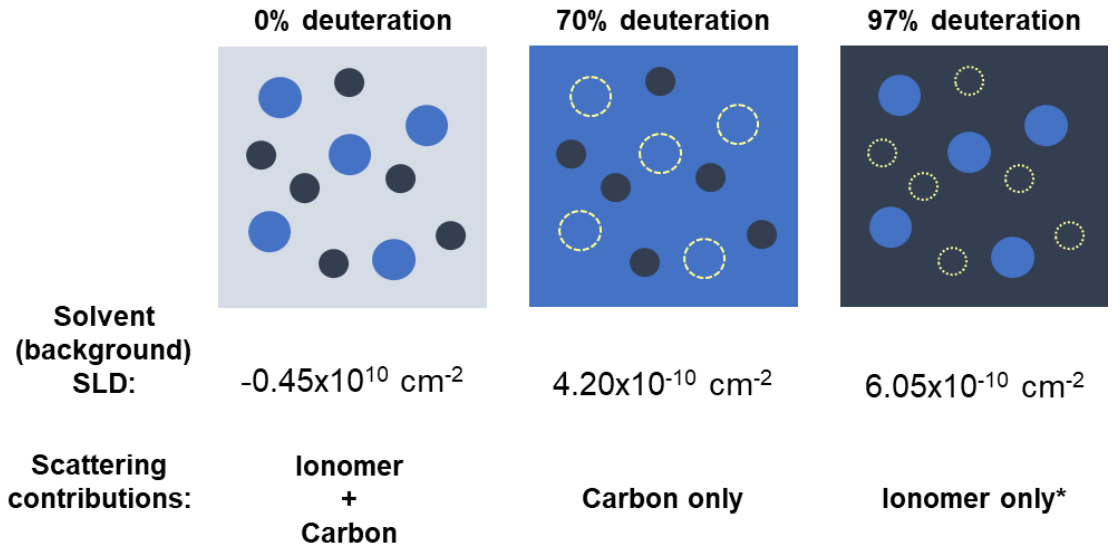


Figure 29. *Schematic of the contrast variation principle applied to the catalyst ink system. Blue spheres represent the ionomer. Dark navy spheres represent the carbon. The coloured box represents the background of the system (solvent). The SLD of the background is adjusted accordingly to the respective components, represented by a colour shift.*

For the ink solvent of choice in this work, comprising of a mixture of 50:50 wt% iPrOH and H_2O, the minimum obtainable SLD is approximately -0.45×10^{10} cm^{-2}, when no deuterated solvents are present. A solvent SLD matching that of the ionomer can be achieved by substituting approximately 70 wt% of the solvent with its deuterated alternative, consisting of iPrOH-d8 and D_2O. At maximum solvent deuteration a SLD of approximately 6.05×10^{10} cm^{-2} can be achieved. Note solvents containing different iPrOH concentrations are also considered, yet the range of SLD obtainable remains comparable.

However, the theoretical carbon SLD is 6.67×10^{10} cm^{-2}, meaning that the maximum SLD obtainable for the iPrOH/H_2O mixture solvent is too low to achieve a contrast match. The neutron scattering from the carbon can only be minimized. Additionally, it is important to note that because the ionomer utilized in this work is commercially available already pre-dispersed in hydrogenated solvents, 100% solvent deuteration is not easily achievable. Utilizing the as-purchased dispersion means a small contribution of hydrogenated solvents from the ionomer dispersion will be present, lowering the achievable SLD slightly. This effect will partially contribute to the inability to contrast match carbon. As carbon scatters neutrons very strongly, due to the high volume of scatterer (equation 2.1.9), this will impede the extraction of information on the ionomer component.

Therefore, in the case of the catalyst ink system, simple contrast variation, where one component is matched out in the scattering function, is not sufficient to extract all necessary details of the system. Indeed, the majority of the carbon structure consists of aggregates and agglomerates which are too large to be probed by SANS, therefore it is the scattering from the ionomer that is of particular interest – where information about the degree of adsorption onto the carbon and the nature of the ionomer layer can be extracted.

One approach to overcoming this obstacle is to decompose the contrast variation data set into partial scattering functions, which describe the scattering from each component individually.

2.2.2 Partial scattering functions

The total scattering intensity of a two component system (e.g. carbon and ionomer) can be expressed as contrast terms and partial scattering functions (PSF)[86]:

$$\sum(\ ) = \sum_{=2} (\Delta\ )^2 \quad (\ ) + 2 \sum_{<} \Delta\ \ \Delta \qquad (\ ) \tag{2.2.1}$$

Where $\Delta\rho_i$, $\Delta\rho_j$ are the contrast factors of component *i* and *j* respectively (in cm^{-2}), S_i is the partial scattering function of component *i* (and concurrently S_j is the PSF of component *j*), and S_{ij} is the cross term (units of cm^3). The defined partial scattering functions, S_i and S_j contain information on both intra- and inter- particle interactions, encompassing both the form and structure factors for each component. S_{ij}, the cross term, expresses correlations between components *i* and *j*.

Partial scattering functions can be extracted from contrast variation data, where the scattering intensities obtained for different contrasts yield a set of linear equations[70,86]:

$$\begin{pmatrix} {}_1(\ ) \\ \dots \\ (\ ) \end{pmatrix} = \begin{pmatrix} (\Delta\ {}_{,1})^2 & (\Delta\ {}_{,1})^2 & 2\Delta\ {}_{,1}\Delta\ {}_{,1} \\ \dots & \dots & \dots \\ (\Delta\ {}_{,})^2 & (\Delta\ {}_{,})^2 & 2\Delta\ {}_{,}\Delta\ {}_{,} \end{pmatrix} \begin{pmatrix} (\ ) \\ (\ ) \\ (\ ) \end{pmatrix} \tag{2.2.2}$$

Partial scattering functions can be obtained through a matrix manipulation approach where: $I_n(Q)$ are SANS scattering functions for n contrasts, $\Delta\rho_i$ is the contrast term resulting from the SLD difference between component *i* and solvent of SLD *n*, $(\rho_i - \rho_n)$, and $S_i(Q)$ is the partial scattering function of *i*. Note the contrast matrix is composed of the contrast term squared, $(\Delta\ )^2$, for terms related to the S_i and S_j output extracted, and $2\Delta\ \Delta$ for the cross-term, S_{ij}, corresponding to terms found in equation (2.2.1).

For x partial scattering functions to be extracted, at least x scattering functions of different contrasts are required. For a two component system x = 3. If x>3, the set of equations is overdetermined, and can be solved using a singular value decomposition algorithm, equivalent to a least squares fit.[86] Utilization of singular valued decomposition (SVD) allows for more precise determination of partial scattering functions by reducing statistical errors present in SANS scattering functions.[70] The choice of the contrast range and the number of experimental data also play an important role towards achieving a reliable output. These parameters will be discussed in more detail below.

Note, that even with the presence of Pt deposited on the carbon support, the ink system can be considered as two components, since the SLD of Pt (6.36×10^{10} cm^{-2}) and carbon (~6.67×10^{10} cm^{-2}) are very similar to one another, and therefore would be indistinguishable through this method. Therefore, the effect of Pt in the system can only be observed by changes induced with respect to the ionomer component, for example

through the degree of adsorption to the Pt/C complex, rather than as the Pt particle structure alone, which would not be altered in the ink system.

Figure 30. presents an example of the input parameters and subsequent output of the SVD-PSF extraction method:

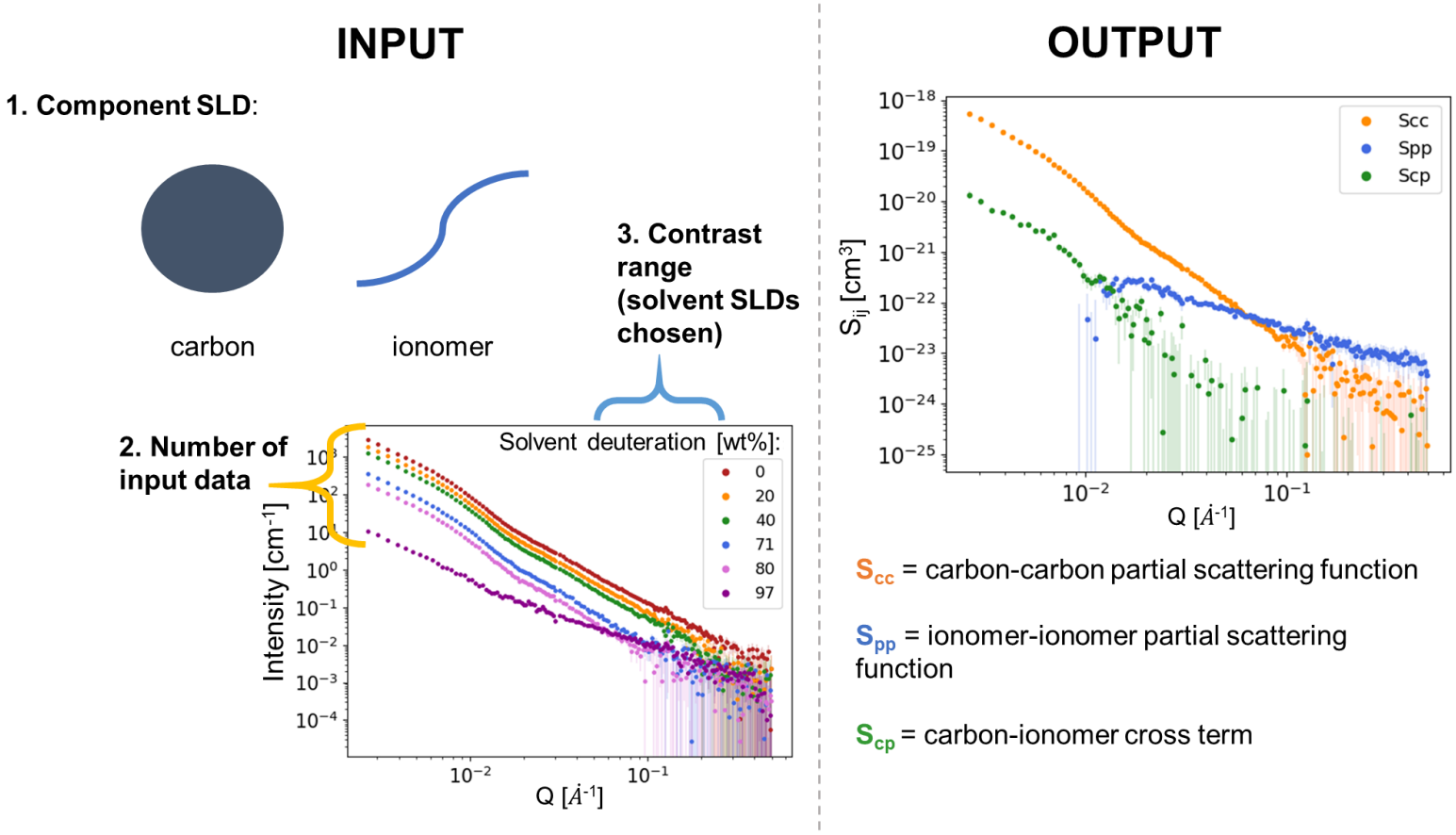


Figure 30. *Visualization of inputs to the PSF extraction method and the corresponding partial scattering function output. HNP is a catalyst ink series measured by CV-SANS in the scope of this work, which the PSF output corresponds to. HNP composition consists of 1 wt% HSAC, Nafion D2020 with I/C = 0.8, 50:50 wt% iPrOH/water solvent.*

Note the outputs are not plotted on an intensity (cm^{-1}) scale common to scattering functions, but rather on a partial scattering function scale, S_{ij} (cm^3). However, conversion between the two scales is facile, and involves multiplying the S_{ij} by the SLD squared, $(\Delta\rho)^2$, of the component that the PSF output relates to. As the cross-term relates to both the carbon and ionomer component, the scaling is slightly different, relying on $2\Delta\rho_c\Delta\rho_p$ instead. Multiple scattering functions, with varying solvent SLDs, are used to obtain partial scattering functions, however the 'solvent' SLD for PSFs is that of vacuum, 0 cm^{-2}. Therefore, $\Delta\rho$ can be simplified to ρ, the component SLD.

The validity of the output can be verified through reconstruction of original SANS data, for which two approaches can be considered. Firstly, the PSF outputs can be multiplied by the contrast matrix utilized for the original extraction, essentially reversing the process and going back to the original scattering function data. Secondly, an optimization method can be used to compare the initial scattering functions and PSF outputs, and compute a contrast matrix that would link the input to the output (appendix 1).

With regards to the input, the number of scattering functions used will of course always be known. If the dispersion medium (solvent) consists of one species of molecules, or a mixture of homogeneously dispersed molecules, and the density is known, the theoretical SLD can be determined from equation (2.1.7).

However, theoretical SLD determination may not be sufficient in the case of component SLDs. For example, carbon black densities can range between 1.8 and 2.1 g/cm^3 [87], depending on the nature of the material, such as degree of porosity. Therefore, a more prudent approach for determination of component SLDs is experimentally for each material in use. This can be achieved through SANS contrast matching measurements.

2.2.3 Contrast matching determination of component SLD

As shown by equation (2.1.9), the scattering intensity is proportional to the contrast term squared ($(\Delta\rho)^2$). The contrast term is defined as the SLD difference between a scatterer (i.e. ink component – ionomer, carbon etc.) and the dispersion medium (i.e. solvent), $\Delta\rho = \rho_{scatterer} - \rho_{dispersion\ medium}$.

Contrast matching experiments are used determine unknown SLD values through defining the dispersion medium SLD required to fully minimize scattering from a component – the point where dispersion medium and component SLDs 'match': $\Delta\rho = \rho_{scatterer} - \rho_{dispersion\ medium} = 0$.

A series of samples is prepared, containing the component of unknown SLD to be determined, dispersed in a medium (solvent, buffer etc.). In each sample the deuteration degree of the medium is varied, resulting in a range of background SLDs, and therefore contrast terms for the scattering component. Since the degree of deuteration as well as corresponding SLD values of the dispersion medium in each sample are known, by finding the deuteration point of the dispersant at which scattering from the component is minimized, its SLD can be determined.

Note in order to obtain an accurate SLD value, the contrast match samples must include only the component whose SLD is to be determined and the dispersion medium, whose SLD will be varied in the sample series. If more than one component is present, the SLD extracted will be related to all the singular SLD component contributions as well as their volume fractions, and may be additionally altered by any arising component interactions.

The specific procedure of obtaining a component SLD using the contrast match method will be presented using an example of the SLD determination of Nafion in 50:50 wt% iPrOH/water solvent, Figure 31.

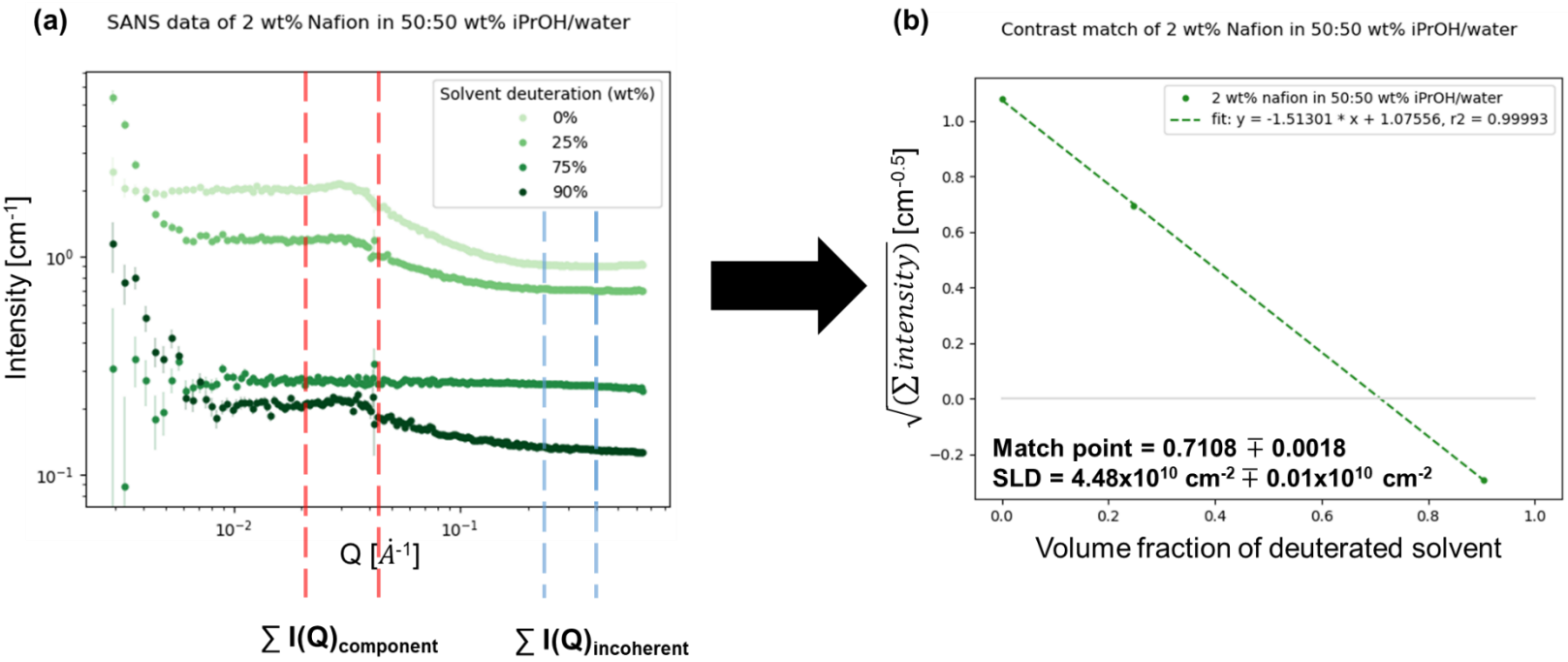


Figure 31. (a) *SANS data series of 2.0 wt% Nafion in 50:50 wt% iPrOH/H_2O solvent at different contrasts (% solvent deuteration). Red dotted lines represent the Q range where summation of intensity is performed for contrast match analysis.* ***(b)*** *Contrast match from SANS data presented in (a). Note error bars are included in 31(b), but are too small to be visualized. For an example of error bar magnitude, please refer to appendix 2.*

In the Nafion SANS data presented in figure 31(a), a peak feature, arising from structural organization of the ionomer, can clearly be observed (Q ≈ 3x10^{-2} $Å^{-1}$). The intensity of the peak diminishes with increasing contrast until 75% of solvent deuteration, where the peak is observed to disappear completely, suggesting this scattering function is close to the contrast match point of Nafion. Note in this case a peak feature can be observed, however, in a more general sense, any structural feature that is at a comparably high intensity to the background can be used. As the solvent deuteration is further increased the peak feature reappears. Note the position of the peak feature however doesn't change with degree of deuteration.

The first step involves the comparison of increased intensity arising from the Nafion-related peak feature to the general intensity arising from the background, mainly in the form of incoherent signal. The intensities in the peak Q range, $I(Q)_{component}$ (Q = 0.026-0.040 $Å^{-1}$), as well as in the incoherent scattering Q range, $I(Q)_{incoherent}$ (Q = 0.28-0.40 $Å^{-1}$), are summed.

To quantify the differences in intensity between the two Q ranges, and therefore the intensity arising from the Nafion-related feature only, the following equation is applied (stemming from equation (2.1.9)):

$$\sqrt{\sum(\qquad)} = \sqrt{\sum(\ ) \qquad - \sum(\ )} \tag{2.2.3}$$

A plot of the square root of this summed intensity as a function of the volume fraction of deuterated solvent is performed, figure 31b. The volume fraction of deuterated solvent is computed from measured component masses during sample preparation and the density of solvents utilized. A perfectly linear relation can be

observed. However, note the data point corresponding to 75 wt% deuterated sample is missing. This is because there is not enough intensity corresponding to the peak feature observed in this scattering functions, and $(\sum \text{Intensity})^{0.5}$ would quantify only noise, potentially impacting the linearity of the plot. Additionally, observe the $(\sum \text{Intensity})^{0.5}$ value obtained from the scattering function of the most deuterated sample is negative.

This is because the match point of Nafion has already been passed, observed in the scattering function of 75 wt% solvent deuteration sample, and in the most deuterated sample (90 wt% solvent deuteration) the peak feature can already be seen reappearing. The match point of Nafion can be determined as the point where $\sqrt{(\sum \quad)} = 0$, and crosses the x-axis. Therefore, in order to obtain a match point when solvent volume fraction is <1, crossing the x axis, all data points arising from scattering functions after the match point must be considered negative. Otherwise, a parabola shape would be obtained, where $\sqrt{(\sum \quad)}$ decreases until the match point, and then increases after the match point is crossed. The component SLD can also be obtained using this approach,[70] fitting the parabola, however, more data points would be required for SLD extraction.

When $\sqrt{(\sum \quad)}$ crosses the x-axis, no scattering intensity from the peak feature is observed, and the contrast factor is 0. The SLD of the solvent matches exactly the SLD of Nafion, resulting in a complete disappearance of the peak feature. The SLD of fully deuterated iPrOH/H_2O (or more appropriately iPrOH-d8/D_2O) is 6.30×10^{10} cm^{-2}. The match point is found to arise when the volume fraction of deuterated solvent in the sample is 0.7108. Therefore, the SLD of Nafion can be worked out to be $(0.7108 \times 6.30 \times 10^{10}\ cm^{-2}) = 4.48 \times 10^{10}\ cm^{-2}$.

2.2.4 Component SLD input for PSF extraction – an experimental queary.

As large-scale facilities are required to perform neutron scattering experiments, ‘beamtime’ is in high demand and subject to an application process. For this reason, results obtained in the scope of this work were performed continuously over the entire PhD duration, spaced approximately every several months. This means that for first results, all contrast matches could not be performed, and some data was preliminarily analysed using theoretical SLD values of 6.67×10^{10} cm^{-2} for carbon and 4.16×10^{10} cm^{-2} for Nafion respectively. After obtaining experimental SLD values from contrast match experiments, of 6.59×10^{10} cm^{-2} and 4.48×10^{10} cm^{-2} for carbon and Nafion respectively, it was observed that the difference in the PSF outputs for the same data series, when theoretical and experimental component SLD values were used, was significant even for such relatively small variations:

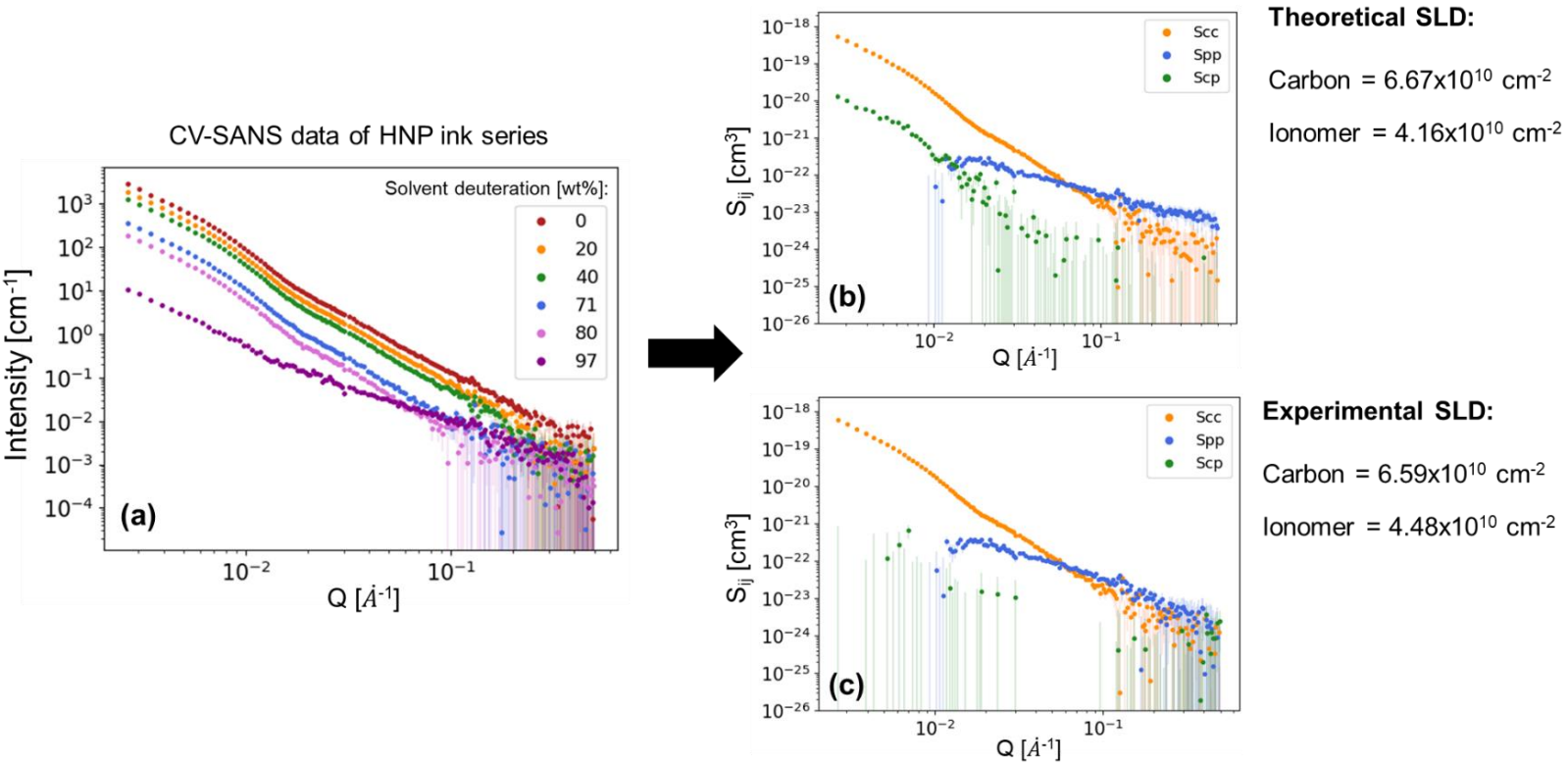


Figure 32. (a) *CV-SANS data of HNP ink series,* ***(b)*** *the PSF output when theoretical component SLDs were used in the input,* ***(c)*** *the PSF output when experimental component SLDs obtained from contrast match measurements were used in the input.*

When theoretical SLD values were applied in the input, the cross-term, S_{cp} can be clearly observed in the low Q regime ($Q<1x10^{-2}$ $Å^{-1}$), however, when experimental values were used, only a handful of points can be observed in the S_{cp}. As such a small change in the input causes variation in the extracted PSFs, a worry arises with regards to the robustness of the PSF method. Indeed, although SLDs can be experimentally extracted, a slight uncertainty (on the second decimal place) in the true value will always be present. Due to this observation, a necessity to evaluate the impact of input variation on the PSF output has be noted, in order to estimate to what an extent the PSFs obtained can be trusted to provide veritable structural information of the system in question. Such a study is not necessary only in the case of the component SLD variation, but also for the other two inputs, the contrast range and the number of input files used.

However, it is impossible to estimate the accuracy of the method when it is not known which PSF output shows the true results for experimental data. Therefore, it was opted to perform such an evaluation on simulated CV-SANS data, where the output could be directly compared with the known simulated structures.

2.2.5 CV-SANS simulations

Data analysis software such as SasView contain a plethora of structural models used to fit experimental data, however these can also be exploited for generation of simulated data through theory mode. In order to check whether the effects of input variation are consistent for different structural information to be extracted, two possible structural cases were considered – when there is no adsorption of the ionomer to carbon, namely where the two components, carbon spheres and Nafion cylinders are not interacting at all (dubbed the spheres + cylinders model); and the case when all of the ionomer is absorbed onto the carbon, the core-shell model. In order to obtain the clearest result possible, each simulated scattering function consists of 10,000 evenly spaced data points. Otherwise, the parameters used for simulations were kept as close to the real-life case as possible. All SLD values, for the carbon (SLD(C)), ionomer (SLD(P)), as

well as the solvents, were chosen from an example of experimental ink series measured by CV-SANS. Additionally, six contrasts were simulated in order to fully comply with the experimental case. Structural parameters chosen were inspired by values found in literature – carbon primary particles range between 20-40 nm in diameter, while the ionomer in question, Nafion, forms rod-like aggregates with radii of few nm.[17] The I/C ratio was fixed at 0.8 as this was the value used in the majority of experimental compositions. Lognormal function polydispersity was included for each component. Instrumental smearing was set at dQ/Q = 2% pinhole smear to approximate instrumental considerations and smooth out simulated scattering functions. As simulated datasets do not contain any error information, error corresponding to 1% scattering intensity was added to each simulated scattering function in order to ensure successful application of the SVD method. Note the simulations consider adsorption of ionomer on carbon primary particles only and therefore are a simplification of the real catalyst ink system.

The no adsorption case – spheres + cylinders model

Spherical carbon primary particles can be described using the form factor of a sphere,[88] ( ):

$$( ) = \frac{}{} \cdot [3 \quad (\Delta \quad) \cdot \frac{\sin(\quad) - \quad (\cos(\quad))}{(\quad)^3}]^2 \qquad (2.2.4)$$

= volume fraction of spherical particles, V_s = volume of the sphere (^{3}), (Δ) = contrast term ($^{-2}$), r = radius of the sphere ( )

Ionomer particles can be described using the form factor of a cylinder[89], (,):

$$(,) = \frac{}{} \quad ^2(,) + \qquad (2.2.5)$$

$$(,) = 2(\Delta \quad) \quad \frac{\sin(\frac{1}{2} \qquad)}{\frac{1}{2}} \frac{_1(\qquad)}{} \qquad (2.2.6)$$

Where = volume fraction of cylindrical particles, α is the angle between the axis of the cylinder and ,
= ^{2} = volume of the cylinder (^{3}), L = length of the cylinder ( ), R = radius of the cylinder ( ), (Δ) = contrast term ($^{-2}$), J_1 = first order Bessel function.

For a dilute scattering system of non-interacting spheres and cylinders, the total scattering intensity can be described as follows:

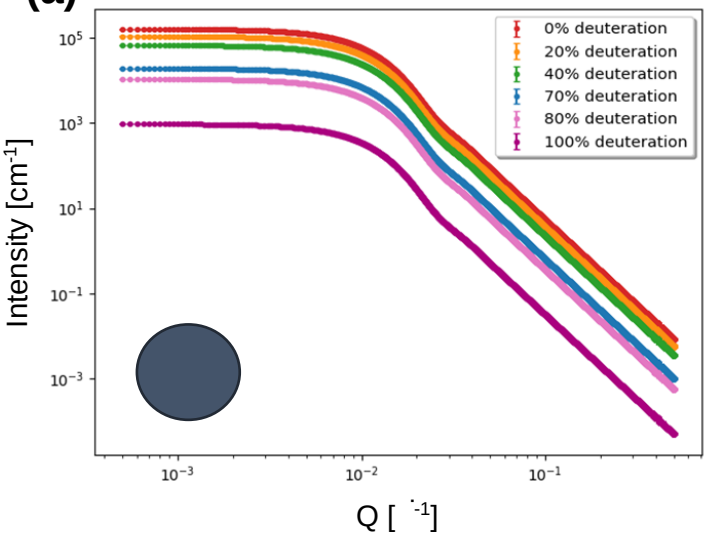
$$( ) = \quad ( ) + \quad ( ) \qquad (2.2.7)$$

Where the volume fraction of all scattering objects in the system, :

$$= \quad + \qquad (2.2.8)$$

Firstly, each component had to be simulated separately. Figure 33 shows simulated CV-SANS data for carbon spheres as well as parameters used for their creation:

(a)



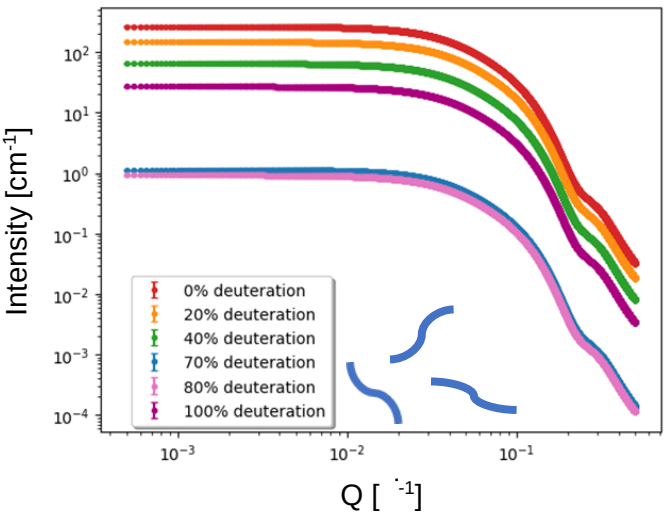
(b)

Parameter	Value
Scale	1.0
Background	0 cm^{-1}
Radius	150 Å
SLD	6.59x10^{10} cm^{-2}
SLD_solvent	[-0.43, 0.81, 2.05, 4.16, 4.77, 6.05] x10^{10} cm^{-}
Polydispersity (radius)	0.25

Figure 33. (a) *CV-SANS data simulated with the sphere model in SasView 5.0.6. % deuteration values correspond to the degree of solvent deuteration used in experimental ink samples.* ***(b)*** *table of parameters used in the simulation.*

Figure 34. shows simulated CV-SANS data for ionomer cylinders as well as parameters used in the simulation:

(a)



(b)

Parameter	Value
Scale	1.0
Background	0 cm^{-1}
Radius	16.2 Å
Length	100 Å
SLD	4.48x10^{10} cm^{-2}
SLD_solvent	[-0.43, 0.81, 2.05, 4.16, 4.77, 6.05] x10^{10} cm^{-}
Polydispersity (radius)	0.20
Polydispersity (length)	0.20

Figure 34. (a) *CV-SANS data simulated with the cylinder model in SasView 5.0.6. % deuteration values correspond to the degree of solvent deuteration used in experimental ink samples (based on 50:50 wt% iPrOH/water).* ***(b)*** *table of parameters used in the simulation.*

The two models were combined together in a manner presented in equation (2.2.4), with volume fraction of 0.556 and 0.444 for carbon and ionomer respectively, chosen to correspond to I/C = 0.8 widely used in experimental compositions, yielding the spheres + cylinders model:

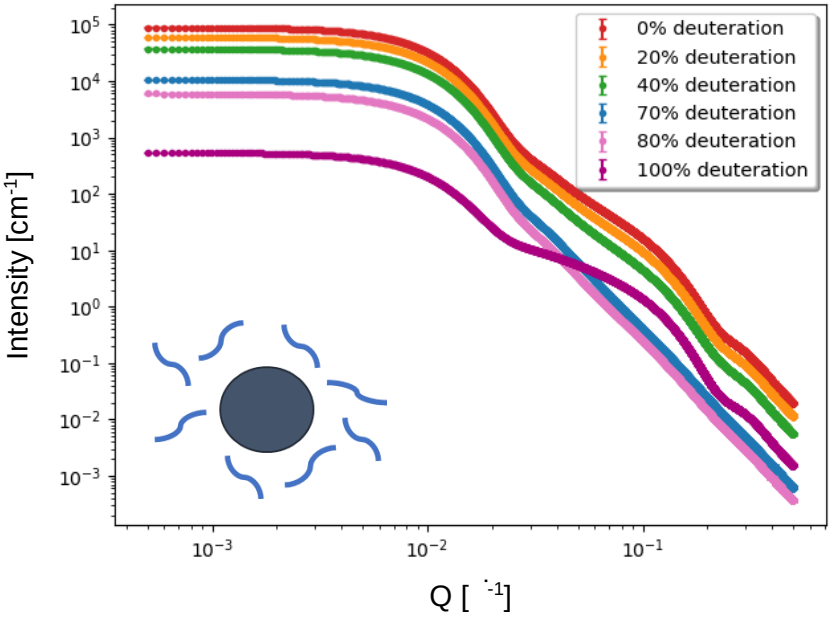


Figure 35. *CV-SANS data corresponding to the spheres + cylinders model – obtained by combining the spheres and cylinders simulations.*

Note that carbon scattering dominates in the low Q regime ($Q<1x10^{-2}$ Å^{-1}) throughout the contrast range, even at maximum achievable deuteration, stressing the fact it is impossible to match out carbon scattering completely and achieve an easy sample structural characterization.

The full adsorption case – core-shell model

For a system depicting a case of full ionomer adsorption to carbon, a form factor of a core-shell sphere was opted for[90]:

$$( ) = \frac{}{} ^2( ) + \qquad (2.2.9)$$

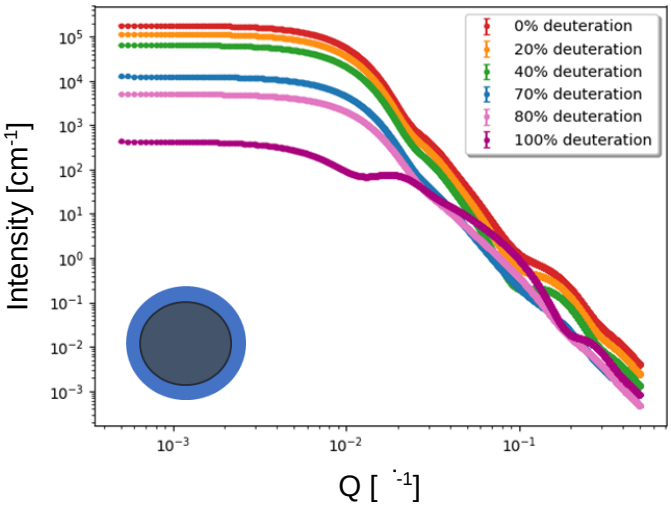
$$( ) = \frac{3}{}[(-)\frac{\sin( ) - \cos( )}{( )^3} + (-)\frac{\sin( ) - \cos( )}{( )^3}] \qquad (2.2.10)$$

Where = volume fraction of whole (core-shell) particle, V_s = volume of the whole particle (Å^3), V_c = volume of the core (Å^3), r_s = radius of whole particle (Å), r_c = radius of the core (Å), = SLD of core (Å^{-2}), = SLD of shell (Å^{-2}), = SLD of solvent (Å^{-2})

The simulated core-shell data as well as parameters used for its generation are presented in figure 36.

For both simulations, the core radius of 15 nm (150 Å) corresponds to spheres of 30 nm diameter, which falls in the middle of the size range of carbon primary particles. The radius of the ionomer chosen for the cylinder simulation is directly linked to the shell thickness in the core-shell model. The shell thickness of

(a)



(b)

Parameter	Value
Scale	1.0
Background	0 cm^{-1}
Radius (core)	150 Å
Thickness (shell)	32.4 Å
SLD_core	6.59x10^{10} cm^{-2}
SLD_shell	4.48x10^{10} cm^{-2}
SLD_solvent	[-0.43, 0.81, 2.05, 4.16, 4.77, 6.05] x10^{10} cm^{-2}
Polydispersity (radius)	0.25
Polydispersity (thickness)	0.20

Figure 36. (a) *CV-SANS data simulated with the core_shell_sphere model in SasView 5.0.6. % deuteration values correspond to the degree of solvent deuteration used in experimental ink samples.* ***(b)*** *table of parameters used in the simulation.*

3.24 nm (32.4 Å) was estimated from the theoretical volume of a core-shell sphere when all of the ionomer is adsorbed to carbon at I/C = 0.8. This ensures that the core-shell model does not have to consider unadsorbed ionomer cylinders as part of the structure, making evaluation of the PSF output more facile, but the two models still correspond to the same ink composition.

Extracting and fitting PSFs from simulated data

Firstly, PSF outputs of both models were extracted to ensure they can be fitted back with the corresponding parameters used to generate simulations. SasView 5.0.6 software was used in data fitting.

Figure 37. shows PSF outputs for the spheres + cylinders (S + C) model. As can be observed, the sphere and cylinder models are a perfect match to the S_{cc} and S_{pp} outputs respectively (when the scale of the fit is adjusted to the cm^3 format). Large error bars appear in the S_{pp} output approximately for Q < 0.01 $Å^{-1}$ (appendix 3). Note that in one of the experimental outputs presented in figure 32(a) no data points were observed for the S_{pp}, in the corresponding range on the logarithmic scale, suggesting that scattering in the low Q range (Q<1x10^{-2} $Å^{-1}$) of the S_{pp} may be prone to missing data points in that region during the PSF extraction. The S_{cp} output shows only a few data points, mainly in the mid Q range (1x10^{-2}<Q<1x10^{-1} $Å^{-1}$), and the data show very high error bars (visualized in appendix 3). Additionally, the S_{ij} magnitude of the S_{cp} is significantly lower than that of the other two outputs. Ultimately, the perfect fit to the S_{cc} and S_{pp} suggests the correct representation of structural information by the PSF outputs. The S_{cp} is more dubious. More appropriately, no cross term at all should be extracted in an event where two components in the system have no interactions to present, so although there is no risk in misinterpreting the output as component interaction, the outputs extracted from the S+C model based simulations may show a limitation of the PSF method.

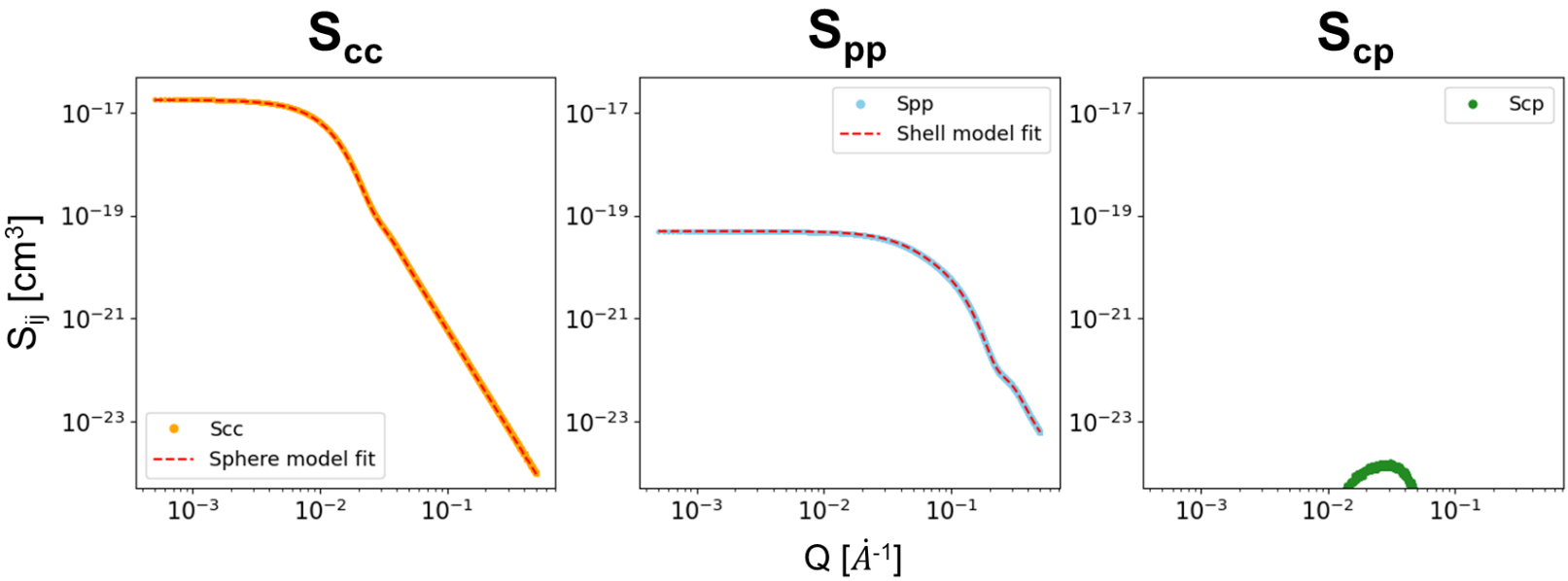


Figure 37. *Partial scattering function outputs extracted for simulated CV-SANS data based on the spheres + cylinders simulation. Scc (orange) was fitted with the sphere model. Spp (blue) was fitted with the cylinder model. No fitting was applied to Scp (green). Models fitted to the data are represented as red dashed lines. Error bars have been left out of the Scp for visualization purposes (contained in appendix figure 3).*

Figure 38 presents the fitted PSF outputs extracted for CV-SANS simulated data based on the core-shell model:

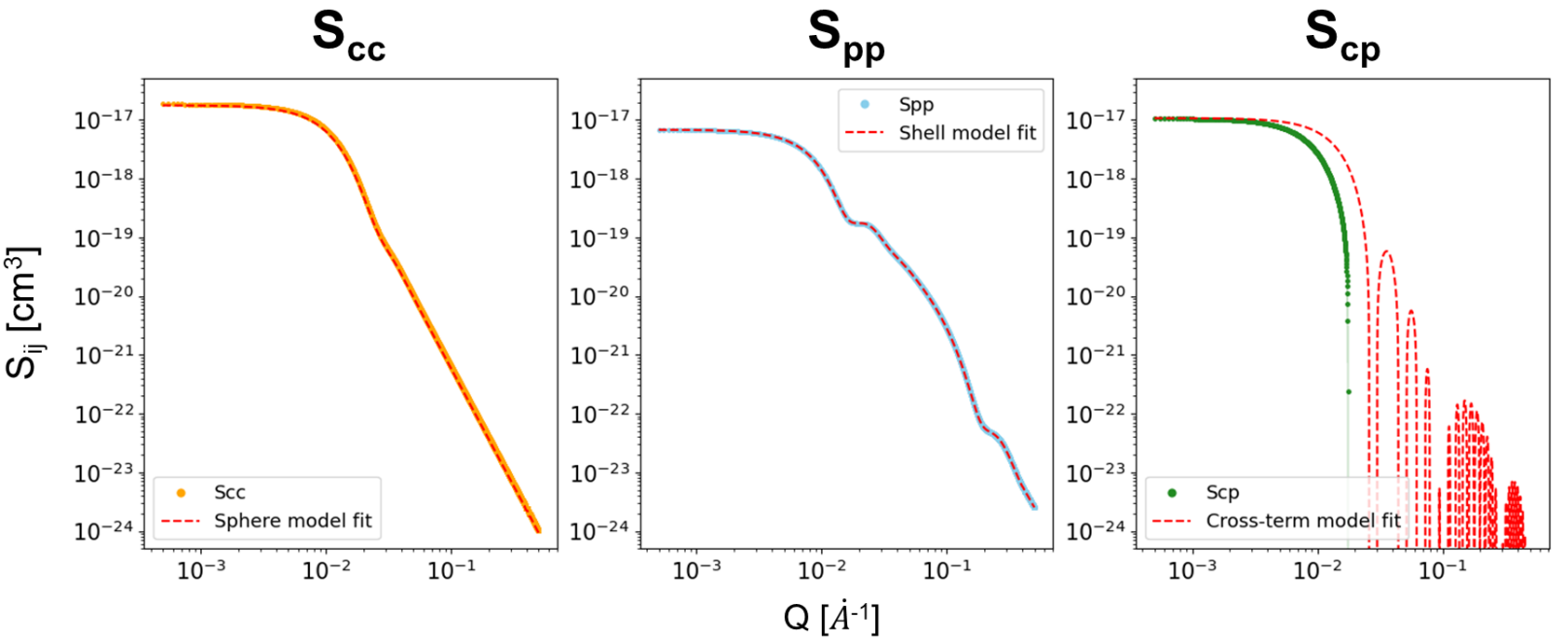


Figure 38. *Partial scattering function outputs extracted for simulated CV-SANS data based on the core-shell simulation. S_{cc} (orange) was fitted with the sphere model, S_{pp} blue was fitted with the core_shell_sphere model with SLD_core = 0, S_{cp} (green) was fitted with the cross-term shell model proposed by Shibayama et al.[70]. Red dashed lines represent the fits applied to PSF outputs.*

The S_{cc} output again showed a perfect fit to the sphere model. The S_{pp} output was an exact match to the core_shell_sphere model when the SLD_core parameter was set to 0, representing a model of the shell scattering only, with the core component matched out. The S_{cp} fit was inspired by the model proposed by Shibayama et al.[70], based on the scattering amplitude of the shell, $A_{coreshell}(Q)$, number density of carbon n_c, and a term related to scattering from spherical objects, Φ_{sph}:

$$( ) = \Phi ( ) \quad (2.2.11)$$

$$\Phi = \frac{\sin( ) - ( )}{( )^3} \quad (2.2.12)$$

where R = radius of a sphere ( )

$$( ) = \Delta \Phi (,) - (\Delta - \Delta) \Phi (,) \quad (2.2.13)$$

where $\Delta\rho$ is the contrast term ($^{-2}$), V is the volume (^{3}). The *out* subscript denotes dimensions of the full core-shell (carbon + ionomer) sphere, while the *core* subscript refers to the core (carbon) sphere.

However, when the model from this work was directly applied to the S_{cp} extracted from the core-shell simulation, an exact fit was not achieved. It was noted that the proposed model shows great similarities to the core_shell_sphere model when polydispersity is set to 0 (appendix figure 4). Importantly to note, it can be observed that the fit suggests an increased number of data in the mid to high Q regions ($Q>1x10^{-2}$ $^{-1}$) that are not present at all in the cross-term. The reason being that there are no polydispersity considerations at all present in this model, resulting in an oscillatory scattering from homogenously sized particles. Indeed, that seems to also be the case for the cross-term, but only the first, biggest, oscillation can be observed. More work must be done to investigate the physical meaning of the S_{cp}, along with finding a model that can explain the cross-term contributions, and for this reason, in this work the S_{cp} outputs obtained from experimental data will not be fitted, but used as a visual indication of potential ionomer-carbon interactions only.

Overall, both structural models yield veritable and fit-able S_{cc} and S_{pp} PSF outputs. However, the two models consider the most extreme structural cases of the catalyst ink – when the ionomer is completely adsorbed to carbon or not at all. In reality, the adsorption will most likely fall somewhere in the middle of the two, and this is what would be represented in the PSF outputs of experimental data. For this reason, a simulation model for a case of partial ionomer adsorption is presented:

$$( ) = ( ) + ( ) + ( ) \quad (2.2.14)$$

Where ( ) = scattering intensity of core-shell model (cm^{-1}), = volume fraction of core-shell objects, ( ) = scattering intensity of sphere model (cm^{-1}), = volume fraction of sphere objects, ( ) = scattering intensity of cylinder model (cm^{-1}), = volume fraction of cylinder objects.

Note = + + = 1

It is the same concept of fractional combination as presented in equations (2.2.7) and (2.2.8), with the assumption that neither of the three structures, the core-shell, spheres, or cylinders are interacting together. Another assumption that must be made is that in the case of ionomer adsorption, the carbon spheres are either fully covered by the ionomer or not at all. Therefore, the idea of partial adsorption relates to the

concept of having both adsorbed and unadsorbed ionomer in the system, rather than to having partially covered carbon particles.

Figure 39 presents PSF outputs for simulated data with a gradually increasing adsorption of ionomer (increasing fraction of the core-shell model used). _ = (——) 100 .

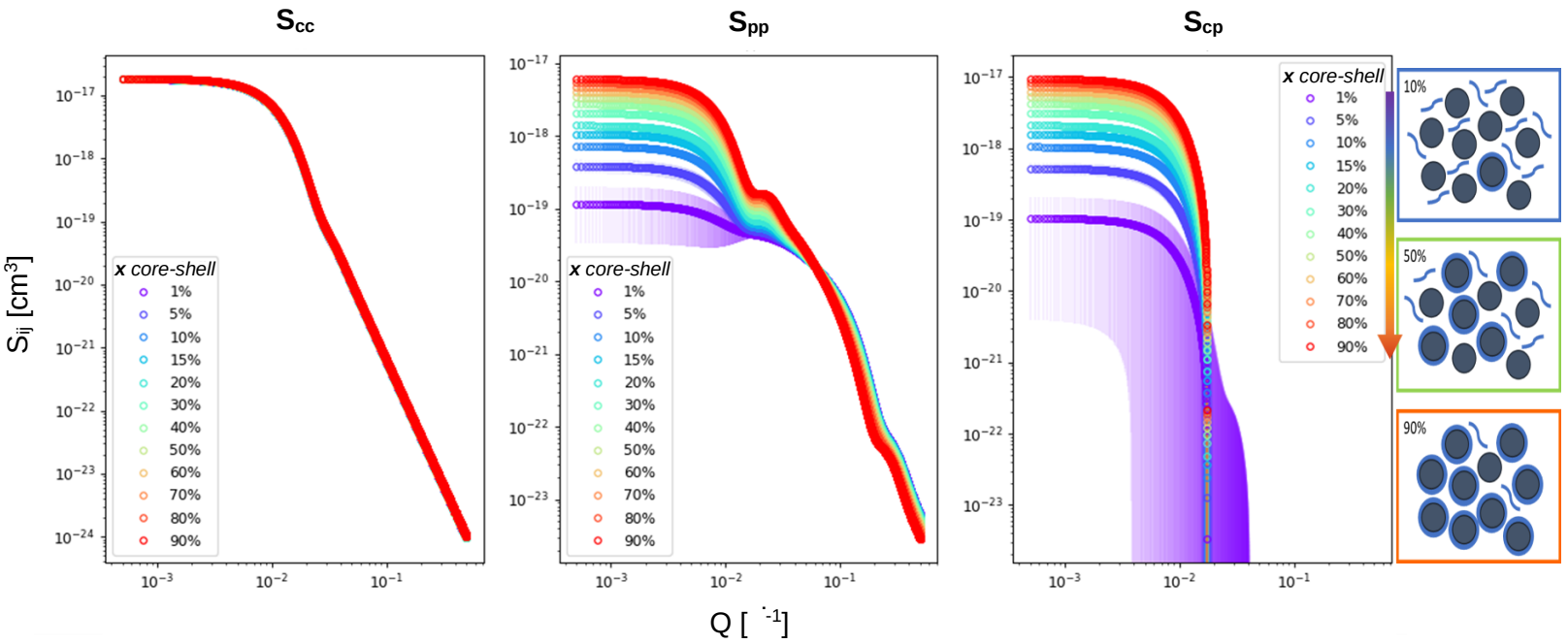


Figure 39. *PSFs extracted from partial adsorption structural model simulations, with the degree of adsorption defined by the % of core-shell model utilized in the simulation.*

Importantly to note, even if $x_{core\text{-}shell}$ = 1% is present in the simulated dataset, the S_{cp} specific to the core-shell structure can already be observed, albeit with very high error bars. However, the magnitude of the error bars is already significantly reduced at 5% of core-shell in model. Additionally, the magnitude of the S_{ij} /cm^3 increases in the low Q regime (Q<1x10^{-2} $^{-1}$) for the S_{pp} and S_{cp} with increasing % of the core-shell model, while the magnitude of the S_{cc} remains constant throughout, which may aid in interpretation of degree of adsorption in experimental datasets. For this reason, partial scattering models will be discussed in more detail later in the results section (2.3). For the upcoming evaluation of the PSF method input effect on outputs extracted, the spheres + cylinders and core-shell models, which show the two most extreme scenarios, are sufficient.

2.2.6 Investigation of PSF input effect

2.2.6.1 component SLD variation

Figure 40. presents the effect of input SLD deviation from the true value on the PSF output of the spheres + cylinders simulation. When the carbon SLD was altered, the polymer SLD was kept constant at its true value of 4.48x10^{10} cm^{-2} and vice versa. It can be observed that the S_{cp} extracted is particularly sensitive to SLD deviation. In both the cases of altering the SLD(C) and SLD(P) by 0.01 (corresponding to a 0.15 and 0.22% change respectively), the cross-term appears over the full Q-range, which is inconsistent with the unadsorbed model. Moreover, the shape of the cross-term does not resemble at all the shape observed in the S_{cp} present in the core-shell simulation, and seems to visually correspond to the carbon sphere and ionomer cylinder structures expected to be extracted in the S_{cc} and S_{cp}. Interestingly, this great sensitivity to the SLD deviation, is observed when increasing the SLD(C) value, and contrastingly when decreasing

the SLD(P) value. In the reverse scenarios no S_{cp} is present, which is closer to the expectation of an unadsorbed model. The S_{cc} seems to be the most robust to SLD deviation, showing only erroneous outputs at SLD values which are critically different from the originals used in the simulation. The S_{pp} output is a lot more robust in the case of SLD(P) alteration, however remains fairly affected by SLD(C), where a difference of approximately 0.1 from the original value starts to show inconsistency to the original result.

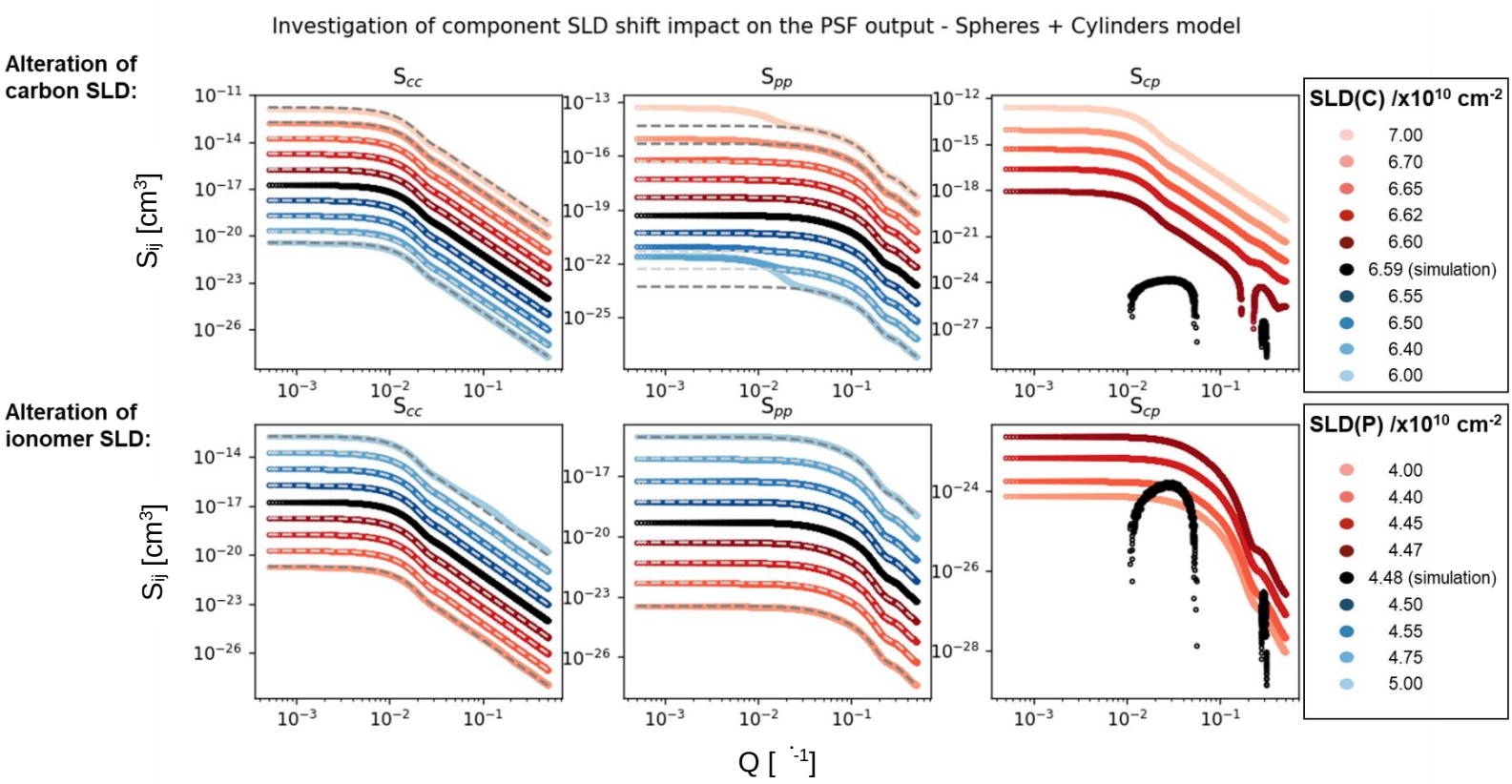


Figure 40. *Partial Scattering Functions of the Spheres + Cylinders model simulated data, extracted by varying the carbon (C) and ionomer (P) input SLDs. The SLD values used in the simulations were 6.59 and 4.48 x10^{10} cm^{-2} respectively for carbon and ionomer, corresponding to experimentally extracted values. The PSF outputs corresponding to these SLD values are marked in black, as well as grey dashed lines, for comparison to other output results. Both outputs presented in black and in grey dashed lines are equivalent to those shown in figure 37. The data is shifted on a logarithmic scale for visualisation purposes. Error bars have been left out for visualization purposes.*

It is also important to consider a case where both SLD(C) and SLD(P) are not exact. This creates an even larger number of possibilities for the PSF output. To reduce the number of variations that need to be investigated, it can be assumed that combining the SLDs of carbon and ionomer that lead to the appearance of a false S_{cp} would enlarge this effect further, and in the reverse case if the SLD shift is small for both, the PSF output should remain relatively veritable. Yet questions remain concerning the cases where contrasting effects are observed, i.e. where the SLD of both components increase or decrease.

Figure 41. shows the effect of altering SLDs of both components by approximately 0.05x10^{10} cm^{-2}, a small change, yet enough for observation of changing PSF output behaviours.

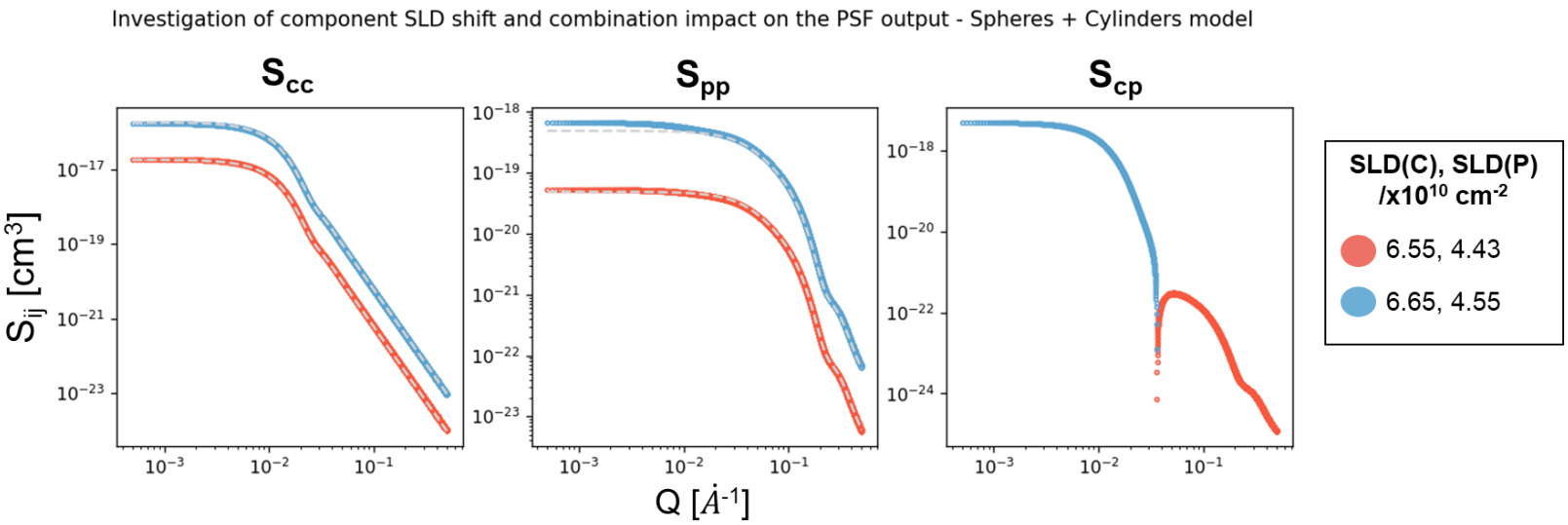


Figure 41. *Effect of SLD shift and combination on the spheres + cylinders simulation PSF output: when SLD(C) and SLD(P) are both decreased (red) and increased (blue). The data is shifted on a logarithmic scale for visualisation purposes. Error bars have not been included for visualization purposes.*

For the case of increasing SLDs, even such a small shift shows a deviation in the S_{pp} from the desired cylinder fit, and an appearance of a cross-term, in this case one which could be easily misinterpreted as that characteristic for the core-shell structure. When both the SLDs are decreased, the S_{cc} and S_{pp} outputs are still congruent with the sphere and cylinder models, however a short S_{cp} appears in the mid/high Q range ($Q>3x10^{-2}$ Å^{-1}).

Figure 42. shows impact of shifting the carbon and ionomer SLDs respectively on the PSF output extracted from the core-shell based simulations. It can be clearly observed that the output for the core-shell structure is a lot more robust than for the spheres + cylinders model. Only when SLD(C) and SLD(P) are shifted to unrealistically high or low values a deviation from the expected case is observed in S_{pp} and S_{cc} outputs respectively. Additionally, for SLD(C) variation, in the most drastic cases the cut-off point for the S_{cp} is also altered, however, the cross-term shape characteristic to the core-shell structure is still observed.

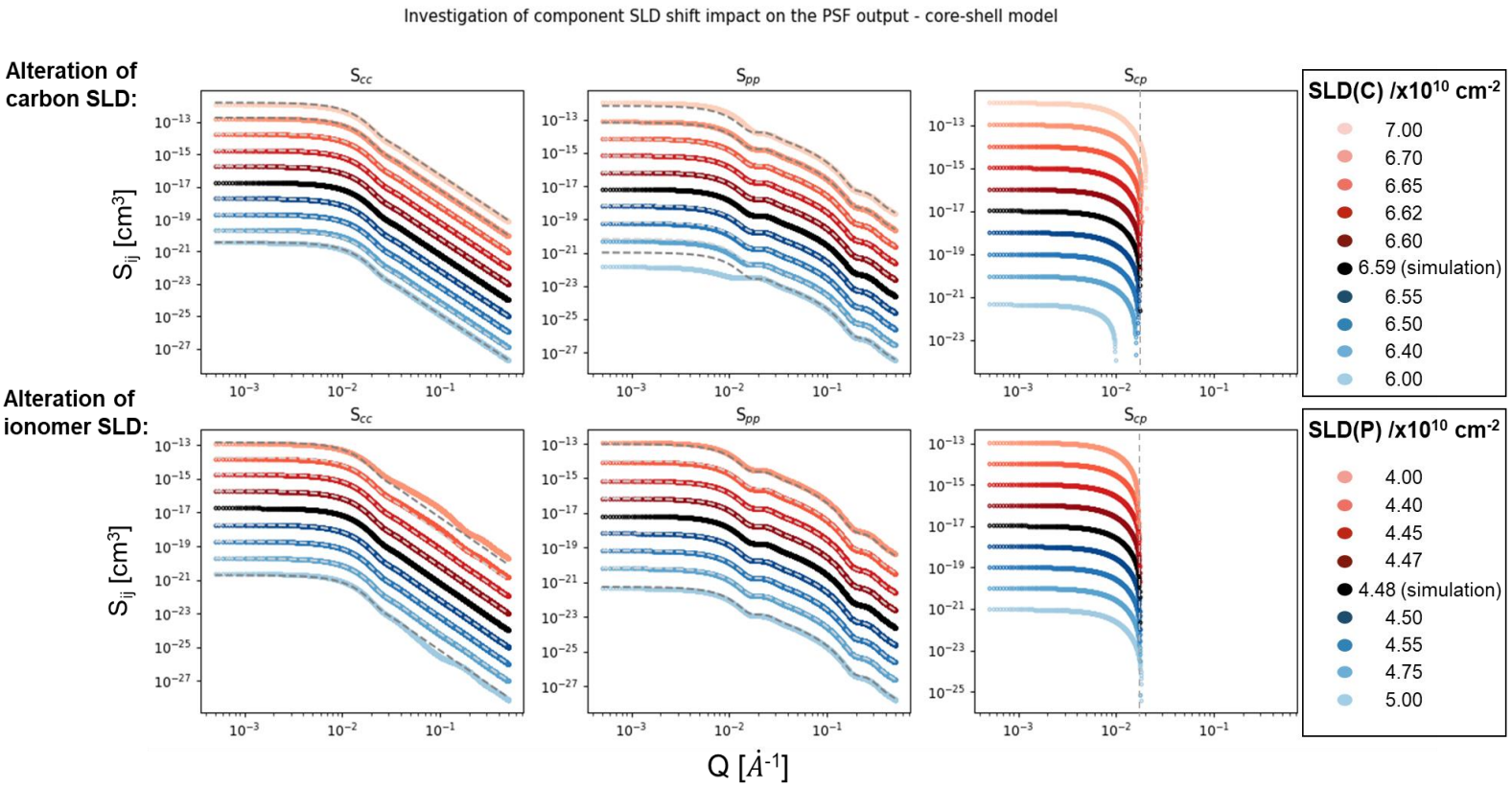


Figure 42. *PSFs of the core-shell model simulated data, extracted by varying the carbon (C) and ionomer (P) input SLDs. The SLD values used in the simulations were 6.59 and 4.48 x10^{10} cm^{-2} respectively for carbon and ionomer. The PSF outputs corresponding to these SLD values are marked in black, as well as grey dashed lines, for comparison to other output results. The data is shifted on a logarithmic scale for visualisation purposes. Error bars have been excluded from this figure for visualization purposes.*

Figure 43. shows the effect of altering SLDs of both components by approximately 0.05x10^{10} cm^{-2} in the core-shell model PSF output. It can be observed that in both shift and combination cases the output is almost exactly as expected for the core-shell simulation.

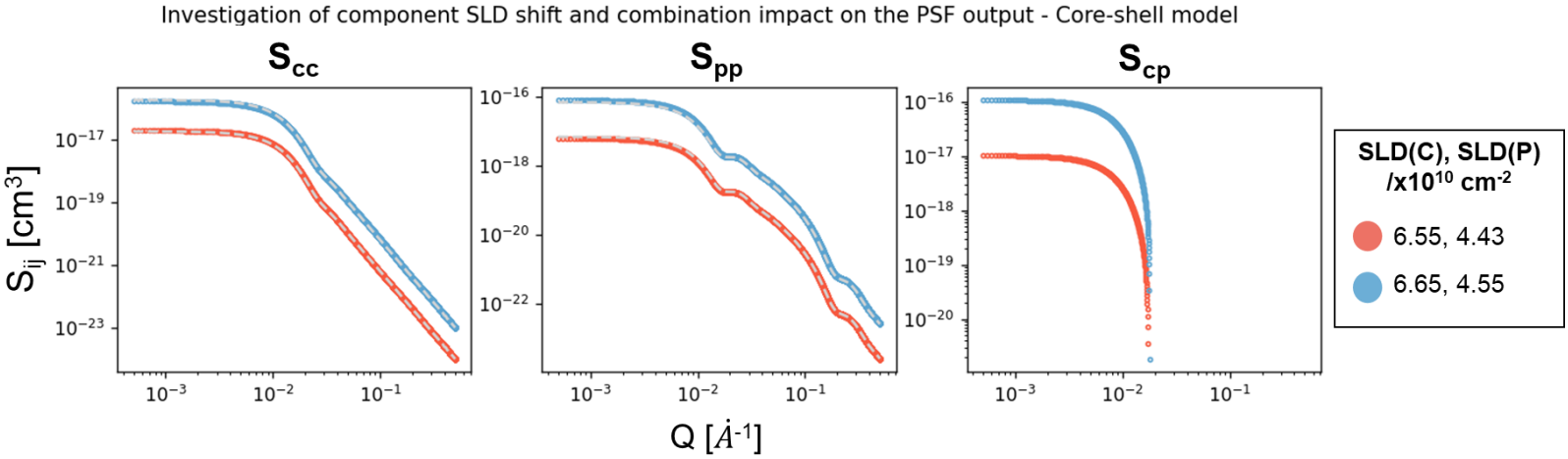


Figure 43. *Effect of SLD shift and combination on the core-shell simulation PSF output: when SLD(C) and SLD(P) are both decreased (red) and increased (blue). The data is shifted on a logarithmic scale for visualisation purposes. Error bars have not been included.*

These insights do not only increase the understanding of how robust the PSF outputs are, but can also be exploited, as a tool for data interpretation. Even when accurate SLD values for each component are known, obtained through contrast match experiments, by modifying the SLD slightly and observing the output behaviour, the structure interpretation of the output can be further confirmed.

This approach can be further extended to the more realistic case of partial adsorption. Through the same approach, PSF outputs of simulations with partial core-shell structure have been evaluated when SLD(C) and SLD(P) were slightly altered in an individual manner (appendix 5). In each case investigated the S_{cc} and S_{pp} outputs were correct. The S_{cp} output suffered, particularly when SLD(C) was altered, in simulations with less than 10% adsorption (% core-shell model). In cases of more than 10% core-shell in model, the robustness particular to a core-shell model output can be assumed for all PSF outputs. Nevertheless, it is important to note that this approach is completely reliant on the assumption that any adsorption to the carbon complex follows the core-shell structure. The case where carbon is partially covered by the ionomer has not been investigated in this work.

It should also be noted that the sensitivity of the SLD input deviation seems to be correlated to the scale of the error bars in the original outputs presented for the two models. The S + C model showed high error bars in the low Q regime for the S_{pp} and unreasonably high error bars for the S_{cp} across the whole Q range (appendix 3). On the contrary, the PSF outputs for the core-shell based simulation showed almost insignificant error bars in each case. However, when the SLD shift was large enough from the true value, even the PSF outputs extracted from the core-shell model showed inconsistencies to the true structure. Therefore, error bars may be used as a suggestion towards how stable the output is, but do not indicate a perfect precision.

Table 2 shows a summary of information that can be obtained when altering the SLD values in both model systems:

Model, PSF output	SLD(C) maximum deviation for correct output (Increase/Decrease)	SLD(P) maximum deviation for correct output (Increase/Decrease)
Spheres + Cylinder, S_{cc}	$+0.41\times10^{10}$ cm^{-2} , -0.59×10^{10} cm^{-2}	$+0.27\times10^{10}$ cm^{-2} , -0.48×10^{10} cm^{-2}
Spheres + Cylinder, S_{pp}	$+0.06\times10^{10}$ cm^{-2} , -0.09×10^{10} cm^{-2}	$+0.27\times10^{10}$ cm^{-2} , -0.03×10^{10} cm^{-2}
Spheres + Cylinder, S_{cp}	$+0.01\times10^{10}$ cm^{-2} , -0.59×10^{10} cm^{-2}	$+0.52\times10^{10}$ cm^{-2}, -0.01×10^{10} cm^{-2}
Core-shell, S_{cc}	$+0.41\times10^{10}$ cm^{-2} , -0.59×10^{10} cm^{-2}	$+0.27\times10^{10}$ cm^{-2}, -0.07×10^{10} cm^{-2}
Core-shell, S_{pp}	$+0.11\times10^{10}$ cm^{-2}, -0.09×10^{10} cm^{-2}	$+0.52\times10^{10}$ cm^{-2}, -0.48×10^{10} cm^{-2}
Core-shell, S_{cp}	$+0.11\times10^{10}$ cm^{-2}, -0.19×10^{10} cm^{-2}	$+0.52\times10^{10}$ cm^{-2}, -0.48×10^{10} cm^{-2}

Table 2. *Summary of maximum allowable deviation from true value of SLD(C) and SLD(P) for veritable S_{cc}, S_{pp} and S_{cp} outputs in the cases of the spheres + cylinders and core-shell models. Green values represent the highest deviation tested in this work. Red values represent the lowest deviation tested in this work.*

In conclusion, it has been shown that extracting a correct SLD value for both the carbon and ionomer components is a very important aspect in obtaining a correct PSF output. The SLD deviation has a particularly strong impact on the spheres + cylinders model, which represents a case where there is no adsorption of the ionomer to carbon, and the two components are not interacting together. The outputs for the core-shell model are a lot more robust to SLD deviation for both components. A case where component SLDs are slightly increased or decreased simultaneously has been investigated for both models, again highlighting the same trends for the respective cases. Furthermore, simulations of partial core-shell based adsorption have been investigated by the same method, albeit with only small SLD deviations. It has been characterized that the S_{cc} and S_{pp} remain accurate throughout, but if the simulation contains less than 10% of the core-shell model, S_{cp} remains sensitive to SLD deviation. It should be noted that in each case the reconstructions of the CV-SANS data showed ideal agreement to the original data, in both reconstruction models (appendix 6). This highlights that the reconstructions are not an indication

of the veracity of the results, but rather should be used to verify that the correct file inputs are present, and in the right order.

Nevertheless, it is near impossible to obtain experimental SLD values correct to the second decimal place, a margin which has shown to affect the veracity of the spheres + cylinders model output in certain instances. Therefore, the investigation of SLD deviation can also be utilized as a handy tool for interpretation of results. If the output changes with the smallest deviation it could be indicative of low or no adsorption. If changes are observed only after higher deviations a higher degree of adsorption can be assumed.

Taking into account how significant utilizing accurate SLD values has been found to be, on top of obtaining each component SLD experimentally through the contrast match method, in the scope of this work PSF output deviation as function of SLD shift studies will be utilized to increase confidence in the variability of extracted PSF results.

As this is a purely mathematical extraction of data, it is possible that a similar output trend is not observed as a function of deviation for different component SLD values (representing different components - carbon or ionomer type), even for the same structural models. Therefore, such an investigation should be handled case by case, albeit a smaller range of deviations should suffice.

2.2.6.2 Solvent SLD range & number of input data

As it has already been shown that deviation in component SLD can create a very profound effect on the PSF output in some cases, the two other inputs of the PSF method, namely the solvent SLD (contrast) range as well as the number of input data supplied must also be investigated.

Firstly, table 3 shows the chosen solvent SLD ranges for the investigation of the PSF outputs:

Identification name	**Solvent SLDs /x10^{10} cm^{-2}**
Experimental solvent range	-0.43, 0.81, 2.05, 4.16, 4.77, 6.05
Low solvent range	-0.43, 0.81, 1.50, 2.50, 3.50, 4.16
Medium solvent range	-0.43, 0.81, 1.50, 2.50, 4.16, 4.77
High solvent range	-0.43, 0.81, 2.05, 4.16, 6.05, 7.00

Table 3. *Solvent SLD ranges chosen to investigate the effect on the PSF output*

The experimental solvent range is a control parameter, used in the original simulations and corresponding to one of the experimentally measured ink series. The low solvent range was designed to exclude either of the component SLDs. The medium range overlaps only with the ionomer SLD of 4.48x10^{10} cm^{-2}, just like the experimental range, however here the maximum solvent SLD is chosen to be as close to that of SLD(P) as possible (and therefore as far away from SLD(C) as possible). The high range was chosen to overlap with both component SLDs.

With regards to input data, the amount chosen must be at least equal to the number of PSF outputs generated, which for the two component catalyst ink systems studied is 3. In this case, straightforward matrix multiplication is sufficient to obtain all PSFs. However, utilization of singular value decomposition allows for a greater number of input data to be used, which may generate more precise results.[86]

Table 4. shows number of input data investigated for output generation utilizing singular value decomposition and the solvent SLDs chosen for each:

Input number	Solvent SLDs /x10^{10} cm^{-2}
3	-0.43, 4.16, 6.05
4	-0.43, 0.81, 4.16, 6.05
5	-0.43, 0.81, 2.05, 4.16, 6.05
6 (experimental)	-0.43, 0.81, 2.05, 4.16, 4.77, 6.05

Table 4. *Number of input files for PSF extraction and the solvent SLDs chosen for each case*

The solvent SLDs were chosen to evenly cover the entire contrast range obtainable experimentally. 6 data inputs correspond to the number utilized in CV-SANS experiments and for generation of original simulations of each structural model.

In both investigations, for both structural models, the results remain unchanged with the introduced variations. Both spheres + cylinders and core-shell models can be re-fitted with structural models utilized for their generation. The only exception was a small variation in the shape of the S_{cp} output for the spheres + cylinders model when solvent SLDs were altered. However, the S_{cp} remained in the mid Q regime ($1x10^{-2}$ $Å^{-1}$<Q<$1x10^{-1}$ $Å^{-2}$) only, with a small number of low intensity data points, suggesting a lack of polydispersity consideration as mentioned before. Nevertheless, this alteration would not lead to misinterpretation of results. Therefore, from the simulated data it can be concluded that the PSF extraction method is not very sensitive to alteration of the contrast and data inputs. The results of these investigations can be viewed in appendix 7 and appendix 8 for the contrast range and data input number respectively.

2.2.6.3 Comparison to experimental data

Simulations are a necessary tool for evaluating the effect of extraction method inputs on the subsequent PSF output, as the expected results are already known, and can be fitted with a certainty. Therefore, aside from using data where structure is already known with certainty (although if that is the case there would be no reason to apply this method), it is the one way to verify whether the output is veritable.

However, for a complete assurance that the input effects remain constant, the variations must also be tested on experimental data. This is because simulated data presents the most ideal case, at least in this work: 10000 evenly spaced data points are generated, ensuring a very detailed scattering function, including a plethora of information at both low and high Q magnitudes on the logarithmic scale. Moreover, no errors are present in the simulated data set, to the point where a small error bar corresponding to 1% of intensity value must be added in to ensure the singular value decomposition method of extraction works. And that is not to mention errors that arise from data cleaning in the experimental case. Therefore, experimental input data may result in higher sensitivities of the PSF outputs.

The component SLD shift and number of input data investigation approaches were tested on an example of experimental data that was the most similar to the simulated models – i.e. used the same component and solvent SLDs (appendix 9 and 10 respectively). With experimental CV-SANS data obtained in the scope of this work, the contrast, and therefore solvent SLDs were kept constant for each ink series, consequently investigation of the contrast range input cannot be reproduced without also altering the number of input data. For the two reproducible investigations, the PSF output followed almost exactly the same observations as with simulated data. One difference observed was that the experimental PSF output was less sensitive to SLD(P) alteration than in the case of simulated data. This could be explained by the slight differences in between simulated and experimental datasets, or may alternatively suggest that the SLD(P) extracted from contrast match experiments is over-estimated. Nevertheless, assuming the latter, if the over-estimation is not extreme, the results should still provide a veritable result, as shown by the deviation study on simulated data. Despite the augmented perfection of simulated data, the input

investigation approach was highly successful and provides a lot of useful information to evaluation of PSF outputs from experimental data.

Nevertheless, one deviation between the outputs of simulation and experimental data has been found. A combination of the SLD solvent range and amount of input effects has been briefly studied utilizing the most dramatic cases, with only 3 data inputs and covering either the first or second half of the experimentally available contrast range. In this scenario again, the simulated core-shell model showed a remarkable robustness (appendix 11). For the spheres + cylinders model, the S_{cc} and S_{pp} remained as expected. However, when utilizing the second half of the contrast range only, the S_{cp} scattering extends over the entire Q range. On the other hand, when a similar investigation was applied to experimental data, the deviation was highly extrapolated in each case.

Figure 44 presents the PSF outputs of each combination scenario, for both the spheres + cylinders model simulated data and experimental ink data with matching component and solvent SLDs.

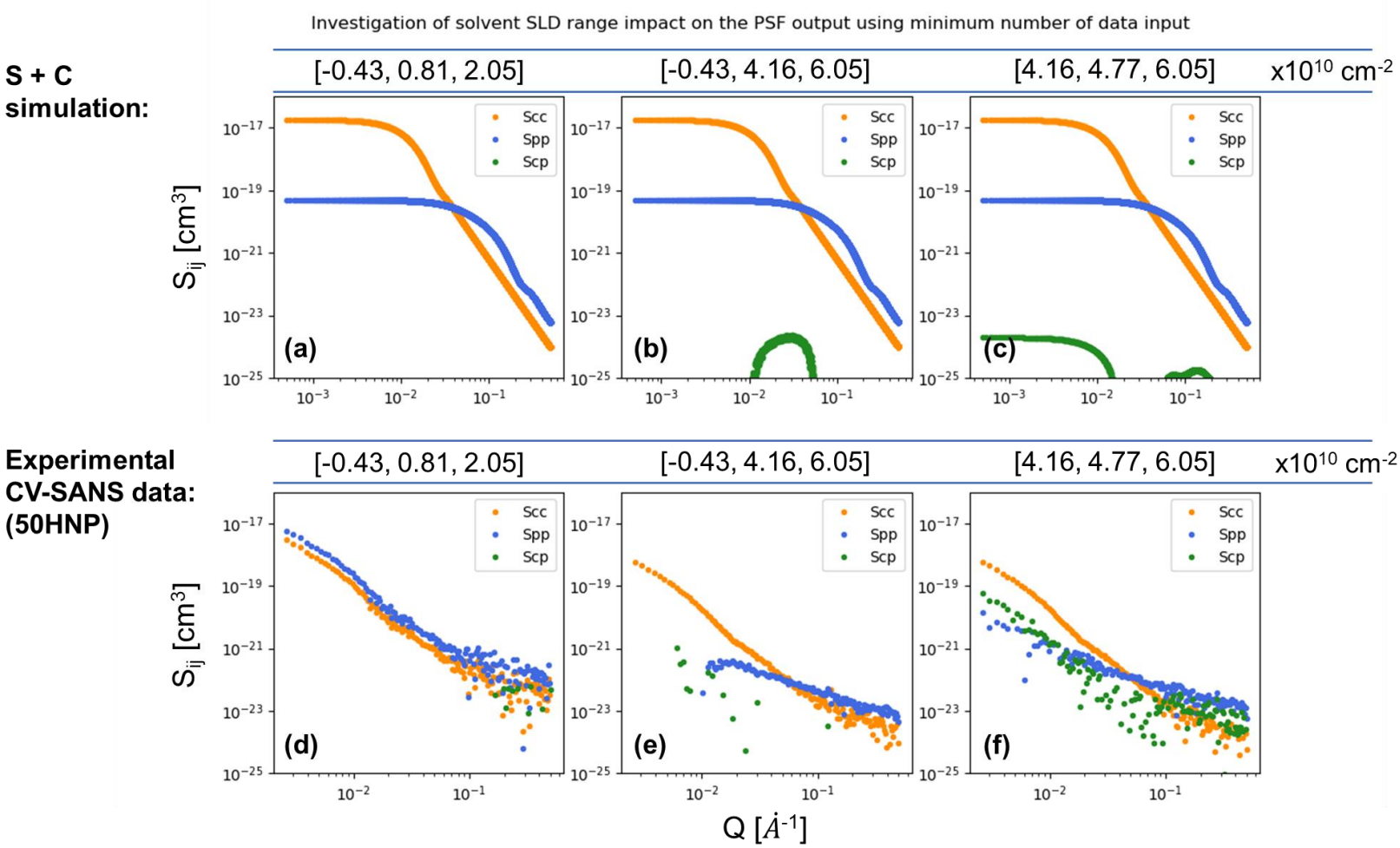


Figure 44. *Investigation of solvent SLD range impact on the PSF output using minimum number of input data.* ***(a), (b), (c)*** *show the PSF outputs of the spheres + cylinders simulation data when the first half, entire, and second half of the SLD solvent range are covered by the input respectively.* ***(d), (e), (f)*** *show the PSF outputs of experimental ink data when the first half, entire, and second half of the SLD solvent range are covered by the input respectively. The Sij scale has been kept constant for (a-f) for comparison purposes. Error bars have not been included for visualization purposes.*

Note a variation in the S_{cp} scattering for the spheres + cylinders simulation described above can be somewhat observed at lower S_{ij} values in figure 44 (a), (b), (c), however, as the S_{ij} scale is fixed in between outputs for improved comparison purposes, some of the S_{cp} outputs are cut-off.

Nevertheless, again, due to the low intensity and number of data points present, this variation would not lead to misinterpretation of data. And indeed, in the experimental data outputs, a similar trend can be observed for the S_{cp}, where a significantly larger number of data points appears when only the second half of the SLD solvent range is covered. However, the biggest difference can be observed in the S_{pp} output of experimental data. When covering the first half of the SLD range the S_{pp} scattering seems to largely mimic the S_{cc}, and therefore shows an interpretation of the carbon structure rather than the polymer. When the whole SLD range is covered in the 3 data inputs, the S_{pp} is over-subtracted in the low Q range ($Q<1x10^{-2}$ $\dot{A}^{-1}$). When the second half of the SLD range is covered, the S_{pp} again covers the entire Q range, however does not longer mimic the S_{cc} scattering.

As stated in literature, more input data yields more precise PSF outputs.[70] Therefore, the question arises, whether this deviation is only present in a case where the minimum number of input data is used, or whether it is caused by using only a section of the solvent SLD (contrast) range. For an extended insight, a similar study was performed on experimental data, but using 5 data inputs instead of 3, with the first and last input removed to avoid covering the entire contrast range, figure 45.

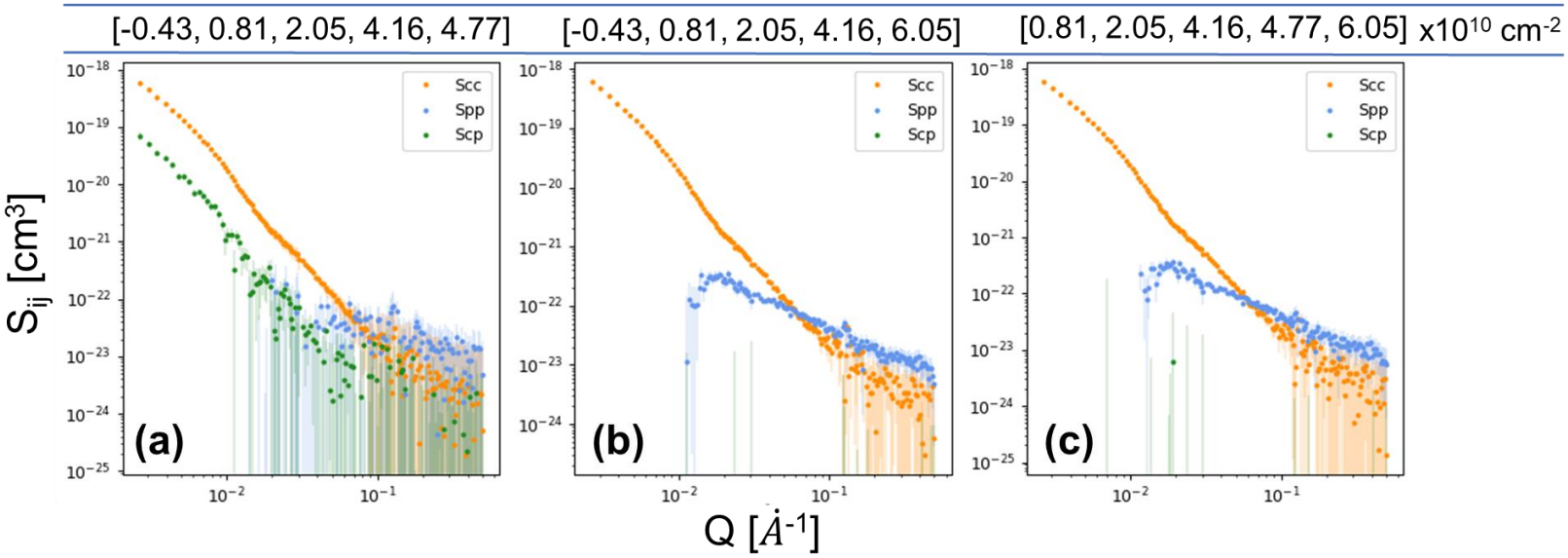


Figure 45. *Investigation of solvent SLD range impact on the PSF output using 5 input data files.* ***(a), (b), (c)*** *show the PSF outputs of experimental ink data when the first part, entire, and second part of the SLD solvent range are covered by the input respectively.*

In this instance, the output generated when the input covers the beginning of the contrast range but not the end again showed deviation, however the outputs generated when the end of the range was favoured, as well as when the whole contrast range was covered were identical. This suggests that the two input variations are correlated, but that indeed using a greater number of input data results in less deviation between the outputs over the chosen solvent SLD range. In order to gain more clarity on the effect of the solvent SLD range alone on experimental data PSF outputs, future work should involve measuring an ink series with a greater number of contrast variations across the entire experimentally available range, allowing for a selection of different input solvent SLD ranges while maintaining the same number of input data.

The question remains, which experimental PSF outputs show the real structural information of the system. Theoretically, 6 data inputs should yield the most trustworthy results, however the output deviation observed throughout this study leaves room for discussion. The carbon scattering can only ever be minimised when solvent SLD is high, but as scattering from carbon is very strong, for the majority of the contrast range available it will be strongly dominant over the scattering from the ionomer. A concern arises of whether any

information on the ionomer is extractable at lower solvent SLD values. Concomitantly, in the middle of the contrast range, and particularly for the two solvent chosen for this study, 4.16 and 4.77 x10^{10} cm^{-2}, the scattering from the ionomer is effectively matched out, again leaving carbon scattering as the sole expression. Therefore, of the three data inputs with the highest solvent SLDs, two are effectively the same, expressing carbon scattering only, and may not include enough information between them for reliable data extraction. In order to solve this obstacle, another data extraction approach is proposed where data manipulation is not as complex or reliant on numerous input parameters – direct scattering subtraction.

2.2.6.4 Direct scattering subtraction

The contrast terms for a two component system measured during CV-SANS experiments, denoted as HNP, where SLD(C) = 6.59x10^{10} cm^{-2} and SLD(P) = 4.48x10^{10} cm^{-2}, are described in table 5:

Sample code	Solvent SLD/ x10^{10} cm^{-2}	Δρ(C) / x10^{10} cm^{-2}	Δρ(P) /x10^{10} cm^{-2}	Component Expression
HNP0	-0.43	7.02	4.91	C > P
HNP20	0.81	5.78	3.67	C > P
HNP40	2.05	4.54	2.43	C > P
HNP71	4.16	2.43	0.32	C
HNP80	4.77	1.82	-0.29	C
HNP97	6.05	0.54	-1.57	P > C

Table 5*. Comparison of component expression in total SANS scattering at different contrast variations*

As shown in equation (2.2.1), total scattering can be expressed in terms of contrast and partial scattering functions. If the polymer component is matched out, and Δρ(P) = 0, carbon scattering can be simply expressed as:

$$\frac{\sum}{}(\quad) = (\Delta \quad)^2 \quad (\quad) \tag{2.2.15}$$

Therefore, if one component can be matched in the CV-SANS series, the subtraction should yield the polymer term and the cross-term combined. Indeed, the two cannot be further separated but can be used for determine which experimental output of the PSF extraction method is the most veritable. Note from table 5 that as there is no solvent SLD which yields Δρ(P) = 0. This is because the solvent SLD range was chosen before the component contrast match measurements were performed (instead solvent SLD of 4.16x10^{10} cm^{-2} corresponds to the theoretical SLD of Nafion). Therefore, it has to be assumed that due to the strong scattering nature of carbon and the almost complete match to the SLD(P), the scattering corresponds to the carbon only. Moreover, as it is the $(\Delta\rho)^2$ that is considered, the differences between contrast terms with a very large and very low values will be further extended. Therefore, Δρ(P) is considered small enough to obtain a valid approximation of expected output.

Consider two experimental data inputs, one containing both carbon and polymer information (HNP0, solvent SLD = -0.43x10^{10} cm^{-2}), and one containing only carbon structural information (HNP71, solvent SLD = 4.16x10^{10} cm^{-2}), (figure 46(a)):

HNP0: $$\frac{\sum}{}(\quad) = (\Delta \quad _{,0})^2 \quad (\quad) + (\Delta \quad _{,0})^2 \quad (\quad) + 2\Delta \quad _{,0}\Delta \quad _{,0} \quad (\quad) \tag{2.2.16}$$

HNP71:

$$\frac{\sum}{}(\ ) = (\Delta\ _{,71})^2\ \ (\ ) \qquad (2.2.17)$$

In order to subtract the carbon structural information common to both the datasets, the S_{cc} must be isolated from the carbon contrast term:

HNP0:

$$\frac{\sum(\ )}{(\Delta\ _{,0})^2} = \ (\ ) + \frac{(\Delta\ _{,0})^2}{(\Delta\ _{,0})^2}\ \ (\ ) + \frac{2\Delta\ _{,0}\Delta\ _{,0}}{(\Delta\ _{,0})^2}\ \ (\ ) \qquad (2.2.18)$$

HNP71:

$$\frac{\sum(\ )}{(\Delta\ _{,71})^2} = \ (\ ) \qquad (2.2.19)$$

(HNP0) – (HNP71):

$$\frac{\sum(\ )}{(\Delta\ _{,0})^2} - \frac{\sum(\ )}{(\Delta\ _{,71})^2} = \frac{(\Delta\ _{,0})^2}{(\Delta\ _{,0})^2}\ \ (\ ) + \frac{2\Delta\ _{,0}\Delta\ _{,0}}{(\Delta\ _{,0})^2}\ \ (\ ) \qquad (2.2.20)$$

Figure 46. shows a visual representation of the above described scattering subtraction manipulation:

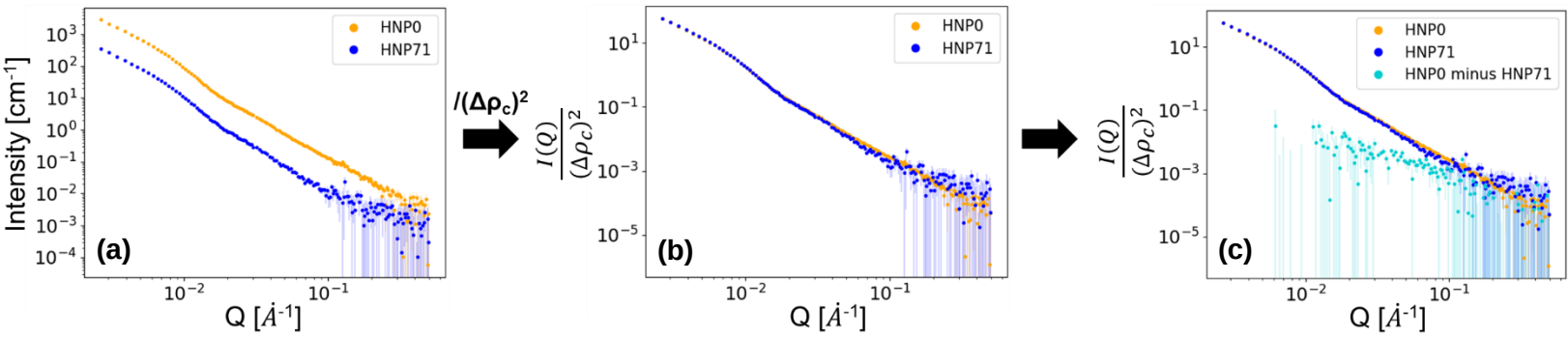


Figure 46. *Scattering subtraction method applied to experimental SANS data for a catalyst ink. Only two data sets from the 6 data set series were selected: HNP0 (orange), which contains structural information of the carbon, ionomer components as well as the cross-term; HNP71 (blue), which contains structural information on the carbon component only.* ***(a)*** *original CV-SANS data after processing,* ***(b)*** *CV-SANS data divided by the carbon contrast term (7.02 and 2.43 for HNP0 and HNP71 respectively),* ***(c)*** *CV-SANS data divided by the carbon contrast term as well as the (HNP0-HNP71) subtraction output (cyan).*

As can be observed, when a division by the carbon contrast term is applied to the data, the datasets are perfectly overlapping in the low Q regime ($Q<1x10^{-2}$ $\dot{}^{-1}$), with deviation observed in the mid Q region ($Q>4x10^{-2}$ $\dot{}^{-1}$) onwards. Predictably, the subtraction output is missing data points in the low Q regime ($Q<1x10^{-2}$ $\dot{}^{-1}$), interestingly already showing similarities to the experimental S_{pp} output of this ink data series from the PSF extraction method when a full solvent SLD range is covered (although the subtraction output contains both the s_{pp} and the S_{cp}). In the mid/high Q regime ($Q>5x10^{-2}$ $\dot{}^{-1}$) large error bars can be observed, due to propagation of uncertainty from the HNP0 and HNP71 scattering functions.

The subtraction output can now be compared to the deviating S_{pp} and S_{cp} outputs arising from each of the conditions imposed on the PSF method inputs, presented in figure 46, by processing with the correct contrast terms as shown in equation (2.2.20):

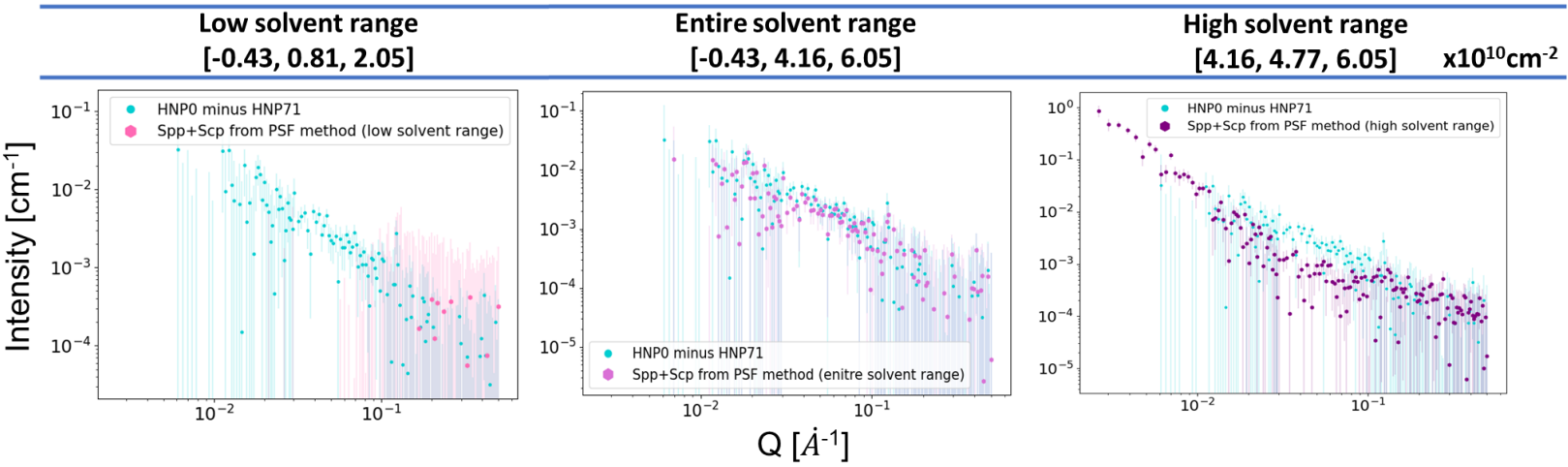


Figure 47. *Comparison of the scattering subtraction output (cyan) to Spp, Scp terms processed by contrast terms (pink/purple), obtained from the PSF extraction method with different solvent SLD inputs and minimum data inputs.*

Figure 47. clearly demonstrates that the scattering subtraction output perfectly matches the processed S_{pp} and S_{cp} outputs from the PSF method when the whole solvent SLD range is utilized in the input. For the instance where only half of the available contrast range is selected as the input, the processed S_{pp} and S_{cp} terms deviate greatly from the scattering subtraction output. This suggests that, at least in the instance of 6 or less data inputs, it is important to include the entire experimentally available contrast range in the PSF extraction input. In order to verify this result is reproducible, the scattering subtraction method has been further evaluated on a CV-SANS ink series, where initial PSF outputs suggested the presence of another structure, as well as on both model simulations presented above (appendix 12). Again for experimental data the processed output which utilised the whole solvent SLD range showed a perfect match to the scattering subtraction approach. In the case of the spheres + cylinders based outputs, a match was obtained no matter the solvent SLD range used. Interestingly, for the core-shell simulation, the processed S_{pp} and S_{cc} outputs never perfectly matched the subtraction outputs, although they were in good agreement. Moreover, this was the case from each solvent SLD range investigated, which suggests this may be a structural effect rather than input related variation. Nevertheless, enough information has been gathered to suggest utilizing the entire contrast range in the solvent SLD inputs is the optimal approach for data processing.

In conclusion, a detailed investigation of the effects of input variation on the PSF extraction has been performed. Simulated data for two structural models, representing the case of no adsorption of ionomer to carbon, and full adsorption of ionomer to carbon were utilized in order to compare the PSF outputs with fully known structural information. The investigation on simulations highlighted that the PSF outputs are the most sensitive to variation in component SLD, where a shift as small as 0.01×10^{10} cm^{-2} from the true SLD resulted in erroneous results in certain cases. This was particularly the case for the spheres + cylinders model based simulation, where small SLD deviation in some instances resulted in an appearance of a cross-term output, which could lead to a misleading suggestion of ionomer adsorption to carbon occurring in the system. On the other hand, the core-shell model based simulation showed overall a higher degree of robustness in the PSF outputs. Additionally, it has been noted that in the case of partial adsorption, if there is less than 10% of core-shell model in simulation, a deviation in the S_{cp} could be observed. In the

case of simulated data, varying the solvent SLD range and the number of input data used showed no difference in PSF outputs for both models.

The component SLD shift and number of input data investigations were applied to experimental data to verify that conclusions reached when looking at simulations could be carried through. The solvent SLD range could not be investigated due to unavailability of required experimental data. Both investigations showed the same behaviours, proving tests on simulations are a viable approach for evaluating the PSF method. However, when minimising the input data to the lowest possible amount (3 datasets), and using different ranges of the experimentally available solvent SLD range, deviation between experimental and simulated outputs was noticed. Simulations remained fairly insensitive to the variation in the input effects combined together, while PSF outputs from experimental data showed significant difference dependent on the solvent SLD range used.

By comparing the varying PSF outputs to S_{pp} and S_{cp} combined scattering obtained through direct CV-SANS data subtraction, it has been concluded that it is important to utilize the entire contrast range when extracting PSFs from experimental data.

As per the conclusions of the investigation the input procedure for extracting PSFs in this work is as follows – use of 6 datasets as inputs for maximum precision, with the contrast covering the entire range available experimentally, and each component SLD measured through contrast matching experiments to obtain the most accurate value possible. In addition, the effect of SLD shift on the PSF output deviation will be utilized to assess the veracity of the PSF outputs obtained using component SLDs extracted from contrast match experiment.

Following such an approach we expect to extract information on the ink with regards to the structure of each component and their location with good reliability.

2.3 CV-SANS experimental results – investigation of catalyst ink structure variation as function of ink composition

Over the course of the PhD project several CV-SANS experiments on the D22 beamline of the ILL were performed, measuring catalyst inks of different compositions, each as a series of 6 samples with altering solvent contrasts. Additionally, component SLD values were extracted from contrast match experiments, for each carbon as well as ionomer component used. In the case of the latter, contrast match experiments were performed for samples of ionomer dispersed in different solvent systems (iPrOH/water with varying ratios) investigated throughout this work, and some analysis on the ionomer conformation itself was performed.

2.3.1 Methodology

2.3.1.1 Sample preparation

Commercially available materials were used throughout this work. High surface area carbon with 50 wt% Pt loading (TEC10E50E) and graphitized carbon with 50 wt% loading (TEC10EA50E), as well as carbon only alternatives (E and EA respectively) were sourced as nanopowders from Tanaka Precious Metals. Nafion D2020 was purchased from Chemours, as a 20-22 wt% dispersion in 40-48 wt% 1-propanol and 30-38 wt% water. For the sake of sample preparation, the following amounts were estimated: Nafion (20 wt%), 1-propanol (45 wt%), water (35 wt%). Aquivion D83-24B was obtained commercially from Solvay Specialty Polymers, as a dispersion of 24 wt% Aquivion and 76 wt% water. Isopropanol ≥ 99.5% purity (purchased from Sigma-Aldrich) and ultrapure water (18.2 mΩ cm^{-2}) were used as hydrogenated solvents. 2-Propanol-d8, ≥99.5 atom % D and D_2O, ≥99.9 atom % D (both sourced from Sigma-Aldrich) were used as deuterated solvents.

For each solvent system of a desired alcohol:water wt% ratio, two solvent stock solutions were prepared – one with fully hydrogenated solvents and one with fully deuterated counterparts.

Two ionomer stock solutions were also prepared, 4 wt% ionomer dispersions in the hydrogenated and the deuterated solvent mixtures respectively. This was achieved by combining desired amounts of the commercially sourced ionomer dispersion and the corresponding solvent stock solutions. Note because the ionomer comes pre-dispersed in hydrogenated solvents, the deuterated ionomer stock solution contained several wt% of hydrogenated solvent contamination.

Figure 48. shows a general procedure for the preparation of catalyst ink samples:

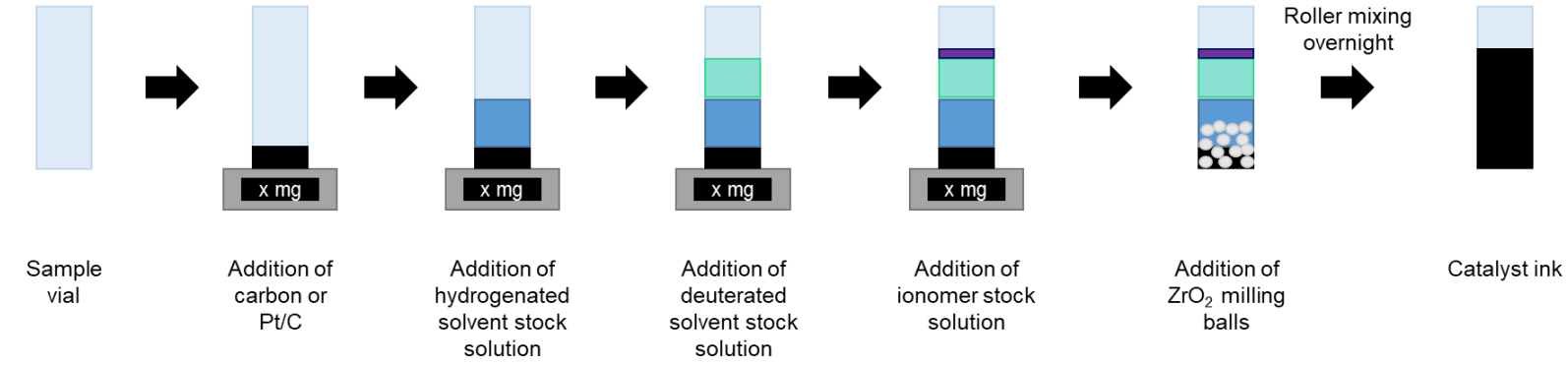


Figure 48. *Schematic of catalyst ink sample preparation.*

For each ink composition, a series of samples with 6 different contrasts was prepared. The sample contrast was altered by adding different proportions of the hydrogenated and deuterated solvent stock solutions to the sample. For samples of lower contrast (0-71 wt%), 4 wt% ionomer stock solution in hydrogenated solvent was used. For samples of higher contrast (80 and 97 wt%), 4 wt% ionomer stock solution in deuterated solvent was used. Note due to hydrogenated solvent contamination in the ionomer stock solution based on deuterated solvent, a maximum of 97 wt% solvent deuteration could be achieved. Therefore, the 6 contrasts used in each series, denoted by wt% of deuterated solvents used, were approximately: 0, 20, 40, 71, 80 and 97.

One alteration of the procedure presented in figure 48 arose in the case of ink compositions requiring both the Pt/C complex and high proportions of alcohol in the solvent, where water and alcohol had to be added separately. The Pt/C complex was hydrated with water first and then alcohol was added to avoid any fire hazards associated with the oxidative nature of dry Pt nanoparticles.

3 mm zirconia balls were added to the ink, and the components in the slurry were dispersed by mixing on a roller mill (Pheonix RS-TR05) overnight. The final dispersed samples were stable over the period of several days.

Each ink series has been given a specific code that describes its composition and follows the pattern described below:

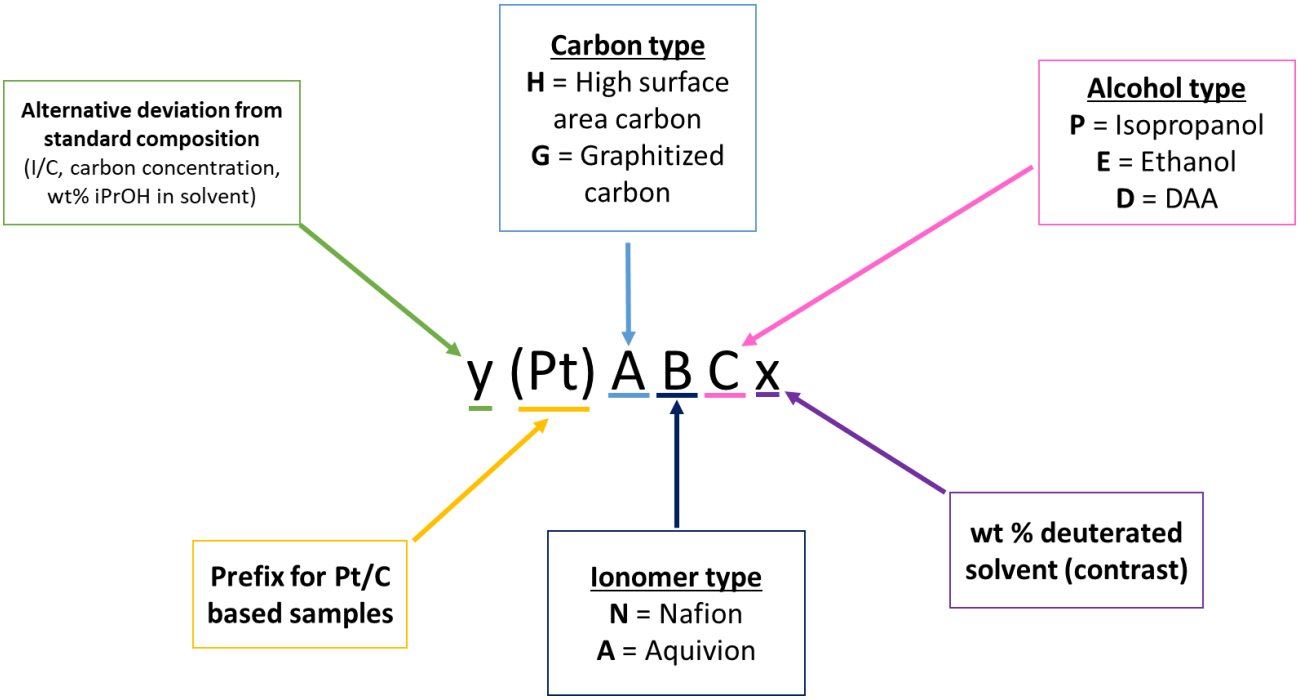


Figure 49. *Schematic for general naming of catalyst inks with different compositions.*

The most fundamental ink compositions can be described by the 'ABCx' parameters. For example, the code HNP20 describes an ink based on HSAC, Nafion and iPrOH/H_2O solvent, which is 20 wt% deuterated. In the case of this notation, the other compositional parameters are fixed as: 1 wt% carbon, I/C = 0.8 and 50 wt% of iPrOH in the solvent mixture. A Pt prefix is given to samples which contain the Pt/C complex (with 50 wt% Pt loading) rather than the carbon only nanopowder. Therefore, an ink denoted as PtHNP20 would include 1 wt% Pt + 1 wt% HSAC, Nafion with I/C = 0.8 and 50:50 wt% iPrOH/H_2O solvent, which is 20% deuterated. The prefix y is a broad term used when one of the normally fixed parameters is being investigated. For example, if the effect of the amount of alcohol in the solvent system is being studied on the HNP ink, notations of 25HNP, 50HNP and 75HNP may be made to describe the % of iPrOH used in the solvent system (25, 50, and 75 wt%).

Ionomer contrast match samples were prepared by mixing the corresponding ionomer and solvent stock solutions to yield a 2 wt% ionomer dispersion in a desired iPrOH:water based medium, with typical solvent deuterations being: 0, 25, 75 and 90 wt%.

Carbon contrast match samples were prepared by firstly creating two 0.1 wt% carbon stock solutions – one in conventional N,N-dimethylformamide (DMF, ≥ 99%), and one in the deuterated version (DMF-d7, ≥ 99.5 atom % D), both purchased from Sigma-Aldrich. Dilution to 0.01 wt% with corresponding solvent stock solutions followed to yield samples of a desired deuteration degree. 6 or 7 samples at the following deuteration degrees were used: 0, 12.5, 25, 50, 75, 85 and 95 wt% of deuterated solvent. DMF solvent and very low concentrations were opted for in order to improve sample stability throughout the SANS data acquisition. Additionally, a large number of samples with different contrasts was chosen in order to allow for a successful SLD extraction from the contrast match method even if some stability concerns remained.

2.3.1.2 Instrumental set-up and data processing

All catalyst ink samples were measured using a 6 Å neutron wavelength, 10x7 mm rectangular beam , at two different configurations, with the back 2D detector placed 4m or 17m away from the sample, resulting in collimation lengths of 4 and 17m respectively. At 17m a large Q range of $2.5x10^{-3}$ – $6.4x10^{-1}$ Å^{-1} was obtained. A measurement with the detector and collimation at 4m from sample yields a shorter Q range of $1.3x10^{-2}$ – $7.1x10^{-1}$ Å^{-1}, however the neutron flux, and consequently measurement statistics are improved. Each data set was reduced as described in section 2.1.2, using the GRASP software, but before any further processing (reference subtraction etc.), the corresponding 4m and 17m datasets were stitched together at approximately Q = 0.035 Å^{-1}. This resulted in a scattering function that has both the benefits of a long Q range from the 17m configuration, as well as good statistics in the mid and high Q regimes (Q>$1.3x10^{-2}$ Å^{-1}) from the 4m configuration. Following this step, the data was processed by removing solvent scattering contributions (subtracting reference scattering functions) and incoherent scattering. During each beamtime, measurements of solvent samples at each contrast used were collected at the 4m configuration. As the scattering from the solvent reference is largely due to the incoherent scattering (no structure is observed) and is a flat signal, the scattering intensity could be extrapolated to cover the extended range present in the measurements collected at 17m. The reference solvent scattering was subtracted from each catalyst ink sample of corresponding contrast to remove the dispersion medium contributions. Following, a Q limit of 0.5 Å^{-1} was applied to disregard the noisiest data in the high Q range. An example of a fully processed dataset for one catalyst ink series can be found in figure 30.

Measurements of the carbon and ionomer only dispersions, destined for contrast match studies, were obtained using the 17 m configuration only. In the event of also using this data for structural analysis of individual components, background was removed by subtracting a constant which was obtained through averaging I(Q) in the high Q regime of 0.4 – 0. 5 Å^{-1}.

2.3.2 SANS on component dispersions

partial scattering functions, it is prudent to evaluate CV-SANS data of singular components. Although the primary Before discussing catalyst inks and corresponding purpose is to extract experimental SLD values for each component, structural information can also be obtained.

2.3.2.1 Ionomer dispersions

CV-SANS data was obtained for 2 wt% ionomer dispersion in iPrOH/water solvents with an increasing concentration of iPrOH, ranging from 0 wt% to 75 wt%, each at solvent deuteration ranging from 0 to

approximately 90 wt%. Figure 50 shows scattering functions of the 2 wt% Nafion dispersions in solvents with varying iPrOH concentration, at 0 wt% solvent deuteration only.

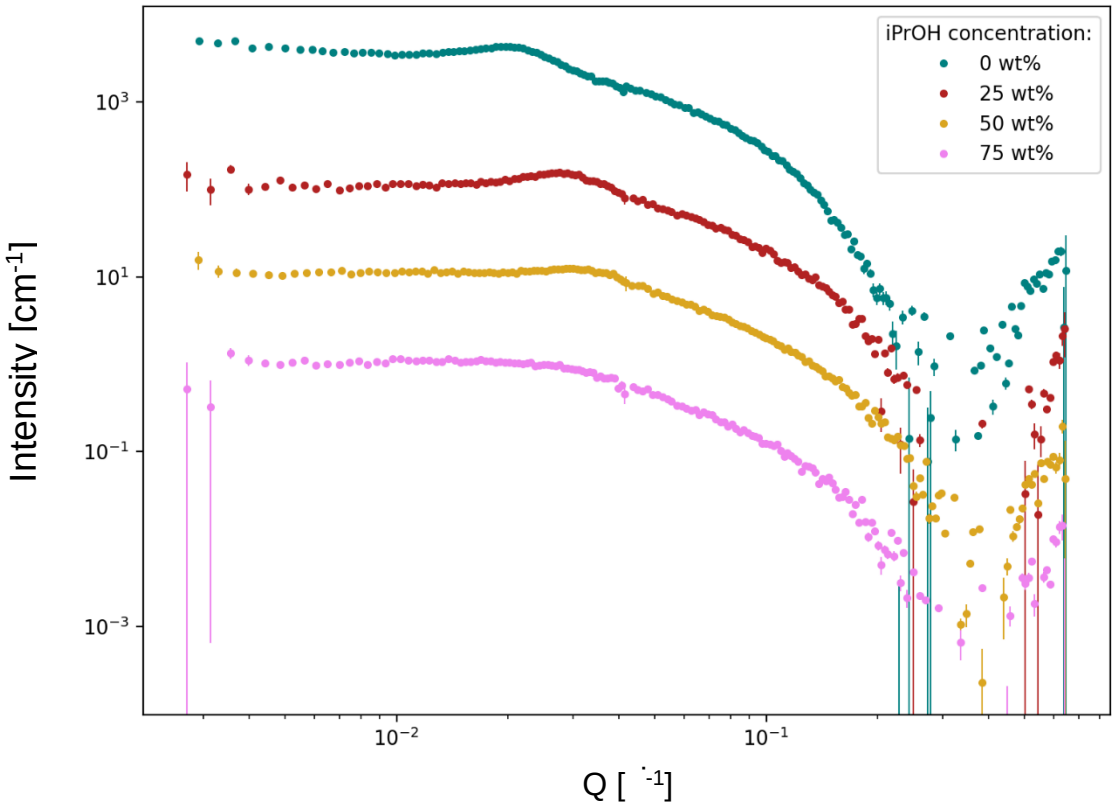


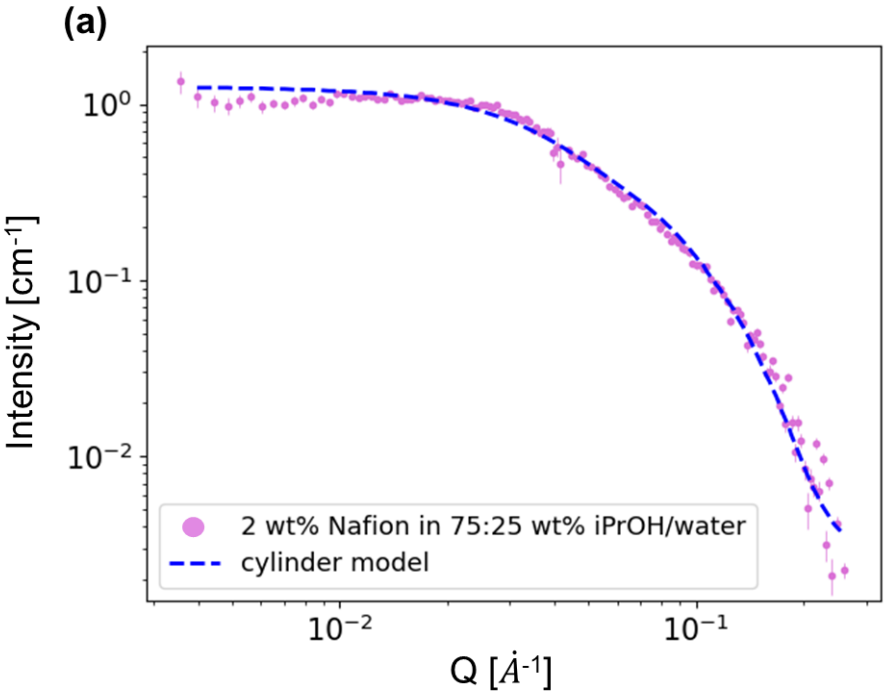
Figure 50. *SANS data of 2 wt% Nafion in solvents with varying iPrOH:water ratios (0 wt% solvent deuteration). Data has been shifted on a logarithmic scale for visualization purposes (original version can be found in appendix 13).*

Nafion forms rod-like aggregates, which display short range ordering in between each other, resulting in a structure factor observable as a peak-like feature.[17] The most notable difference in the scattering functions of Nafion in different iPrOH concentrations is a shift of the said inter-particle interference term[17] from Q ≈ 0.035 to 0.020 Å^{-1}. The position of the interference term is related to the inter-particle ordering, as well as the concentration of the scatterer. Through dilution studies Gebel et al.[91] showed that the interference peak position shifts with the square root of the concentration, indicating bidimensional dilution of rod-like aggregates. It was noted such a behavior suggests that the size and the shape of the aggregates is independent of concentration.

As the concentration of iPrOH in the solvent decreases, the peak feature becomes more pronounced and its position shifts to lower Q values, associated with larger sizes. In the low Q regime (Q<1x10^{-2} Å^{-1}), a flat scattering, I(Q) Q^0, can be observed, associated with a lack of further structural features in this size domain. In the mid and high Q regimes, after the peak feature (Q>3x10^{-2} Å^{-1}), power law type scattering remains fairly consistent for each dispersion that contained some iPrOH. The scattering from Nafion dispersed in water deviates slightly from the others, where a steeper power law can be observed in the high Q regime (Q>1x10^{-1} Å^{-1}). Moreover, in the low Q regime (Q<1x10^{-2} Å^{-1}) scattering does not completely tend to Q^0 (flat scattering), which may be indicative of bigger structural features not observed for iPrOH containing dispersion.

Gebel et al.[17] determined the shape and size of Nafion aggregates, with a typical value of 2 nm extracted for the aggregate radius, and noted the scattering function could be well fitted using a cylinder form factor model. However, this was the case for very dilute samples where no structure factor (interference term) related features could be observed in the scattering function.

The presence of the structure factor will interfere with accurate extraction of the cylinder shape parameters (length and radius), and there is no distinct structure factor model designed to fit anisotropic elongated objects, such as the cylinder. More dilute versions of the Nafion dispersion, with no structure factor scattering, should be measured in order to extract the ionomer structure. Nevertheless, in figure 50 it can be observed that the scattering function related to a 2 wt% Nafion dispersion in 75:25 wt% iPrOH/water solvent shows no structure factor related peak feature, and is suitable for fitting. Figure 51 shows a fitting of the above mentioned scattering function with the cylinder form factor.



(b)

Cylinder

Scale = 4.62e-03 ± 3.00e-05
Sld = 4.53x10^{10} cm^{-2}
Sld_solvent = -0.38x10^{10} cm^{-2}

Radius = 14.63 ± 6.52e-02 Å
Length = 131.14 ± 1.23 Å

Distribution of radius = 0.20
Distribution of thickness = 0
(function:lognormal)

Chi^2/Npts = 12.07

Fitting performed using SasView 5.0.6, SasModels version 1.0.7, Fit optimizer DREAM

Figure 51. (a) *Scattering function of 2 wt% Nafion in 75:25 wt% iPrOH/water solvent, fitted with the cylinder model using SasView 5.0.6 software.* ***(b)*** *Parameters extracted from fitting.*

The fit performed using the cylinder model is coherent to the Nafion scattering function, with a satisfactory chi^2 value of 12.1 reported. A smaller radius of 1.5 nm has been extracted, in comparison to values reported by Gebel et al.[17], however, note this is most likely as a result of different solvent systems utilized in the two works. Additionally, a length value of 13.1 nm was obtained, confirming Nafion forms anisotropic, rod-like aggregates in 75:25 wt% iPrOH/water solvent also. Considering a shape similarity (with the exception of a structure factor) between scattering functions of Nafion observed in figure 50, it can be assumed both scattering functions of 2 wt% Nafion in 50:50 and 25:75 wt% iPrOH/water solvent would also be coherent with the cylinder model.

Nevertheless, the primary purpose of this data was the determination of accurate SLD values for the Nafion component in varying solvent systems, to be utilized during extraction of PSF outputs from catalyst inks. Four scattering functions with different contrasts were used for SLD extraction using the contrast match method, following the procedure demonstrated in section 2.2.3.

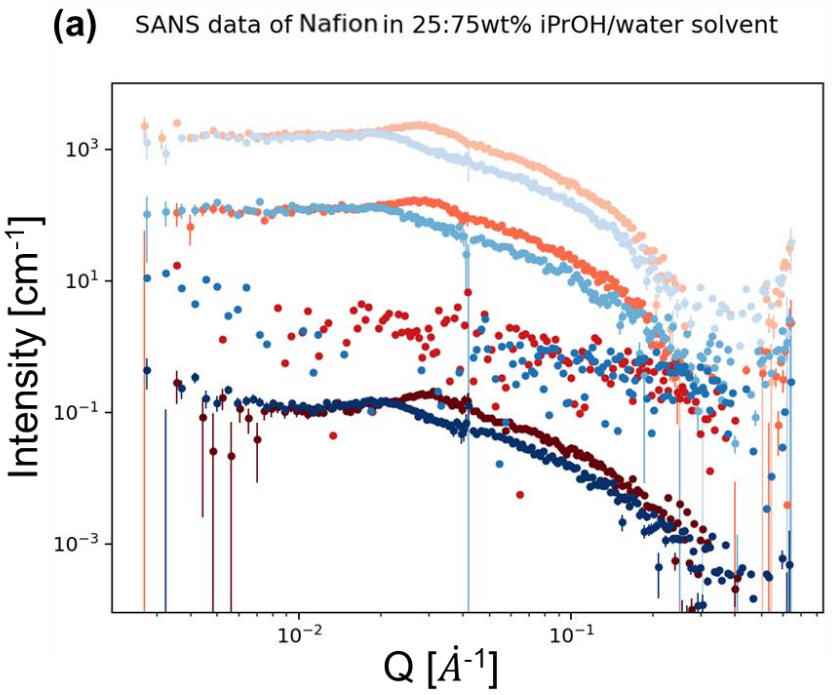
Table 6 shows SLD values for Nafion ionomer in different solvent systems (full figures of CV-SANS data and contrast match linear plots in appendix 14). Note the concentration of the ionomer, and therefore the volume fraction, was kept constant for all the samples.

iPrOH:water (wt%)	**Extracted SLD ($x10^{10}$ cm^{-2})**
0:100	3.77 ± 0.01
25:75	4.22 ± 0.02
50:50	4.48 ± 0.01
75:25	4.53 ± 0.01

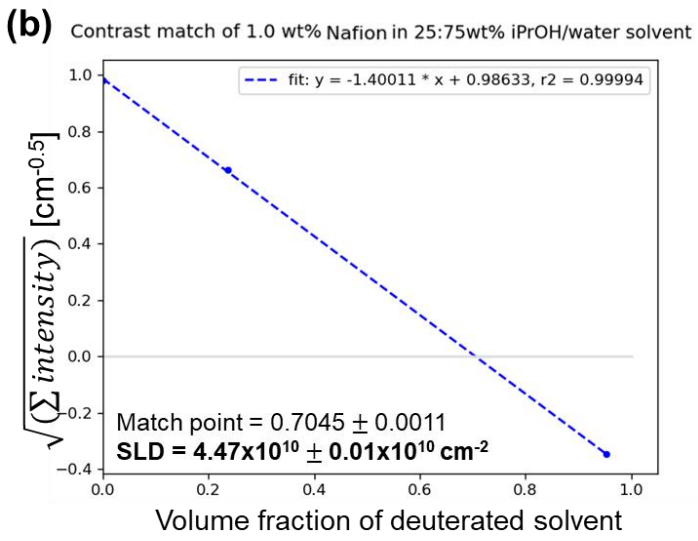
Table 6. *Extracted SLD values of 2 wt% Nafion in solvent systems with varying iPrOH concentration.*

Variations can be observed in the extracted SLD values, where the SLD shows a non-linear decreasing trend with decreasing iPrOH concentrations. The difference is again the most pronounced for the Nafion in water dispersion, with a comparably low SLD of $3.77x10^{10}$ cm^{-2}. Because the SLD is directly related to density (equation (2.1.9)), with no changes to the material composition itself, a decreasing SLD would also signify a decreasing density (from Nafion density of 2 g/cm^3)[17], indicating variation in molecular volume with decreasing concentrations of iPrOH in solvent. However, as contrast matching is a technique designed to measure the SLD of the molecule, irrelevant of structural conformations, it is unclear where this change may arise from. One possibility would be if solvent molecules are present in between the monomer chains making up the elongated aggregate, creating a less compact structure, which could be interpreted as decreasing density of the overall molecule. Another option could consider altered interfacial interactions with the solvents, or a varying degree of crystallinity present in the hydrophobic ionomer backbone.[92]

Moreover, the SLD extracted from contrast matching experiments should not change with concentration of the molecule. However, interestingly, such a variation was observed for Nafion dispersed in 25:75 wt% iPrOH/water solvent. Figure 51 compares the scattering functions as well as contrast matches of 2 and 1 wt% Nafion dispersed in the above mentioned solvent.



Solvent deuteration [wt%]	1 wt% Nafion	2 wt% Nafion
0		
25		
75		
100		



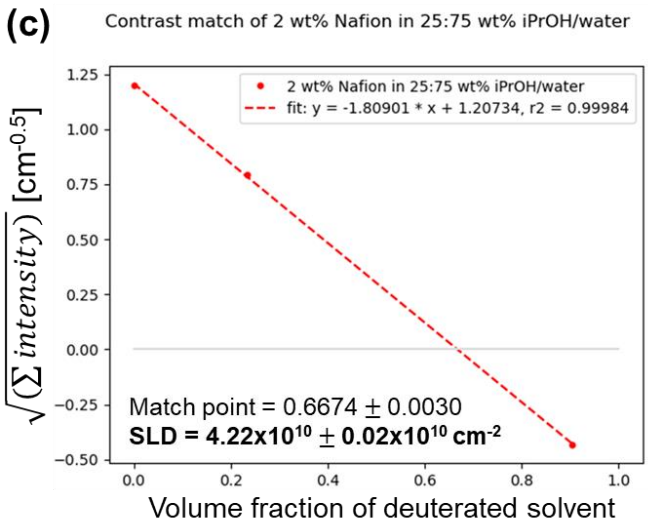


Figure 51. (a) *SANS data of Nafion in 25:75 wt% iPrOH/water solvent. Data has been shifted, and error bars have been excluded in data corresponding to 75 wt% solvent deuteration for visualization purposes.* ***(b)*** *contrast match of 1 wt% Nafion in 25:75 wt% iPrOH/water solvent.* ***(c)*** *contrast match of 2 wt% Nafion in 25:75 wt% iPrOH/water solvent.*

The SLD determined from contrast match measurements, of 2 wt% Nafion dispersion was 4.22×10^{10} cm^{-2}. On the other hand, for contrast match measurements of 1 wt% Nafion dispersion the SLD extracted was 4.47×10^{10} cm^{-2}, a value much closer to that for Nafion dispersed in solvents with higher iPrOH concentrations. In both instances the intensity in the Q range where a peak feature was observed was used for contrast match determination (Q ≈ 0.02-0.04 and 0.015-0.02 Å^{-1} for 2 wt% and 1 wt% Nafion scattering functions respectively). In figure 51(a) it can also be observed that the position of the peak related to the structure factor is different for the data of Nafion at two different concentrations (Q ≈ 0.03 and 0.01 Å^{-1} for 2 and 1 wt% Nafion scattering functions respectively). However, this is to be expected as this feature is indeed concentration dependent, yet should not influence the SLD of the material. As was shown by Gebel et al.[91] using dilution studies, the size and shape of the aggregates should not change with the concentration of the scatterer. Yet these findings were made when the ionomer was dispersed in a 50:50 wt% EtOH/water solvent, therefore it is possible the dilution behaviour would be different for the samples presented in this work. The significant difference could also be related to the error bar, where small changes

in the match point could result in significant variation of extracted SLD value, although the calculated uncertainty does not point towards this.

Nevertheless, it is important to consider that the variation observed could suggest the structure of Nafion aggregates may be concentration dependent in this type of solvent. Contrast match experiments on very dilute Nafion dispersions, with no inter-particle interference term, may aid to shed light on the accurate SLD value of the material, and/or the concentration dependent ionomer aggregate structure. Additionally, re-measurement of the 1 and 2 wt% samples should be performed to confirm the validity of the SLD discrepancy.

As thoroughly discussed in section 2.2.6.1, the component SLD has a big impact on the PSF outputs extracted from CV-SANS data. This alteration suggests that component SLDs should not only be determined experimentally, but also using similar component concentrations as in the ink samples. However, this may not always be possible. For example, obtaining a stable carbon dispersion can be arduous at higher concentrations.

The effect of variation in ionomer SLD as a function of concentration on the extracted PSF outputs was investigated for an ink series with the corresponding solvent composition, 25HNP.

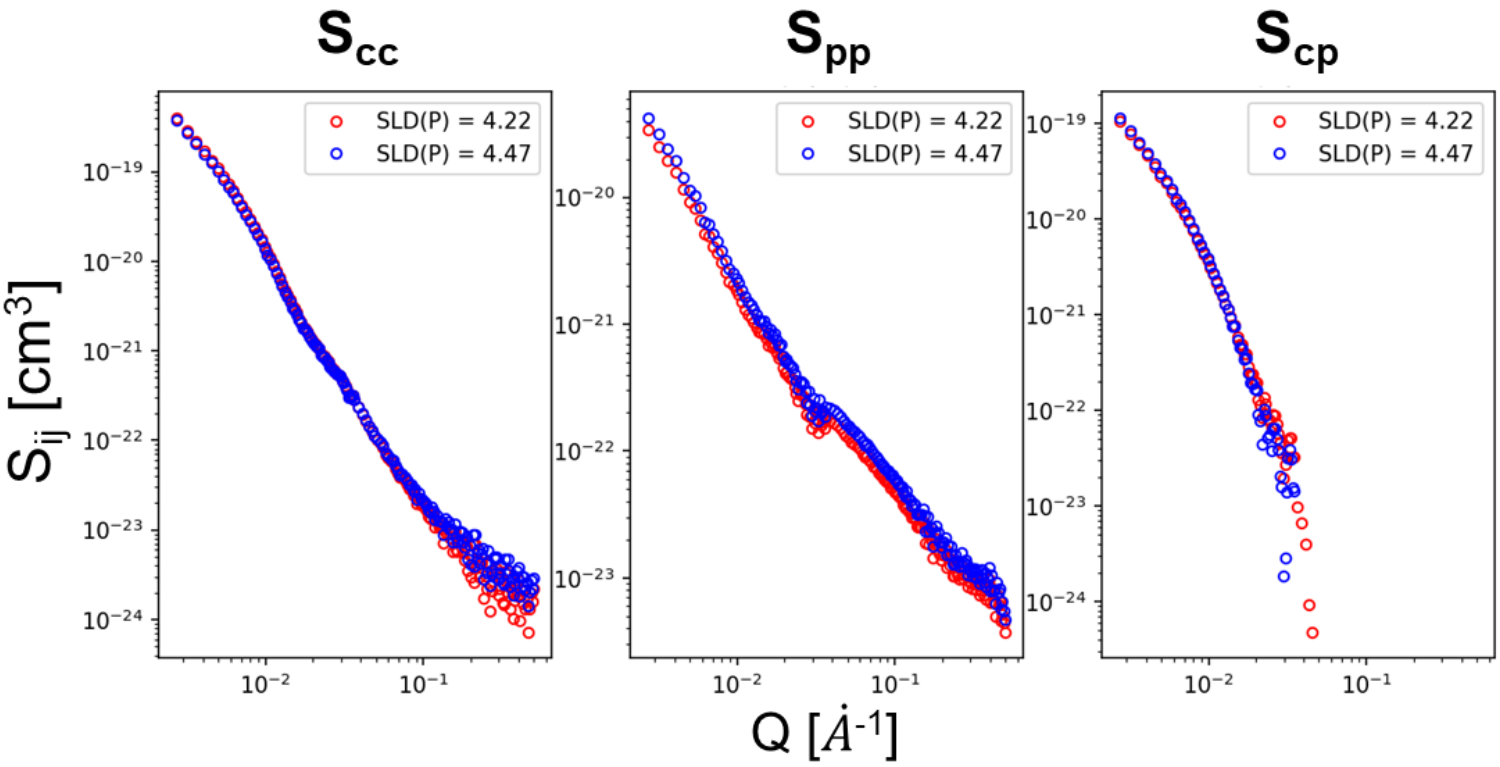


***Figure 52**. Partial scattering functions extracted from 25HNP ink series (1 wt% HSAC, Nafion with I/C = 0.8, 25:75 wt% iPrOH/water solvent), with the ionomer component SLD inputs of 4.22x10^{10} cm^{-2} (red) and 4.47x10^{10} cm^{-2} (blue). The carbon component SLD was kept fixed at 6.59x10^{10} cm^{-2}, a value extracted from contrast match measurements.*

The variation in extracted Nafion SLD does not have a great impact on the PSFs extracted for the corresponding ink series. Concurrently, when investigating the effect of component SLD input on PSF extraction from experimental data, it was also noted that deviation in ionomer SLD does not have a great impact on the PSF outputs extracted (unlike the deviation in carbon SLD).

Moreover, dispersions of Nafion with higher iPrOH content do not seem to show the same Nafion concentration effect. SLDs determined from 0.8 and 2 wt% Nafion in 50:50 wt% iPrOH/water solvent were

4.50 and 4.48 x10^{10} cm^{-2}, very coherent values (appendix 15). Therefore, it can be deduced that either Nafion behaves very differently in water-rich solvent to mixture solvents with higher alcohol proportions, or more probably an error is present in one of the two sample series measured in 25:75 wt% iPrOH/water solvent.

As it has been shown that the extracted SLD does not have a major impact on extracted partial scattering functions, for the sake of consistency, the input SLD chosen for the ionomer component will always be from contrast match measurements performed on 2 wt% Nafion based dispersions. This is because, although the 1 and 0.8 wt% Nafion dispersions were closer in concentration to the Nafion present in catalyst inks, contrast match measurements of the ionomer at this concentration were not measured for all the solvent systems investigated in this work. Moreover, considering that ionomer SLD should be independent of concentration, scattering intensity from 2 wt% ionomer dispersions would be greater, yielding improved measurement statistics, and making the SLD extraction more reliable. Overall, maintaining the values from 2 wt% Nafion dispersion allows for a better cross-comparison of data.

2.3.2.2 Carbon dispersions

Graphitized and high surface area carbon dispersions were prepared at 0.01 wt% concentration in DMF and deuterated DMF (DMF-d7) solvents, depending on the solvent deuteration degree desired. For successful SLD extraction, a fixed concentration that yields a stable dispersion throughout the measurement time must be ensured in each sample. In the catalyst ink, the ionomer also acts as a stabilizer between carbon aggregates. However, pure carbon does not yield very stable dispersions. The DMF based solvent and low concentrations were chosen to boost the stability of carbon dispersions. It must be assumed that unlike in the case of the ionomer, the SLD of carbon will not vary with concentration or solvent. Additionally, an increased number of samples across the deuteration range was measured to ensure a precise SLD value can be obtained. As the samples were very dilute and consequently no distinct structural features can be observed, intensity in the low Q region (3x10^{-2} – 6x10^{-2} $\dot{-}^{-1}$) was utilized for the contrast

match method. Figure 53 shows CV-SANS measurements of carbon dispersions, along with their respective contrast matches.

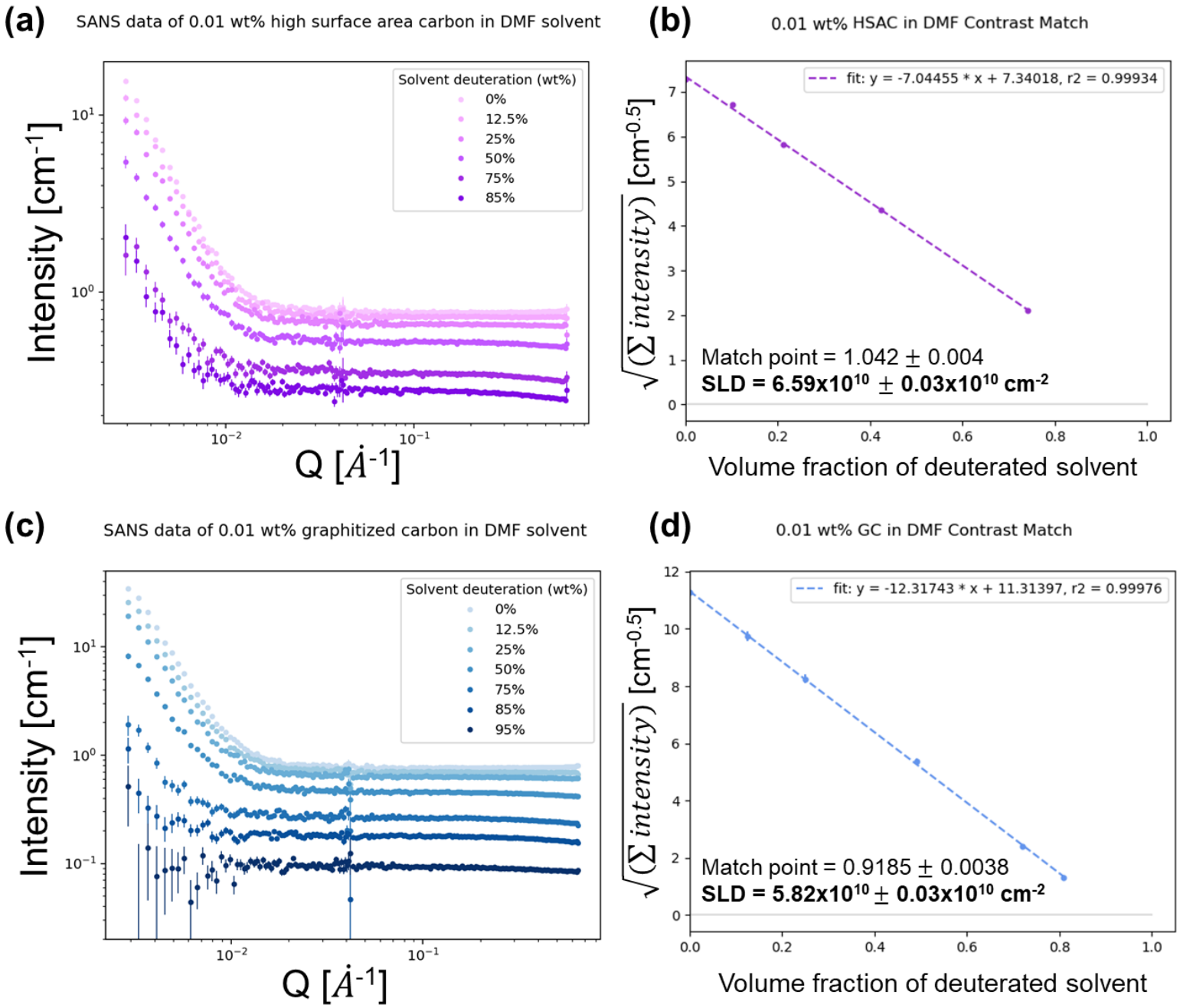


Figure 53. ***(a)*** *CV-SANS data of 0.01 wt% high surface area carbon in DMF solvent.* ***(b)*** *high surface area carbon contrast match and SLD extraction.* ***(c)*** *CV-SANS data of 0.01 wt% graphitized carbon in DMF solvent.* ***(d)*** *graphitized carbon contrast match and SLD extraction.*

Due to very low carbon concentrations in samples, the scattering functions do not show many features. For this reason, unlike for the ionomer component, structural analysis of carbon from singular component dispersion cannot be carried out. However, a shifting intensity with the contrast term is still clearly present, and component SLD can be calculated. The extracted SLD of 6.59×10^{10} cm^{-2} for HSAC is a lot higher than for GC at 5.82×10^{10} cm^{-2}, and also a lot closer to the theoretical SLD value for carbon black of 6.67×10^{10} cm^{-}

^{2}. Indeed, in the CV-SANS data of GC, a minimization of scattering in the low Q regime ($Q<1x10^{-2}$ $\dot{}^{-1}$) at high solvent deuterations can be observed. The large deviation in SLD between the two carbon types most likely relates to the structure of the carbon primary particles – where HSAC contains a large degree of porosity accessible to small molecules, and GC contains a void space that is completely closed off by a layer of graphitized carbon, figure 54. The void in GC can be expected to result in lower overall particle density and therefore lower SLD.

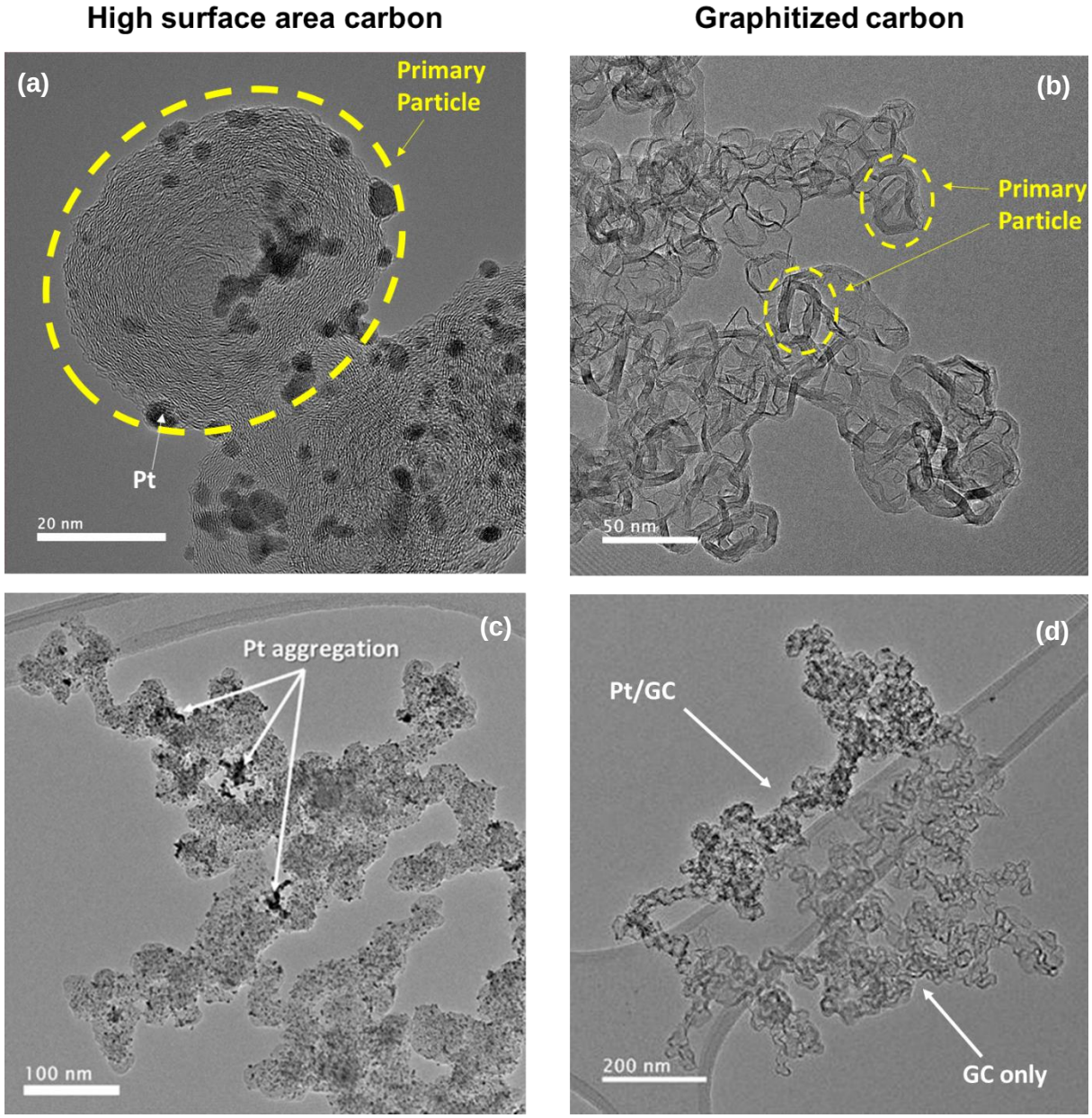


Figure 54. *High Resolution TEM (HRTEM) images of* ***(a)*** *high surface area carbon primary particles* ***(b)*** *graphitized carbon primary particles,* ***(c)*** *high surface area carbon aggregates (with Pt),* ***(d)*** *graphitized carbon aggregates (sections with Pt and without Pt loading). Images obtained by Dr. Laure Guetaz.*

Contrast match measurements for corresponding Pt/C complexes were also performed, however even at low concentrations and in DMF based solvent, stability for the duration of the measurement could not be

achieved, and therefore viable SLD values could not be extracted. Knowing that deviation from the exact carbon component SLD value can cause erroneous PSF output extractions, presence of Pt was accounted for by combining theoretical SLD of Pt and experimentally extracted carbon SLD in proportions related to volume fraction of each material in the Pt/C complex. Since Pt and C SLDs are very similar (Pt SLD = 6.23×10^{10} cm^{-2}), and the volume fraction of Pt in the Pt/C complex is fairly low (approximately 10%), the calculated SLD of the Pt/C complex is quite close to that of the carbon only. For example, the SLD of Pt/HSAC was calculated to be 6.56×10^{10} cm^{-2}. Nevertheless, since it is known even small changes in component SLD can have an impact on the extracted PSFs, an output robustness approach may be applied to certain results from inks containing this component, as described in section 2.2.6.1, shedding light on the veracity of the structure suggested through the output deviation behaviour.

2.3.3 CV-SANS measurements of catalyst inks – results and discussion

2.3.3.1 Effect of carbon support

High surface area carbon (HSAC) and graphitized carbon (GC) are two industrially relevant carbon supports utilized in catalyst inks. HSAC has a large degree of porosity, and primary particles can be segmented into two types – 'hollow' particles, with large pores accessible through wider openings on the particle surface, and denser particles, with smaller pores, accessible through narrow channels of 2-5 nm in diameter.[16] Approximately 70% of Pt is situated in the pores of HSAC,[18] leading to improved catalyst distribution and lower poisoning by the ionomer, which can't penetrate the pores, yielding improved electrode performance. GC primary particles are composed of a graphitic shell, which surrounds a void pocket, that is completely inaccessible to Pt or other molecules. GC improves electrode stability through increased tolerance to oxidation, however, Pt nanoparticles, all located on the surface, have a tendency to nucleate and amass into crevices in-between primary particles.[18]

Unquestionably, the biggest alteration that different carbon types introduce is in varied Pt distributions, however this will be discussed in detail later. Another variation in between such contrasting carbon supports is the degree of surface functionalization, which affect chemical properties of the support itself, such as hydrophobicity and electronic interactions.[93] A question arises, whether the inherent nature of the carbon support alters the adsorption of ionomer onto the carbon surface, even if Pt and the variation in distribution on different carbon supports is disregarded. To attempt and answer this question, the structures of pseudo inks containing the two starkly different carbon supports, HSAC and GC, were investigated by CV-SANS. Ink series were coded HNP and GNP for each carbon type respectively.

HNP = 1 wt% **high surface area carbon**, Nafion with I/C = 0.8, 50:50 wt% iPrOH/H_2O solvent

GNP = 1 wt% **graphitized carbon**, Nafion with I/C = 0.8, 50:50 wt% iPrOH/H_2O solvent

Each series contained six samples, with solvent deuteration ranging from 0 to 97 wt%. Figure 55 shows CV-SANS data of the two ink series, post processing and reference subtraction.

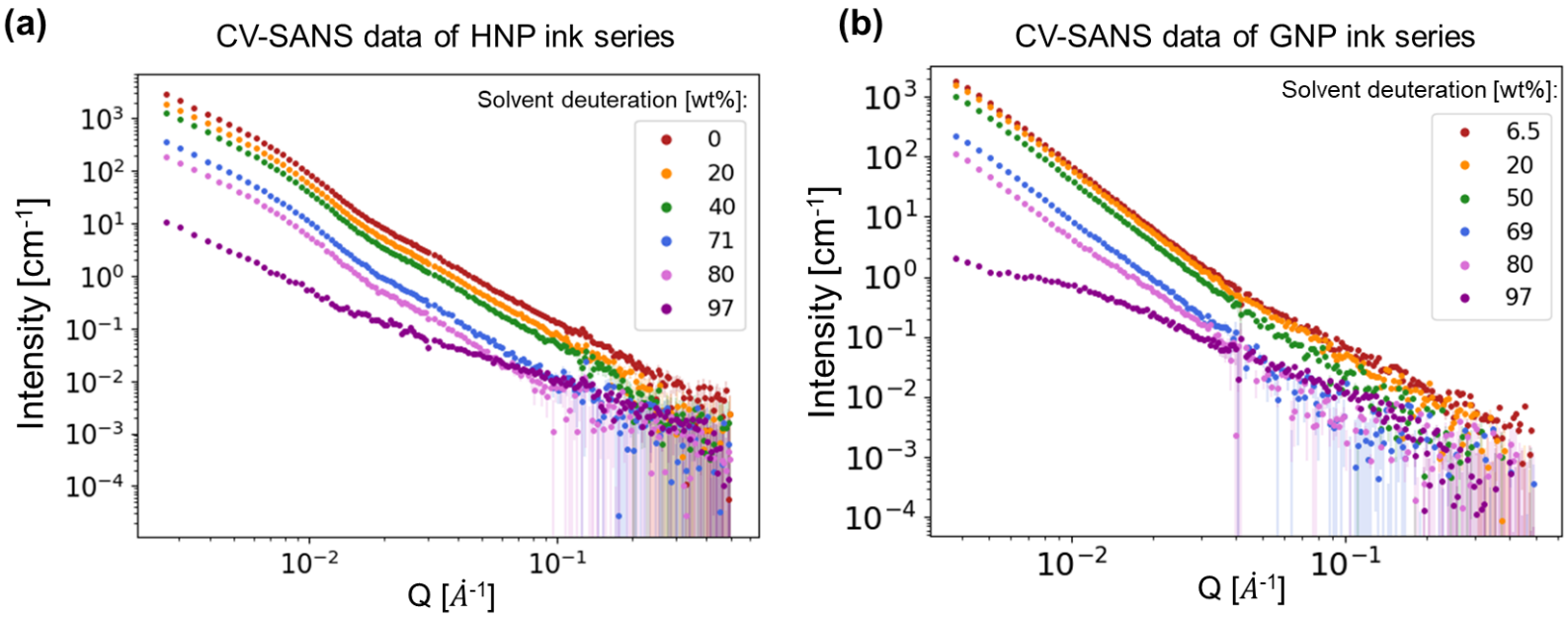


Figure 55. *CV-SANS data of* ***(a)*** *HNP ink series and* ***(b)*** *GNP ink series. Each series is composed of 6 samples with solvent deuteration ranging from 0 to 97 wt%.*

In both ink series a similar scattering behaviour can be observed for samples up to 80 wt% solvent deuteration, with progressively decreasing intensity due to an alteration of the contrast term. Moreover, in both ink series, in the scattering function corresponding to the sample with 97 wt% solvent deuteration, a change in power law scattering from the mid Q range ($Q>1x10^{-2}$ $\dot{A}^{-1}$) onwards can be observed. This is an indication of minimization of carbon scattering, and an appearance of ionomer contribution in the scattering functions. In the case of HNP (HSAC based inks), a shoulder-like feature is observed at approximately Q = 0.015 $\dot{A}^{-1}$. Such a feature is not observable for GNP (GC based) inks.

Figure 56 shows partial scattering functions extracted for the HNP and GNP ink series.

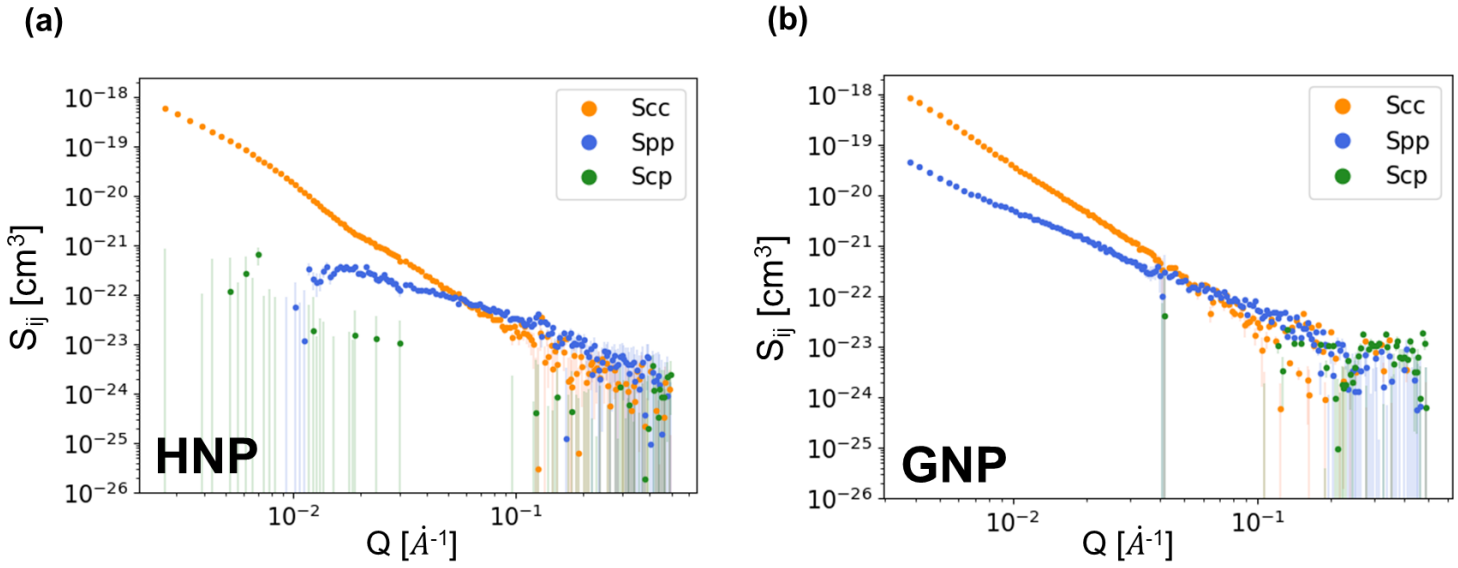


Figure 56. *Partial scattering functions extracted for* ***(a)*** *HNP ink series and* ***(b)*** *GNP ink series. S_{cc} shows carbon-carbon interactions (orange), S_{pp} shows ionomer-ionomer interactions (blue), S_{cp} shows the cross-term between carbon and ionomer (green).*

The SLD of Nafion was 4.48×10^{10} cm^{-2}, as extracted from a contrast match experiment in the corresponding solvent. The carbon component SLDs were 6.59×10^{10} and 5.82×10^{10} cm^{-2} respectively, corresponding to values extracted from contrast match experiments for the two carbon types dispersed in DMF solvent.

The most evident observation related to the PSF outputs for both ink series is the lack of a cross-term, with only a handful of data points with high error bars apparent in both instances. The S_{cc} for both compositions corresponds to the scattering observed from samples with solvent deuteration around 70-80 wt%. This is expected as in these instances the solvent SLD is almost exactly that of Nafion, meaning it is mostly matched out and scattering from carbon makes up the majority of the scattering intensity. For the HNP series the S_{pp} shows no data points in the low Q regime ($Q<1 \times 10^{-2}$ $\dot{}^{-1}$). Conversely, for the S_{pp} arising from the GNP series, strong scattering can be observed in the low Q regime.

Analysis of the S_{cc} outputs

The S_{cc} output extracted from the HNP based ink series shows a broad shoulder feature in the low Q regime ($Q<1 \times 10^{-2}$ $\dot{}^{-1}$), which continues to trend to higher intensities outside of the Q range measured, followed by a smaller feature in the mid Q regime ($Q \approx 1.5 \times 10^{-2}$ $\dot{}^{-1}$) and a power law. The power law in the high Q regime gives an indication of the roughness of the surface of carbon primary particles by $I \quad Q^{Ds-6}$, where D_s is the surface fractal dimension. A value of $D_s = 2$ is indicative of smooth particles, while rough particles show a D_s value between 2 and 3.[46, 94] It is known HSAC primary particles are rough spheres with diameters ranging between 20-40 nm.[16] A fitting of the S_{cc} output from the HNP series was attempted with the sphere model (equation (2.2.4)) using SasView 5.0.6 software, the same model that was used in previously to fit PSF outputs extracted from simulated datasets (figures 37, 38). However, the sphere model considers spherical particles with smooth interfaces,[80] which show a characteristic Q^{-4} power law scattering in the mid/high Q regimes ($Q>1 \times 10^{-2}$ $\dot{}^{-1}$). On the contrary, the HSAC carbon structure extracted in the S_{cc} shows a Q^{-3} power law scattering instead, which is evidence of rough surfaces that are expected for such highly porous particles.[46] This deviation means a primary particle radius cannot be reliably extracted using the sphere model available. Nevertheless, identification of scattering features and rough size gauging can be attempted. The scattering from a model sphere shown in figure 57 has been extracted using sphere radius of 22 nm with a polydispersity (lognormal) of 0.25, proving that although two features can be observed in the scattering, the structure corresponds to primary particles only. Not only can the deviation in power law in the mid/high Q regime ($Q>1 \times 10^{-2}$ $\dot{}^{-1}$) be clearly observed, but also a nonconformity in the low Q regime ($Q<1 \times 10^{-2}$ $\dot{}^{-1}$), where the model suggests scattering should be flatter than the increasing intensity observed.

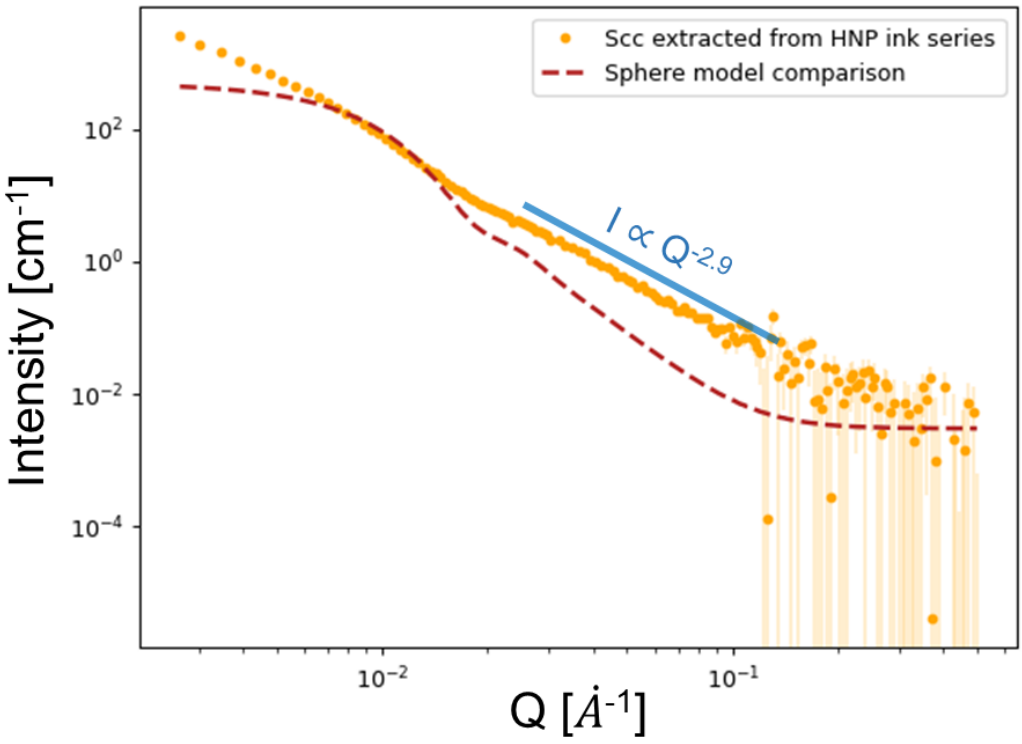


Figure 57. *Scc output extracted from HNP ink series (orange) compared to a sphere model (red). Note no parameter fitting of the sphere model has been performed, and the parameters have been adjusted visually only for comparison purposes. However, an estimation of the power law (blue) was obtained using the power law fitting model.*

This deviation corresponds to the aggregate structure which should be observed in Q ranges lower than those available using SANS. Because of these mismatches, the structure of the carbon particles cannot be reliably extracted. To overcome the issue arising from rough spheres, the unified power model developed by Beaucage has been previously utilized to fit scattering from carbon.[95, 96] However, as this model is shape independent, the sizes extracted will be dependent entirely on the Q range rather than on the particle structure, and the fitting should be carefully controlled based on previous structural observations. Another approach, utilized in this work, is to combine the sphere model together with a power law model to account for the slope variation[88,97,98]:

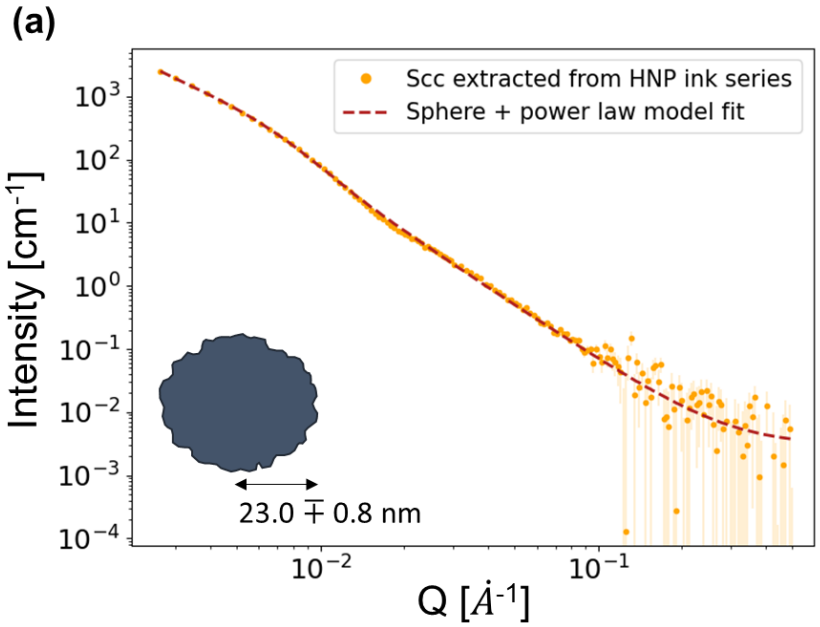
$$\{\ (\qquad\qquad) + (1 - \ )(\qquad\qquad)\} + \tag{2.3.1}$$

$$(\ ) = \frac{1}{\ } \cdot [3\ \ (\Delta\ ) \cdot \frac{\sin(\ \ ) - \ \ (\cos(\ \ ))}{(\ \ )^3}]^2 \tag{2.3.2}$$

$$(\ ) = \ ^{-} \tag{2.3.3}$$

Equations (2.3.2) and (2.3.3) present the sphere and power law models respectively. Note the sphere model is the same as in equation (2.2.4), however, the scatterer volume fraction parameter, , common to both models has been moved to the overall equation (2.3.1). *x* defines the proportion of the volume fraction applied to the sphere model in the overall fit. As the overall proportion of the combined models should equate to 1, the scale of the power law model is therefore defined as (*1-x*) and applied through the use of a constrained fit. Note such a model combination occurs across the entire Q range used for fitting.

Figure 58 shows a fit of the S_{cc} with a combined sphere + power law model:



(b) **Sphere + power_law**

Scale = 1.01e-03 ± 6.38e-05

Sphere_scale = 0.90 ± 8.63e-03
Sphere_sld = 6.59x10^{10} cm^{-2}
Solvent_sld = 0 cm^{-2}
Radius = 229.8 ± 7.50 $\dot{A}$

Distribution of radius = 0.36 ± 0.02
(function: lognormal)

Power_law_scale = 0.10 ± 8.63e-03
Power = 2.80 ± 0.03

Chi^2/Npts = 5.98

Fitting performed using SasView 5.0.6, SasModels version 1.0.7, Fit optimizer DREAM

Figure 58. (a) *S_{cc} extracted from the HNP ink series, fitted with the sphere + power_law model.* ***(b)*** *Parameters extracted from fitting.*

It can be observed that by proportionally combining 0.9 and 0.1 of the sphere and power_law models respectively (represented by the scale parameters), the power law resulting from the rough surface of porous primary particles is completely accounted for. The power is a bit lower than what was initially measured, with a returned value of 2.8 instead of 2.9, but the D_s value of 3.2 can still be related to the surface roughness of porous particles. The extracted radius of 23 nm is in good agreement with the estimated radius from the sphere model. The radius value indicates primary particles that are on the larger end of the expected spectrum, based on TEM images of Pt/HSAC particles, however, this may be a result of the large polydispersity value of 0.36, resulting in an overestimation of the average radius. Nevertheless, a large polydispersity is consistent with a carbon particle dispersion. The disadvantage of this combined model is that the smaller shoulder-like feature, related to the primary particle polydispersity is not reproduced due to the power law model contributions. Yet based on the remainder of the fitting, including that of the scattering that arises due to the size of primary particles directly, overall the fit provides a good quasi-quantitative overview of the carbon structure.

The S_{cc} extracted from the GC based ink series, GNP, shows a lot less features in comparison the carbon structure observed in the HNP ink series. Only a single power law, yielding a value of 2.8, can be observed over the entire Q range. Moreover, no features indicative of primary particle structure can be observed. The power law extracted from the fit can be quantified, however, with only one feature, structural interpretation becomes very difficult. A mass fractal dimension, D_m, is characterized by $I \quad Q^{Dm}$, where D_m ranges between 0 and 3.[99] A fractal dimension of 3 suggests a 'uniformly random' 3D structure,[100] which the value extracted of 2.8 could potentially indicate. However, considering that no scattering from primary particles can be observed, surface fractal dimension, D_s, obtained from $I \quad Q^{6-Ds}$ should also be taken into account. On the other hand, characterization of surface roughness, D_s, which takes values ranging between 2 and 3,[99] it can be argued that the magnitude of the power law indicates the roughness of larger aggregates and/or agglomerates. An ultra-small angle scattering measurement is necessary to obtain enough information for accurate structural determination.

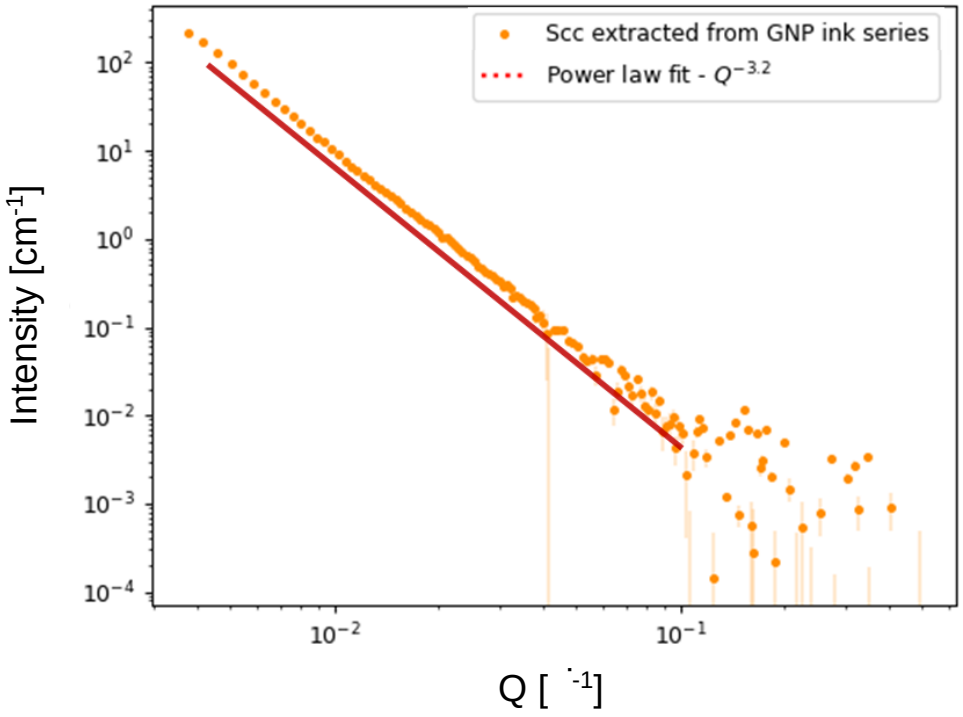


Figure 59. *S_{cc} extracted from the GNP ink series (orange), showing a power law scattering of $I \quad Q^{-3.2}$ (red).*

Analysis of the S_{cp} and S_{pp} outputs

With regards to the S_{cp} output, looking back to PSF outputs extracted from simulated datasets (section 2.2.5.3, figures 37, 38), the lack of a significant amount of positive values in the cross-term clearly corresponds to the outputs observed for the spheres + cylinder model, suggesting no Nafion adsorption to either carbon type in these ink compositions. Moreover, in the case of the HNP series, the S_{pp} output corresponds almost exactly to the 0.8 wt% Nafion in 50:50 wt% iPrOH/water solvent scattering function measured, figure 60.

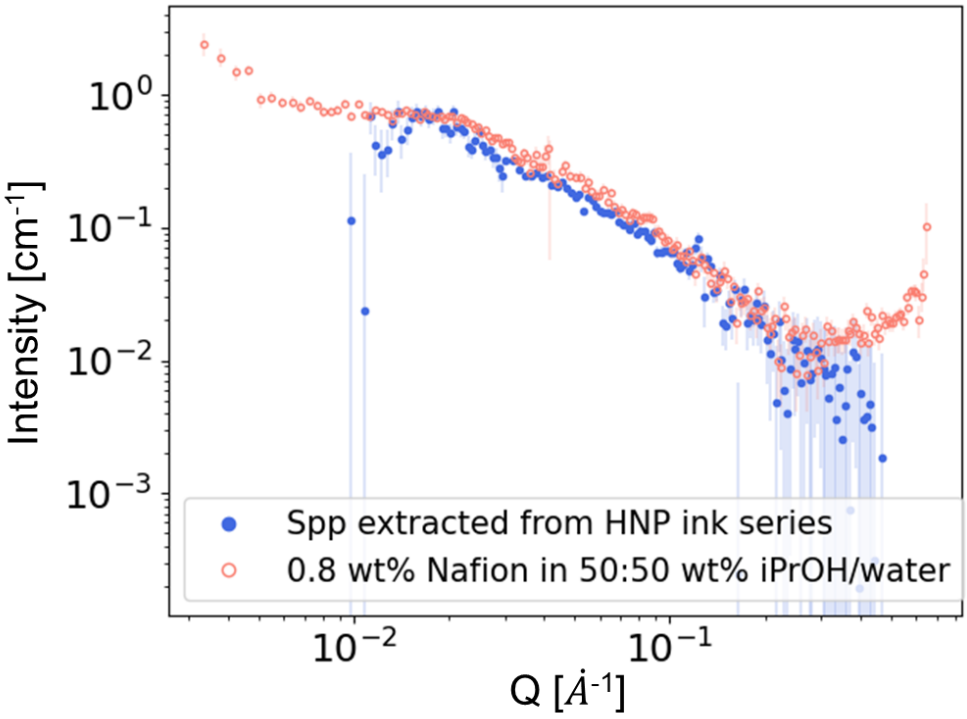


Figure 60. *S_{pp} output extracted from HNP ink series (blue) and scattering function of 0.8 wt% Nafion in 50:50 wt% iPrOH/water solvent (pink). The Spp output has been scaled to the scattering intensity [cm^{-1}] format.*

The region where data points start to disappear in the S_{pp} output – the 'cut-off point', corresponds directly to the Q range where Nafion scattering starts to show a I(Q) Q^0 linear behaviour ($Q \approx 2x10^{-2}$ $\dot{}^{-1}$). Looking back to the PSF outputs extracted from the spheres + cylinders model based simulated data (figure 37), the point in the Q range where such Q^0 behaviour began ($Q \approx 1x10^{-2}$ $\dot{}^{-1}$) also corresponded to the appearance of very large error bars. Therefore, it can be stipulated that in the case of experimental results, data points showing such a behaviour are not well extracted. Moreover, Yoshimune et al.[31] have shown in their work that unadsorbed ionomer in a catalyst ink behaves in the same manner as ionomer in dispersion, which supports the idea that similar scattering between the pure Nafion dispersion and the unadsorbed ionomer present in the HNP ink series is to be expected. Based on this observation, and the lack of S_{cp} extracted, it can be deduced that Nafion does not adsorb to HSAC, in the case of inks with the specified I/C ratio and solvent. In order to support the qualitative observations, the S_{pp} extracted from the HNP ink series was fitted to obtain quantitative information.

To account for both the presence of unadsorbed ionomer in the system, as well as any potential adsorbed ionomer in a shell structure, a combination created using the vesicle and cylinder models was opted for:

$$\{ (\quad) + (1 - \quad)(\quad)\} + \qquad (2.3.4)$$

$$(\quad) = \frac{}{}[\frac{3 \quad (\quad - \quad)_1(\quad)}{} + \frac{3 \quad (\quad - \quad)_1(\quad)}{}]^2 \qquad (2.3.5)$$

The cylinder model can be found in equations (2.2.5) and (2.2.6). The vesicle model is presented in equation (2.3.5), where = volume fraction of adsorbed ionomer, V_{shell} = volume fraction of the shell material ($^{\cdot 3}$), V_{core} = volume of the core ($^{\cdot 3}$), V_{tot} = total volume ($^{\cdot 3}$), R_{core} = radius of the core ($^{\cdot}$), R_{tot} = radius of core + shell thickness ($^{\cdot}$), ρ_{shell} = SLD of shell ($^{\cdot -2}$), $\rho_{solvent}$ = SLD of solvent ($^{\cdot -2}$).

represents the total ionomer volume fraction in the sample. Pre-factors x and 1-x denote the proportion of each model present in the overall combination, with x + (1-x) = 1. The pre-factor value for each model represents the fraction of weighted into the corresponding model, and therefore the volume fraction of ionomer present in the modelled structures, such that:

$$= (\quad) + (1 - \quad)(\quad) \qquad (2.3.6)$$

Where = total ionomer volume fraction, = ionomer adsorbed to carbon (represented by the vesicle model), = unadsorbed ionomer (represented by the cylinder model)

The validity of the vesicle-cylinder combination model was verified by reconstruction of a S_{pp} output obtained from a simulated data set containing x = 50% of the core-shell model, representing a partial ionomer adsorption case (equation (2.2.14)), appendix 16. Applying known parameters, including the ionomer volume fraction and pre-factors corresponding to 50% shell and 50% cylinder model, resulted in a perfect reconstruction of the S_{pp} output extracted for this data set.

Note that although the core_shell_sphere model has been previously applied to S_{pp} outputs of simulated datasets to fit shell scattering, the vesicle model has been opted for in this combination model as it takes into account the ionomer volume fraction only (unlike the former which also considers the carbon volume fraction, even when the core component is matched out to fit the shell). As the proportion of each model (*x* and *1-x*) utilized will be affected by the scale (volume fraction) parameter, combining the two models, vesicle and cylinder, which both consider the volume fraction of the ionomer only is bound to provide more accurate results.

In order to minimize the number of free parameters in the complex combination model, the radius of the core, as well as its polydispersity, were fixed at 23 nm and 0.36 respectively, in accordance with fitting of the S_{cc} output representing HSAC primary particles (figure 58). Moreover, although the presence of a structure factor hinders extraction of exact parameters (as discussed in section 2.3.2.1), the radius and length of unadsorbed Nafion cylinders were also estimated by fitting a scattering function of 0.8 wt% Nafion in 50:50 wt% iPrOH/water, yielding values of 1.2 and 20 nm respectively (appendix 17).

Therefore, the remaining parameters to be extracted from the vesicle-cylinder combined fit were the shell thickness and , calculated from the vesicle proportion parameter, .

Figure 61 presents the S_{pp} output extracted from the HNP ink series fitted with the vesicle-cylinder combination model:

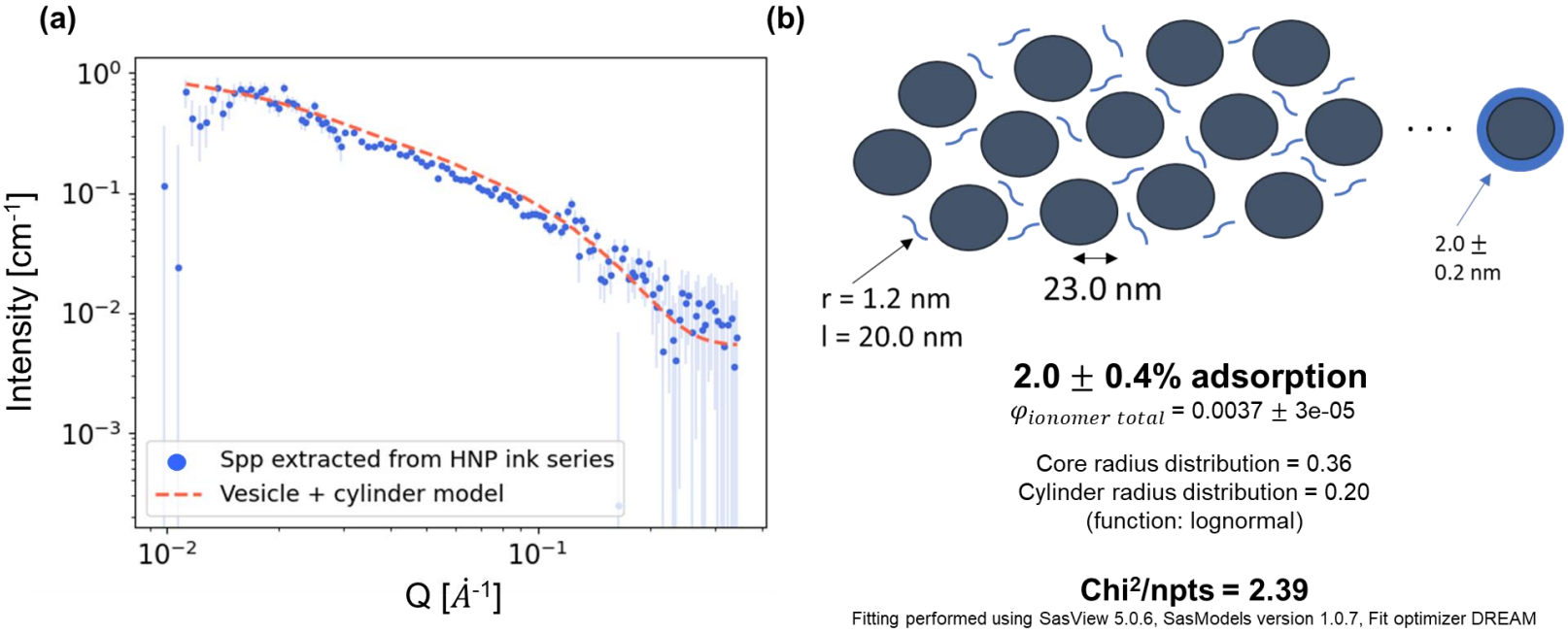


Figure 61. (a) *S_{pp} extracted from the HNP ink series, fitted with the vesicle + cylinder model.* ***(b)*** *Parameters extracted from fitting represented in a system schematic. r = radius, l = length. Degree of adsorption computed from vesicle proportion, (x) pre-factor.*

A good fit is achieved, with a low chi^2 value of 2.39. The fitting does suggest a low degree of ionomer adsorption at 2%, with a shell thickness of 2 nm, however, this can be explained by the presence of scattering intensity arising from the structure factor in the S_{pp} related to the Nafion unadsorbed cylinders. Indeed, the S_{pp} output is identical to the scattering function of 0.8 wt% Nafion in the corresponding solvent, where a structure factor can be observed, and the model considers the form factor of cylinders only.

In addition to the qualitative evidence– lack of cross-term output and a perfect match between the S_{pp} and a Nafion-only scattering function, the very low degree of 2% adsorption extracted from the vesicle + cylinder model corroborates the conclusion that Nafion does not adsorb to HSAC primary particles in 50:50 wt% iPrOH/water solvent.

On the other hand, despite the fact that the cross-term output is also lacking, the S_{pp} output extracted from the GNP ink series does not show such a great similarity to scattering from the Nafion-only dispersion, figure 62.

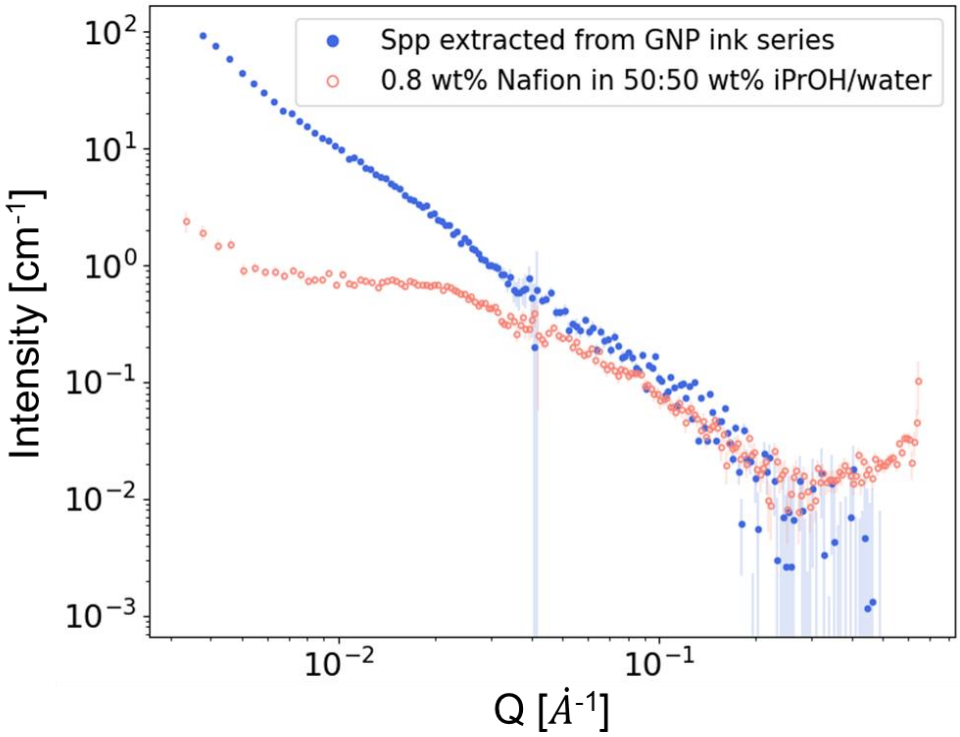


Figure 62. *S_{pp} output extracted from GNP ink series (blue) and scattering function of 0.8 wt% Nafion in 50:50 wt% iPrOH/water solvent (pink). The Spp output has been scaled to the scattering intensity [cm^{-1}] format.*

The S_{pp} output shows a more intense scattering in the mid/low Q regimes ($Q<4x10^{-2}$ $Å^{-1}$), suggesting bigger structural features present. Such scattering would be consistent with an ionomer shell structure, however, the lack of S_{cp}, which has been shown to be quite a robust feature in the core-shell simulations, is not present. Due to this discrepancy, a SLD shift study has been undertaken. A set of S+C (spheres + cylinders) as well as core-shell models have been simulated, using experimental component and solvent SLDs from the GNP ink series, and the SLD has been deviated from the true value to evaluate the effect on PSF outputs (appendix 18). The output deviation trend observed was almost the same as the previously discussed simulation data (section 2.2.6.1, figures 40, 41), with the core-shell based simulations showing a great output robustness despite SLD shifts, with an increased sensitivity seen for the S + C based simulations.

Indeed, the PSF outputs obtained for the GNP ink series can be directly compared to the S+C simulation PSF outputs, when SLD is shifted, figure 63.

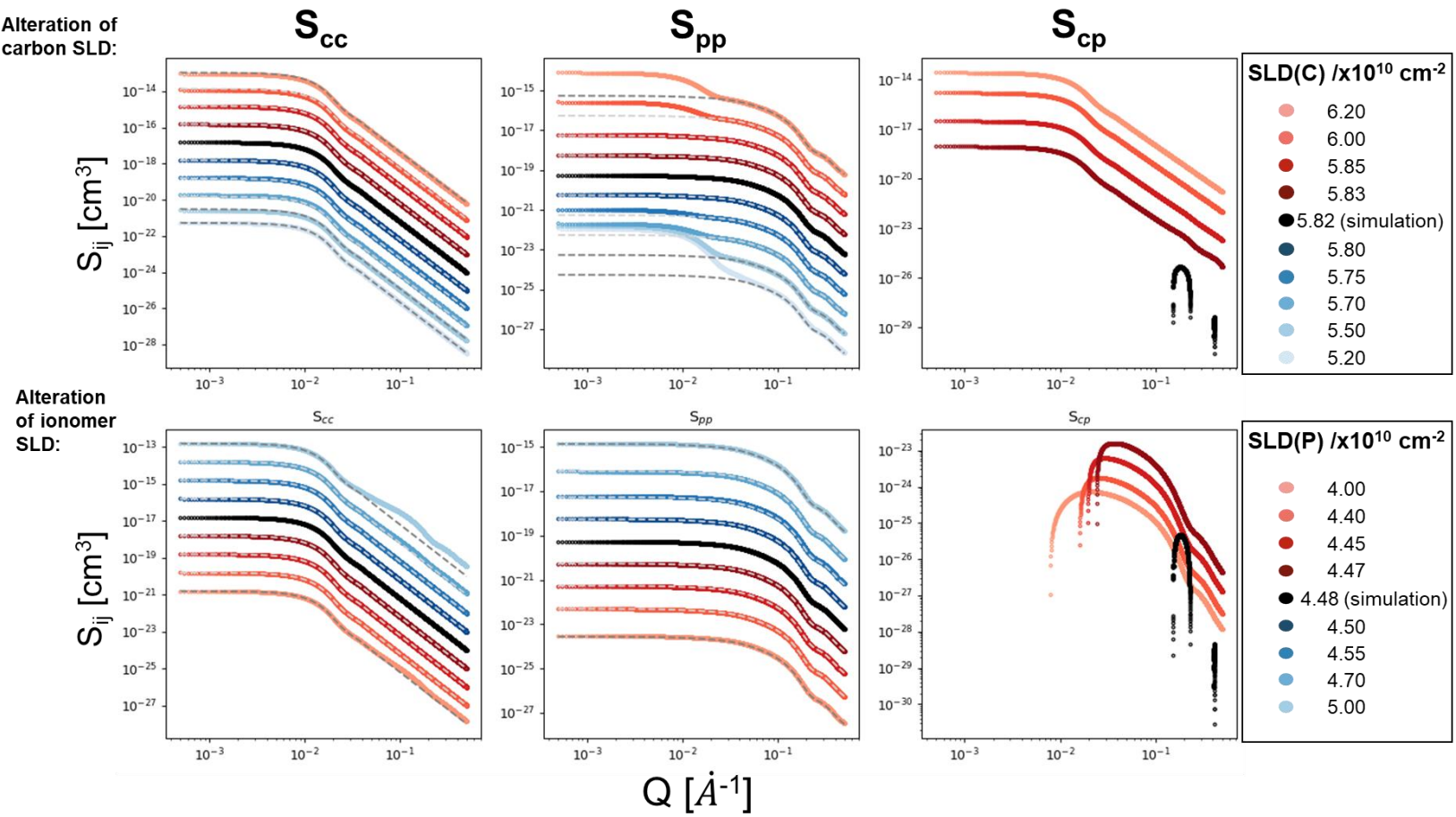


Figure 63. *Investigation of SLD shift impact on the S+C model based dataset, simulated using experimental SLD values of the GNP ink series. Scattering functions plotted in black and grey dashed lines represent the original PSF outputs, extracted using component SLD values obtained from contrast match experiments (GC and Nafion in 50:50 wt% iPrOH/water). Data has been shifted on a logarithmic scale and error bars have been excluded for visualization purposes.*

The GNP ink series outputs resemble the case where SLD(C) is underestimated in the S+C based simulation – when the SLD(C) is decreased by at least 0.07×10^{10} cm^2, an increasing intensity in the low Q regime ($Q < 1 \times 10^{-2}$ Å^{-1}) of the S_{pp} can be observed, yet the cross-term in the S_{cp} remains missing.

Furthermore, when an SLD shift study was performed on the GNP ink series itself, completely different observations were noted, not resembling behaviours with shifting SLDs from the true value in either S+C or core-shell simulations, figure 64.

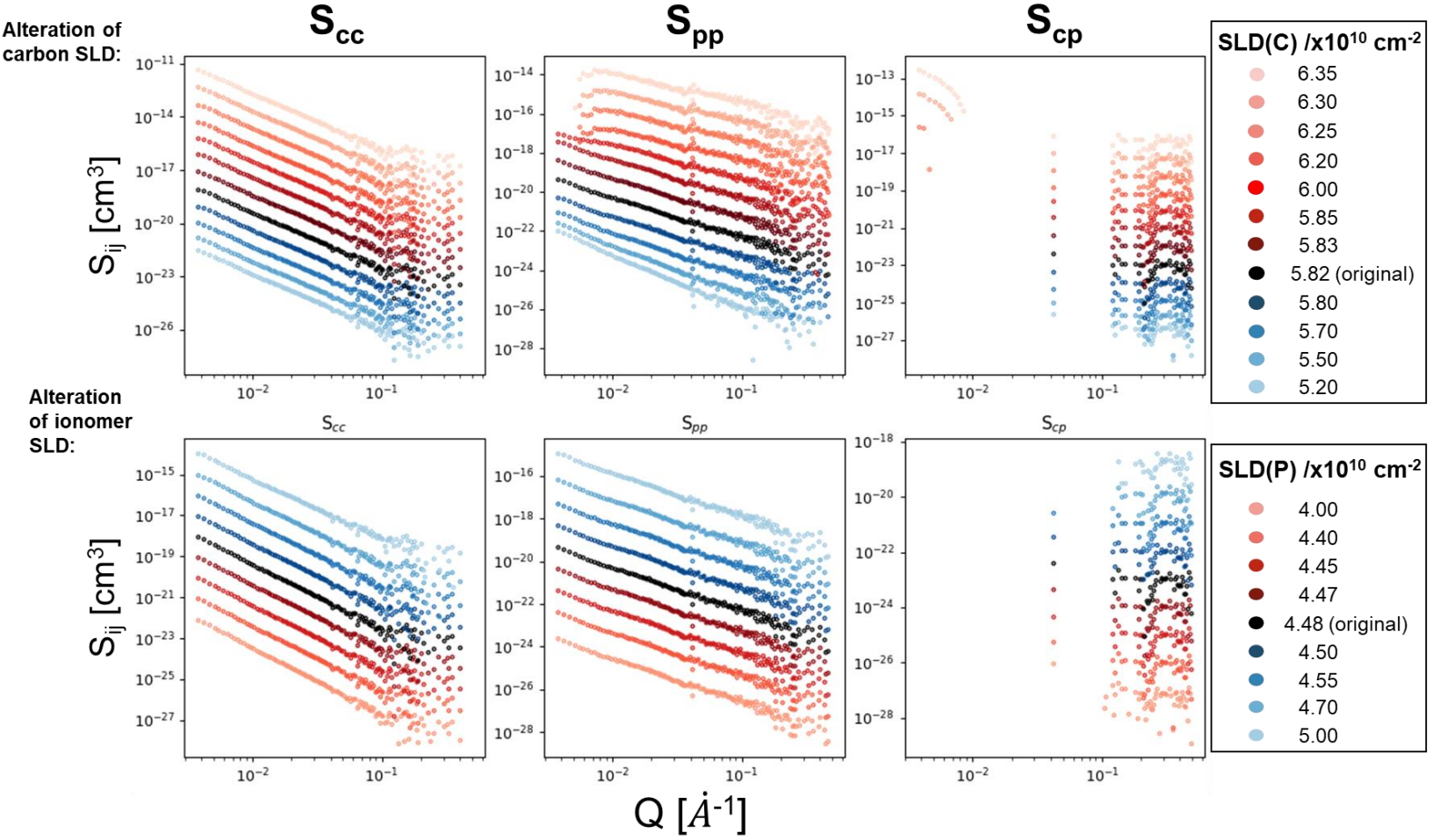


Figure 64. *Investigation of SLD shift impact on the GNP ink series. Scattering functions plotted in black represent the original PSF outputs, extracted using component SLD values obtained from contrast match experiments. Data has been shifted on a logarithmic scale and error bars have been excluded for visualization purposes.*

Shifting ionomer SLD from the original values for experimental datasets resulted in almost no change in output whatsoever. This has been previously noted and discussed in section 2.2.6.3 as well as visualized in appendix 9, following a somewhat expected trend. On the other hand, in previous investigations based on the no adsorption case, both on simulated and experimental data sets, shifting the carbon SLD upwards by even a small value resulted in an appearance of an erroneous cross-term, a feature that is not observed in the GNP ink series study. Indeed, no major differences in the PSF outputs are observed until the carbon component SLD is shifted as high as +0.4x10^{10} cm^{-2}, and no major deviation at all when it is decreased. Additionally, the S_{pp} output originally observed, with increasing intensity in the low Q regime (Q<1x10^{-2} Å^{-1}), shows similarity to scenarios from simulation datasets where SLD(C) is significantly underestimated. Such a behaviour, along with cross-term appearance only when the SLD is increased, supports the idea of a highly underestimated carbon SLD extracted from contrast match experiments. When carbon SLD is adjusted to 6.20x10^{10} cm^{-2} a variation in the S_{pp} output is observed, showing missing data points in the low Q regime (Q<1x10^{-2} Å^{-1}), resembling the S_{pp} output from the HNP ink series. When SLD(C) is increased further to 6.30x10^{10} cm^{-2}, a cross-term output also starts to appear, suggesting the true SLD of graphitized carbon may lie somewhere between 6.20 and 6.30x10^{10} cm^{-2}. This hypothesis is further supported by the scattering subtraction method. In one of the first steps, where the two scattering functions are scaled by $(\Delta\rho_c)^2$ in order to isolate the S_{cc} term (equation (2.2.18)), it is expected data points in the low Q regime

($Q<1x10^{-2}$ Å^{-1}) of the two scattering functions will overlap or be relatively close in intensity. However, for scattering functions in the GNP in series, a large intensity gap can be observed even after scaling (appendix 19), suggesting the carbon SLD utilized (from the contrast match) is not correct. Moreover, this may also be the reason why no primary particle structure was observed in the S_{cc} output.

It is possible the reason for the erroneous extraction of the SLD value for graphitized carbon is due to the void space in the primary particles that cannot be filled by solvent molecules, effectively creating a two component system that is incompatible with the contrast match technique. For this reason, CV-SANS data of ink series based on graphitized carbon will not be discussed further. However, the structure of graphitized carbon in the inks will be discussed again later on in chapter 3, focusing on USAXS experiments.

Conclusions

The structure of HNP ink (1 wt% HSAC, Nafion, I/C = 0.8, 50:50 wt% iPrOH/water) was successfully determined using CV-SANS measurements and PSF extraction.

The S_{cc} showed scattering from rough primary particles, whose radius was estimated as 23.1 nm using fitting with a combined sphere + power law model.

Evaluation of the S_{cp} and S_{pp} showed that no adsorption of Nafion to HSAC is evident in this ink composition. Simulated data based on the partial ionomer adsorption scenarios (figure 39) suggested even 1% of ionomer adsorption would yield a cross-term, but the S_{cp} output for the HNP ink series showed only a handful of data points across the entire Q range, consistent with the S + C, no adsorption case, simulation. Additionally, the S_{pp} output from the HNP ink series showed an almost exact match to the scattering function of 0.8 wt% Nafion in the same solvent system, further proving only scattering from unadsorbed ionomer can be observed in the ink PSF outputs. Fitting of the S_{pp} output with a vesicle-cylinder combination model, which considers structure related both to adsorbed and unadsorbed ionomer, further suggested a very low degree of ionomer adsorption at 2%. Considering the qualitative evidence presented above, this slight discrepancy can be attributed to the presence of a structure factor in the S_{pp} output, which is identical to the scattering function of 0.8 wt% Nafion-only dispersion. The structure factor feature leads to an increased scattering intensity in the Q ≈ 0.15 Å^{-1} region that may be incorrectly interpreted as a shell structure by a model designed to consider the vesicle and cylinder form factors only. Overall, the strong evidence for no ionomer adsorption to HSAC primary particles in the sample remains distinct.

The structure of GNP ink (1 wt% GC, Nafion, I/C = 0.8, 50:50 wt% iPrOH/water) could not be confidently evaluated. SLD shift investigations suggested the SLD(C) extracted from contrast match experiments is severely underestimated, which was further supported by the direct scattering subtraction method (as it could not be reliably performed due to contrast term scaling issues). The SLD extraction was most likely hindered by the structure of GC primary particles, which have a void space inaccessible to solvent molecules, surrounded by a shell of graphitic carbon, effectively creating a two component system. If the SLD of the graphitic shell could be accurately worked out through another method, for example directly calculated from the density of the material, the PSF method could be applied to samples based on graphitized carbon. However, in this instance, more partial scattering functions would have to be considered to account for the additional air component: $S_{air\text{-}air}$ and $S_{carbon\text{-}air}$. **Additional work needs to be done in order to ensure the SLD of graphitized carbon is properly determined. Due to this, in this work inks based on graphitized carbon will not be further evaluated by CV-SANS. This system shows that time must not only be taken to determine the SLD of each component experimentally, but also care must be applied when selecting the ink system to investigate. Graphitized carbon proved a challenging choice for such a study, yet it remains of interest due to its favourable chemical stability. On the other hand, Vulcan carbon may be a better alternative for comparing ionomer adsorption to carbon**

supports of varying porosity, already showing good compatibility with the CV-SANS method in studies published.[31, 80]

2.3.3.2 Effect of ionomer-to-carbon (I/C) ratio

The amount of ionomer is an important factor to control when manufacturing catalyst layers.[101] The ionomer not only acts as a proton conductor towards the ORR, but also aids in stabilizing the carbon dispersion via mechanical and electronic repulsion mechanisms.[35] Nevertheless, too much ionomer coverage in the catalyst layer inhibits gas transport towards the Pt catalyst, creating a poisoning effect.[25] Catalyst layers prepared from inks with Nafion ionomer and I/C in the range of 0.75 - 1.1 show the best performance,[32-34] yet a question remains of how altering I/C in the ink composition affects its structure. In this work, three different I/C ratios were investigated: 0.5, 0.8 and 1.3. Corresponding CV-SANS ink series were coded as follows:

0.5HNP = 1 wt% high surface area carbon, Nafion with **I/C = 0.5**, 50:50 wt% iPrOH/H_2O solvent

HNP = 1 wt% high surface area carbon, Nafion with **I/C = 0.8**, 50:50 wt% iPrOH/H_2O solvent

1.3HNP = 1 wt% high surface area carbon, Nafion with **I/C = 1.3**, 50:50 wt% iPrOH/H_2O solvent

Note the ink composition with I/C = 0.8, HNP, has already been discussed in section 2.3.3.1, with regards to the effect of carbon support on ink structure, yet a lack of ionomer adsorption onto carbon has been noted. Consequently, it can be expected that 0.5HNP, a composition with a lower I/C of 0.5, will also present a lack of ionomer adsorption to carbon. Nevertheless, a variation in the low Q regime ($Q<1x10^{-2}$ $\dot{A}^{-1}$) of the S_{cc} relating to the dispersion quality (i.e. size of aggregates) of carbon may still be observed. A higher ionomer content in 1.3HNP, where I/C is as high as 1.3, may result in a degree of ionomer adsorption onto carbon particles. Figure 65. presents CV-SANS data of each ink series, as well as extracted PSF outputs.

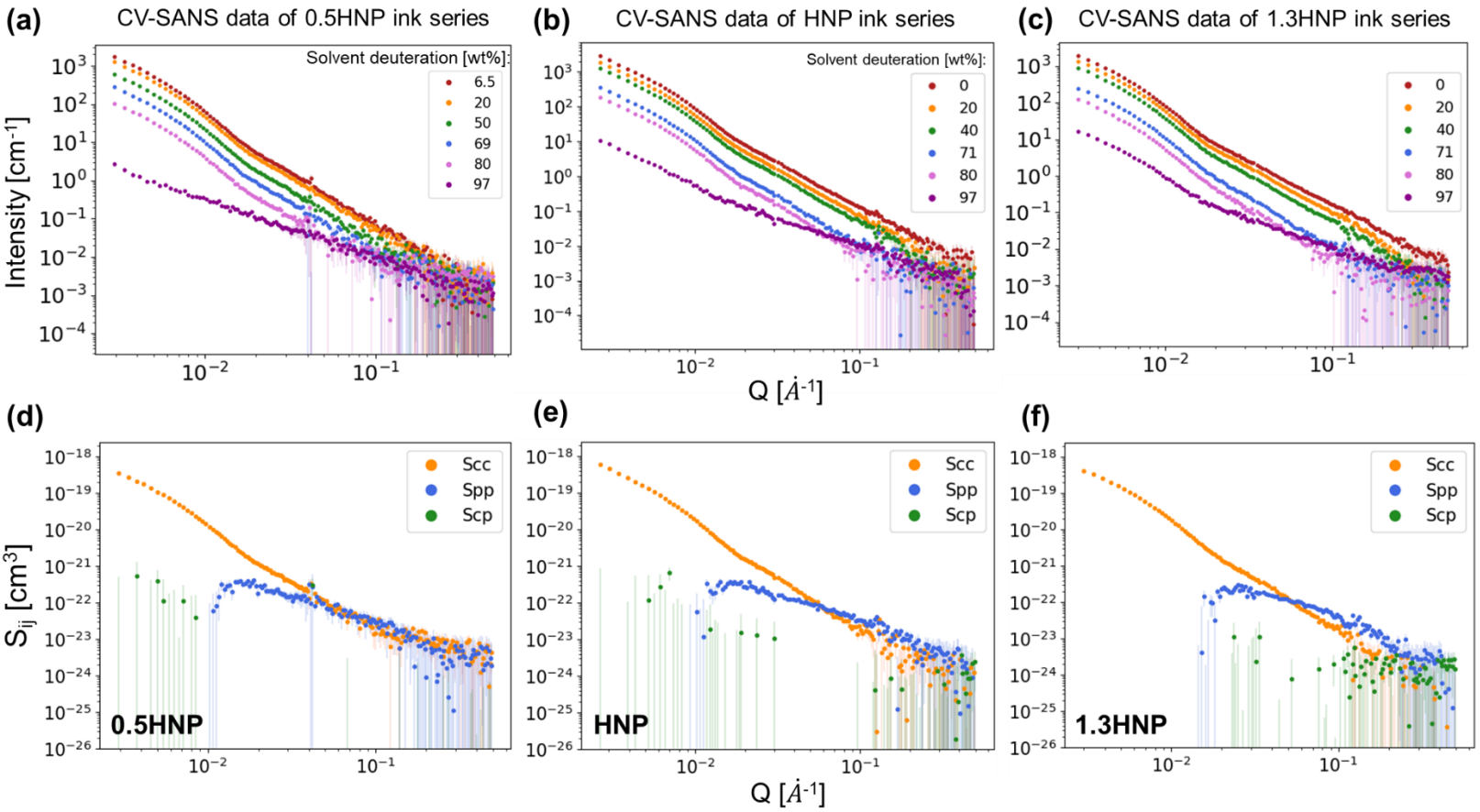


Figure 65. *CV-SANS scattering functions of* ***(a)*** *0.5HNP,* ***(b)*** *HNP,* ***(c)*** *1.3HNP ink series. PSF outputs extracted from* ***(d)*** *0.5HNP,* ***(e)*** *HNP,* ***(f)*** *1.3HNP ink series.*

Component SLDs utilized were 6.59 and 4.48×10^{10} cm^{-2} for the carbon and Nafion components respectively. Solvent SLDs were obtained for each individual sample through evaluating solvent masses measured during sample preparation.

All PSF outputs extracted from each ink series show a similar trend. The S_{cc} outputs show scattering consistent with the structure of primary particles described in the section above (2.3.3.1.1). The S_{pp} shows scattering with data points missing in the low Q regime ($Q<1 \times 10^{-2}$ $\dot{A}^{-1}$). Only a handful of data points can be observed in the S_{cp} outputs. The PSF outputs therefore suggest that no matter the I/C ratio in the ink, no ionomer adsorption onto the carbon particles occurs. Figure 66 presents all analogous PSF outputs plotted together for a detailed view of differences in between the outputs extracted.

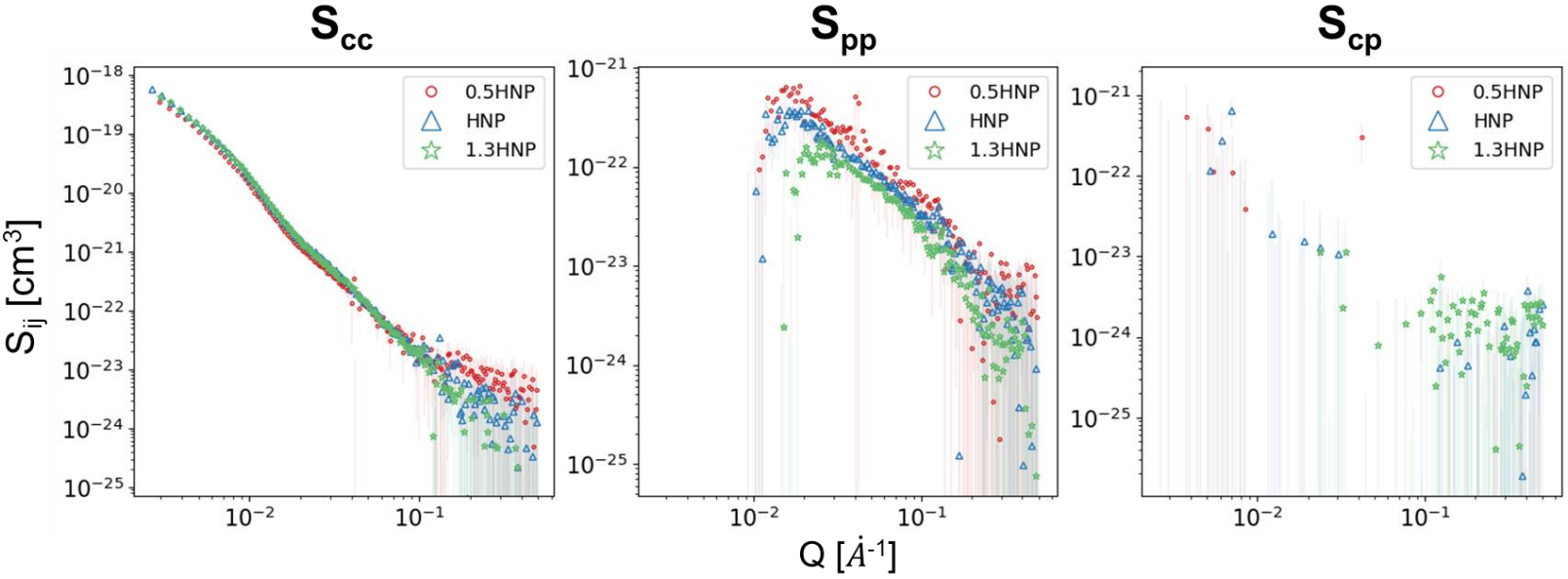


Figure 66. *Comparison of equivalent PSF outputs extracted from ink compositions with varying I/C ratios: 0.5HNP (red), HNP (blue), 1.3HNP (green). S_{pp} outputs from 0.5HNP and 1.3HNP have been scaled by the ionomer volume fraction for comparison purposes.*

In the S_{cc} there is a very good overlap between the PSFs extracted, suggesting there is no change to the size of the carbon aggregates, or more likely, that any present alteration is not visible in the Q range probed. There is small deviation arising in the high Q regime ($Q>1x10^{-1}$ $\dot{}^{-1}$) that arises as a consequence of data processing. With each series consisting of six individual scattering functions, discrepancies in the quality of data processing will unavoidably arise, translating into the PSF outputs extracted. In the S_{pp} outputs it can be observed the 'cut-off' point shifts to higher Q values (from 0.01 to 0.015 $\dot{}^{-1}$) with increasing ionomer concentration in the system. This resembles the concentration dependent shift of the structure factor related peak feature observed in Nafion-only scattering functions (figure 50). Moreover, the intensity of the slope present just before the cut-off point can be observed to increase with decreasing ionomer content, which may be related to the position of the cut-off point itself. Nevertheless, even considering these differences, it can be observed that each S_{pp} matches well with the scattering function of a Nafion-only dispersion, as interpreted by the structural similarity of the S_{pp} output to the HNP ink series (figure 60). In each S_{cp} output most data points are missing, consistent with a case of no ionomer adsorption.

Conclusions

For ink composition based on 1 wt% HSAC, Nafion ionomer and 50:50 wt% iPrOH/water solvent, increasing the I/C ratio does not boost adsorption of Nafion to carbon, and indeed no adsorption is observed throughout. This observation is consistent with literature. Yoshimune et al.[31] observed that for inks based on Pt/Vulcan complex, Nafion ionomer, and iPrOH/EtOH/water solvent mixture, adsorption to carbon does not increase when I/C is higher than 0.25. The S_{cc} outputs were also consistent for each ink series, showing no change in carbon structure in the Q range in question. Moreover, Khandavalli et al.[25] showed through rheology measurements that full stabilization for HSAC based inks is achieved when I/C = 0.5, which could be another reason for the lack of variation observed. Although it is evident that adsorption is not boosted with increasing I/C for this type of ink composition, an extension of this section could include measuring ink series with I/C ratios lower than 0.5 to investigate whether a change in the S_{cc} output indicative of varying carbon dispersion quality could be observed.

2.3.3.3 Effect of solvent

The dispersion solvent used in catalyst inks is a mixture of water and alcohol, with ethanol and isopropanol being the most common candidates. In the ink, the solvent system plays a complex role, affecting the conformation of ionomer molecules, which contain both hydrophobic and hydrophilic domains, resulting in altered interactions with carbon particles, and subsequently an altered dispersion quality. As a consequence, physical properties of the ink, such as viscosity are also influenced, affecting the manufacturing of the catalyst layers throughout processes such as ink deposition onto substrate, or drying. In this work, focus was placed on the effect of alcohol concentration in the solvent system on ionomer adsorption to carbon particles in the catalyst ink. The alcohol in the solvent was isopropanol throughout, and three different concentrations were chosen to yield the following ink compositions:

25HNP = 1 wt% high surface area carbon, Nafion with I/C = 0.8, **25:75 wt%** iPrOH/H_2O solvent

HNP = 1 wt% high surface area carbon, Nafion with I/C = 0.8, **50:50 wt%** iPrOH/H_2O solvent

75HNP = 1 wt% high surface area carbon, Nafion with I/C = 0.8, **75:25 wt%** iPrOH/H_2O solvent

Note the ink composition HNP, has been previously discussed in detail in section 2.3.3.1, and also section 2.3.3.2. Figure 67 shows CV-SANS data of the above-mentioned ink series, as well as corresponding partial scattering functions extracted. Note that as different SLD values for Nafion have been extracted in varying solvent systems using the contrast match method, the SLD(P) input has been adjusted based on values obtained from 2 wt% Nafion dispersions (section 2.3.2.1, table 6).

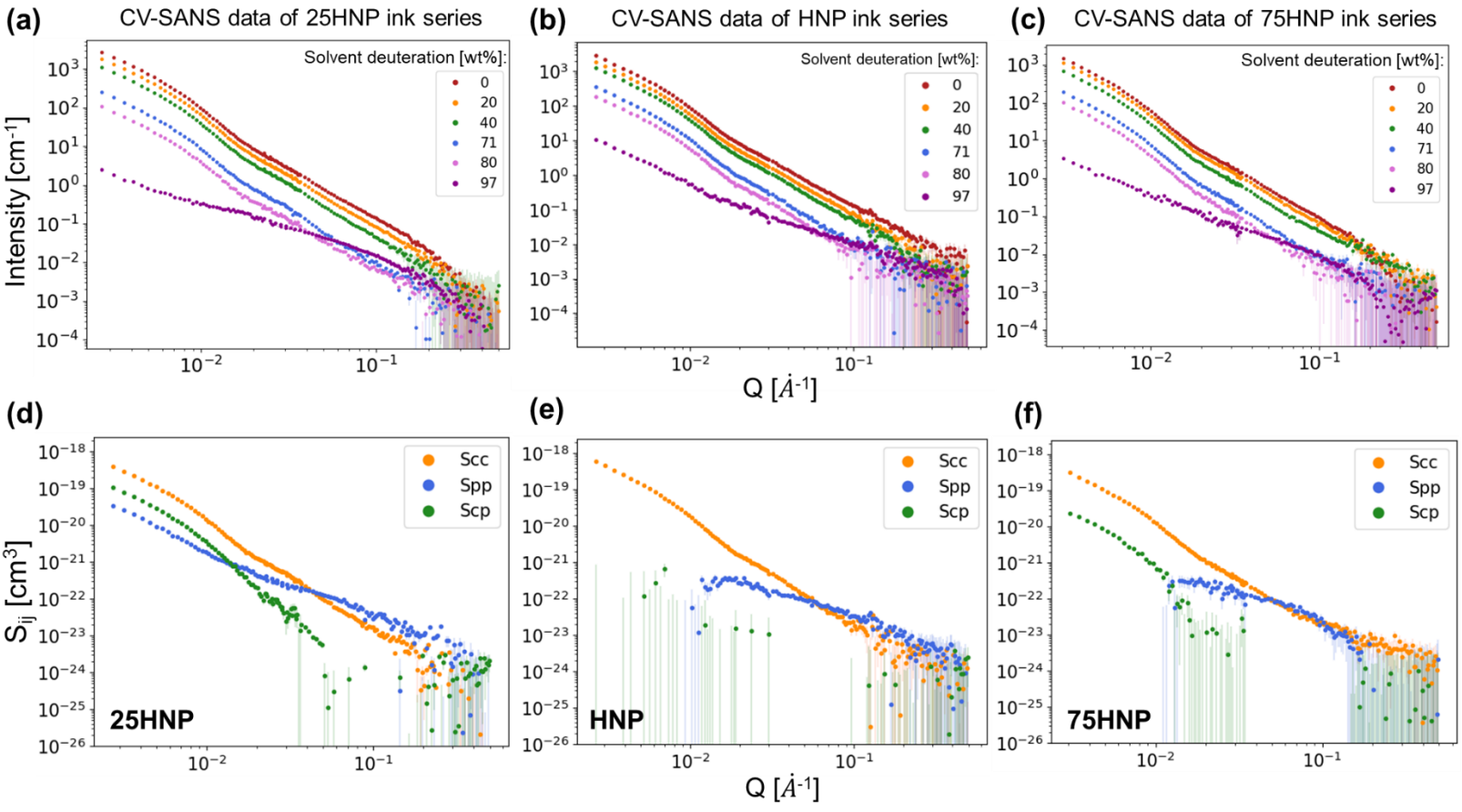


Figure 67. *CV-SANS scattering functions of* ***(a)*** *25HNP,* ***(b)*** *HNP,* ***(c)*** *75HNP ink series. PSF outputs extracted from* ***(d)*** *25HNP,* ***(e)*** *HNP,* ***(f)*** *75HNP ink series.*

An immediate observation can be made that unlike in the HNP ink series, PSF outputs extracted from 25HNP and 75HNP ink compositions both show scattering in the S_{cp} in the low/mid Q regimes ($Q<5x10^{-2}$ $\dot{A}^{-1}$), reminiscent of the cross-term observed for outputs of the core-shell based simulation, suggesting adsorption of Nafion molecules to carbon particles. Moreover, the S_{pp} output of the 25HNP ink series shows scattering across the entire Q range, with scattering in the low Q regime ($Q<1x10^{-2}$ $\dot{A}^{-1}$) indicative of an ionomer presence on carbon aggregates. Equivalent PSF outputs from each ink series were plotted together for a more detailed structural evaluation, figure 68:

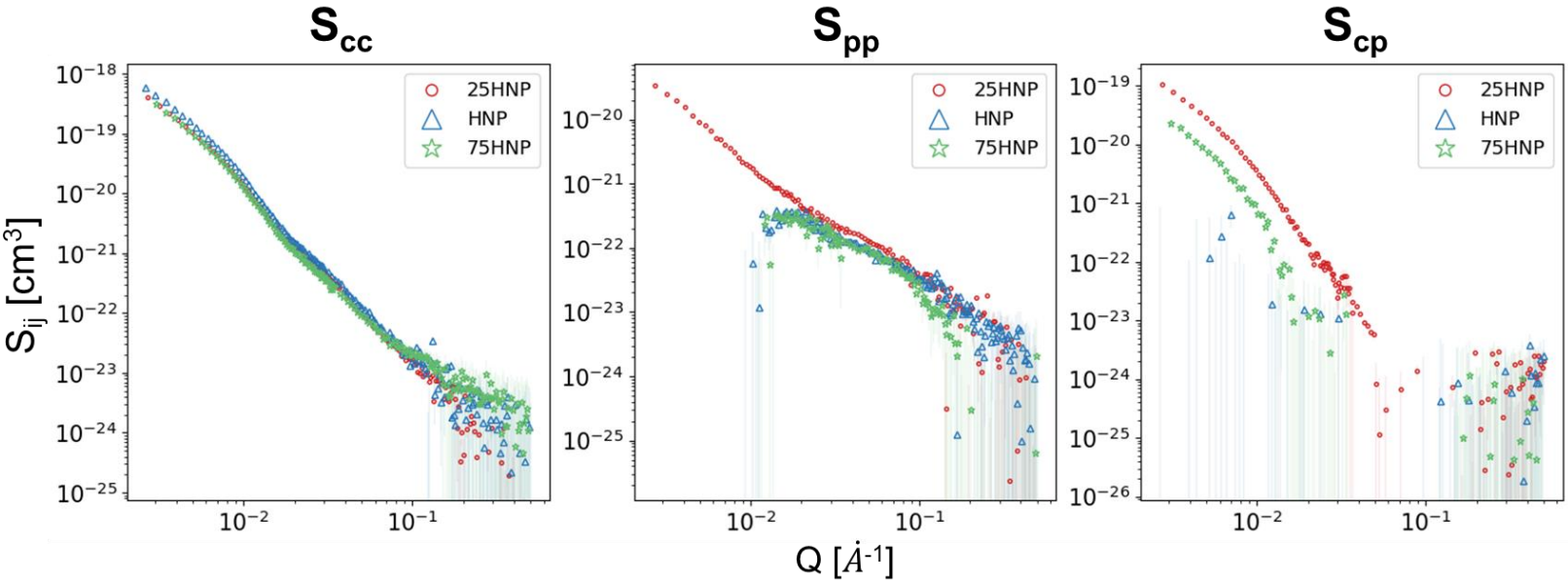


Figure 68. *Comparison of equivalent PSF outputs extracted from ink compositions with varying iPrOH concentrations in the solvent system: 25HNP (red), HNP (blue), 75HNP (green).*

Fitting PSF outputs extracted from the 25HNP ink series

As can be expected, the S_{cc} output remains unchanged to that previously evaluated for the HNP ink series. Please refer to section 2.3.3.1 for detailed analysis of the HSAC structure.

The S_{pp} output of the 25HNP ink series seems to display a slightly overall higher intensity than the outputs of HNP and 75HNP, and scattering extends into the low Q regime ($Q<1x10^{-2}$ $\dot{A}^{-1}$), suggesting a presence of an ionomer structure on a bigger size scale. This is consistent with shell scattering, also observed in the S_{pp} output extracted from core-shell based simulated data, which corresponds to an overall size scale of the carbon particle and the ionomer shell together. A fit of the S_{pp} with the shell model was attempted (appendix 20), and a good coherence in the low/mid Q regimes ($Q<3x10^{-2}$ $\dot{A}^{-1}$) was achieved. However, in the mid/high Q regimes ($Q>3x10^{-2}$ $\dot{A}^{-1}$) an increased scattering could not be accounted for with just the shell model alone. This observation can be explained by a more realistic case of partial ionomer adsorption in the system, and therefore also a contribution from the unadsorbed ionomer in the mid/high Q regimes of the S_{pp}. Therefore, the vesicle-cylinder combination model (equations (2.3.4) - (2.3.6)) was used to fit the S_{pp} output extracted from the 25HNP ink series, accounting for both scattering from the adsorbed and unadsorbed ionomer. As no change was observed in the S_{cc} output, once again the core radius and polydispersity were fixed based on parameters extracted from previous fitting (figure 58). In order to minimize the number of free parameters, the radius and length of unadsorbed ionomer cylinders were estimated using the scattering function of 1 wt% Nafion in 25:75 wt% iPrOH/water (appendix 21). Note that because the structure factor present was significantly prominent, fitting of the data itself was unsuccessful, and the parameters could only be roughly gauged. Nevertheless, the minimization of free parameters in the

complex combination fit is imperative to allow for as accurate information extraction on the shell thickness and degree of ionomer adsorption as possible.

Figure 69 presents the fitting of the combined model to the 25HNP S_{pp} output.

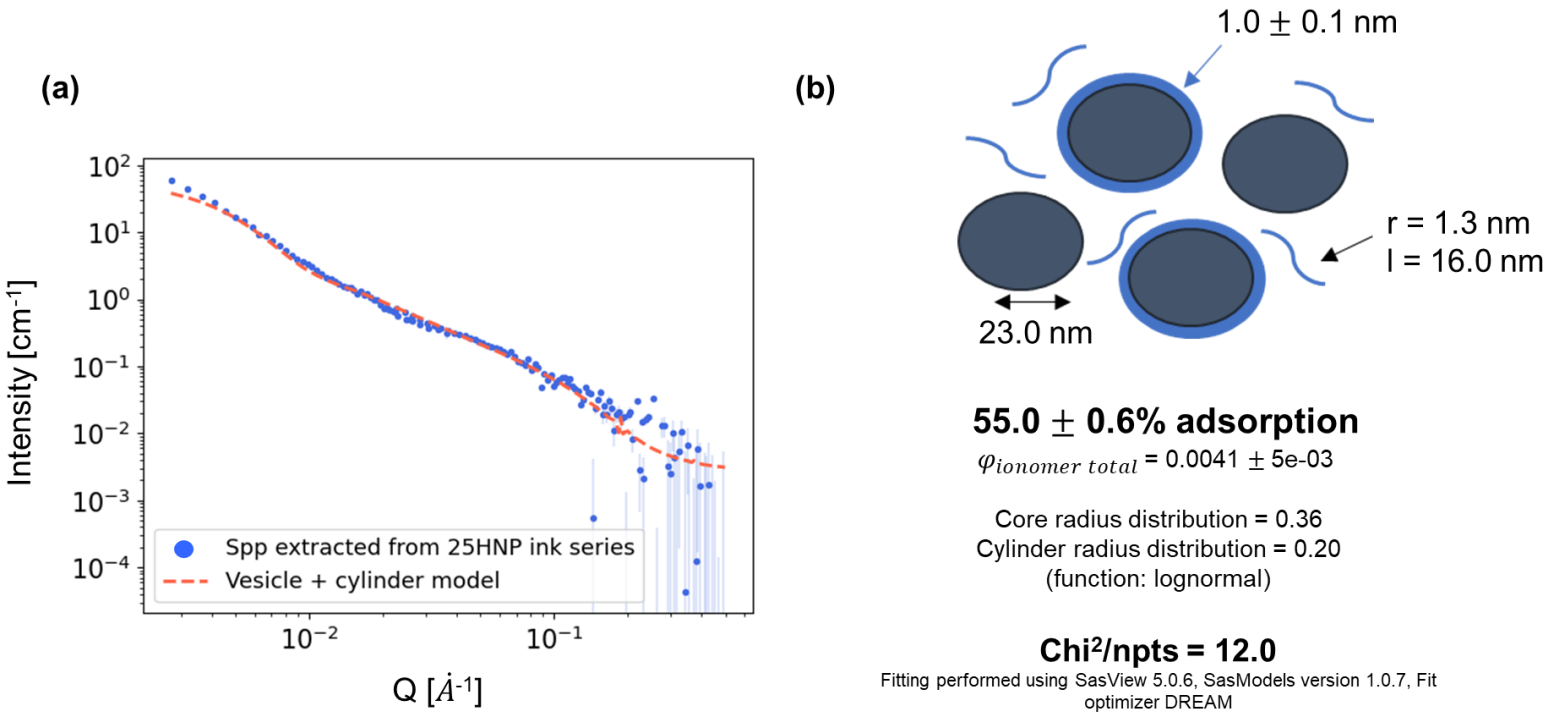


Figure 69. (a) *S_{pp} extracted from the 25HNP ink series, fitted with the vesicle + cylinder model.* ***(b)*** *Parameters extracted from fitting represented in a system schematic. r = radius, l = length. Degree of adsorption computed from vesicle scale (x) pre-factor.*

A good fit with a relatively low chi^2 value of 12.0 is achieved, with low errors bars obtained for both the shell thickness and degree of adsorption parameters. A thickness value of 1.0 nm is extracted with a low error of 0.01 nm, suggesting Nafion forms a thin shell around the carbon.

Scattering in the mid/high Q regimes (Q>3x10^{-2} $\dot{}^{-1}$) was well fitted with the cylinder form factor, using values of 1.3 and 16.0 nm estimated for the cylinder radius and length respectively from the Nafion-only scattering function (appendix 21). Both the radius and the length parameters are somewhat similar to the 1.4 and 12.5 nm values obtained for the Nafion only dispersion (section 2.3.2.1, figure 51). Note that in the latter case the solvent used was 75:25 wt% iPrOH/water, which might account for the differences. Considering the similarity in scattering function shape (figure 50) as well as suggested structural dimensions, it can be concluded that the unadsorbed Nafion forms small, rod-like aggregates even with lower concentrations of iPrOH present in the solvent.

Considering the proportions of each model applied in the combination fit, 55% of the total ionomer was found to be adsorbed to the carbon particles, with the remainder present as unadsorbed ionomer. Moreover, the extracted scale of 0.0041, representing the total ionomer volume fraction, is precisely consistent with the value of 0.0041 calculated from measured masses during sample preparation. Note a 10% upper and lower boundary was applied to the scale fitting parameter to account for errors arising during sample preparation, as well as other experimental considerations, such as the volatility of iPrOH or the unavoidable interaction of carbon aggregates with zirconia milling balls.

With regards to the cross-term, as mentioned in section 2.2.5, a suitable model has not been yet identified for fitting of the S_{cp} output. Indeed, it was noted by Endo et al.[68] that interpretation of the cross-term remains challenging. Nevertheless, as a result a section of the data remains only interpreted through a qualitative manner. Moreover, considering that although the ionomer does adsorb onto the carbon, the resulting structure is most likely not as simplistic as a uniform shell expressed by the core-shell or vesicle models. And certainly, it is highly probable that in a real-life scenario carbon has a number of defect or functionalized sites with varied surface energies that the ionomer may preferentially interact with. For this reason, the parameters extracted from fitting the S_{pp} will be regarded as quasi-quantitative only.

Fitting PSF outputs extracted from the 75HNP ink series

The S_{cc} output extracted from the 75HNP ink series again is unchanged with regards to the outputs extracted for the HNP and 25HNP ink series. On the other hand, although a cross-term output is clearly present, the S_{pp} shows a similar scattering to unadsorbed Nafion, similarly to the HNP output. This is contrary to the notion of an adsorbed ionomer shell structure. A brief investigation into the effect of SLD deviation on PSF outputs was performed for 75HNP ink series to verify if the outputs presented in figures 67 and 68 were veritable (appendix 22). The outputs extracted were fairly robust despite SLD deviation, a feature more consistent with a core-shell structure. However, unlike for the investigation performed on the core-shell model based simulated data, a decrease in SLD(C) greater than 0.1×10^{10} cm^{-2} resulted in a complete disappearance of the cross-term, an observation that can also be made for PSFs extracted from the S+C simulated dataset when SLD is shifted. In summary, 75HNP shows PSF outputs and behaviour that is partially consistent with both lack and presence of ionomer adsorption. And indeed, the answer may lie in the case of partial ionomer adsorption. As figure 39 demonstrates, in simulations of partial ionomer adsorption, even 1% of the core-shell model in the dataset resulted in extraction of the S_{cp} output that is a signature of the core-shell structure. Moreover, in SLD shift investigation of the simulated dataset based on 1 wt% adsorption the S_{cp} output was also seen to disappear when SLD(C) was decreased by approximately 0.05×10^{10} cm^{-2}. Furthermore, a lower degree of adsorption is also consistent with the lower intensity of the S_{cp} output when comparing to S_{cp} extracted from the 25HNP ink series. With regards to the S_{pp}, figure 70 compares the output extracted form 75HNP ink series, and scattering from 2 wt% Nafion dispersion in the same solvent system:

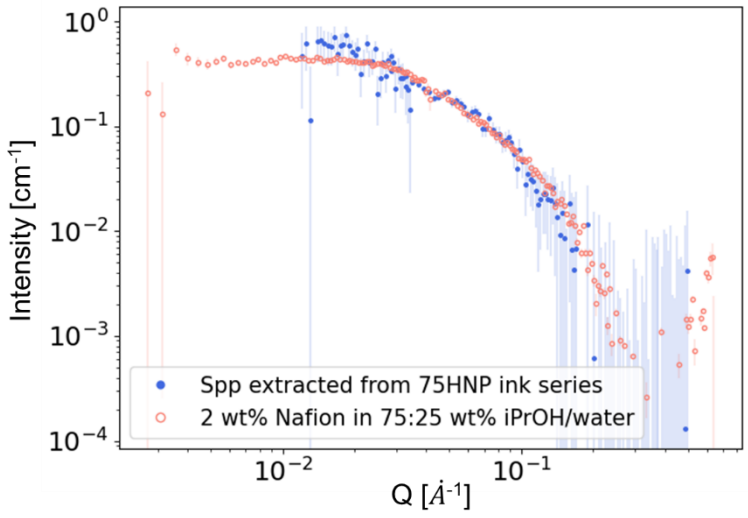


Figure 70. *S_{pp} output extracted from 75HNP ink series (blue) and scattering function of 2.0 wt% Nafion in 75:25 wt% iPrOH/water solvent (pink). The Spp output has been adjusted to the intensity [cm^{-1}] scale, as well as to account for an increased scattering intensity arising from the more than doubled concentration in the Nafion-only dispersion.*

It can be observed that unlike in the case of HNP, the S_{pp} output extracted and the Nafion scattering function are somewhat mismatched in the mid/low Q regimes ($Q<3x10^{-2}$ $\dot{A}^{-1}$). It could be argued that this is because the concentration of Nafion in the dispersion was more than double that in the ink, shifting the position of the structure factor related peak feature. However, to begin with the Nafion scattering function does not show any features related to a structure factor that would shift with concentration (which is the reason why this scattering function is fully fit-able, figure 51). Instead, the increasing intensity that can be observed in the S_{pp} output close to the cut-off point in the low/mid Q regime ($Q \approx 3x10^{-2}$ $\dot{A}^{-1}$) may suggest a presence of an ionomer structure aside from the unadsorbed Nafion aggregates. A fitting was attempted with a combined vesicle and cylinder model, figure 71. Note because of the good agreement of the S_{pp} and Nafion-only scattering functions in the mid/high Q regimes ($Q>3x10^{-2}$ $\dot{A}^{-1}$) observed in figure 70, the cylinder related parameters (radius, length and polydispersity) were fixed to values obtained from the fitting of the latter (figure 51), in addition to fixed core radius and polydispersity parameters (figure 58).

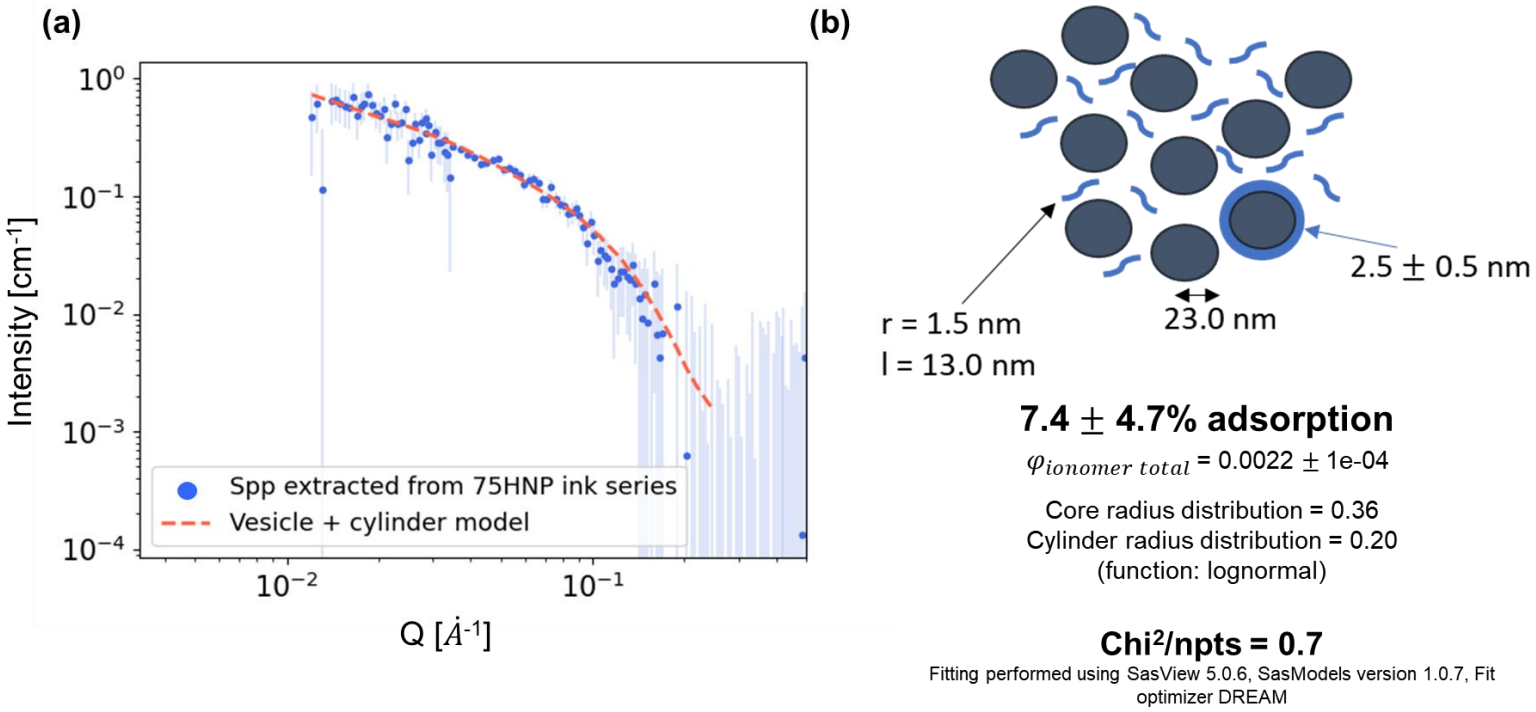


Figure 71. (a) *S_{pp} extracted from the 75HNP ink series, fitted with the vesicle + cylinder model.* ***(b)*** *Parameters extracted from fitting represented in a system schematic. r = radius, l = length. Uncertainty for fitted cylinder length/radius parameters can be found in original fitting of corresponding Nafion-only scattering function (figure 51). Degree of adsorption computed from vesicle proportion (x) pre-factor.*

A good fit is achieved, with a low chi^2 value of 0.7, accounting for all data points in the S_{pp} scattering function. In the mid/high Q regime ($Q>3x10^{-2}$ $\dot{A}^{-1}$) the scattering from unadsorbed Nafion aggregates is well expressed with the cylinder form factor, using parameters obtained when fitting the Nafion only dispersion in the corresponding solvent. With regards to the ionomer shell, a low degree of adsorption is extracted at 7.4%, with shell thicknesses of 2.5 nm. However, a large error of 4.7% is also present in the adsorption parameter, which is most likely due to the missing data points in the low Q regime ($Q<1x10^{-2}$ $\dot{A}^{-1}$), resulting in a low amount of information corresponding to the adsorbed ionomer in the scattering function to be fitted. This further stresses the quasi-quantitative nature of the fitting.

Nevertheless, the low degree of ionomer adsorption suggested by the fit, also when the error is taken into account, is consistent with the lacking data points of the S_{pp} output itself, which is reminiscent of the S_{pp} output obtained for the HNP ink series, where no ionomer adsorption was observed. Furthermore, partial

adsorption simulations with less than 5% core-shell model present were found to display higher error bars in the S_{pp} output low Q regime ($Q<1x10^{-2}$ $\dot{}^{-1}$), figure 39. Moreover, where less than 10% of the core-shell model was present, the PSF outputs from partial adsorption simulations were found to behave similarly to the spheres + cylinders, no adsorption model simulations in sensitivity studies (section 2.2.6). These observations suggest S_{pp} outputs obtained from ink systems with low degree of adsorption also may be susceptible to poor extraction of data in the low Q regime ($Q<1x10^{-2}$ $\dot{}^{-1}$).

Note the parameter extracted from the fit, at 0.0022, is significantly lower than the value of 0.0038 calculated from masses measured during sample preparation, and well outside the 10% error boundary estimated. It is likely some material was deposited on the zirconia balls used for dispersion, and the entire component concentration was not present in the liquid sample measured, however, even considering such an explanation, the discrepancy remains very high.

Conclusions

CV-SANS data for the 25HNP, HNP and 75HNP ink series were successfully obtained, and PSF outputs for each case were extracted, allowing for investigation of the effect of iPrOH concentration in the ink solvent on Nafion adsorption to HSAC. Figure 71 summarizes key parameters extracted from fitting of the S_{pp} outputs (% adsorption, shell thickness), as well as Nafion-only in corresponding solvent scattering functions, which were then used as fixed parameters (cylinder radius, length) in the fitting of the more complex S_{pp} outputs:

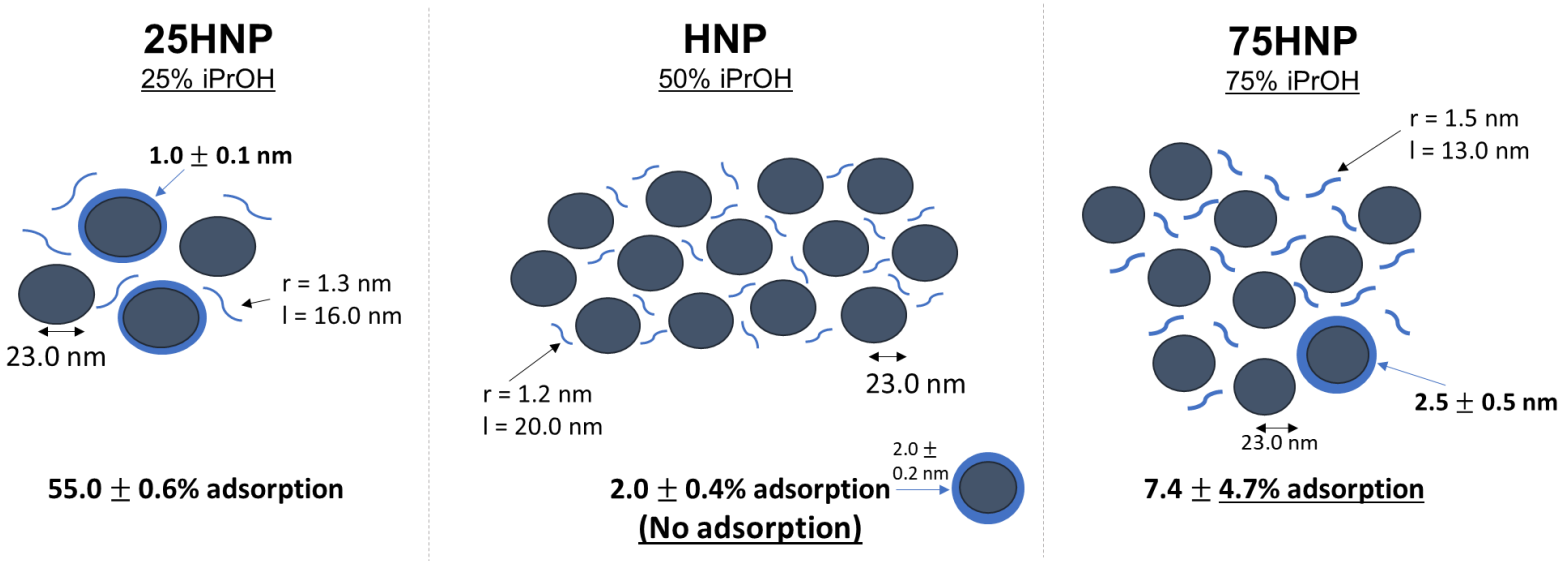


Figure 72. *Schematic visualizing structural differences between ink systems based on solvents with varying iPrOH concentrations: 25HNP, HNP and 75HNP, as extracted from quasi-quantitative and qualitative analyses.*

HNP, which was based on a 50:50 wt% iPrOH/water solvent, was concluded to show no ionomer adsorption to carbon, as indicated by a lack of S_{cp} output, perfect match of the S_{pp} output and Nafion-only scattering functions, as well as very low adsorption of 2% extracted from fitting with the vesicle/cylinder combined model.

On the other hand, its alcohol-poor and alcohol-rich counterparts, 25HNP and 75HNP, both showed a degree of ionomer adsorption, made evident by the presence of a cross-term in the outputs extracted.

Fitting the S_{pp} output of the 25HNP ink series suggested approximately 55% of ionomer adsorption to carbon, with a shell thickness of 1.0 nm. On the other hand, the S_{pp} output of the 75HNP ink series suggested approximately 7.4% of ionomer adsorption, with a thicker shell of 2.5 nm. Including the large

error of 4.7% on the adsorption parameter extracted for 75HNP, the difference in degree of adsorption between these two ink systems is evident. Moreover, the extracted shell thicknesses are consistent with the 'cut-off' Q values observed in the S_{cp} outputs of the two ink series – for 25HNP, where a thinner ionomer shell was suggested by fitting of the S_{pp}, the S_{cp} output tends towards higher Q magnitudes ($Q \approx 5x10^{-2}$ Å^{-1}), consistent with a smaller size domain. On the other hand, the S_{cp} output of the 75HNP ink series is 'cut-off' at approximately $Q \approx 1x10^{-2}$ Å^{-1}, consistent with the larger shell thickness extracted from fitting of the corresponding S_{pp} output.

Parameters extracted for unadsorbed ionomer aggregates were obtained by analysis of Nafion-only (in corresponding solvents) scattering functions using the cylinder form factor. However, it is important to note only the scattering function of Nafion in 75:25 wt% iPrOH/water was fully fit-able. Distinct structure factors were observable in the other two cases, because of which Nafion in 50:50 wt% iPrOH/water could only be approximately fitted, and the Nafion in 25:75 wt% iPrOH/water fit could only be estimated (appendix 17 and appendix 21 respectively). Although the estimated information was crucial in minimizing the large number of free parameters in the complex vesicle/cylinder combination model, commenting on the differences between the extracted unadsorbed ionomer parameters remains difficult, particularly with regards to the cylinder length. The Nafion-only scattering functions should be re-measured using samples of very low ionomer concentrations, ensuring no scattering related to the structure factor is present and all data is fully fit-able, allowing for a direct structure comparison and more accurate information that can be used in the vesicle/cylinder model also.

In summary, it can be concluded that higher degrees of adsorption are observed in the case of 25HNP, with formation of a thinner ionomer shell. 75HNP showed very little ionomer adsorption (with a thicker ionomer layer), and HNP displayed clear behaviour corresponding to no ionomer adsorption.

Although the adsorption trend is not linear with varying iPrOH concentration, in general it can be observed that adsorption of ionomer to carbon is increased in ink compositions based on water-rich solvents.

Obtaining a more detailed picture, by measuring additional datasets with a more gradual increase of iPrOH content could shed light on the detailed ionomer-to-carbon adsorption mechanism - whether the adsorption gradually decreases with increasing iPrOH concentration, or whether a critical iPrOH value exists, causing the degree of adsorption to change significantly.

2.2.3.4 Effect of ionomer type

Nafion has been the ionomer of choice for application in PEM fuel cells for a long time since its commercialization in the 1960s. In recent years, Aquivion has also been garnering significant research attention due to its improved mechanical stability, improved conductivity, and reduced gas crossover properties[59,102,103] Aquivion, a short side chain (SSC) ionomer, displays an increased polarity in comparison to nafion,[59] and therefore its conformation in the ink solvent medium, along with adsorption to carbon, can be expected to differ. This section will investigate such differences, comparing inks based on Nafion and Aquivion with the following compositions and naming:

25HNP = 1 wt% high surface area carbon, **Nafion** with I/C = 0.8, 25:75 wt% iPrOH/H_2O solvent

25HAP = 1 wt% high surface area carbon, **Aquivion** with I/C = 0.8, 25:75 wt% iPrOH/H_2O solvent

Note the 25:75 wt% iPrOH/H_2O solvent is being used in the ink compositions instead of the standard 50:50 wt% iPrOH/H_2O. A composition based on Aquivion and the standard solvent was also measured, however was deemed invalid due to an error in sample preparation. Nevertheless, as CV-SANS data sets for two ink series with a matching solvent system were obtained, a proper investigation of the effect of ionomer on

the catalyst ink dispersion structure can still be performed. The SLD of Aquivion in 25:75 wt% iPrOH/water solvent has been obtained using the contrast match approach, yielding a value of 4.94×10^{10} cm^{-2} (appendix 23). Figure 73 presents the CV-SANS data as well as corresponding PSF outputs extracted for the two ink compositions.

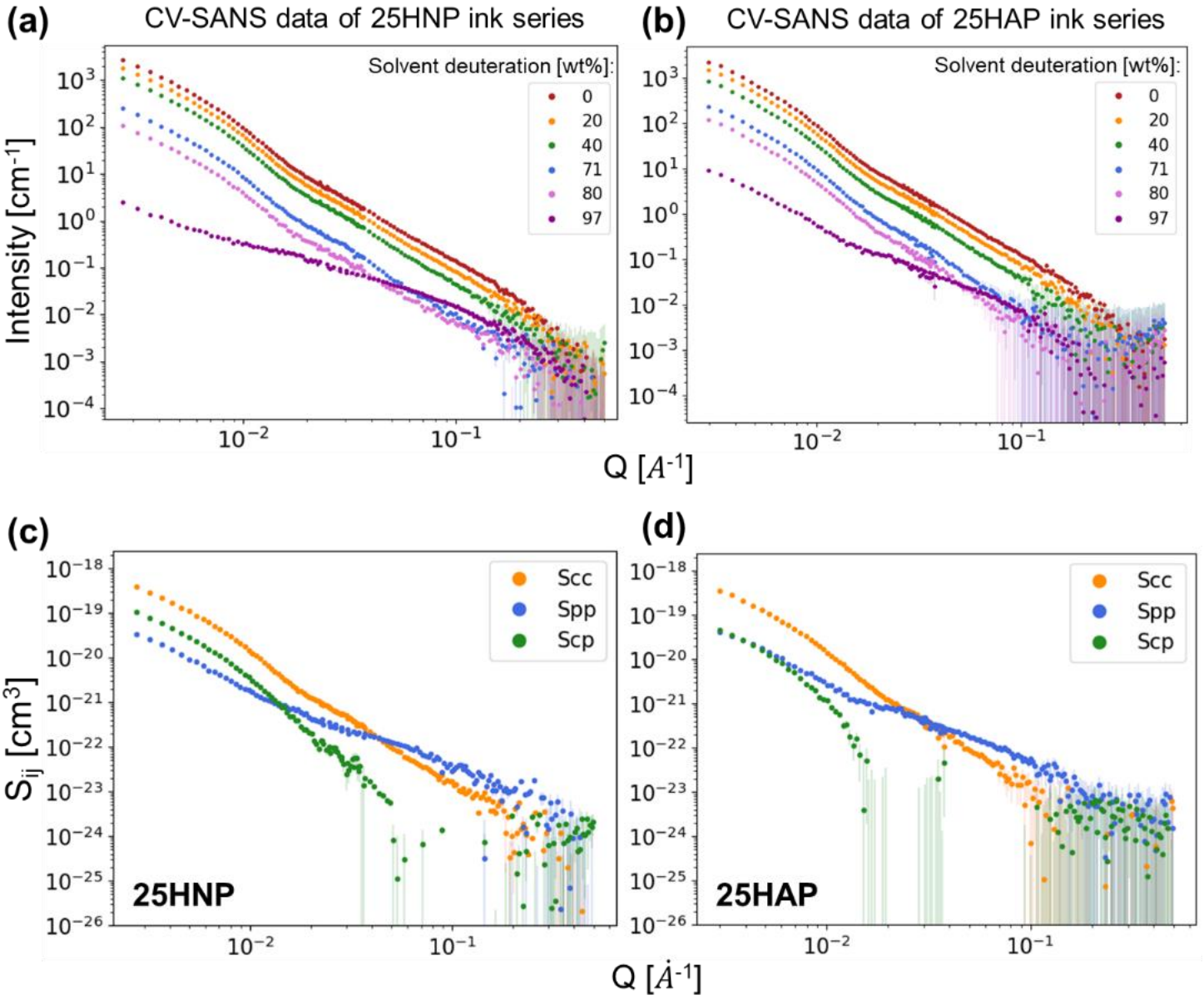


***Figure 73**. CV-SANS scattering functions of **(a)** 25HNP**, (b)** 25HAP ink series. PSF outputs extracted from **(c)** 25HNP, **(d)** 25HAP ink series.*

Both PSF outputs contain a cross-term, indicating a degree of adsorption of both Nafion and Aquivion onto HSAC in the 25:75 wt% iPrOH/water solvent. The PSF outputs from the two ink series were plotted together for a closer inspection, figure 74.

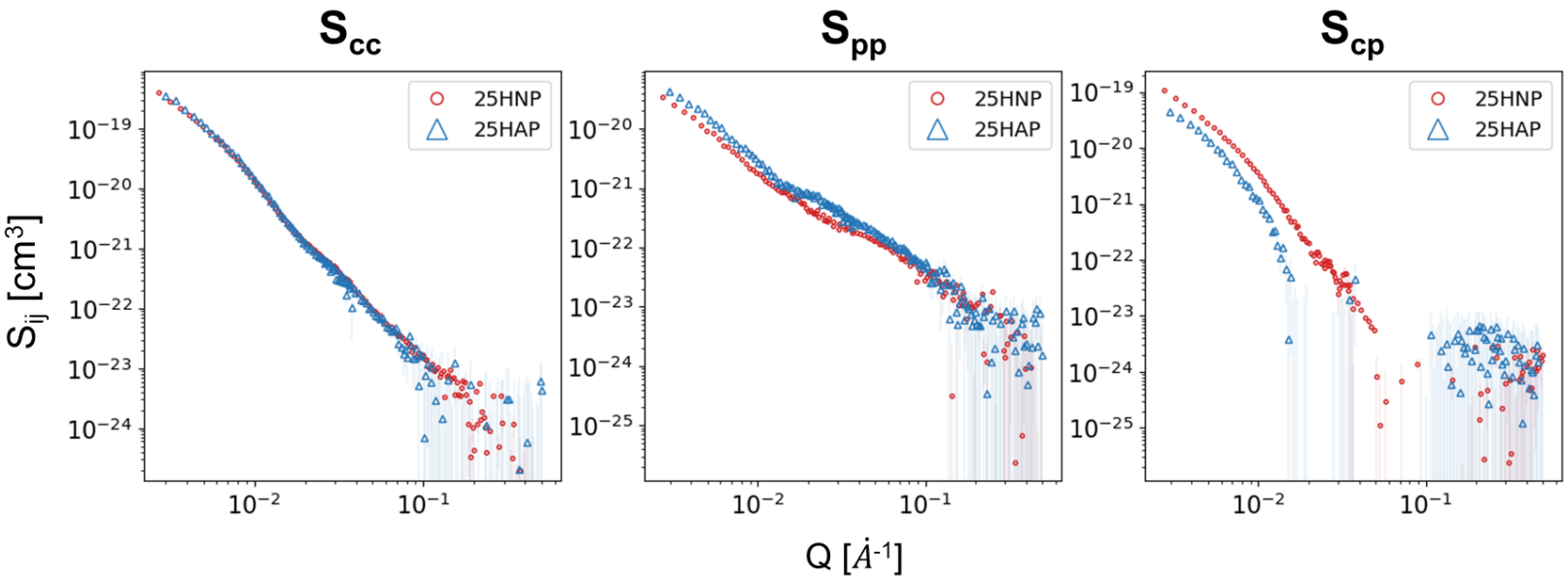


Figure 74. *Comparison of equivalent PSF outputs extracted from ink compositions based on different ionomer types: 25HNP (red), 25HAP (blue).*

The S_{cc} output remains constant throughout the different ink compositions, showing the unchanging structural nature of carbon primary particles. The S_{cp} output of the 25HAP ink series falls at a lower intensity compared to the S_{cp} of 25HNP, and is cut-off at a lower Q value ($Q \approx 2x10^{-2}$ $\dot{A}^{-1}$), indicating a potentially lower degree of adsorption and a thicker shell layer. On the other hand, the S_{pp} output of 25HAP has a higher intensity, which does not match with the idea of a lower degree of adsorption, as shown through simulations of the partial adsorption case. However, note that in the simulated data, in each case of partial adsorption the shell thickness is kept as a constant parameter. It is possible that if the shell thicknesses are very different between the two samples, the idea of estimating degree of adsorption from the PSF output intensity becomes invalid. The S_{pp} extracted for the 25HAP ink series was fitted with the vesicle + cylinder combination model to estimate degree of adsorption and shell thickness, figure 75. As no significant variation was observed in the S_{cc} outputs of 25HNP and 25HAP, the core radius and polydispersity remained fixed based on the initial fitting performed (figure 58). However, because the structure factor in the corresponding Aquivion-only scattering function was too prominent, no size estimation could be extracted. Therefore, the radius and length from cylinder form factor used to model the unadsorbed ionomer structure remain free parameters in the combination model.

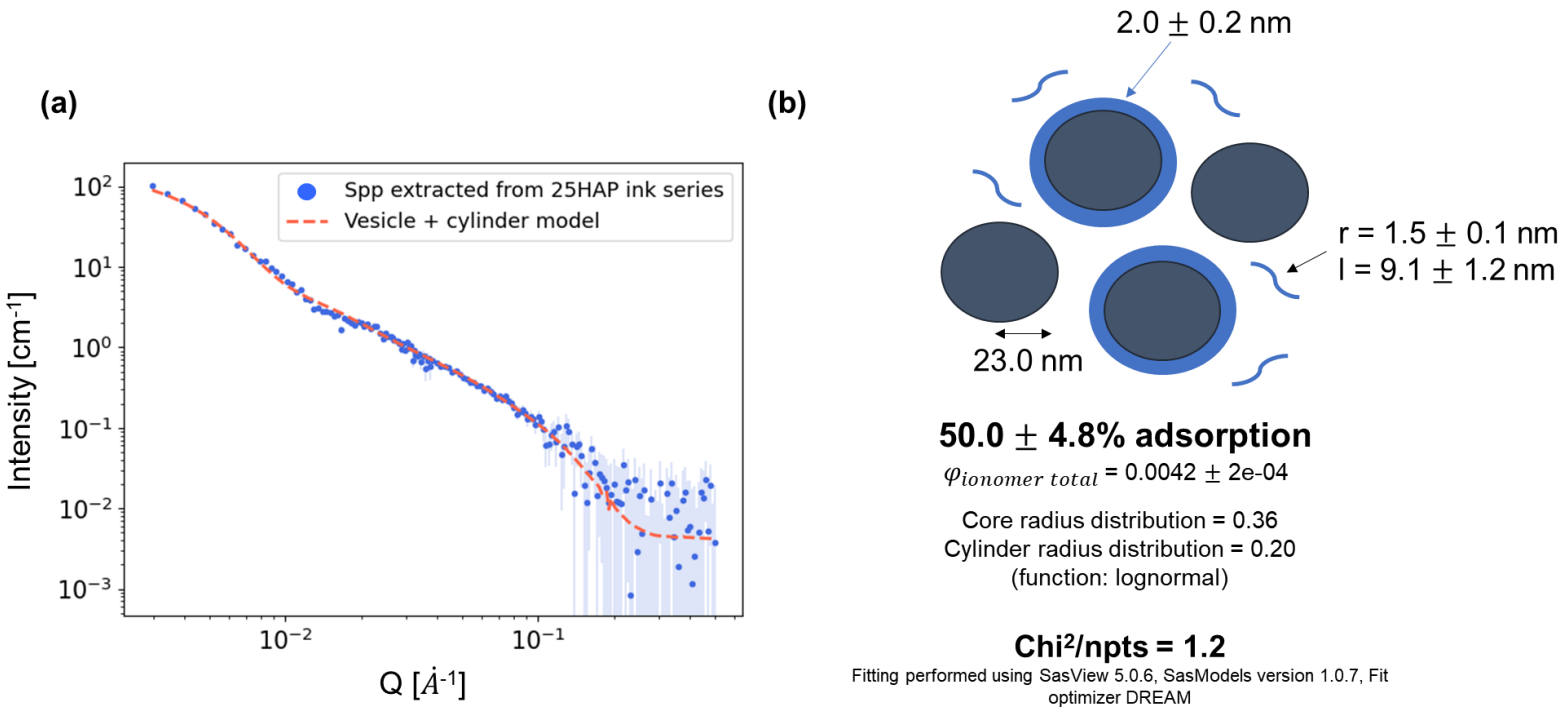


Figure 75. (a) *S_{pp} extracted from the 25HNP ink series, fitted with the vesicle + cylinder model.* ***(b)*** *Parameters extracted from fitting represented in a system schematic. r = radius, l = length. Degree of adsorption computed from vesicle proportion (x) pre-factor.*

The vesicle + cylinder model fits the S_{pp} output well, with a chi^2 value of 1.2, suggesting Aquivion adsorbs to HSAC, forming a shell layer, and also forms rod-like aggregates in the water-rich solvent like Nafion.

The radius and length values extracted for the Aquivion unadsorbed aggregates were 1.5 and 9.1 nm. Despite the very good fit, the veracity of these parameters, in particular the length, should be verified by fitting of a scattering function of a very dilute Aquivion sample, with no structure factor present.

With regards to the ionomer shell, extracted parameters suggest a 2.0 nm thick shell, and a significant degree of adsorption at 50%. Notably, a high error of 4.8% is present, yet despite this a high degree of Aquivion adsorption to HSAC can be concluded.

Figure 76 compares key parameters extracted from the 25HNP and 25HAP ink series. In both systems, high degrees of adsorption (55 and 50% respectively) can be observed. This suggests ionomer type has little effect on the degree of ionomer to carbon adsorption in the 25:75 wt% iPrOH/water solvent system. The similar degrees of adsorption could also indicate the alcohol concentration is a more crucial parameter in determining ionomer-carbon interaction. The higher degree of adsorption in water rich solvents may be related to reduction of the interfacial energy between the hydrophobic carbon surface and water through the presence of an ionomer layer, with SO_3^- groups orientated towards the solvent.[30] Nevertheless, in order to confirm such a hypothesis, ink compositions based on Aquivion with varying iPrOH concentrations must also be studied in order to observe similarities or differences when iPrOH concentration is increased.

The shell thickness extracted from the 25HAP sample is twice as big at 2 nm in comparison to the value obtained for 25HNP (1 nm). This is surprising considering the shorter side-chain length of Aquivion, which may instinctively suggest thinner shells in the case of monolayer adsorption. Nevertheless, comparison of the S_{cp} outputs of the two inks series supports the idea of a thicker ionomer shell in the Aquivion based

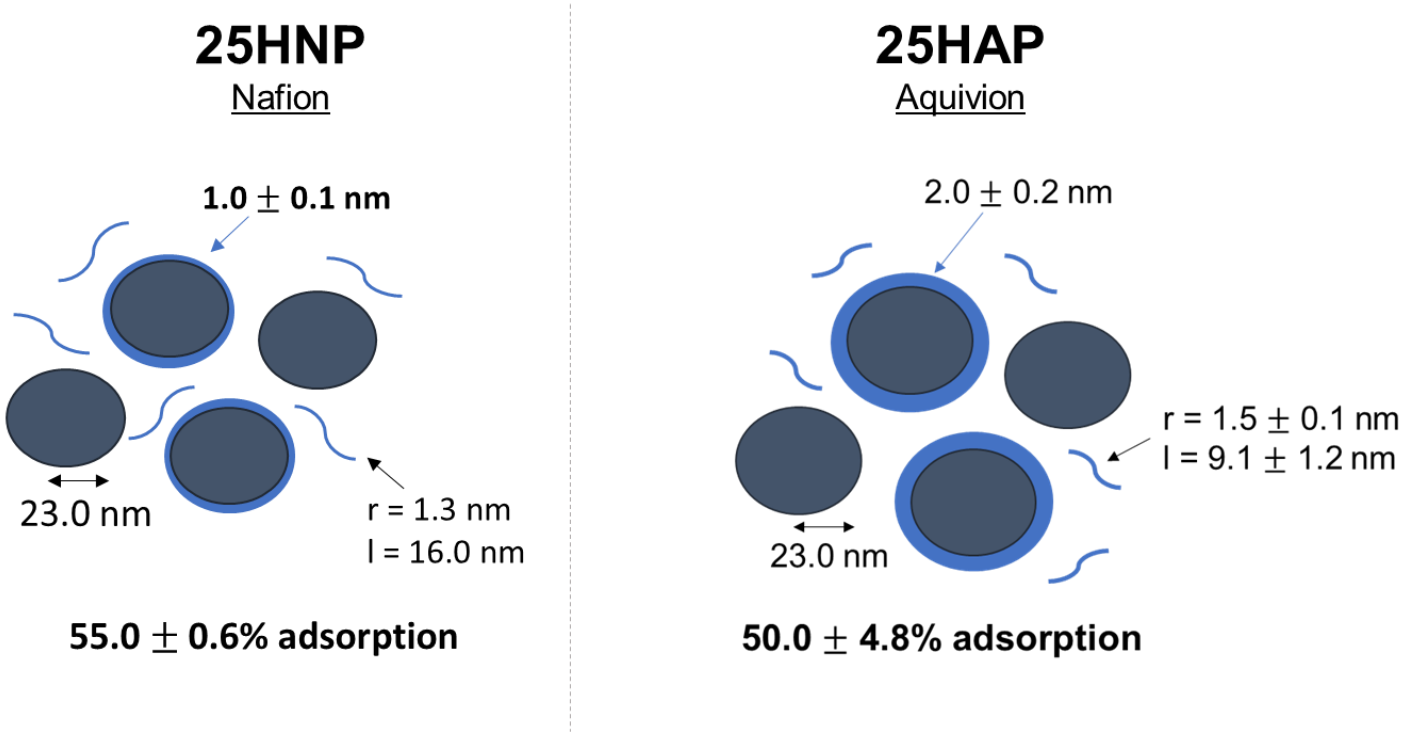


Figure 76. *Schematic visualizing structural differences between ink systems based on different ionomer types in 25:75 wt% iPrOH/water solvent: 25HNP and 25HAP, as extracted from quasi-quantitative and qualitative analyses.*

sample, with a 'cut-off' Q magnitude of approximately $1x10^{-2}$ $\dot{}^{-1}$ indicating an object of a bigger dimension ($Q \approx 5x10^{-2}$ $\dot{}^{-1}$ for 25HNP). The difference may be explained by a different conformation of the two ionomer types. Indeed, the radius and length parameters of the unadsorbed ionomer are rather different for 25HNP and 25HAP, in particular with regards to the length. Nevertheless, since in both instances a proper fitting of the ionomer-only scattering functions could not be achieved, further data (scattering functions of dilute samples) is necessary for verification of this notion.

Conclusions

PSF outputs of 25HAP were successfully extracted and the S_{pp} was fitted using a combined vesicle/cylinder model. A high degree of adsorption at 50% could be observed, with shell thickness of 2 nm. Comparison of 25HNP and 25HAP ink series, which were based on Nafion and Aquivion respectively, suggested the ionomer type does not have a great impact on the degree of ionomer-carbon interactions, yet does affect the shell thickness, which may be linked to variations in ionomer conformation.

Inks based on Aquivion with varying iPrOH concentration in the solvent should be further studied in order to explore a potential ionomer type/solvent cross-correlation effect, and dilute ionomer-only scattering functions need to be obtained for an in-depth understanding of the conformation of the two different ionomers in the specified solvent system.

2.3.3.5 Concentration effect

In this work the standard ink composition is based on 1 wt% carbon, yielding an ink solid content of approximately 3 wt% (when Pt is also considered). However, the most common industrial manufacturing process of catalyst layers involves blade coating of inks onto a substrate, which requires inks of approximately 10 wt% solid content. Therefore, it is imperative to verify whether component concentrations

in the ink impact its structure. The following ink compositions were chosen for the investigation of this variable:

HNP = **1 wt%** high surface area carbon, Nafion with I/C = 0.8, 50:50 wt% iPrOH/H_2O solvent

2HNP = **2 wt%** high surface area carbon, Nafion with I/C = 0.8, 50:50 wt% iPrOH/H_2O solvent

Note an ink based on 2 wt% carbon would still correspond to a solid content of only 6 wt%, which is lower than in the industrially applicable case, however, inks based on 3 wt% carbon (10 wt% solid content) proved difficult to handle during sample preparation due to their increased viscosity. Nevertheless, a doubled concentration, and therefore solid content, should prove sufficient for investigation of the concentration effect in general. Figure 77 presents CV-SANS data of the two ink series, along with extracted PSF outputs.

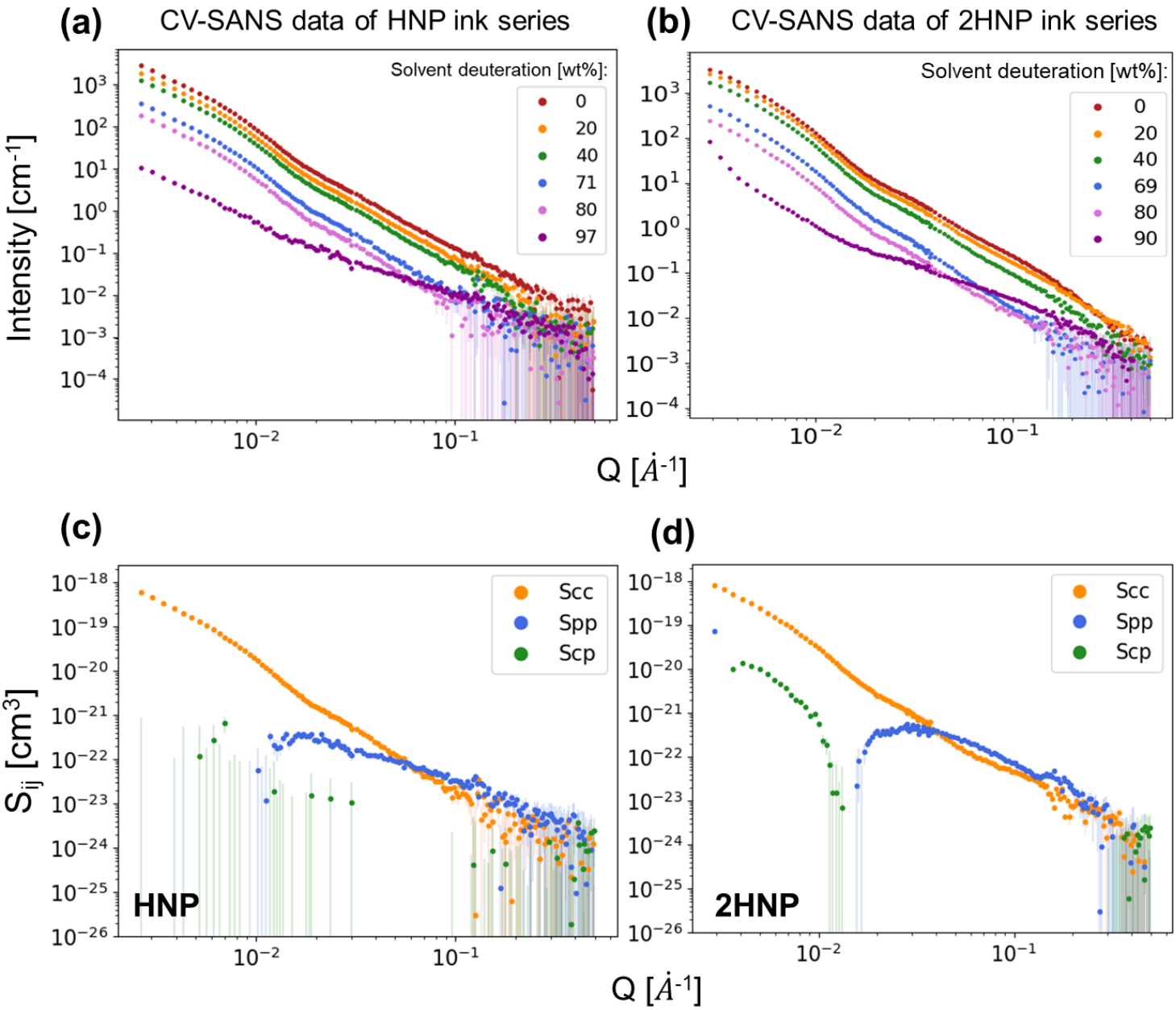


Figure 77. *CV-SANS scattering functions of* ***(a)*** *HNP,* ***(b)*** *2HNP ink series. PSF outputs extracted from* ***(c)*** *HNP,* ***(d)*** *2HNP ink series.*

Already in the CV-SANS data a difference can be observed in the low Q regime ($Q<1x10^{-2}$ $\dot{A}^{-1}$) of the scattering function that corresponds to the most deuterated sample, where scattering from carbon is minimized. Where in HNP the low Q regime looks similar to all the other samples in the ink series, in the 2HNP series the most deuterated sample displays an upturn that was not visible in other scattering functions investigated. Concurrently, a cross-term can be observed in the S_{cp} output of the 2HNP ink series. The S_{pp} remains over-subtracted in the low Q regime ($Q<1x10^{-2}$ $\dot{A}^{-1}$), suggesting a lower degree of Nafion adsorption to carbon. Corresponding outputs extracted from the two ink series were plotted together for a detailed overview. Note for comparison purposes, PSF outputs extracted from 2HNP were scaled by the volume fraction difference of 2 to account for increased scattering intensity originating from the concentration difference. An unscaled version can be found in appendix 24.

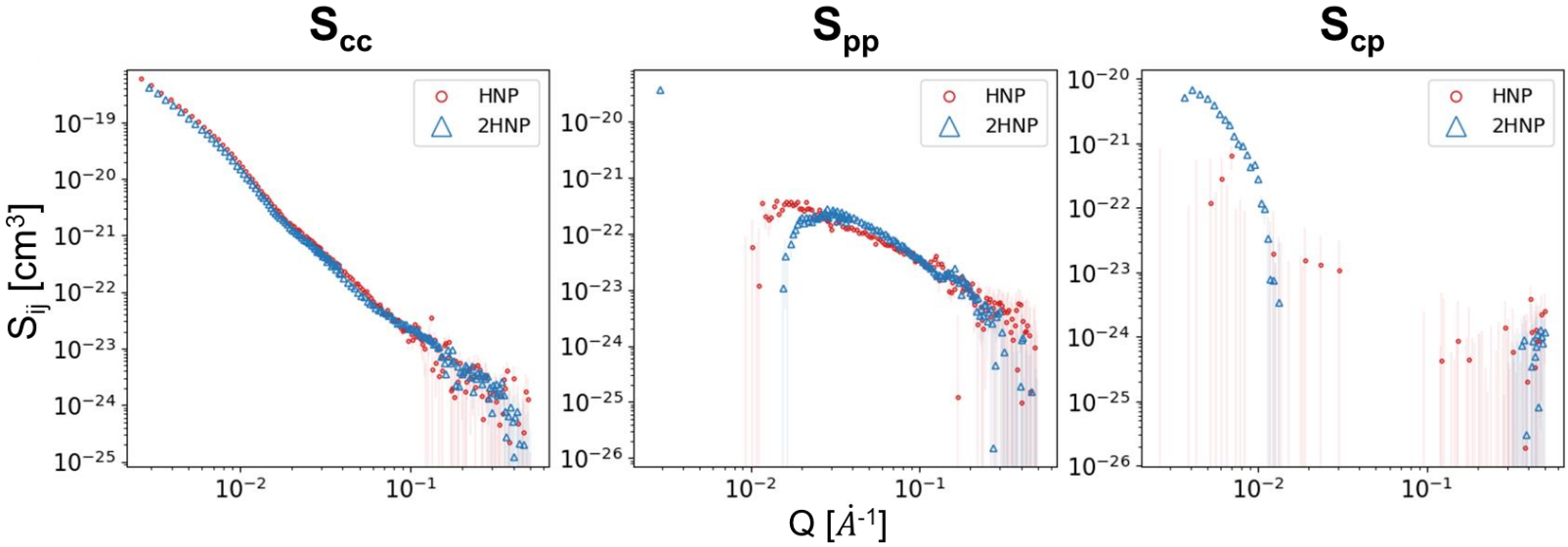


Figure 78. *Comparison of equivalent PSF outputs extracted from ink compositions based on different component concentrations: HNP (red), 2HNP (blue). PSFs outputs extracted from 2HNP ink series have been scaled by a factor of 2 to account for concentration discrepancies.*

The S_{cc} output remains unchanged between the two ink series, corresponding to carbon primary particles that make up further aggregates and agglomerates, which are not visible in the Q range measured, but might be affected by concentration differences.

On the other hand, aside from missing data points in the low Q regime ($Q<1x10^{-2}$ $\dot{A}^{-1}$), the S_{pp} outputs of the two ink series do not look much alike.

However, it is prudent to recall that ionomer concentration impacts the Q position where a peak feature related to the structure factor is present, which may be a justification for the difference in cut-off point observed between the two S_{pp} outputs. Consequently, the S_{pp} extracted from 2HNP should be compared to SANS data of a 2 wt% Nafion dispersion in the corresponding solvent instead, figure 79.

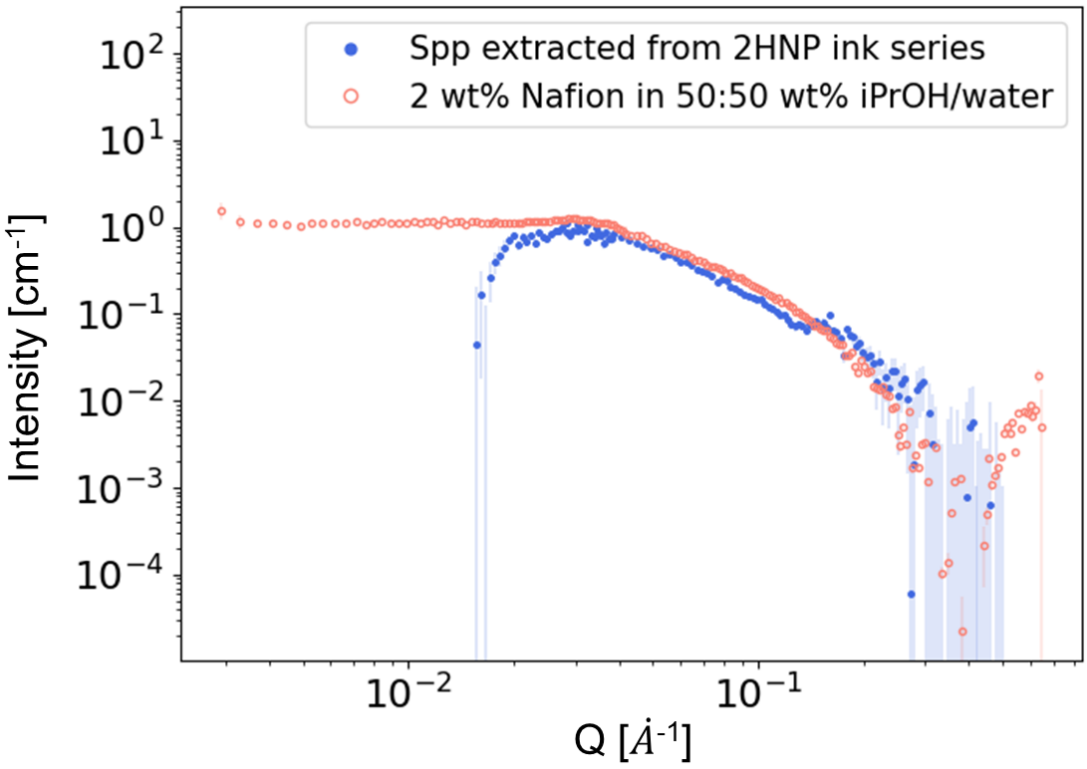


Figure 79. *Comparison of Spp output extracted from the 2HNP ink series to SANS data of 2 wt% Nafion in 50:50 wt% iPrOH solvent.*

Indeed, the cut-off point observed in the S_{pp} perfectly corresponds to the point in the 2 wt% scattering function where I Q^0 type scattering commences towards the low Q regime onwards ($Q<3x10^{-2}$ $\dot{}^{-1}$). A good agreement is also observed in the power law scattering present in the mid Q regime ($3x10^{-2}$ $\dot{}^{-1} < Q < 1x10^{-1}$ $\dot{}^{-1}$). However, in the high Q regime ($Q>1x10^{-1}$ $\dot{}^{-1}$), increased scattering can be observed in the S_{pp} output that is not present in the 2 wt% Nafion scattering function. Since the scattering has a distinct, peak-like shape (clearly visible in figure 77d), background noise seems an unlikely explanation. Indeed, the peak corresponds well to a feature observed in the shell and vesicle models, arising from the thickness of the ionomer layer on carbon particles, however in such an instance it should be present at significantly reduced intensities. Moreover, the observation of such a distinct feature is inconsistent with the lack of increased scattering observed in the low/mid Q regimes ($Q<3x10^{-2}$ $\dot{}^{-1}$). The reason for this deviation remains unclear.

Conclusions

The concentration effect on the catalyst ink structure was successfully investigated. The appearance of a cross-term in the ink composition with based on 2 wt% carbon, 2HNP, suggests that higher component concentrations results in an increased ionomer adsorption to carbon particles. This is most likely as the components are in closer proximity in a more concentrated system to begin with. Albeit, an over-subtracted S_{pp} output, where the data cut-off point corresponds exactly to scattering from a Nafion only dispersion, suggests that the degree of adsorption in the 2HNP ink composition remains very low.

Nevertheless, the outputs extracted suggest the component concentration is not insignificant with respect to the overall structure of the system. As future work, investigating a cross-correlation between component concentration and other parameters, such as the solvent system or ionomer type, would be of interest.

2.3.3.6 Effect of Pt

It is widely agreed that the presence of Pt on the carbon support alters the adsorption mechanism of the ionomer, however, it is disputed whether the ionomer preferentially interacts with the carbon,[38,39] or with the Pt component.[25,53] In this section the effect of Pt addition on the catalyst ink structure will be investigated, as a singular parameter, as well as in combination with other variables studied earlier in this section such as iPrOH concentration and ionomer type. Note that contrast match measurements of the Pt/C complex proved unsuccessful due to issues with sample stability. Due to this reason, SLD(Pt/C) had to be estimated by combining the theoretical SLD of Pt with the experimentally determined carbon-only SLD in a manner corresponding to the volume fraction of each component. SLD(Pt/HSAC) has been approximated to be 6.56×10^{10} cm^{-2}.

2.3.3.6.1 Introduction of Pt

The impact of Pt presence in the system on ionomer adsorption was investigated by comparing the standard HNP ink series with its Pt containing counterpart. The ink compositions were labelled as follows:

HNP = 1 wt% high surface area carbon, Nafion with I/C = 0.8, 50:50 wt% iPrOH/H_2O solvent

PtHNP = 1 wt% high surface area carbon **+ 1 wt% Pt**, Nafion with I/C = 0.8, 50:50 wt% iPrOH/H_2O solvent

CV-SANS data obtained for the two compositions as well as corresponding PSF outputs extracted are visualized in figure 80.

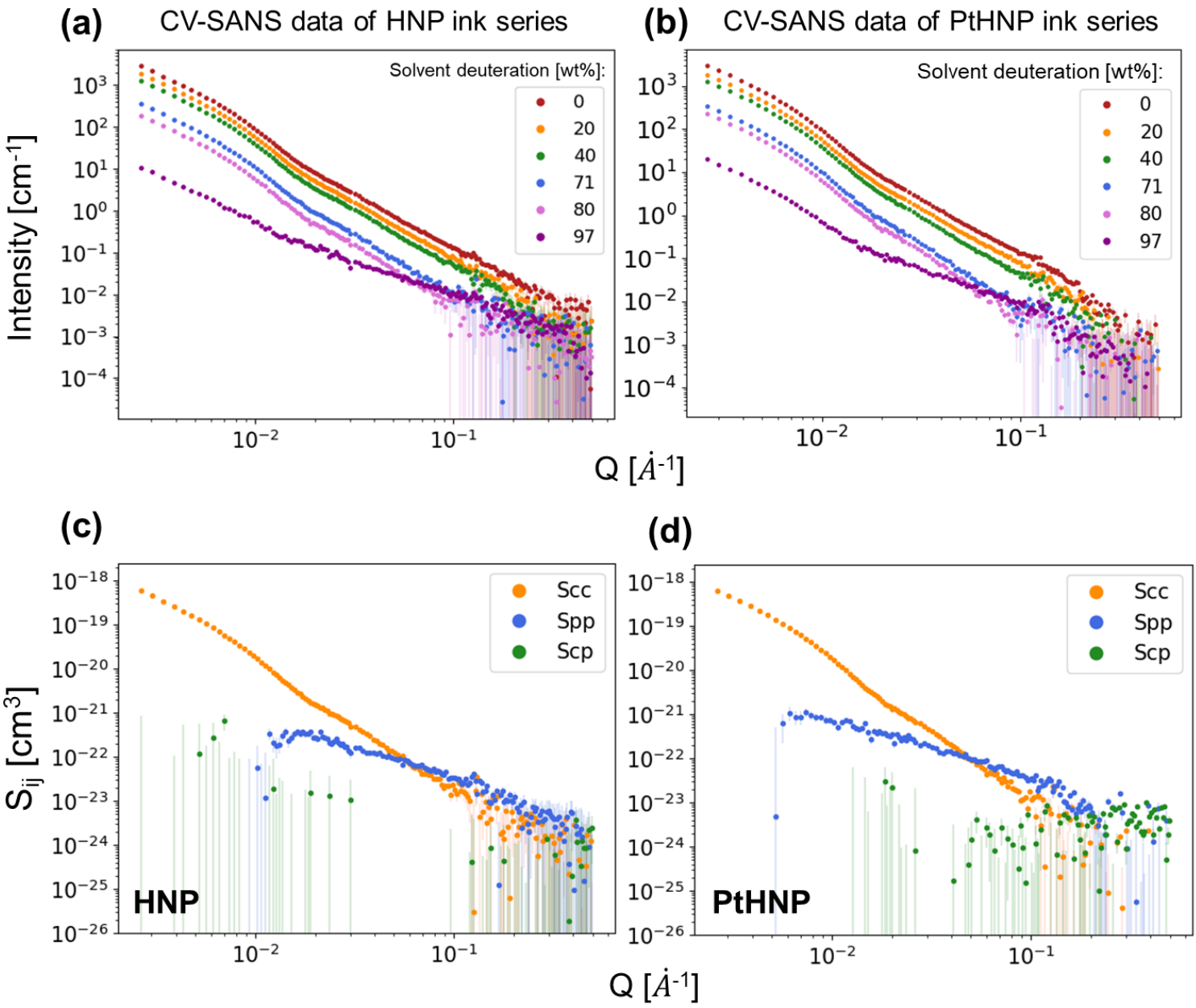


Figure 80. *CV-SANS scattering functions of* ***(a)*** *HNP,* ***(b)*** *PtHNP ink series. PSF outputs extracted from* ***(c)*** *HNP,* ***(d)*** *PtHNP ink series.*

It can immediately be observed that neither of the S_{cp} outputs contains any scattering reminiscent of the cross-term, suggesting the presence of Pt does not boost ionomer adsorption in the HNP based ink composition. As SLD(Pt/C) had to be estimated rather than extracted experimentally, a SLD shift investigation was performed on the PtHNP ink series in order to determine the validity of the output (appendix 25). Indeed, the behaviour of the PSF outputs with deviating component SLD values was very coherent with the observations made in the case of spheres + cylinders based simulations, confirming the veracity of the obtained PSF outputs.

Corresponding PSF outputs of the two ink series were plotted together for enhanced comparability, figure 81.

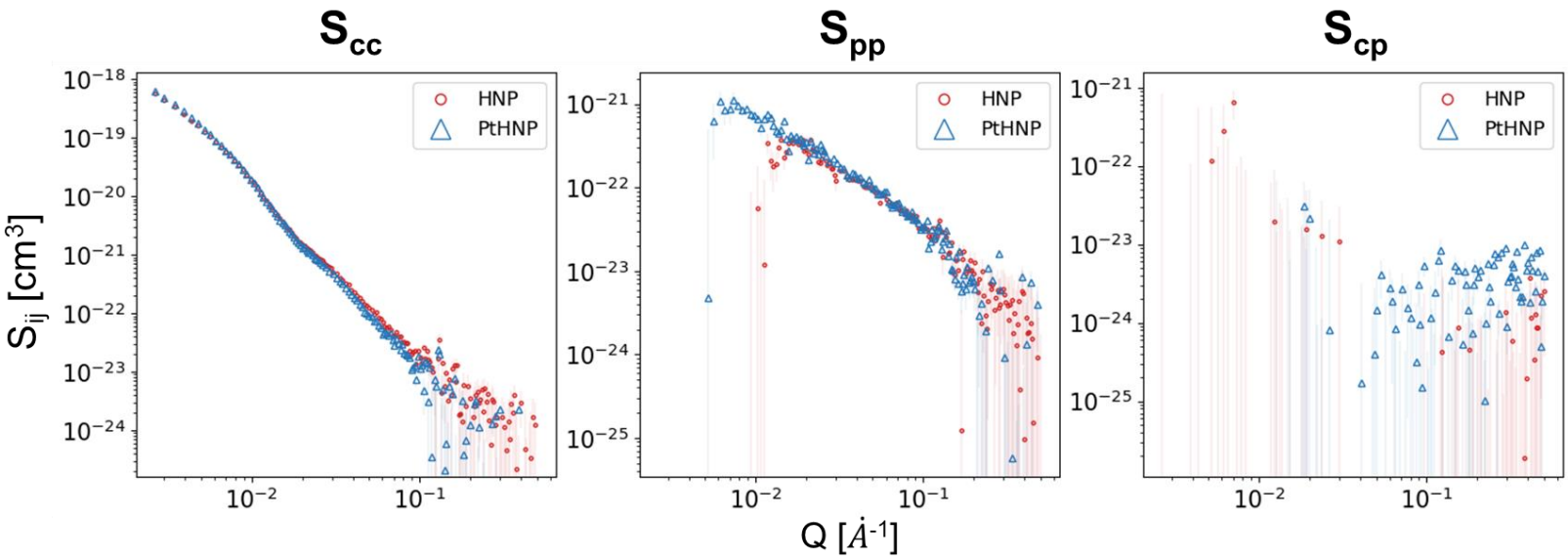


Figure 81. *Comparison of equivalent PSF outputs extracted from ink compositions based on different component concentrations: HNP (red), PtHNP (blue).*

The S_{cc} output remains unchanged between the ink series, demonstrating that scattering from Pt is negligible compared to that of carbon. The S_{pp} outputs are both missing data points in the low Q regime ($Q<1x10^{-2}$ Å^{-1}), however the S_{pp} extracted from the PtHNP ink series is cut-off at a lower Q value ($Q \approx 6x10^{-3}$ Å^{-1}) than the S_{pp} of the HNP ink series, showing additional data points. As the concentration of ionomer remains constant throughout the two ink compositions, and it has been shown that the S_{pp} arising from the HNP ink series matches perfectly with the scattering function of a Nafion only dispersion, from the deviation it can be deduced that an additional structure related to the ionomer may be present in the PtHNP ink composition. However, the lack of scattering in the S_{cp} output points towards no adsorption of ionomer onto the carbon particles. This manner of scattering could be evident of a shift in the position of the peak feature related to the structure factor in unadsorbed ionomer scattering with lower concentrations. Nevertheless, this explanation seems dubious considering the lack of concentration change in-between the two ink series. A fitting attempt of the PtHNP S_{pp} output was made using the vesicle + cylinder combined model in order to search for structural explanations of the output deviation, figure 82. The core radius and polydispersity as well as unadsorbed ionomer radius and length parameters remain fixed as previously described.

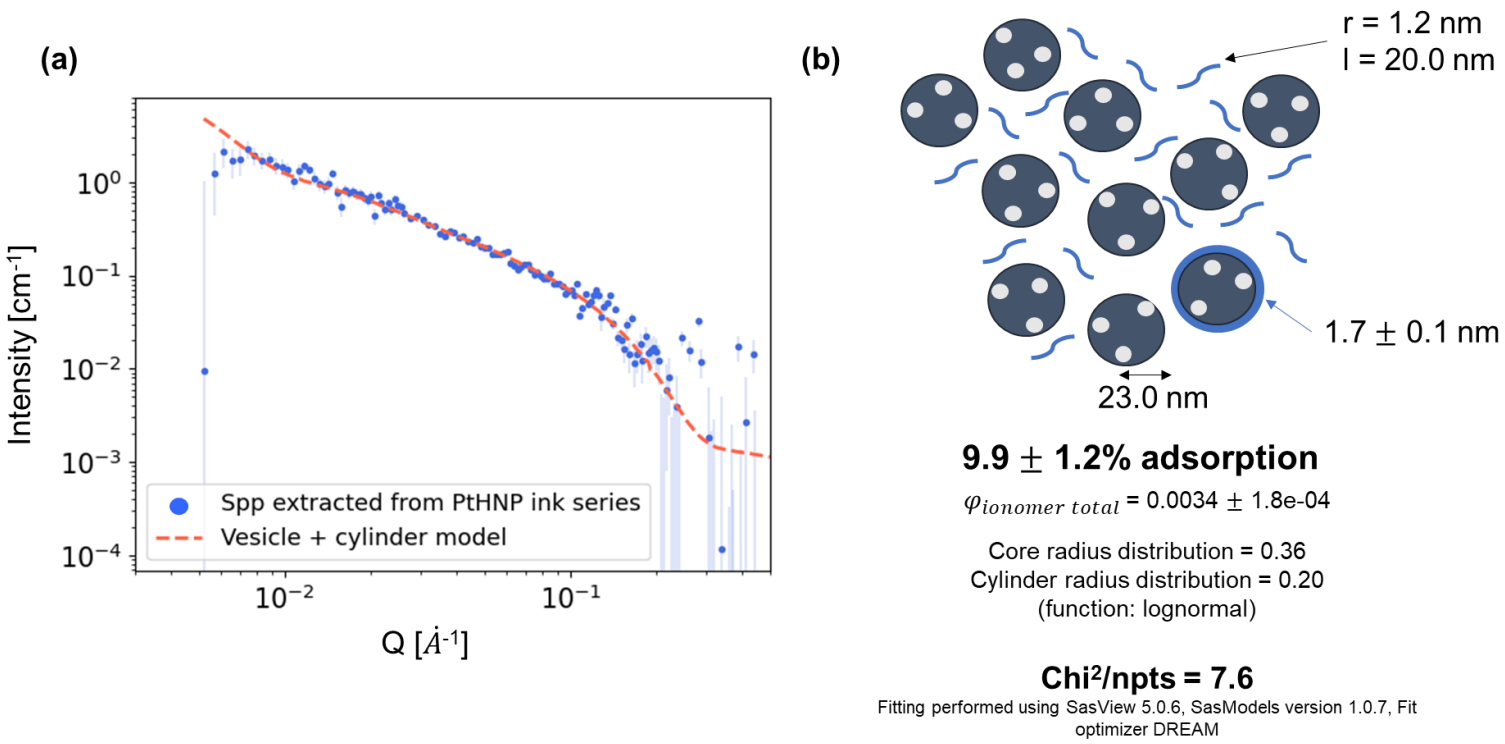


Figure 82. (a) *S_{pp} extracted from the PtHNP ink series, fitted with the cylinder + vesicle combination model.* ***(b)*** *Parameters extracted from fitting represented in a system schematic. r = radius, l = length. Degree of adsorption computed from vesicle proportion (x) pre-factor.*

Parameters extracted from the fit suggest a low degree of ionomer adsorption, approximately 10%, accounting for the additional data points observed in the S_{pp} in comparison the HNP, no Pt ink series counterpart. Nevertheless, it can be observed the fit deviates from the scattering function in the low Q regime ($Q<1x10^{-2}$ $\dot{A}^{-1}$) where the additional data points commence, trending towards higher intensities, suggesting bigger ionomer structures outside of the fitting range. This discrepancy makes the fit dubious, indicating the vesicle/cylinder model may not be an appropriate choice for fitting of this scattering function. The fit was chosen for the sake of consistency when fitting the S_{pp} outputs, allowing for a direct comparison of the quasi-quantitative results, however, considering the lack of cross-term output in the S_{cp}, a no-adsorption scenario remains highly plausible, and a different model should be applied to fit this S_{pp} output.

Nevertheless, at this point it remains unclear what the additional data points in the scattering function could represent. A conformation change of the unadsorbed ionomer in the presence of Pt is highly unlikely, particularly if a case of no interaction is considered.

Another hypothesis could be that the ionomer binds to the Pt particles only, not interacting with the carbon surface, forming a long chain that is loosely adsorbed to the complex surface. However, as no interactions with carbon particles occur, a cross-term output is not generated. Yet, to justify such a claim, one would have to assume that, just like in the S_{cc}, in the S_{cp} also scattering from carbon dominates enough to negate any Pt-ionomer related interaction in the output. To confirm this, in theory a much more complex PSF output could be performed, considering the ink system as 3 components and yielding 3 additional partial scattering function: $S_{Pt\text{-}Pt,}$ $S_{Pt\text{-}C}$ and $S_{Pt\text{-}P}$. Most likely such an endeavour, while not only posing a bigger challenge, would also require a larger amount of data inputs for a successful output extraction. On the other hand, obtaining more information from supporting techniques may not only prove easier, but also more useful in aiding to explain the phenomenon observed in the S_{pp} output.

From the data presented in this work, it can only be deduced with certainty that no Nafion adsorption is observed <u>onto the carbon primary particles</u> in the 50:50 wt% iPrOH/water solvent, irrespective of Pt presence.

2.3.3.6.2 Effect of Pt + I/C ratio

In section 2.3.3.2 it has been shown that the I/C ratio alone does not boost adsorption of Nafion onto HSAC. However, if the ionomer preferentially interacts with Pt its addition into the ink system may alter adsorption behaviour observed with varying I/C ratios. The following ink compositions were used for this investigation:

0.5PtHNP = 1 wt% high surface area carbon **+ 1 wt% Pt**, Nafion with **I/C = 0.5**, 50:50 wt% iPrOH/H_2O solvent

PtHNP = 1 wt% high surface area carbon **+ 1 wt% Pt**, Nafion with **I/C = 0.8**, 50:50 wt% iPrOH/H_2O solvent

1.3PtHNP = 1 wt% high surface area carbon **+ 1 wt% Pt**, Nafion with **I/C = 1.3**, 50:50 wt% iPrOH/H_2O solvent

Unfortunately, during the experiment it was noticed 1.3PtHNP samples were not stable and the dispersion would create a settlement during the measurement. For this reason, the CV-SANS data acquired for this ink series will not be evaluated. Figure 83 shows CV-SANS data and consequent PSF outputs extracted for the 0.5PtHNP and PtHNP ink series.

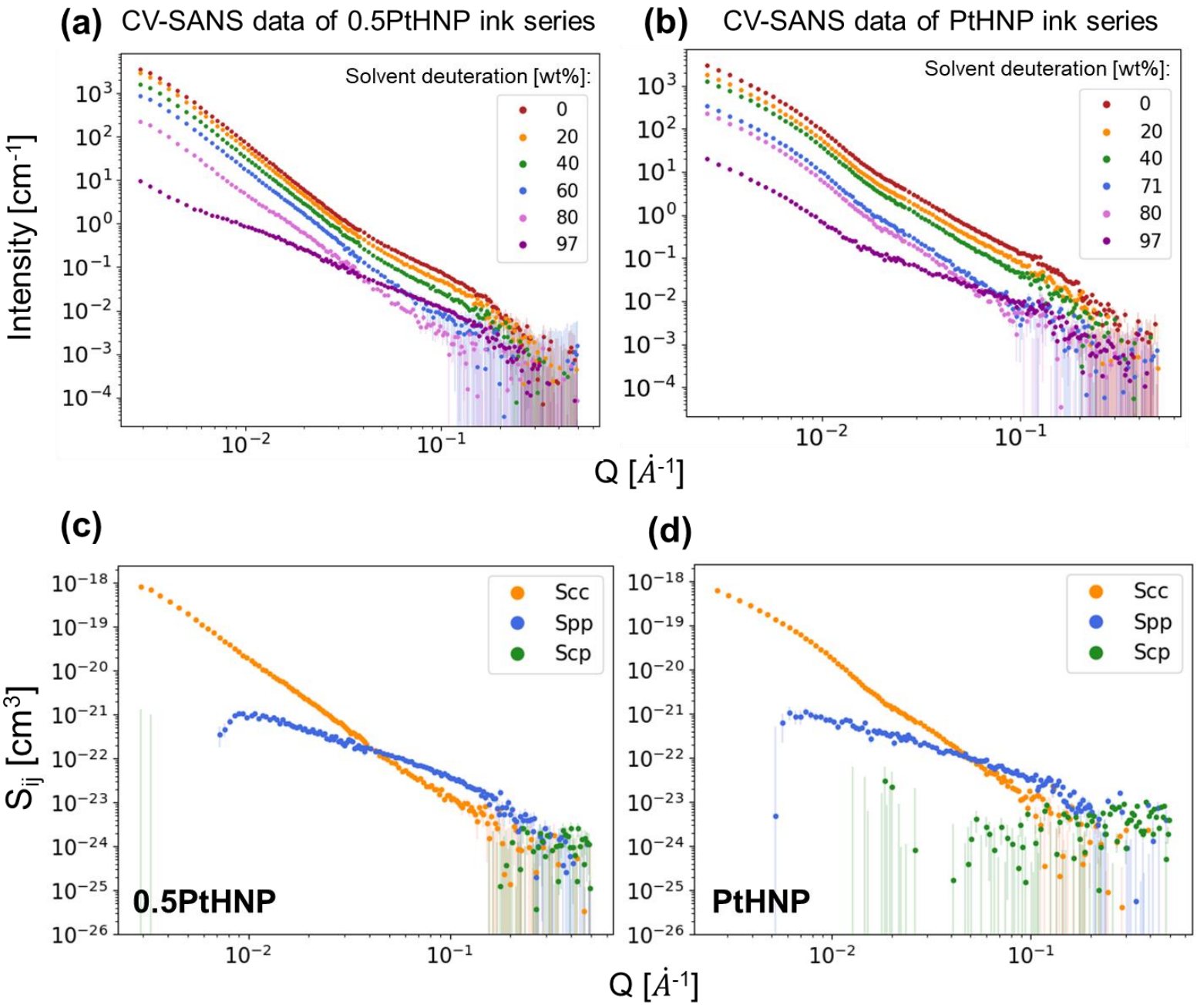


Figure 83. *CV-SANS scattering functions of* ***(a)*** *0.5PtHNP,* ***(b)*** *PtHNP ink series. PSF outputs extracted from* ***(c)*** *0.5PtHNP,* ***(d)*** *PtHNP ink series.*

Just like when investigating this variable in carbon-only ink compositions, decreasing the I/C ratio to 0.5 does not yield major differences in the S_{pp} and S_{cp} outputs. However, interestingly the S_{cc} output seems to vary in the case of 0.5PtHNP. The shoulder arising from the size of primary particles is not as evident as in all the other previous ink series investigated. Figure 84 shows corresponding outputs from the two ink series plotted together, with the 0.5PtHNP S_{pp} output scaled by the ionomer volume fraction difference.

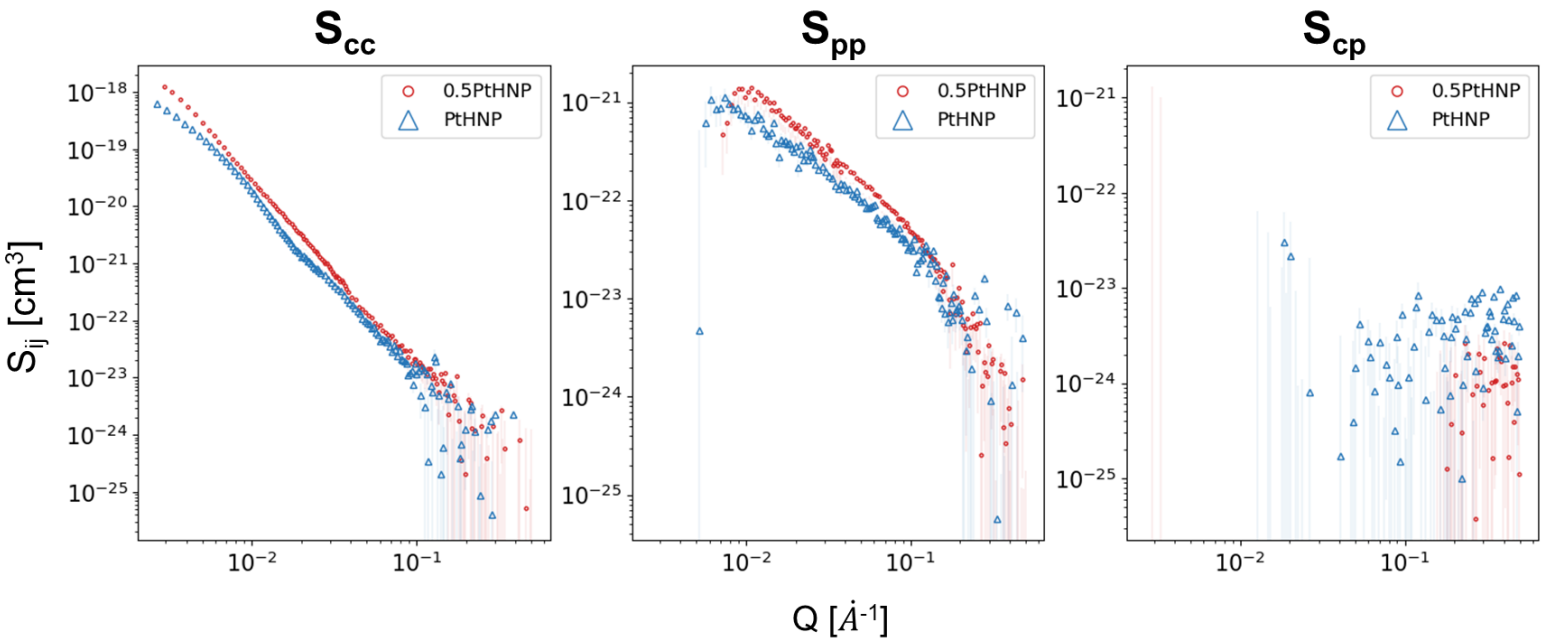
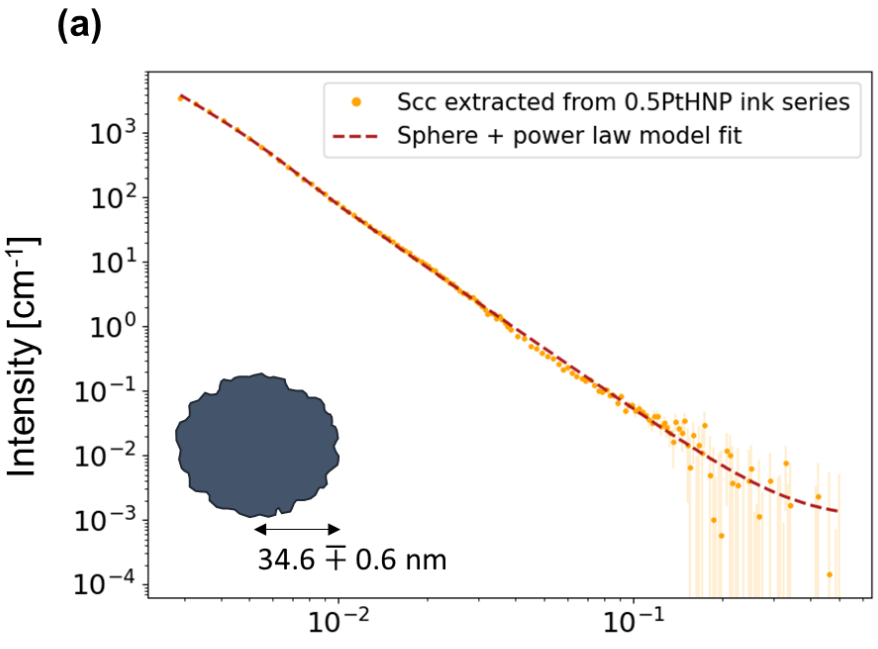


Figure 84. *Comparison of equivalent PSF outputs extracted from Pt containing ink compositions based on varying I/C ratios: 0.5PtHNP (red), PtHNP (blue). S_{pp} output of 0.5PtHNP has been scaled by the ionomer volume fraction for comparison purposes.*

The difference in the S_{cc} outputs becomes even more evident. However, considering the structure of primary particles would not be altered by the ink preparation process, and the Pt/C complex utilized in the inks was obtained from the same batch, the reason for this change is unclear. A fit with the sphere + power_law combined model was applied to the S_{cc} output extracted from the 0.5PtHNP ink series, figure 85.



(b)

Sphere+power_law

Scale = 6.64e-04 ± 2.54e-05

Sphere_scale = 0.94 ± 1.66e-03
Sphere_sld = 6.56x10^{10} cm^{-2}
Solvent_sld = 0 cm^{-2}
Radius = 346.18 ± 6.36 Å

Distribution of radius = 0.33 ± 0.01
(function: lognormal)

Power_law_scale = 0.06 ± 1.66e-03
Power = 3.11 ± 5.79e-03

Chi^2/Npts = 10.20

Fitting performed using SasView 5.0.6, SasModels version 1.0.7, Fit optimizer DREAM

Figure 85. (a) *S_{cc} extracted from the 0.5PtHNP ink series, fitted with the sphere + power_law model.* ***(b)*** *Parameters extracted from fitting.*

The proportions of the sphere and power law models remain similar to the values extracted when fitting the S_{cc} output extracted from the HNP ink series. Moreover, the value of the power law, 3.11, again indicates rough particles. However, the particle radius extracted is a lot higher with a value of 34.6 nm (although the radius polydispersity value again is cohesive). Where already in the initial S_{cc} fitting from the HNP ink series the radius extracted seemed over-estimated, a value of 34.6 nm is completely incoherent with the known size ranges of HSAC primary particles (20 - 40 nm in diameter). It is possible that the decreased ionomer content results in increased degree of particle agglomeration, with primary particles forming small clusters composed of 2-3 primary particles. However, no observations related to a poor quality dispersion, such as increased deposition of material onto zirconia milling balls, resulting in increased sample viscosity, were made during the experiment. Furthermore, if increased agglomeration is the reason, then the effect should be even more evident in the 0.5HNP ink series, where no Pt is present to provide additional electrostatic repulsions between carbon particles. Additionally, it would be expected that increased aggregation would result in an additional feature related to an extra structural regime, rather than shifting the shoulder feature associated with the size of primary particles. The sample should be re-measured to evaluate whether this scattering is sample specific or an anomaly, perhaps related to incorrect sample preparation.

The S_{pp} output of the 0.5PtHNP ink series is also rather different to that of the PtHNP ink series. Just like in the case of their carbon-only counterparts, the S_{pp} output of 0.5PtHNP shows higher intensities than PtHNP. However, where previously the cut-off point in the low Q regime ($Q<1x10^{-2}$ $\dot{}^{-1}$) fell at lower Q values for S_{pp} extracted from 0.5HNP, consistent with the concentration dependent shift of the ionomer interference term, in the outputs of Pt containing inks, a reversed observation can be. The S_{pp} PSF of PtHNP is longer than that of 0.5PtHNP ($Q \approx 6x10^{-3}$ and $7x10^{-3}$ $\dot{}^{-1}$ respectively), which is not consistent anymore with the varying ionomer concentration. As the structure of ionomer aggregates is not expected to vary with ionomer concentration in this solvent system, as suggested by comparable SLD values extracted using the contrast match method for 1 and 2 wt% Nafion dispersions (appendix 15), this may further suggest an additional ionomer structure in the PtHNP ink series. **On the other hand, due to the unexpected deviation observed in the S_{cc}, the 0.5PtHNP ink series must be re-measured, and all PSF outputs must be extracted again to confirm this observation.**

2.3.3.6.3 Effect of Pt + solvent system

Section 2.3.3.3 demonstrated the concentration of iPrOH in the solvent system dramatically altered ionomer adsorption to carbon. The ink composition based on a water-rich solvent, 25HNP, showed the most Nafion adsorption to HSAC (55%), followed by little adsorption observed in the alcohol rich composition, 75HNP (7.4%), and no adsorption in the composition based on a 50-50 iPrOH/water mixture, HNP. A question arises whether in Pt containing inks the same pattern will be observed, or whether the presence of Pt will alter the adsorption mechanism in one or more samples. Ink series with the following compositions were investigated:

25PtHNP = 1 wt% high surface area carbon **+ 1 wt% Pt**, Nafion with I/C = 0.8, **25:75 wt%** iPrOH/H_2O solvent

PtHNP = 1 wt% high surface area carbon **+ 1 wt% Pt**, Nafion with I/C = 0.8, **50:50 wt%** iPrOH/H_2O solvent

75PtHNP = 1 wt% high surface area carbon **+ 1 wt% Pt**, Nafion with I/C = 0.8, **75:25 wt%** iPrOH/H_2O solvent

Figure 86. shows CV-SANS data of each ink series along with extracted PSF outputs. The general observations remain the same as for the carbon-only, pseudo-ink counterparts. 25PtHNP shows the most pronounced S_{cp} output, along with an S_{pp} that stretches across the entire Q range. PtHNP, which has been evaluated in detail in section 2.3.3.6.1, shows no cross term in the S_{cp}, suggesting no ionomer adsorption to carbon particles, and an S_{pp} which is missing data points in the low Q regime. A short cross-term can be

observed in the S_{cp} output of the 75PtHNP ink series, along with a short S_{pp} output reminiscent of scattering from unadsorbed ionomer.

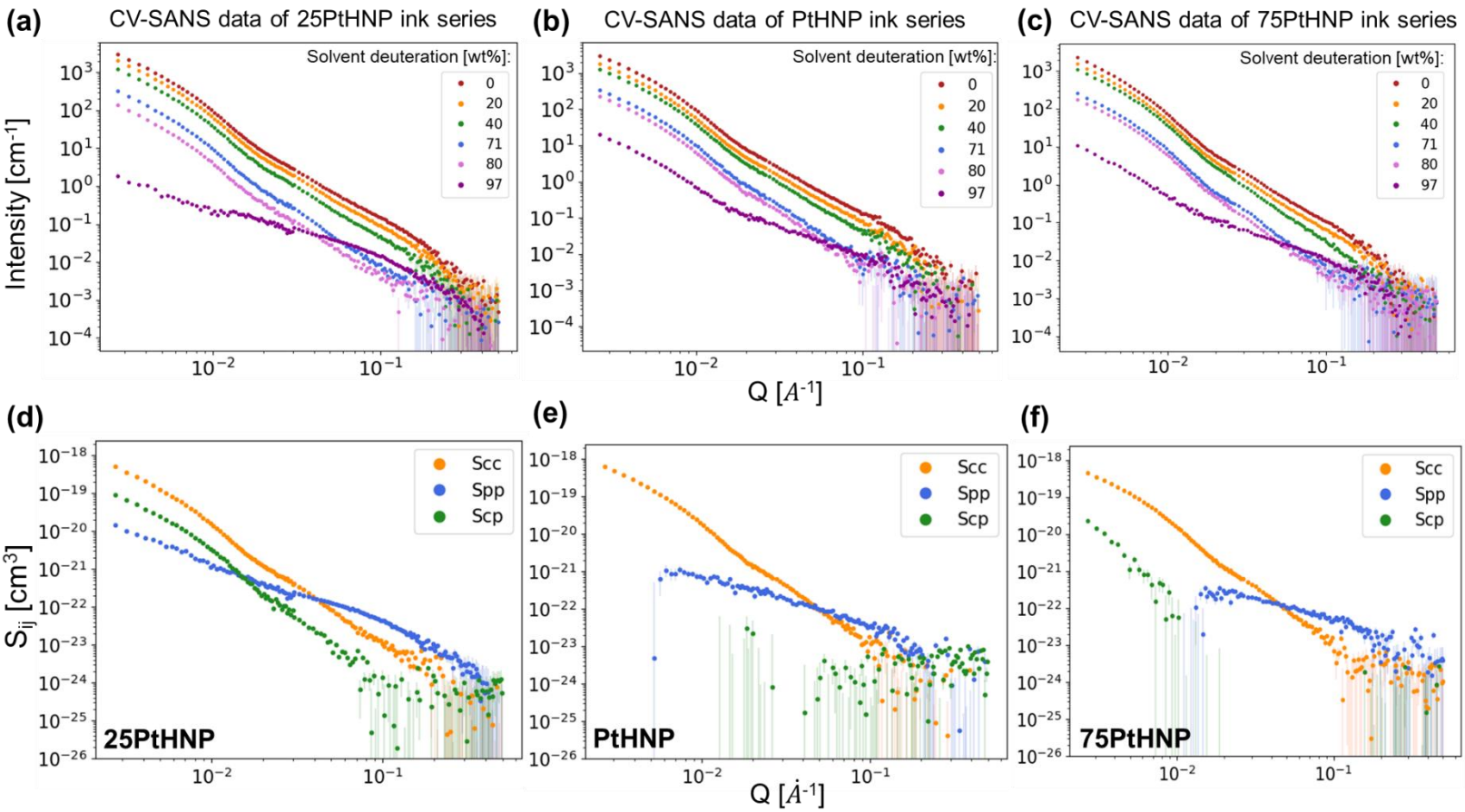


Figure 86. *CV-SANS scattering functions of* ***(a)*** *25PtHNP,* ***(b)*** *PtHNP,* ***(c)*** *75HPtNP ink series. PSF outputs extracted from* ***(d)*** *25PtHNP,* ***(e)*** *PtHNP,* ***(f)*** *75PtHNP ink series.*

As the general observations remain the same, instead of plotting all the data presented in figure 86d-f together, PSF outputs extracted from 25PtHNP and 75PtHNP will be plotted with their carbon-only equivalents, 25HNP and 75HNP respectively, for a detailed visualisation of differences that the presence of Pt introduces.

25PtHNP and 25HNP

Figure 87 presents PSF outputs extracted from 25PtHNP and 25HNP ink series plotted together.

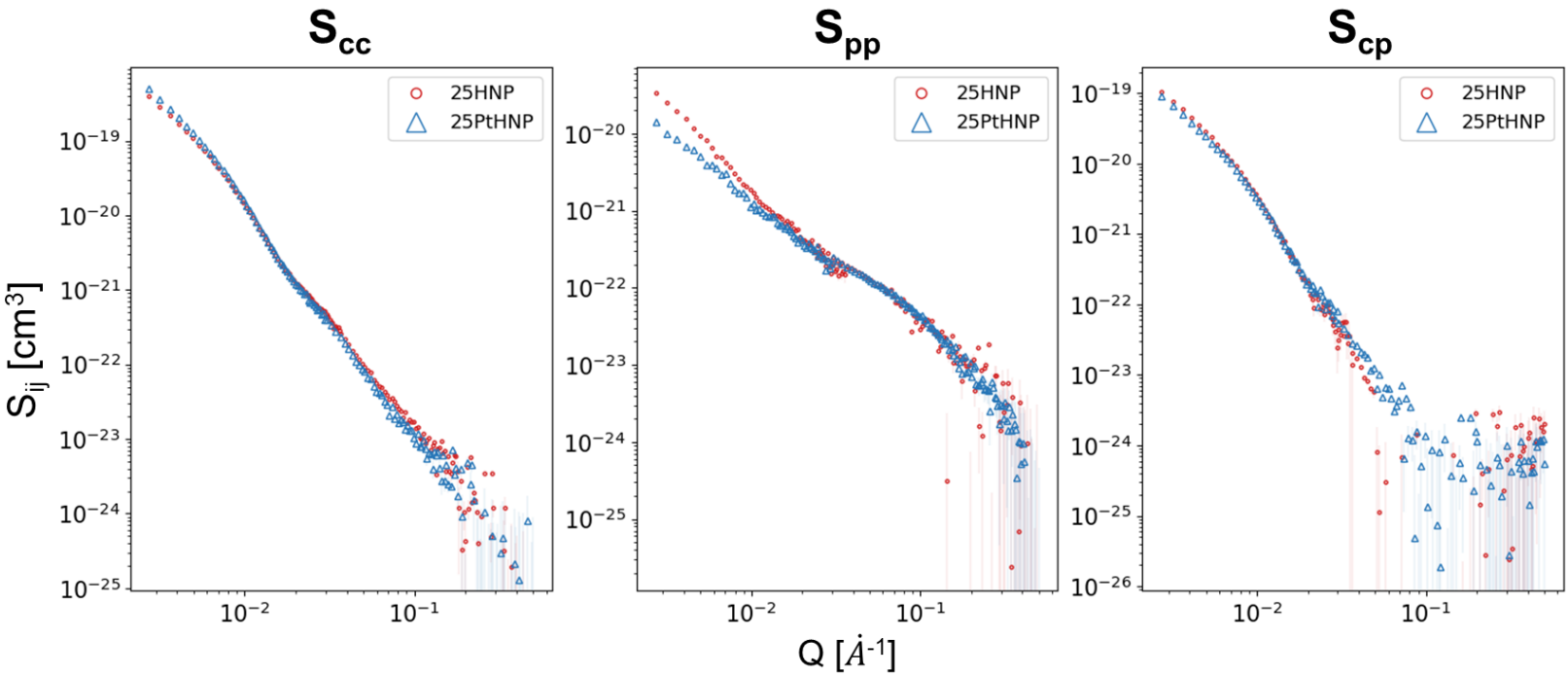


Figure 87. *Comparison of equivalent PSF outputs extracted from ink compositions based on 25:75 wt% iPrOH/water solvent with and without Pt: 25HNP (red), 25PtHNP (blue).*

The S_{cc} and S_{cp} outputs remain fairly unchanged. A handful of additional data points can be observed in the mid Q regime ($Q \approx 7x10^{-2}$ Å^{-1}) of the 25PtHNP cross-term, which may be indicative of a thinner ionomer shell. The biggest difference can be observed in the low Q regime ($Q<1x10^{-2}$ Å^{-1}) of the S_{pp} output extracted from 25PtHNP, where a lower scattering intensity can be observed in comparison to the 25HNP S_{pp} output. The S_{pp} output extracted from 25PtHNP was fitted with the vesicle + cylinder model, figure 88. The core radius and polydispersity, as well as parameters describing the unadsorbed ionomer structure remain fixed.

A satisfactory fit is achieved with a chi^2 value of 12.6, yet an intensity discrepancy between the model and fit can be observed between the data and fit in the low/mid Q regimes ($Q<2x10^{-2}$ Å^{-1}), related to the overall size of the carbon primary particles with ionomer layer. Nevertheless, note no variation in the primary particle structure was suggested by the S_{cc}. Increased polydispersity arising from non-uniform ionomer distribution on the carbon surface may provide a potential explanation for the observed deviation.

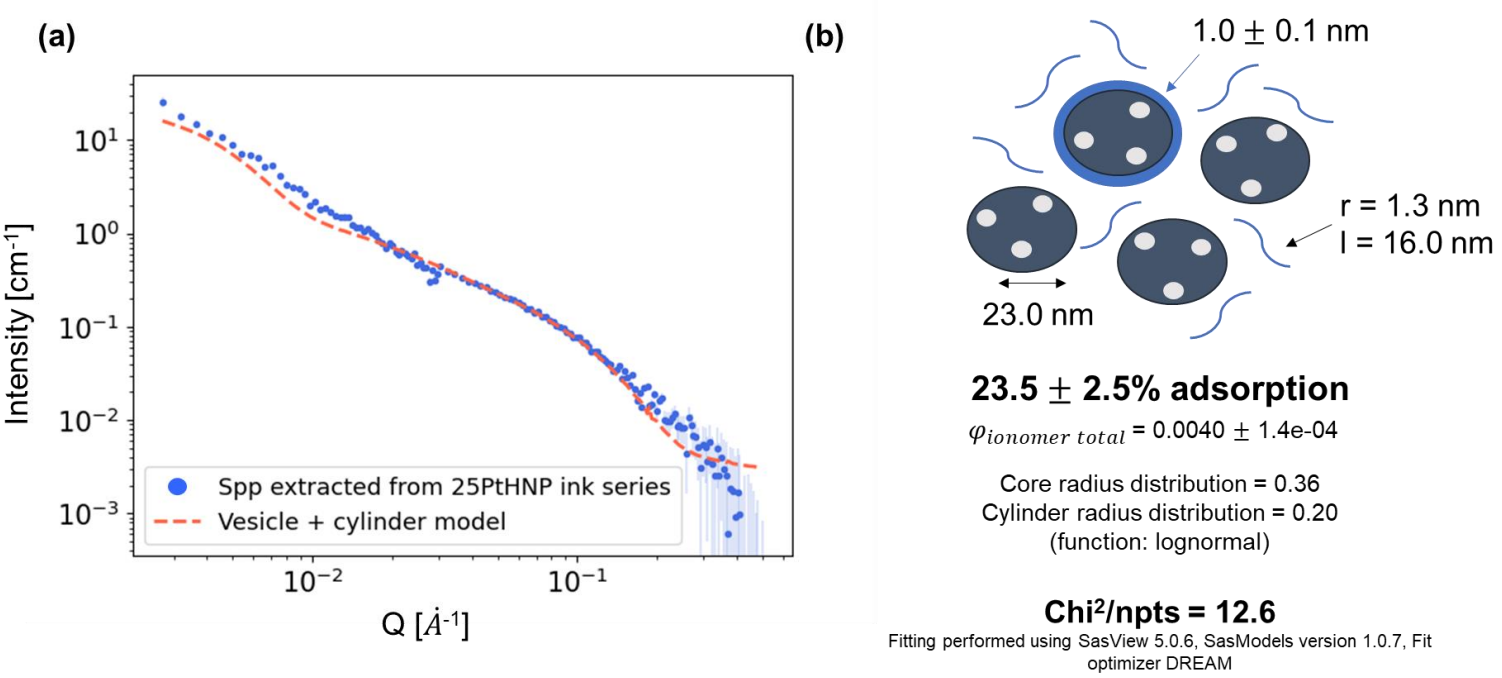


Figure 88. (a) *S_{pp} extracted from the 25PtHNP ink series, fitted with the vesicle + cylinder model.* ***(b)*** *Parameters extracted from fitting represented in a system schematic. r = radius, l = length. Degree of adsorption computed from vesicle proportion (x) pre-factor.*

Figure 89 compares key parameter values extracted from the 25HNP and 25PtHNP ink series:

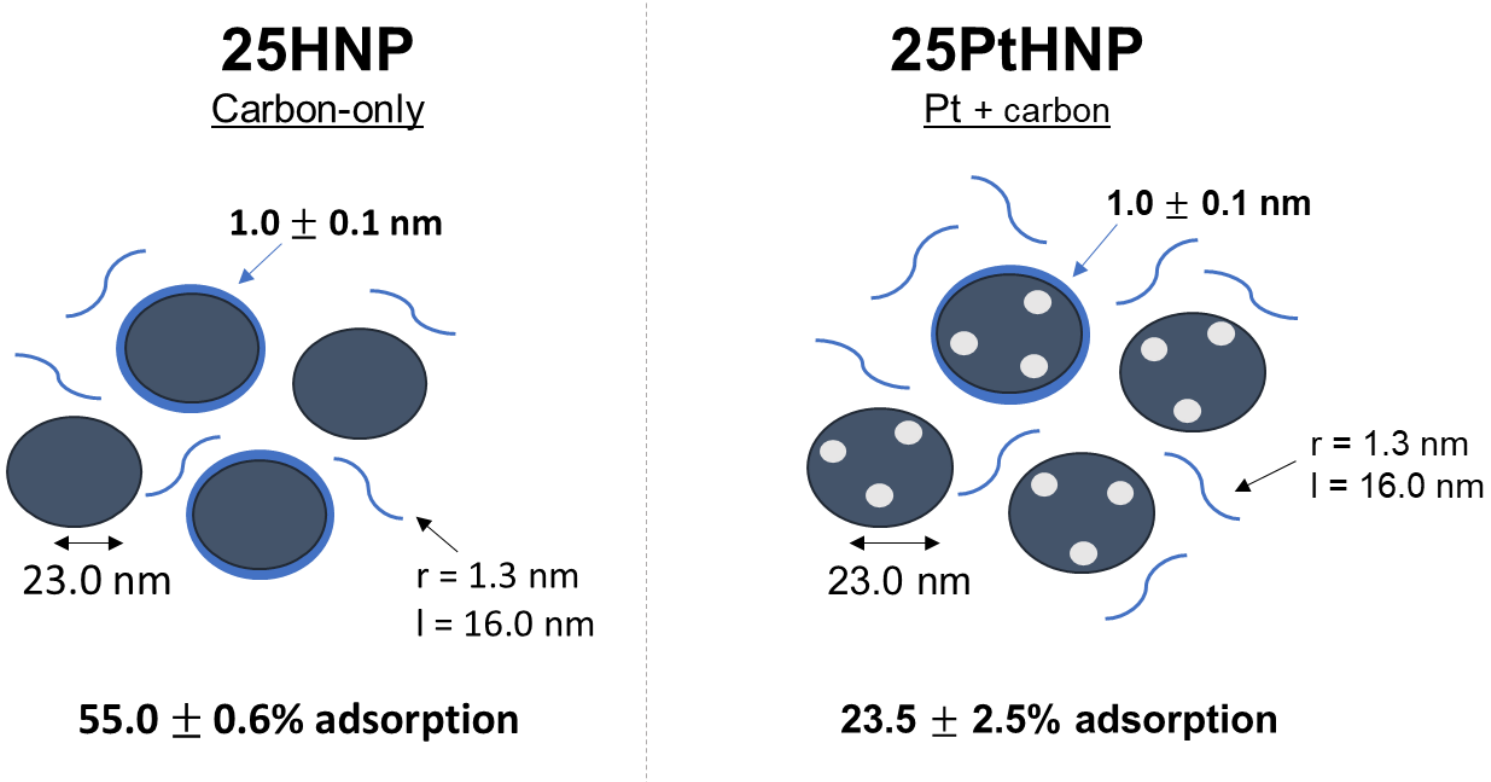


Figure 89. *Schematic visualizing structural differences between ink systems without and with Pt in 25:75 wt% iPrOH/water solvent: 25HNP and 25PtHNP, as extracted from quasi-quantitative and qualitative analyses.*

The fit of 25PtHNP suggests the same shell thickness to 25HNP, 1 nm, which is consistent with the alike cross-term outputs observed for the two ink series in figure 87. However, the degree of adsorption is suggested to reduce by half in the presence of Pt, from 55 to 23.5%, indicating presence of Pt reduces adsorption of ionomer to the Pt/C complex. Favourable adsorption of Nafion to carbon in catalyst inks has previously been reported,[31,39] nevertheless, considering to low volume of Pt nanoparticles in comparison to the carbon spheres, such a large change in adsorption is unexpected. A further investigation into ionomer-Pt interactions is necessary in order to obtain a more in depth explanation for such a result.

75PtHNP and 75HNP

Figure 90 presents PSF outputs extracted from 75PtHNP and 75HNP ink series plotted together.

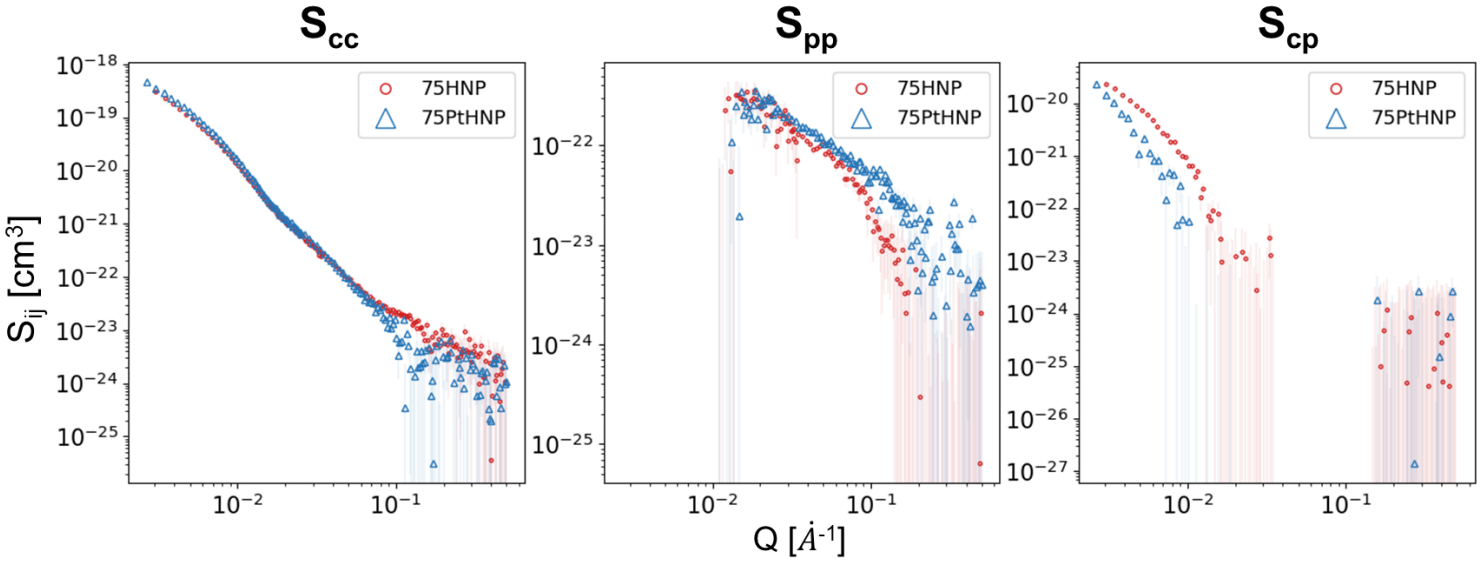


Figure 90. *Comparison of equivalent PSF outputs extracted from ink compositions based on 75:25 wt% iPrOH/water solvent with and without Pt: 75HNP (red), 75PtHNP (blue).*

The S_{cc} output remains mostly consistent, however a deviation can be observed in the high Q regime ($Q>1x10^{-1}$ $\dot{A}^{-1}$), with 75HNP showing an increased degree of scattering. However, as this difference appears in the high Q regime, where no structural information of primary particles is expected, it can be attributed to variations arising from the data processing procedure. The most significant change can be observed in the S_{pp} outputs, where although the cut-off point in the low/mid Q regime remains the same ($Q \approx 1.5x10^{-2}$ $\dot{A}^{-1}$), an alteration of power law scattering can be observed in the high Q regime ($Q>1x10^{-1}$ $\dot{A}^{-1}$). The S_{cp} extracted from 75PtHNP falls at a comparable intensity to the corresponding output of 75HNP. A cut-off point at a higher Q value may suggested a slightly thicker Nafion shell in the 75PtHNP ink composition. A fitting attempt of the S_{pp} extracted from 75PtHNP was performed using the vesicle + cylinder model, with the core radius and polydispersity, as well as parameters describing the structure of unadsorbed ionomer fixed.

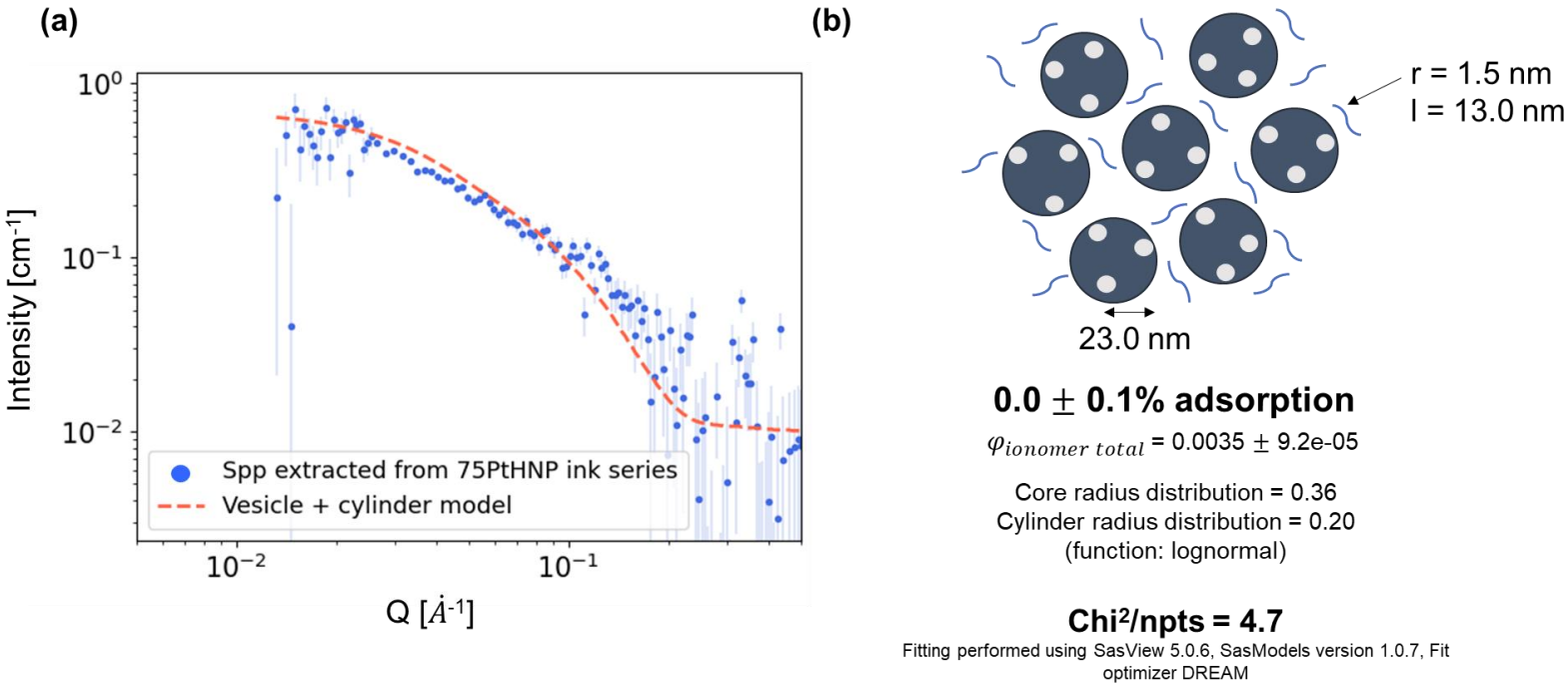


Figure 91. (a) *S_{pp} extracted from the 75PtHNP ink series, fitted with the vesicle + cylinder model.* ***(b)*** *Parameters extracted from fitting represented in a system schematic. r = radius, l = length. Degree of adsorption computed from vesicle proportion (x) pre-factor.*

A good fit with a low chi^2 value of 4.7 was achieved. However, unlike in the case of 75HNP, the adsorption parameter extracted for 75PtHNP was 0%, indicating the entire scattering function is well fitted by the cylinder form factor alone. Despite the lack of information on the adsorbed ionomer in the S_{pp}, the presence of the cross-term scattering in the S_{cp} cannot be ignored. An SLD shift investigation performed on the 75PtHNP ink series (appendix 26) suggests the cross term output is veritable, and just like in the case of 75HNP, the output behaviour with shifting component SLD resembles that of partial adsorption simulations with low degrees of ionomer adsorption (appendix 5). Therefore, it can be concluded that some semblance of adsorption may be present in the 75PtHNP ink composition, albeit at very low degrees.

In the high Q regime (Q>1x10^{-1} Å^{-1}) the scattering associated with the unadsorbed ionomer aggregate radius remains well fitted by the fixed parameters extracted from fitting of the Nafion-only scattering function (figure 51), implicating no ionomer conformation change in the presence of Pt as expected. Therefore, the discrepancy in the high Q regime (Q>1x10^{-1} Å^{-1}) between 75HNP and 75PtHNP may be a result of processing of the two datasets, just like the difference observed in the high Q regime of the S_{cc} outputs.

Figure 92 compares structural schematics of the 75HNP and 75PtHNP ink series, as suggested by key parameters extracted from fitting of the PSF outputs:

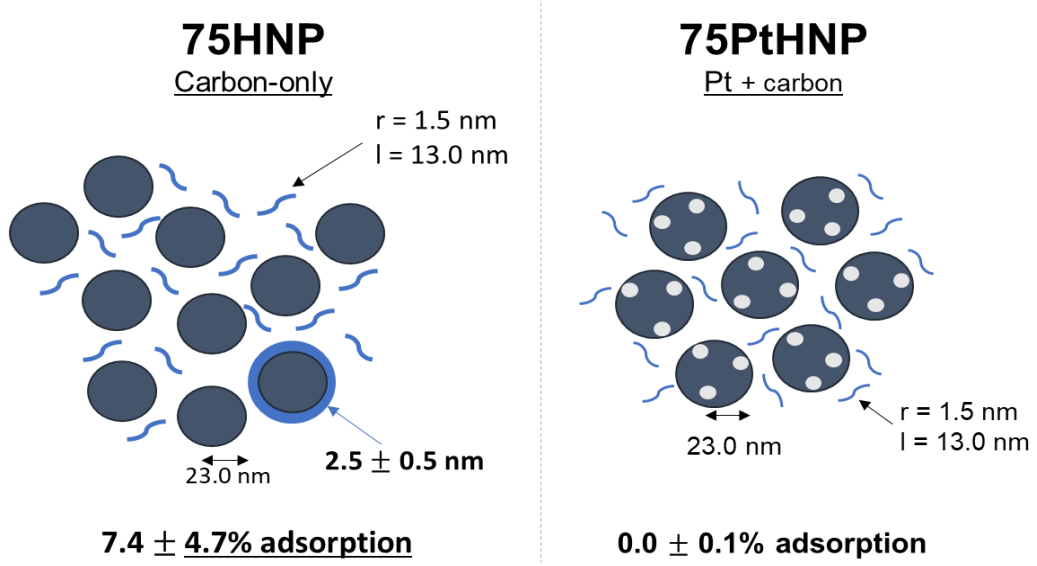


Figure 92. *Schematic visualizing structural differences between ink systems without and with Pt in 75:25 wt% iPrOH/water solvent: 75HNP and 75PtHNP, as extracted from quasi-quantitative and qualitative analyses.*

Again, just like in the case of 25HNP/25PtHNP, addition of Pt into the systems seems to decrease the amount of ionomer adsorption to the Pt/HSAC complex in comparison to HSAC alone. As has been observed in all instances of PSF outputs obtained from ink compositions containing Pt, the interpretation of results becomes more arduous, and additional information may need to be acquired on the system for a more comprehensive understanding of the effect of Pt.

The physical rationality for such a phenomenon remains unclear, yet such an alteration remains unexpected as no significant variation in the mid Q regime ($1x10^{-2}<Q<1x10^{-1}$ $\AA^{-1}$) could be observed between the S_{pp} outputs of 75HNP and 75PtHNP. Note in this region additional data points in the S_{pp} extracted from 75HNP were observed in comparison to the scattering function of Nafion-only in corresponding solvent.

One potential explanation could be found when looking at the total ionomer volume fractions extracted from fitting of both S_{pp} outputs. The value of 0.0035 obtained for 75PtHNP is consistent with the expected total ionomer volume fraction calculated from masses measured during sample preparation. However, it has been noted in section 2.3.3.3 that the total ionomer volume fraction of 0.0022 is almost half of the expected value of 0.0038 calculated from sample preparation data. Looking back to equation (2.3.4) it is crucial to note the (x) parameter, denoting the proportion of the total scale (and therefore ionomer volume fraction) applied to the vesicle mode is directly linked to determining the % adsorption parameter. The variation in volume fraction extracted from the fit could justify the difference in adsorption suggested by the combination model for the two ink series, despite significant variation in the obtained S_{pp} outputs. The low volume fraction suggested by the fit performed on 75HNP could be a result of erroneous sample preparation or poor sample stability, and for these reasons the sample should be re-measured.

2.3.4 Conclusions

In section 2.3.3 a large number of CV-SANS, and consequently PSF output results were evaluated, relating to the effects of a large plethora of variables on the catalyst ink structure, mostly pertaining to ionomer interaction with carbon primary particles. The most notable difference was observed when altering iPrOH concentration in the solvent system, where most ionomer adsorption was observed in inks based on 25:75 wt% iPrOH/water solvent (55%), little degree of adsorption in 75:25 wt% iPrOH/water (7.4%), and no

adsorption in 50:50 wt% iPrOH/water. Most definitely, the largest change in degree of adsorption can be observed in the case of inks with 25:75 wt% iPrOH/water, which may suggest ionomer adsorption is driven by reduction of the carbon/solvent interfacial energy. Indeed, change in adsorption is very small for inks based on 50:50 and 75:25 wt% iPrOH/water solvent systems, suggesting higher degrees of iPrOH may aid in stabilizing the carbon/solvent interface.

Moreover, the ionomer conformation doesn't seem to vary greatly with the solvent composition. Analysis of the Nafion structure using the cylinder form factor suggests rod-like aggregates on the scale of 1 nm in each solvent system, with aggregate length between 10 and 20 nm. Note because of the presence of structure factors in scattering functions of Nafion in 25:75 and 50:50 wt% iPrOH/water solvent, the parameters, in particular aggregate length, can only be considered estimations. In future data of very dilute Nafion dispersions should be obtained for extraction of the precise structure. Nevertheless, the estimated parameters model well the structure of the unadsorbed ionomer in S_{pp} outputs of the various ink systems, which allows for minimization of free parameters in the complex combination model.

On the other hand, alteration in ionomer type from Nafion to Aquivion (in the ink system based on 25:75 wt% iPrOH/water) showed no significant variation in degree of ionomer adsorption. In both cases the adsorption was relatively high, 55% in the Nafion based ink (25HNP), and 50% in the Aquivion based ink (25HAP). This observation further suggests the choice of solvent may be a key parameter in dictating ionomer-carbon interactions, potentially due to the need for minimization of carbon-solvent interfacial energy.[30] Nevertheless, more investigation on the behaviour of Aquivion in solvents with varying iPrOH concentrations should be performed in order to obtain more extensive information on this phenomenon. On the other hand, the shell thicknesses of the ionomer layer extracted for the two ink series were significantly different, at 1 and 2 nm for 25HNP and 25HAP respectively. This may suggest a conformational difference between the two ionomer types in the same solvent, which has to be further researched through analysis of data from dilute ionomer dispersions.

On the other hand, no change in adsorption could be observed as a function of varying I/C ratio in the ink, as suggested by a consistent lack of cross-term output. Some variation in the S_{pp} output could be discerned for inks with varying I/C ratio, with regards to the Q magnitude of the 'cut-off' point, and scattering intensity, however, this was consistent with a concentration dependent shift of the interference term (for carbon-only based inks). Such observations were unexpected, as the I/C ratio seems to be a parameter heavily correlated with performance of the catalyst layer itself.[34-38] This may suggest either the drying process is more critical to determining the final ionomer distribution in the catalyst layer, or that the I/C ratio plays a more crucial role in determining the Pt/C aggregate size in the ink, a feature that could not be probed in the Q magnitude investigated by CV-SANS. The latter will be discussed in chapter 3, focusing on the USAXS technique.

Surprisingly, component concentration also played a part in ionomer adsorption to carbon. Where no adsorption could be observed in the case of 1 wt% HSAC based, HNP ink composition, doubling all component concentrations, resulting in the 2HNP ink series, showed a little ionomer adsorption to carbon particles. Moreover, the doubled concentration resulted in the observation of a peak feature, which could be potentially related to the ionomer shell in the high Q regime of the S_{pp} output, yet at higher intensities then expected, therefore it remains to be verified.

The effect of Pt presence, alongside with its correlation to other variables, was heavily investigated. In particular, ink compositions based on different solvent systems, with and without Pt, proved highly insightful. Figure 93 compares key structural findings for such inks:

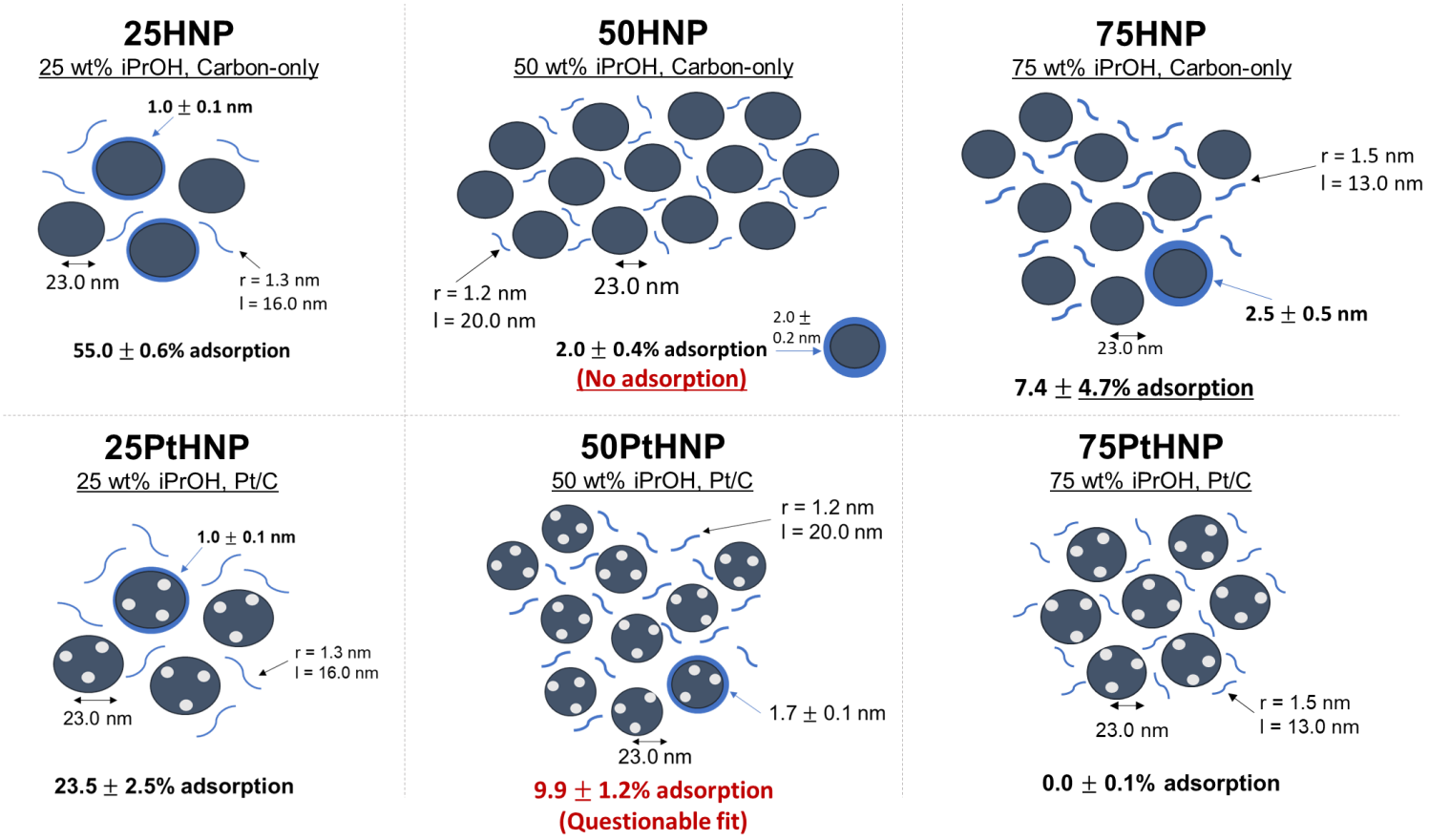


Figure 93. *Schematics representing key structural findings for inks with varying solvent systems, with and without Pt.*

Overall, it can be concluded that the presence of Pt did not boost ionomer adsorption to carbon greatly in any instance, and in certain cases lower adsorption was noted (25HNP/25PtHNP and 75HNP/75PtHNP), which may be indicative of preferred ionomer-carbon interaction as suggested by Yoshimune and Harada.[31]

However, the high degree of decreased adsorption (in the case of 25HNP/25PtHNP from 55 to 23.5%) is rather surprising, considering the low volume fraction of Pt nanoparticles on the carbon surface, particularly with the HSAC support used, where approximately 70% of Pt is found in pores of the carbon support inaccessible to the ionomer itself. The knowledge of the Pt/C structure suggests the coverage of Pt on the surface should be rather low, so it is unclear why the effect on ionomer adsorption would be so significant. Moreover, in the case of 50HNP/50PtHNP, the lack of cross-term presence in either S_{cp} output suggests no ionomer adsorption in the two ink systems, yet the S_{pp} output obtained from 50PtHNP contains additional scattering points that cannot be accounted for by scattering from the unadsorbed ionomer only (like in the case of 50HNP). For the above reasons, the ionomer interactions and structure in Pt containing ink systems remains unclear.

Two potential explanations can be considered – from a structural perspective and that of method limitation.

The shell model used to describe the adsorbed ionomer structure throughout this work considers a uniform layer of ionomer adsorbed to carbon. It has been already discussed that in reality the nature of the ionomer is most likely more complex – potentially not fully uniform across the carbon particles, rendering the results obtained quasi-quantitative and an approximation of the real system. However, if a case of very strong Pt-ionomer interactions is considered, where in the presence of Pt the ionomer binds predominantly in the proximity of these particles, the adsorption could be thought of as 'patchy'. In such an instance, the ionomer layer, which in the uniform shell model is related to the average adsorbed mass of the ionomer, would be misinterpreted as a thinner uniform shell. On the other hand, the degree of adsorption parameter should remain unaffected.

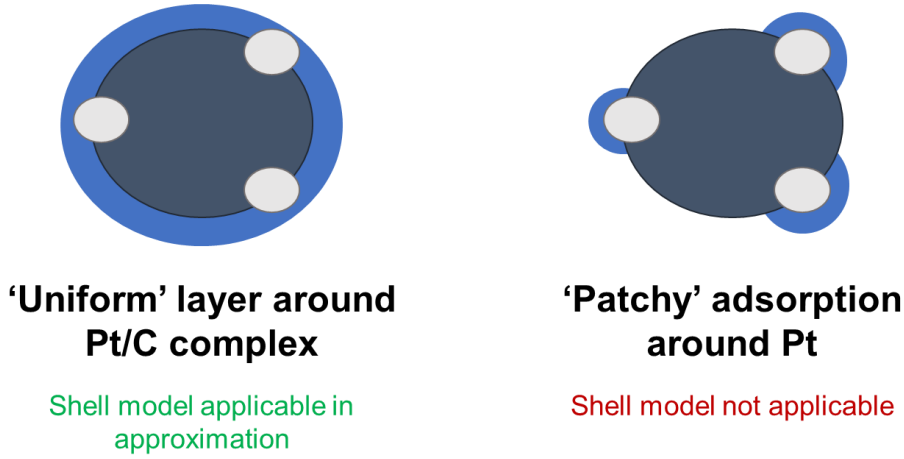


Figure 94. *Schematics of different potential ionomer adsorption models.*

In order to model a 'patchy' adsorption of ionomer, a much more complex numerical model would have to be created using computational methods.

Another potential explanation for the variation in degree of adsorption and ionomer conformation extracted could be the notion of a limitation in the PSF method itself. It is assumed that Pt scattering is negligible in comparison to carbon due to their similar SLDs as well as the significantly lower volume fraction of the former. However, if that were not the case, a more complex computation may be required in order to obtain a full deconvolution of the system, considering Pt as a separate component and yielding three additional PSFs: $S_{Pt\text{-}Pt}$, $S_{C\text{-}Pt,}$ $S_{Pt\text{-}P}$. However, this explanation also seems rather unlikely, as even in the instance that the cross-term is affected by the factors stated above, increased adsorption should be evident in the S_{pp} output, where only the ionomer structure is considered, in the form of low Q scattering from a shell structure. Nevertheless, in most cases addition of Pt did not significantly alter the S_{pp} output in the low/mid Q regime ($Q<3x10^{-2}$ $\dot{A}^{-1}$) where size feature related to the shell structure can be observed.

Because of this, the effect of Pt should be further studied. Despite the close proximity of carbon and Pt SLD values, computing more complex PSF outputs, which consider Pt as a separate component to carbon, may yield additional insights, although more datasets per ink series may be required for precise PSF extraction. On the other hand, investigation of inks based on the Vulcan carbon support, where a large majority of Pt is found on the surface, would allow for perception into how Pt surface density affects ionomer interactions. Additionally, using complimentary method such as SAXS, where scattering from Pt is greatly pronounced, may additionally shed light on Pt-ionomer interactions.

The effect of solvent electro-oxidation in the presence of Pt is also important to highlight. Several studies have demonstrated that both 1-propanol (1-PrOH) and isopropanol (iPrOH) decompose in standard conditions in the presence of Pt.[104-106] In particular, Kircher et al.[106] investigated inks based on a similar composition as in this work, based on Nafion and iPrOH/water solvents, and demonstrated using GC-MS

that even in freshly prepared inks the presence of acetone can already be detected. Moreover, the acetone content has been found to constantly increase over a period of 4 weeks (672 h), from 1250 ppm, w. to 2750 ppm, w., with a sharpest increase observed in the first 2 days (50 h), from 1250 ppm, w. to 2000 ppm, w.

This work demonstrates that in the case of Pt containing inks, the initial composition is most likely not identical than that of the ink during the measurement. Nevertheless, 2000 ppm of acetone corresponds to 0.2 wt%, which is a minute change in the solvent composition, particularly after a time period of 672 h (the inks presented in this work were measured by SANS on average 12-24 h after initial sample preparation). It is unlikely that such a small composition change would result in a significant alteration of the ionomer conformation that may explain some of the structural variation observed in the scattering functions, yet quantification of acetone content in Pt-containing inks over a set aging period would be recommended for verification purposes.

With regards to the CV-SANS/PSF method itself, the data analysis definitely provided unique insights into the effect of several variables on the catalyst ink structure, most notably on the effect of iPrOH concentration on the ionomer adsorption to HSAC, as well as the use of the SSC ionomer Aquivion. On the other hand, in certain cases, such as for the I/C ratio, it has also been shown the parameter might not have an extreme effect on the ionomer structure in the ink, and processes such as the ink drying or Pt/C aggregation may be more worthwhile to consider in order to justify the final variation in electrode performance observed.

The method for obtaining the structural results is most definitely difficult. It has been shown that obtaining veritable partial scattering function outputs can be challenging, where a rigorous set of conditions, both in the sense of choosing the right contrasts and components, as well as acquiring near-perfect experimental component SLDs must be satisfied. Especially the latter may be arduous, particularly in the case of carbon and the Pt/C complex, where stability concerns pose a hurdle that must be overcome. Although the SLD of HSAC was successfully obtained through the use of DMF solvent and very low component concentrations, the solvent choice may be further optimized for an increased dispersion stability. A stable dispersion of Pt/C was not obtained, and additional investigation into obtaining improved stability is required to achieve a fully veritable SLD component value. In feature measurements sample viability should also be further evaluated, potentially by performing turbidity measurements, where any changes in scattering intensity due to sample sedimentation can be observed as a function of time.

Some components may also not be fully suitable to begin with, as shown in the case of graphitized carbon, where the presence of a void space inaccessible to solvent proved hindering in carbon SLD extraction. Nevertheless, GC remains a component of interest, and further work into obtaining a veritable SLD would prove worthwhile. With respect to ionomer SLD determination, it is suggested samples contain a component concentration that corresponds to the ink composition itself, as it has been shown that, particularly in water-rich solvents, concentration may have an effect on the SLD extracted.

Simulated data considering the case of no ionomer adsorption, complete, and partial adsorption proved key in not only understanding the various input effects on the extracted PSF output, but also in the interpretation of outputs arising from experimental data, particularly by comparison of output behaviour with shifting component SLD values, which were indicative of specific structures in the ink system.

However, the simulated data considered very idealized structural scenarios, with the core-shell model assuming a shell of uniform thickness on spherical particles, and the generated partial adsorption models stipulating either a full coverage of particles, creating again a shell of uniform thickness, or no adsorption at all. Indeed, ultimately the vesicle model proved to be more suitable for fitting of experimental data, and simulations based on such a model should also be studied for the sake of consistency.

Nevertheless, both the shell and vesicle models consider a uniform ionomer layer adsorbed to a carbon core particle. In a realistic scenario such a behaviour is very unlikely, where a partial coverage of the carbon structure with regions of altering ionomer thicknesses can be deemed more appropriate. However, in order to characterize such a structural scenario, a much more specific and complex numerical model would have to be created. Therefore, due to the simplified nature of the models used, PSF outputs arising from experimental data sets proved more challenging to evaluate, and in the case of data fitting, mostly of the S_{pp} outputs, only a quasi-qualitative data interpretation could be obtained. In almost every case a combination model had to be used to account for both the adsorbed and unadsorbed ionomer scattering, and in many instances missing data points in the low Q regime heavily hindered the extraction of accurate parameters. Additionally, the S_{cp} could not be fitted with the shell model containing no polydispersity consideration, like in the case of core-shell simulated data, proving the nature of the shell may be different to that designed into the model itself. Nevertheless, the veracity of the cross-term output was in most cases confirmed by investigation of the SLD shift impact on output extraction, where a distinct output robustness was observed in partial adsorption simulated data containing at least 5% of the core-shell model.

It is therefore evident that although the CV-SANS/PSF method poses many challenges, it is a credible method for obtaining insights into the catalyst ink structure, in particular with regards to the ionomer component, whose structure can be characterized directly, uniquely using this method. Nevertheless, it was shown the method may not be as sensitive to Pt-ionomer interactions, which may require increasing the amount of supporting data using a combination of technique for precise system analysis. Moreover, as this method visualized only a specific nanoscale part of the system, the effect of certain parameters may be underestimated. For example, the I/C ratio may play a bigger role on the size of carbon aggregates in the ink, which is an important parameter in obtaining optimal ECSA. For this reason, methods which look to the bigger size scale should also be opted for. In combination with other supporting methods, such as TEM or USAXS for carbon structure analysis, thermogravimetric analysis (TGA) for adsorption kinetics evaluation, or GC-MS for solvent composition evaluation in Pt containing inks, a thorough picture of the catalyst ink system can be constructed.

Many interesting variables remain to be studied related to the catalyst ink. Comparison of HSAC and Vulcan based inks would allow for an investigation of the carbon support variable. Already adsorption differences could be observed between compositions based on Nafion and Aquivion, and a general study considering Aquivion inks in different solvent systems, with and without Pt, could yield a plethora of information on the varying behaviours of the two ionomers. In this work only a solvent system based on iPrOH and water was considered, however, 1-propanol and ethanol also remain popular alcohol choices for catalyst ink preparation. It is highly possible the alteration of the alcohol type would result in ionomer adsorption differences that remain to be evaluated, not to mention the changes that could be observed in the presence of Pt, perhaps due to different oxidation products.

Indeed, a lot of possible variations remain to be investigated, for which the CV-SANS/PSF method may prove highly beneficial. Each such systematic alteration will aid in building a more comprehensive understanding of inter- and intra- component interaction in the catalyst ink system overall. It is the hope of the author this work will act as a guide for a comprehensive extraction of partial scattering functions, and information one can expect to extract using this approach.

2.4 Catalyst Layer SANS

In section 2.3 the structure of the catalyst ink as a function of composition was thoroughly investigated. As a next step, it is important to consider what impact structural variation in the catalyst ink may have on the final structure of the catalyst layer. For this reason, powders of cathode catalyst layers manufactured from some of the ink compositions analysed in the previous section were also investigated using SANS. However, in this instance the contrast variation method was not employed. Instead, the relative humidity of the

samples was controlled in order to investigate the hydration behaviour of ionomer in the catalyst layer, which is relevant to its proton and gas transport properties.[65,67] The variations observed with increasing ionomer hydration can yield insight into the ionomer structure in the catalyst layer. Such changes can be slight, however, they can be accentuated directly through subtraction of a dry catalyst layer reference scattering function.

Because of the most prominent difference in the degree of adsorption observed, ink compositions based on varying iPrOH concentrations in the solvent were chosen for the catalyst layer study, allowing for a clear correlation between the variation observed in the PSFs extracted from the ink series, and the arising catalyst layers. Additionally, despite the incompatibility with the CV-SANS method, catalyst layers based on graphitized carbon with iPrOH concentration variation will also be investigated. As no SLD determination is required for the catalyst layer analysis, a comparison between HSAC and GC based compositions can be performed, yielding some insights into the effect of carbon support chosen. Furthermore, Pt/HSAC based catalyst layers were characterized using transmission electron microscopy (TEM) and elemental mapping (EDS), allowing for a comparison of the overall structure and information obtained from SANS.

2.4.1 Sample preparation and methodology

Commercially available materials were used throughout this work. Pt/HSAC with 50 wt% Pt loading (TEC10E50E), and heat-treated Pt/GC with 30 wt% Pt loading (TEC10EA30E-HT) were purchased from Tanaka Precious Metals. Nafion D2020 was purchased from Chemours, as a 20-22 wt% dispersion in 40-48 wt% 1-propanol and 30-38 wt% water. Isopropanol ≥ 99.5% purity (purchased from Aldrich), Ethanol ≥ 99.9% purity (purchased from Technic Micropor), and ultrapure water (18.2 mΩ cm^{-2}) were used as solvents.

For the anode catalyst layer, a set composition was maintained, and prepared as follows:

Pt/HSAC (TEC10E50E) nanopowder was mixed with ultrapure water in a glove box, in order to mitigate risks related to the pyrophoric nature of Pt, as well as the use of nanoparticles. Subsequently, the mixture was removed from the glovebox and Nafion D2020 solution was added in proportions yielding an I/C ratio of 0.8. Ethanol was introduced into the mixture, in an amount yielding a 25:75 wt% EtOH/water solvent system.

The cathode catalyst layer, which is the most limiting PEMFC component, and which was studied by SANS in powder form, was prepared following a similar procedure as the anode catalyst layer. However, variations in ink composition, pertaining to the Pt/C complex used, as well as through use of isopropanol instead of ethanol, in varying concentrations, were introduced.

The ink compositions used to manufacture the cathode catalyst layers were characterized as follows:

Ink composition	C + Pt	Ionomer and I/C ratio	Solvent (iPrOH:water wt%)
25PtHNP	3.5 wt% high surface area carbon + 3.5 wt% Pt	Nafion with I/C = 0.8	25:75
50PtHNP			50:50
75PtHNP			75:25
25PtGNP	3.5 wt% graphitized carbon + 3.5 wt% Pt		25:75
50PtGNP			50:50
75PtGNP			75:25

Table 7. *Ink compositions used in catalyst layer manufacture.*

Note the component concentration is approximately 3 times higher than that of inks investigated using CV-SANS, yielding an ink solid content of approximately 10 wt%. During sample preparation, it has been noted that the 75PtHNP ink was a lot more viscous than the other Pt/HSAC based inks. Conversely, all inks based on Pt/GC appeared relatively fluid.

3 mm zirconia beads were added to the inks, and the slurries were mixed overnight using a roller mill (IKA roller 10 basic) at room temperature. The inks were coated onto a 250µm PTFE substrate using the blade coating method, with the blade height adjusted to yield an average Pt loading of 0.2 mg/cm^2 for the cathode and 0.1 mg/cm^2 for the anode. The coating table was heated to 60^{o}C, allowing for the drying process to occur directly after coating in the space of a few minutes.

The Pt loading and uniformity was confirmed by weighing and X-ray fluorescence on dried catalyst layers. Almost all inks were well transferred onto the substrate, with the exception of 75PtGNP, where only a partial catalyst layer transfer was achieved.

In order to evaluate the catalyst layer structure after the whole processing protocol, the anode and cathode were transferred to a reinforced PSFA membrane (MX788.12 obtained from Gore) using the hot-press method at 145^{o}C, under 1 MPa pressure for 180 seconds, yielding the catalyst coated membrane (CCM).

Note the resulting CCMs were fairly large, approximately 7x7 cm each. Approximately a quarter of this area was utilized to obtain the cathode catalyst layer powder analysed by SANS, by lightly scratching the cathode side of the CCM using a sharp scalpel, with care taken to avoid damaging the Nafion membrane. The remainder of the CCM was used for electrochemical characterization (chapter 5) and TEM/EDS characterization. This ensured all results were obtained from the same batch, allowing for direct correlation of observations from different experimental methods applied.

2.4.1.1 TEM/EDS characterization

TEM/EDS measurements on Pt/HSAC based CCMs, obtained from inks with 25, 50, and 75 wt% iPrOH in solvent, were kindly performed by Dr. Laure Guetaz. A small piece of each CCM was embedded in epoxy resin. Subsequently, LEICA UC6 ultramicrotome was used to obtain 100 nm thick CCM cross-sections, which were then deposited on a lacey carbon TEM copper grip. TEM measurements were performed using a FEI THEMIS microscope equipped with a Cs probe corrections and a Super X system for EDS analysis, at 200 kV in high-angle annular dark field/scanning transmission electron microscopy (HAADF/STEM)

mode. EDS elemental maps are acquired under similar conditions, with a pixel size of 1 nm, beam current of 90 pA, and short acquisition time of 1 ms per pixel, in order to account for fluorine evaporation under the electron beam.

2.4.1.2 SANS measurements

SANS measurements of catalyst layer powders were performed on the D22 beamline of the ILL. Figure 73 shows a schematic of a 5 slot cell used throughout measurements, allowing for relative humidity control.

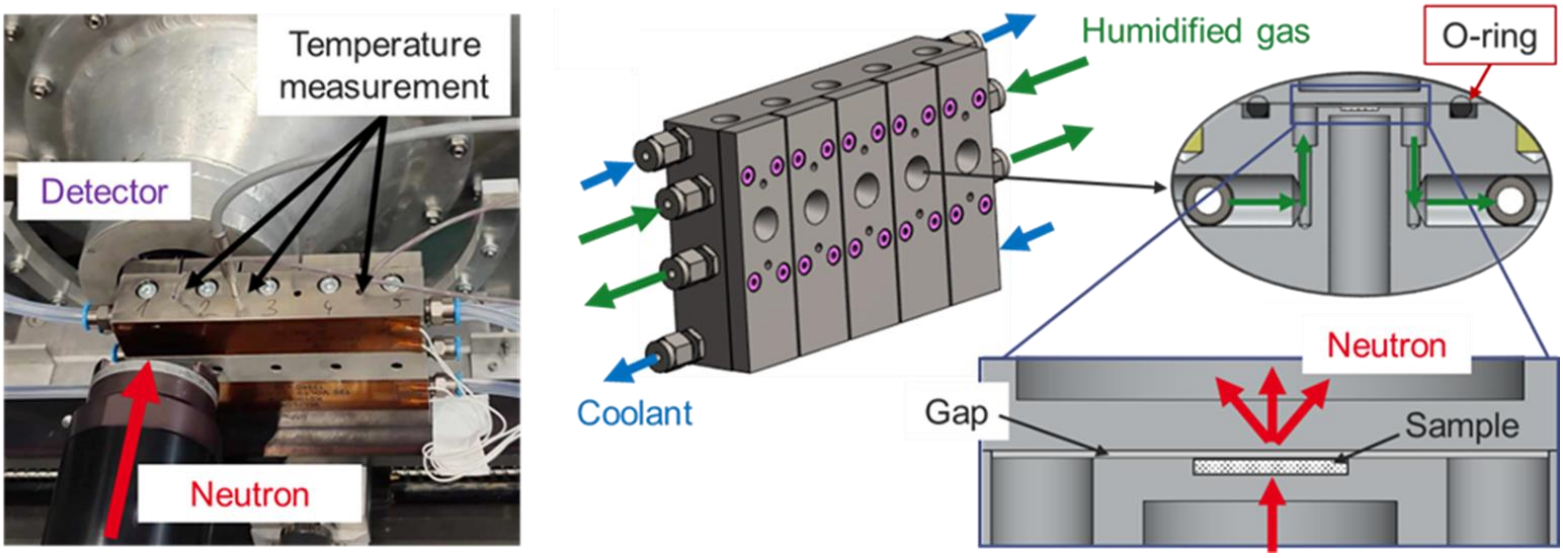


***Figure 95**. Schematic of sample cell used to measure catalyst layer powders in an environment with controlled relative humidity.*

Small amounts (tens of mg) of powdered sample were inserted into the sample slot. An O-ring was used to ensure sealing, and a lid was screwed onto the slot. Tubing was used to provide controlled gas flows of dry and humidified air, achieving a desired relative humidity inside the cell. The gas flow could be controlled externally through the use of software. Coolant was also run through the cell, allowing for specific temperature management.

Each sample was measured for 25 minutes using a 6 Å neutron beam at the 4m collimation/detector configuration. As a particular focus is placed on the structure of the ionomer component, a Q range of 0.013 – 0.7 $Å^{-1}$ was sufficient, and measurements with very good statistics were obtained. The temperature was kept constant at 20°C. Each sample was measured at four different relative humidity (RH) values in an ascending manner: 8%, 70%, 80% and 95%. The samples measured at 8% relative humidity represent the 'dry' reference samples, as lower humidity values would be near-impossible to achieve.

Since powdered samples result in isotropic scattering, a similar reduction process using the GRASP software could be undertaken as for ink samples previously (please refer to sections 2.1.2 and 2.3.1.2). Firstly, measurements of the incident beam and blocked beam, containing a beam stop, were acquired. Scattering from an empty slot was measured in order to calculate transmission from the sample cell with respect to the incident beam, as well as to remove scattering arising from the cell itself from that of the sample. The transmission of the sample could then be calculated with respect to transmission of the cell. Azimuthal radial averaging was used to convert the signal from the 2D detector into a 1D scattering function suitable for analysis. Sample processing involved removing incoherent scattering using the IQ^4 vs Q^4 Porod plot method (see section 2.1.3).

In order to allow for a direct comparison between different catalyst layer samples, variations in sample volume fractions must be accounted for. This was achieved by scaling each scattering function with RH 70-95% by an invariant calculated from the scattering function of RH = 8% of corresponding samples. The invariant value was calculated by integrating the scattering intensity of the 8% RH sample over the entire Q range[46]:

$$= \frac{1}{2^{2}} \int_{0.01}^{0.7} (\ )^{2} . \qquad (2.4.1)$$

Where Q= wavevector transfer ($^{-1}$), $I(Q)$ = intensity at give value of Q(cm^{-1})

2.4.2 Results

2.4.2.1 TEM/EDS characterization

TEM images were acquired for three CCMs containing Pt/HSAC based cathode catalyst layers (CCLs), which were manufactured from inks containing 25, 50 and 75 wt% iPrOH in the solvent composition (table 7).

Figure 96 presents images on the micrometre scale, focusing on the cathode/membrane interface.

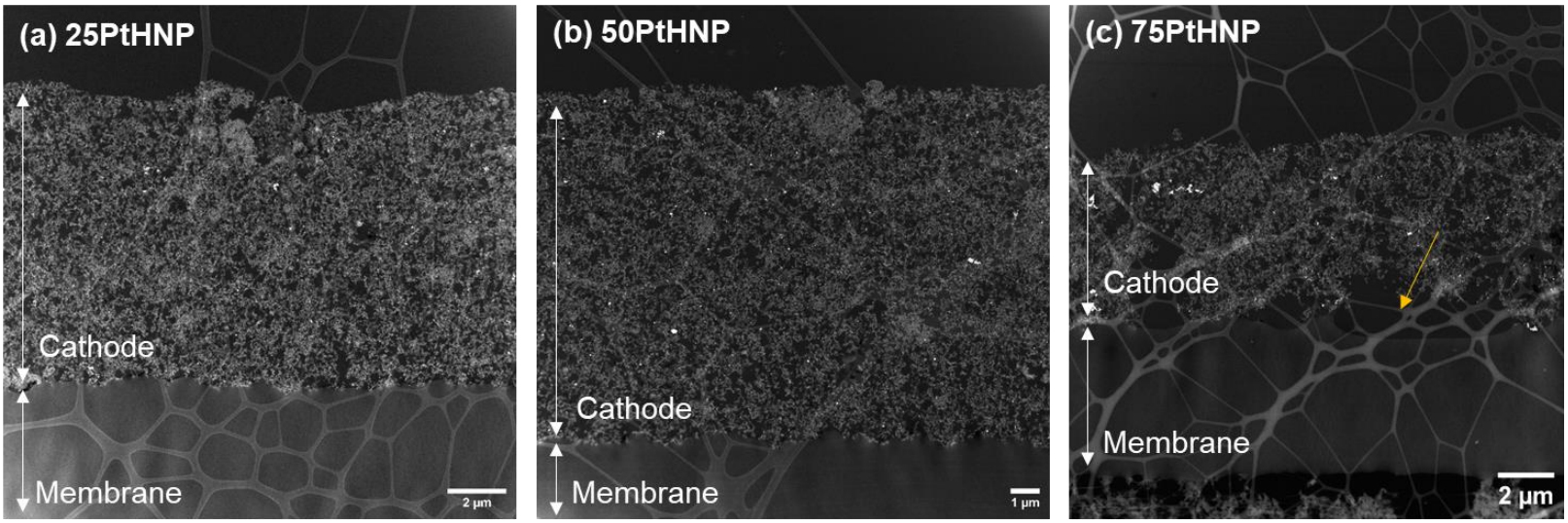


Figure 96. *HAADF/STEM images of* ***(a)*** *25PtHNP,* ***(b)*** *50PtHNP and* ***(c)*** *75PtHNP catalyst layer cross-sections.*

Good contact between the cathode and membrane, as well as homogeneity in CCL thickness were observed for both 25PtHNP and 50PtHNP samples. On the other hand, a more pronounced variation in the CCL thickness, along with areas with no cathode/membrane contact were observable in the case of 75PtHNP. More examples of micrometre scale images obtained for the three samples can be visualized in appendix 27.

Figure 97 presents HAADF/STEM images on the nanometre scale, with and without EDS mapping (both for F and Pt). For 25PtHNP and 75PtHNP, EDS mapping reveals regions of increased fluorine content (pointed to by arrows), which may suggest a less homogenous ionomer distribution on the Pt/C complex. On the other hand, in the case of 50PtHNP, a more uniform fluorine distribution was observed, suggesting an improved ionomer coverage. Nevertheless, note some patches of increased fluorine content could also be observed in some regions for 50PtHNP. Please refer to appendix 28 for more examples of HAADF/STEM images with EDS mapping.

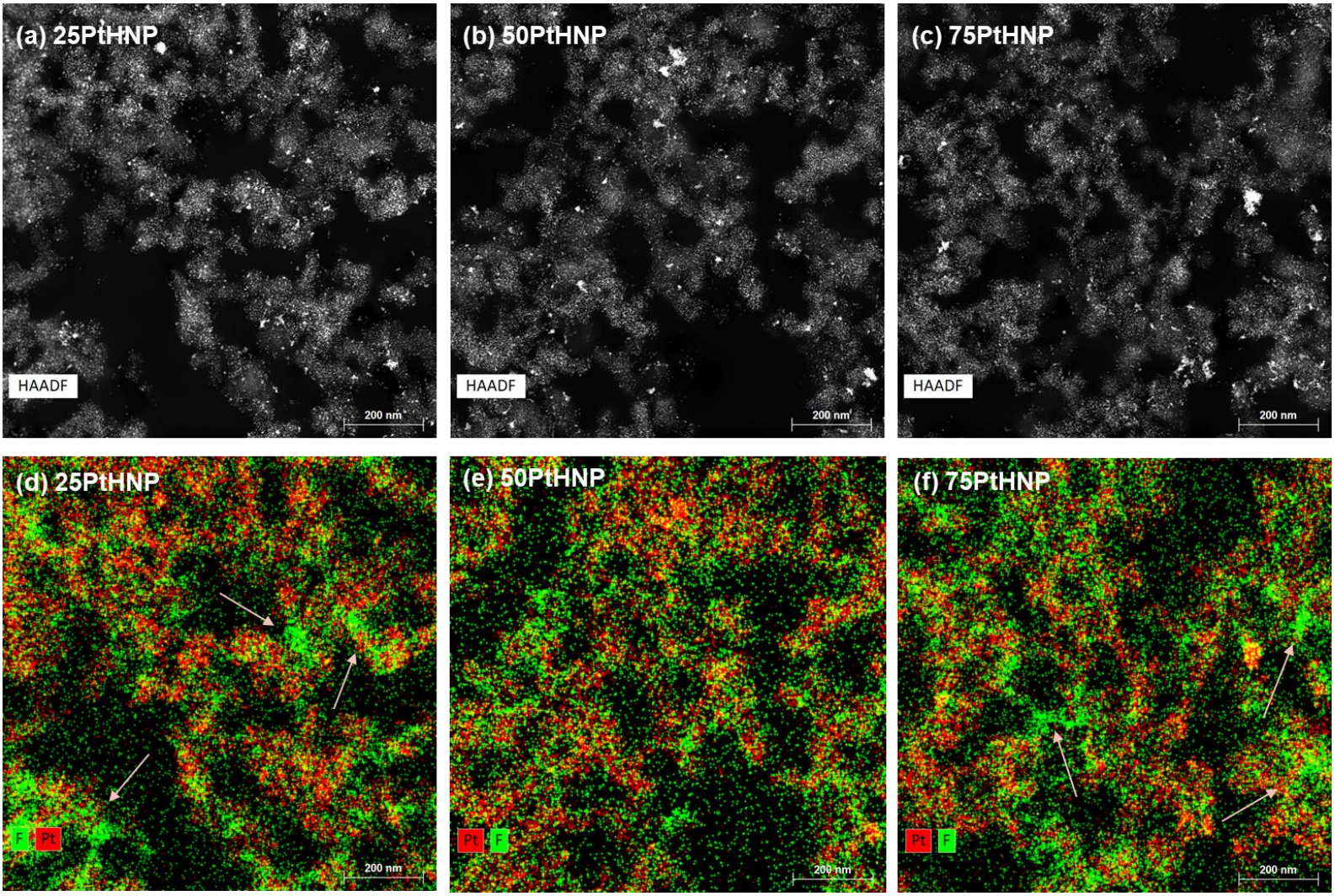


Figure 97. *HAADF/STEM images of* ***(a)*** *25PtHNP,* ***(b)*** *50PtHNP and* ***(c)*** *75PtHNP. Corresponding HAADF/STEM images with Pt and F EDS mapping* ***(d-f).***

In summary, HAADF/STEM images with EDS mapping suggest 50PtHNP was the CCM of best quality, with a homogenous CCL thickness, good cathode/membrane contact, and the most uniform ionomer distribution implied by fluorine mapping. 25PtHNP also showed a fairly homogenous CCL thickness and good cathode/membrane contact, however, regions of increased fluorine content could be observed in EDS, suggesting some ionomer aggregation. This was likewise the case for 75PtHNP, which in addition displayed varying CCL thicknesses and regions of reduced contact between the cathode and membrane, suggesting poor transfer of the catalyst layer onto the membrane. Little can be concluded on the Pt/C aggregation itself from a handful of images. In general, all samples show a connected network of Pt/C particles, forming aggregates of approximately few hundred nm, as expected.

On the other hand, the differences in ionomer coverage observed can give some insight into the effect of solvent system on the catalyst layer post processing. Indeed, it is interesting to note that 50PtHNP, where no ionomer adsorption to Pt/C was observed in the ink, shows the most uniform distribution. Moreover, where some degree of ionomer adsorption was observed for both 25PtHNP and 75PtHNP in the ink, in the catalyst layers the ionomer seems to show increased aggregation. This suggests that no ionomer interaction with Pt/C in ink yields an improved ionomer distribution post drying, an idea contrary to

hypotheses made in a number of published works.[30,62,63] It is of utmost importance to correlate these observations to SANS data as well as electrochemical performance of each CCL.

2.4.2.2 SANS results

Figure 98 shows processed (incoherent scattering removed using the Porod plot method) scattering functions of Pt/HSAC and Pt/GC based cathode catalyst layers, manufactured from ink compositions with varying iPrOH concentration in the solvent system.

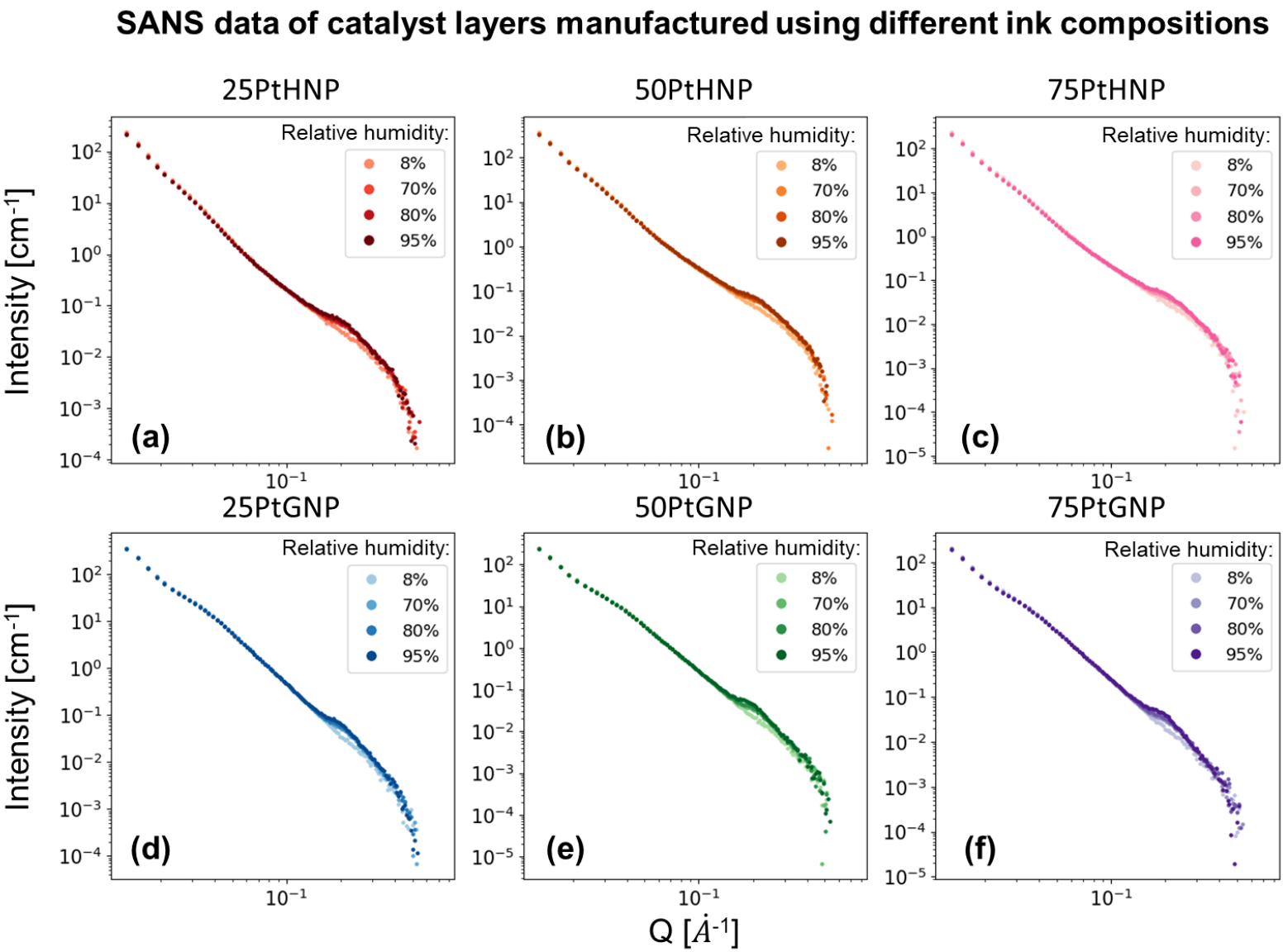


Figure 98 *SANS data of catalyst layers (with incoherent scattering removed) manufactured using different ink compositions:* ***(a)*** *25PtHNP,* ***(b)*** *50PtHNP,* ***(c)*** *75PtHNP,* ***(d)*** *25PtGNP,* ***(e)*** *50PtGNP,* ***(f)*** *75PtGNP. Error bars have not been included for visualization purposes. For corresponding figure with error bars included please refer to appendix 29.*

In each instance the scattering functions are identical in the low/mid Q regimes ($Q<1x10^{-1}$ $\dot{A}^{-1}$), showing a shoulder feature related to the size of carbon primary particles in the lower mid Q range ($Q \approx 3x10^{-2}$ $\dot{A}^{-1}$). However, in the catalyst layer SANS measurements only a 4m detector configuration was used, resulting in a lower range of Q magnitudes (0.013-0.7 $\dot{A}^{-1}$). For this reason, the shoulder feature can be attributed to the polydispersity variation of carbon primary particles, as deduced by a rough fit with the sphere form factor

(figure 57), rather than the primary particle size itself, whose feature was observed at lower Q values ($8x10^{-3}$ $Å^{-1}$), not covered by the Q range in question. Note this feature is also distinctly visible in the case of GC-based catalyst layers, suggesting that it has no relation to the primary particle porosity present in HSAC-based sample.

Furthermore, this suggests the S_{cc} output for GNP ink series discussed in section 2.3.3.1 has been most likely erroneously extracted due to the incorrect GC SLD value. The lack of change with increasing relative humidity confirms no alteration in the carbon primary particle structure occurs with increasing water saturation for both Pt/C complexes. Nevertheless, it is important to highlight water would interact with the primary particles themselves. Chabot et al.[46] observed the filling of HSAC pores by water molecules by comparing scattering function acquired in the presence of H_2O and D_2O. However, as the SLD of H_2O and air are very similar (-0.56 and 0 $x10^{10}$ cm^{-2} respectively), it is likely this alteration is not observed in scattering functions presented in figure 76 because the contrast difference is too low. The CV-SANS method could be further applied to catalyst layers, using H_2O and D_2O, in order to investigate water accumulation near the primary particles with increasing RH.

In the high Q range ($Q > 1x10^{-1}$ $Å^{-1}$), as relative humidity is increased from 8%, in the case of each catalyst layer sample a peak feature related to the hydration of the ionomer can be observed. In the catalyst layer, the ionomer exists in two general forms – as a thin film covering the carbon particles, as observed in CV-SANS data discussed in section 2.3.3, and as aggregates separating carbon aggregates/agglomerates. In this Q region two features related to the ionomer can be expected – the structure factor related to the aggregates and their inter-particle interaction, as well as the form factor of the thin ionomer shell. At this point, it is impossible to say with certainty which of the two structural domains the feature can be attributed to. However, note HAADF/STEM images and EDS mapping (figure 97) suggest a fairly good ionomer distribution in all samples, with only a handful of ionomer aggregates implied by increased fluorine content in 25PtHNP and 75PtHNP. For this reason, a form factor of a thin ionomer shell seems a more likely explanation for the contribution observed in the high Q regime of scattering functions. Nevertheless, characterizing its behaviour with increasing RH will shed more light onto the nature of the ionomer.

However, how this feature evolves as relative humidity increases from 70 to 95% is not evident on this scale. To accentuate the ionomer-related feature, allowing for an improved evaluation, scattering from 8%

RH catalyst layer samples, the ‘dry’ reference, was subtracted from scattering functions obtained at increased RH values, figure 99.

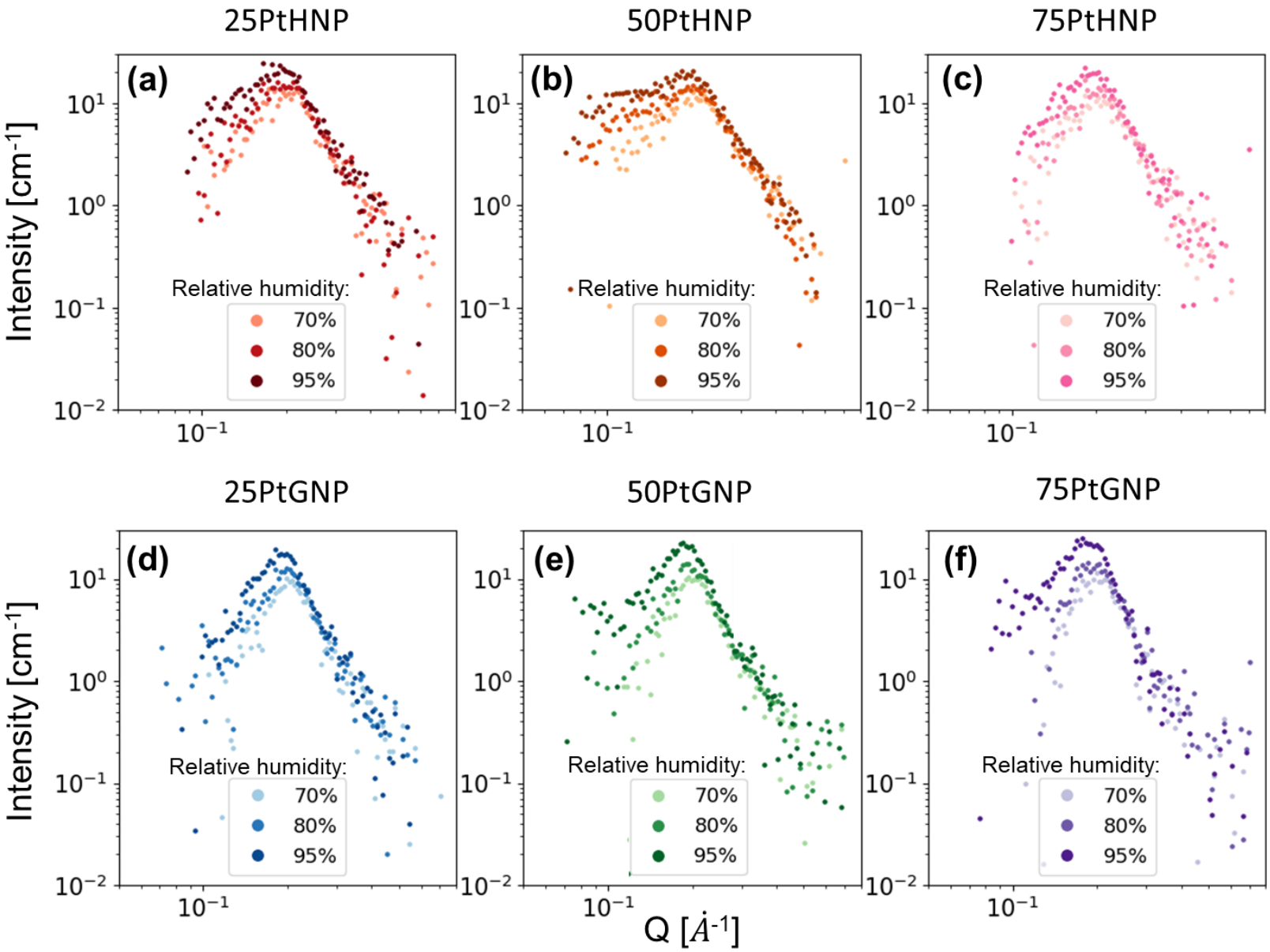


Figure 99. *Scattering functions obtained at 70-95% RH, with scattering of the ‘dry’ reference sample removed, accentuating a peak-like feature related to the ionomer.* ***(a)*** *25PtHNP,* ***(b)*** *50PtHNP,* ***(c)*** *75PtHNP,* ***(d)*** *25PtGNP,* ***(e)*** *50PtGNP,* ***(f)*** *75PtGNP. Error bars have not been included for visualization purposes. For corresponding figure with error bars included please refer to appendix 30.*

In this format, a shift in position of maximum feature intensity can be clearly observed in the case of each sample. A small shift is observed when RH is increased from 70% to 80%, and a more significant one with a further RH increase to 95%. The scattering from each ionomer-related feature was fitted with a Gaussian distribution in order to determine the Q values of maxima observed. Figure 100 presents the quantified Q values of maxima, focusing on their change with relative humidity, for Pt/HSAC and Pt/GC based inks. Additionally, table 8 presents the % shift of the peak maximum Q magnitudes for each sample.

Sample	% Shift of peak maximum Q magnitude from 75 to 95% RH
25PtHNP	6.5
50PtHNP	5.9
75PtHNP	5.4
25PtGNP	6.9
50PtGNP	7.9
75PtGNP	8.9

Table 8. *Quantified peak maximum Q magnitude % shift as relative humidity is increased from 70 to 95% for each sample.*

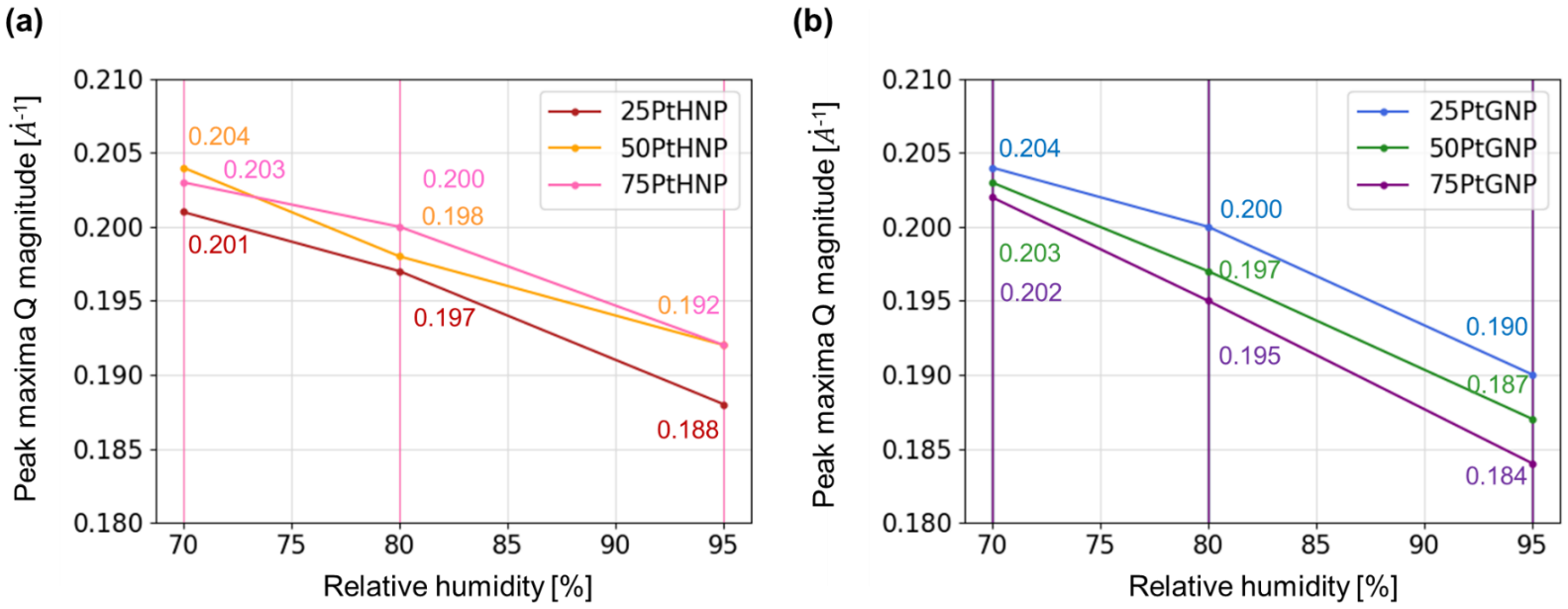


Figure 100. *Quantification of Q magnitude of peak maxima as a function of relative humidity of* ***(a)*** *Pt/HSAC based* ***(b)*** *Pt/GC based catalyst layers manufactured from ink compositions with varying iPrOH concentration in the solvent system. Note error bars, ΔQ, are in the range of 0.025 – 0.0037 Å^{-1}.*

For the case of each sample, the Q position of the peak maximum decreases with increasing RH, indicating an increased structural size, coherent with the data presented in figure 99. Although a general size increase is evident on hydration, in the case of Pt/HSAC based cathode catalyst layers, the size of the ionomer structure increases with increasing iPrOH concentration used in the preceding ink, while a reverse observation can be made in the case of Pt/GC based catalyst layers. Moreover, considering the peak positions extracted for the 50PtHNP and 75PtHNP, where only a difference of 0.001 Å^{-1} can be observed at 70% RH and the peak position is identical at 95% RH, the size regime can be considered unchanged for the two catalyst layers. Indeed, evaluating the Q values extracted, it can be observed that the shift in peak maxima Q magnitude with RH is generally very small, varying by approximately 0.010 – 0.015 Å^{-1} between 70 and 95% RH measurements. Looking to table 8, it can be observed the % shift remains fairly similar for the Pt/HSAC based samples, between 5.4 (75PtHNP) and 6.5% (25PtHNP). Although not much difference can be observed between the samples with respect to degree of peak maxima shift, it is worth noting that the Q magnitudes extracted for 25PtHNP sample peak maxima are overall smaller than for the other two samples irrespective of RH. On the other hand, the Q magnitudes of 50PtHNP and 75PtHNP remain fairly close, and even have the same value at 95% RH. A correlation could potentially be made between this general Q magnitude and the degree of ionomer adsorption in the catalyst inks of corresponding samples – 25PtHNP which showed significant ionomer adsorption (23.5%) in the ink displays larger ionomer features

in the catalyst layer, while 50PtHNP and 75PtHNP where no/little adsorption was deduced in the inks show smaller ionomer features, closer in size.

The difference is more pronounced for Pt/GC based inks, with shift increasing by 1% point with increasing iPrOH concentration, from 6.9 to 8.9%. Moreover, the peak maxima Q magnitudes are overall lower for 75PtGNP, suggesting a bigger size domain for the ionomer feature, and again a progressive increase in general Q magnitude can be observed with decreasing iPrOH concentration.

Using a simple conversion from the Q domain to d spacing, d = 2π/Q, a size shift from 3.1 to 3.3/3.4 nm can be determined when shifting from 70 to 95% RH. These values take into account the smallest and highest Q magnitudes determined at both 70 and 95% RH across all samples, showing the differences observed in the peak positions between different samples at the same RH are very slight on the nanoscale.

The extracted size changes on hydration are comparable to shell thickness values reported by Chabot et al.[46] of 3 nm for CCLs based on Pt/HSAC and Pt/Vulcan, which were manufactured from inks dispersed by a planetary mixing/ball-milling procedure. Note in their study the ionomer, I/C and Pt loading used were also comparable, although the component concentrations and solvent system (60:40 by volume DAA/water) were different. However, in their work the swelling of ionomer aggregates in the CCL was also investigated by SANS by comparing peak maxima shift with increasing hydration, and the results obtained likewise show similarity to those presented in this work. Swelling of the Nafion N117 membrane resulted in a peak maxima shift from 0.173 to 0.184 $\dot{A}^{-1}$ with an RH change from 70 to 95%. Swelling of Nafion (EW = 1000 g/mol^{-3}) aggregates in a catalyst layer obtained from a poorly dispersed ink showed a shift from 0.195 to 0.215 $\dot{A}^{-1}$ with an RH change from 70 to 95%. Such small shifts in Q magnitude, approximately 0.01 – 0.02 $\dot{A}^{-1}$, are similar to those presented in figure 100.

Figure 101 shows inter-sample comparison, with each scattering function scaled by the invariant calculated as described in equation (2.4.1). Comparisons are made in between catalyst layers based on different Pt/C complexes, but manufactured from inks with the same solvent compositions. Note only scattering functions at 95% RH will be compared, where the peak feature is the most pronounced.

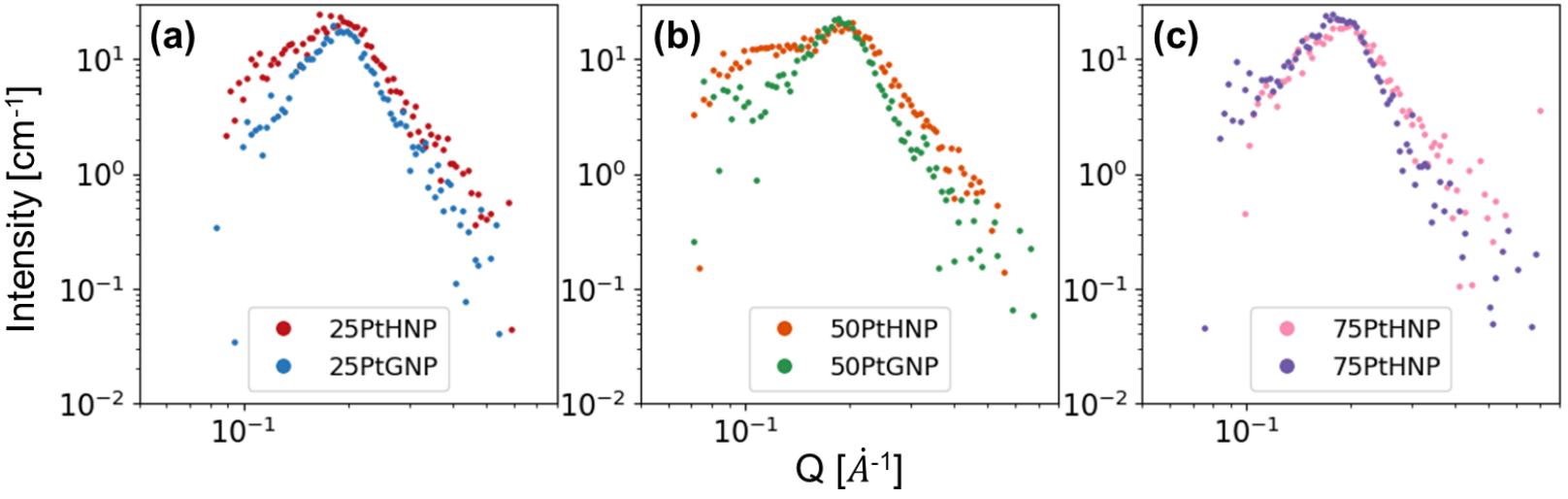


***Figure 101**. Comparison of ionomer-related peak like feature arising from scattering functions measured at 95%RH: comparison of catalyst layers based on different Pt/C complexes, but manufactured from inks with the same solvent composition – **(a)** 25:75 wt% iPrOH/water, **(b)** 50:50 wt% iPrOH/water, **(c)** 75:25 wt% iPrOH/water.*

In each case a general difference in the peak shape can be clearly observed, with sharper peaks present in the case of Pt/GC based samples, and broader peaks in the case of Pt/HSAC based samples. The peak shape will relate to the nature of the ionomer structure, where a correlation length specific to the shell form

factor would result in broader peaks, while scattering from the bulk ionomer, where inter-domain distance is more well defined, would result in a sharper peak shape. This may suggest that in fact, dependent on the Pt/C complex, the ionomer distribution in the catalyst layer varies greatly, and both thin ionomer layers as well as aggregates are observed, depending on the sample. Nevertheless, in order to confirm such a hypothesis, a more detailed analysis must be performed, including fitting of the SANS data obtained. Moreover, obtaining measurements of bulk ionomer swelling in the membrane, or in a catalyst layer manufactured from a poorly dispersed ink, would allow for a direct comparison of the peak shape variation with altering ionomer dispersion.

2.4.3 Conclusions

SANS measurements of catalyst layers obtained from varying ink compositions, at several relative humidity levels, were successfully obtained. At RH values between 70 and 95% a peak-like feature related to the hydration of the ionomer component could be observed. Evaluation of the position of the peak maximum using a Guinier distribution fit showed that, in the case of Pt/HSAC based catalyst layers, the layer thickness increases with iPrOH concentration in the corresponding ink solvent system, while a reverse pattern was observed for Pt/GC based catalyst layers. Nevertheless, it remained inconclusive whether the ionomer-related peak feature could be attributed to the ionomer thin film or ionomer aggregates.

Chabot et al.[46], who also performed SANS on catalyst layers with varying RH conditions, extracted shell thicknesses of 3 nm, and almost the same size domain was indicated by the extracted peak maxima positions for all catalyst layers studied (figure 78). On the other hand, in their work peak position shift associated with the swelling of ionomer aggregates was also very similar to the peak position shifts observed in this work. Furthermore, variation in peak shape between Pt/HSAC and Pt/GC based catalyst layers may suggest that in fact both ionomer thin films and aggregates are potentially present, depending on the catalyst layer composition.

Based on these comparisons, it remains difficult to conclude whether the ionomer related feature can be attributed to a thin ionomer shell on the carbon support or the swelling of ionomer aggregates. In the work by Chabot et al.[46] a contrast variation between H_2O and D_2O was applied in order to ultimately conclude the feature relates to the ionomer shell, along with a thin water layer present at the carbon/ionomer interface. Such a study would be necessary in order to confirm the nature of the ionomer observed. Moreover, obtaining measurements of the bulk ionomer only (membrane) swelling behaviour in varying RH content may aid in pinpointing the nature of the ionomer feature in the catalyst layer through comparisons of peak shape that could be made.

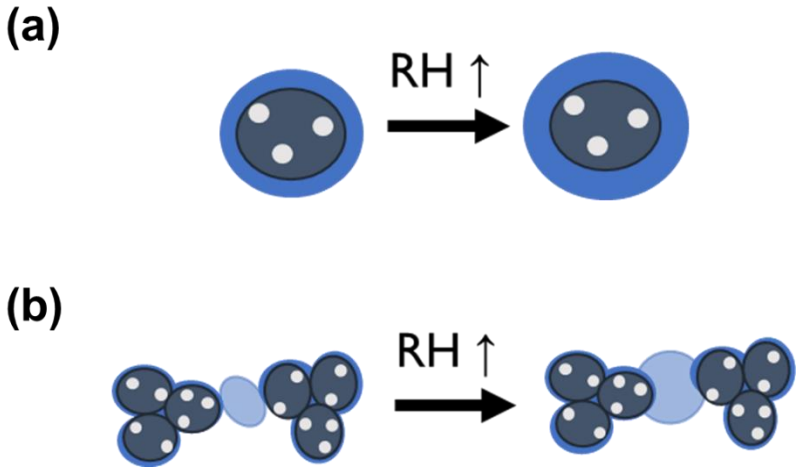


Figure 102. *Potential mechanisms that could be attributed to the shift of ionomer related peak-like feature with increasing RH:* ***(a)*** *hydration of the thin ionomer layer,* ***(b)*** *hydration of ionomer aggregates present in between Pt/C aggregates.*

Overall, it remains difficult to relate the ink structure variation (with respect to the ionomer component) as a function of varying iPrOH concentration in the solvent system to information obtained from catalyst layer SANS. One possible correlation could be observed, where the Q magnitude of the peak maximum of the 25PtHNP sample was always lower than for 50PtHNP and 75PtHNP, irrespective of RH. This sample was the only one to show significant ionomer adsorption in the ink (23.5%). On the other hand, 50PtHNP and 75PtHNP, which showed little or no ionomer adsorption in the inks, displayed peak maxima at more similar Q magnitudes at 70 and 95% RH. Nevertheless, it is also important to note the uncertainty obtained for the quantified peak maxima positions were also very high, ranging from 0.025 to 0.037 $^{-1}$ for all samples. This error is much higher than any differences between the obtained peak maxima Q magnitudes, and therefore reasonable scepticism has to be applied when discussing these values. Therefore, obtaining more information on the catalyst layer SANS data as a whole is imperative. Fitting of the data already acquired may shed more light onto the nature of the ionomer related feature, and obtaining additional contrast variation as well as bulk ionomer measurements would be a great aid.

On the other hand, the choice of Pt/C complex had a noteworthy impact on the peak shape (figure 101), as well as the trend in peak position extracted as a function of varying iPrOH content in preceding inks (figure 100). This suggests the choice of Pt/C, either due to the nature of the carbon support, Pt distribution, or both, plays a major role in dictating the final catalyst layer structure, even with respect to the ionomer component, and should be considered a key component to investigate further.

With regards to the carbon component in catalyst inks, as mentioned before CV-SANS may not be the ideal method for characterization of GC based samples, however, differences in catalyst ink/layer structures between HSAC and Vulcan may be insightful. SAXS may be another method to consider, particularly if a method to remove Pt scattering contributions can be applied.[67] Additionally, USAXS can yield insight into Pt/C behaviour on the aggregate scale.

3. Ultra Small Angle X-ray Scattering

Chapter 3 focuses on the ultra-small angle X-ray scattering technique (USAXS).

In **section 3.1** the theory of small-angle X-ray scattering (SAXS) will be discussed. Note the theory of SAXS is very similar to the theory of SANS (presented in section 2.1), with the two techniques often generalized under the term small-angle scattering (SAS). Therefore, the theory presented in this section will focus on the differences that arise when using X-rays instead of neutrons for structural characterization. This mainly pertains to the method of interaction with matter, and an alteration in the contrast term.

Section 3.2 will focus on experimental results obtained using USAXS, with an investigation of the structure of the high surface area carbon (HSAC) and graphitized carbon (GC) supports, as well as its variation with increasing ionomer content and Pt presence.

Section 3.3 presents conclusions made based on results and discussion in section 3.2.

Le chapitre 3 se concentre sur la technique de diffusion des rayons X aux ultra-petits angles (USAXS).

*Dans la **section 3.1**, nous aborderons la théorie de la diffusion des rayons X aux petits angles (SAXS). Il convient de noter que la théorie de la SAXS est très similaire à la théorie de la SANS (présentée dans la section 2.1), les deux techniques étant souvent généralisées sous le terme de diffusion aux petits angles (SAS). Par conséquent, la théorie présentée dans cette section se concentrera sur les différences qui apparaissent lors de l'utilisation des rayons X au lieu des neutrons pour la caractérisation structurelle. Cela concerne principalement la méthode d'interaction avec la matière et une altération du terme de contraste.*

*La **section 3.2** se concentrera sur les résultats expérimentaux obtenus à l'aide de l'USAXS, avec une étude de la structure des supports en carbone à haute surface spécifique (HSAC) et en carbone graphité (GC), ainsi que de sa variation avec l'augmentation de la teneur en ionomères et de la présence de Pt.*

*La **section 3.3** présente les conclusions tirées des résultats et de la discussion de la section 3.2.*

3.1 Theory

Small-angle X-ray scattering (SAXS) follows an almost identical concept as presented in section 2.1 - SANS theory. For this reason, the two methods are often generalized under the name small-angle scattering (SAS).

The principal difference between the two techniques can be observed in the name – where in SANS it is the neutrons that interact with the nuclei of atoms, in SAXS X-ray radiation interacts with the electrons of the atom instead:

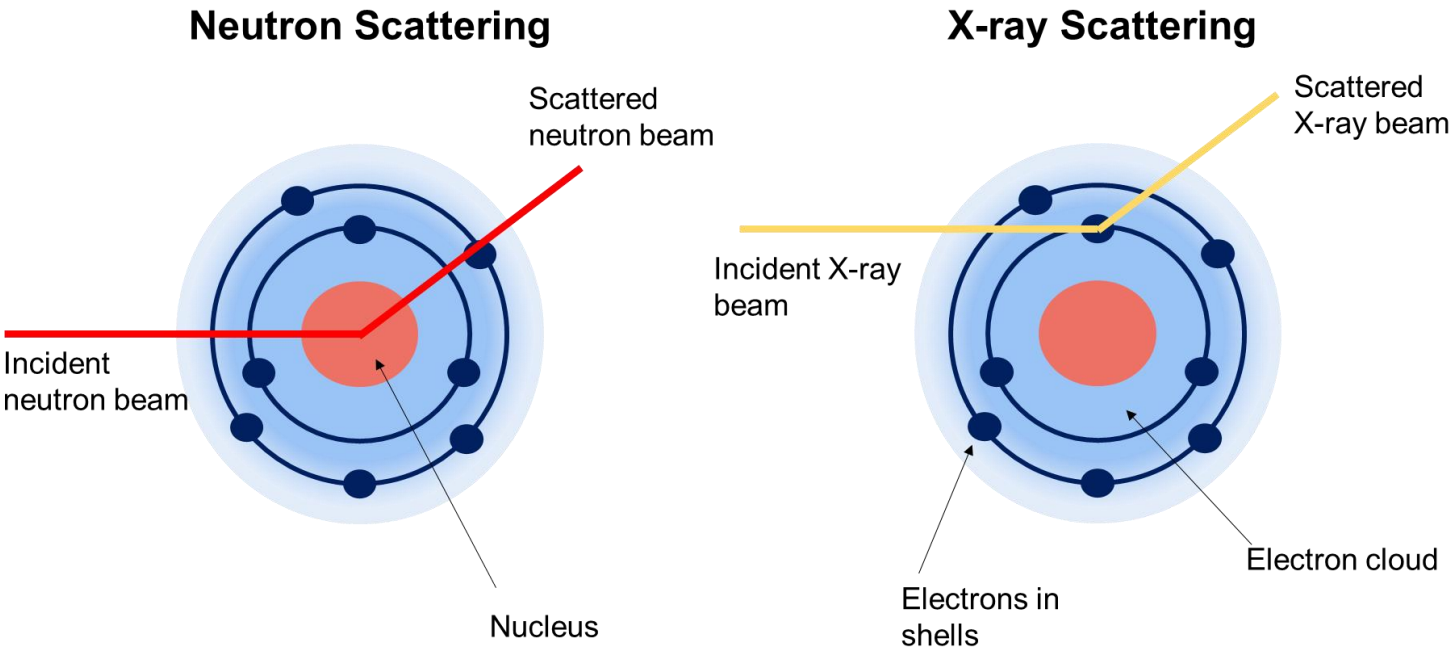


Figure 103. *A very basic, generalized, representation of an atom, with schematic showing neutron scattering from the nucleus, and X-ray scattering from the electron.*

The basic measurement set up for the two techniques is comparable, where a sample is placed in a monochromatic, parallel beam of radiation, obtained with the aid of a wavelength selector and collimation set-up. Scattered radiation through a size domain specific angle, θ, is recorded on a 2D detector located inside a vacuum chamber, placed at a certain distance from the sample. As particles in solution are randomly orientated, again, isotropic scattering is observed on the 2D detector.[107]

Scattering from alike scatterers (molecules/molecular domains in the range one to several hundred nm in the case of SAS) results in constructive interference, increasing the amplitude of the beam wave, resulting in coherent scattering detected. Scattering from unalike scatterers results in out of phase waves and destructive interference. As a result, incoherent scattering 'noise' is obtained.

SAXS again assumes elastic scattering only and the scattering angle θ can be related to the wavevector transfer Q, through equations (2.1.2– 2.1.5).

Here the first difference between neutrons and X-rays must be introduced, which regards the energy of the particles. The energy of an X-ray photon is on the scale of 10 keV, while the kinetic energy of a thermal neutron is 10 meV (although in a typical SANS experiment cold neutrons are used, whose kinetic energy is deliberately reduced further). The kinetic energy resulting in motion of atoms at ambient temperature is approximately 20 meV. Therefore, in X-ray scattering, the elastic scattering consideration arises from the fact that the energy change of an X-ray photon associated with energy transfer to an atom is negligible.[108]

The intensity arising from coherent scattering can be described by equation (2.1.9)[107]:

$$\frac{\sum}{}(\ ) = (—)\ \ ^2(\Delta\ )^2\ \ (\ )\ (\ ) \qquad (2.1.9)$$

Where N = number of scatterers in sample volume, V (cm^3), V_p = volume of individual scatterer (cm^3), $P(Q)$ = form factor containing information on the size and shape of scatterer, $S(Q)$ = structure factor pertaining to the inter-particle interactions of like-scatterers, $\Delta\rho^2$ = contrast term (cm^{-2}).

The second major difference between neutrons and X-rays is the contrast term. Recall in neutron scattering the contrast is based on an inherent property called scattering length, that varies in a somewhat random manner between atoms of different elements as well as different isotopes. In X-ray scattering, for samples in solution, the contrast term arises due to variation in between the electron density of the scatterer and the dispersion medium:

$$\Delta\ =\ \ \ \ \ \ \ \ -\qquad (3.1.1)$$

As heavier elements, containing more electrons, will have a higher electron density, ρ increases with the atomic number, Z, across the periodic table.

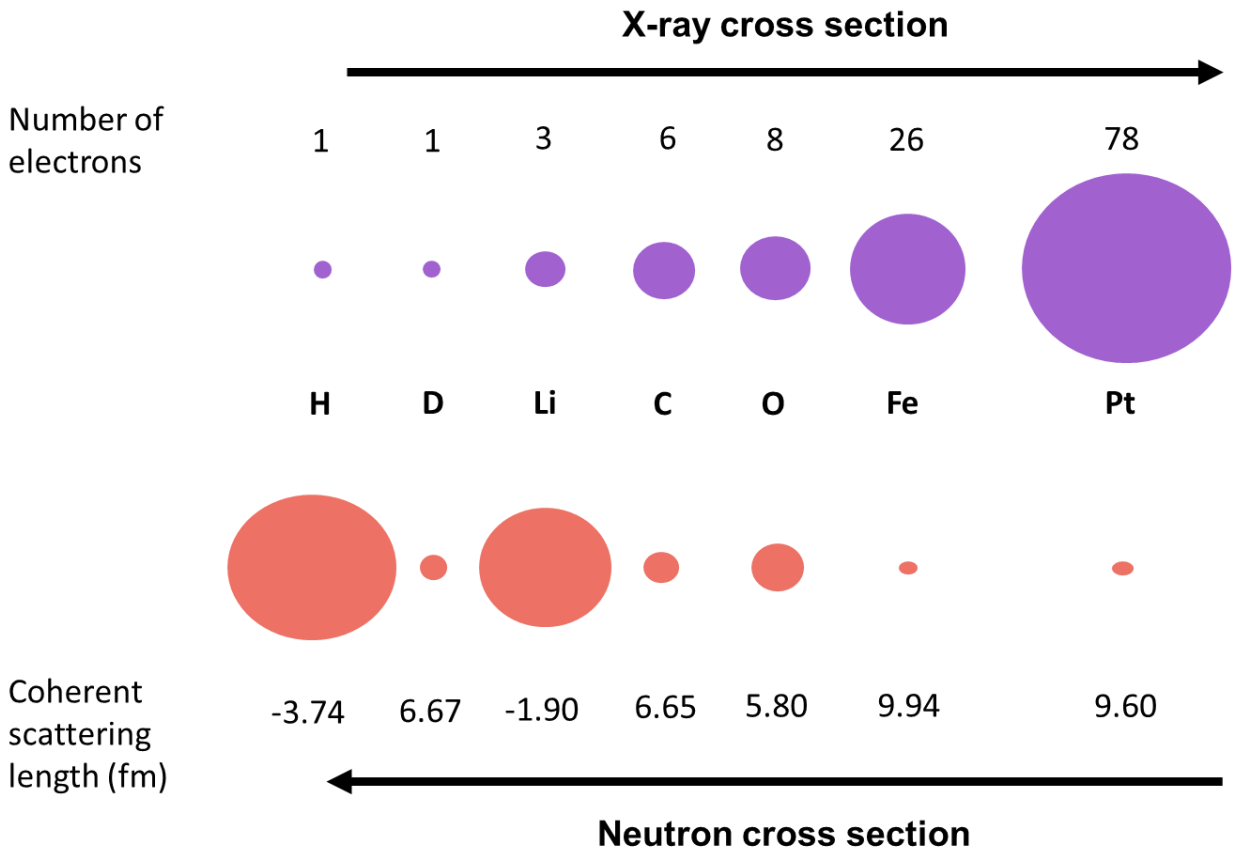


Figure 104. *Generalized schematic of variation in X-ray and neutron cross section across some elements and isotopes of the periodic table.[109] Coherent scattering length numbers were obtained from the NIST neutron scattering length list.[110]*

Just like in SANS, for molecular considerations, the electronic density of a molecule, namely the number of electrons per unit volume, must be taken into account:

$$= \frac{\sum_{=1}}{} = \frac{\sum_{=1}}{\sum_{=1}} \quad (3.1.2)$$

$\sum_{=1}$ represents the summation of the number of electrons in all atoms in the molecule, V_m (cm^3) is the molecular volume which can be expressed in terms of bulk density ρ (g/cm^3), the Avogadro number (N_a) and a summation of the molecular masses, M_i (g/mol) of all the atoms in the molecule.

Note equation (3.1.2) is almost identical as equation (2.1.7), however in the former case, the number of electrons in an atom, N_e, is used.

Table 9 compares theoretical SLDs and electronic densities of catalyst ink specific components:

Component	**Density (g/cm^3)**	**SLD (cm^{-2})**	**Electronic density (cm^{-2})**
Carbon	2.00	$6.67x10^{10}$	$1.70x10^{11}$
Nafion D2020	2.00	$4.19x10^{10}$	$1.64x10^{11}$
Pt	**21.45**	**$6.36x10^{10}$**	**$1.31x10^{12}$**
iPrOH	0.79	$-0.33x10^{10}$	$7.56x10^{10}$
iPrOH-d8	0.89	$6.22x10^{10}$	$7.55x10^{10}$
H_2O	1.00	$-0.56x10^{10}$	$9.44x10^{10}$
D_2O	1.11	$6.38x10^{10}$	$9.40x10^{10}$

Table 9. *Comparison of theoretical SLD and electronic density values relevant for Neutron and X-ray scattering respectively of catalyst ink specific components that were utilized throughout this work.*

The differences in the contrast between neutrons and X-rays mean the two techniques are suited to usually quite different, yet complimentary investigations.

To take the catalyst ink system as an example, SANS is a superior method for the study of interactions between the carbon support and the ionomer, molecules which are both composed of light atoms, however, SAXS and WAXS (wide-angle X-ray scattering) prove better equipped for the study of the Pt structure itself.[111,112]

Another example of the SAXS and SANS methods used in tandem is in the study of synthesis/functionalization of semiconductor nanoparticles.[113] A sol-gel synthesis approach results in a core-shell structure, where the variation in structure of the organic shell, and core based on heavier elements, as a function of ligand exchange can be studied using SANS and SAXS respectively.[114]

One of the most important advantages that still need to be discussed is that high-brilliance synchrotron X-ray sources offer access to X-ray beams of high flux and high energy.

In addition to the electron density dependence, X-ray cross-section varies with the photon energy in a reciprocal manner. Moreover, the short wavelengths associated with high energy X-rays pose several advantages, including increased sample penetration, and the ability to work in complex sample environments, while accessing increasingly smaller Q values that arise with ever lower scattering angles.[115, 116]

Furthermore, the high flux of the incident X-ray beam results in very short measurement times, on the order of milliseconds. Increased flux signifies drastically increased number of scattering events; therefore, sufficient intensity can be observed on the detector in very short time periods. The short measurement times arising from high X-ray flux result in the ability of performing time resolved measurements, which is

perfect for monitoring fast structural changes in in-situ and operando studies. Koga et al.[71] investigated the change in Pt/C aggregation structure during the ink drying process using Grazing incidence small-angle X-ray scattering (GI-SAXS), showing the aggregation process finishes as soon as 250s into the 1600s long drying process. Moreover, Hasegawa et al.[44] utilized time resolved USAXS to show Pt/C agglomeration during drying is suppressed in the presence of low content of high boiling solvent propylene glycol in the ink solvent composition. Povia et al.[117] used operando SAXS and XAS (X-ray absorbance spectroscopy) in tandem to investigate the change in Pt/C fractal aggregation structure and Pt degradation respectively during fuel cell operation conditions.

On the other hand, note increased radiation energies and high flux carry a risk of sample damage with prolonged exposure.[118] Therefore, it is prudent to verify sample stability for a specified exposure time through preliminary measurements.

From a practical point of view, since beamtime at large scale facilities is hard to come by, if a large number of samples needs to be measured, and the method proves suitable, X-ray scattering is the appropriate option.

For the latter reason, ultra-small angle X-ray scattering (USAXS) has been opted for in order to perform an investigation on the variation of carbon structure between different carbon supports, in the presence of increasing ionomer content as well as Pt. In section 2.3.3, focusing on results obtained concerning ink structure using CV-SANS, some insights into the HSAC structure was obtained, however, the standard Q range of $2.5x10^{-3}$ – $6.4x10^{-1}$ $\dot{}^{-1}$ yielded information on primary particles only. As expected, it was observed the inherent structure of the primary particles does not change with varying ink composition. Utilizing longer Q ranges of $1.2x10^{-4}$ – $5.1x10^{-1}$ $\dot{}^{-1}$ may yield additional insights into the carbon aggregate structure. As in the Q range of interest only carbon structural information is expected, no simplification of scattering functions associated with multi-component systems is necessary, making USAXS a suitable method, where such information can be obtained in the matter of hours.

3.2 Methodology

Samples based on HSAC, GC, Pt/HSAC (50 wt% Pt loading) and Pt/GC (50 wt% Pt loading) were prepared to each yield the following compositions:

1) 0.002 wt% carbon, no ionomer, DMF solvent
2) 2 wt% carbon, Nafion D2020, with I/C = 0.1, 50:50 wt% iPrOH/water solvent
3) 2 wt% carbon, Nafion D2020, with I/C = 0.8, 50:50 wt% iPrOH/water solvent

All components were obtained from the same sources as described in section 2.3.1.1. Note no deuterated solvents were used in the samples. Otherwise, the sample preparation procedure was the same as for inks and component dispersions (for carbon contrast match) studied by CV-SANS, described in section 2.3.1.1. A 50:50 wt% iPrOH/water stock solution was prepared. A 4 wt% Nafion stock solution was created through combination of Nafion D2020 and the solvent stock solution in correct proportions. The carbon (or Pt/C) nanopowder, Nafion stock solution and solvent stock solution were combined in appropriate proportions, zirconia balls were added, and the slurries were mixed on a roller mill overnight.

For the carbon (or Pt/C) in DMF samples, 0.02 wt% carbon (0.04 wt% Pt/C) stock solutions were prepared and a 10-fold dilution with DMF was performed to ensure low concentrations, boosting sample stability.

Additionally, two reference samples were prepared, one containing 50:50 wt% iPrOH/water solvent and one containing DMF only.

Each sample was placed in a quartz capillary tube of 1.5 mm diameter.

USAXS experiments were performed on the ID02 beamline of the ESRF using an X-ray beam of 1 Å wavelength (12.2 keV), with dimensions of 50 μm x 120 μm (vertical and horizontal respectively). Each sample was measured at two configurations, with the collimation and back detector distance from sample of 30.7 and 10 m. Each measurement took 0.005 s and was performed 10 times. Data reduction was performed directly on the beamline. The same corrections are applied as in the case of neutron data reduction, described in section 2.1, yielding scattering functions corresponding to the sample + solvent, on the absolute intensity scale. No evolution in the scattering functions was observed over the 10 measurements collected per sample, suggesting no sample damage over the exposure time. An average of the 10 measurements was taken to yield the final scattering function. The averaged measurements obtained for the two detector configurations were merged at approximately Q = 0.05 $Å^{-1}$, yielding a scattering function over a very long Q range of $1.2x10^{-4}$ – $5.1x10^{-1}$ $Å^{-1}$, with good resolution in the mid/high Q range ($Q>5x10^{-2}$ $Å^{-1}$). Data was processed by subtracting the scattering functions of the corresponding solvent containing reference sample from the carbon dispersions and ink samples.

3.3 USAXS results

3.3.1 Comparison of scattering functions obtained from USAXS and CV-SANS

Before delving into structural alteration introduced by varying ionomer content, it is prudent to evaluate the consistency of data obtained using USAXS and CV-SANS. In section 2.3.3 the structure of carbon was evaluated using the S_{cc} output extracted from the HNP ink series, showing the scattering function obtained in the Q = $2.5x10^{-3}$ – $6.4x10^{-1}$ $Å^{-1}$ range contained almost exclusively information on the carbon primary particle structure (figure 58). Throughout the evaluation of S_{cc} outputs obtained from different ink compositions it was noted the scattering function remains unaffected, which is consistent with the lack of change expected from the building blocks that are primary particles.

Therefore, it would be expected that for the USAXS data the scattering related to the carbon structure in the Q = $2.5x10^{-3}$ – $5.0x10^{-1}$ $Å^{-1}$ range also remains consistent, and is in very close proximity to the S_{cc} output extracted from the HNP ink series. For this reason, scattering functions of 0.002 wt% HSAC-only in DMF (HC-DMF) and the S_{cc} extracted from the HNP ink series were compared.

It is important to highlight that although the HNP ink series measured by CV-SANS and ink series based on 2 wt% HSAC and Nafion with I/C = 0.8 (0.8HNP) measured by USAXS are closer in composition, in the case of USAXS the scattering function is not deconvoluted into PSF outputs, and therefore contributions related to the ionomer structure can also be expected in the high Q regime (Q>0.1 $Å^{-1}$). Consequently, a more appropriate comparison of the carbon primary particle structure can be made using the USAXS data of the low concentration HSAC component only, dispersed in DMF (HC-DMF).

Figure 105 presents the comparison of HC-DMF scattering function and the S_{cc} output extracted from HNP ink series. Note although both measurements are on the absolute intensity scale, due to differences in the contrast term definition in between the methods, as well as in sample concentration, the scattering functions

had to be scaled together for comparability. An original, unscaled version of the figure can be found in appendix 31.

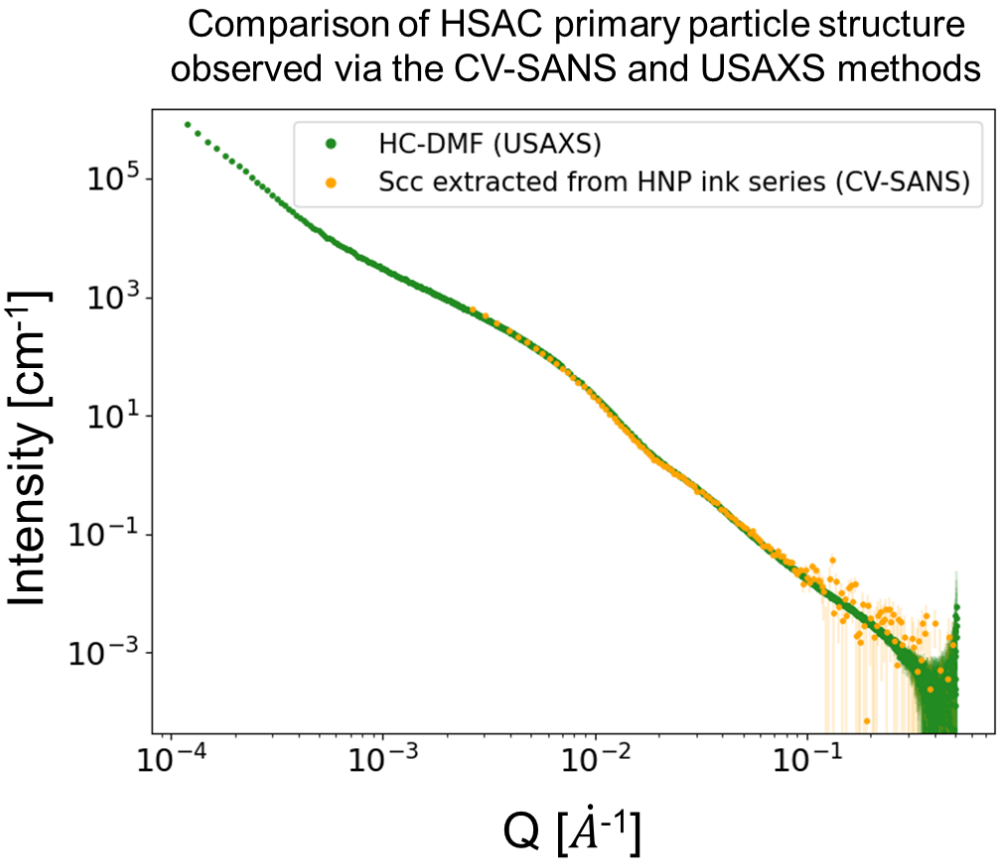


Figure 105. *Comparison of S_{cc} output extracted from the HNK ink series investigated using the CV-SANS method, showing the structure of the HSAC component in the ink, to the scattering function of HSAC in DMF sample obtained using USAXS. HC-DMF scattering function was scaled for comparison purposes.*

The USAXS scattering function of 0.002 wt% HSAC in DMF (HC-DMF) shows a very good agreement to the S_{cc} output extracted from CV-SANS measurements of the HNP ink series, further proving that indeed the latter scattering function pertains to the carbon primary particle structure, which remains constant throughout. Note, the lack of variation between the S_{cc} extracted from the HNP ink series, which was based on 50:50 wt% iPrOH/water, and the scattering function of HSAC dispersed in DMF increases confidence in the SLD extracted for HSAC primary particles using the contrast match method by proving no structural alterations that may affect the SLD extraction take place as a result of altering the solvent system (as expected for primary particles).

3.3.2 Effect of Pt on aggregate size

To commence the analysis of aggregate size variation, it is important to consider what effect the presence of Pt itself has on the large-scale aggregate structure. It is stipulated that Pt provides additional stabilization by electrostatic repulsion,[25,53] so a question arises whether a general decrease in aggregate size can be observed with addition of Pt. As it has been previously discussed in chapter 1, addition of ionomer may have contrasting effects on aggregate size in samples with and without Pt, depending on the carbon support chosen.[25,52,53] Therefore, carbon as well as Pt/C component only dispersions in DMF of the following compositions will be utilized to answer this question:

HC-DMF = 0.002 wt% high surface area carbon in DMF solvent

Pt/HC-DMF = 0.002 wt% high surface area carbon **+ 0.002 wt% Pt** in DMF solvent

GC-DMF = 0.002 wt% graphitized carbon in DMF solvent

Pt/GC-DMF = 0.002 wt% graphitized carbon **+ 0.002 wt% Pt** in DMF solvent

Figure 106 presents a comparison of USAXS scattering functions obtained for samples with no ionomer content, based on a corresponding carbon supports, with and without Pt. The two scattering functions can be observed to have distinctly different scattering intensities, with Pt containing samples showing higher intensities across the entire Q range, and particularly in the mid/high Q regimes ($Q>1x10^{-2}$ $\dot{A}^{-1}$). This may be linked to the significantly increased electronic density of Pt, which is found in close proximity to the carbon particles, resulting in an overall stronger scattering from the complex. In particular, this effect is pronounced for HSAC based samples, which may be linked to the presence of Pt inside the carbon support pores, further convoluting the electronic densities of the complex together.

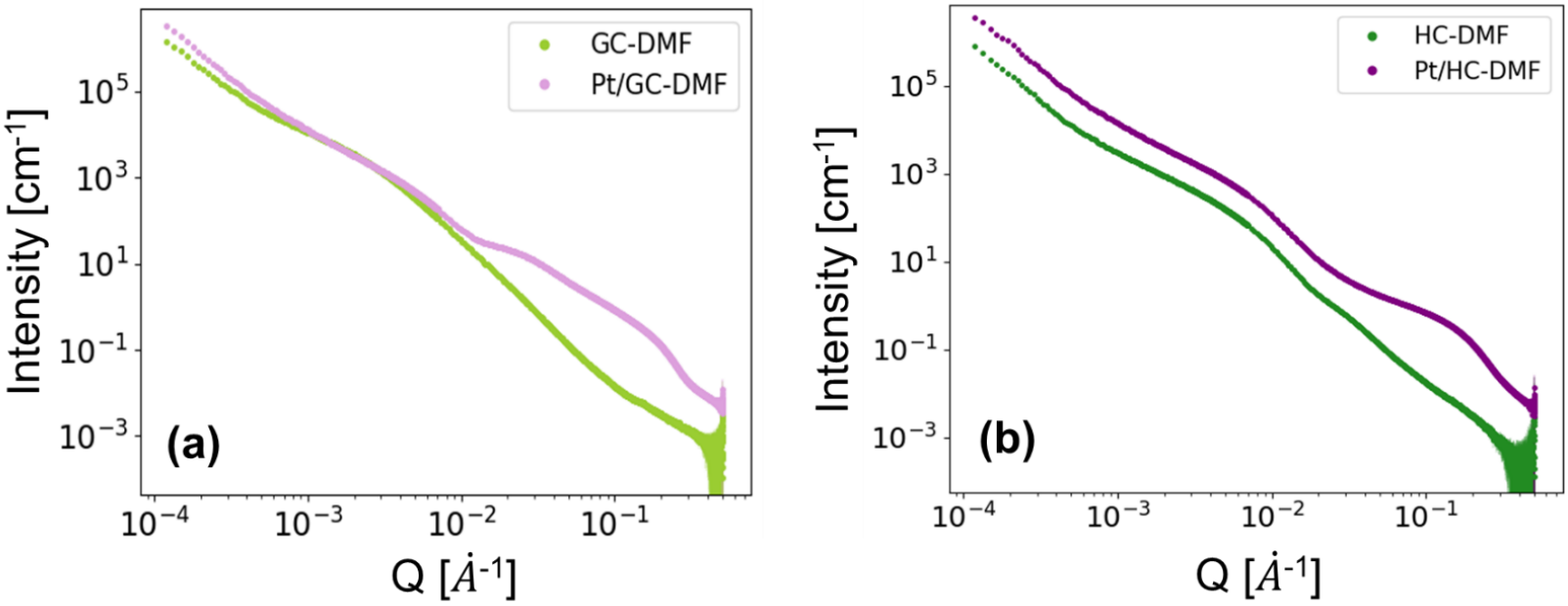


Figure 106. *Comparison of USAXS scattering functions with and without Pt based on* ***(a)*** *graphitized carbon,* ***(b)*** *high surface area carbon, with no ionomer content present. No scaling has been applied to scattering functions.*

Nevertheless, despite intensity variations, the scattering functions remain consistent. In the mid/high Q regimes ($Q>1x10^{-2}$ $\dot{A}^{-1}$) an increased intensity for Pt-containing samples related to the Pt particle structure can be observed. Note the feature is much broader for Pt/GC-DMF than for Pt/HC-DMF, which is consistent with an increased degree of Pt particle agglomeration in the primary particle edge sites of graphitized carbon, resulting in a larger Pt size distribution. On the other hand, the porosity of HSAC acts as a physical blockade for increased Pt particle agglomeration, and the average particle size, as well as the size distribution, remain smaller.

In the low Q regime ($Q<1x10^{-2}$ $\dot{A}^{-1}$) it can be noted that in the case of both GC and HSAC based samples no significant variation in intensity in the low Q regime related to shifting aggregate size is present when Pt is introduced to both carbon types. For HSAC based samples with and without Pt the shape of the scattering functions appears to be near identical. For GC based samples, slightly increased intensity at $Q<5x10^{-3}$ $\dot{A}^{-1}$ can be observed when Pt is introduced, suggesting conversely to expectations, that addition of Pt increased aggregate size. However, it is important to highlight that comparable samples containing the Pt/C complex

only were found not to be very stable previously during SANS experiments, and therefore this is also most likely the case in USAXS. For this reason, the deviation in intensity between GC-DMF and Pt/GC-DMF observed at low Q ($Q<1x10^{-3}$ $\dot{}^{-1}$) may be explained by a potential concentration discrepancy between the two samples. Although no variation in scattering functions was noted across the 10 repeated measurements performed (in a millisecond time frame), settling down of material could have occurred prior to placing the sample in the beam, and the two GC based samples would have to be re-measured to verify whether this difference in intensity observed is reproducible. Despite this, based on the results presented, it can be concluded the presence of Pt has no major impact on carbon (or Pt/C) aggregation.

3.3.3 Effect of increasing ionomer content on aggregate size

In this section the effect of increasing ionomer content in the ink on the carbon aggregate structure will be investigated. For each carbon support and Pt/C complex three different conditions were chosen: no ionomer in sample, little ionomer in sample (I/C = 0.1), and a conventional amount of ionomer (I/C = 0.8). The sample with no ionomer, namely the carbon component dispersion in DMF solvent, will allow for interpretation of structure arising from the type of carbon support itself. Ensuing, it is of interest to evaluate whether significant changes in the aggregate structure can be observed even when only a low ionomer concentration is present (in comparison to the concentration used in conventional catalyst inks). Lastly, the carbon structure in the presence of ionomer concentrations typically found in ionomer inks can be delved into. The I/C ratio of 0.8 chosen will allow for further comparisons to ink compositions studied using CV-SANS.

The structural changes will be discussed for each of the two carbon supports, with and without Pt, before moving to a cross comparison of structural evolution between the different supports/complexes.

3.3.3.1 High surface area carbon (HSAC)

The three sample compositions investigated in this section are:

HC-DMF = 0.002 wt% high surface area carbon in DMF solvent

0.1HNP = 2 wt% high surface area carbon, Nafion D2020 with I/C = 0.1, 50:50 wt% iPrOH/water solvent

0.8HNP = 2 wt% high surface area carbon, Nafion D2020 with I/C = 0.8, 50:50 wt% iPrOH/water solvent

Note the naming convention for ionomer containing sample compositions remains unchanged to inks investigated by CV-SANS (section 2.3.1.1). The HSAC dispersion in DMF has been identified as HC-DMF.

Figure 107 shows scattering functions of HC-DMF, 0.1HNP and 0.8HNP plotted together. Note no scaling of scattering functions has been performed, unless stated otherwise.

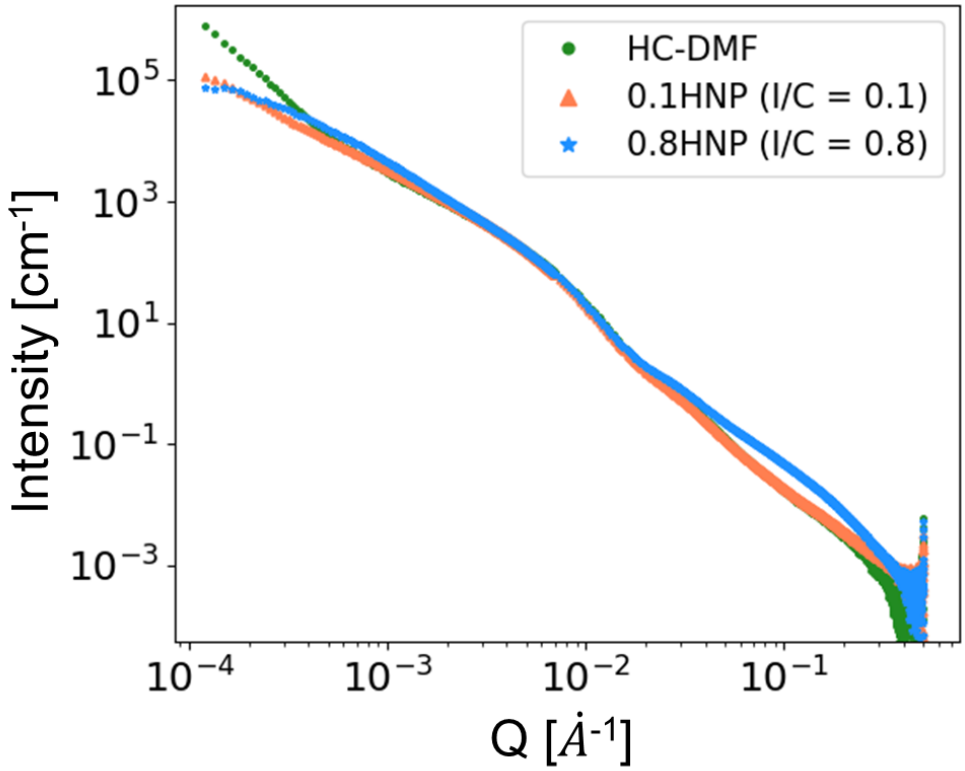


Figure 107. *Comparison of USAXS scattering functions obtained from HSAC based samples with varying ionomer content: no ionomer (HC-DMF, green), I/C = 0.1 (0.1HNP, red), I/C = 0.8 (0.8HNP blue).*

Consistent with expectations, the shoulder feature related to the size of primary particles remains unchanged in the scattering functions of the three samples. However, in the $Q<1x10^{-3}$ $\dot{A}^{-1}$ regime, significant variation can be observed. Firstly, it can be remarked that the intensity of HC-DMF scattering function trends towards much higher intensities, suggesting a much larger aggregate size when no ionomer is present in the sample. For 0.1HNP and 0.8HNP the intensity is much lower and closer together, suggesting even a small amount of ionomer reduces the carbon aggregate size and helps to stabilize the dispersion. Where generally in the low Q regime ($Q<1x10^{-3}$ $\dot{A}^{-1}$) the intensity of 0.8HNP was higher than of 0.1HNP, at approximately $Q = 1x10^{-4}$ $\dot{A}^{-1}$ a cross-over can be observed, where the scattering function of 0.1HNP continues to trend towards higher intensities, while the intensity of 0.8HNP seems to plateau. Additionally, in the mid/high Q regime ($Q>5x10^{-2}$ $\dot{A}^{-1}$), an increased intensity for the 0.8HNP scattering function can clearly be observed. As mentioned before, the scattering functions obtained from USAXS contain information on all the components in the sample, from which it can be deduced the increased intensity arises due to scattering from the ionomer component. Although 0.1HNP contains some ionomer, it is logical to expect the scattering to be much more intense in the case of 0.8HNP, where the volume fraction of Nafion is closer to that of HSAC, than in the case of 0.1HNP, where the Nafion concentration is ten times less than that of HSAC.

Figure 108 presents the three scattering functions plotted separately, with power law scattering analysis.

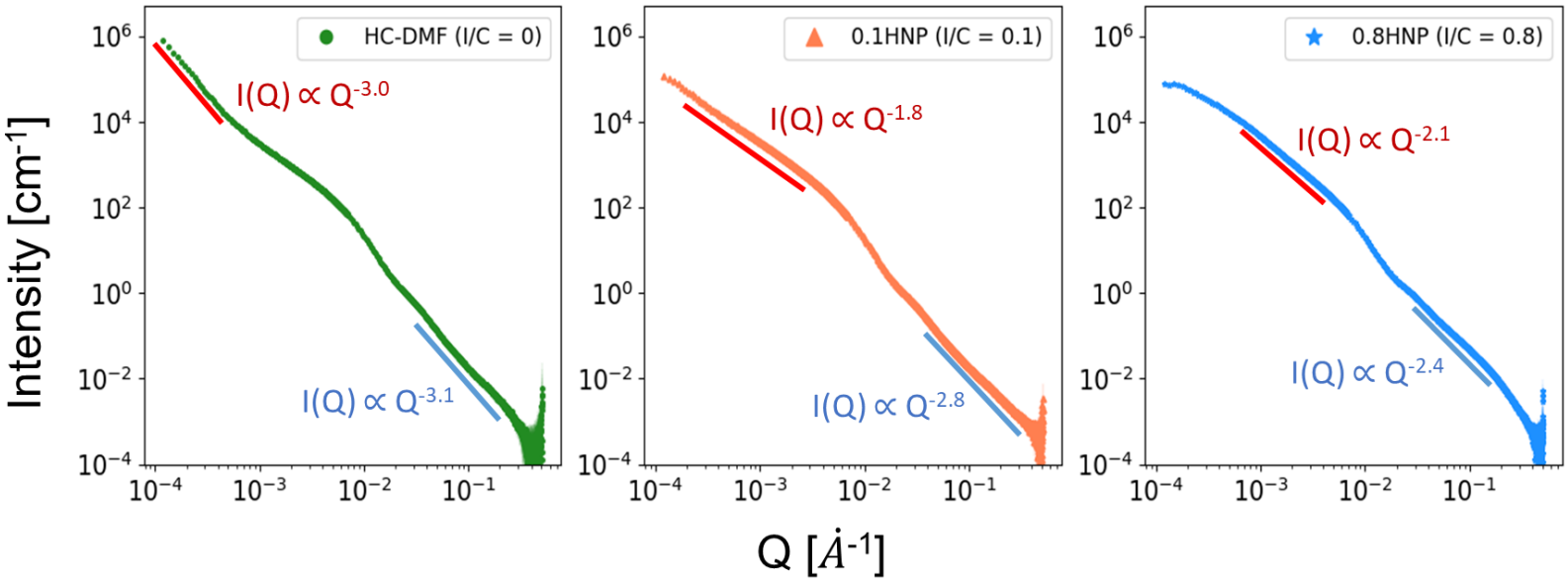


***Figure 108**. Scattering functions obtained using USAXS for HSAC based samples with varying ionomer content: HC-DMF (I/C = 0, green), 0.1HNP (I/C = 0.1, red), 0.8HNP (I/C = 0.8, blue). Power law type scattering is quantified in the low Q regime (red) and in the mid Q regime (blue).*

The contrasting scattering trends in the low Q regime between HC-DMF and 0.1HNP/0.8HNP become evident. Where scattering intensity of HC-DMF continues to trend upwards, for 0.1HNP and 0.8HNP the intensity seems to comparably almost 'level-off'. This observation is quantified by the difference in power law scattering in the low Q regime, with I(Q) Q^{-3} for HC-DMF, and an approximate relation of I(Q) Q^{-2} for 0.1HNP and 0.8HNP. Moreover, the shoulder feature related to the primary particle size is much more pronounced in the case of HC-DMF, and could be referred to as a 'bump'. Indeed, these two distinct types of scattering can be attributed to the structural features of non-fractal and fractal aggregates respectively.

Non-fractal aggregates show scattering behaviour that could be attributed to two spherical objects – a bigger sphere of radius R that is made up of smaller spheres of radius r. The size of the two objects is described by two Guinier shoulders, where after each such feature power law scattering characterizing the surface dimensionality (i.e. surface roughness), D_s, can be observed.

Fractal aggregates do not necessarily possess such a defined shape as a sphere, ellipsoid, cylinder etc., that could be fitted with a specific form factor. For this reason, a shoulder feature associated with such structures is characterized instead by the 'outer cut-off distance', ξ, which is defined as 'the largest distance separating two points inside the fractal'.[119] ξ can therefore be linked to the size of the fractal aggregates. The following power law quantifies the fractal dimension, D_m, where I(Q) Q^{-Dm}. D_m takes values between 1 and 3, and indicates a 1D, 2D or 3D structure. The shoulder feature corresponding to the size of primary

particles, or otherwise 'the inner cut-off distance',[119] along with the power law characterizing the surface dimension of primary particles remain unchanged.

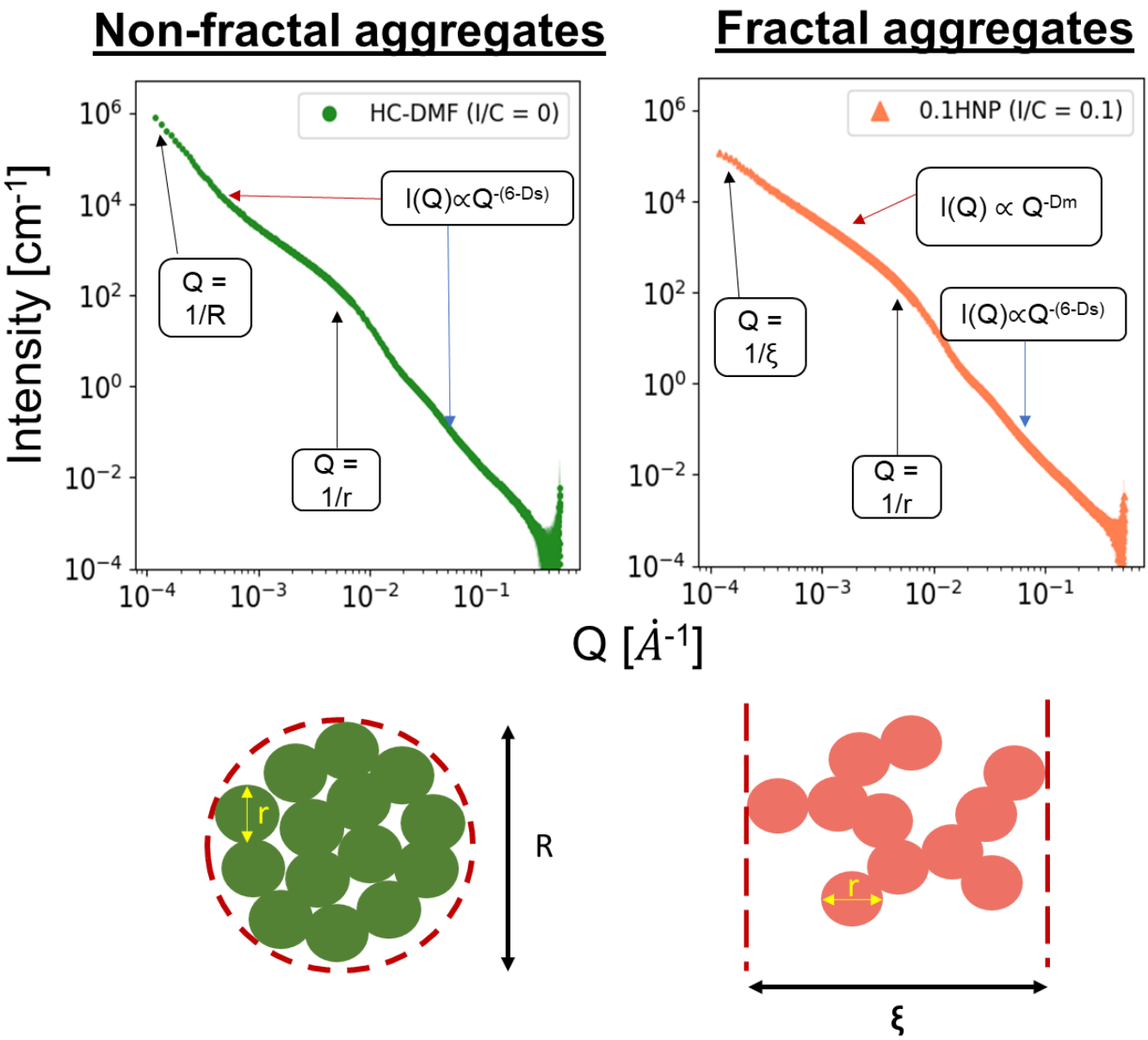


Figure 109. *Schematic of scattering features of non-fractal and fractal aggregates displayed on corresponding examples.* [94,119]

In the case of HC-DMF, and the scattering corresponding to a non-fractal aggregate system, the power law scattering behaviour of I(Q) $Q^{-3.0}$ in the low Q regime ($Q<1x10^{-3}$ $^{-1}$) suggests rough surface aggregates. However, as no Guinier shoulder feature is observable, the size of the aggregates itself cannot be extracted. It can only be deduced that with no ionomer present in the system the carbon particles form very large, non-fractal aggregates.

On the other hand, the mass fractal model (equations *3.3.1 – 3.3.3*)[120] can be used to extract information on the structure of carbon aggregates in 0.1HNP and 0.8HNP:

$$(\ ) = (\ )(\ ) + \qquad (3.3.1)$$

$$( ) = \{\frac{3[\sin( ) - \quad ( )}{( )^3}\}^2 \tag{3.3.2}$$

$$( ) = \frac{\Gamma(\quad -1) \quad ^{-1}}{(1+(\quad)^2)(\quad ^{-1)/2}} \frac{\sin((\quad -1) \quad ^{-1}( ))}{} \tag{3.3.3}$$

Where = volume fraction of carbon aggregates, *P(Q)*= form factor, *S(Q)*= structure factor, *r* = radius of primary particles ( ), D_m = mass fractal dimension, ξ = fractal cut-off length ( )

Figure 110 presents 0.1HNP and 0.8HNP scattering functions fitted using the mass fractal model.

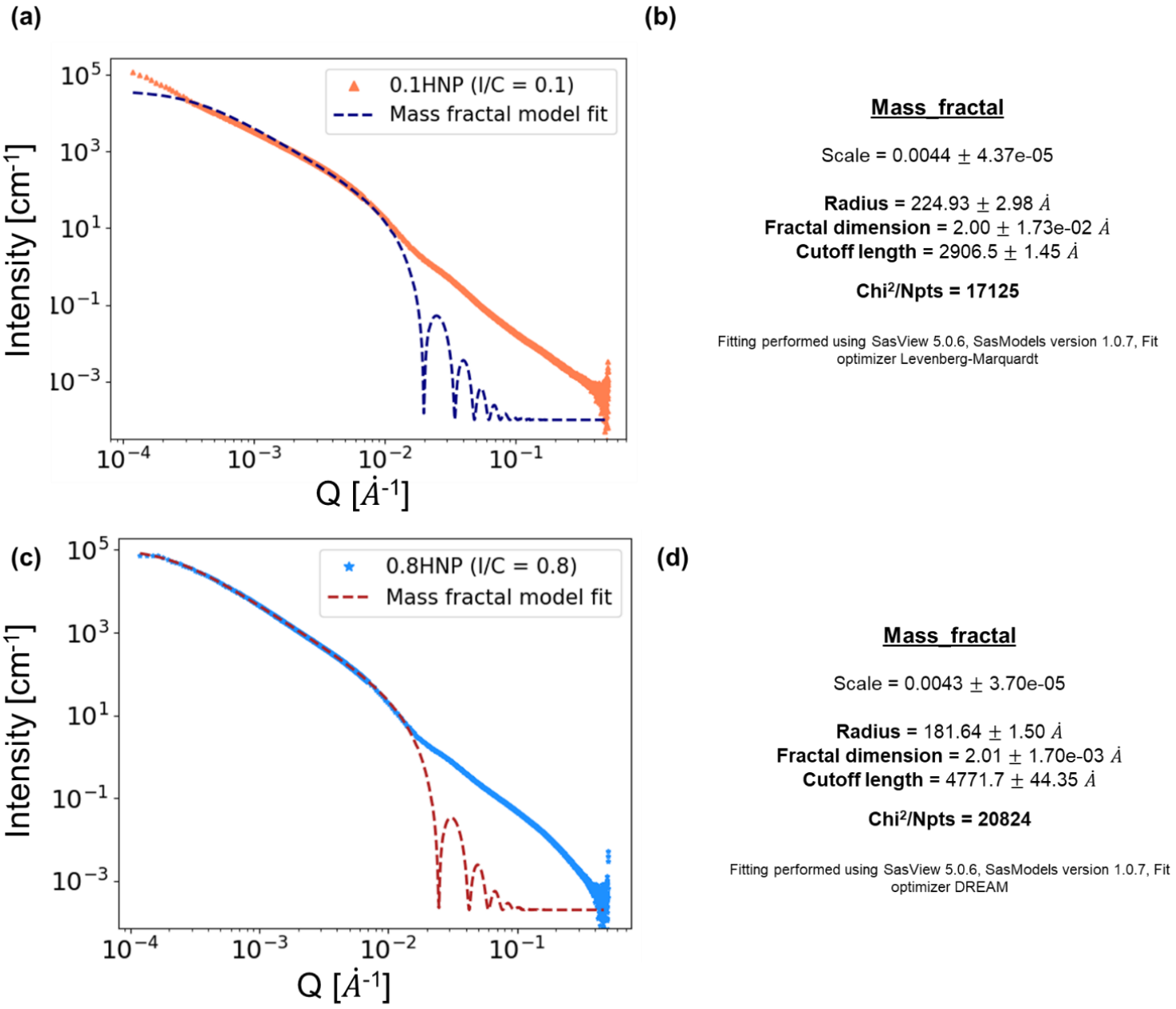


Figure 110. (a) *USAXS scattering function of 0.1HNP fitted with a mass fractal model,* ***(b)*** *parameters extracted from fitting,* ***(c)*** *USAXS scattering function of 0.8HNP fitted with a mass fractal model,* ***(d)*** *parameters extracted from fitting.*

In both cases the chi^2 values extracted are very large, and arise from the lack of conformity of the fit in the mid Q ($Q>1x10^{-2}$ $\dot{}^{-1}$) regime onwards. Nevertheless, in the case of 0.8HNP (figure 110c, d), a very good agreement is reached between the data and model in the low/mid Q regimes ($Q<1x10^{-2}$ $\dot{}^{-1}$). The plateauing intensity at $Q \approx 1x10^{-4}$ $\dot{}^{-1}$ can be correlated to the commencement of a feature related to the cut-off length, for which the value extracted of 477 nm is consistent with the expected size of carbon aggregates. The radius of 18.2 nm is consistent with the size of primary particles (although lower than previously extracted value from CV-SANS), and the fractal dimension of 2 suggests a 2D fractal structure.

On the other hand, a suitable fit could not be achieved in the case of 0.1HNP. Around $Q = 4x10^{-4}$ $\dot{}^{-1}$ the fitting suggests a plateauing intensity, resulting in a cut-off length of 291 nm extracted. However, in this Q range the scattering function intensity keeps trending upwards. Nevertheless, this discrepancy can't be interpreted as a non-fractal aggregate structure due to the I(Q) Q^{-2} power law scattering that is observed, and the clear variation in scattering function shape between HC-DMF and 0.1HNP. Therefore, it can be concluded that fractal aggregates are formed even with smaller ionomer content, however the cut-off length is higher, and cannot be properly characterized with the available Q-range through fitting of data. Note a fit using a mass fractal + power law combination model was attempted for 0.1HNP, however, even just 1% proportion of the power law model resulted in an inconsistent fit for the low/mid Q regimes (appendix 32).

In conclusion, scattering functions of HSAC based samples using USAXS suggest addition of ionomer alters the size of carbon aggregates. Moreover, the data of 0.002 wt% HSAC in DMF, HC-DMF, showed scattering consistent with non-fractal aggregates. On the other hand, the scattering functions of 2 wt% HSAC based samples in 50:50 wt% iPrOH/water solvent, with Nafion I/C = 0.1 and 0.8 respectively, could be identified as fractal aggregates. The size of the fractal aggregates, characterized by the cut-off length, could be seen to decrease with increasing ionomer content. The fractal aggregates are consistent with TEM images presented in figure 54c, d, as well as with observations previously made in literature. Khandavalli et al.[25] noted a yield stress exhibited in rheological measurements of a 1.5 wt% HSAC based ink, which suggested the formation of a percolated aggregate network. However, this observation was not made when HSAC concentration was 0.75 wt%. This concentration related effect is interesting, and sheds doubt on whether the addition of ionomer is responsible for the shift from non-fractal to fractal aggregate conformation.

In order to achieve a stable carbon dispersion, 0.002 wt% HSAC was dispersed in DMF. On the other hand, ionomer containing samples contained 2 wt% HSAC and were based on a 50:50 wt% iPrOH/water solvent, similar to ink compositions studied by CV-SANS. Therefore, it can be argued the samples are too different to compare, both in terms of the concentration, that could introduce changes in aggregation as showed by Khandavalli et al.[25], and the solvent system. Because of this, the carbon or Pt/C dispersions in DMF will not be further compared to ionomer containing, higher concentration samples. USAXS measurements of ionomer containing samples based on a 0.002 wt% HSAC concentration and DMF solvent system would be necessary to make this comparison with confidence.

From the ionomer containing samples investigated it can simply be concluded that an increase in ionomer content results in a decreasing fractal aggregate size. However, the magnitude of Q utilized in the USAXS measurements was not low enough to capture a plateau arising from the fractal cut-off length for the low Nafion content sample 0.1HNP, which impeded fitting of data. For this reason, additional use of other methods which capture information on a larger size scale, such as TEM, may also prove necessary for further investigation of carbon aggregation behaviour.

3.3.3.2 High surface area carbon and platinum (Pt/HSAC)

Section 2.3.3 showed that the addition of Pt into HSAC based ink compositions did not affect the carbon primary particle structure, concluded by a lack of change observed in the S_{cc} output. However, the evaluation of the aggregate structure was not possible with the Q range obtained ($2.5x10^{-3}$ – $6.4x10^{-1}$ $\dot{}^{-1}$). Moreover, Khandavalli et al.[25] noted HSAC-only and Pt/HSAC systems showed contrasting rheological behaviours in the presence of increasing ionomer content. For this reason, ink compositions with varying ionomer content, based on the Pt/HSAC complex, were also investigated. The two sample compositions explored in this section are:

0.1PtHNP = 2 wt% high surface area carbon + **2 wt% Pt**, Nafion D2020 with I/C = 0.1, 50:50 wt% iPrOH/water solvent

0.8PtHNP = 2 wt% high surface area carbon **2 wt% Pt**, Nafion D2020 with I/C = 0.8, 50:50 wt% iPrOH/water solvent

Figure 111 shows scattering functions obtained for the two compositions plotted together.

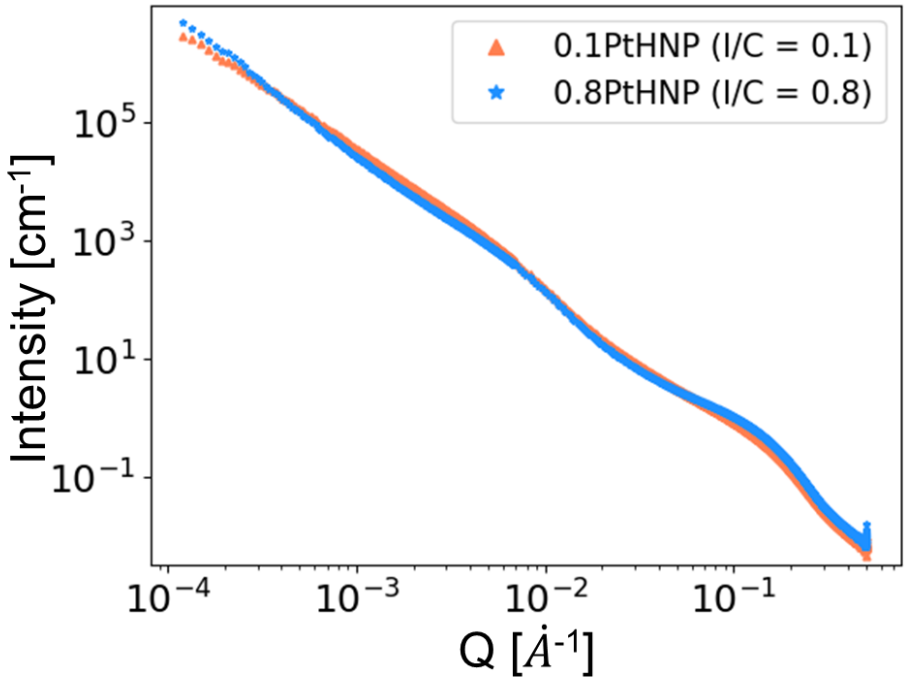


Figure 111 *Comparison of USAXS scattering functions obtained from Pt/HSAC based samples with varying ionomer content: I/C = 0.1 (0.1PtHNP, red), I/C = 0.8 (0.8PtHNP, blue).*

Indeed, a different behaviour can be observed in comparison to HSAC-only based samples. Again the shoulder feature related to primary particle size remains consistent, however, at Q ≈ $1x10^{-4}$ $\dot{}^{-1}$ an increasing intensity with ionomer content can be observed. Note the overall intensity is also higher than for HSAC-only based samples, due to increased electronic density of Pt particles. In the high Q regime (Q > $1x10^{-1}$ $\dot{}^{-1}$) a new peak feature can be observed, with no significant increase in intensity with increasing ionomer content. This is because the feature is attributed to the Pt nanoparticles themselves, and as Pt has a much greater electron density than Nafion, scattering related to the latter is masked in the presence of the former.

Figure 112 presents the two scattering functions plotted alongside each other, with quantification of power law behaviour in the low Q regime.

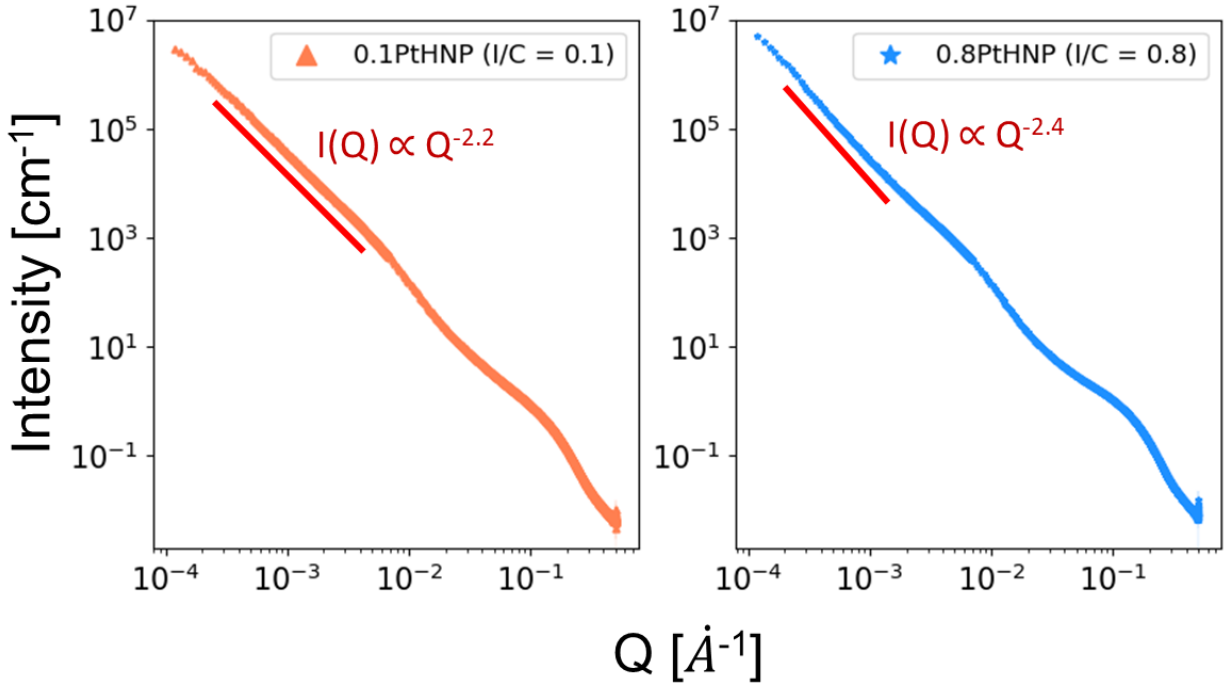


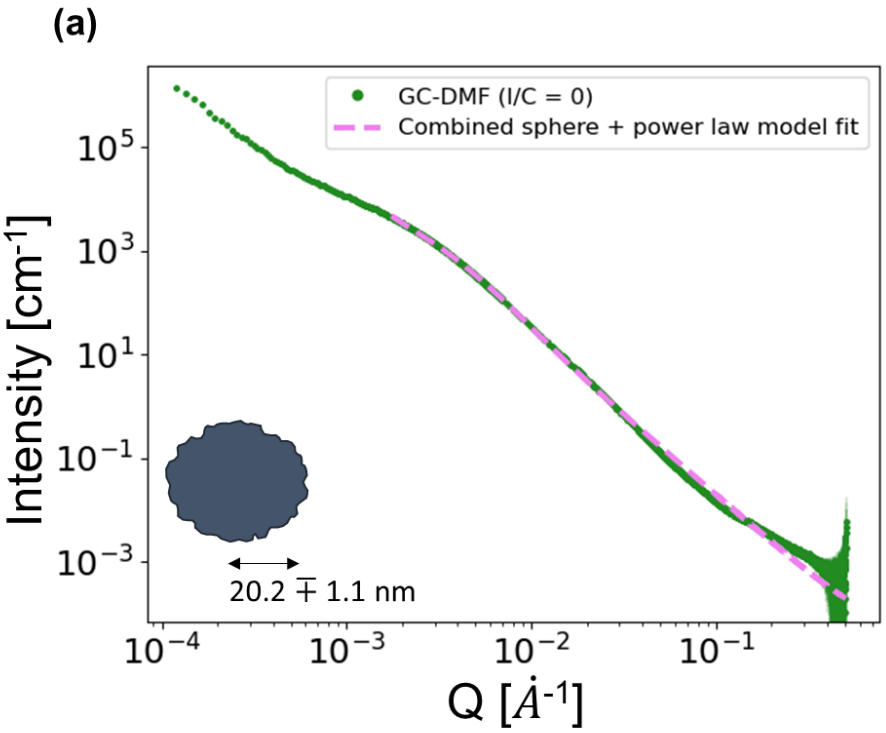
Figure 112. *Scattering functions obtained using USAXS for HSAC based samples with varying ionomer content: 0.1PtHNP (I/C = 0.1, red), 0.8PtHNP (I/C = 0.8, blue). Power law type scattering is quantified in the low Q regime (red).*

The shape of both the 0.1PtHNP and 0.8PtHNP scattering functions is again indicative of fractal aggregates, with D_m values of 2.2 and 2.4 respectively suggesting two-dimensional fractal aggregates. Just like in the case of 0.1HNP no plateau behaviour of scattering intensity can be observed at Q = 1x10^{-4} Å^{-1}, suggesting a large cut-off length for fractal aggregates (that cannot be reliably extracted from a mass fractal model fit). Khandavalli et al.[25] used rheology to investigate the carbon aggregate structure in HSAC based inks with and without Pt, and with increasing ionomer content. The study found that increasing ionomer content in HSAC only compositions up to a critical value decreased the ink viscosity due to electrostatic stabilization of carbon aggregates. However, in the case of Pt/HSAC based compositions, increasing ionomer content led to a contrasting behaviour of increasing ink viscosity, which was attributed to flocculation of carbon aggregates. The flocculation behaviour can be interpreted as an increase in the size of the fractals, and may explain the increasing intensity in the low Q regime for 0.1PtHNP and 0.8PtHNP.

3.3.3.3 Graphitized carbon (GC)

In section 2.3.3.1 the structure of graphitized carbon (GC) was briefly investigated, however, due to the void space inaccessible to solvent molecules in the primary particle structure, GC proved incompatible with the CV-SANS method. On the other hand, some primary particle related features could be observed in SANS data of Pt/GC based catalyst layers, therefore it is most probable the GC structure in the ink suggested by the corresponding S_{cc} output was incorrect. However, where for SANS measurements of catalyst layers a shorter Q range was opted for (Q = 0.013 – 0.7 Å^{-1}), not covering sufficient Q magnitude for primary particle characterization, USAXS can be utilized for this purpose. Indeed, the size of the primary particles themselves can be extracted utilizing the same combined sphere + power law model as for HSAC (figure 58). The GC-DMF sample is the most suitable for this evaluation, as it is based on the carbon component only (although fitting of 0.1GNP should yield identical results). Note only the Q range

of 2.5x10^{-3} – 5.0x10^{-1} Å^{-1}, comparable to that obtained in CV-SANS experiments, will be used. This is because the models utilized in the combination are both applied to data points across the entire Q range , and the additional alteration in power law observed in the low Q regime (Q<1x10^{-3} Å^{-1}) would hinder extraction of veritable results. Figure 113 presents the fitting results for the GC-DMF scattering function



(b)

Sphere+power_law

Scale = 3.69e-04 ± 2.16e-05

Sphere_scale = 0.95 ± 1.20e-02
Sphere_sld = 17.0x10^{10} cm^{-2}
Solvent_sld = 8.78x10^{10} cm^{-2}
Radius = 201.98 ± 11.37 Å

Distribution of radius = 0.52 ± 2.88e-02
(function: lognormal)

Power_law_scale = 0.05 ± 1.20e-02
Power = 3.00 ± 0.07

Chi^2/Npts = 7.36e+05

Fitting performed using SasView 5.0.6, SasModels version 1.0.7, Fit optimizer DREAM

Figure 113. (a) *Scattering function of GC-DMF sample, fitted with the sphere + power_law model in Q range = 2.5x10^{-3} – 5.0x10^{-1} Å^{-1}.* ***(b)*** *Parameters extracted from fitting. The sphere and solvent SLDs of 17 and 8.78 x10^{10} cm^{-2} respectively consider GC and DMF specific SLD values associated with X-rays of 1 Å wavelength. These value were obtained using the SLD calculator tool available in SasView 5.0.6.*

and the combined sphere + power law model.

Visually a fairly good fit is obtained, however the chi^2 value is very high at 7.36e+05, which may relate to the very low error bars present in USAXS data as well as a deviation between the scattering function and model fit in the mid/high Q regimes (Q>4x10^{-2} Å^{-1}). The reason for this deviation may stem from a slight alteration in scattering behaviour in the high Q regime (Q>1x10^{-1} Å^{-1}). Nevertheless, the radius value of 20.2 nm obtained from the fit is consistent with the expected size of GC primary particles. The extracted radius polydispersity value of 0.52 is much higher than the value of 0.36 obtained for HSAC primary particles (figure 58), however, note that unlike in the case of HSAC, the scattering function of GC does not show an additional, distinct shoulder feature related to the primary particle polydispersity. This observation is consistent with the higher polydispersity value obtained.

Furthermore, the effect of ionomer content on GC aggregation will be investigated, utilizing the following sample compositions:

0.1GNP = 2 wt% graphitized carbon, Nafion D2020 with I/C = 0.1, 50:50 wt% iPrOH/water solvent

0.8GNP = 2 wt% graphitized carbon, Nafion D2020 with I/C = 0.8, 50:50 wt% iPrOH/water solvent

Figure 114. shows scattering functions of the two varying composition samples obtained using USAXS plotted together.

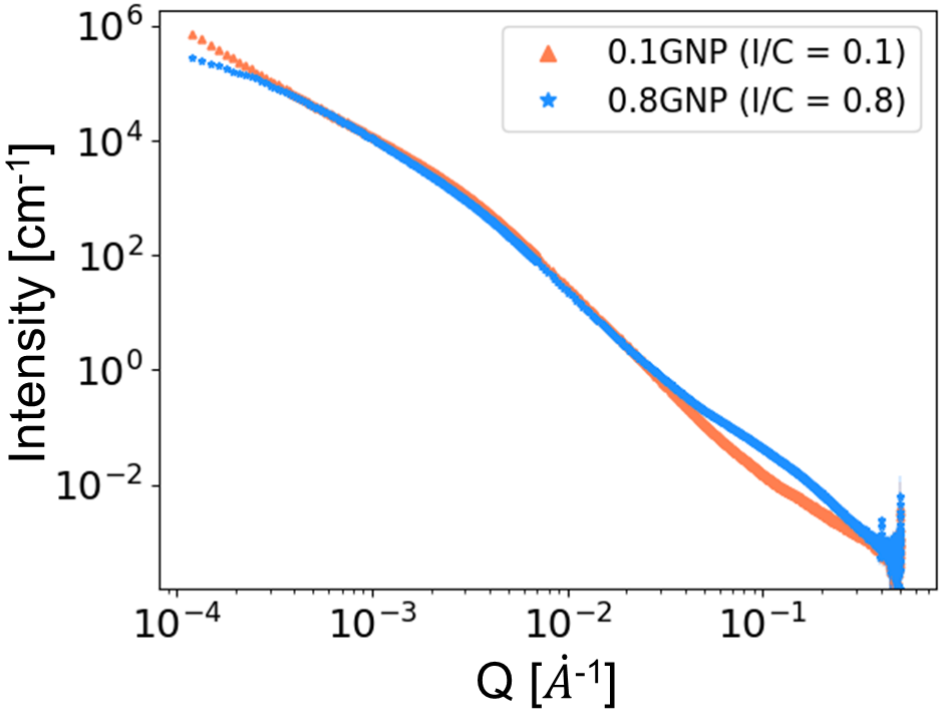


Figure 114. *Comparison of USAXS scattering functions obtained from GC based samples with varying ionomer content: I/C = 0.1 (0.1GNP, red), I/C = 0.8 (0.8GNP blue).*

Indeed, each scattering function obtained by USAXS shows a Guinier shoulder feature related to the size of carbon primary particles, that remains unchanged with increasing ionomer content. In addition, similar behaviour with increasing ionomer content to HSAC based inks can be observed – in the Q = $1x10^{-4}$ $Å^{-1}$ region scattering intensity decreases for compositions with increasing ionomer content, suggesting a reduced aggregate size. In the high Q regime (Q>$1x10^{-1}$ $Å^{-1}$) the scattering function 0.8GNP shows increased intensity associated with scattering from the Nafion component.

Figure 115 shows the scattering functions plotted alongside each other, with quantification of power law type scattering.

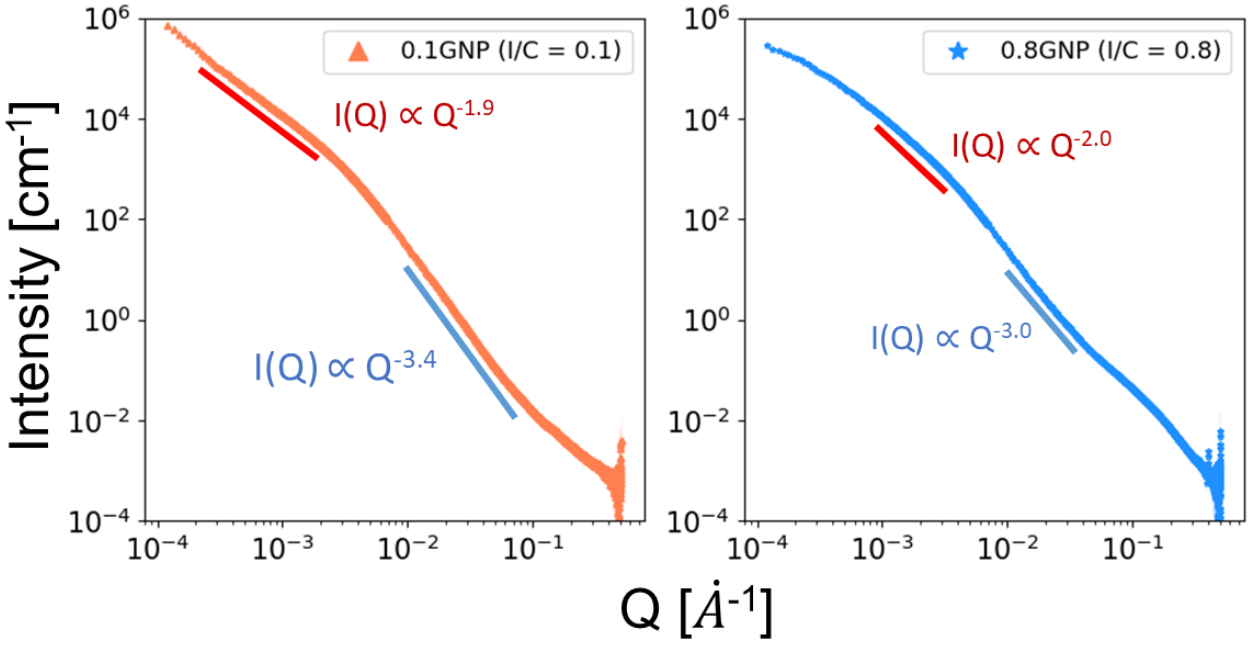


Figure 115. *Scattering functions obtained using USAXS for GC based samples with varying ionomer content: 0.1GNP (I/C = 0.1, red), 0.8GNP (I/C = 0.8, blue). Power law type scattering is quantified in the low Q regime (red) and in the mid Q regime (blue).*

Once more, the general scattering function shape, as well as the power law behaviours quantified in the low Q regime suggest a fractal aggregate structure of a 2D dimensionality in both cases. However, the power law scattering behaviour in the mid/high Q regimes ($Q>1x10^{-2}$ $\dot{}^{-1}$) varies, with I(Q) $Q^{-3.4}$ behaviour observed for 0.1GNP, and I(Q) $Q^{-3.0}$ for 0.8GNP. This variation most likely arises due to the presence of Nafion related scattering in the mid/high Q regime ($Q>5x10^{-2}$ $\dot{}^{-1}$), which may also convolute with the power law scattering arising from primary particle interfaces. For this reason, interpretation of the primary particle structure remains more accurate from scattering functions of samples with low/no ionomer content.

As was the case for 0.1HNP, the scattering function of 0.1GNP shows consistently increasing scattering intensity at $Q = 1x10^{-4}$ $\dot{}^{-1}$, which renders cut-off length size extraction from the mass fractal model unreliable. On the other hand, the scattering function of 0.8GNP shows a progressively plateauing intensity at this Q value and may be suitable for fitting. Figure 116 shows fitting of 0.8GNP scattering function fitted with the mass fractal model.

Just like in the case of 0.8HNP (figure 110c, d) the mass fractal model provides a good fit to the low/mid Q regime, however the chi^2 value of the fit remains very high. Nevertheless, the radius value extracted of 20.7 nm is very consistent with the primary particle radius obtained from the sphere + power law model (figure 113), and the fractal dimension of 2.1 is well representative of the 2D fractal aggregates suggested by quantification of power law behaviour in the low Q regime (figure 115). The cut-off length of 583 nm suggests the presence of larger fractal aggregates in GC based inks in comparison to HSAC based inks, where a cut-off length of 477 nm was extracted for a sample with the same ionomer content.

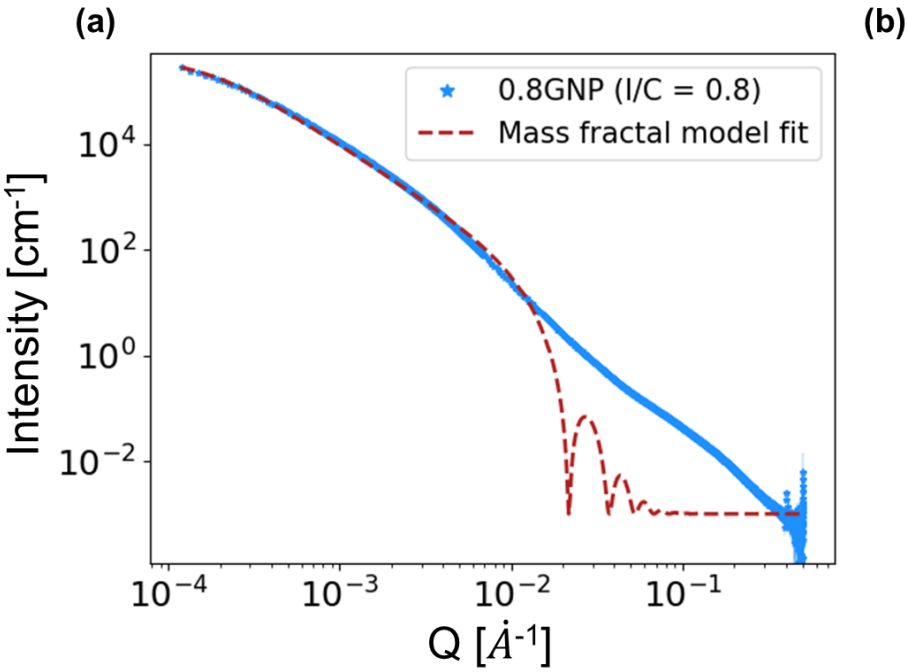


Figure 116. (a) *USAXS scattering function of 0.8GNP fitted with a mass fractal model,* ***(b)*** *parameters extracted from fitting.*

In summary, comparison of GC based samples with varying ionomer content showed a decreasing aggregate size with increasing ionomer content, and both scattering functions are indicative of a fractal aggregate structure. These observations remain unchanged between HSAC and GC based samples.

Additionally, in the scattering functions obtained by USAXS a shoulder feature related to the primary particle size could be clearly observed. The scattering function of the GC-DMF sample was fitted with the combined sphere + power law model. Despite a variation in the mid/high Q regime ($Q>0.4x10^{-2}$ - $^{-1}$) between the model fit and the scattering function, a primary particle size of 20.2 nm could be extracted, consistent with the expected size range. The successful primary particle size extraction further demonstrates the power of using neutron and X-ray scattering in tandem.

3.3.3.4 Graphitized carbon and platinum (Pt/GC)

As GC based inks proved incompatible with the CV-SANS method (section 2.3.3), the effect of Pt addition on the ink structure in these ink compositions was not investigated at all. It is known the Pt distribution on HSAC and GC supports is very different, arising due to the inherent differences between the two (section 2.3.2). It was already observed that Pt/HSAC based samples show a contrasting behaviour of increasing aggregate size with increasing ionomer content in comparison to samples containing HSAC-only. Analysing Pt/GC based compositions will aid in determining whether this behaviour is related to the presence of Pt itself, or the distribution of Pt specific to the HSAC support. The sample compositions used in this investigation were:

0.1PtGNP = 2 wt% graphitized carbon + **2 wt% Pt**, Nafion D2020 with I/C = 0.1, 50:50 wt% iPrOH/water solvent

0.8PtGNP = 2 wt% graphitized carbon **2 wt% Pt**, Nafion D2020 with I/C = 0.8, 50:50 wt% iPrOH/water solvent

Figure 117 presents scattering functions of the above mentioned samples plotted together.

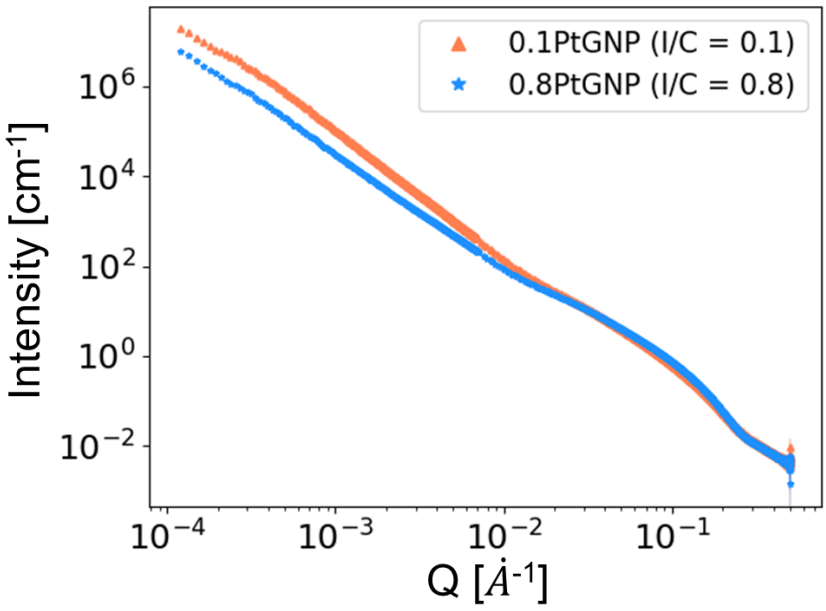


Figure 117. *Comparison of USAXS scattering functions obtained from Pt/GC based samples with varying ionomer content: I/C = 0.1 (0.1PtGNP, red), I/C = 0.8 (0.8PtGNP, blue).*

The most notable difference can be observed in the low/mid Q regime ($Q<1x10^{-2}$ $\dot{A}^{-1}$) where the scattering function of 0.1PtGNP shows a significantly higher intensity than 0.8PtGNP. Moreover, this intensity deviation also falls in the Q magnitude region where a shoulder feature from primary particles is expected, which in both cases is not clearly visible. In previous samples the scattering feature of primary particles was always reproducible, even when comparing the low concentration HC-DMF to 0.1HNP and 0.8HNP (section 3.3.3.1). For this reason, scattering functions of 0.1PtGNP and 0.8PtGNP were compared to the low concentration Pt/GC-DMF:

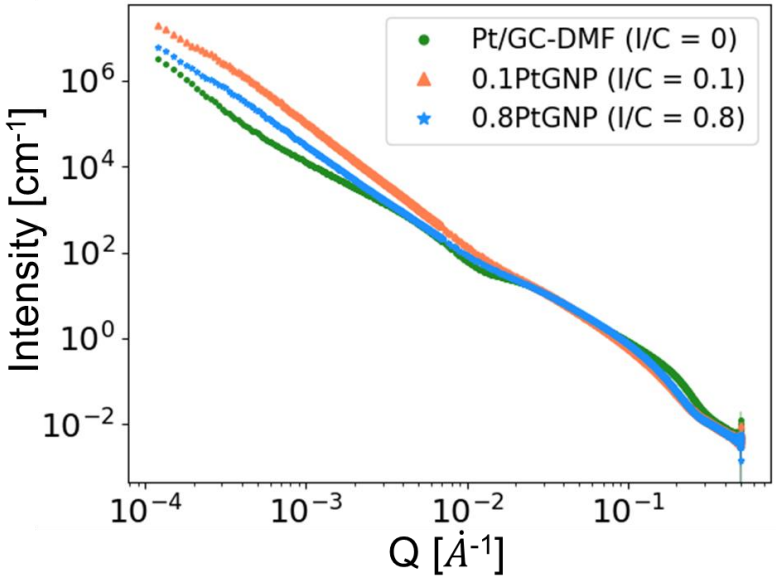


Figure 118. *Comparison of USAXS scattering functions obtained from Pt/GC based samples with varying ionomer content: I/C = 0 (Pt/GC-DMF, green), I/C = 0.1 (0.1PtGNP, red), I/C = 0.8 (0.8PtGNP, blue).*

It can be observed that although the primary particles related shoulder remains indistinguishable, the scattering intensity of 0.8PtGNP in the feature region remains similar to Pt/GC-DMF. On the other hand, the large deviation in scattering intensity observed for 0.1PtGNP, in particular with regards to the primary particle region, suggest either a great change in the carbon structure, or an erroneous scattering function, of which the latter is more probable. It is possible that either an error arose during sample preparation, or the sample was not sufficiently stable throughout the measurement. Therefore, the scattering function of 0.1PtGNP presented in figures 117 and 118 will be considered an outlier, and should be re-prepared and measured again for structural evaluation purposes.

For 0.8PtGNP a steady intensity increase at $Q \approx 1x10^{-4}$ $^{-1}$ suggests a growth in aggregate size on addition of ionomer, just like in the case of Pt/HSAC based samples. Therefore, the flocculation behaviour discussed above may arise due to the presence of Pt itself. The power law scattering behaviour of $I(Q)$ $Q^{-2.5}$ quantified for 0.8PtGNP remains consistent with two dimensional fractal aggregates.

In summary, investigation of effect of ionomer content on aggregates size for Pt/GC based samples was attempted for ionomer containing samples 0.1PtGNP and 0.8PtGNP, yet a lack of primary particle related feature, as well as varying intensity in the corresponding Q region, suggested an issue with the obtained scattering functions. By comparing the two to scattering from the low concentration Pt/GC-DMF sample, where a shoulder feature related to the primary particles could be clearly observed, it was revealed the intensity of 0.8PtGNP was more similar to the scattering function of the low concentration sample, and it was the intensity of 0.1PtGNP that was unusually high. For this reason, the latter was considered an outlier, and the sample should be re-prepared for an in-depth comparison. Nevertheless, the reason as to why the primary particle feature is not observable in 0.8PtGNP remains unclear, as the structure of the primary particle itself has not been observed to change in any other case, and it may be worthwhile to re-measure this sample also. Despite this, steadily increasing intensity at $Q \approx 1x10^{-4}$ $^{-1}$ suggests an increase in aggregate size in the presence of Pt and ionomer, indicating the flocculation effect previously discussed for Pt/HSAC samples may be related to the presence of Pt in general rather than its distribution on the carbon support.

3.3.5 Comparison of carbon supports, with and without Pt

With regards to the effect of varying ionomer content on aggregate structure, it was shown that for samples based on a carbon support only, increasing ionomer content resulted in decreasing aggregate size. On the other hand, in Pt/C based samples aggregate size increased with ionomer content, which was attributed to a flocculation effect. The size of fractal aggregates was estimated for the carbon support only samples 0.8HNP and 0.8GNP using a mass fractal model fit, with values of 477 and 583 nm extracted respectively, suggesting generally bigger aggregates in GC-based samples. However, a visual comparison of corresponding GC and HSAC based samples, with and without Pt may provide more information on variation in carbon aggregation between the two different carbon supports. Figure 119 shows scattering functions of GC and HSAC, as well as Pt/GC and Pt/HSAC based samples with corresponding ionomer content plotted together.

In the case of samples containing the carbon support only, either HSAC or GC, it can be remarked that the scattering intensity in the mid/low Q regimes ($Q<1x10^{-2}$ $^{-1}$) is higher for GC based samples, irrelevant of the ionomer content. Therefore, it can be deduced that the use of GC support results in generally bigger carbon aggregates.

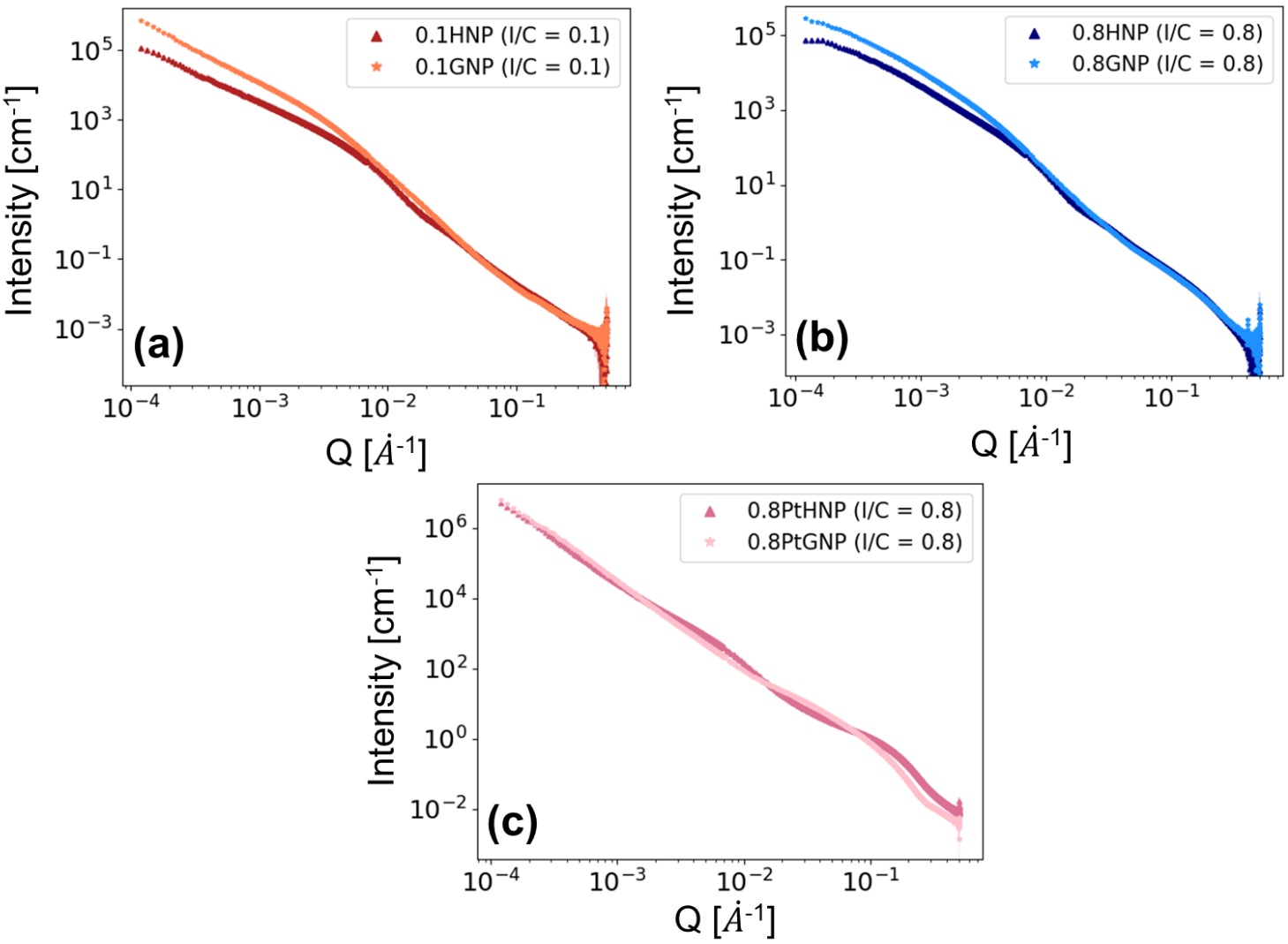


Figure 119. *Comparison of USAXS scattering functions of samples with corresponding ionomer content, based on different carbon supports:* ***(a)*** *carbon support only in 50:50 wt% iPrOH/water (I/C = 0.1),* ***(c)*** *carbon support only in 50:50 wt% iPrOH/water (I/C = 0.8),* ***(d)*** *Pt/C complex in 50:50 wt% iPrOH/water (I/C = 0.8).*

On the other hand, in the case of Pt containing samples, it was noted addition of ionomer results in increasing aggregates size. Interestingly, when comparing Pt/HSAC and Pt/GC based samples containing Nafion with I/C = 0.8 (0.8PtHNP/0.8PtGNP), figure 95c, no apparent variation in intensity at Q ≈ $1x10^{-4}$ $Å^{-1}$ can be observed. This suggests that, unlike in the case of samples based on the carbon support only, variation in Pt/C complex used results in a comparable size of carbon aggregates. However, note the primary particle feature is not well expressed in 0.8PtGNP, for which the reason remains unclear, and such a variation may alter the resulting low Q intensity. For this reason, 0.8PtGNP sample should also be re-made and measured, to verify whether this phenomenon is consistent.

3.4 Conclusions

In conclusion, USAXS was successfully employed for investigation of carbon structure variation as a function of Pt presence and increasing ionomer content.

Comparing carbon and Pt/C dispersions in DMF based on the same carbon support revealed introduction of Pt into the system had little to no impact on the aggregate size.

Furthermore, scattering functions of low concentration carbon or Pt/C component dispersion in DMF showed scattering consistent with non-fractal aggregates, while ionomer containing inks, with compositions similar to the samples investigated by CV-SANS showed scattering typical of fractal aggregates. Because of the very different compositions, with regards to concentration, solvent, and ionomer content, the specific reason for the shift in aggregate conformation could not be established. In order to reach this deduction, low concentration, DMF based samples, containing ionomer should be investigated, which can be compared to the carbon or Pt/C only dispersions.

With respect to variation in ionomer content, for carbon support-only based samples it was found that increasing ionomer content results in smaller carbon aggregates, however with GC based compositions showing generally larger fractal aggregates than those based on HSAC. Aggregate sizes for compositions with Nafion I/C = 0.8 were quantified at 583 and 477 nm for GC and HSAC based samples through fitting with the mass fractal model.

For Pt/C based samples, conversely to C-only compositions, it was found that increasing ionomer content resulted in a size increase of carbon aggregates, which can be attributed to a flocculation effect. This phenomenon was previously proposed by Khandavalli et al.[25], who found that samples based on Pt/HSAC showed increasing viscosities with ionomer content, an observation that was not made in the case of HSAC-only samples. Such a significant change in aggregation behaviour in the presence of Pt may be suggestive of ionomer-Pt interactions in the ink system. Nevertheless, note a similar observation was not noted by Li et al.[53], who investigated rheological behaviour of Pt/GC based inks with varying ionomer content, noting decreasing viscosities with increasing ionomer concentrations in the ink.

Moreover, this observation is somewhat inconsistent with the CV-SANS and PSF output results obtained for 0.8PtHNP, which suggested no ionomer adsorption to the Pt/C surface due to a lack of S_{cp} output extracted. However, note this may be a limitation of the CV-SANS technique, where it is possible the similar SLDs of carbon and Pt, as well as low volume fractions of the latter, hinder the extraction of ionomer-Pt interactions. The varying behaviour observed between literature and the USAXS results, along with the uncertainty in interpretation of CV-SANS data suggest the effect must be investigated further.

On the other hand, the ability to visualize carbon aggregate structure, as well as to obtain information on graphitized carbon based compositions, which proved highly arduous by SANS, show how SAXS and SANS can be utilized in tandem in order to extract a more complete picture of the catalyst ink system. Indeed, it is highly likely X-ray scattering could be exploited further to gain more information on the above mentioned Pt-ionomer interactions themselves, as well as on the effect of various variables (e.g. iPrOH concentration or ionomer type) on the larger aggregates structure.

4 Isothermal Titration Calorimetry (ITC)

In this chapter ITC will be investigated as a supporting technique to characterizing ionomer adsorption behaviour on different carbon supports, with and without Pt.

Section 4.1 presents the general theory behind ITC and describes the general experiment protocol, with links made to the titration of ionomer to carbon specifically.

Section 4.2 defines the methodology specific to ITC measurements carried out in the scope of this work.

Section 4.3 contains results obtained from ITC. Firstly, titration of Nafion into carbon-only samples is discussed, followed by titration of Nafion into Pt/C samples.

Section 4.4 summarizes conclusion drawn based on results and discussion presented in section 4.3.

Isothermal titration calorimetry (ITC) is a high-resolution method used to study the thermodynamics of interaction of components in a solvent based system.[121] Just the definition provides insight into the usefulness of this method applied to catalyst ink systems – to investigate ionomer adsorption to the carbon or Pt/C component.

Dans ce chapitre, l'ITC sera étudiée comme technique de soutien à la caractérisation du comportement d'adsorption des ionomères sur différents supports de carbone, avec et sans Pt.

*La **section 4.1** présente la théorie générale derrière l'ITC et décrit le protocole expérimental général, avec des liens établis spécifiquement avec le titrage de l'ionomère sur le carbone.*

*La **section 4.2** définit la méthodologie spécifique aux mesures ITC réalisées dans le cadre de ce travail.*

*La **section 4.3** contient les résultats obtenus par ITC. Tout d'abord, le titrage du Nafion dans des échantillons contenant uniquement du carbone est abordé, suivi du titrage du Nafion dans des échantillons Pt/C.*

*La **section 4.4** résume les conclusions tirées sur la base des résultats et de la discussion présentés dans la section 4.3.*

La calorimétrie de titration isotherme (ITC) est une méthode à haute résolution utilisée pour étudier la thermodynamique de l'interaction des composants dans un système à base de solvant.[121] La définition elle-même donne un aperçu de l'utilité de cette méthode appliquée aux systèmes d'encre catalytique - pour étudier l'adsorption d'ionomère sur le composant carbone ou Pt/C.

4.1 Theory

All chemical processes associated with the breaking or creation of bonds, as well as physical processes associated with structural rearrangement, can be described as exothermic or endothermic – namely whether energy is released by the system, or must be provided to the system, for the change to occur.[122] This energy change can be measured in the form of heat release or adsorption respectively, and monitored with respect to a reference cell where no such changes are taking place. Through the use of titration, one component can be gradually introduced to a system containing the other slowly, monitoring how interaction changes with concentration. In the case of the catalyst ink system this feature is useful for assessing degree of ionomer adsorption to carbon – not only can adsorption be observed in the form of a heat change, but also a critical ionomer concentration, when all adsorption to carbon is complete and the system becomes saturated, can also be quantified.

Aside from the suitability of the general concept, ITC probes the bulk system, making it suitable for the heterogeneous nature of the catalyst ink. Moreover, as the method is not based on optics, such as many other laboratory techniques used to study component dispersions (dynamic/elastic light scattering, laser diffraction etc.), the opaque nature of carbon does not hinder the measurement process, and concentration directly comparable to the catalyst ink system can be used. These features make ITC a promising method for the study of catalyst inks.

Figure 120 presents a generalized schematic of the ITC principle.

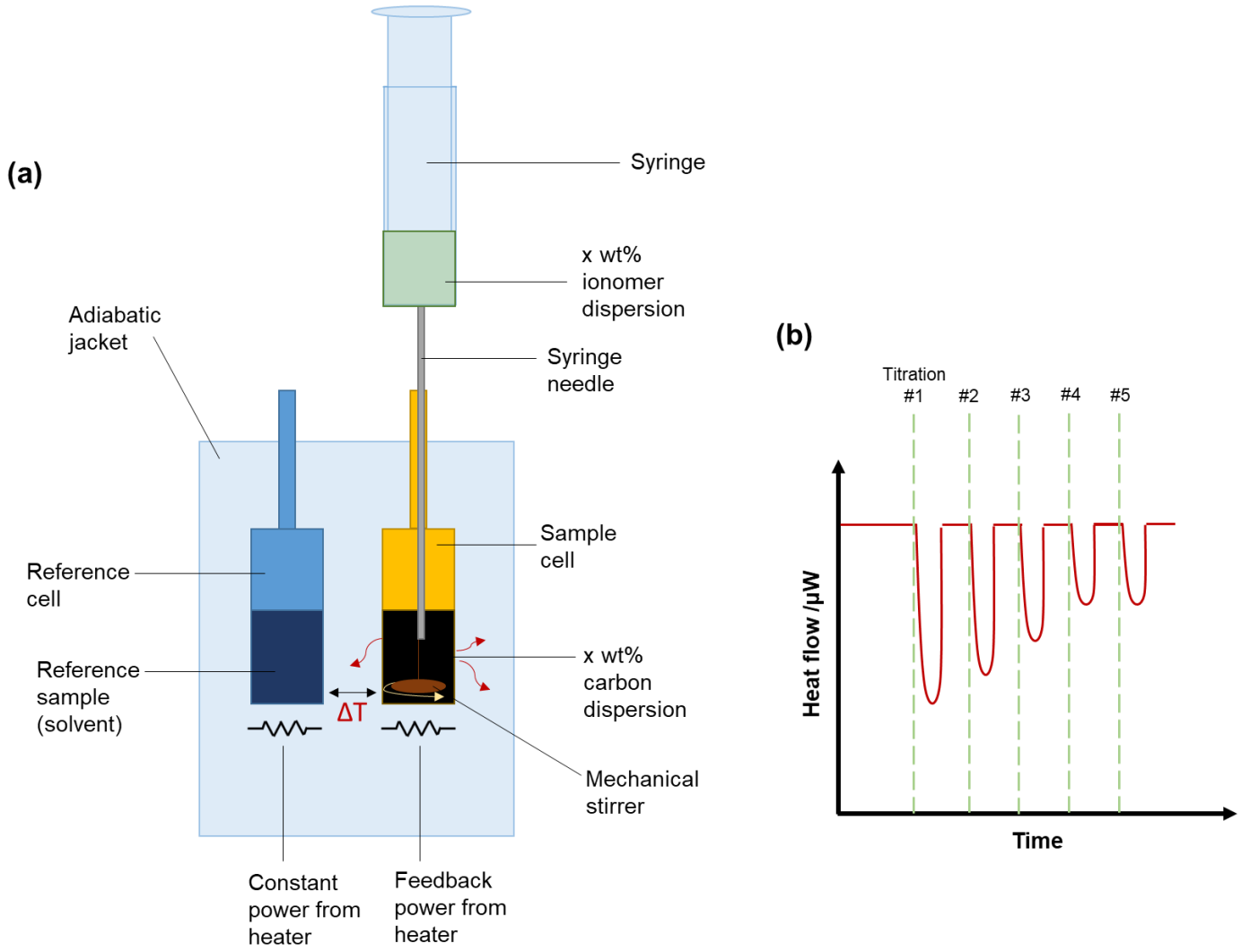


Figure 120. (a) *schematic of ITC principle applied to the catalyst ink system,* ***(b)*** *signal collected from the ITC measurement.* [123,124]

The sample and reference cells are filled with an x wt% carbon dispersion and the corresponding dispersion medium respectively. A mechanical stirrer is present in the sample cell, which prevents carbon sedimentation, negating any stability concerns that may arise with regards to the carbon dispersion. The cells are surrounded by an adiabatic jacket to prevent any heat loss to the environment during the measurement. An automated syringe is utilized to inject a set volume of the ionomer dispersion into the sample cell during each titration step. The system detects temperature variation in the sample cell as a result of heat release/loss caused by component interaction. Subsequently, power is supplied to both the reference and sample cells to maintain a constant temperature between them, $\Delta T = 0$. The output of the measurement is the power required to maintain the $\Delta T = 0$ condition between the reference and sample cells, heat flow /W. The heat flow over time with each titration step can be monitored. As the carbon dispersion becomes saturated with the ionomer component the adsorption process gradually becomes less pronounced, resulting in lower heat flow recorded, until only heat flow related to the addition of the ionomer itself into the sample cell is being recorded and the heat flow remains constant with each titration step.[123] The area of each peak can be integrated to obtain the total heat flow per titration step.

Note the titration of ionomer into the solvent system itself will also result in a temperature alteration that will be recorded during the heat flow measurement. For this reason, a reference measurement must be

collected where the ionomer dispersion is titrated into the sample cell that contains the dispersion medium only. The arising heat flow should be constant, assuming no alteration in interactions related to concentration, and can then be subtracted from the sample measurement.

Subsequently, results can be interpreted as cumulative heat flow as a function of ionomer concentration added into the system. That is to say, the total heat flow obtained from integrating each consecutive titration peak is summed and compared to the increasing ionomer intensity which results from each progressive titration. As the concentration of carbon in the sample cell is known, the I/C ratio in the sample cell at each titration step can be determined.

Thoma et al.[59] used the ITC approach to study the adsorption behaviour of Aquivion ionomer with varying effective weight (EW) per mol of SO_3^- on the surface of Vulcan carbon support. It was found that use of Aquivion with increasing EW resulted in a higher maximum carbon coverage, but the number of deposited ionic groups per carbon black surface remained constant. Extraction and analysis of adsorption isotherms from the ITC data allowed for calculation of the free energy of adsorption, ΔG, which indicated the adsorption of Aquivion to Vulcan is a spontaneous physisorption process, favoured both entropically and enthalpically.

It has already been shown deconvolution of scattering functions of catalyst inks obtained using CV-SANS into PSF outputs can be a tricky process, with the outputs obtained proving quite sensitive to input information provided. Therefore, in the scope of this work ITC was identified as a promising supporting technique, which could be used to verify whether similar information on ionomer adsorption to carbon can be obtained as suggested by CV-SANS analysis. Additionally, where no reliable information was obtained on ionomer adsorption to graphitized carbon based compositions using the CV-SANS/PSF method, ITC most likely could bridge this gap, as only information related to ionomer interactions with the accessible particle surface is acquired. For these purposes, Nafion adsorption to varying carbon and Pt/C components in 50:50 wt% iPrOH/water solvent was investigated. ITC measurements were performed at the Institute of Particle Technology of the University of Erlangen-Nuremberg, with the kind assistance of Prof. Wolfgang Peukert and Dr. Cornelia Damm.

4.2 Methodology

For carbon dispersions of HSAC (EA), GC (E), Pt/HSAC (TEC10E50E) and Pt/GC (TEC10EA50E), nanopowders obtained from Tanaka Precious Metals were utilized. Both Pt/C complexes had a 50 wt% Pt loading on carbon support. For the ionomer dispersion, Nafion D2020 obtained from Chemours was employed. In both cases the dispersion medium was composed of 50:50 wt% iPrOH/water, which utilized isopropanol ≥ 99.5% purity purchased from Sigma-Aldrich and ultrapure water (18.2 mΩ cm^{-2}).

A 50:50 wt% iPrOH/water stock solution was prepared by combining corresponding masses of each solvent and mixing.

Initially, 1 wt% carbon and 2 wt% Nafion dispersion were opted for to correspond to concentrations used in catalyst ink compositions studied by CV-SANS. However, the 2 wt% Nafion dispersion proved incompatible with the very thin syringe needle and blocked it. For this reason, 0.1 and 0.2 wt% dispersions were utilized for the carbon and ionomer components respectively.

The dispersions were prepared by weighing out an appropriate mass of the carbon, Pt/C, or Nafion D2020 component and diluting with the solvent stock solution to achieve a desired concentration. The carbon component was mixed using shear dispersion for approximately 30 seconds. The Nafion component was dispersed by mixing using a magnetic stirrer bar for several minutes. Note the dispersions were prepared in excessive volumes, and the same batch was utilized for each corresponding measurement. Moreover, the carbon component was re-dispersed before each measurement using the shear dispersion method for approximately 10 seconds.

The TAM III thermostat equipped with a nanocalorimeter (TA instruments) were utilized for ITC measurements. 4 mL stainless steel cells were used for both the reference and sample. Approximately 1.2 mL of the solvent stock solution and 1 mL of the carbon dispersion were inserted into the reference and sample cells respectively. As soon as the carbon dispersion was introduced into the cell, stirring at 80 rpm was commenced. The cells were inserted into the thermostat stepwise, allowing for signal equilibration between each step. A 500 μL glass syringe was filled with the 0.2 wt% Nafion dispersion, the needle was inserted into the sample cell, and time was given to allow for signal equilibration. Each measurement was performed at 25^{o}C, with 22 aliquots of 20 μL ionomer dispersion injected into the sample cell, resulting in a stepwise increase of I/C = 0.04 with each titration. The titrations were performed every 30 minutes to allow for signal equilibration back to background level after each heat release recorded.

For each carbon or Pt/C complex investigated, 3 or 4 repeat measurements were performed. Baseline signal was removed, and the total heat release for each titration step was obtained through peak area integration. The heat release values for corresponding titration steps from each repeated measurement were summed to yield the cumulative heat of adsorption, *Q*, as a function of I/C ratio, which were then averaged. A reference measurement, titrating the ionomer dispersion into the 50:50 wt% iPrOH/water solvent only, was performed twice and averaged in the same manner. The two reference ITC measurements, the resulting cumulative heat release as function of ionomer concentration of each, as well as the cumulative heat release average obtained can be visualized in appendix 33.

4.3 Results

4.3.1 Adsorption of ionomer to carbon support only

Figure 121 presents an example of the heat release as a function of time measurement obtained by titration of 0.2 wt% Nafion to 0.1 wt% HSAC and GC respectively, as well as the cumulative heat release as function of I/C ratio plot for each repeat measurement performed.

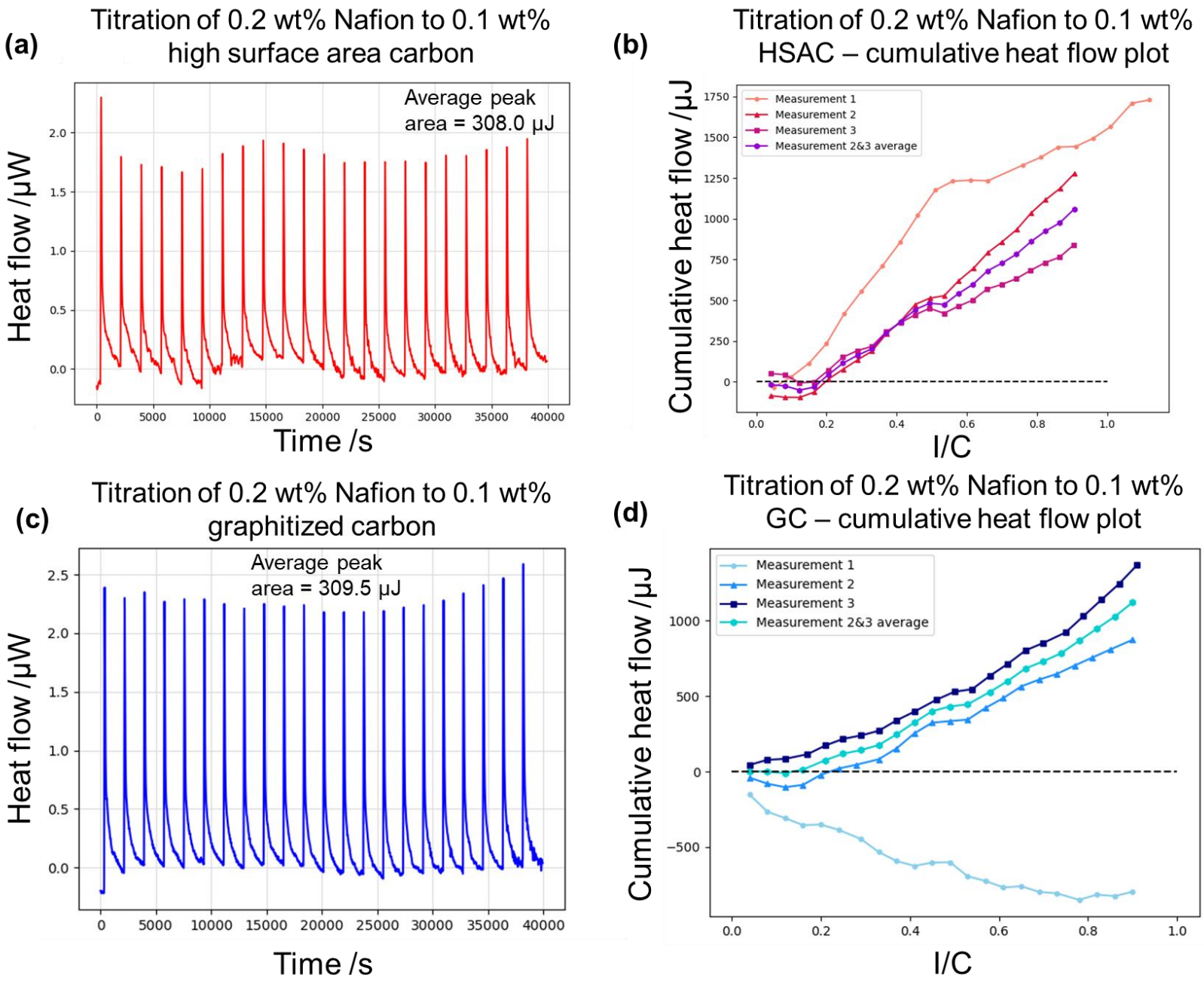


Figure 121. (a) *ITC signal resulting from titration of 0.2 wt% Nafion to 0.1 wt% high surface area carbon,* ***(b)*** *plot of cumulative heat flow (reference cumulative heat flow subtracted) as a function of I/C for repeated measurements of Nafion titration to high surface area carbon, along with the average of measurement 2 and 3,* ***(c)*** *ITC signal resulting from titration of 0.2 wt% Nafion to 0.1 wt% graphitized carbon,* ***(d)*** *plot of cumulative heat flow (reference cumulative heat flow subtracted) as a function of I/C for repeated measurements of Nafion titration to graphitized carbon, along with the average of measurement 2 and 3.*

In the ITC signals (figure 121a, c) it can be observed most peaks have a fairly comparable signal and width. Only in the case of Nafion titration to HSAC the first peak shows an increased heat flow. Indeed, such small variations in peak height can also be observed for the reference measurement (appendix 33), suggesting the differences may not correspond to heat changes associated with the interaction of Nafion and carbon. In the cumulative heat flow plot of Nafion titration to HSAC it can be observed measurements 2 and 3 are fairly consistent, while measurement 1 shows higher cumulative heat flow than both. The variation for measurement 1 may be a result of issues with cell filling. 1 mL of the carbon dispersion was added to the sample cell using a micropipette, however, during the cell preparation it was noted the tip of the micropipette was leaking slightly. Consequently, the mass of the carbon dispersion in the sample cell was 0.8 g for measurement 1, while the mass of carbon dispersion in samples prepared for measurement 2 and 3 was approximately 1g in both cases. This means the overall system in measurement 1 was more concentrated, as indicated by the higher overall I/C ratio achieved. Due to this issue, measurement 1 was disregarded as an outlier, and measurements 2 and 3 were averaged to obtain the final cumulative heat flow as function of I/C ratio plot for titration of Nafion to HSAC.

In the case of Nafion titration to GC, again measurements 2 and 3 are cohesive, but measurement 1 shows discrepancy. In fact, the cumulative heat flow over the entire I/C range is negative, suggesting on average the integrated peak areas were lower than those measured for the reference. Measurement 1 is clearly another outlier, for which possible explanations may include issues throughout the measurement, such as a somewhat blocked titration needle by Nafion. However, no observation of concerns was made when preparing the samples, the measurement set-up, or after the titrations were finished. Nevertheless, again, measurement 2 and 3 were averaged to yield the final cumulative heat flow for titration of Nafion to GC.

Figure 122 compares the averaged cumulative heat flows for titrations of Nafion to HSAC and GC.

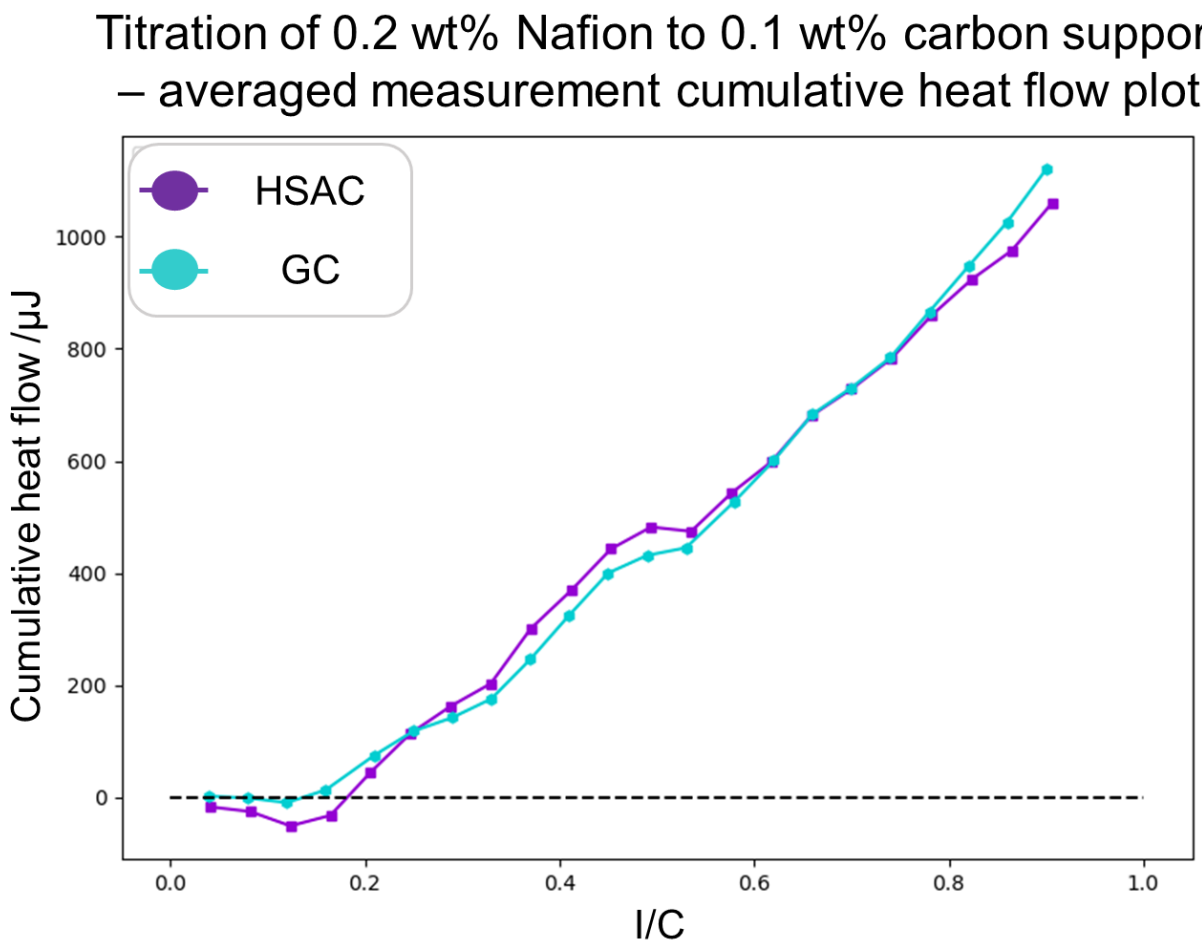


Figure 122. *Comparison of cumulative heat flow as function of ITC when titrating 0.2 wt% Nafion to 0.1 wt% HSAC (purple) and 0.1 wt% GC (blue). Cumulative heat flow of an averaged reference measurement has been subtracted in both cases.*

Interestingly, no major differences between the cumulative heat flow plots obtained for the two very different carbon supports can be observed. Moreover, in either case a plateau in cumulative heat flow related to system saturation is not present either. This may signify the I/C range probed, up to I/C = 0.88, was not enough for complete carbon saturation with the ionomer, and any interactions are still continuing to take place up to this point. However, recall results obtained from the CV-SANS/PSF method suggested there is no adsorption of Nafion to carbon taking place in the 50:50 wt% iPrOH/water solvent system. And indeed, ITC seems to support this observation. Consider the minimum, maximum, and average heat flow obtained from titration peak integrations for several measurements:

Measurement	**Titration of Nafion to:**	**Heat flow minimum /µJ**	**Heat flow maximum /µJ**	**Average heat flow /µJ**
2	**HSAC**	264	343	317
3	**HSAC**	262	472	308
2	**GC**	288	381	310
3	**GC**	301	466	332
1 (reference)	**Solvent**	225	388	299
2 (reference)	**Solvent**	199	461	241

Table 10. *Comparison of the minimum, maximum, and average heat flow obtained from titration peak integration when titrating Nafion to varying samples.*

The average heat flows obtained for reference measurements are somewhat lower than the average heat flows of titration to carbon dispersions. However, the latter fall within the range of heat flow (minimum-maximum) obtained across the reference measurements. In other words, this suggests the titration of Nafion to a carbon support results in a similar heat release as titration of Nafion to solvent, indicating no further heat change related to carbon-ionomer interactions. It could be argued that in figure 121a, the heat flow spike from the first titration of Nafion to HSAC is bigger and may suggest some degree of initial adsorption, however, note such a spike could also be observed in the ITC signal of reference measurements (appendix 33), and could be linked to initiation of the titration process. Moreover, in the ITC study performed by Thoma et al.[59] the same ITC instrument was used, as well as low concentrations of 9.75 and 3.25 g/L for the carbon and ionomer components respectively, yet figure S10 shows heat release of the first several titrations were on the order of mJ instead of μJ. Furthermore, a change in the heat release recorded was clearly visible with progressive titrations. **Based on these comparisons, it can be concluded that no adsorption of Nafion can be observed to either HSAC or GC in the 50:50 wt% iPrOH/water solvent.** On the other hand, it is worth noting in the work by Thoma et al.[59] the I/C range investigated was much smaller, up to I/C = 0.15, resulting in a lower concentration stepwise increase. Moreover, a plateau in adsorption isotherms related to saturation of carbon by an ionomer monolayer was already observed at approximately I/C = 0.03, which is lower than the I/C ratio resulting from the first titration of ionomer into the carbon dispersion. It can be expected that in the instance of adsorption the increased heat release would be observed irrelevant of the initial concentration of ionomer introduced to the system, however, the low I/C value at which full adsorption to carbon was previously deduced suggest in future work it may be prudent to perform titrations that result in a smaller step wise concentration increases in the sample, and cover a lower I/C range, where results can already be expected.

4.3.2 Adsorption of ionomer to Pt/C complexes

In section 2.3.3, results obtained using the CV-SANS/PSF method suggested introduction of Pt into the catalyst ink system may not have a significant impact on ionomer adsorption. However, in section 3.3, the completely altered carbon aggregation behaviour observed by USAXS for Pt/C based samples with increasing ionomer content threw doubt on the former conclusion. For this reason, more information on the effect of Pt addition on the behaviours of the catalyst ink system is desired, obtained using other methods. ITC measurements were collected for 0.2 wt% Nafion titration to 0.1 wt% HSAC + 0.1 wt% Pt and 0.1 wt% GC + 0.1 wt% Pt dispersions. Regrettably, the use of Pt/C dispersions proved incompatible with the ITC method. Figure 123 presents examples of ITC measurements collected for Nafion titrations to Pt/HSAC and Pt/GC.

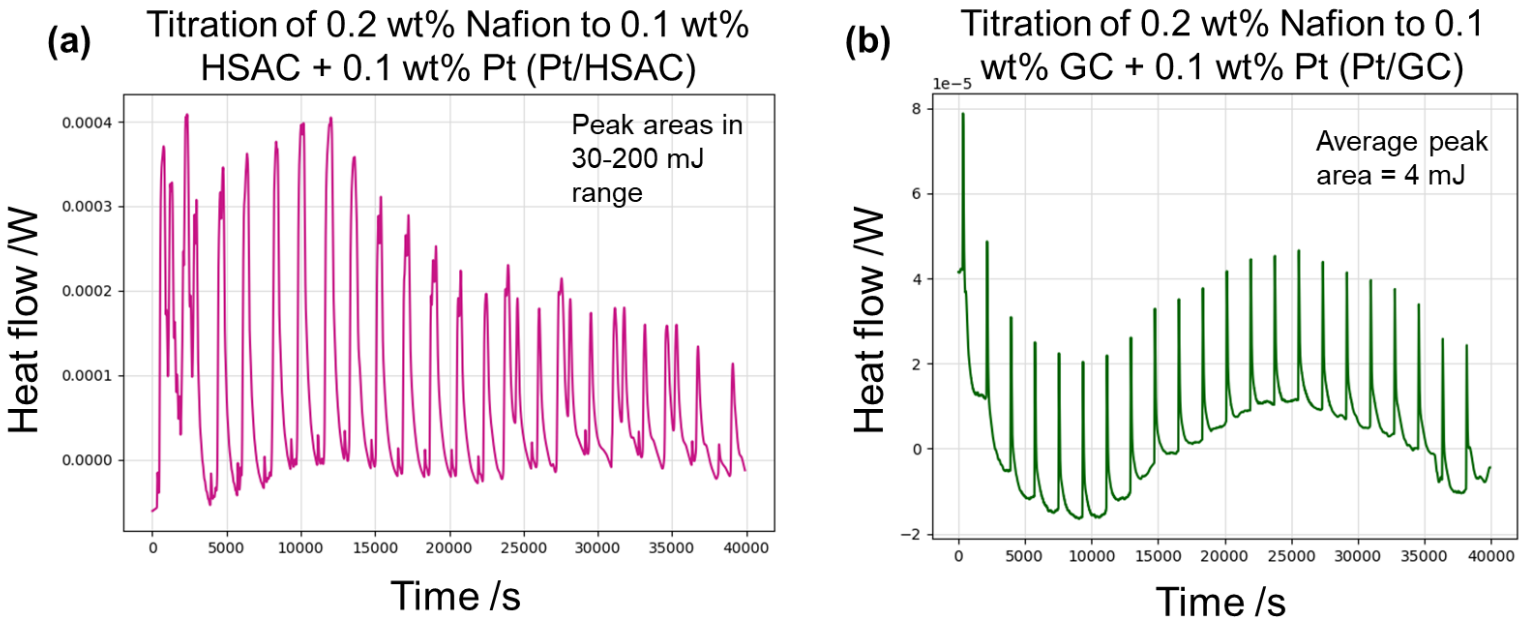


Figure 123. (a) *ITC signal resulting from titration of 0.2 wt% Nafion to 0.1 wt% high surface area carbon + 0.1 wt% Pt,* ***(c)*** *ITC signal resulting from titration of 0.2 wt% Nafion to 0.1 wt% graphitized carbon + 0.1 wt% Pt.*

In both instances the heat flow signal is in the mJ range, much higher than for the titrations to carbon only dispersions. In the case of Pt/HSAC each titration step resulted in the appearance of a small peak, followed by considerably larger peaks that were in most cases convoluted together. Moreover, in the last few titration steps an additional peak can also be observed. A preliminary quantification of the peak areas showed heat flow values in the range of 100-200 mJ for the first half of titration steps, followed by 30-50 mJ in the second half. In the case of Pt/GC the peak shapes themselves were more consistent with what was observed before in section 4.3.1, however, the background signal showed no equilibration throughout the measurement, resulting in a poor baseline. Although the measurement behaviour is quite different between Pt/HSAC and Pt/GC based measurements, in both instances proper quantification of the heat flow per titration step is challenging. Moreover, although several repeated measurements were performed for both titrations to Pt/HSAC and Pt/GC, no reproducible results were obtained. Indeed, measurements presented in figure 123 are the best case scenarios (other examples can be found in appendix 34). Additionally, the heat flow measured per titration never reached the μJ scale that could be associated to the reference measurement, namely heat release associated with the addition of Nafion into the solvent only. In order to confirm whether this much increased heat flow arises due to interactions between Nafion and the Pt/C, or whether this effect is inherently linked to the presence of Pt/C, dilution measurements were performed. This involved titration of the solvent only into the Pt/C dispersion. Figure 124 presents ITC measurements of the Pt/HSAC and Pt/GC dilutions.

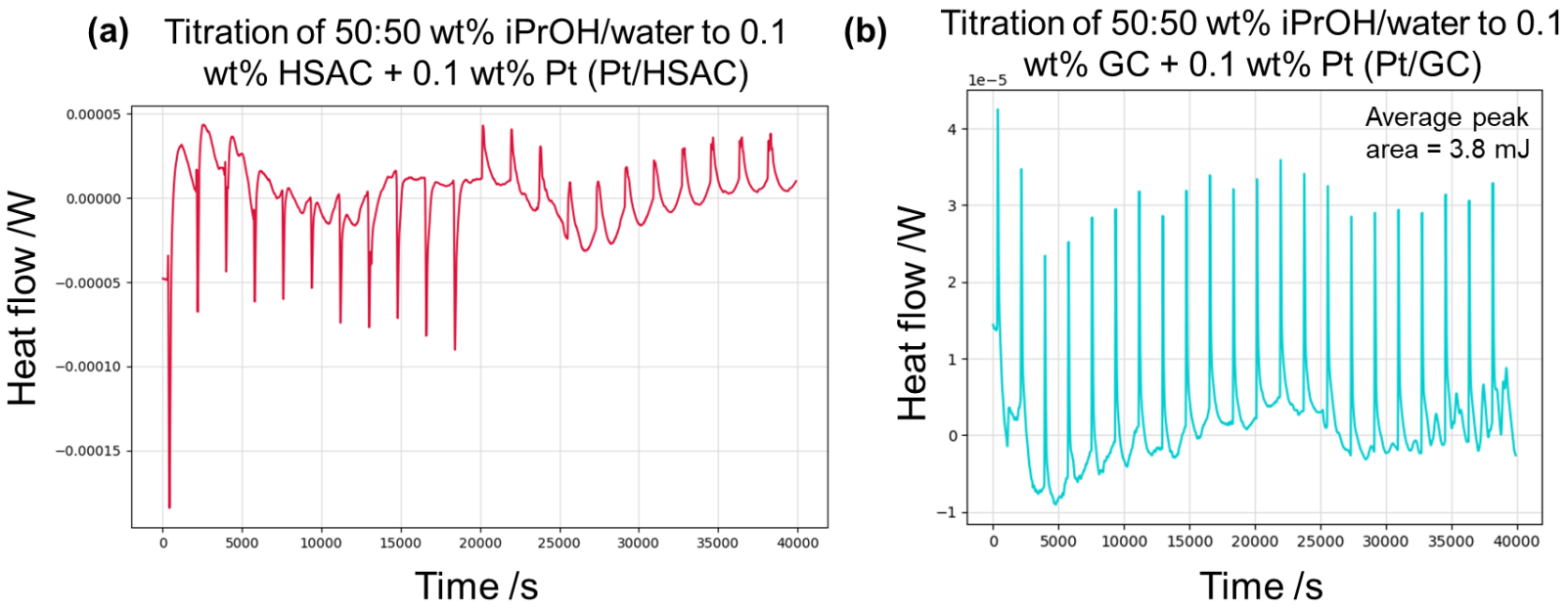


Figure 124. (a) *ITC signal resulting from titration of 50:50 wt% iPrOH/water to 0.1 wt% high surface area carbon + 0.1 wt% Pt,* ***(b)*** *ITC signal resulting from titration of 50:50 wt% iPrOH/water to 0.1 wt% graphitized carbon + 0.1 wt% Pt.*

It can be observed the scale corresponding to heat flow on the order of mJ is maintained in both instances, suggesting the increased signal may be related to other processes occurring between the Pt/C and solvent. The phenomenon of iPrOH oxidation to acetone was discussed in detail in section 2.3.3., and these measurements are a clear evidence of this process. Indeed, such a reaction would result in heat alterations that would be picked up in the ITC measurement. The dilution titration of Pt/GC shows fairly consistent peaks; whose integrations yield an average heat flow of 3.8 mJ. On the other hand, the results of Pt/HSAC dilution shows a very peculiar behaviour, where the first half of titrations show inversed peaks, suggesting an exothermic process, but in the second half peaks show an increasing heat flow suggesting an endothermic process. The reason for this change is unclear, but considering that a large proportion of Pt is present inside of HSAC pores, it is not unreasonable to stipulate that factors associated to reactant and product diffusion may make iPrOH oxidation a much more complex process.

In summary, the phenomenon of iPrOH electro-oxidation to acetone makes Pt/C complexes incompatible with ITC based investigation of ionomer adsorption behaviour. Moreover, the inability to achieve reproducible measurements render any meaningful observations impossible.

This is rather disappointing, as information on the thermodynamics of Pt/C-ionomer interactions would have aided a lot in interpreting both the CV-SANS and USAXS data, which suggest rather contrasting hypotheses with regards to the Pt-ionomer interactions. In future work, ITC measurements could be attempted on Pt-containing compositions, but with degassing of the inks prior to measurement, which ay aid in reducing the electro-oxidation effect. Furthermore, increasing time in between each titration may result in more reproducible results.

4.4 Conclusions

ITC proved to be a viable method for the study of ionomer adsorption behaviour to the carbon support. The bulk system can be easily studied, sample preparation is facile, and the technique is compatible with many components, including graphitized carbon. However, sample concentrations comparable to those utilized in the ink could not be achieved as a 2 wt% Nafion dispersion was found to block the titration needle. Note

concentration effects were suggested by both CV-SANS and USAXS regarding the ionomer adsorption and carbon aggregation respectively. Therefore, the systems studied are not fully representative of those that were investigated by methods mentioned above. For future investigations, finding a way in which 2 wt% Nafion could be utilized would be preferable.

Nevertheless, titrations of 0.2 wt% Nafion to 0.1 wt% HSAC and 0.1 wt% GC dispersions showed no evidence of carbon-ionomer interactions in the 50:50 wt% iPrOH/water solvent system. For HSAC, this result is consistent with observations made using the CV-SANS/PSF method (despite the variation in concentration between the compositions studied using the two techniques), increasing the confidence in the latter technique itself. Moreover, additional insights into compositions based on GC, as well as the effect of carbon support on ionomer adsorption could be made. The use of this method should definitely be considered further in the future, for example by collecting ITC measurements for Nafion titrations to HSAC and GC in other solvent systems.

On the other hand, Pt/C dispersions proved incompatible with the use of ITC for investigation of ionomer adsorption, due to the hindering effect of iPrOH electro-oxidation, which results in significant heat release throughout the measurements. In addition, obtaining any reproducible measurements proved difficult. Due to these two factors no observations regarding Nafion-Pt/C interactions could be made. Attempting to degas the Pt/C dispersion prior to measurement, in hope of reducing the effect of iPrOH electro-oxidation may be worthwhile. In addition, as insight into Pt/C-ionomer interactions would be highly useful in understanding the effect of Pt on the ink structure, other techniques should be found for such an investigation.

It is worth noting one general downside to the ITC method is the time taken per measurement of approximately 12 hours. In tandem with the need to ensure reproducibility of results by collecting repeated measurements for each sample, as well as references, obtaining a sufficient dataset might take weeks. Thoma et al.[59] also noted this downside, and suggested densitometry or thermogravimetric analysis could also be applied to the study of ionomer adsorption behaviour in catalyst inks. Where ITC has been proven to yield valid results in the case of compositions based on the carbon support only, it is suggested other approaches are also attempted in the future to verify whether a more efficient method to obtain such results can be employed.

5 Electrochemical Characterization

In previous sections the impact of composition of catalyst inks as well as catalyst layers was investigated. However, it is also important to understand what effect said alterations have on the electrochemical performance of the electrode itself. Electrochemical characterization allows for monitoring the electrode performance in different operating conditions as a function of potential difference, current, and resistance measured. The cathode catalyst layer is known to be one of the most limiting components on the performance of the fuel cell. Performance related processes in the cathode include the kinetics of the oxygen reduction reaction (ORR), mass transport through the cathode as well as the cathode ohmic drop. In this work, three methods will be used for electrochemical characterization of catalyst layers using the MEA (membrane-electrode assembly set up): polarization curves, impedance spectroscopy, and cyclic voltammetry.

The theory behind each method will be described in **section 5.1**.

Section 5.2 covers the preparation of cell containing the MEA to be measured, electrochemical characterization protocols, as well as specifications of different conditions used throughout the measurements.

Section 5.3 presents results obtained using the various characterization methods, first focusing on MEAs containing Pt/HSAC based catalyst layers, followed by MEAs containing Pt/GC based catalyst layers, and lastly the two cases mentioned above are compared.

Section 5.4 summarizes the most important observations arising from section 5.3, and presents conclusions based on results obtained.

Dans les sections précédentes, l'impact de la composition des encres catalytiques ainsi que des couches catalytiques a été étudié. Cependant, il est également important de comprendre l'impact de ces altérations sur les performances électrochimiques de l'électrode elle-même. La caractérisation électrochimique permet de surveiller les performances de l'électrode dans différentes conditions de fonctionnement en fonction de la différence de potentiel, du courant et de la résistance mesurée. La couche de catalyseur cathodique est connue pour être l'un des composants les plus limitants sur les performances de la pile à combustible. Les processus liés aux performances dans la cathode comprennent la cinétique de la réaction de réduction de l'oxygène (ORR), le transport de masse à travers la cathode ainsi que la chute ohmique de la cathode. Dans ce travail, trois méthodes seront utilisées pour la caractérisation électrochimique des couches de catalyseurs en utilisant le MEA (assemblage membrane-électrode) : courbes de polarisation, spectroscopie d'impédance et voltamétrie cyclique.

*La théorie derrière chaque méthode sera décrite dans la **section 5.1**.*

*La **section 5.2** couvre la préparation de la cellule contenant le MEA à mesurer, les protocoles de caractérisation électrochimique, ainsi que les spécifications des différentes conditions utilisées tout au long des mesures.*

*La **section 5.3** présente les résultats obtenus en utilisant les différentes méthodes de caractérisation, en se concentrant d'abord sur les MEA contenant des couches de catalyseur à base de Pt/HSAC, suivis des MEA contenant des couches de catalyseur à base de Pt/GC, et enfin les deux cas mentionnés ci-dessus sont comparés.*

*La **section 5.4** résume les observations les plus importantes découlant de la section 5.3 et présente des conclusions fondées sur les résultats obtenus.*

5.1 Theory

The theoretical cell voltage (U_{rev}) of the PEMFC at operating conditions (increased pressure, air as reactant, water by-product generation) can be calculated as 1.18V at standard operating conditions (25°C, 1 bar pressure)[125] using the Nernst equation:

$$(,) = -\frac{\Delta ( )}{} - \ln\left(\frac{}{\cdot \sqrt{}}\right) \quad (5.1.1)$$

Where T = temperature (K), P = pressure (Pa), ΔG = Reaction free enthalpy of H_2O formation (J), n = number of electrons exchanged in the overall reaction, F = Faraday constant, R = universal gas constant, a_{H2O} = activity of water, a_{H2} = activity of hydrogen, a_{O2} = activity of oxygen

Note the Nernst equation assumes the proton activity is the same at each electrode.

Nevertheless, the U_{rev} value of 1.18V is never achieved as the theoretical system used to compute this value, considering the O_2/H_2O and the H^+/H_2 redox couples at the cathode and anode, both at equilibrium, is not representative of the real life scenario. The open circuit voltage (OCV), measured when no current is flowing through the external circuit, is lower than this value. This is attributed to the complexity of the catalyst layer, where other species of the fundamental components may be also found. For example, presence of water and oxygen results in oxidation of Pt to PtOH or PtO.[125] H_2 crossing towards the cathode and O_2 towards the anode result in H^+/H_2 and O_2/H_2O redox couples respectively. Taking such redox processes into account, the electrodes are no longer at equilibrium, and the total potential at each potential arises as a function of the mixed potential contributions from the numerous processes taking place. The potential at the cathode is lower than for the O_2/H_2O redox couple at equilibrium. On the other hand, the potential at the anode is higher than for $H^=/H_2$ at equilibrium. As a result, the potential difference measured across the cell itself, U_{rev}, is lower than the theoretical value arising from the Nernst equation.

Moreover, the Nernst equation doesn't take into account kinetic limitations that are always present during fuel cell operation, as the electrochemical reactions themselves are not at equilibrium. Different types of losses are present during fuel cell operation and can be characterized using polarization curves.

5.1.1 Polarization curves

The electrochemical overpotential can be defined as 'the difference between the applied potential at the working electrode and equilibrium potential of the net redox reation'.[74] Namely, the presence of an overpotential indicates more energy is required to drive a reaction than would be expected by thermodynamic calculations, making it directly related to potential losses present throughout the fuel cell[126]:

$$= \quad . + \quad . + \quad + \quad , + \quad , + \quad (5.1.2)$$

where η_{tot} = total cell overpotential, $\eta_{act,c}$ = activation overpotential at the cathode, $\eta_{act,a}$ = activation overpotential at the anode , η_{ohm} = ohmic overpotential, $\eta_{mt,a}$ = mass transport overpotenital at the anode, $\eta_{mt,c}$ = mass transport overpotenital at the cathode, η_{other} = overpotential resulting from other effects

Note the activation overpotential at the anode, $\eta_{act,a}$, as well as mass transport overpotential at the anode, $\eta_{mt,a}$, are considered negligible in comparison to that at the cathode due to much faster kinetics of the HOR and faster diffusion of protons respectively.

The potential difference of the cell can then be described as:

(5.1.3)

= – = –

Where E_{we} and E_{ce} are the potentials of the working and counter electrodes respectively.

The various potential losses can be observed on a polarization curve, where E_{we} is measured as a function of current density, I.

Figure 125 presents a generalized polarization curve.

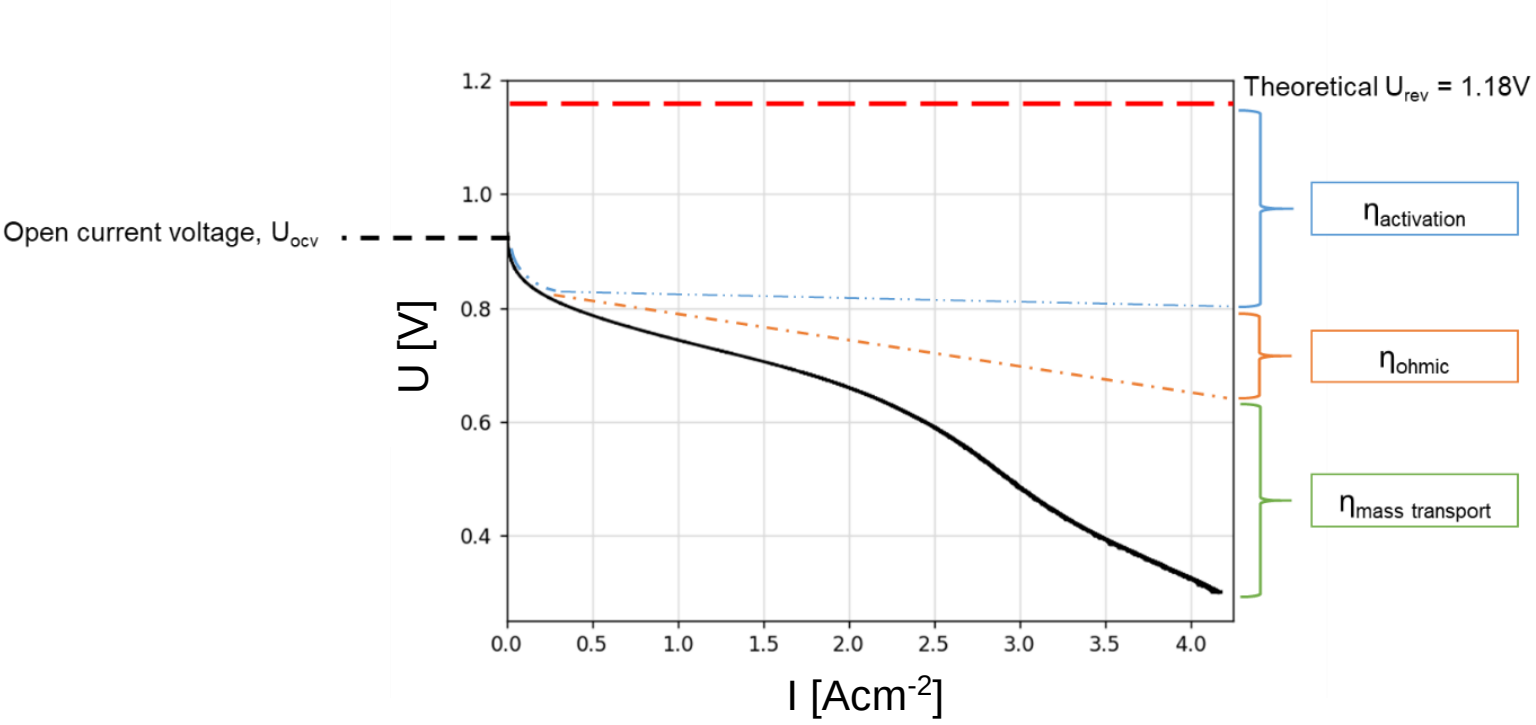


Figure 125. *An example of a polarization curve, with labels pertaining to different potential losses.*[73]

The activation loss, $\eta_{activation}$, is characterized by an initial sharp drop from the U_{ocv} with increasing current density, and is related to the reaction kinetics of the ORR and HOR at the cathode and anode respectively. As mentioned above, in the PEMFC the activation loss arising from the anode can be considered negligible as the reaction kinetics of the HOR are generally much faster than reaction kinetics of ORR. Although the activation losses are significant at all current densities, it is particularly dominant at low current densities, where ohmic and mass transport losses can be considered negligible.[125] For this reason, characterization of activation losses is performed at low current densities.

In a first approximation the current density, I, can be linked to activation overpotential associated with ORR kinetics, , by the Butler-Volmer equation[125]:

$$= \left[\frac{}{} - \frac{-(1-)}{} \right] \qquad (5.1.4)$$

where I_o = exchange current density (A/cm^2), = charge transfer coefficient

The exchange current density is the current when the oxidation and reduction half-equations of the full reaction are at equilibrium, and consequently no overpotential is present. I_0 can be expressed as[126]:

$$_0 = \quad , \quad 0, \quad -\!\!\!- \tag{5.1.5}$$

where $C_{ox,\,surf}$ is the concentration of reactants at the electrode surface for the oxidation reaction (mol/cm^3), $_{0,}$ is the rate constant of the reduction reaction (cm/s).[127] Higher values of $_0$ indicate lower activation losses at the electrode.

Ohmic losses are introduced due to charge transport resistance of ionic species through the fuel cell – protons and electrons. The voltage drop can be linked to the ohmic resistance by[126]:

$$= \tag{5.1.6}$$

$$= -\!\!\!- \tag{5.1.7}$$

where = conductivity (S/m), = thickness of electrode/membrane (m), = area of the charge flow (m^2)

Note R_{ohmic} contributions are measured across the entire cell – including the GDLs, contact between the GDL and the bipolar plate as well as the GDL and catalyst layer. Moreover, R_{ohmic} will vary with cell hydration and current density.

Component interfaces also contribute to increased ohmic resistance. In the case of electron movement through the catalyst layer the resistance depends on inter-component interface quality and degree of component compression. In the case of proton movement, the electrolyte/catalyst layer is considered, as well as the nature of the ionomer shell in the electrode itself – its thickness, temperature and humidity.[125] Note the electrolyte refers to proton conducting species, namely the ionomer thin film as well as water molecules present at the Pt/C surface. Both have the ability to propagate protons towards the ORR active site.

The mass transport losses relate to the reaction rate limitations, which are linked to the concentration of reactants at the anode or cathode, for the HOR and ORR respectively. Namely, the reactants are used up faster than can be supplied. The three reactant transport processes applicable in the fuel cell are migration, diffusion and convection.[126] Migration relates to transport of ionic species such as protons through the ion conductive membrane, or electrons from the external circuit through the carbon support, towards the active sites. Diffusion is relevant to the movement of gas reactant species, such as H_2 or O_2, through the catalyst layer itself. Convection describes bulk motion by mechanical forces, namely the initial reactant gas supply.

Supplying reactants and their subsequent movement towards active sites results in a concentration gradient across the cell. The higher the reactant concentration, the higher the exchange current density (equation *5.1.5*). In addition, a pressure gradient is created between the inlet and the outlet of the flow filed, with lower pressures at the outlet aiding in removing excess water from the cell (however some water is required for efficient fuel cell operation). The concentration and pressure gradients can be controlled by the stoichiometry of reactants at the electrodes, namely the ratio between amount of reactants supplied and the amount of reactants needed for the electrochemical reaction. Providing stoichiometries of 1, where all reactants that are provided are also used up in the corresponding reactions, would result in insufficient gas flow towards the outlet for water removal, causing flooding of the electrodes and therefore a severe degradation. In addition, in the case of the cathode, with all reactants effectively used up as soon as they are provided the entire surface of the active sites would not be efficiently utilized. On the other hand, if the

stoichiometry is too high, large pressure gradients are created, which result in increased H_2O removal, to the point where the catalyst layer may no longer be sufficiently hydrated for optimal performance. This effect becomes more pronounced at low RH conditions. Therefore, the stoichiometry must provide a balance between sufficient reactant concentrations for efficient utilization of the catalyst layer, as well as a pressure gradient that aids in preventing flooding of the electrode, but is not so large as to remove the water content in the cell needed for operation.

Commonly used stoichiometries of 1.2-1.5 and 1.6-2.0 are provided for the anode and cathode respectively. Lower stoichiometries can be applied at the anode due to the fast diffusion kinetics of H_2, which result in low mass transport losses, and the reactant can be more efficiently provided from the inlet to the active site. In the case of the cathode, as air flow is supplied, containing only 20% of the O_2 reactant (majority is N_2), higher flows are required to provide sufficient concentration of reactant to the active site. In addition, because the diffusion of O_2 is slower, concentrations must be kept higher to allow for sufficient reactant diffusion across the entire catalyst layer.

Where polarization curves give a general overview of overpotential losses with varying current density, impedance spectroscopy is a useful method which can be utilized to quantify some of the resistance arising from the reactant mass transport, charge transfer, as well as the rate of the electrochemical reaction itself.

5.1.2 Electrochemical Impedance spectroscopy (EIS)

EIS is a tool for probing the dynamics of electrochemical processes in a perturbative manner through measurements of impedance of the electrochemical system to the passage of a sinusoidal alternating current. An AC current of a very small amplitude (approximately 10 mA), is applied on top of the controlled DC current. Alternating the frequency of the applied AC current allows for acquisition of information on electrochemical processes that occur on different time scales. For example, low frequencies yield information on the dynamics of slower process related to the kinetics of the ORR reaction (charge transfer between the electrode/electrolyte interface) and reactant mass transport. On the other hand, high frequencies result in probing of faster processes such as charge migration of H^+ in the membrane or electrolyte, and electrons in the electron conducting phase. Note in order to calculate the proton transfer resistance on the local scale it must be assumed operation is homogenous in the thickness of the catalyst layer - namely that the proton transport within the catalyst layer does not affect the kinetics of the ORR.[128] A gradient of potential will be present in the electrolyte though the electrode thickness, however, it Is considered to be small enough to have no impact on the reaction kinetics.

Impedance embodies the opposition of an electrochemical system to the current flow applied. Where resistance observed in DC circuits follows Ohm's law directly, the response of an electrochemical system to impedance is linear, with an acquired phase-shift, while the response of current to a sinusoidal potential is a sinusoid at the applied frequency.[129] The system impedance can be expressed as:

$$( ) = — = \ _0( ) \ ^{(\ ( ))} = \ _0( )(\quad ( ) + \quad ( )) \tag{5.1.8}$$

Note in this work, as characterization of the catalyst layer specifically is of interest, impedance measured at small dc current densities of 25 mA/cm^2 will be considered. Such small current density values correspond to the region where activation losses dominate, and mass transport losses related to the entire cell are negligible. For this reason, the impedance measured can be more effectively analysed with regards to the catalyst layer specific processes, such as the charge transfer across the electrolyte/catalyst interface, or the proton migration through the catalyst layer specifically.

The impedance is commonly represented by a Nyquist plot, where the total expression is segmented into a real part (Re(Z)) and an imaginary part (Im(Z)). Note as the imaginary part of the impedance is predominantly negative, -Im(Z) is plotted on the y-axis. Each point of the Nyquist plot corresponds to impedance at a set frequency value.[129] When Im(Z) is 0, the high and low frequency resistance can be calculated.

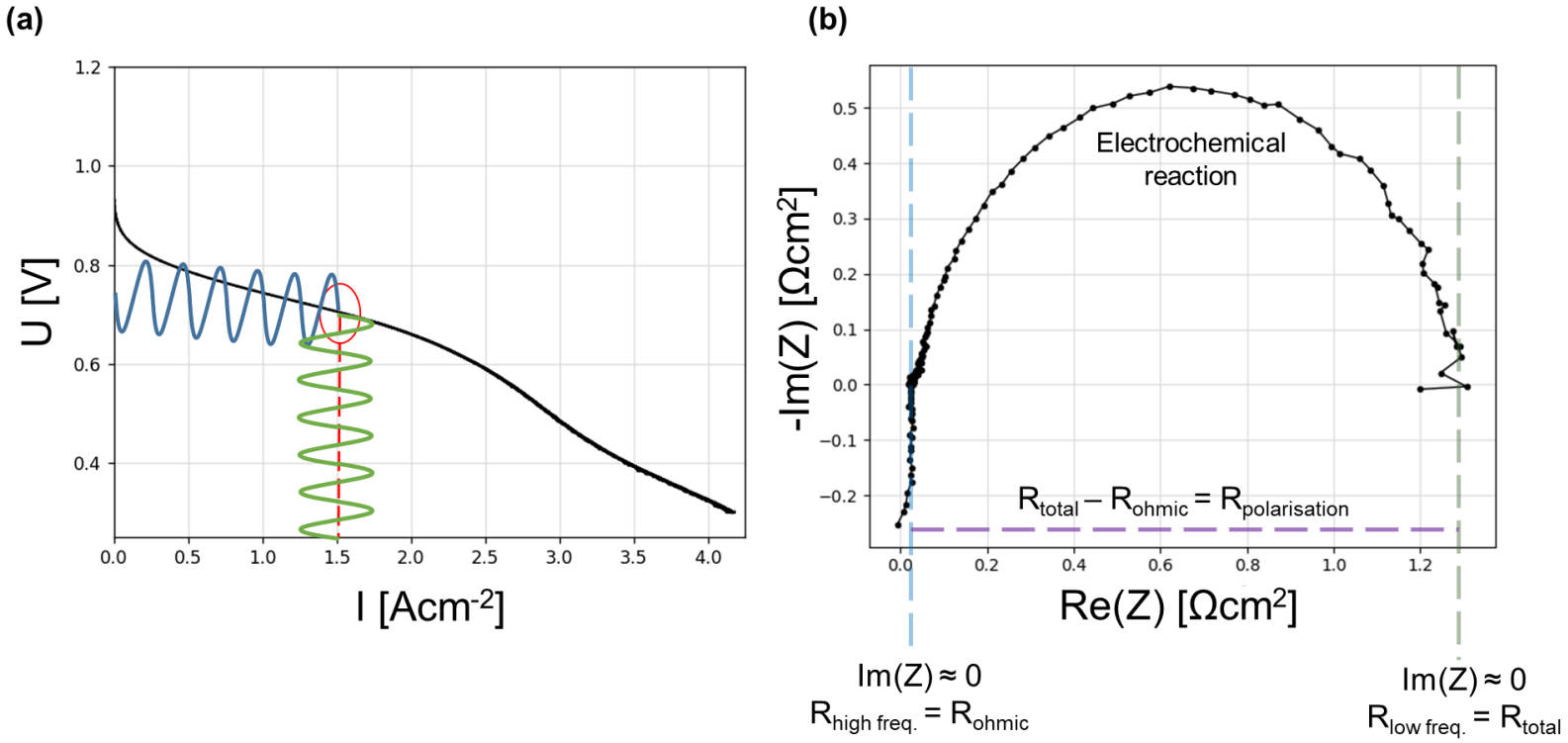


Figure 126. (a) *Schematic representation of impedance of small amplitude ac current at fixed dc point of I,* ***(b)*** *an example of a Nyquist plot[128] obtained at 25 mA/cm^2. Conditions included fuel cell temperatures of 80^{o}C, high H_2/Air gas flows (47/118 NL/h) at the anode and cathode respectively, pressure of 2.5 bar.*

The low frequency resistance, $R_{low\ freq.}$, is associated with the total resistance, as well as the slope of the polarization curve at the fixed dc current density. The total resistance, R_{tot}, mainly corresponds to the polarization resistance, $R_{polarisation}$, which is related to the difference between the applied potential and equilibrium potential needed to flow current produced by the cell. $R_{polarisation}$ includes the mass transport resistance, as well as charge transfer resistance related to the ORR mechanism. However, as impedance is performed at very low current densities of 25 mA/cm^2 the contributions from mass transport losses can be considered negligible, and R_{tot} predominantly describes charge transfer specific to the ORR mechanism. This can be related to the α parameter, charge transfer coefficient, in equation (5.1.5). Again, as the HOR is a much faster process than the ORR, R_{tot} describes the kinetics, and therefore efficiency at the cathode only.

$R_{high\ freq.}$, corresponds to ohmic resistance and characterizes comparably faster process such as the charge migration through the respective conductive phases in the catalyst layer. The slope of approximately 45^o in the high frequency regime corresponds to the proton transport through the catalyst layer specifically.

Note the impedance characterizes the entire electrochemical system, however, if impedance is performed at a low fixed dc current, resistance related to the catalyst layer only can be probed. This is because at low current densities activation losses related to the electrolyte/catalyst interface kinetics inside the catalyst

layer are dominant, and mass transfer related to gaseous reactants as well as ohmic losses associated with proton/electron migration through the system are comparably negligible.

EIS data obtained at low dc current values can be fitted with the following model to extract quantified resistance values related to the various losses[130]:

$$Z(\omega) = \frac{}{\sqrt{}} \sqrt{} + \frac{}{} + \qquad (5.1.9)$$

where $Z(\omega)$ = impedance (Ωcm^2) at frequency, ω (rad/s), R_{ohmic} = protonic resistance of the cathode catalyst layer (Ωcm^2), R_{ct} = charge transfer resistance (Ωcm^2), C_{dl} = double layer capacitance (F/cm^2), R_{ohmic} = ohmic resistance (Ωcm^2)

Charge transfer resistance, R_{ct}, is assumed to be constant under homogenous operation in the catalyst layer, with all active species having the same speed of reaction and producing the same current.

5.1.3 Cyclic voltammetry (CV)

Cyclic voltammetry (CV) is a technique used to probe the electrochemical reduction and oxidation behaviours of chemical species, initiated by the transfer of electrons. A gradually increasing potential at a defined scan rate, , is applied to the system and the current response is monitored.[131] With regards to the catalyst layer, cyclic voltammetry can be utilized to study oxidative and reductive electrochemical reactions occurring at the electrolyte/catalyst interface. This includes processes linked to the catalytic reaction itself, as well as the evolution of components present at the interface. Moreover, the Pt availability can be determined, which is one of the most important factors in the rate of ORR and hence fuel cell performance. Note in order to characterize the physical nature of the interface itself the system is probed when no ORR is taking place. To achieve this the working electrode is saturated with humidified nitrogen. Humidified hydrogen flow is still applied to the counter electrode, allowing for migration of protons and electrons towards the working electrode. Moreover, this also permits the counter electrode to act as a reference electrode (whose potential = E_{ref}), assuming the kinetics of H^+/H_2 electroreduction are so fast no potential changes as a result are recorded.

Figure 127 presents an example of a cyclic voltammogram obtained with a scan rate of 100 mV/s. The potential is varied between 0.07 and 1.2V with respect to H^+/H_2. To commence, as E_{we} is increased up to 0.4V vs H^+/H_2, oxidation of protons can be observed as they are desorbed from the surface of Pt. Increasing E_{we} further, up to 1.2V vs H^+/H_2, results in oxidation of the Pt/C complex itself, both with regards to the carbon and Pt components, which can form several products on oxidation. As E_{we} is decreased, alteration in current density corresponding to the reversibility through reductive reactions of the above-mentioned processes can be observed. Additionally, it can be noted that in the reductive direction when $E_{we} < 0.1$V vs

H^+/H_2, an extra spike in the current density measured is present. This spike corresponds to reduction of protons to hydrogen, a reversibility of the proton production process.

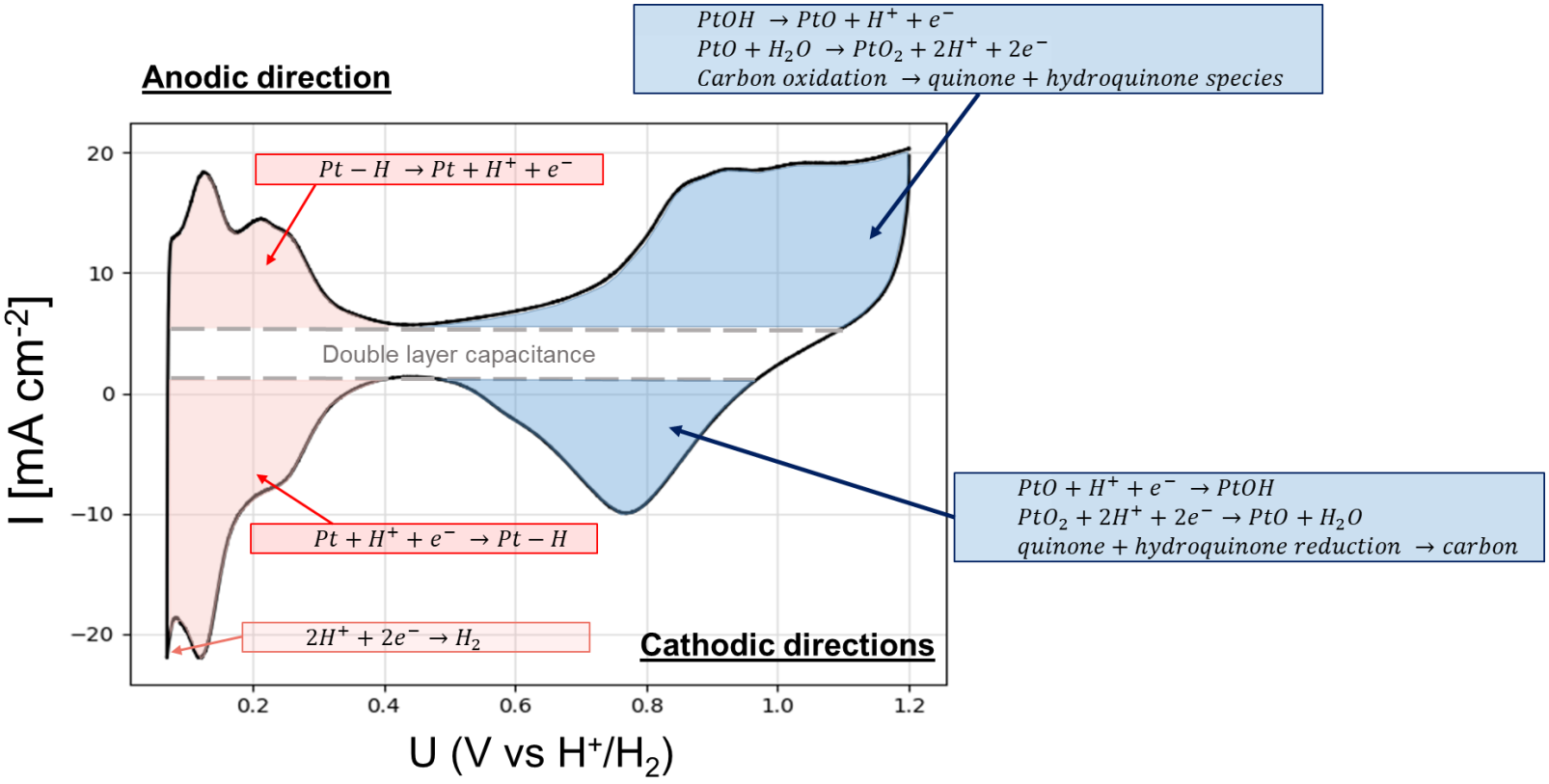


Figure 127. *Example of measurement obtained from cyclic voltammetry performed at a 100 mV/s scan rate.[128] The potential is measured with respect to the counter electrode and the corresponding H^+/H_2 reduction couple. Current alteration associated with oxidative processes are recorded with increasing potential. Subsequently, when potential is step-wise decreased back to 0V vs the reference electrode, reductive processes are observed, and changes in current are recorded on the negative scale.*

In figure 127, grey dotted lines can be observed dividing the peaks related to oxidative and reductive processes. This zone represents current variation arising from the capacitive nature of the electrolyte-catalyst interface, where charge rearrangement occurs with alternating E_{we} through charge diffusion processes. Note the magnitude of current arising from the capacitance phenomenon remains constant with varying magnitudes of E_{we}, and is equal in both the anodic and cathodic directions. As mentioned above, the available catalytic Pt surface area can be estimated from cyclic voltammetry, by integrating the peak area corresponding to hydrogen desorption from the Pt surface at E_{we} < 0.4 V vs H^+/H_2. The hydrogen adsorption to Pt peak is less appropriate for this determination due to the convoluted contributions of H_2 production present in the same E_{we} range. Before the peak integration can be performed, contributions from the double layer capacitance have to be removed. Additionally, the gradient observable in the 0.45 – 0.6 V vs H^+/H_2 range, arising from the internal short circuit across the membrane, must be estimated and also corrected for.

The integration of the proton desorption peak can be linked to the available Pt surface area by[128]:

$$= \frac{1}{} \int \ . \qquad (5.1.10)$$

Where I = current density (A/cm^2), E = Potential (V), V_b is the hydrogen underpotiential deposition (Hupd) desorption roughness factor (cm^{2}Pt/cm^{2}geo) and Q= Hupd charge (C/cm^{2}geo). Although the Hupd charge is known to vary with the crystallographic orientation of Pt, the value most commonly used to determine the Pt surface area is the Hupd charge of Pt (100), 210 μC/cm$^2_{Pt}$.[128]

Note as both the ionomer and water present in proximity to the Pt/C surface can act as a proton conducting electrolyte, the obtained active Pt surface area cannot be directly linked to the quality of coverage of Pt/C by the ionomer in fully humidified conditions. Instead, polarization curves and EIS data may provide more insight into the ionomer distribution.

5.2 Sample preparation and methodology

In order to correlate electrode performance to its structure, pre (catalyst inks) and post (catalyst layers) manufacturing, the effect of Pt/C complex used in the catalyst layer, as well as the solvent system composition of the ink it was manufactured from, were investigated. Therefore, the same CCMs were utilized for electrochemical testing as prepared for catalyst layer measurements by SANS. Please refer to section 2.4.1 for details of CCM preparation.

The interior of the sample cell set up can be visualized in figure 128.

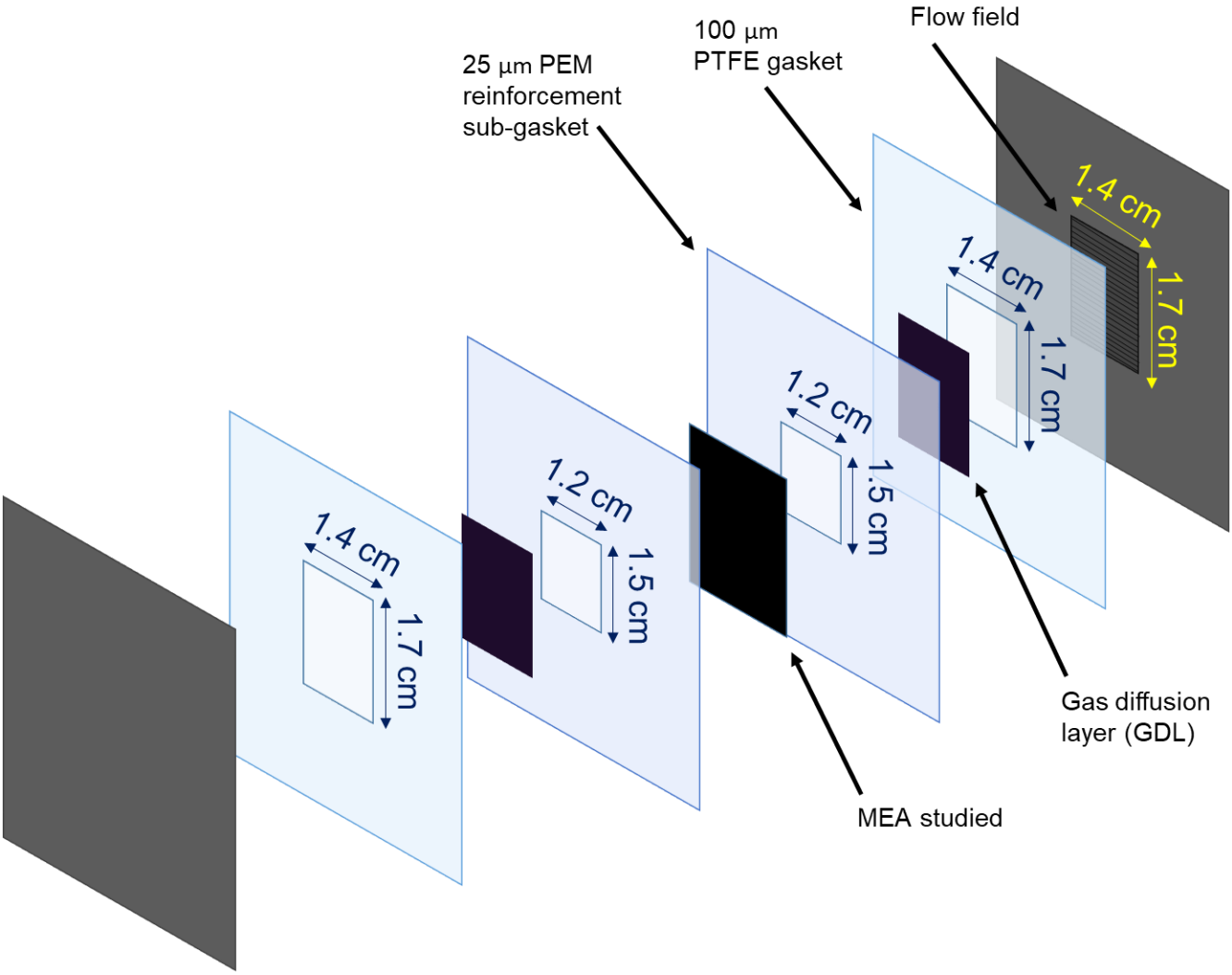


Figure 128. *Schematic of internal cell set up for MEA electrochemical characterization.*

The 1.8 cm^2 cell used allows for characterization of low surface area catalyst coated membranes (CCMs) with high stoichiometry of reactant gases resulting from high gas flow. Such a set up favours homogenous operation at the surface of the catalyst layer. Reactant gases enter the cell through 250 µm wide and 400 µm deep flow field channels, that are spaced apart by 250 µm from each other. A 100 µm thick PTFE gasket is placed on top of the cell, with a 1.4x1.7 cm gap accommodating the gas diffusion channel on one side and the gas diffusion layer (GDL) of same dimensions on the other. The GDL used in all cells was H14CX653 (Lot no. 916289/1/1) obtained from Freudenberg. The GDL was arranged in such a manner so that the microporous layer faces the CCM. Next a 25 µm PEM reinforcement sub-gasket is introduced, which limits the active surface area of the set up. Both the gasket and sub-gasket ensure proper sealing and compression (which ensures good electrical contact), within the cell set up. Finally, the CCM investigated is presented, and the sub-gasket/GDL/gasket/flow field set up is repeated on the other side before the cell is sealed using screws. Figure 129 presents a picture of the cell set up on a homemade electrochemical characterization bench:

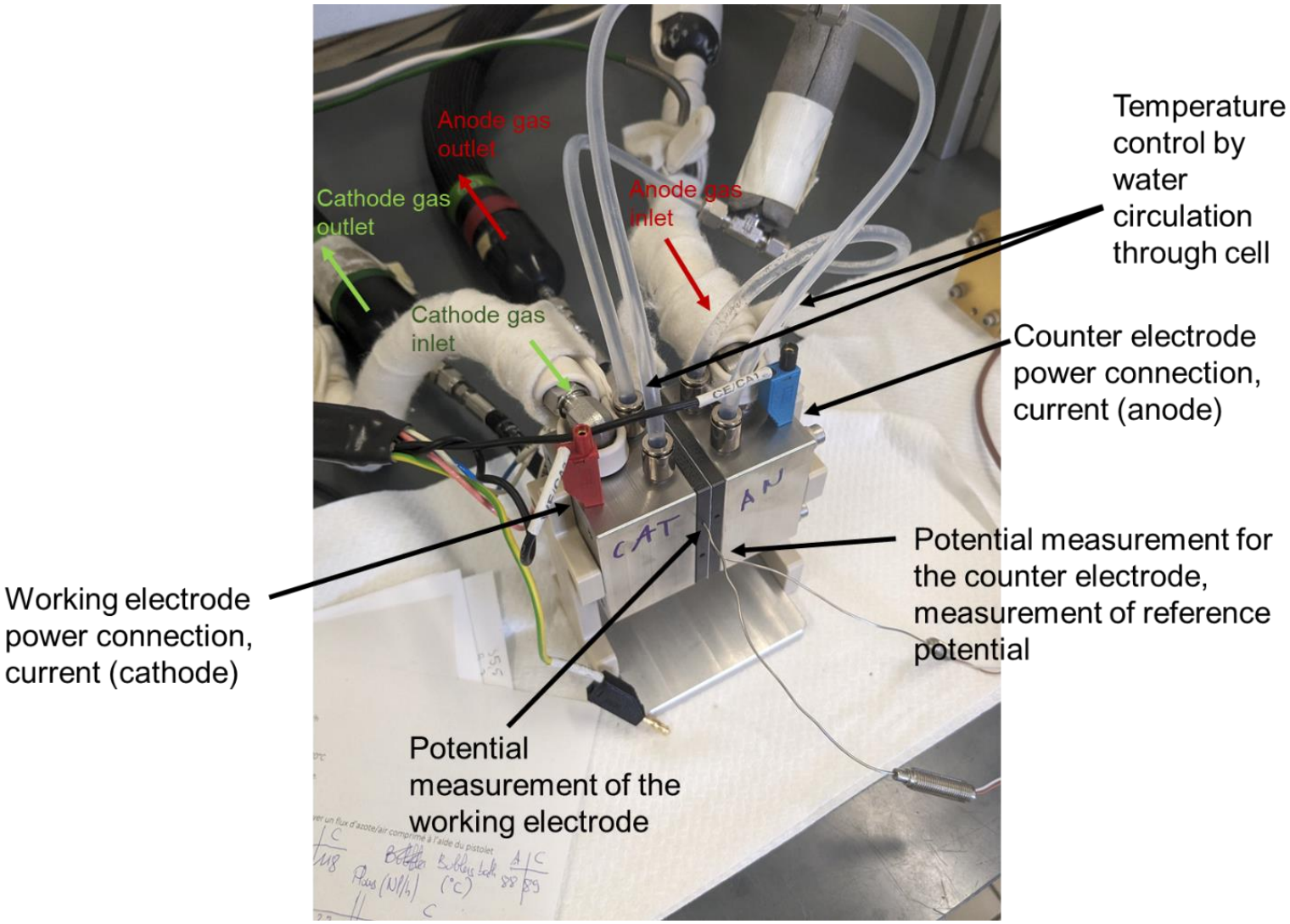


Figure 129. *Picture of cell set up on a homemade electrochemical characterization test bench.*

The cathode and anode sides of the cell are connected to inlets and outlets that allow for gas flow through the cell. H_2, O_2, N_2 and air can be utilized with precisely controlled flow rates between 0.5 and 200 NL/h (normal litres per hour). In addition, mixtures of the above mentioned gasses can be flown to the anode and/or cathode, with a control of relative humidity provided by running the reactant gasses through temperature-controlled bubblers, allowing for their hydration. The inlet supply lines are thermally controlled to ensure no water condensation occurs when hydrated gasses are flown towards the cell. The gas inlets are additionally surrounded by insulation fibre to ensure as little temperature loss as possible. The temperature of the cell is also controlled by constant passing of water through an internal circuit that is heated to a desired temperature using a thermostatically controlled bath. The working electrode, counter electrode, and references are connected to a Biologic SP-150 potentiostat joined to a 20A booster that are used to perform the experiments and collect measurement data.

5.2.1 Measuring protocols

Catalyst coated membranes (CCMs) tested were obtained from the same batch which was utilized in catalyst layer SANS. For this reason, please refer to section 2.4.1 for the manufacturing protocol. The anode

composition was kept constant, while in the cathode variations were introduced with regards to the Pt/C complex as well as iPrOH concentration utilized in the catalyst ink that the cathode catalyst layers were manufactured from. The Pt loading was kept constant at 0.1 mgPt/cm^2 and 0.2 mgPt/cm^2 for the anode and cathode respectively.

Each arising MEA, set up as shown in figure 128, has been characterized using three different operating conditions, during which different processes inside the cell can be accentuated:

1. **Air, high RH conditions** – 95% RH, H_2/Air with gas flow of 47/118 NL/h at the anode and cathode respectively, 2.5 bar pressure, cell temperature = 80^{o}C

2. **O_2, high RH conditions** – 100% RH, H_2/O_2 with gas flow of 47/118 NL/h at the anode and cathode respectively, 1.5 bar pressure, cell temperature = 80^{o}C

3. **O_2, low RH conditions** – 50% RH, H_2/O_2 with gas flow of 47/118 NL/h at the anode and cathode respectively, 1.5 bar pressure, cell temperature = 80^{o}C

As mentioned above high gas flows, which are maintained in each protocol, yield high reactant stoichiometry, ensuring the amount of reactant consumed in the cell is negligible compared to the amount provided to the cell. In addition, the water produced by the electrochemical reaction is very low in comparison to the amount of water supplied by the humidified gas flow. Therefore, the concentration of both products and reactants is thought of as constant from the inlet to the outlet. Moreover, the design of the flow field results in a low pressure drop from the inlet to the outlet, and pressure of the overall cell is maintained manually. As a result, an environment of homogenous operation is created throughout the entire catalyst layer, creating an ideal case, which is easier to study and understand.

The air, high RH conditions mimic real-life fuel cell operation, however in a very idealized scenario. High pressures of 2.5 bar result in higher O_2 concentrations provided to the active site. On the other hand, transport resistance, for both the reactants and products is increased. However, in this instance the effect is countered by high reactant stoichiometry used. Additionally, high pressures ensure a more uniform and greater hydration throughout the cell.

In the O_2, high RH condition, utilizing 100% RH ensures proton transport resistance through the cell is minimized. Additionally, the use of pure O_2 as the reactant gas instead of air results in increased reactant concentrations, and subsequently reduced O_2 transport resistance. Moreover, this allows for use of lower pressure of 1.5 bar, corresponding to a partial pressure of 0.5 bar and 1.0 bar for H_2 and O_2 respectively, applied in many literature works to assess catalytic activity. As both the proton transport and O_2 transport resistances are minimized, contributions corresponding to ORR kinetics, namely the charge transfer resistance at the electrolyte/catalyst interface are emphasized.

In the low RH condition, again use of O_2 instead of air minimizes O_2 transport resistance contributions. On the other hand, low RH of 50% means proton transport resistance is emphasized, as fewer water molecules are present to act as an electrolyte.

By combining information obtained at each operating condition, an optimized picture of the processes occurring inside the catalyst layer can be obtained.

Before measuring polarization curves and EIS at each of the above-described conditions, a break-in step is first performed to commence the experiment. This essentially corresponds to the ‘activation’ of the MEA and achieving optimal performance. The break-in process entailed resting at OCV for 90 seconds, followed by a change in potential from OCV to 0.1V vs potential of the reference electrode (E_{ref}) with a scan rate of 100 mV/s, after which the potential was kept constant at 0.1V vs E_{ref} for 60 seconds. This cycling process

was repeated a total of 14 times, however, after the first cycle OCV was maintained for 30 second only (instead of the initial 90).

Moreover, before the measurement of polarization curves in operating conditions, E_{we} was increased from 0.1V to 0.65V vs E_{ref} (H^+/H_2) using a scan rate of 100 mV/s, and E = 0.65V vs E_{ref} was maintained for 15 minutes. Finally, E_{we} was altered from 0.65V vs E_{ref} back to OCV in a 100 mV/s scan rate. The same process was performed in the case of high and low RH conditions, however the E_{we} of 0.65V vs E_{ref} was maintained for 30 minutes instead.

Polarization curves in operating conditions were recorded by first maintaining OCV for 30 seconds, and then shifting the potential from OCV to 0.3V vs E_{ref}, and back, using a scan rate of 2 mV/s. Current density, I, was recorded over the last 50% of each stepwise shift of E_{we}, and was averaged over two steps. In the case of high and low RH conditions, the potential was shifted from OCV to 0.5 vs E_{ref}, and back, instead. Moreover, this cycling was repeated an additional two times.

EIS was measured using a multi sine mode, at a set dc current density of I = 25 mA/cm^2, a zone where resistances contributing to the activation overpotential are dominant (figure 101). The amplitude of the sinusoidal ac current was 1 mA, and impedance was recorded for frequencies between 100 mHz and 200 kHz.

Before performing cyclic voltammetry, the temperature of the cell was reduced to 30^{o}C. 100% humidified H_2 and N_2 were flown through the counter electrode (CE) and working electrode (WE) at 47 and 50 NL/h respectively for 30 minutes. The introduction of pure nitrogen to the cathode ensured any O_2 present from previous cell operation was flushed out, and an environment where no ORR could take place was created. As a result, E_{we} dropped from OCV to approximately 200 mV vs E_{ref}. Afterwards, the flow of N_2 was completely terminated (H_2 was retained at 47 NL/h), and cyclic voltammetry was commenced when a further drop of E_{we} to approximately 50 mV vs E_{ref} was observed. Note a drop to 0 mV vs E_{ref} that would be indicative of complete O_2 depletion was impossible to achieve using the characterization test bench in use. However, the change from OCV of approximately 0.65V when N_2 flow was first introduced, to 50 mV when the measurement was commenced, was significant.

Cyclic voltammetry was performed by altering the E_{we} from 0.07V vs E_{ref} to 1.2V vs E_{ref} and back, using a scan rate of 100 mV/s. The current density, I, was measured over the last 50% of E step-wise increase, and averaged over 10 steps. The cycling was performed 20 times in total.

In addition to CV, EIS measurements were also performed at the same operating conditions. However, in this set up, a fixed E_{we} point of 0.4V was chosen, and a sinus wave of amplitude 5 mV was utilized instead, with impedance measured at frequencies from 100 mHz to 200 kHz. With ORR thwarted by the lack of O_2 reactant, EIS performed at the fixed point of 0.4V vs E_{ref} yields information on the resistance associated with the movement of protons, electrons, and the double layer capacitance only.[128] No resistance associated with mass transport of reactants through the CCM or the kinetics of the ORR reaction are probed.

For each CCM composition (acquired from the same batch) based on Pt/HSAC, 3 repeats of electrochemical characterization were performed. Additionally, a new batch of CCMs was prepared using ink compositions with varying solvent systems, to ensure repeatability is maintained when the catalyst layers are made from scratch. The measurement reproducibility was evaluated by comparing polarization curves obtained at the air, high RH condition as well as the cyclic voltammogram of each sample. Note in each instance significant variations could be observed in polarization curves at I > 1.7 A/cm^2. At high current densities > 1 A/cm^2 the impact of mass transport losses becomes significant, particularly with high RH and lower O_2 concentrations present in this operating condition. The mass transport losses are strongly related to the GDL material, which can be stochastic, with low pressure drops for water evacuation, particularly in

a differential cell type such as used in this work. Therefore, small variations in the GDL structure may have a large impact on the mass transport losses observed. For this reason, the observed discrepancies were attributed to inhomogeneity in the GDL batch used in the cell set-up, and therefore the reproducibility was evaluated at I < 1.7 A/cm^2, with particular focus on the losses associated with the activation overpotential observed. Additionally, due to this observation, polarization curves obtained at air, high RH conditions will be analysed in the I < 1.7 A/cm^2 region only in section 5.3 focusing on results. In each instance at least 2 of the 3 measurements were reproducible, along with the extra measurement utilizing a Pt/HSAC based CCM from a different preparation batch. Examples of data reproducibility can be visualized in appendix 35. Note obtaining an averaged result proved arduous as each measurement resulted in a varied number of data points, and therefore one representative of the repeatable datasets will be used in the results section. Unfortunately, due to insufficient time, only 2 repeated measurements were obtained for CCM compositions based on Pt/GC, and so the reproducibility could not be as accurately evaluated. For this reason, observations for the Pt/GC based CCMs can only be considered preliminary. An example of reproducibility for Pt/GC based CCMs can be found in appendix 35.

5.3 Results

MEAs containing cathode catalyst layers based on varying Pt/C complexes and manufactured from inks with varying solvent systems were characterized, allowing for a correlation of structural differences observed in the inks/catalyst layers by SANS directly to electrochemical performance of the resulting fuel cell. As the MEAs are exactly the same as for SANS catalyst layer studies, the same naming conventions will be maintained: 25/50/75 PtHNP as well as 25/50/75 PtGNP. For details of each ink composition used to manufacture the corresponding cathode catalyst layer (CCL) please refer to section 2.1.4. Firstly, polarization curves and EIS data of MEAs containing catalyst layers based on the same Pt/C complex obtained in different conditions will be compared, followed by data acquired from cyclic voltammetry and EIS measured when ORR was inhibited. Secondly, a comparison of MEAs containing catalyst layers based on varying Pt/C complexes will be made, focusing on data obtained using operating conditions as well as cyclic voltammetry.

5.3.1 Pt/HSAC based CCMs

Figure 130 presents a comparison of polarization curves and EIS data obtained during air, high RH operating conditions for MEAs containing CCLs based on Pt/HSAC, which were manufactured from inks

with varying solvent compositions. Note decreasing current density as a function of potential difference yields higher performance than increasing current density as function of potential difference.

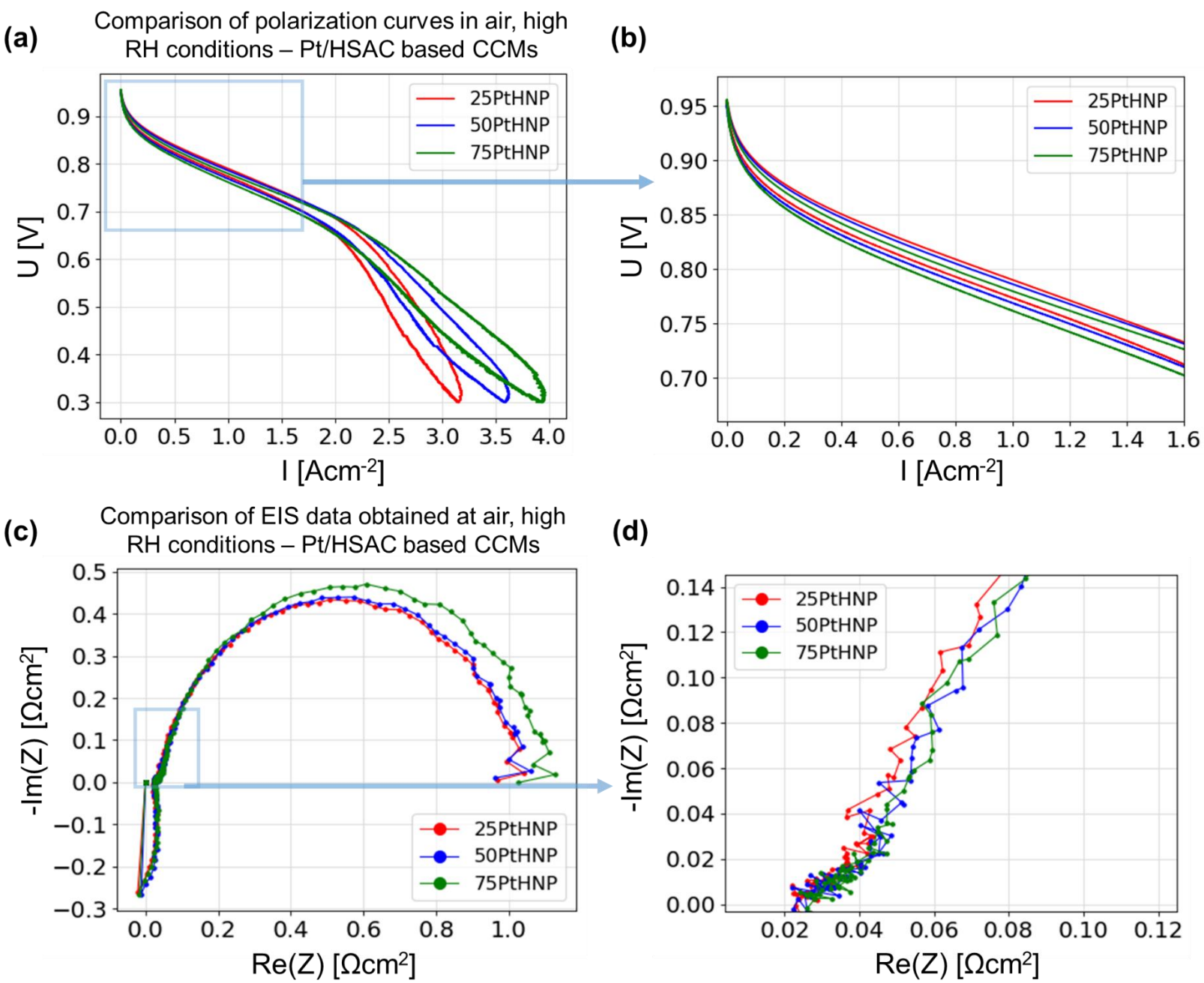


Figure 130. *Electrochemical characterization of MEAs containing Pt/HSAC based CCLs in air, high RH conditions:* ***(a)*** *polarization curves,* ***(b)*** *polarization curves focusing on the activation overpotential region,* ***(c)*** *EIS data obtained at 25mA/cm^2,* ***(d)*** *EIS data focused on high frequency impedance.*

On first glance, the most visible difference between polarization curves obtained for the different MEAs lies at high current density, however, it has been noted above that similar variations were observed in repeating measurements of the same batch CCMs, which most likely arise due to inhomogeneity in the GDL batch that was used throughout all characterizations. Therefore, a better comparison can be made when focusing on the low current density region related to activation overpotential losses, figure 130b. Indeed, slight

variations can be observed, with 75PtHNP showing a slightly bigger drop in U, indicating a higher activation overpotential. On the other hand, the polarization curves of 25PtHNP and 50PtHNP are almost identical in this region, suggesting similar resistance related to the ORR mechanism. Moreover, this idea is further suggested by the low frequency EIS data presented in figure 130c, where 75PtHNP shows significantly increased impedance at low frequencies. In the high frequency region, enhanced in figure 130d, such major differences are not noticeable. Perhaps it could be argued 25PtHNP shows less resistance to the dynamic processes (proton/electron transport resistance) occurring in the catalyst layer. Note fitting of EIS data was attempted using the model presented in equation (*5.1.9*), however a suitable fit was not achievable (example in appendix 36). No variation of R_p, C_{dl}, R_{ct} and R_{ohmic} could be found which would satisfy the entire EIS data set. This was a recurring issue, suggesting an alternative to the model proposed in (5.1.9) has to be applied. Further work most definitely will include finding an appropriate model for extraction of qualitative resistance values from the EIS data obtained. Nevertheless, in the scope of this work EIS data will be evaluated based on visual observations only.

Figure 131 presents a comparison of polarization curves and EIS data obtained during O_2, high RH conditions for the same MEAs, highlighting kinetic resistance related to the ORR, with proton and O_2 transport resistance minimized.

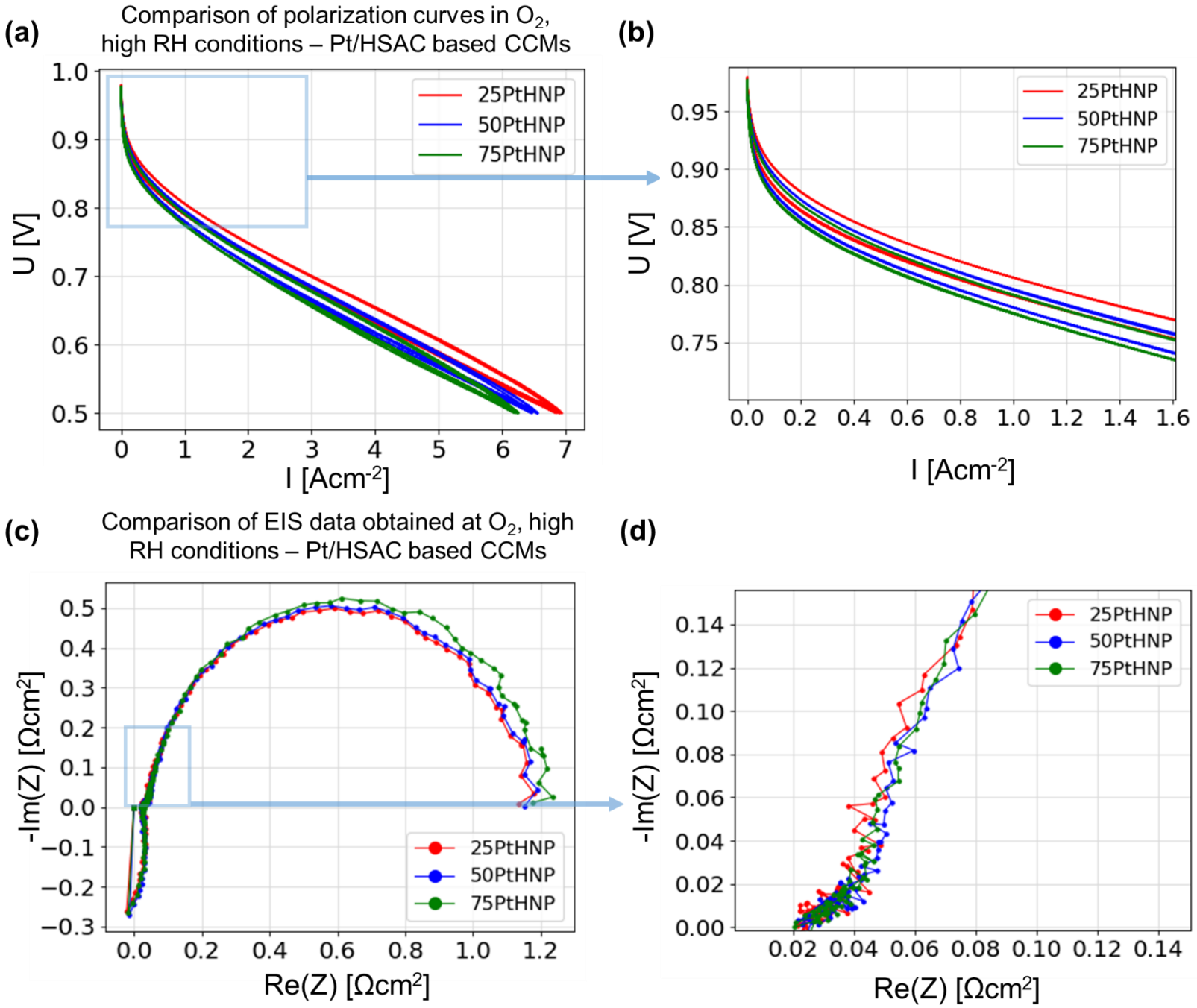


***Figure 131**. Electrochemical characterization of MEAs containing Pt/HSAC based cathode catalyst layer in O_2, high RH conditions: **(a)** polarization curves, **(b)** polarization curves focusing on the activation overpotential region, **(c)** EIS data obtained at 25 mA/cm^2, **(d)** EIS data focused on high frequency impedance.*

In figure 131b it can be observed the trend in decreasing U at low current densities (and therefore increasing activation overpotential) is maintained between the three samples, however, the difference between 25PtHNP and 50PtHNP seems more pronounced.

Table 11 compares upper E_{we} values measured at 0.3 A/cm^2 for different MEAs in both air, high RH and O_2, high RH conditions for an in-depth analysis:

Catalyst layer in MEA	**E_{we} at 0.3 A/cm^2 in air, high RH conditions (V vs E_{ref})**	**E_{we} at 0.3 A/cm^2 in O_2, high RH conditions (V vs E_{ref})**
25PtHNP	0.867	0.869
50PtHNP	0.864	0.862
75PtHNP	0.859	0.858

Table 11. *Comparison of upper E_{we} value measured at – 500 mA in operating and high RH conditions for different MEAs.*

Indeed, at high RH conditions the difference in U between 25PtHNP and 50PtHNP becomes more pronounced, however, this is a result of small U shifts observed in both MEAs, an increase and decrease of 2mV for 25PtHNP and 50PtHNP respectively. Since the differences between U measured at operating conditions are so small, it is impossible to make any deductions relating to the reaction kinetics itself. And indeed, in EIS the trend remains consistent, with 75PtHNP showing higher impedance at low frequencies, suggesting higher polarization resistance, while at higher frequencies 25PtHNP seems to show lower resistance in comparison to the other two MEAs. The increased U loss observed in polarization curves, as well as EIS data obtained at high RH for 75PtHNP suggest increased resistance related to the proton transport and ORR mechanism. Note the charge transport associated with the ORR mechanism is affected by the potential applied and RH, however should remain unchanged between the MEAs. For this reason, variation in the low frequency impedance may arise from mass transport within the catalyst layer, although at 25mV current density these shouldn't be prominent. On the other hand, it can be observed the polarization resistance is overall higher in the O_2, high RH conditions than in air, high RH, across all MEAs. This may be suggestive of an alteration in the charge transfer resistance and ORR mechanism when the reactant gas is varied. Please refer to appendix 37 and 38 to visualize polarization curves and EIS data obtained in different conditions for each CCM plotted together.

Figure 132 presents a comparison of polarization curves and EIS data obtained during O_2, low RH conditions for the above discussed MEAs, where O_2 transport resistance remains minimized, however proton transport resistance becomes more pronounced.

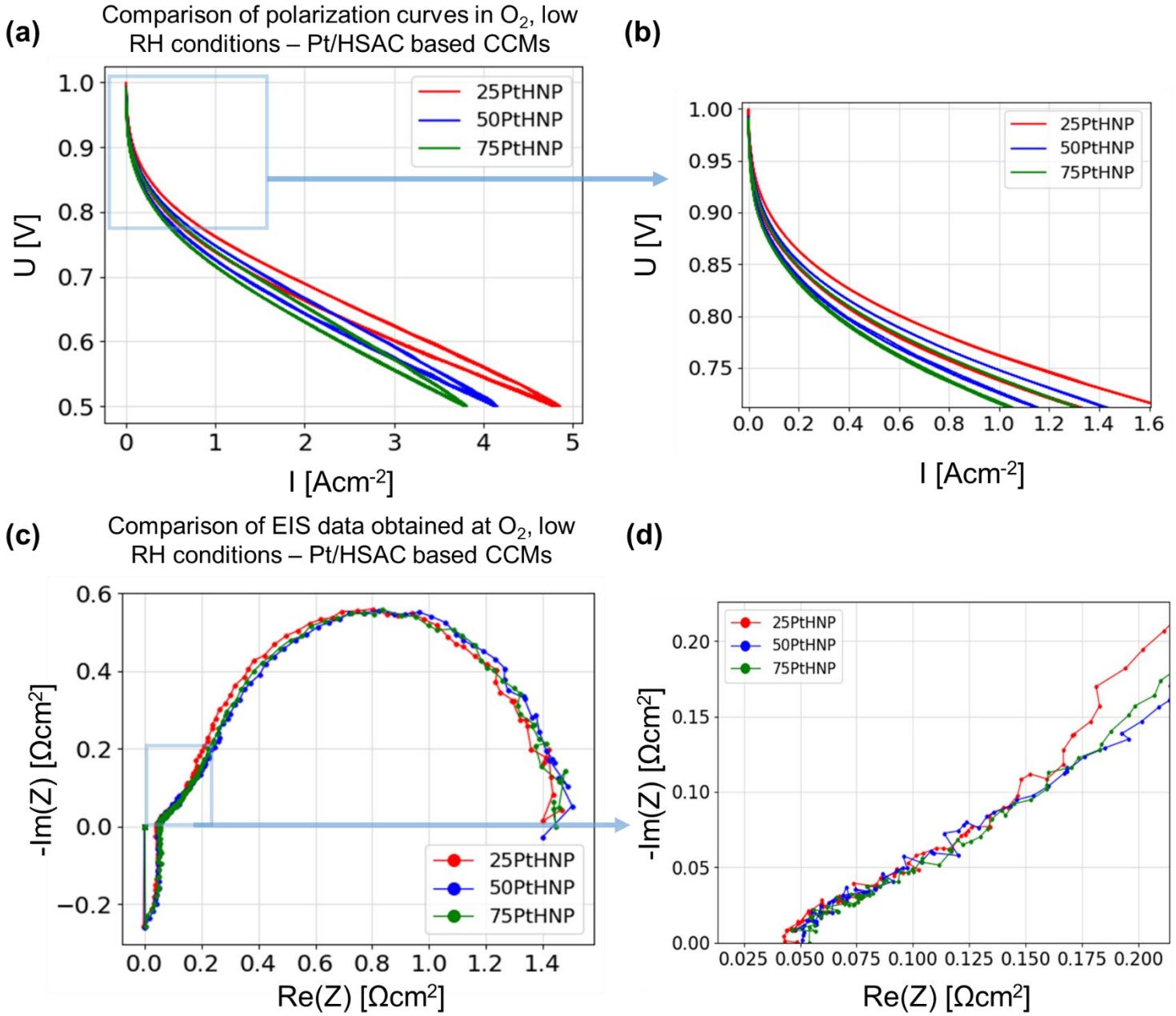


***Figure 132**. Electrochemical characterization of MEAs containing Pt/HSAC based cathode catalyst layer in O_2, low RH operating conditions: **(a)** polarization curves, **(b)** polarization curves focusing on the activation overpotential region, **(c)** EIS data collected at 25 mA/cm^2, **(d)** EIS data focused on high frequency impedance.*

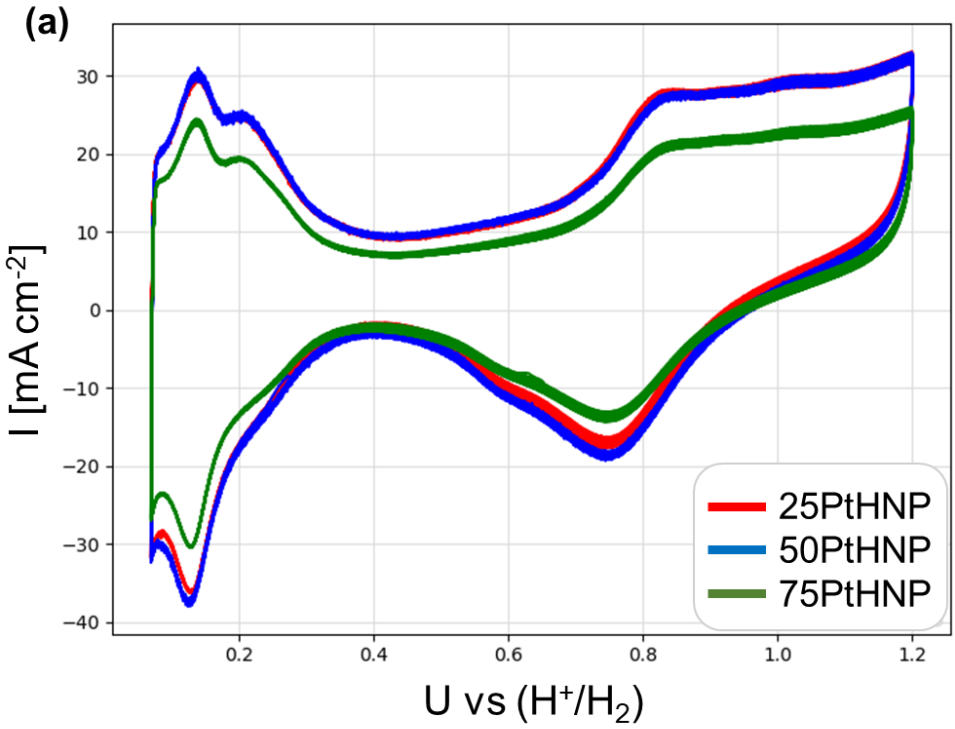
In figure 132b a drop in U can be observed for each MEA, in comparison to values observed in polarization curves measured at operating and high RH conditions, along with increased real and imaginary impedance values in EIS (figure 132c). In the activation overpotential region, the U measured for 25PtHNP is significantly higher than for the other MEAs, and at 0.5V current densities over 4.5 A/cm^2 are achieved. Impedance obtained at high frequencies shows the Tafel slope related to the proton migration is higher

than for 50PtHNP and 75PtHNP, suggesting lower proton transport resistance. As at low RH conditions the ability for water to act as an electrolyte is reduced, this may indicate an improved ionomer coverage in the case of 25PtHNP. The differences in activation losses observed in polarization curves are related to the reaction kinetics only, rather than proton transport itself, however, proton transport limitations may lead to the misuse of the catalyst and increased kinetic losses. For this reason, the observations of lower activation losses and lower proton migration resistance for 25PtHNP can be considered consistent.

On the other hand, low frequency impedance is similar for all MEAs studied.

Figure 133 presents cyclic voltammetry measurements of the three samples, along with extracted Pt per surface area values from the peak associated with proton desorption from Pt.

(a)



(b)

Sample	Hupd desorption charge (mC/cm² geo)	Hupd desorption roughness factor (cm²Pt/cm²geo)	ECSA (m²/g)
25PtHNP	34.5	163	74.1
50PtHNP	34.8	164	78.1
75PtHNP	27.6	135	67.5

Figure 133. (a) *cyclic voltammetry data obtained from MEAs containing cathode catalyst layers based on Pt/HSAC, but manufactured from inks with different solvent compositions,* ***(b)*** *quantified Hupd desorption charge from integration of peak corresponding to proton desorption from Pt surface, and subsequent Hupd desorption roughness factor, corresponding to Pt active area available. Electrochemically active surface area (ECSA) was computed from Hupd desorption roughness factor and known Pt loading.*

In cyclic voltammetry, both visually and in terms of extracted ECSA, a significant difference in the case of 75PtHNP can clearly be observed. This observation correlates with the consistently lower performance indicated by polarization curves, as well as increased impedance observed at low frequency for 75PtHNP in high RH conditions (both in air and O_2). Nevertheless, charge transfer resistance associated with the ORR mechanism is assumed to remain constant during homogenous operation of all CCMs, and cannot explain the impedance variation. The low current density chosen for EIS measurements should also negate any mass transport resistance in the catalyst layer. On the other hand, the presence of an internal short circuit, indicated by increasing current density in the 0.4-0.5V region observed in cyclic voltammetry, may result in an overall increased current density. In this instance, in reality EIS was performed at current density values slightly higher than 25mA/cm^2, and mass transport activation losses may no longer be negligible. Although this explanation is plausible, and consistent with cyclic voltammetry data, further investigation must be performed into the reason for impedance variation observed at low frequencies at high RH conditions.

The ECSA is very comparable for 25PtHNP and 50PtHNP, and the discrepancy observed for 75PtHNP can also be linked to TEM/EDS characterization presented in section 2.4.2.1. In HAADF/STEM images obtained on the micrometre scale (figure 96) it was observed that the contact between the cathode and the membrane is much poorer for the 75PtHNP CCM. Moreover, the thickness of the cathode was seen to vary. In particular, the former observation could account for the lower ECSA obtained, with poor transfer of the CCL to the membrane. Where before it was debated whether such a poor transfer could be an anomaly, the repeatability of electrochemical results may suggest poorer quality of catalyst layers obtained from inks based on alcohol-rich solvents. On the other hand, increased carbon aggregation, could also explain a lower ECSA measured. Such a case was not necessarily observed in TEM, however, note the technique is not essentially representative of the bulk system, especially on the nanometre scale. Therefore, verification of carbon aggregate size as a function of solvent system by USAXS would be favourable in resolving this query.

Manufacturing related aspects could be studied by methods such as rheology, to evaluate ink viscosity change as a function of solvent, or time resolved USAXS, allowing for observation of carbon aggregation during the drying of inks with varying solvent systems, combined with microscopy to estimate the final quality of the catalyst layer.

Figure 134 shows EIS data collected at 30°C, with 47NL/h flow of humidified H_2 at the anode and no gas flow at the cathode, namely when the ORR reaction was completely inhibited.

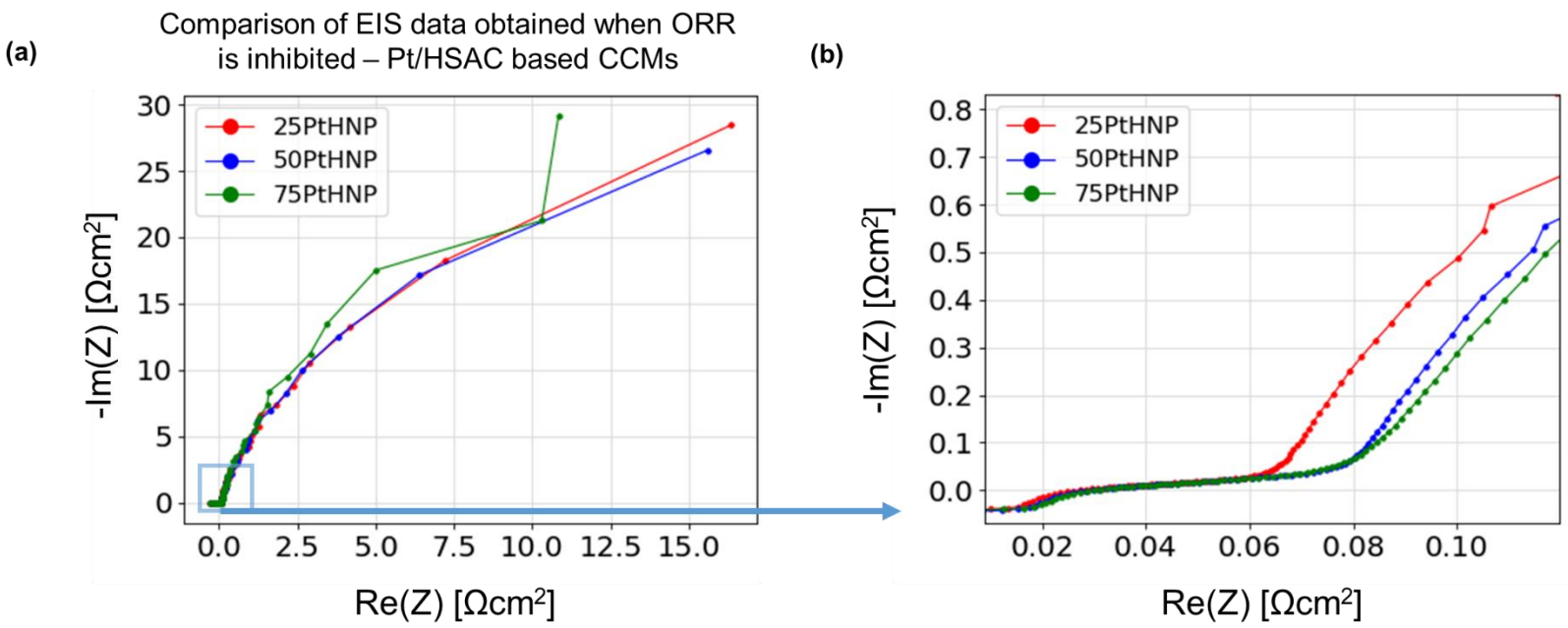


Figure 134. *Characterization of MEAs containing Pt/HSAC based cathode catalyst layer when ORR is inhibited (same conditions as for cyclic voltammetry):* ***(a)*** *EIS obtained at 0.4V,* ***(b)*** *EIS data focused on high frequency impedance.*

As ORR is inhibited, the characteristic half-spherical shape of EIS is not retained, as no sluggish ORR kinetics remain to be characterized in the low frequency region. Instead, looking into the high frequency impedance, a large decrease in resistance can be observed in the case of 25PtHNP. This corresponds to the reduced proton transport resistance through the catalyst layer, and may justify the improved performance observed for 25PtHNP in each operating condition.

In summary, throughout characterization in operation as well as high RH conditions, 25PtHNP and 50PtHNP showed similar U losses related to the activation overpotential, with 75PtHNP consistently showing higher losses than the other two CCMs. EIS data revealed 75PtHNP showed higher impedance at low frequencies, however with the ORR mechanism assumed unchanged between the three compositions, and mass transport resistance negligible due to the low current density chosen for EIS measurements, the reason for this discrepancy remains unknown. Furthermore, cyclic voltammetry revealed 75PtHNP has a lower ECSA of 67.5 m^2/g in comparison to 25/50PtHNP which showed values of 74.1 and 78.1 m^2/g respectively. This variation can be directly linked to the increased impedance observed in EIS, and may be a result of incompatibility of inks based on a high alcohol solvent system with the catalyst layer manufacturing process, either in terms of the coat-ability of the ink or the transfer process of the catalyst layer to the membrane. Investigating properties such as viscosity of the ink, or processes such as crack formation during drying of the ink, may give more insight into the reasons of lower Pt active area observed. Additionally, it is suggested USAXS is applied to verify effect of ink solvent system on Pt/C aggregation.

With regards to the other two MEAs, EIS measured in conditions where ORR is inhibited suggested 25PtHNP exhibits reduced proton transport resistance, showing significantly lower impedance values at high frequencies than 50PtHNP and 75PtHNP. Moreover, the EIS performed at low RH conditions also showed lower impedance at high frequency for 25PtHNP, suggesting the reduced

proton transport resistance observed could be related to improved ionomer coverage due to the low water content in the cathode.

This suggests that although in operating conditions 25PtHNP and 50PtHNP showed almost identical activation losses, 25PtHNP was the best performing CCM, showing least proton transport resistance, which may be related to an improved coating of the ionomer on Pt/C, as suggested by small activation losses in conditions that enhanced proton transport resistance. Looking back to section 2.3, the catalyst ink based on 25:75 wt% iPrOH/water solvent, 25PtHNP, showed a significantly higher ionomer adsorption to the Pt/HSAC particles. Moreover, in section 2.4 it was noted the corresponding catalyst layer displayed a bigger size domain of the ionomer-related peak-like feature, irrespective of the sample relative humidity. These observations correlate with the EIS data at low RH and when the ORR is inhibited, conditions where proton transport resistance is minimized, and may explain the significantly reduced impedance at high frequencies in comparison to the other two samples (25PtHNP and 50PtHNP), where little or no ionomer adsorption was observed in corresponding ink samples.

5.3.2 Pt/GC based CCMs

Figure 135 presents a comparison of polarization curves and EIS data obtained during air, high RH conditions for CCMs containing cathode catalyst layers (CCLs) based on Pt/GC, which were manufactured from inks with varying solvent compositions.

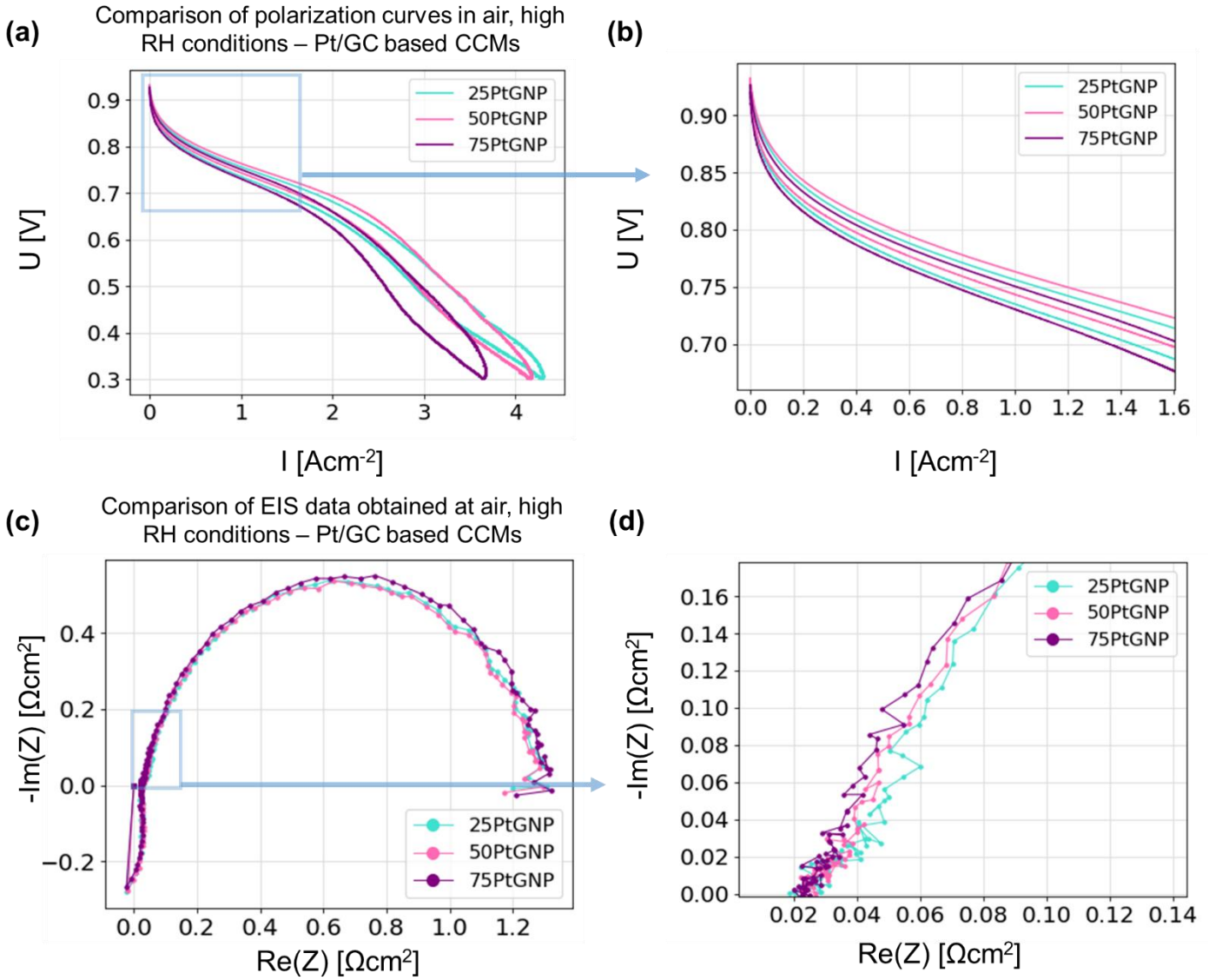


Figure 135. *Electrochemical characterization of MEAs containing Pt/GC based cathode catalyst layer in air, high RH operating conditions:* ***(a)*** *polarization curves,* ***(b)*** *polarization curves focusing on the activation overpotential region,* ***(c)*** *EIS data obtained at 25 mA/cm^2,* ***(d)*** *EIS data focused on high frequency impedance.*

Again in polarization curves no major difference in activation overpotential can be observed between the different MEAs, however, the slight variation observed is more gradual, with highest U values observed for 50PtGNP, followed by 25PtGNP and 75PtGNP. Looking to EIS data (figures 135c, d) a similar trend can be observed in impedance measured at low frequencies, with 50PtGNP showing lowest resistance, and 75PtGNP the highest. This variation in low frequency impedance measured between 75PtGNP and the two other MEAs is not as significant as in the case of Pt/HSAC based MEAs in the same conditions. At high frequencies, impedance seems fairly similar for all the CCMs.

Figure 136 presents characterization data obtained for the three Pt/GC based MEAs in high RH conditions.

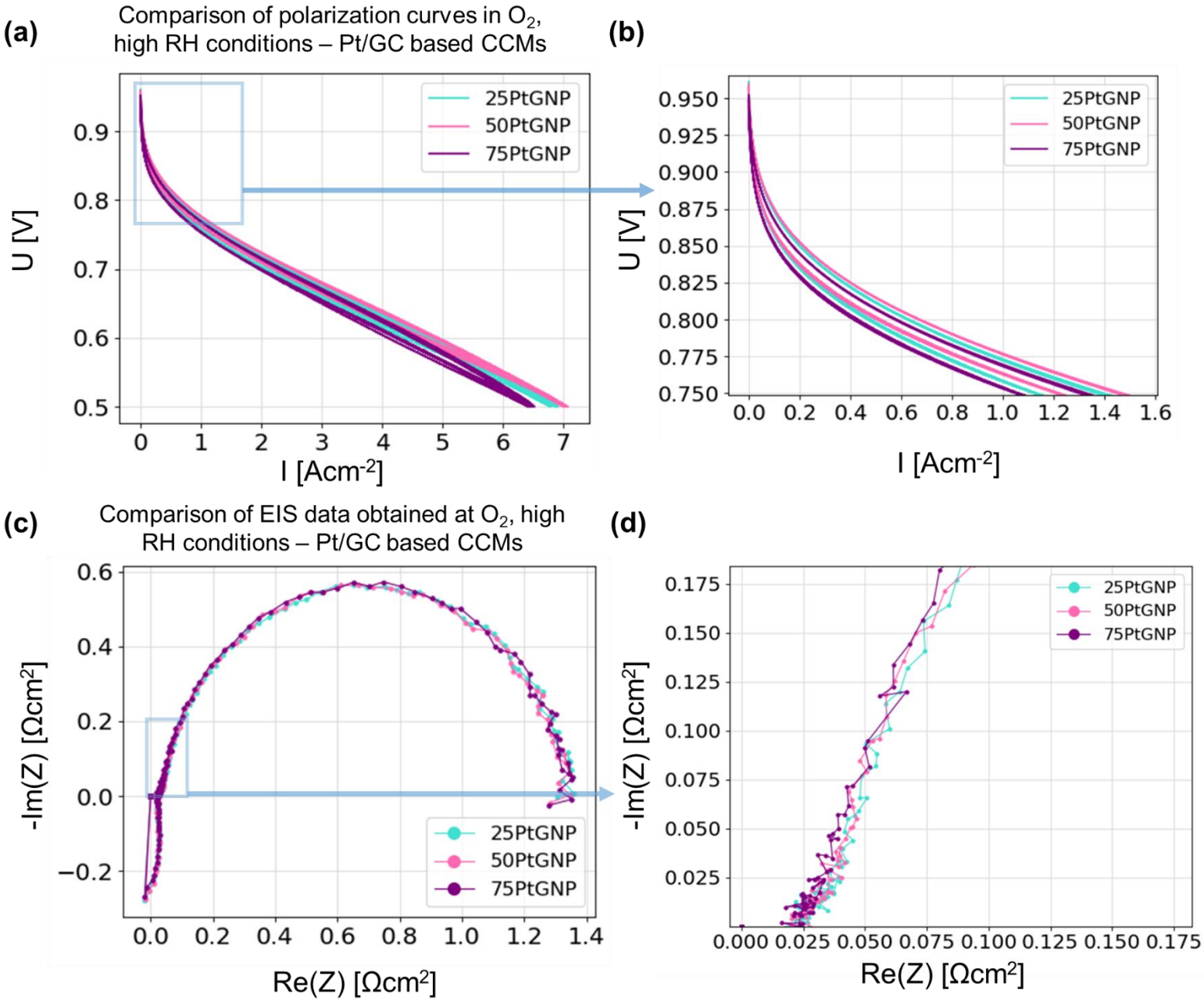


Figure 136. *Electrochemical characterization of MEAs containing Pt/GC based cathode catalyst layer in O_2, high RH conditions:* ***(a)*** *polarization curves,* ***(b)*** *polarization curves focusing on the activation overpotential region,* ***(c)*** *EIS data obtained at 25 mA/cm^2,* ***(d)*** *EIS data focused on high frequency impedance.*

In high RH conditions a similar trend in activation losses can be observed as in operating conditions – 50PtGNP shows the smallest losses and 75PtGNP the highest. Moreover, the current density achieved at 0.5V vs U is also the highest for 50PtGNP and the lowest for 75PtGNP. However, in the EIS data no major differences in impedance can be observed, either at low or high frequencies. Since O_2 and proton transport are both optimized under the high RH conditions, this observation suggests resistance related to electrode operation is unchanged in between the samples, as expected at low current densities of 25mA/cm^2. Note just like in the case of MEAs containing Pt/HSAC based CCMs, overall the impedance is higher at lower

frequencies than in air, high RH operating conditions, which may be indicative of variation in ORR mechanism under different reactant gasses supplied (appendix 38 compares polarization curves and EIS obtained in different operating conditions for each Pt/GC based CCM).

Figure 137 presents characterization data obtained for the same CCMs at O_2, low RH conditions.

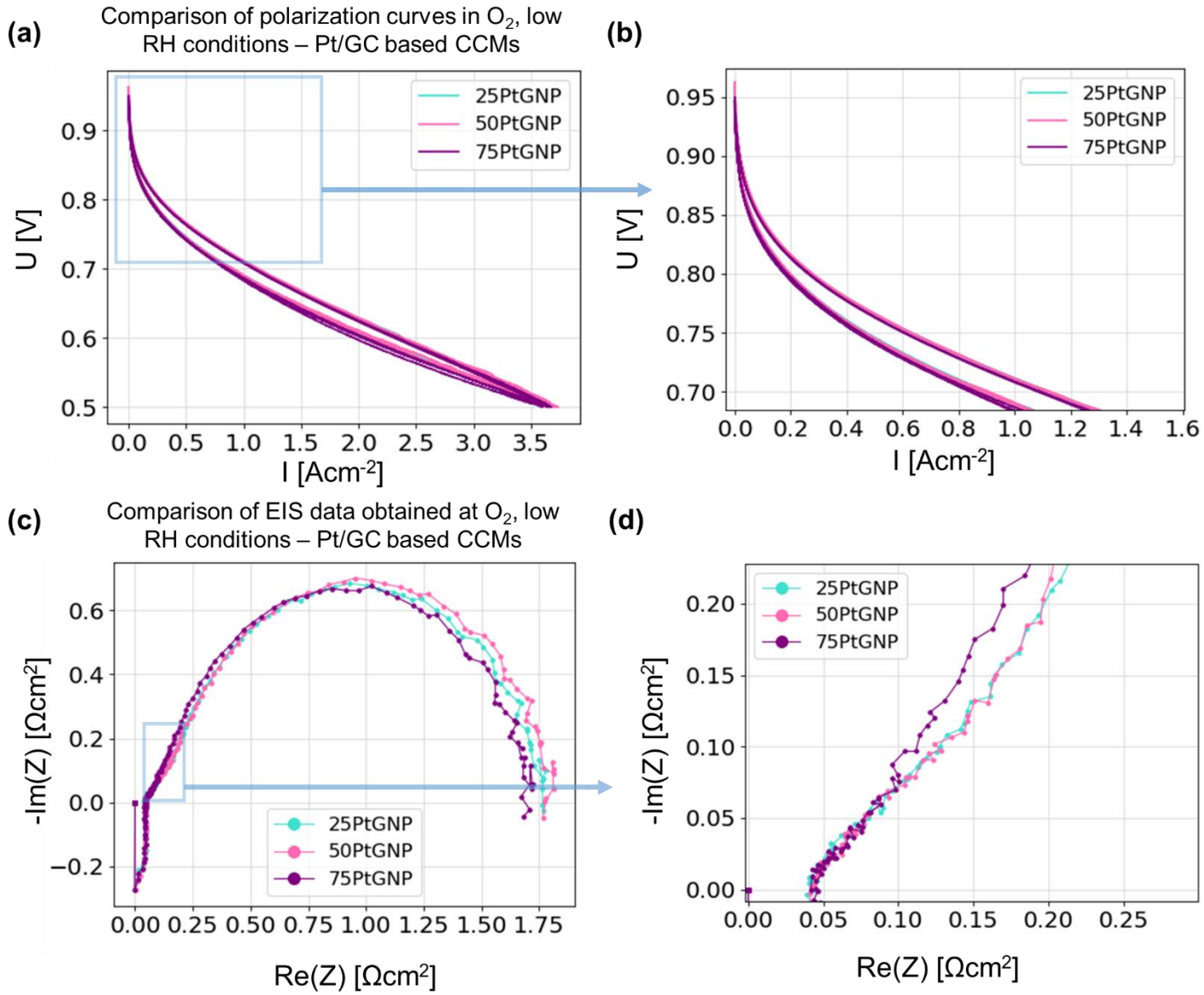


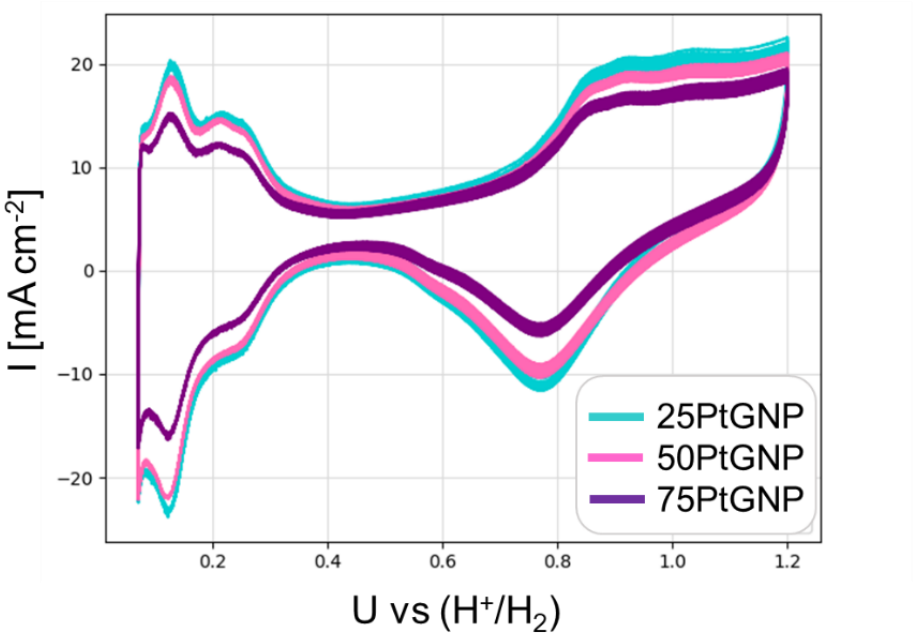
Figure 137. *Electrochemical characterization of MEAs containing Pt/GC based cathode catalyst layer in O_2, low RH conditions:* ***(a)*** *polarization curves,* ***(b)*** *polarization curves focusing on the activation overpotential region,* ***(c)*** *EIS data obtained at 25 mA/cm^2,* ***(d)*** *EIS data focused on high frequency impedance.*

A contrasting trend to characterization data obtained in high RH can be observed. Where polarization curves show effectively no difference over the entire U range, significant variation can be observed in EIS, both with regards to impedance measured at high and low frequencies. At high frequencies, 50PtGNP, which previously was noted to show the lowest polarization resistance, shows the highest impedance, and conversely 75PtGNP the lowest. Moreover, at high frequencies the impedance of 75PtGNP is also significantly lower than for 25PtGNP and 50PtGNP, despite the fact 75PtGNP shows consistently the highest losses across all polarization curves. EIS measured in the low RH conditions indicates variation in

proton transport resistance, however, the unchanging activation overpotential across all MEAs suggests this may not be a limiting factor for the ORR reaction.

Figure 138 presents cyclic voltammetry measurements obtained for the three Pt/GC based MEAs, along with extracted Hupd desorption roughness factors, with subsequently calculated ECSA values using known Pt loading.

(a)



(b)

Sample	Hupd desorption charge (mC/cm² geo)	Hupd desorption roughness factor (cm²Pt/cm²geo)	ECSA (m²/g)
25PtGNP	23.1	109	49.5
50PtGNP	21.4	101	45.9
75PtGNP	16.8	79	32.9

Figure 138. (a) *Cyclic voltammetry data obtained from MEAs containing cathode catalyst layers based on Pt/GC, but manufactured from inks with different solvent compositions,* ***(b)*** *quantified Hupd desorption charge from integration of peak corresponding to proton desorption from Pt surface, and corresponding Hupd desorption roughness factor, corresponding to Pt active area available. Electrochemically active surface area (ECSA) was computed from Hupd desorption roughness factor and known Pt loading.*

Cyclic voltammetry measurements again show significantly lower current densities across the cycling potential for 75PtGNP, which explains the highest activation losses observed for this MEA in both air and O_2 high RH conditions. The significant decrease in the ECSA for both Pt/GC and Pt/HSAC based samples, where inks contained high alcohol content in the solvent compositions, suggest a solvent specific issue that results in poorer Pt/C dispersion quality. Pt/GC based CCMs should also be characterized using TEM to verify whether the same issue with cathode/membrane contact that was present for 75PtHNP can be observed for 75PtGNP also.

With regards to 25PtGNP and 50PtGNP, again the difference in ECSA obtained remains low, however in this instance the ECSA of 25PtGNP is higher.

Figure 139 presents EIS data obtained with cell temperature of 30ºC, 47NL/h flow of humidified H_2 at the anode and no gas flow at the anode – therefore, when the ORR was inhibited.

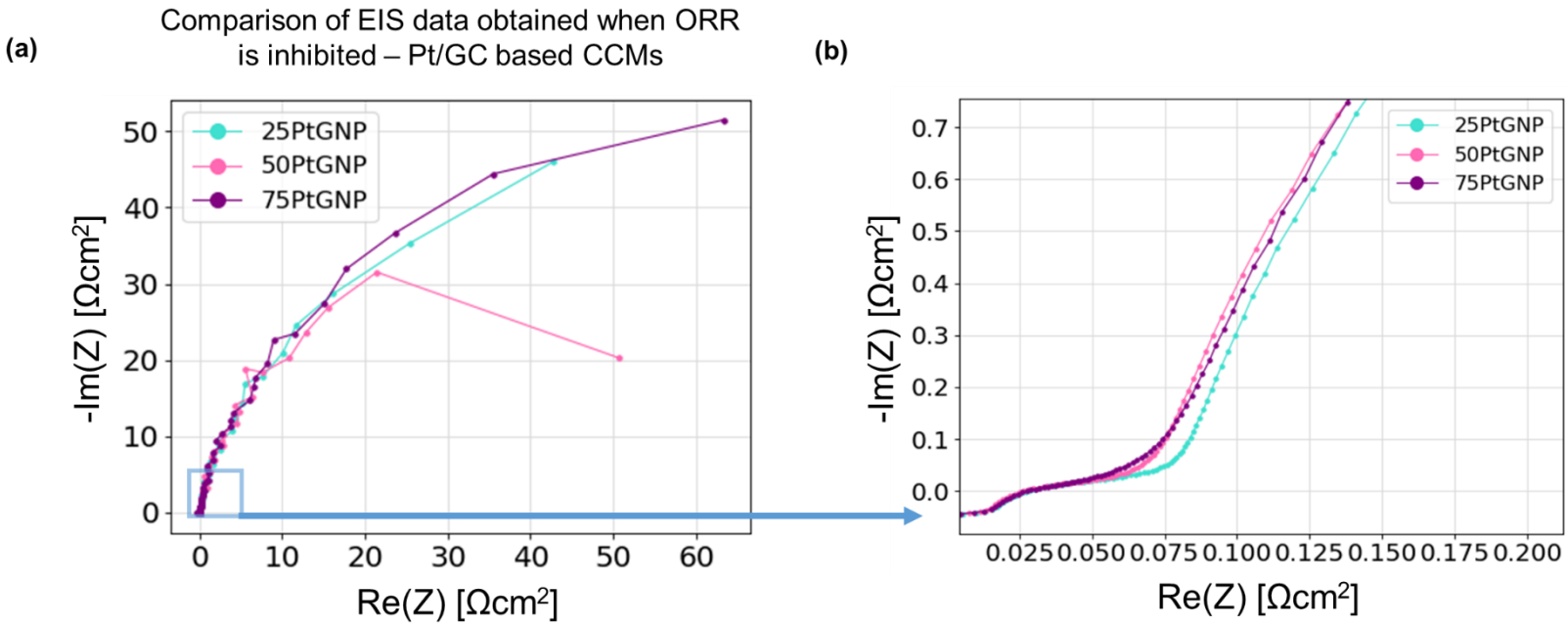


Figure 139. *Characterization of MEAs containing Pt/HSAC based cathode catalyst layer when ORR is inhibited (same conditions as for cyclic voltammetry measurements):* ***(a)*** *EIS obtained at 0.4V,* ***(b)*** *EIS data focused on high frequency impedance.*

At the highest frequencies (figure 139b), the impedance of 25PtGNP can be observed to be bigger, suggesting greater proton transport resistance. This is contrary to Pt/HSAC based MEAs (figure 132b), where 25PtHNP showed the lowest proton resistance. Moreover, this difference is not as pronounced as in the case of Pt/HSAC based samples.

In summary, for Pt/GC based MEAs again it was observed the use of CCLs manufactured from inks containing high alcohol concentrations in the solvent composition proved detrimental to the Pt active surface availability, suggesting a poorer Pt/C dispersion in the catalyst layer. The effect of lower Pt availability could be observed as higher activation overpotentials in polarization curves obtained in air and O_2 high RH operating conditions.

In general, 50PtGNP showed lower activation losses and higher achievable current densities than 25PtGNP in the polarization curves obtained, however, the extracted ECSA was lower for the former, suggesting Pt availability alone cannot justify the differences in performance observed. Looking to EIS data, in low RH conditions, where proton transport resistance is enhanced, 50PtGNP showed a higher impedance at low frequencies than 25PtGNP. On the other hand, at O_2, high RH conditions no significant difference in impedance could be observed, coherent with the lack of change in the ORR mechanism expected. In EIS obtained at air, high RH conditions, low frequency impedance of 50PtGNP is lower than that of 25PtGNP. The contrasting impedance behaviours observed in low RH and operating conditions may suggest thicker ionomer shells for 25PtGNP, which would boost proton transfer, but impede oxygen permittivity, and if reactant gas transport is considered the limiting factor, the increased activation losses observed for 25PtGNP can be perhaps explained. Concurrently, higher impedance at low frequency observed in O_2, low RH EIS, but lower impedance measured at operating conditions may suggest thinner ionomer shells in the case of 50PtGNP

which would result in improved reactant gas transport. Nevertheless, again it is important to note the EIS is performed at very low current densities of 25 mA/cm^2, where no losses associated with mass transport should be probed. In further work it must be verified whether EIS at these current densities also probes transport on the catalyst layer local scale, perhaps by obtaining EIS at even lower current density values and comparing the results.

5.3.3 Comparison of MEAs based on different Pt/C complexes

Figure 140 presents characterization data obtained at air, high RH conditions for MEAs containing catalyst layers based on different Pt/C complexes, but manufactured from inks with the same solvent compositions.

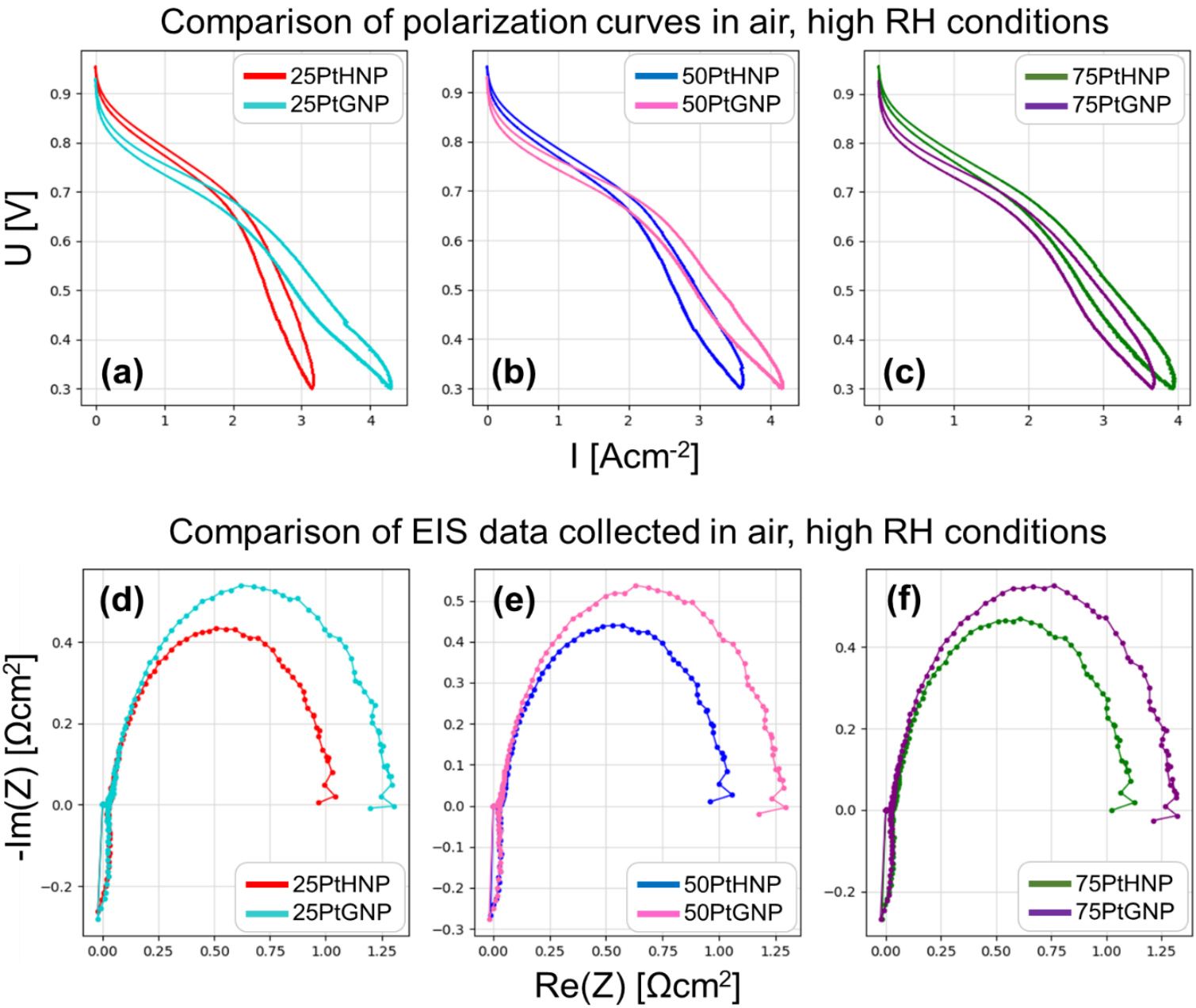
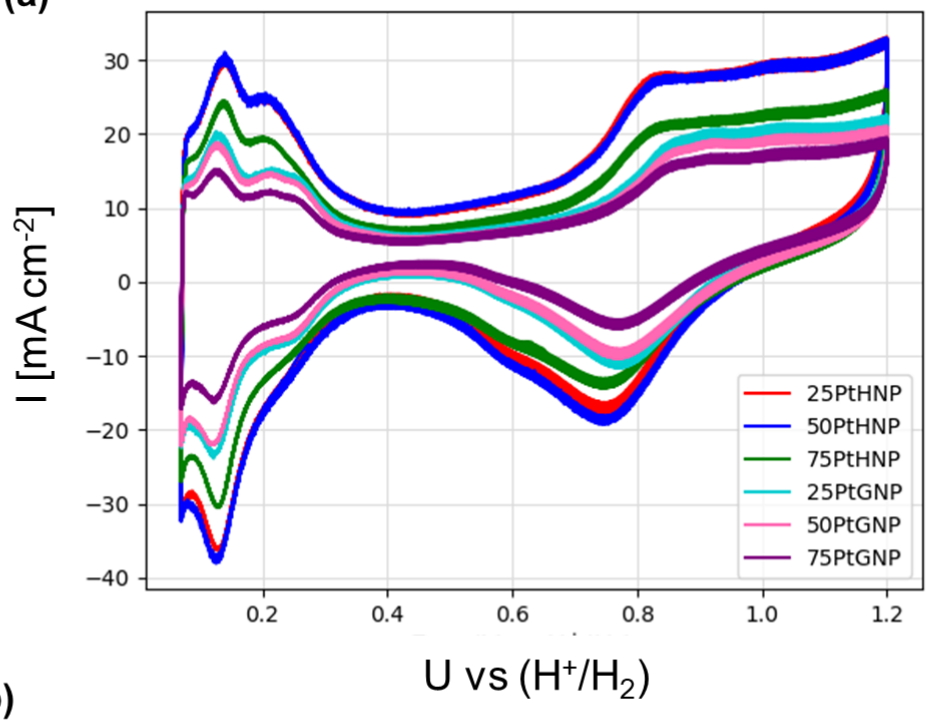


Figure 140. *Comparison of polarization curves (a-c) and EIS data obtained at 25 mA/cm^2 (d-f) collected in air, high RH conditions for MEAs containing cathode catalyst layers based on different Pt/C complexes, manufactured from inks with same alcohol concentrations in the solvent composition.*

Immediately clear differences between Pt/HSAC and Pt/GC based MEAs can be observed. Firstly, losses associated with the activation overpotential are much higher for Pt/GC based MEAs. Secondly, the low frequency impedance is much higher for Pt/GC based MEAs. Both of these aspects suggest increased resistance associated with the charger transfer across the electrolyte/catalyst interface related to the ORR mechanism. Indeed, differences in data obtained using cyclic voltammetry allows for a presentation of a clear conclusion, figure 141. It is evident that Pt/GC based MEAs show significantly reduced Pt active surface areas (characterized by the ECSA). Furthermore, a clear correlation can be made between the Pt

(a)



(b)

Sample	Hupd desorption charge (mC/cm^2 geo)	Hupd desorption roughness factor (cm^{2}Pt/cm^{2}geo)	ECSA (m^2/g)
25PtHNP	34.5	163	74.1
50PtHNP	34.8	164	78.1
75PtHNP	27.6	135	67.5
25PtGNP	23.1	109	49.5
50PtGNP	21.4	101	45.9
75PtGNP	16.8	79	32.9

***Figure 141**. **(a)** Comparison of cyclic voltammetry data (cycles 5-15) obtained for MEAs containing cathode catalyst layers based on different Pt/C complexes, manufactured from inks with different alcohol concentrations in the solvent composition. (**b**) Comparison of Hupd desorption charge and Hupd desorption roughness factor values obtained for the different MEAs.*

active surface area and observed activation losses in polarization curves as well as low frequency impedance in EIS. Therefore, it can be concluded the difference in performance between Pt/HSAC and Pt/GC based MEAs arises due to the availability of Pt active sites.

Nevertheless, it is known that Pt shows increased coalescence on the GC support due to preferential accumulation in the many defect sites and inter-particle crevices present,[18] resulting in bigger Pt particle size, which makes this observation unsurprising. Indeed, the use of Pt/GC catalyst layers is noteworthy due to its corrosion resistance resulting in improved durability. Therefore, a durability characterization may also be necessary for a more comprehensive comparison of Pt/HSAC and Pt/GC containing MEAs.

5.4 Conclusions

CCMs containing cathode catalyst layers based on Pt/GC and Pt/HSAC, manufactured from inks with varying solvent composition were characterized using electrochemical tests performed under different operating conditions.

In the case of CCLs manufactured from inks containing 75:25 wt% iPrOH/water solvent, based on both Pt/HSAC and Pt/GC, corresponding MEAs showed reduced performance to their counterparts containing CCLs manufactured from inks with lower alcohol content in the solvent. This observation could be directly linked to lower Pt active surface area available, extracted using cyclic voltammetry measurements. The most likely explanation could relate to the physical properties of the ink, such as viscosity, which could affect the ink coating process. The drying process would also be affected by the ink solvent composition, which could result in different qualities of the catalyst layer obtained. Moreover, in TEM characterization of 75PtHNP it was noted the contact between the cathode and membrane was poorer in comparison to the other compositions, suggesting issues with transfer of the cathode onto the membrane. On the other hand, structural differences in the ink itself cannot be disregarded. In USAXS it was observed that carbon aggregation in inks corresponding to the 50PtHNP and 50PtGNP compositions was unchanged, however, the variation in size of aggregates was not investigated for ink compositions based on different solvent systems. Obtaining such USAXS data would aid in pinpointing which stage of catalyst layer manufacturing is most impacted by the ink solvent composition.

For CCMs containing Pt/HSAC based catalyst layers, 25PtHNP (ink based on 25:75 wt% iPrOH/water solvent) and 50PtHNP (ink based on 50:50 wt% iPrOH/water solvent) showed very similar performance, with marginally higher activation losses observed for 50PtHNP in polarization curves studied. EIS data obtained suggests this may be as a result of increased resistance associated with proton transport when compared to 25PtHNP, which shows in particularly significantly lower proton transport resistance at the electrolyte-catalyst interface, observed through lower impedance measured at high frequencies when ORR is inhibited. This lower proton transport resistance can be correlated to both the CV-SANS and SANS data of corresponding catalyst inks and catalyst layers respectively, presented in section 2.3 and 2.4. 25PtHNP showed significantly higher ionomer adsorption to Pt/HSAC in the ink, and also a larger size domain was suggested for the ionomer-related peak-like feature in the catalyst layer. On the other hand, 50PtHNP and 75PtHNP showed little or no ionomer adsorption in the inks, and comparable, smaller size domains of the ionomer-related peak-like feature in the catalyst layer.

For MEAs containing Pt/GC based catalyst layers, a more gradual increase in activation overpotential was observed, from 50PtGNP to 75PtGNP. The difference observed between 50PtGNP and 25PtGNP may be attributed to the thickness of the ionomer layer, where combined analysis of EIS obtained at low RH and operating conditions suggests 50PtGNP may contain a thinner ionomer layer, indicated by greater impedance in the high frequency region when proton mass transport resistance is emphasized (O_2, low RH conditions), but lower impedance in air, high RH conditions,

suggesting improved reactant gas transport, when compared to 25PtHNP. Although Pt/GC-based inks could not be investigated, in Pt/GC based catalyst layers, 75PtGNP showed the largest size domains of the ionomer-related peak-like feature, which again could be related to the lower high frequency impedance observed in O_2, low RH conditions. Nevertheless, in Pt/GC based catalyst layers the size domain increase was more gradual, from 25PtGNP to 75PtGNP, and such a trend is not observed in the EIS data. Moreover, for EIS obtained when ORR is inhibited, 75PtGNP no longer shows significantly lower impedance in comparison to the other two samples. Further data of Pt/GC inks and catalyst layers must be obtained in order to establish a correlation between the results of the various techniques.

Additionally, it is important to highlight the deviations in low frequency impedance are unexpected, and must be investigated further.

Comparing MEAs containing CCLs based on Pt/HSAC and Pt/GC, which were manufactured from inks of the same solvent compositions, showed the activation losses and low frequency impedance are greatly increased in the case of Pt/GC based CCLs. This could be directly linked to the electrochemically active surface area of Pt extracted from cyclic voltammetry, suggesting availability of Pt is a major performance limitation in all catalyst layers.

Electrochemical characterization yielded a lot of details on the performance of the various CCMs, and ultimately the number of Pt active sites and their availability seemed to be the factor resulting in the biggest performance differences, which was affected by both the choice of Pt/C complex and choice of solvent composition in the ink. Moreover, a correlation between the results of the various techniques can be observed in the instance of Pt/HSAC based inks, but it is more challenging for Pt/GC based inks. Further investigation should be performed to fully correlate the composition of the catalyst ink to the final electrochemical performance observed.

6 Conclusions

In conclusion, a systematic study on the catalyst ink structural variation as function of composition was successfully performed, with the final catalyst layer structure and electrochemical performance also characterized for inks containing varying iPrOH concentrations.

A number of methods have been applied to study the catalyst inks. The CV-SANS/PSF method resulted in a plethora of results for numerous ink compositions, with characterization of the ionomer structure and degree of ionomer adsorption to carbon possible. Considering the complexity of the system, including large polydispersity and inhomogeneous component distribution, the results could only be considered quasi-qualitative. Nevertheless, unique information on the structure of the ionomer was successfully obtained, and clear variations could be observed for several ink compositions, shedding light onto which variables have the biggest impact on the ionomer distribution in the catalyst ink.

The impact of several input parameters on extracted PSF outputs was investigated in detail with the aid of simulated datasets, instructing on critical considerations to be taken into account during sample measurement, such as the necessity of performing contrast match measurements for experimental component SLD extraction. This evaluation ensured the veracity of PSF outputs obtained from the ink series studied, also through the development of a helpful tool where the PSF output behaviour as a function of shifting component SLD could be directly linked to the PSF exactness as well as structural nature of the catalyst ink.

The accuracy of the results was confirmed using ITC, through investigation of thermodynamics of ionomer adsorption for carbon and ionomer compositions based on 50:50 wt% iPrOH/water solvent, where observations were consistent with those made through analysis of CV-SANS/PSF data.

Additionally, USAXS was applied for the study of carbon (or Pt/C) aggregate size with varying ionomer content in the ink, contributing information on an additional size scale, and thus aiding in building a more complete picture of the catalyst ink system

Through analysis of results obtained through CV-SANS and USAXS several noteworthy observations with regards to the catalyst ink structure as function of composition could be made.

Regarding the results obtained, the iPrOH concentration in the ink solvent system was found to have a distinct effect on the degree of Nafion adsorption, with the highest proportion observed for 25HNP ink series, a composition based on a water rich solvent, where 55% of the total ionomer was found adsorbed to HSAC. On the other hand, ink series based on 50 and 75 wt% iPrOH, 50HNP and 75HNP, showed no and 7.4% of the total Nafion content adsorbed. Moreover, no significant variation in the conformation of unadsorbed ionomer could be observed between the three compositions, as suggested by analysis of Nafion-only dispersion. Nevertheless, due to the presence of an interference term in the scattering functions of Nafion in 25:75 and 50:50 wt% iPrOH/solvents, fitting of the data proved challenging or impossible. For this reason, dilute Nafion dispersions, where no interference term in the scattering functions is present, must be obtained and analysed in order to confirm such an observation. A potential explanation for the variation in ionomer adsorption observed in inks based on different solvent systems could involve the notion of stabilization of the carbon/solvent interfacial energy, which would be greater in water-rich solvents, and may lead to promoted Nafion adsorption.

This idea is also supported by the degree of adsorption that was observed between Aquivion and Nafion based inks in 25:75 wt% iPrOH/water solvent, 25HAP and 25HNP, where 50 and 55% of total ionomer respectively was determined to be adsorbed to HSAC. The lack of significant variation in ionomer adsorption could point towards the idea that the solvent system is a more critical parameter towards dictating carbon-ionomer interactions. Further studies on variation in Aquivion adsorption to carbon as a function of solvent composition would yield further insights into such a hypothesis.

I/C ratio proved to have little impact on the nanostructure of the ink, however, USAXS measurements revealed it was found to alter both carbon and Pt/C aggregation. This proves that not all information on the catalyst ink structure as a function of composition variation can be acquired using CV-SANS alone, and utilization of USAXS in tandem may lead to important insights that have been omitted by CV-SANS (for example how carbon aggregation changes in different solvent systems).

With respect to the effect of Pt on the catalyst ink system, the CV-SANS/PSF method may also be at its limitation. Comparison of PSF outputs obtained from carbon-only and Pt containing inks showed very similar observations no matter which other parameter was varied (Pt + I/C ratio, Pt + solvent system etc.). Introduction of Pt resulted in no additional adsorption into the system, as suggested by the cross-term extraction, and in fact in certain cases adsorption was seen to decrease (25HNP/25PHNP – 55 to 23.5%, 75HNP/75PtHNP – 7.4 to 0%). Moreover, no significant variation in shell thickness was observed between 25HNP and 25PtHNP, suggesting the nature of the layer itself does not change.

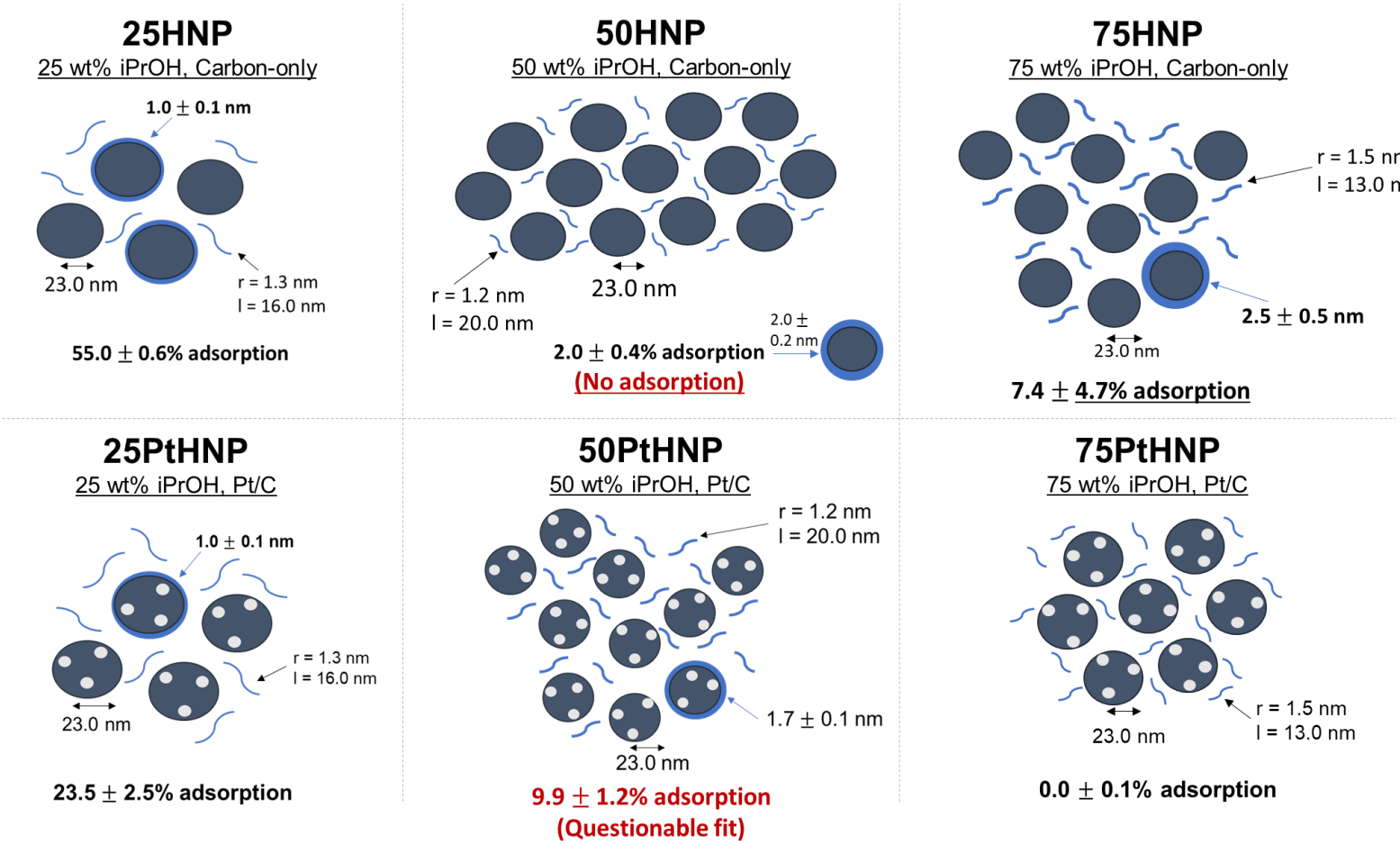


Figure 93. *Schematics representing key structural findings for inks with varying solvent systems, with and without Pt.*

However, the notion that the presence of Pt nanoparticles could reduce the degree of ionomer adsorption to carbon is startling, especially considering the carbon support chosen, HSAC, where approximately 60-70% of Pt nanoparticles are found in internal pores that the ionomer cannot penetrate. As a result, the amount of Pt on the HSAC surface itself would be minimal, making such a large shift in adsorption questionable.

It was noted iPrOH electro-oxidation to acetone in the presence of Pt would induce a change in the solvent composition, albeit a very small one (approximately 0.2 wt% of iPrOH converted to acetone),[106] unlikely to affect the ionomer conformation to such a degree.

Considering the physical nature of the system itself, assuming very strong Pt-ionomer interactions it can be envisioned that the ionomer adsorbs in 'patches' in the proximity of Pt nanoparticles on the HSAC surface. In such an instance the uniform shell model used to fit the S_{pp} outputs is no longer a good approximation for the adsorbed ionomer structure. Nevertheless, it was noted the shell thickness parameter would be misinterpreted as thinner than in reality, however the ionomer adsorption parameter, related to the ionomer volume fraction found on the carbon surface, should remain unaffected.

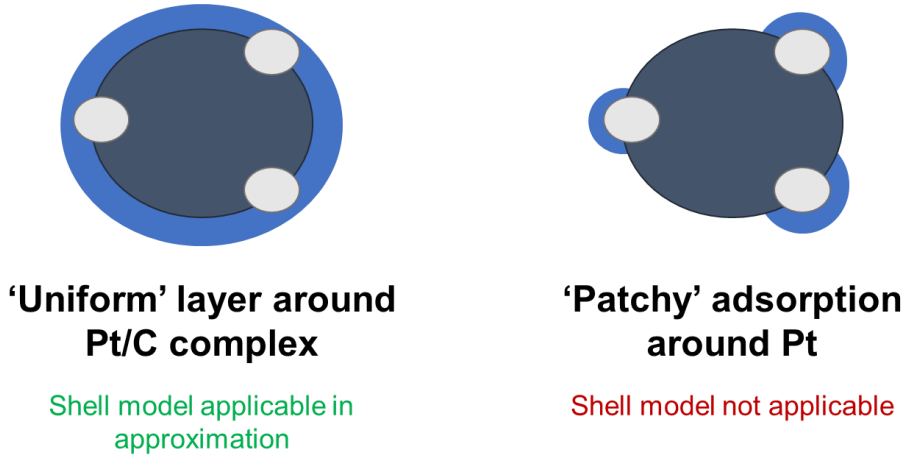


Figure 94. *Schematics of different potential ionomer adsorption models.*

Another hypothesis which may account for the Pt related observations is the idea that because Pt/C is considered to be one component during the PSF extraction, information on the Pt-ionomer interactions may not be taken into account by the PSF outputs generated. A more complex PSF extraction, which takes into account three additional outputs – $S_{Pt\text{-}Pt}$, $S_{Pt\text{-}C}$ and $S_{Pt\text{-}P}$, should be performed in order to evaluate the information encoded in the total scattering intensities in more detail. However, note at this point the minimum number of input data required should be 6, and the use of an increased number of scattering functions is further recommended. On the other hand, the S_{pp} alone should contain information on the entirety of the ionomer component, regardless of whether it interacts with Pt or carbon.

Furthermore, in USAXS data a contrasting behaviour in aggregate size variation as function of ionomer content was observed for carbon-only and Pt/C based inks. Where in carbon-only inks increasing ionomer resulted in smaller aggregate size, the contrary was true for Pt/C based inks. Moreover, this was the case irrespective of support type used (HSAC or GC). Khandavalli et al.[25] observed Pt/HSAC based inks showed an increasing viscosity with increasing I/C ratio, while the reverse behaviour was noted for HASC-only inks. In their work, this was attributed to flocculation of aggregates due to ionomer-Pt interactions. However, no such behaviour was noted in inks based on Vulcan and Pt/Vulcan, and Li et al.[53] also observed decreasing viscosities for Pt/GC based inks with increasing ionomer content. The reason for increasing aggregate size with increasing ionomer content in the presence of Pt remains unclear, yet it is highly suggestive of Pt-ionomer interactions, supporting the idea that such contributions were not properly extracted in PSFs obtained from CV-SANS data.

Further study of thermodynamics of ionomer adsorption to the Pt/C complex was attempted using ITC, yet the results proved invalid due to heat release related to the solvent electro-oxidation. Nevertheless, such information might provide a crucial insight into the Pt-ionomer interactions, which would shed light on the behaviours observed using USAXS and CV-SANS. For this reason, the use of ITC to study Pt/C based systems should be further investigated, with methods such as sample degassing perhaps aiding in

mitigating the electro-oxidation effect. Furthermore, additional techniques where insights into Pt-ionomer interactions could be gained should be further explored.

Since significant variation in degree of ionomer adsorption was observed with altering iPrOH concentration in the catalyst ink solvent system, this variable was chosen to investigate further through characterization of the resulting catalyst layer structure by TEM and SANS, as well as through correlation to electrochemical performance of subsequent MEAs.

TEM images on the nanometre scale revealed the ionomer was generally well distributed in all resulting catalyst coated membranes (CCMs), yet with some level of ionomer aggregation observed in each case. The lowest number of ionomer aggregates was observed in the case of 50PtHNP sample (made from ink containing 50 wt% iPrOH). On the other hand, TEM images on the micrometre scale suggested a significantly deteriorated CCM quality in the case of 75PtHNP, with poor cathode/membrane contact and increased CCL thickness inhomogeneity in comparison to the other two samples.

SANS measurements at increasing RH conditions showed progressive hydration of the ionomer in each CCL, yet the nature of the ionomer related, peak-like feature could not be identified. Comparison to previously published results revealed similarities to both ionomer thin film and ionomer aggregate related behaviours.[46] Moreover, variations in the feature shape were noted between scattering functions of Pt/HSAC and Pt/GC based CCL powders, which may suggest the presence of both thin ionomer layers and ionomer aggregates, depending on the sample. On the other hand, some structural variation as function of the iPrOH concentration in preceding inks could be made, characterized by the extracted Q magnitude of the 'peak' maxima at 95% RH. For Pt/HSAC based compositions, the Q value extracted decreased with decreasing iPrOH concentrations used in the ink. For Pt/GC based compositions, the reverse was true. Moreover, it was noted the size domain suggested by lower Q magnitudes of peak maxima for the ionomer-related peak-like feature of 25PtHNP was consistently bigger than for 50PtHNP or 75PtHNP, irrespective of RH. This could potentially be related to the increased degree of ionomer adsorption suggested by the analysis of the corresponding ink sample.

Nevertheless, ultimately, the structure of the ionomer in the catalyst layers definitely unclear, and a more rigorous analysis of the SANS results is required for a proper characterization. In addition, obtaining additional data, such as H_2O/D_2O CV-SANS of catalyst layers, as well as measurements of the bulk Nafion hydration itself, may greatly aid in result interpretation.

Electrochemical characterization was performed for MEAs based on the same CCLs with variation in Pt/C complex as well as iPrOH concentration used in preceding inks.

The performance observed in high RH conditions, both in air and O_2, characterized by activation losses at low current densities, revealed a direct correlation to the Pt electrochemical surface area (ECSA) obtained from cyclic voltammetry measurements. In general, MEAs containing Pt/HSAC based CCLs showed higher ECSA than for their Pt/GC counterparts, along with higher performance. However, this is to be expected based on the known structures of the two Pt/C complexes. With regards to the iPrOH concentration variation, for both Pt/C supports MEAs containing CCLs manufactured from 75 wt% iPrOH containing inks (75PtHNP and 75PtGNP) showed reduced ECSA in comparison to their lower alcohol content counterparts, consequently resulting in higher activation losses observed and poorer performance. This may be related to the reduced contact observed between the cathode and the membrane in TEM images of 75PtHNP (although this would have to be verified for 75PtGNP also), and may be indicative of poorer catalyst layer quality obtained from high-alcohol content inks. However, it is also important to consider variation in Pt/C aggregation in inks as function of varying solvent system, which was not investigated in this work. USAXS measurements characterizing this effect may aid in pinpointing the reason for poorer quality of CCLs obtained from inks containing 75 wt% iPrOH.

With regards to the CCLs manufactured from inks with lower alcohol content (25 and 50 wt% iPrOH), the ECSA extracted was similar in the case of both Pt/HSAC and Pt/GC (although the ECSA of Pt/GC CCLs

was generally significantly lower). However, some variation in activation loss and performance could be observed. In the case of Pt/HSAC based compositions, 25PtHNP consistently showed the best performance. This may relate to the lowest proton transport resistance deduced using EIS obtained at low current densities of 25 mA/cm^2 in O_2, low RH conditions as well as when the ORR was inhibited (no reactant gas flow to the cathode), suggesting potentially improved ionomer distribution on Pt/HSAC.

With regards to EIS, interestingly the proton transport resistance deduced from high frequency impedance can be correlated to the pattern of ionomer-related peak position observed in SANS measurements for different catalyst layers. **25PtHNP showed the lowest proton transport resistance, and the ionomer-related peak-like feature maximum was present at the lowest Q value in SANS scattering functions. Concurrently, the corresponding ink also showed a significant higher degree of ionomer adsorption, and a correlation can be established:**

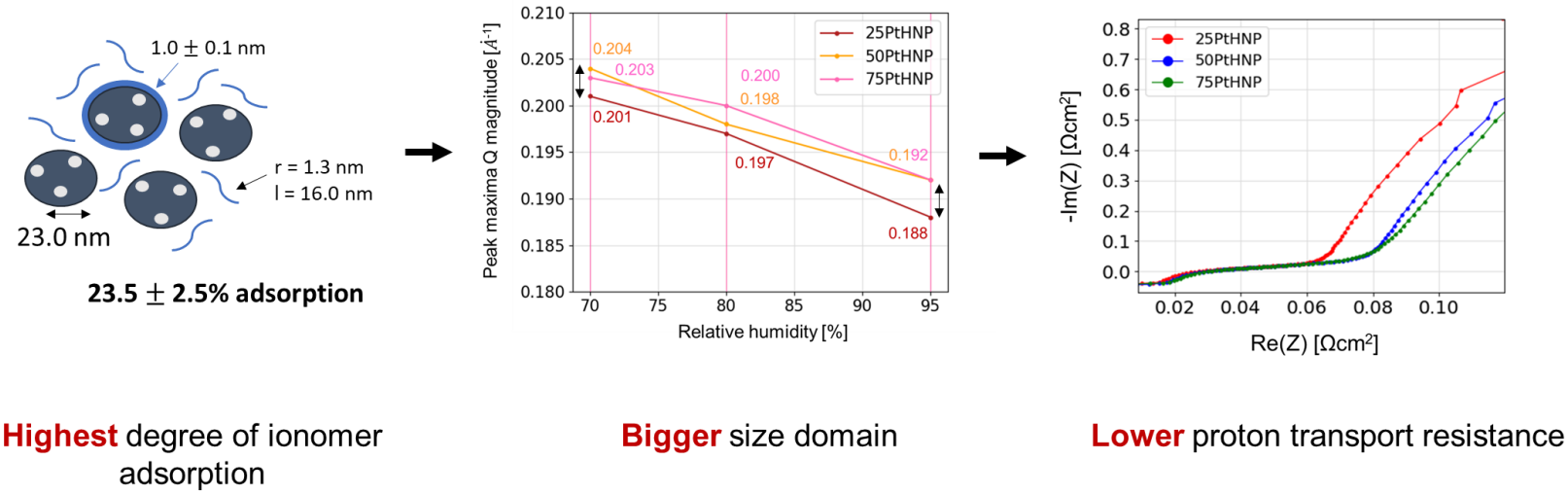


Figure 142. *Schematic presenting correlation of CV-SANS, SANS and electrochemical characterization results for catalyst ink/layer samples based on compositions with varying iPrOH content in the ink solvent system.*

Moreover, 50PtHNP and 75PtHNP, who showed little or no ionomer adsorption in the ink samples, also display very similar ionomer-feature peak maxima Q magnitudes in the catalyst layer SANS data, as well as alike impedance in the EIS results designed to enhance proton transport limitations. This shows the established correlation can be extended to all the Pt/HSAC based samples with variations in the ink solvent system composition, across all the three stages of investigation: ink structure, resulting electrode structure, and final performance.

This result is a promising start to obtaining a comprehensive understanding of the structure-performance relation of the PEMFC catalyst layer, commencing with the ink it is manufactured from. It has been shown correlating results from the various stages together can lead to valuable insight of the system overall.

Nevertheless, this is just the beginning, and further compositional variation should be investigated using such a schematic to verify whether such a correlation holds true throughout. In such complex systems as the catalyst ink and the catalyst layer, amassing a large, consistent, dataset is imperative for accurate interpretation.

With regards to the methods themselves and future prospects, overall, it can be concluded investigation of catalyst ink structure with systematic variation of composition was a success. Valuable insight was gained into the ink structure using the CV-SANS/PSF method, particularly with regards to successful characterization of the ionomer structure (albeit only quasi-quantitatively). Some doubt remains with regards to information obtained for Pt containing compositions, and more complex PSF extraction may have to be applied. Nevertheless, significant variation in ionomer structure could already be observed for carbon-only inks with differing compositions, and characterizing such systems may result in a good foundation for building further understanding of the inter-component interaction in the catalyst ink system. That being said, despite the large number of compositions characterized, due to the complexity of the system and often combined effects of certain components (e.g. solvent and ionomer type), obtaining definite conclusions on component behaviours remained challenging.

Indeed, the larger the number of ink compositions that is characterized, the clearer the understanding of component interactions will become. This may include delving into new variations, for example studying Vulcan based inks, or inks utilizing a different alcohol type such as EtOH. On the other hand, more detailed investigations of already studied variations, for example by measuring inks with a more gradual change in iPrOH concentration, or expanding on the effect of iPrOH concentration on Aquivion adsorption may just as likely be worthwhile. In any case, the plethora of compositions that remain to be investigated (and that is when taking only the industrially relevant components into account) may seem daunting, especially considering how difficult neutron beamtime is to come by. Nevertheless, because inks scatter well and consequently measurement times per sample remain short, even one day of beamtime can result in a plethora of data that may yield new insights. And it is the hope of the author that the work presented in this thesis, with regards to developing a measurement protocol, assessing the veracity of PSF outputs, as well as in potential methods that can be applied for analysing the ensuing data, results in a more efficient interpretation of obtained data, leading to a large number of results to draw information from.

Aside from the CV-SANS/PSF method, USAXS proved to be a valuable, and even an essential technique to allow for characterization of the entire catalyst ink system. That is because where some variables, such as the I/C ratio, may not have a direct impact on the ionomer structure observed on the nanoscale, aggregation behaviour of carbon or Pt/C may change, which would also significantly impact the final catalyst layer structure. Indeed, because information on the effect of iPrOH concentration on carbon aggregation is lacking, it is impossible to pinpoint whether the reduced quality of resulting catalyst layers can be linked to the ink structure. For this reason, it is recommended USAXS results are also obtained for each ink composition studied by CV-SANS, in order to create a full picture of the ink system on several size scales.

Supporting methods such as ITC would also prove worthwhile, aiding to answer some queries present (nature of Pt-ionomer interactions), but also for verification of observations made by CV-SANS. Other methods such as thermogravimetric analysis or rheology also may prove suitable for such endeavours.

Although a successful link could be established, with regards to further correlation of structural variation observed in catalyst inks to that of the resulting catalyst layers, and observed electrochemical performance, plenty of work remains to be done. This is particularly true for characterization of the ionomer structure in the catalyst layer, where interpretation of SANS results remained challenging, and subsequently, a significant gap in information remains between the structure of the ink and observed electrochemical performance. That is also not to mention the lack of information on the effect of the drying process, which will have a significant impact on the final catalyst layer structure.

Nevertheless, even with the gap in knowledge created by lack of information on the catalyst layer as well as the nature of Pt-ionomer interactions, it has been shown a correlation of ink structure to electrochemical performance can be established. The overall approach of characterizing the catalyst ink structure using CV-SANS and USAXS, followed by correlation to the final catalyst layer structure and electrochemical performance remains a promising approach for developing and in-depth, fundamental understanding of the system, which would ultimately result in improved pathways for electrode optimization. Results presented in this work are a good starting point, with

successful insights into the ink structure as function of composition, however, work remains plenty before the final goal of improved electrode optimization pathways can be achieved. In particular, the methodology presented may prove crucial in making catalyst ink characterization more efficient and clear-cut, with a developed understanding of what is important to consider and acquire for extraction of best results. In tandem with complimentary methods such as USAXS, indeed eventually the whole picture of the catalyst ink system could be clearly revealed.

En ce qui concerne les méthodes elles-mêmes et les perspectives d'avenir, on peut conclure que l'étude de la structure de l'encre catalytique avec variation systématique de la composition a été un succès. Des informations précieuses ont été obtenues sur la structure de l'encre à l'aide de la méthode CV-SANS/PSF, notamment en ce qui concerne la caractérisation réussie de la structure de l'ionomère (bien que de manière quasi quantitative). Des doutes subsistent quant aux informations obtenues pour les compositions contenant du Pt, et une extraction PSF plus complexe pourrait devoir être appliquée. Néanmoins, une variation significative de la structure ionomère a déjà pu être observée pour les encres uniquement au carbone avec des compositions différentes, et la caractérisation de ces systèmes peut constituer une bonne base pour une meilleure compréhension de l'interaction entre les composants dans le système d'encre catalyseur. Cela étant dit, malgré le grand nombre de compositions caractérisées, en raison de la complexité du système et des effets souvent combinés de certains composants (par exemple, le type de solvant et d'ionomère), l'obtention de conclusions définitives sur les comportements des composants reste difficile.

En effet, plus le nombre de compositions d'encre caractérisées est élevé, plus la compréhension des interactions entre les composants sera claire. Cela peut inclure l'exploration de nouvelles variantes, par exemple l'étude des encres à base de Vulcan ou des encres utilisant un type d'alcool différent tel que l'EtOH. D'un autre côté, des investigations plus détaillées des variantes déjà étudiées, par exemple en mesurant les encres avec un changement plus progressif de la concentration en iPrOH, ou en approfondissant l'effet de la concentration en iPrOH sur l'adsorption d'Aquivion, peuvent tout aussi bien être utiles. Dans tous les cas, la pléthore de compositions qui restent à étudier (et cela en ne prenant en compte que les composants pertinents sur le plan industriel) peut sembler décourageante, surtout si l'on considère la difficulté d'obtenir du temps de faisceau de neutrons. Néanmoins, comme les encres se dispersent bien et que les temps de mesure par échantillon restent donc courts, même une journée de temps de faisceau peut donner lieu à une pléthore de données susceptibles d'apporter de nouvelles perspectives. L'auteur espère que le travail présenté dans cette thèse, en ce qui concerne le développement d'un protocole de mesure, l'évaluation de la véracité des résultats PSF, ainsi que les méthodes potentielles qui peuvent être appliquées pour analyser les données qui en découlent, aboutira à une interprétation plus efficace des données obtenues, conduisant à un grand nombre de résultats à partir desquels tirer des informations.

Outre la méthode CV-SANS/PSF, l'USAXS s'est avérée être une technique précieuse, voire essentielle, pour permettre la caractérisation de l'ensemble du système d'encre catalytique. En effet, lorsque certaines variables, telles que le rapport I/C, peuvent ne pas avoir d'impact direct sur la structure ionomère observée à l'échelle nanométrique, le comportement d'agrégation du carbone ou du Pt/C peut changer, ce qui aurait également un impact significatif sur la structure finale de la couche catalytique. En effet, comme les informations sur l'effet de la concentration en iPrOH sur l'agrégation du carbone font défaut, il est impossible de déterminer avec précision si la qualité réduite des couches catalytiques résultantes peut être liée à la structure de l'encre. Pour cette raison, il est recommandé d'obtenir également les résultats de l'USAXS pour chaque composition d'encre étudiée par CV-SANS, afin de créer une image complète du système d'encre à plusieurs échelles de taille.

Des méthodes complémentaires telles que l'ITC pourraient également s'avérer utiles, en contribuant à répondre à certaines questions posées (nature des interactions Pt-ionomère), mais aussi à vérifier les observations faites par CV-SANS. D'autres méthodes telles que l'analyse thermogravimétrique ou la rhéologie peuvent également s'avérer adaptées à de telles démarches.

Bien qu'un lien positif ait pu être établi, en ce qui concerne la corrélation plus poussée entre la variation structurelle observée dans les encres catalytiques et celle des couches catalytiques résultantes et les performances électrochimiques observées, beaucoup de travail reste à faire. Cela est particulièrement vrai pour la caractérisation de la structure ionomère dans la couche catalytique, où l'interprétation des résultats SANS reste difficile, et par la suite, un écart important d'informations subsiste entre la structure de l'encre et les performances électrochimiques observées. Sans parler du manque d'informations sur l'effet du processus de séchage, qui aura un impact significatif sur la structure finale de la couche catalytique.

Néanmoins, malgré le manque de connaissances créé par le manque d'informations sur la couche de catalyseur ainsi que sur la nature des interactions Pt-ionomère, il a été démontré qu'une corrélation entre la structure de l'encre et les performances électrochimiques peut être établie. L'approche globale de caractérisation de la structure de l'encre du catalyseur à l'aide de CV-SANS et USAXS, suivie d'une corrélation avec la structure de la couche de catalyseur finale et les performances électrochimiques, reste une approche prometteuse pour développer une compréhension approfondie et fondamentale du système, ce qui aboutirait finalement à de meilleures voies d'optimisation des électrodes. Les résultats présentés dans ce travail sont un bon point de départ, avec des aperçus réussis sur la structure de l'encre en fonction de la composition, cependant, il reste beaucoup de travail avant que l'objectif final d'amélioration des voies d'optimisation des électrodes puisse être atteint. En particulier, la méthodologie présentée peut s'avérer cruciale pour rendre la caractérisation de l'encre du catalyseur plus efficace et plus claire, avec une compréhension développée de ce qui est important à prendre en compte et à acquérir pour l'extraction des meilleurs résultats. En tandem avec des méthodes complémentaires telles que USAXS, en effet, à terme, l'image complète du système d'encre du catalyseur pourrait être clairement révélée.

References

[1] Global Greenhouse Gas Emissions Data | US EPA, URL: https://www.epa.gov/ghgemissions/global-greenhouse-gas-emissions-data, (accessed 11/02/2022)

[2] European Environment Agency, EEA greenhouse gases – data viewer, URL : https://www.eea.europa.eu/data-and-maps/data/data-viewers/greenhouse-gases-viewer, (accessed 25/04/2024)

[3] European Commission – Horizon, URL: https://projects.research-and-innovation.ec.europa.eu/en/horizon-magazine/heavy-duty-trucks-drive-clean-hydrogen-next-level, (accessed 25/04/2024)

[4] Kongkanand A., Mathias M. F., *J. Phys, Chem. Lett.*, 2016, **7**, 1127-1137, DOI : 10.1021/acs.jpclett.6b00216

[5] Girod R., Lazaridis T., Gasteiger H. A., Tileli V., *Nature Catalysis*, 2023, **6** 383-391, DOI : 10.1021/acs.jpclett.6b00216

[6] Office of Energy Efficiency & Renewable Energy – Fuel Cell Systems, URL: https://www.energy.gov/eere/fuelcells/fuel-cell-systems, (accessed 27/09/24)

[7] Wang H., Turner J. A., *Fuel Cells*, 2010, **10**, 510-519, DOI: https://doi.org/10.1002/fuce.200900187

[8] TMN Etching – Differences Between Monopolar Plates and Bipolar Plates, URL: https://tmnetch.com/differences-between-monopolar-plates-and-bipolar-plates/, (accessed 27/09/2024)

[9] Porstmann S., Wannemacher T., Drossel W. –G., *J. Manuf. Process.*, 2020, **60**, 366-383, DOI: 10.1016/j.jmapro.2020.10.041

[10] Toyota Technical Review - Volume 66, URL: https://global.toyota/pages/global_toyota/mobility/technology/toyota-technical-review/TTR_Vol66_E.pdf, (accessed 27/09/2024)

[11] Park S., Lee J. W., Popov B. N., *Int. J. Hydrogen Energ.*, 2012, **37**, 5850-5865, DOI: 10.1016/j.ijhydene.2011.12.148

[12] Cindrella L., Kannan A. M., Lin J. F., Saminathan K., Ho Y., Lin C. W., Wertz J., *J. Power Sources*, 2009, **194**, 146-160, DOI: 10.1016/j.jpowsour.2009.04.005

[13] Fuel Cell Store – Gas Diffusion Layers, URL: https://www.fuelcellstore.com/gas-diffusion-layers, (accessed 29/09/2024)

[14] Vandenberghe F., PhD thesis, Université Grenoble Alpes, 2023

[15] Tellez-Cruz M. M., Escorihuela J., Solorza-Feria O., Compañ V., *Polymers*, 2021, **13**(18), 3064, DOI : 10.3390/polym13183064

[16] Padgett E., Andrejevic N., Liu Z., Kongkanand A., Gu W., Moriyama K., Jiang Y., Kumaraguru S., Moylan T. E., Kukreja R., Muller D. A., *J. Electrochem. Soc.*, 2018, **165**, F173-F180

[17] Gebel G., Loppinet B., *J. Phys. Chem. B*, 1997, **101**, 1884-1892, DOI: 10.1021/jp9623047

[18] Sneed B. T., Cullen D. A., Reeves K. S., Dyck O. E., Langlois D. A, Mukundan R., Borup R. L., More K. L., *ACS Appl. Mater. Interfaces*, 2017, **9**, 29839-29848, DOI: 10.1021/acsami.7b09716

[19] Balachandran M., *Handbook of Research on Inventive Bioremediation Techniques*, ed. Bhakta J. N., IGI Global, 2017, Chapter 12, 287-300

[20] Sharma S., Pollet B. G., *J. Power Sources*, 2012, **208**, 96-119, DOI: 10.1016/j.jpowsour.2012.02.011

[21] Pérez-Rodríguez S., Pastor E., Lázaro M. J., *Int. J. Hydrogen Energ.*, 2018, **43**, 7911-7922, DOI: 10.1016/j.ijhydene.2018.03.040

[22] Yano H., Akiyama T., Bele P., Uchida H., Watanabe M., *Phys. Chem. Chem. Phys.,* 2010, **12**, 3806-3814, DOI: 10.1039/B923460H

[23] Hara M., Lee M., Liu C. H., Chen B. H., Yamashita Y., Uchida M., Uchida H., Watanabe M., *Electrochim. Acta*, 2012, **70**, 171-181, DOI: 10.1016/j.electacta.2012.03.043

[24] Wang C., Ricketts M., Soleymani A. P., Jankovic J., Waldecker J., Chen J., *J. Electrochem. Soc.*, 2021, **168**, 004507, DOI: 10.1149/1945-7111/abf265

[25] Khandavalli S., Park J., Kariuki N. N., Myers D. J., Stickel J. J., Hurst K., Neyerlin K. C., Ulsh M., Mauger S. A., *ACS Appl. Mater. Interfaces*, 2018, **10**, 43610-43622

[26] Gatto I, Saccà A., Sebastián D., Baglio V., Aricò A. S., Oldani C., Merlo L., Carbone A., *Polymers*, 2021, **13**, 3832, DOI: 10.3390/polym13213832

[27] Harden S., Riewald F., Hirschfeld J. A., Perchthaler M., *J. Power Sources*, 2017, **335**, 36-43, DOI: 10.1016/j.jpowsour.2017.04.051

[28] Ono Y., Ohma A., Shinohara K., Fushinobu K., *J. Electrochem. Soc.*, 2013, **160**, F779, DOI: 10.1149/2.040308jes

[29] Liu Y., Ji C., Gu W., Baker D. R., Jorne J., Gasteiger H. A., *J. Electrochem. Soc.*, 2010, **157**, B1154, DOI: 10.1149/1.3435323

[30] Mashio T., Ohma A., Tokumasu T., *Electrochim. Acta*, 2016, **202**, 14-23, DOI: 10.1016/j.electacta.2016.04.004

[31] Yoshimune W., Harada M., *Chem. Lett.* 2019, **48**, 487-490, DOI: 10.1246/cl.190017

[32] Xue Q., Zhang R., Yang D., Li B., Ming P., Zhang C., *Int. J. Hydrogen Energ.*, 2022, **47**, 23335-23347, DOI : https://doi.org/10.1016/j.ijhydene.2022.05.122

[33] Suzuki T., Tsushima S., Hirai S., *Int. J. Hydrogen Energ.*, 2011, **36**, 12361-12369

[34] Antolini E., Giorgi L., Pozio A., Passalacqua E., *J. Power Sources*, 1999, **77**, 136-142, DOI: https://doi.org/10.1016/S0378-7753(98)00186-4

[35] Ishikawa H., Sugawara Y., Inoue G., Kawase M., *J. Power Sources*, 2018, **374**, 196-204, DOI: 10.1016/j.jpowsour.2017.11.026

[36] Ohma A., Mashio T., Sato K., Iden H., Ono Y., Sakai K., Akizuki K., Takaichi S., Shinohara K., *Electrochim. Acta*, 2011, **56** 10832-10841, DOI : 10.1016/j.electacta.2011.04.058

[37] Andersen S. M., *Appl. Catal. B-Environ.*, 2016, **181**, 146-155, DOI: 10.1016/j.apcatb.2015.07.049

[38] Yoshimune W., Harada M., *ECS Trans.*, 2020, **98**, 447-454, DOI : 10.1149/09809.0447ecst

[39] Berlinger S., McCloskey B., Weber A., *ACS Energy Lett.*, 2021, **6**, 2275-2282, DOI: 10.1021/acsenergylett.1c00866

[40] Guo Y., Mabuchi T., Li G., Tokumasu T., *Macromolecules,* 2022, **55**, 4245-4255, DOI: 10.1021/acs.macromol.2c00533

[41] Kang J., Zheng W., Chen S., Yang D., Li B., Zhang C., Ming P., *J. Power Sources*, 2024, **623**, 235269, DOI: 10.1016/j.jpowsour.2024.235269

[42] Saha M. S., Tam M., Berejnov V., Susac D., McDermid S., Hitchcock A. P., Stumper J., *Electrochem. Soc.*, 2013, **58**, 797, DOI: 10.1149/05801.0797ecst

[43] Wang Z., Nagao Y., *Electrochim. Acta*, 2014, **129**, 343-347, DOI: 10.1016/j.electacta.2014.02.133

[44] Hasegawa N., Kamiya A., Matsunaga T., Kitano N., Harada M., *Colloid. Surface. A*, 2021, **628**, 127153, DOI: 10.1016/J.COLSURFA.2021.127153

[45] Lei C., Macauley N., Spinetta M., Purdy G., Jankovic J., Cullen D. A., More K. L., Kim Y. S., Xu H., *J. Electrochem Soc.*, 2021, **168**, 044517, DOI: 10.1149/1945-7111/abf2b0

[46] Chabot J., Lee J., Vandenberghe F., Guétaz L., Gebel G., Lyonnard S., Porcar L., Rosini S., Morin A., *ACS Appl. Energy Mater.*, 2023, **6**, 1185-1196

[47] Balu R., Choudhury N. R., Mata J. P., de Campo L., Rehm C., Hill A. J., Dutta N. K., *ACS Appl. Matter. Interfaces*, 2019, **11**, 9934-9946, DOI: 10.1021/acsami.8b20645

[48] Taning A. Z., Lee S., Woo S., Park S. H., Bae B., Yim S. D., *J. Electrochem. Soc.*, 2021, **168**, 104506, DOI: 10.1149/1945-7111/ac2c13

[49] Zhao J., Tu Z., Chan S. H., *J. Power Sources*, 2021, **488**, 229434, DOI: 10.1016/j.jpowsour.2020.229434

[50] Qi Y., Huang Y., Gao Z., Chen C. H., Perego A., Yildirim H., Odgaard M., Asset T., Atanassov P., Zenyuk I. V., *J. Power Sources*, 2022, **551**, 232209, DOI: 10.1016/j.jpowsour.2022.232209

[51] Oyarce A., Zakrisson E., Ivity M., Lagergren C., Baumann Ofstad A., Bodén A., Lindbergh G., *J. Power Sources*, 2014, **254**, 232-240

[52] Du S., Guan S., Mehrazi S., Zhou F., Pan M., Zhang R., Abel Chuang P. Y, Sui P. C., *J. Electrochem. Soc.*, 2021, **168**, 114506, DOI : 10.1149/1945-7111/ac3598

[53] Li B., Guo Y., Yang D., Yang D., Ming P., Zhang C., *ACS Appl. Mater. Interfaces*, 2021, **13**, 27119-27128, DOI: https://doi.org/10.1021/acsami.1c07070

[54] Yakovlev Y. V., Lobko Y. V., Vorokhta M., Nováková J., Mazur M., Matolínová I., Matolín V., *J. Power Sources*, 2021, **490**, 229531, DOI: 10.1016/j.jpowsour.2021.229531

[55] Ren H., Teng Y., Meng X., Fang D., Huang H., Geng J., Shao Z., *J. Power Sources*, 2021, **506**, 230186, DOI: 10.1016/j.jpowsour.2021.230186

[56] Kodama K., Motobayashi K., Shinohara A., Kudo K., Jinnouchi R., Osawa M., Morimoto Y., *ACS Catal.*, 2018, **8**, 694-700

[57] Huang X., He Y., Sun Y., Sun L., Wang T., Zhang X., *J. Power Sources*, 2024, **603**, 234488, DOI: 10.1016/j.jpowsour.2024.234488

[58] Lyu X., Van Cleve T., Young E., Li J., Yu H., Cullen D. A., Neyerlin K. C., Serov A., *J. Power Sources*, 2023, **556**, 232530, DOI: 10.1016/j.jpowsour.2022.232530

[59] Thoma M., Lin W., Hoffmann E., Sattes M., Segets D., Damm C., Peukert W., *Langmuir*, 2018, **34**, 12324-12334, DOI: 10.1021/acs.langmuir.8b02726

[60] Takahashi S., Shimanuki J., Mashio T., Ohma A., Tohma H., Ishihara A., Ito Y., Nishino Y., Miyazawa A., *Electrochim. Acta*, 2017, **224**, 178-185, DOI: 10.1016/j.electacta.2016.12.068

[61] Woo S., Lee S., Taning A. Z., Yang T. H., Park S. H., Yim S. D., *Curr. Opin. Electrochem.*, 2020, **21**, 289-296, DOI: 10.1016/j.coelec.2020.03.006

[62] Orfanidi A., Rheinländer P. J., Schulte N., Gasteiger H. A., *J. Electrochem. Soc.*, 2018, **165**, F1254, DOI : 10.1149/2.1251814jes

[63] Ren H., Meng X., Lin Y., Shao Z., *J. Energ. Chem.*, 2022, **73**, 588-598, DOI: 10.1016/j.jechem.2022.06.034

[64] Harada M., Takata S., Iwase H., Kajiya S., Kadoura H., Kanaya T., *ACS Omega*, 2021, **6**, 15257-15263, DOI: 10.1021/acsomega.1c01535

[65] Lee J., Escribano S., Micoud F., Gebel G., Lyonnard S., Porcar L., Martinez N., Morin A., *ACS Appl. Energy Mater.*, 2020, **3**, 8393-8401, DOI: 10.1021/acsaem.0c00853

[66] Martinez N., Porcar L., Escribano S., Micoud F., Rosini S., Tengattini A., Atkins D., Gebel G., Lyonnard S., Morin A., *ACS Appl. Energy Mater.*, 2019, **2**, 8425- 8433, DOI: 10.1021/acsaem.9b01266

[67] Toudret P., Wolanin J., Gebel G., Morin A., *J. Power Sources*, 2023, **586**, 233671, DOI: 10.1016/j.jpowsour.2023.233671

[68] Martens I., Chattot R., Drnec J., *J. Power Sources,* 2022, **521**, 230851, DOI: 10.1016/j.jpowsour.2021.230851

[69] Schröder J., Pittkowski R. K., Martens I., Chattot R., Drnec J., Quinson J., Kirkensgaard J. J. K., Arenz M., *ACS Catal.*, 2022, **12**, 2077-2085, DOI: 10.1021/acscatal.1c04365

[70] Shibayama M., Matsunaga T., Kusano T., Amemiya K., Kobayashi N., Yoshida T., *J. Appl. Polym. Sci.*, 2014, **131**, 39842, DOI: 10.1002/app.39842

[71] Koga M., Matsumoto M., Tokita M. Masunaga H., Sugimori H., Sasabe T., Yoshida T., Shinohara L., Hirai S., *ECS Trans.*, 2018, **86**, 157-616, DOI: 10.1149/08613.0157ECST/XML

[72] Purdue University Division of Chemical Education - The Atom and Electromagnetic Radiation, URL: https://chemed.chem.purdue.edu/genchem/topicreview/bp/ch6/atom_emrframe.html, (accessed 14/09/2024)

[73] ISIS Neutron and Muon Source – What is a neutron?, URL: https://www.isis.stfc.ac.uk/Pages/What-is-a-neutron-About.aspx, (accessed 14/09/2024)

[74] Chadwick J. *Nature*, 1932, **129**, 312, DOI: 10.1038/129312a0

[75] Brückel T., Heger G., Richter D., *Neutron Scattering – Lectures of the JCNS Laborator Course held at Forschunszentrum Jülich and the research reactor FRM II of TU Munich In cooperation with RWTH Aachen and Univeristy of Münster, Volume 39*, ed. Roth G., Zorn R., Forschungszentrum Jülich GmbH, Jülich, 2012, Chapter 1, Page 7

[76] Cousin F., *EPJ Web conf.*, 2015, **104**, 01004, DOI: https://doi.org/10.1051/epjconf/201510401004

[77] Boothroyd A. T., *Principles of Neutron Scattering from Condensed Matter*, Oxford University Press, Oxford, First edition, 2020, Chapter 1, Pages 2 – 12

[78] Frewein M.P.K, *Coupling of Leaflet Structure and Collective Fluctuations in Assymetric Lipid Vesicles,* PhD thesis, Karl-Franzens-Universität Graz, 2022

[79] Boothroyd A. T., *Principles of Neutron Scattering from Condensed Matter*, Oxford University Press, Oxford, First edition, 2020, Chapter 1, Page 17

[80] Squires G. L., *Introduction to the Theory of Thermal Neutron Scattering*, Cambridge University Press, Cambridge, First edition, 1978, Chapter 1, Page 8

[81] GISAXS – Scattering Length Density, URL: http://gisaxs.com/index.php/Scattering_Length_Density, (accessed 01/08/2024)

[82] Hammouda B., *Probing Nanoscale Structures – The SANS Toolbox*, National Institute of Standards and Technology Center for Neutron Research, Gaithersburg, 2016

[83] Institut Laue-Langevin - GRASP User Manual, URL: https://www.ill.eu/sites/saxs-sans/Manuals/grasp_manual.pdf, (accessed 06/10/2024)

[84] Wagner N. J., Tande B. M., Mackay M. E., Hawker C. J., Jeong M., *Macromolecules*, 2001, **34**, 8580-8585, DOI: 10.1021/ma011265g

[85] Kreuger S., W. Lynn, Russell J. T., Nossal R., *J. Appl. Crystallogr.*, 1989, **22**, 546-555, DOI: 10.1107/S0021889889007491

[86] Endo H., Schwahn D., Cölfen H., *J. Chem. Phys.*, 2004, **120**, 9410-9423, DOI: 10.1063/1.1691736

[87] GESTIS-Stoffdatenbank – Carbon Black, URL: https://gestis.dguv.de/data?name=091940&lang=en, (Accessed 01/08/2024)

[88] SasView – sphere, URL : https://www.sasview.org/docs/user/models/sphere.html, (accessed 07/10/2024)

[89] SasView – cylinder, URL: https://www.sasview.org/docs/user/models/cylinder.html, (accessed 07/10/2024)

[90] SasView – core_shell_sphere, URL: https://www.sasview.org/docs/user/models/core_shell_sphere.html, (accessed 07/10/2024)

[91] Gebel G., Loppinet B., *Langmuir*, 1998, **14**, 1977-1983

[92] Aldebert P., Dreyfus B., Gebel G., Nakamura N., Pineri M., Volino F., *J. phys. France*, 1988, **49**, 2102-2109

[93] Matsumoto M., Arao M., Katayama S., Kudo S., Asaoka T., Tsuji Y., Sakurai Y., Uchimoto Y., Imai H., *Meet. Abstr.*, 2023, **MA2023-02**, 1745, DOI: 10.1149/MA2023-02371745mtgabs

[94] Weth M., Mathias J., Emmerling A., Kuhn J., Fricke J., *J. Porous Mat.*, 2001, **8**, 319-325

[95] Beaucage G., *J. Appl. Cryst.*, 1995, **28,** 717-728, DOI : 10.1107/S0021889895005292

[96] Xu F., Zhang H., Ilavsky J., Stanciu L., Ho D., Justice M. J., Petrache H. I., Xie J., *Langmuir*, 2010, **26**, 24, 19199-19208, DOI : https://doi.org/10.1021/la1028228

[97] SasView – power_law, URL : https://www.sasview.org/docs/user/models/power_law.html, (accessed 07/10/2024)

[98] SasView – fitting, URL: https://www.sasview.org/docs/user/qtgui/Perspectives/Fitting/fitting_help.html, (accessed 19/09/2024)

[99] Anitas E. M., *Complexity in Biological and Physical Systems – Bifurcation, Solitons and Fractals*, IntechOpen, 2017, Chapter 10, Pages 169-191

[100] Reidy R. F., Allen A. J., Krueger S., *J. Non-Cryst. Solids*, 2001, **285**, 181-186

[101] Wang Y., Liu T., Sun H., He W., Fan Y., Wang S., *Electrochim. Acta*, 2020, **353**, 136491, DOI: 10.1016/J.ELECTACTA.2020.136491

[102] Malek A., Sadeghi E., Jankovic J., Eikerling M., Malek K., *J. Phys. Chem. C*, 2020, **124**, 6, 3429-3438, DOI: https://doi.org/10.1021/acs.jpcc.9b08969

[103] Navessin T., Lei C., Bessarabov D., Ye S., Xie Z., Holdcroft S., *J. Power Sources*, 2011, **196**, 6168-6176, DOI: 10.1016/j.jpowsour.2011.03.024

[104] Uemura S. Yoshida T., Koga M., Matsumoto H., Yang X., Shinohara K., Sasabe T., Hirai S., *J. Ekectrochem. Soc.*, 2019, **166**, F89, DOI: 10.1149/2.0411902jes

[105] Liu P., Yang D., Li B., Zhang C., Ming P., *Membranes*, 2022, **12**, 541¸ DOI: 10.3390/membranes12050541

[106] Kircher M., Roschger M., Koo W. Y., Blaschke F., Grandi M., Bodner M., Hacker V., *Energies*, 2023, **16**, 7011, DOI: 10.3390/en16197011

[107] Small Angle X-ray Scattering – The last resort of the desperate!, URL: https://www.diamond.ac.uk/dam/jcr:fb6f93b8-2cd2-4646-b6ae-4a426d85c19b/Scattering%20101.pdf, (Accessed 16/09/2024)

[108] Roe R. J., *Methods of X-ray and Neutron Scattering in Polymer Science*, Oxford University Press, Inc., New York, 2000

[109] Block T., Gruber M., Gurbuz S., Kaminski J., Lupberger M., Rodriguez Gomez L., Schwaebig P., Desch K., *Nuclear Inst. And Methods in Physcis Research, A,* 2023, **1046**, 167753, DOI: https://doi.org/10.1016/j.nima.2022.167753

[110] NIST Neutron Scattering Length List, URL: https://www.nist.gov/ncnr/neutron-scattering-lengths-list, (Accessed 16/09/2024)

[111] Ronovsky M., Pan L., Klingenhof M., Martens I., Fusek L., Kus P., Chattot R., Mirolo M., Dionigi F., Burdett H., Sharman J., Strasser P., Martinez Bonastre A., Drnec J., *ACS Appl. Energy Mater.*, 2023, **6**, 17, 8660-8665

[112] Fuchs T., Drnec J., Calle-Vallejo F., Stubb N., Sandbeck D. J. S., Ruge M., Cherevko S., Harrington D. A., Magnussen O. M., *Nature Catalysis*, 2020, **3** 754-761

[113] Metwalli E., Götz K., Lages S., Bär C., Zech T., Noll D. M., Schuldes I., Schindler T., Prihoda A., Lang H., Grasser J., Jacques M., Didier L., Cyril A., Martel A., Porcar L., Unruh T., *J. Appl. Crystallogr.*, 2020, **53**, 722-733

[114] Schindler T., Lin W., Schmutzler T., Lindner P., Peukert W., Segets D., Unruh T., *ChemNanoMat*, 2019, **5**, 116-123

[115] Ren Y., Zuo X., *Small Methods*, 2018, **2**, 1800064, DOI: https://doi.org/10.1002/smtd.201800064

[116] Schneider J. R., *Synchrotron Radiation News*, 2020, **33**, 6, 2-4

[117] Povia M., Herranz J., Binninger T., Nachtegaal M., Diaz A., Kohlbrecher J., Abbott D. F., Kim B., Schmidt T. J., *ACS Catal.*, 2018, **8**, 7000-7015, DOI: 10.1021/acscatal.8b01321

[118] Xenocs – 6 sample pitfalls to look out for when preparing SAXS experiments, URL: https://www.xenocs.com/saxs-sample-preparation-6-sample-pitfalls-to-look-out-for/, (Accessed 17/09/2024)

[119] Anitas E. M., *Symmetry*, 2020, **12**, 65, DOI: 10.3390/sym12010065

[120] Sasview – Mass Fractal model, URL: https://www.sasview.org/docs/user/models/mass_fractal.html, (Accessed 18/09/2024)

[121] TA Instruments – Isothermal Titration Calorimeters, URL: https://www.tainstruments.com/products/microcalorimetry/isothermal-titration-calorimetry/, (Accessed 20/09/2024)

[122] TA Instruments – TAM IV, URL: https://www.tainstruments.com/tam-iv/, (Accessed 20/09/2024)

[123] Saponaro A., *Bio-Protocol*, 2018, **8**, 1-11, DOI: 10.21769/BioProtoc.2957

[124] Malvern Panalytical – Isothermal Titration Calorimetry (ITC), URL: https://www.malvernpanalytical.com/en/products/technology/microcalorimetry/isothermal-titration-calorimetry, (Accessed 20/09/2024)

[125] EG&G Technical Services, Inc., *Fuel Cell Handbook ed.7*, U.S. Department of Energy – Office of Fossil Energy – National Energy Technology Laboratory, Morgantown, 2004

[126] Lund University, Department of Energy Sciences, Faculty of Engineering – Polarization curves and voltage losses, (Accessed 21/09/2024)

[127] LibreTexts Chemistry, 2.7: Electrochemistry – Cyclic Voltammetry Measurements, URL: https://chem.libretexts.org/Bookshelves/Analytical_Chemistry/Physical_Methods_in_Chemistry_and_Nano_Science_(Barron)/02%3A_Physical_and_Thermal_Analysis/2.07%3A_Electrochemistry, (Accessed 21/09/2024)

[128] Chabot F., PhD thesis, Université Grenoble Alpes, 2023

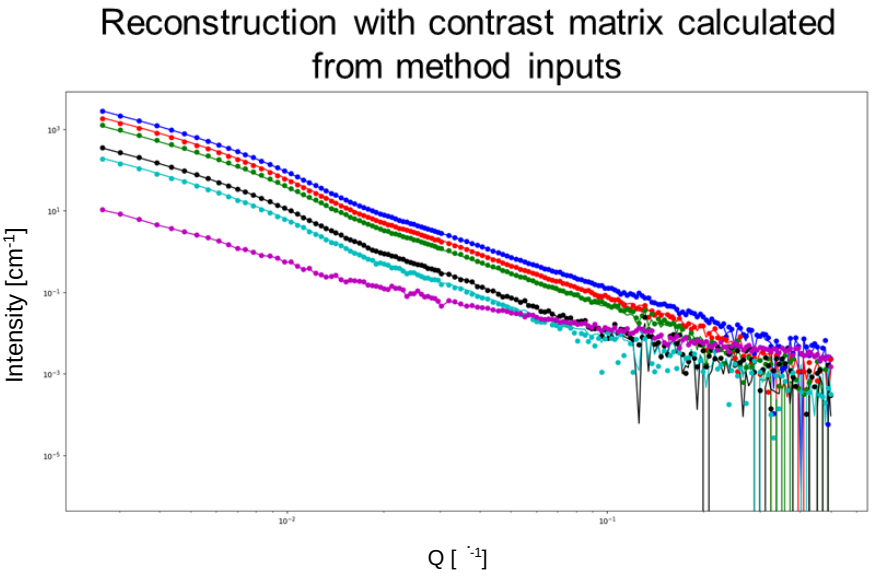
[129] H. S. Magar, R. Y. A. Hassan, A. Mulchandani, *Sensors*, 2021, **21**, 6578, DOI : https://doi.org/10.3390/s21196578

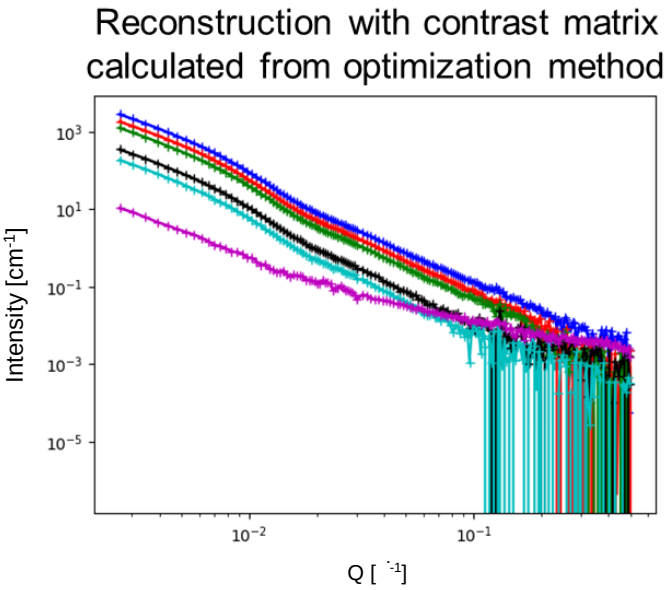
[130] Gaumont T., PhD thesis, Université de Lorraine, 2017

[131] Elgrishi N., Rountree K. J., McCarthy B. D., Rountree E. S., Eisenhart T. T., Dempsey J. L., *J. Chem. Educ.*, 2018 **95**, 197-206, DOI: https://doi.org/10.1021/acs.jchemed.7b00361

Appendix

1. SANS scattering function reconstructions from PSF outputs obtained by (a) performing matrix manipulation with contrast matrix calculated from inputs provided into the method, (b) performing matrix manipulation with a contrast matrix obtained through an optimization approach, based on the extracted PSFs as input. Both reconstructions correspond to the PSF output presented in **figure 30.** for the HNP experimental ink series. It can be observed both reconstructions yield a very good match to the original CV-SANS data inputs. The original contrast matrix computed using input values, as well as the contrast matrix obtained using the optimization method in (b) were also found to be comparable.





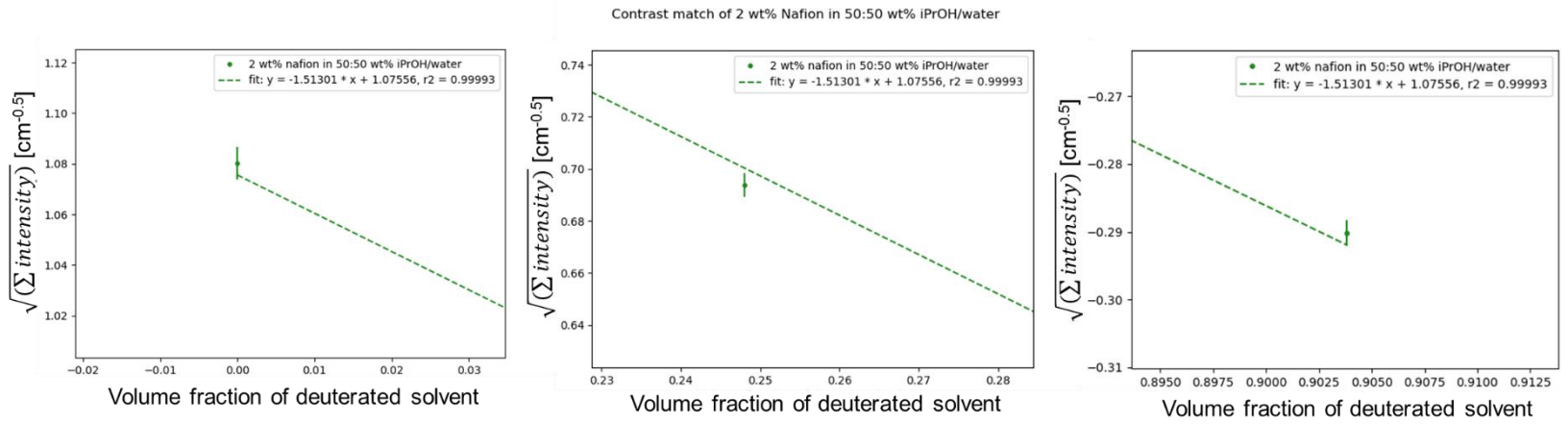
Contrast matrix computed from input values (ρ_c = 6.67x10^{10} cm^{-2}, ρ_p = 4.16x10^{10} cm^{-2})

Solvent SLD, n (cm^{-2})	$(\Delta\rho_{cn})^2$ (cm^{-2})	$(\Delta\rho_{pn})^2$ (cm^{-2})	$2\Delta\rho_{cn}\Delta\rho_{pn}$ (cm^{-2})
-0.43x10^{10}	5.04x10^{21}	2.11x10^{21}	6.52x10^{21}
0.81x10^{10}	3.43x10^{21}	1.12x10^{21}	3.93x10^{21}
2.05x10^{10}	2.13x10^{21}	4.45x10^{20}	1.95x10^{21}
4.16x10^{10}	6.30x10^{20}	0.00	0.00
4.77x10^{10}	3.61x10^{20}	3.72x10^{19}	-2.32x10^{20}
6.05x10^{10}	3.84x10^{19}	3.57x10^{20}	-2.34x10^{20}

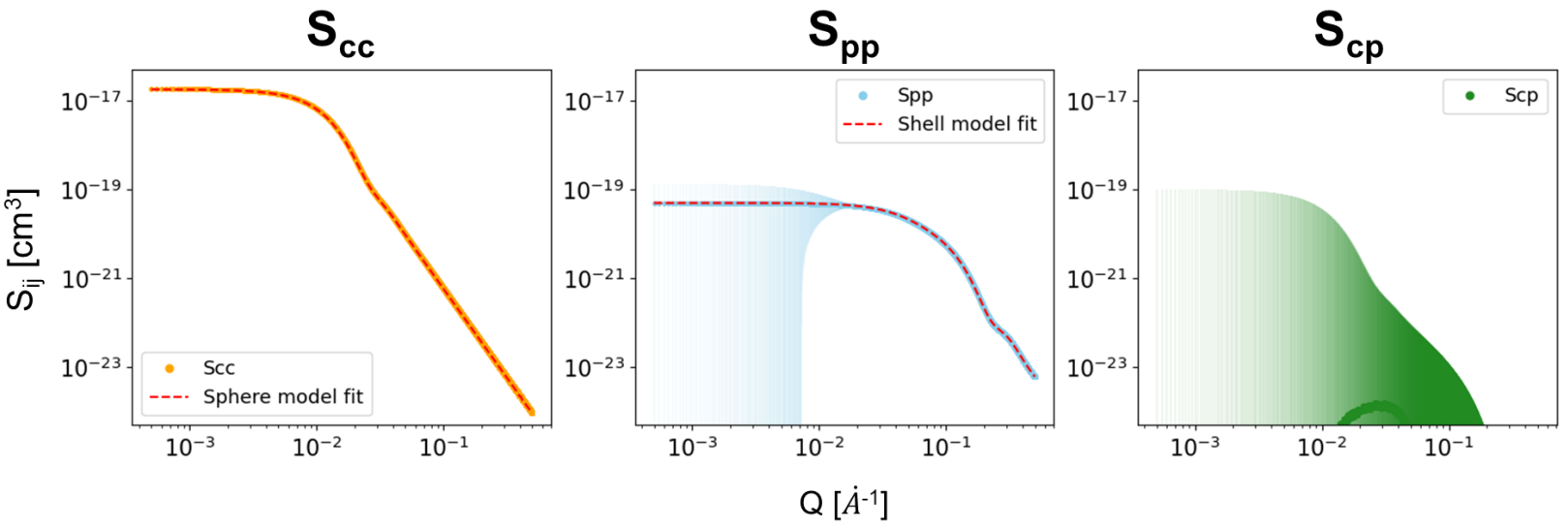
Optimized contrast matrix computed for reconstruction purposes

$(\Delta\rho_{cn})^2$ (cm^{-2})	$(\Delta\rho_{pn})^2$ (cm^{-2})	$2\Delta\rho_{cn}\Delta\rho_{pn}$ (cm^{-2})
5.09x10^{21}	2.14x10^{21}	6.46x10^{21}
3.28x10^{21}	1.05x10^{21}	4.01x10^{21}
2.26x10^{21}	5.27x10^{20}	2.03x10^{21}
6.41x10^{20}	-2.19x10^{19}	-2.60x10^{20}
3.42x10^{20}	-7.83x10^{17}	-7.63x10^{19}
3.95x10^{19}	3.70x10^{20}	-2.46x10^{20}

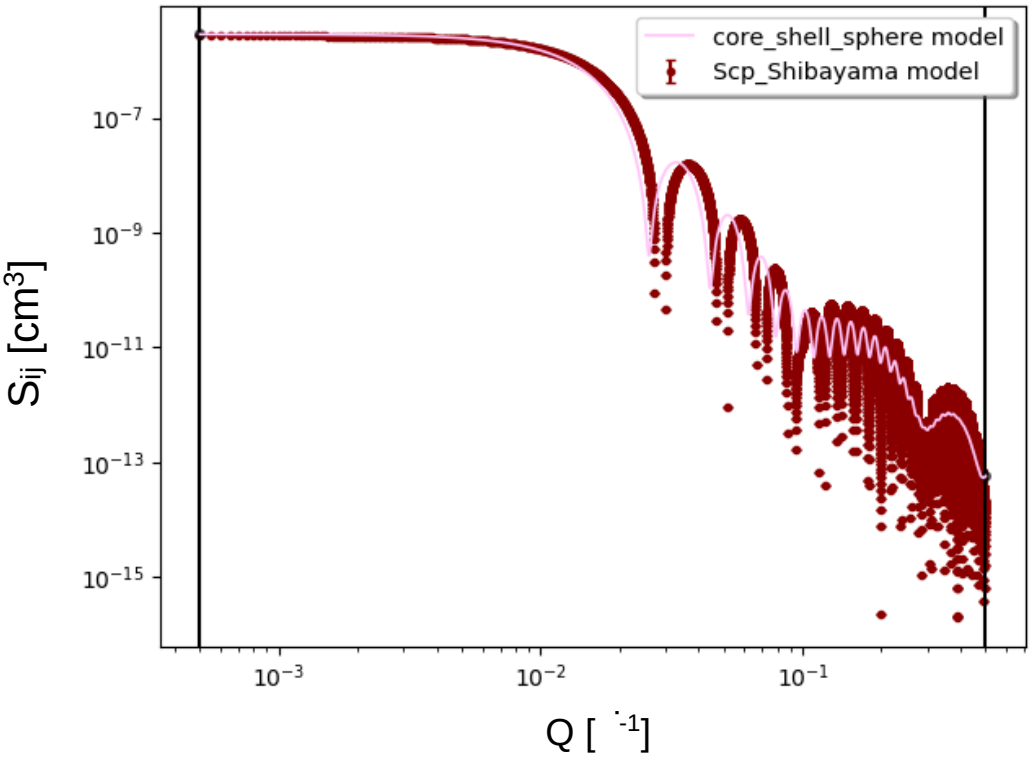
2. Visualization of error bars in **figure 31(b)** – contrast match of 2 wt% Nafion in 50:50 wt% iPrOH/water.



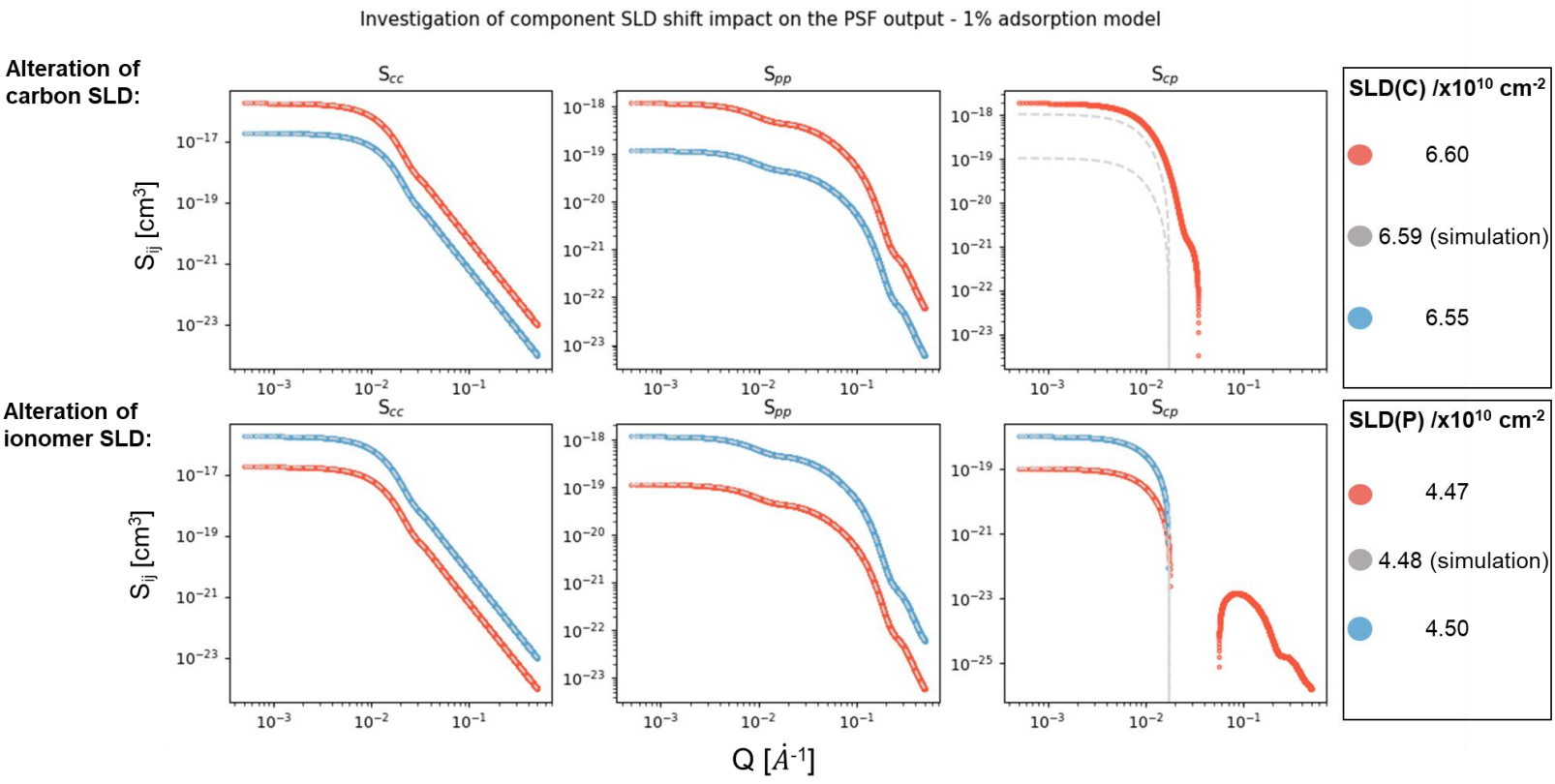
3. PSF outputs obtained from the spheres + cylinders model based simulated data (**figure 37**), with error bars for the S_{cp} visualized:

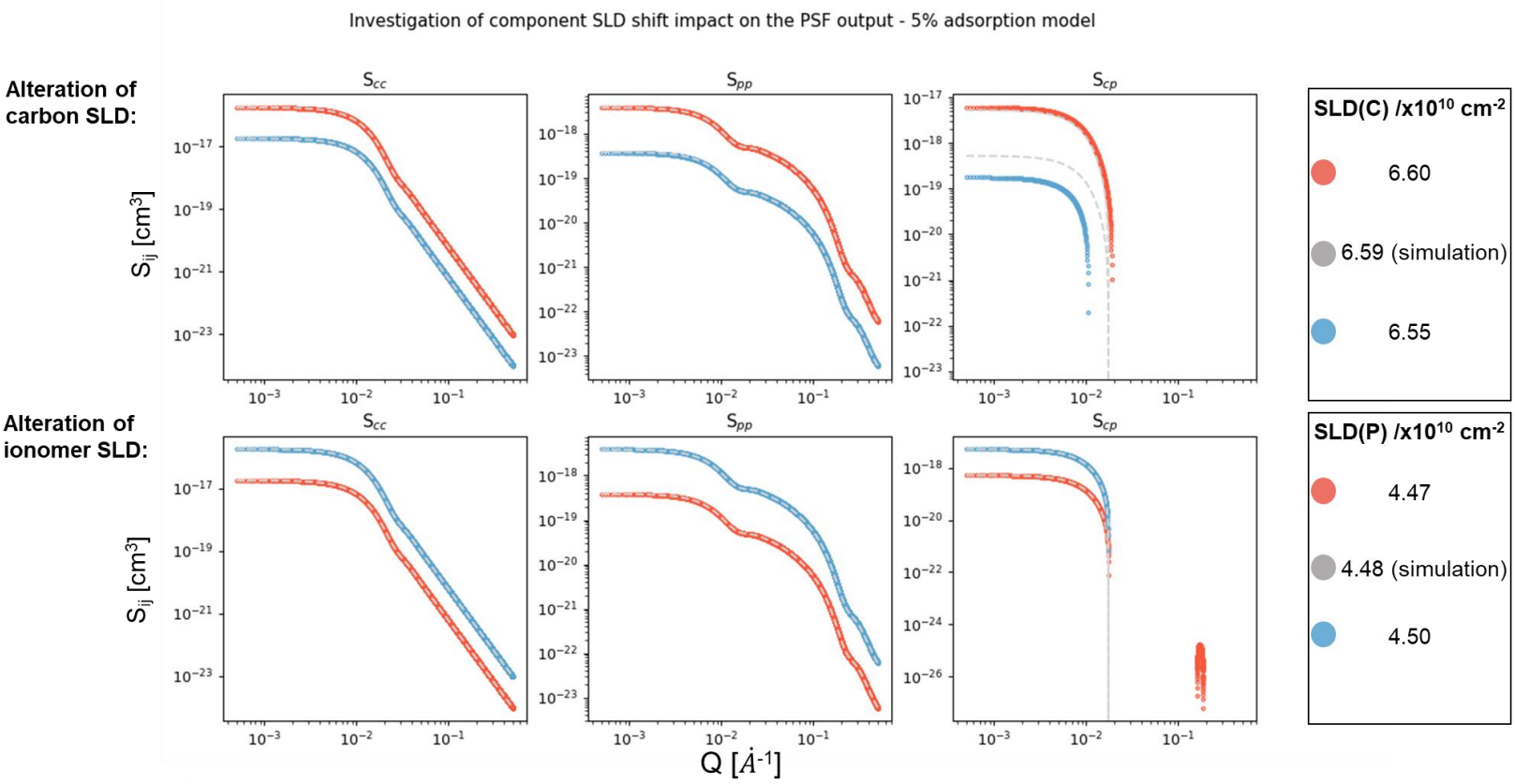


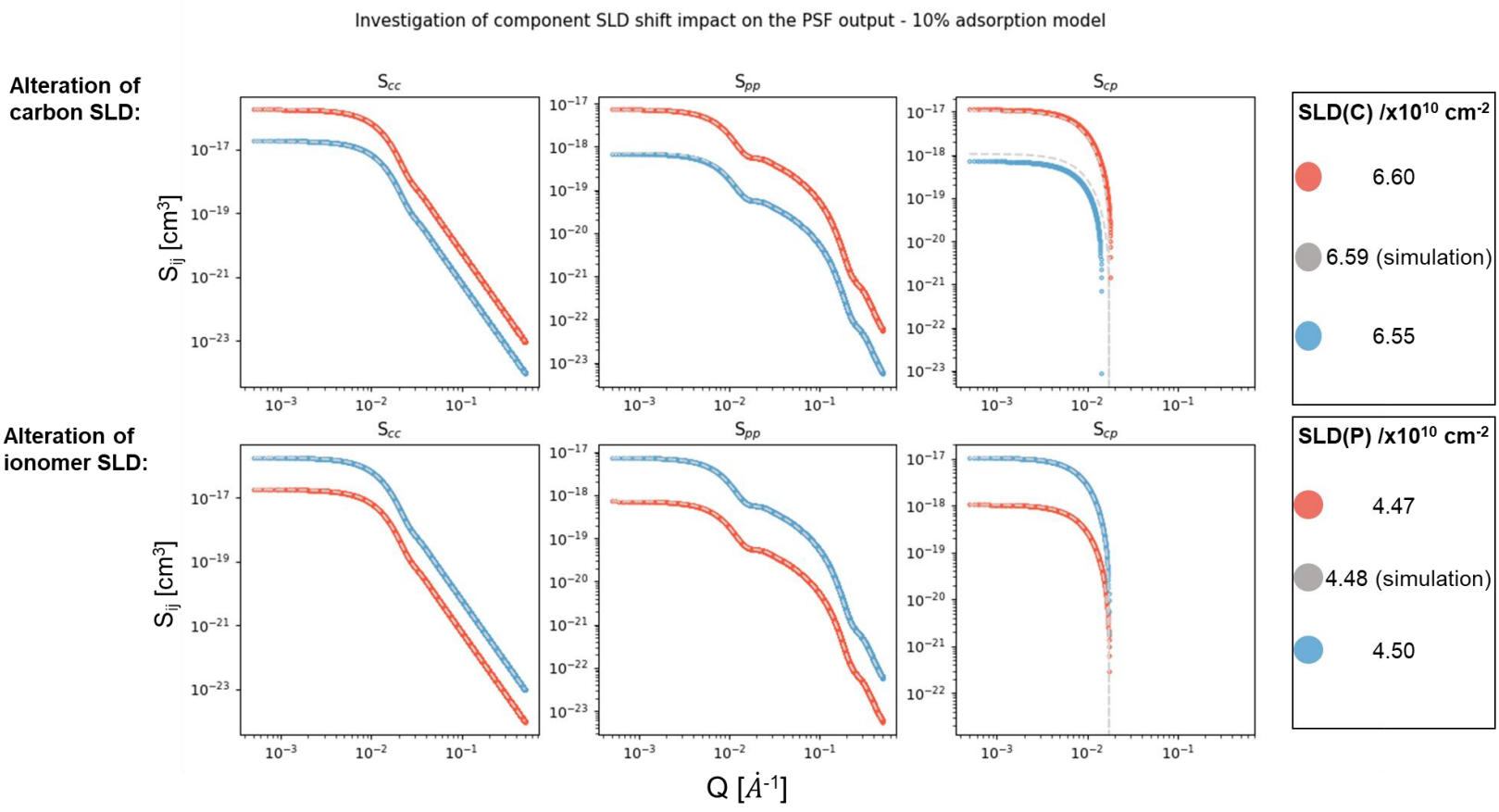
4. Comparison of the model proposed by Shibayama et al.[70] to the SasView 5.0.6 core_shell_sphere model when polydispersity is set to 0:



5. Investigation of SLD shift for partial adsorption model based simulations, for up to 10% core-shell in dataset. After 10% core-shell it can be assumed the behaviour will be the same as for SLD shift investigation on the core-shell based dataset. The validity of the outputs was confirmed by comparing with PSF outputs when the original SLD values used in the simulations were applied as input. Error bars have been left out for visualization, as well as figure generation reasons. Data was shifted on a logarithmic scale for visualization purposes.



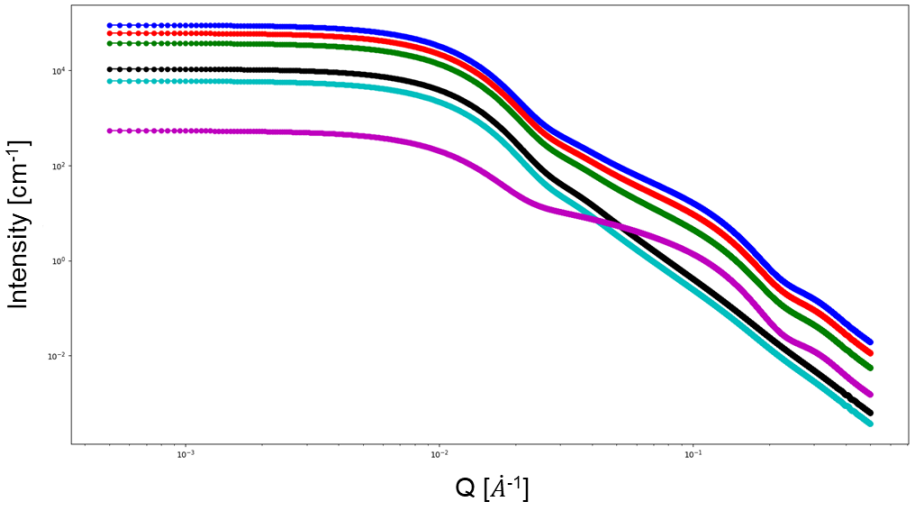

Investigation of component SLD shift impact on the PSF output - 5% adsorption model
Alteration of carbon SLD:
Alteration of ionomer SLD:
S_{cc}
S_{pp}
S_{cp}
S_{ij} [cm^3]
Q [$\dot{A}^{-1}$]
SLD(C) /x10^{10} cm^{-2}
6.60
6.59 (simulation)
6.55
SLD(P) /x10^{10} cm^{-2}
4.47
4.48 (simulation)
4.50


Investigation of component SLD shift impact on the PSF output - 10% adsorption model
Alteration of carbon SLD:
Alteration of ionomer SLD:
S_{cc}
S_{pp}
S_{cp}
S_{ij} [cm^3]
Q [$\dot{A}^{-1}$]
SLD(C) /x10^{10} cm^{-2}
6.60
6.59 (simulation)
6.55
SLD(P) /x10^{10} cm^{-2}
4.47
4.48 (simulation)
4.50

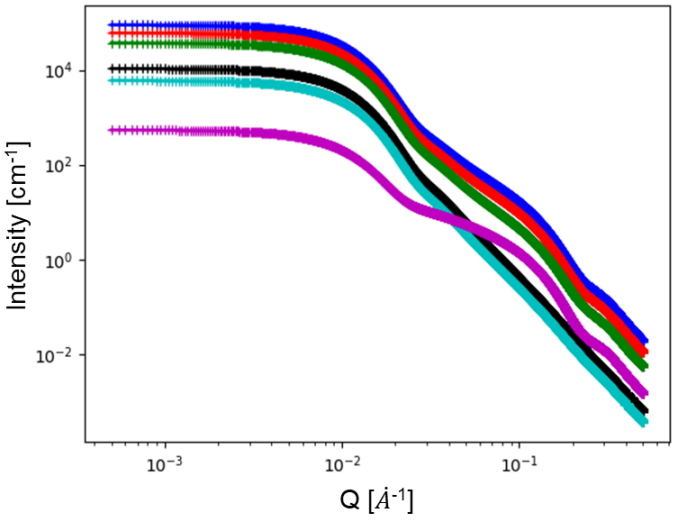
6. An example of data reconstruction arising from PSF output extraction for both the S + C and core-shell model based datasets when SLD(P) was set to 4.00×10^{10} cm^{-2}. For both models erroneous PSF outputs were extracted, however a perfect data reconstruction can be observed:

For S+C model based dataset PSF extraction when SLD(P) = 4.00×10^{10} cm^{-2}:

Reconstruction with contrast matrix calculated from method inputs

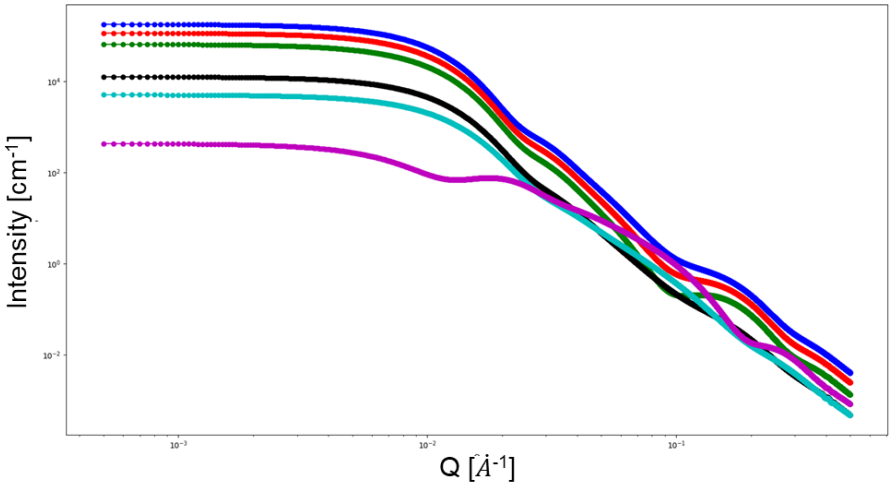


Reconstruction with contrast matrix calculated from optimization method

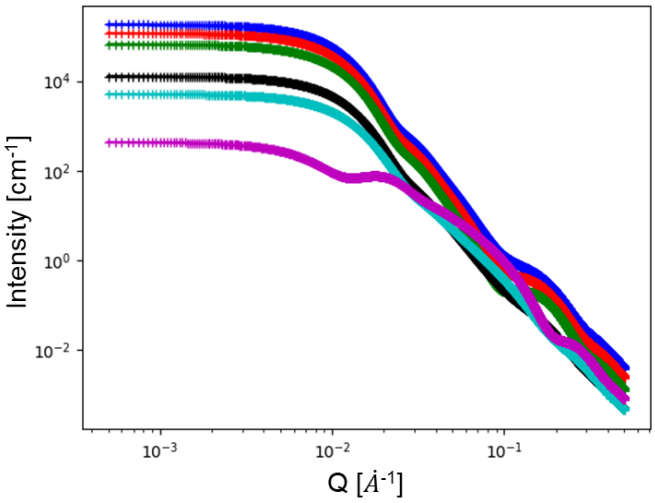


For core-shell model based dataset PSF extraction when SLD(P) = 4.00×10^{10} cm^{-2}:

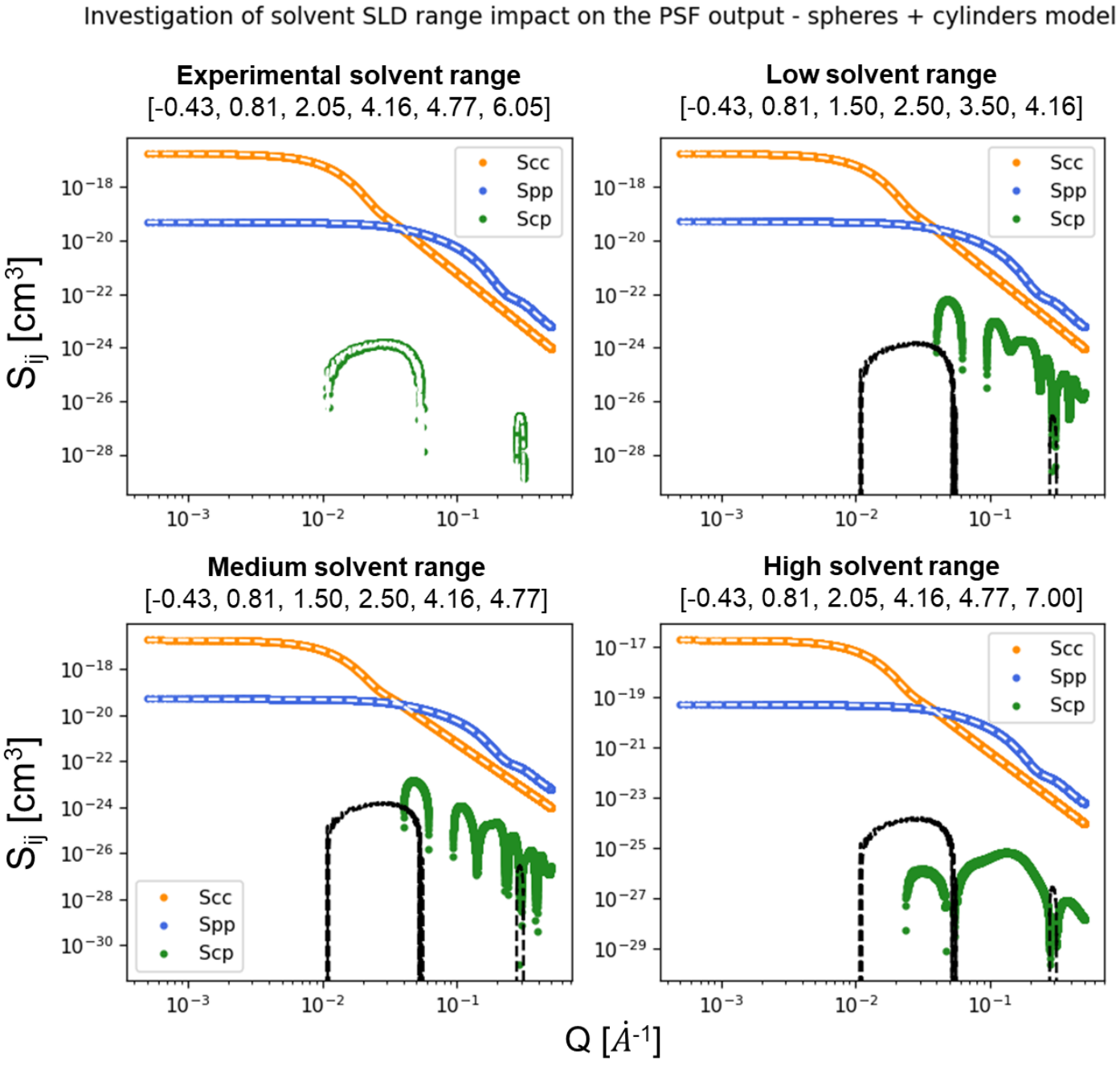
Reconstruction with contrast matrix calculated from method inputs

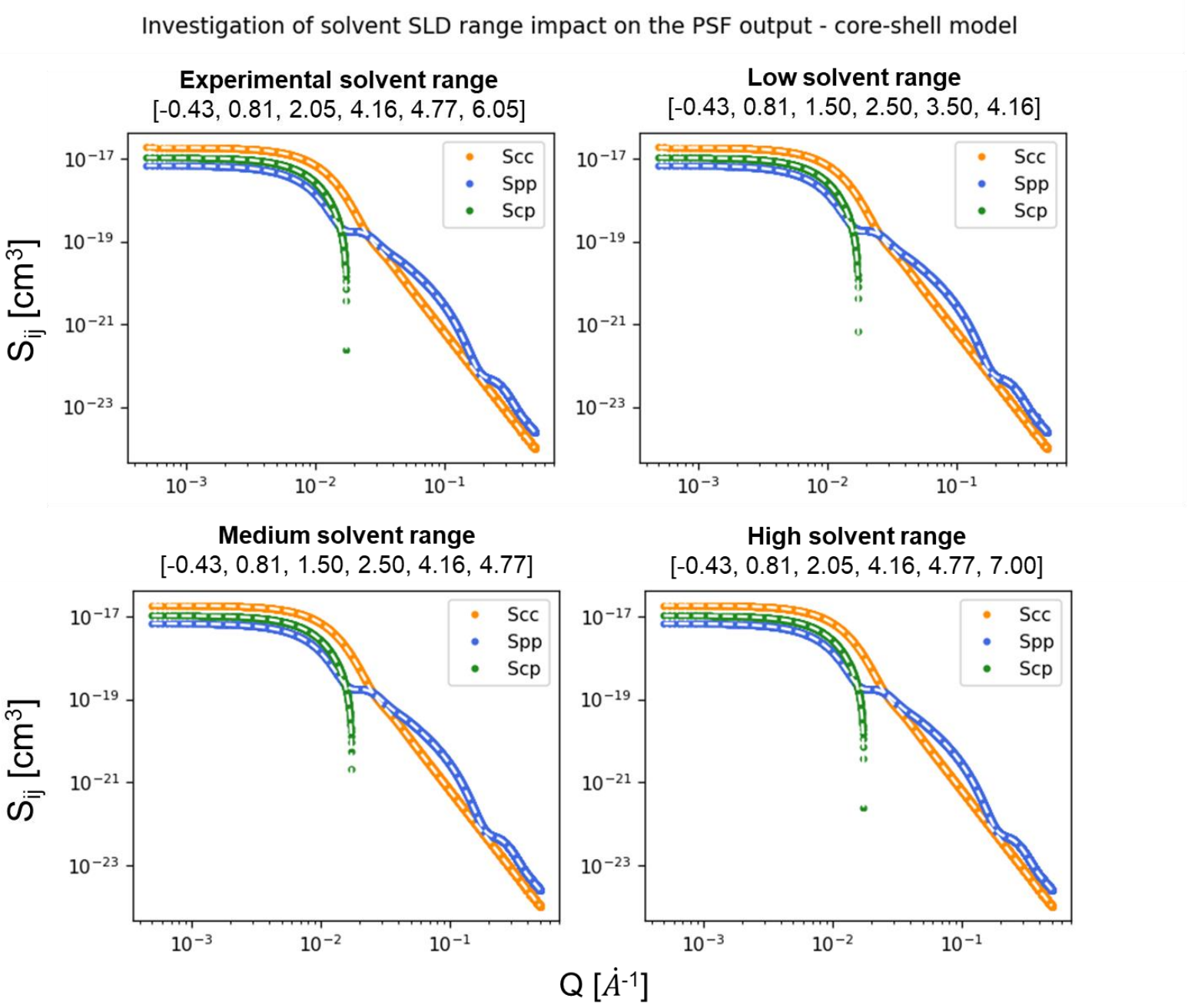


Reconstruction with contrast matrix calculated from optimization method

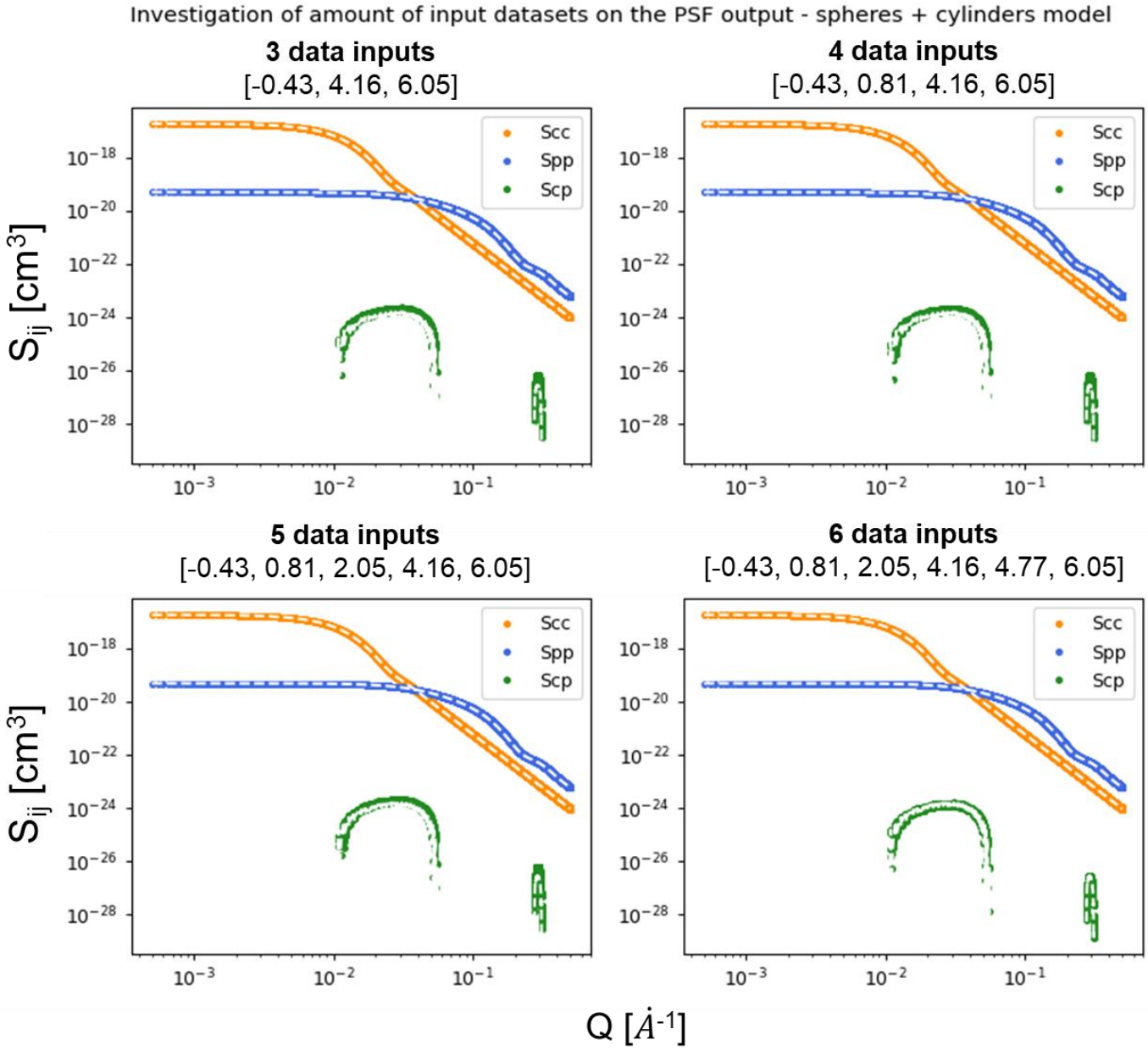


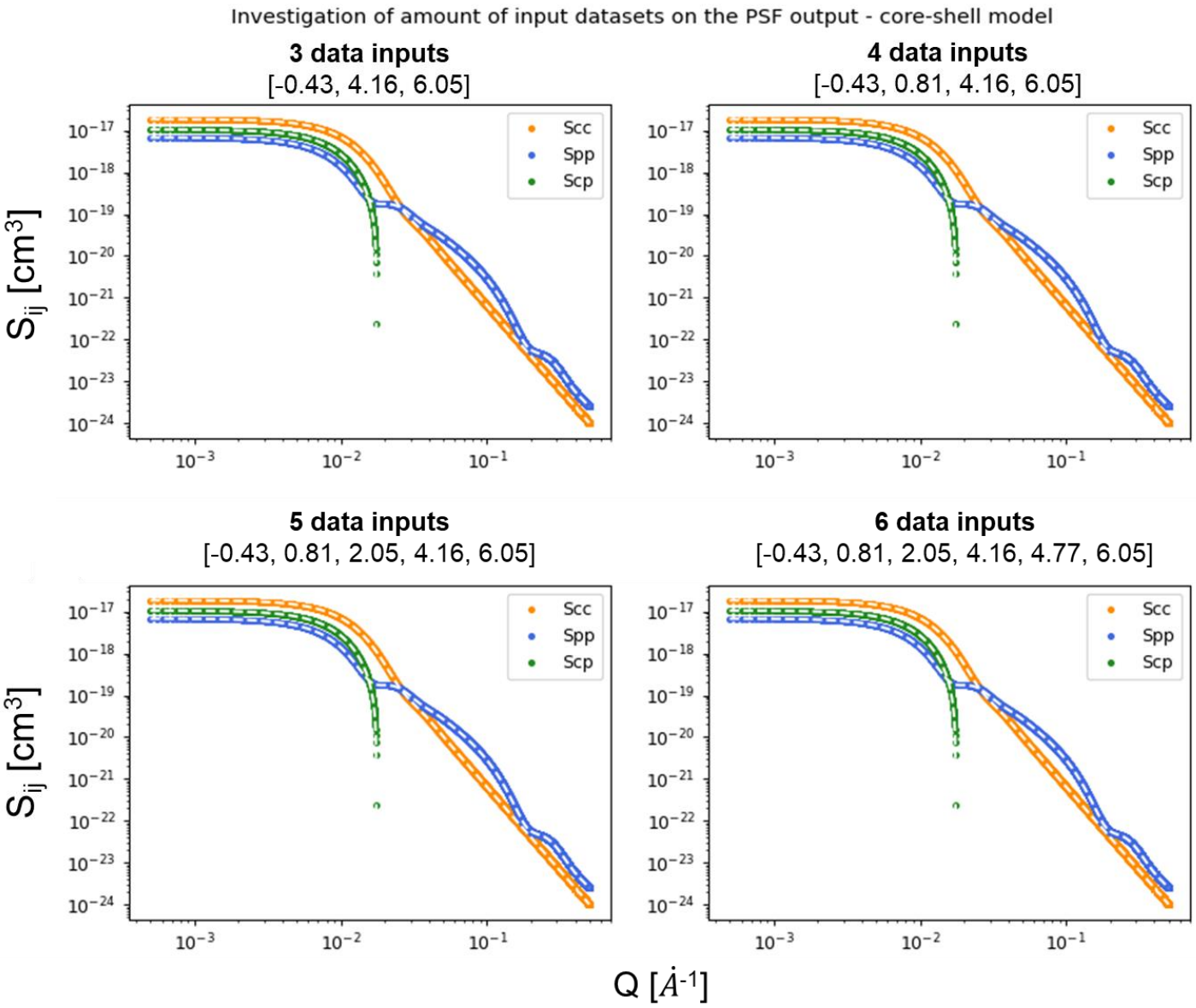
7. Investigation of the effect of solvent range on the PSF outputs extracted for the S + C and core-shell simulations. The veracity of the outputs has been verified by comparing to original PSF extractions (**figures 37, 38**), visualized by dashed white and black lines, which could be perfectly fitted with corresponding models. Error bars have not been included for visualization purposes.



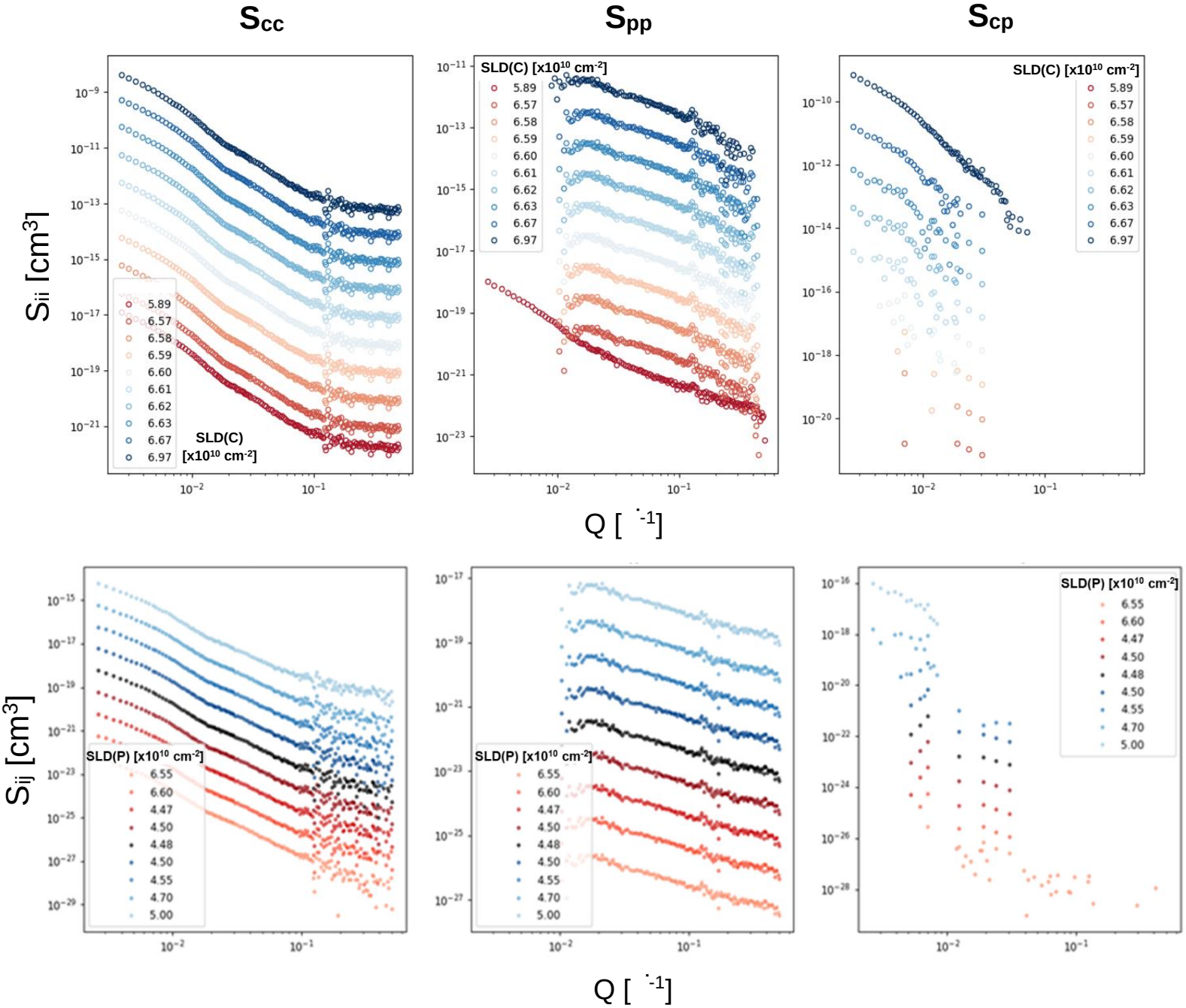

Investigation of solvent SLD range impact on the PSF output - core-shell model
Experimental solvent range
[-0.43, 0.81, 2.05, 4.16, 4.77, 6.05]
Low solvent range
[-0.43, 0.81, 1.50, 2.50, 3.50, 4.16]
Medium solvent range
[-0.43, 0.81, 1.50, 2.50, 4.16, 4.77]
High solvent range
[-0.43, 0.81, 2.05, 4.16, 4.77, 7.00]
Scc
Spp
Scp
S_{ij} [cm^3]
Q [$\dot{A}^{-1}$]

8. Investigation of the effect of data input amount on the PSF outputs extracted for the S + C and core-shell simulations. The veracity of the outputs has been verified by comparing to original PSF extractions (**figures 37, 38**), which could be perfectly fitted with corresponding models. Error bars have not been included for visualization purposes.

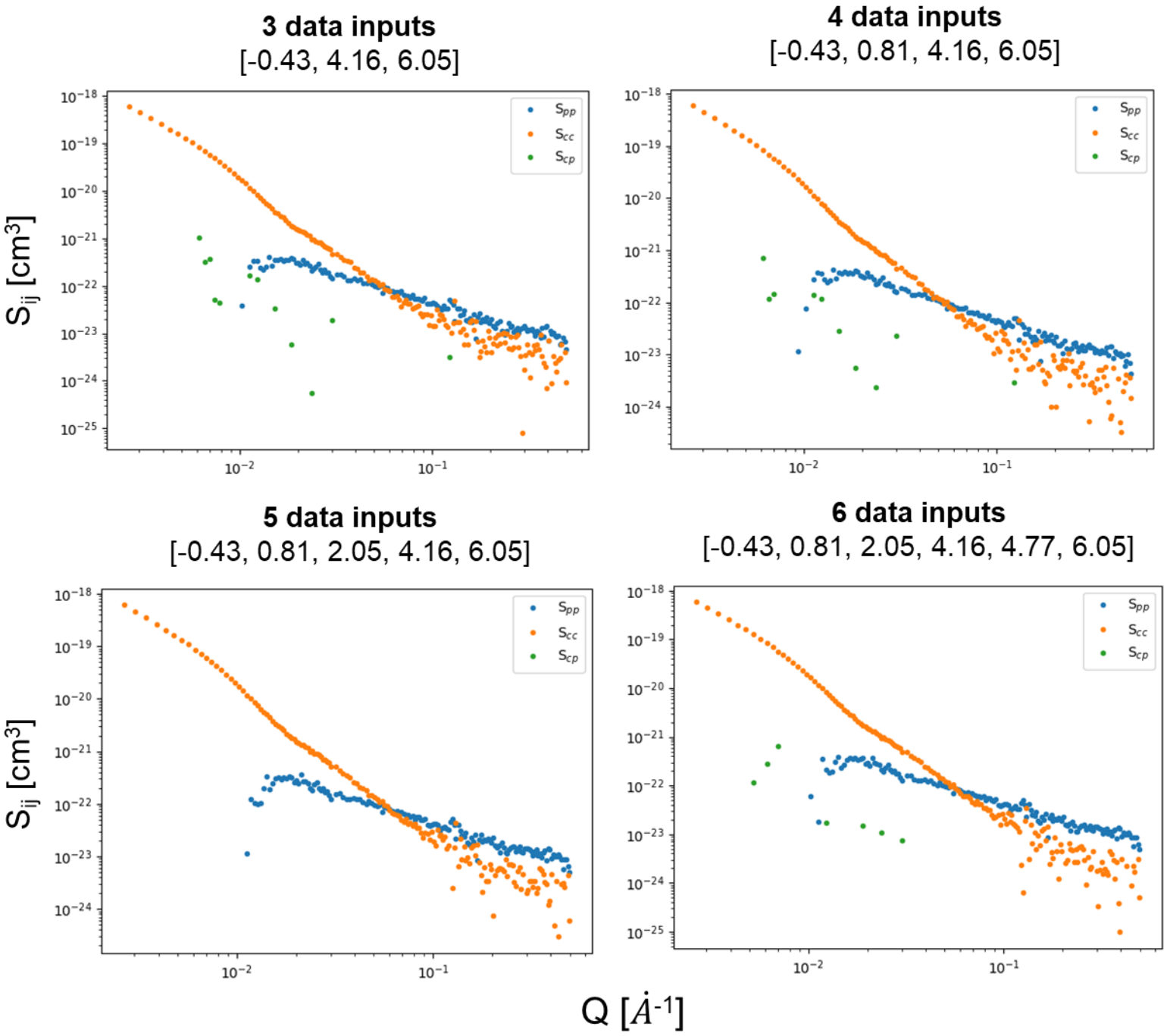



Investigation of amount of input datasets on the PSF output - core-shell model
3 data inputs
[-0.43, 4.16, 6.05]
4 data inputs
[-0.43, 0.81, 4.16, 6.05]
5 data inputs
[-0.43, 0.81, 2.05, 4.16, 6.05]
6 data inputs
[-0.43, 0.81, 2.05, 4.16, 4.77, 6.05]
Scc
Spp
Scp
S_{ij} [cm^3]
Q [$Å^{-1}$]

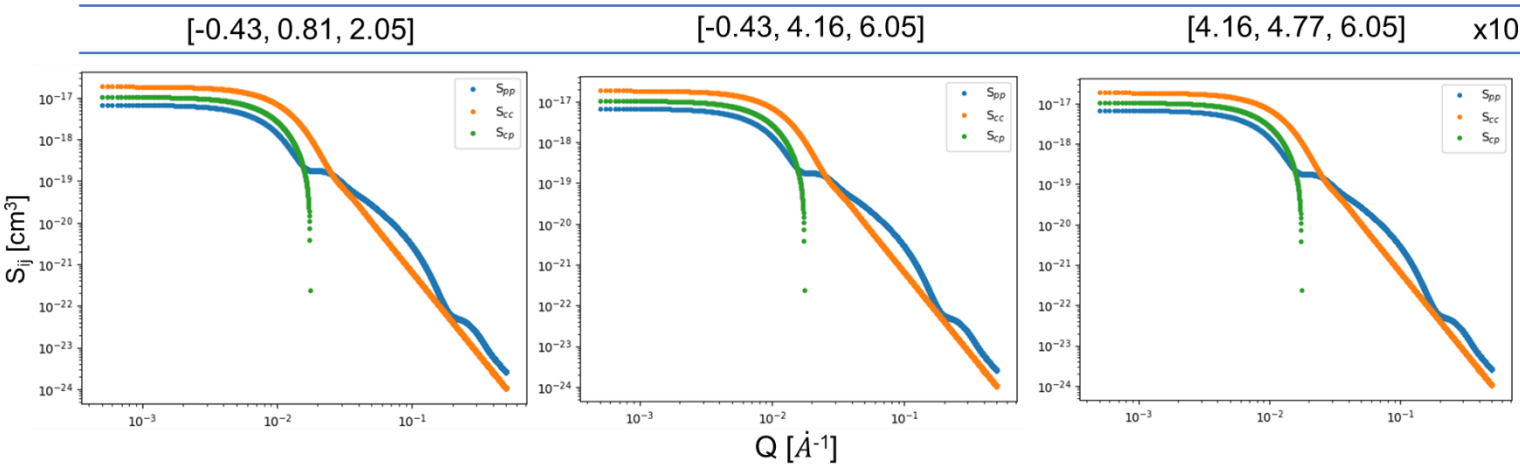
9. Effect of SLD(C) and SLD(P) individual shift on an experimental dataset (HNP) that has the same component and solvent SLD values as the simulated datasets. Data has been shifted on a logarithmic scale and error bars have been left out for visualization purposes. Note a similar behaviour to the spheres + cylinder model based data can be observed.



10. Effect of number of input data on an experimental dataset (HNP) that has the same component and solvent SLD values as the simulated datasets. Error bars have not been included.

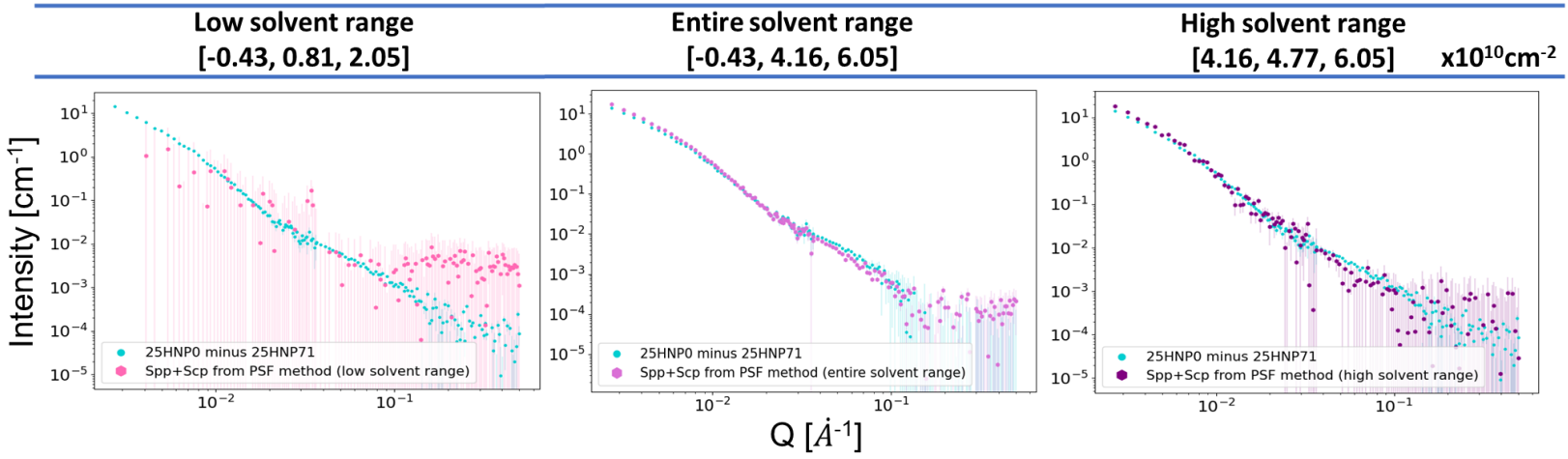


11. Effect of contrast range variation when minimum number of data inputs are used on the core-shell model based simulation PSF outputs extracted. Error bars have not been included.

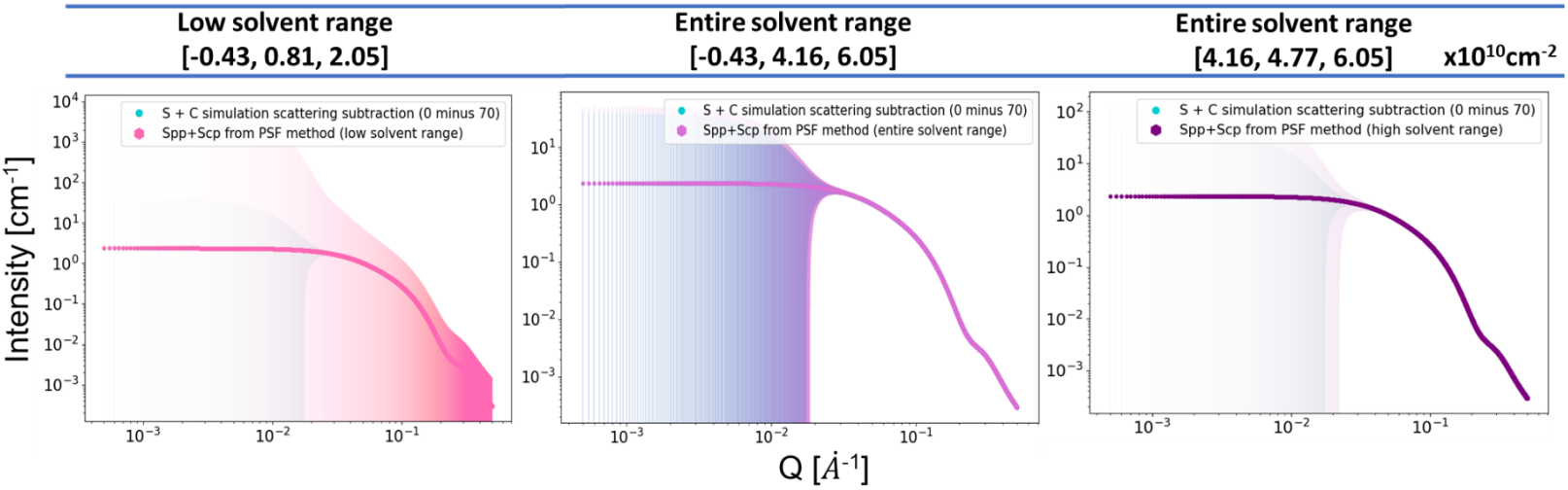


12. Scattering subtraction method applied to another experimental dataset (HNP25), S+C and core-shell model based simulations.

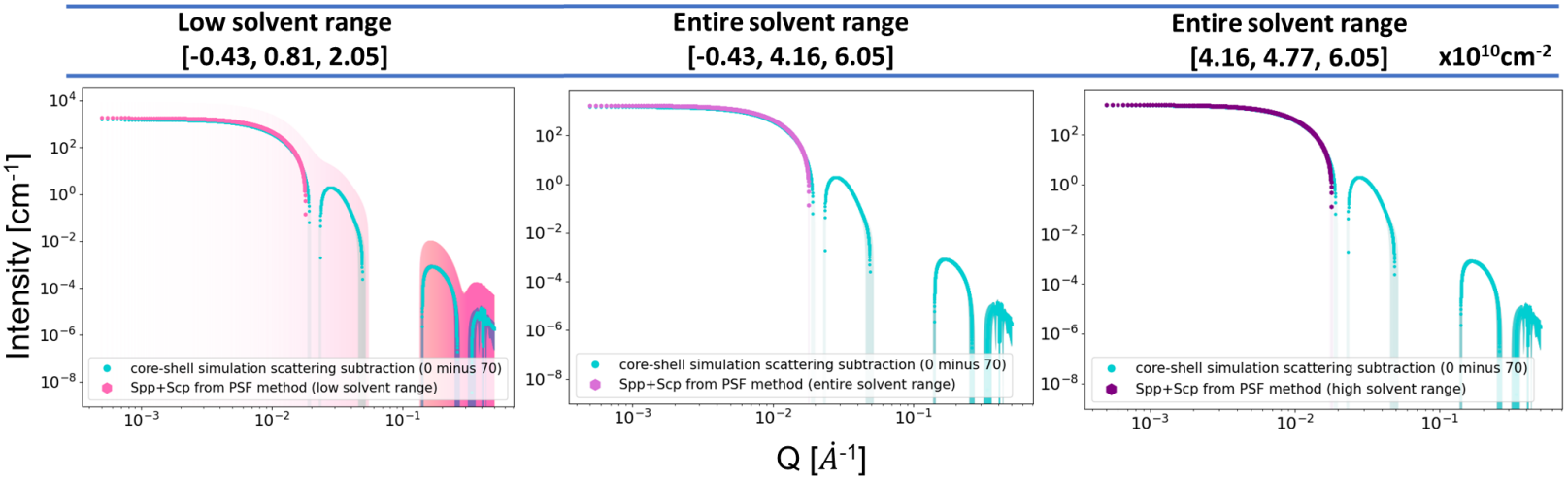
Experimental data set 25HNP:



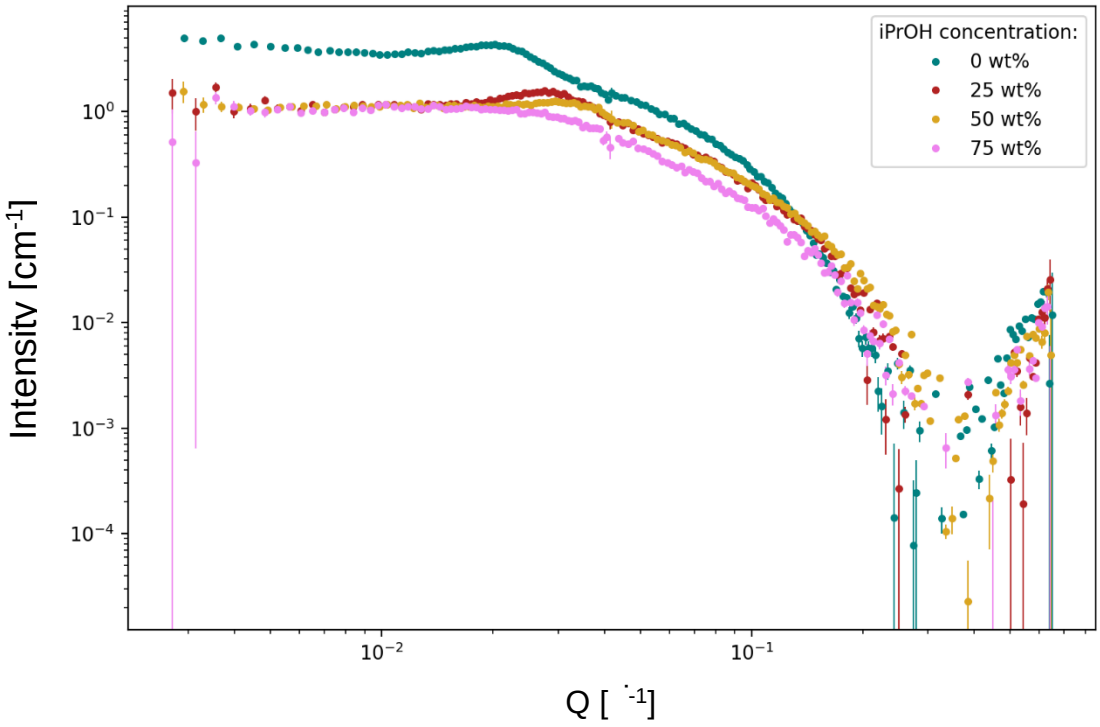
Spheres + cylinders model based simulated data:



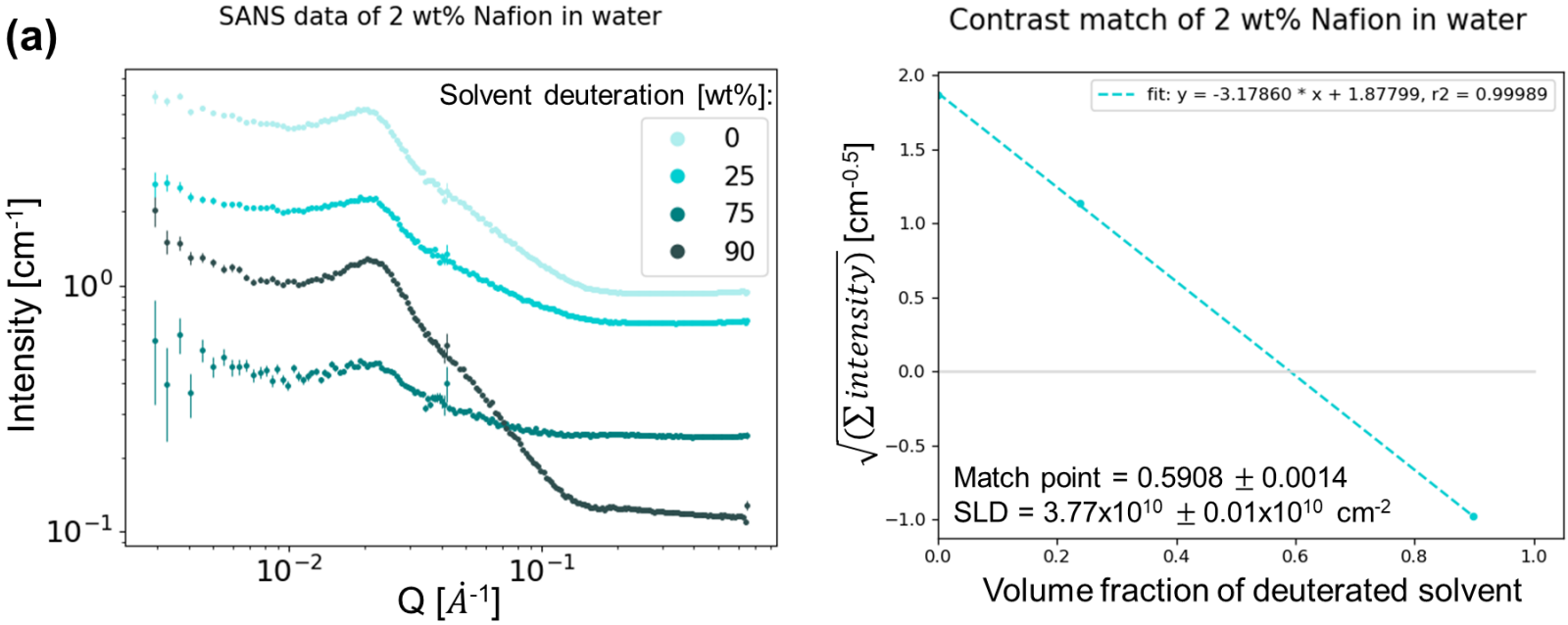
Core-shell model based simulated data:

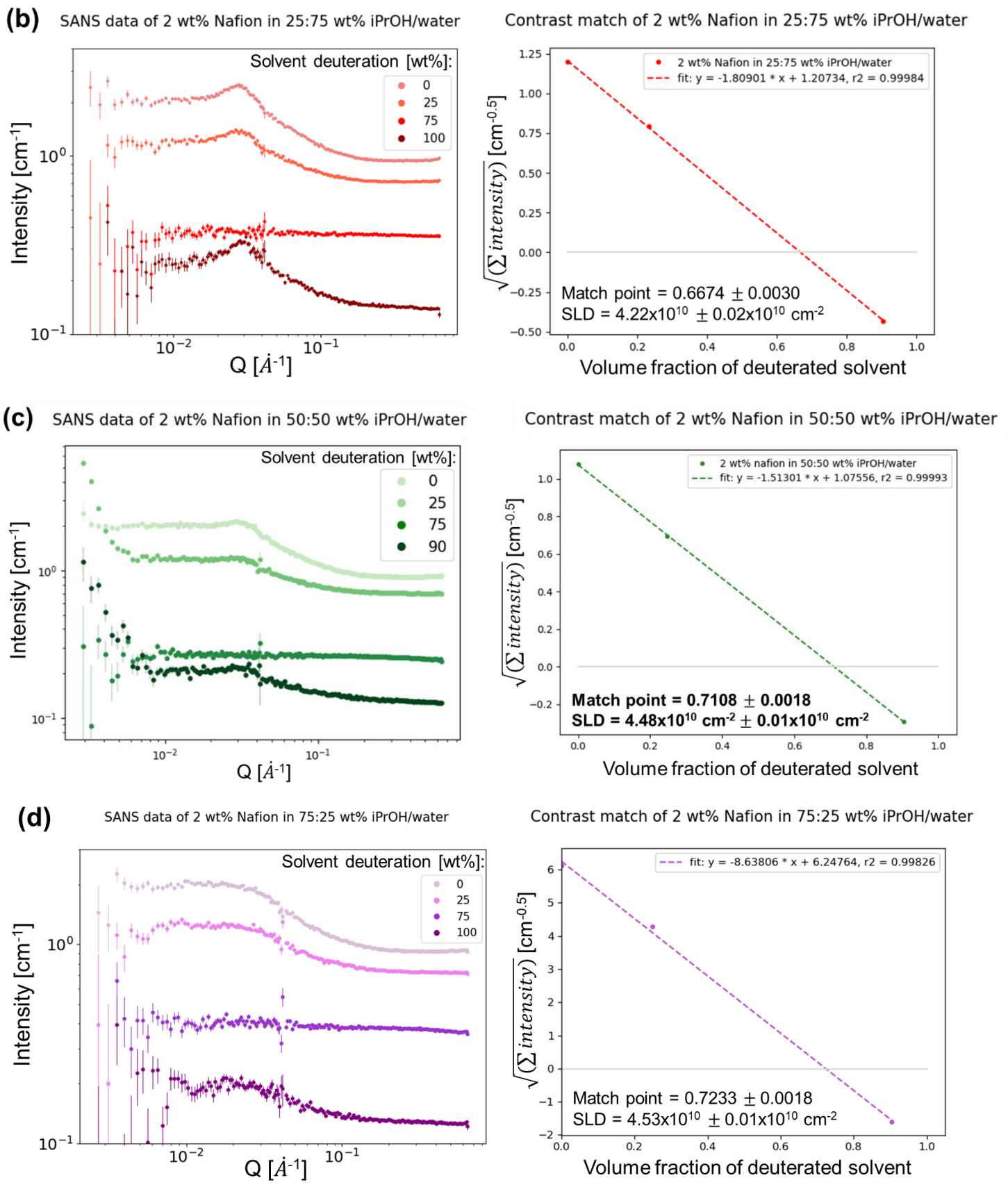


13. SANS data of 2 wt% nafion in solvent with varying iPrOH:water ratios (0 wt% solvent deuteration)

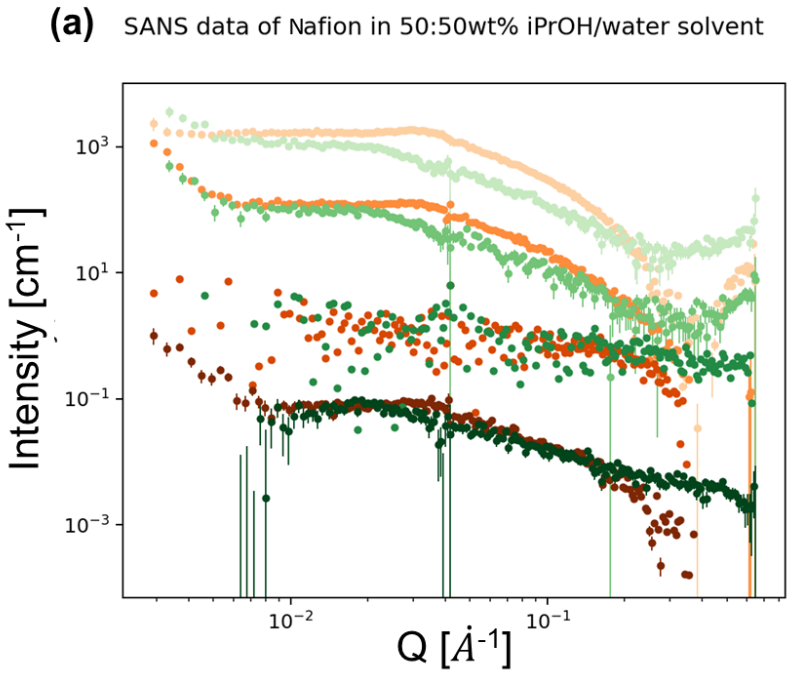


14. CV-SANS measurements, and corresponding contrast matches of 2 wt% Nafion in solvents with varying iPrOH concentration.

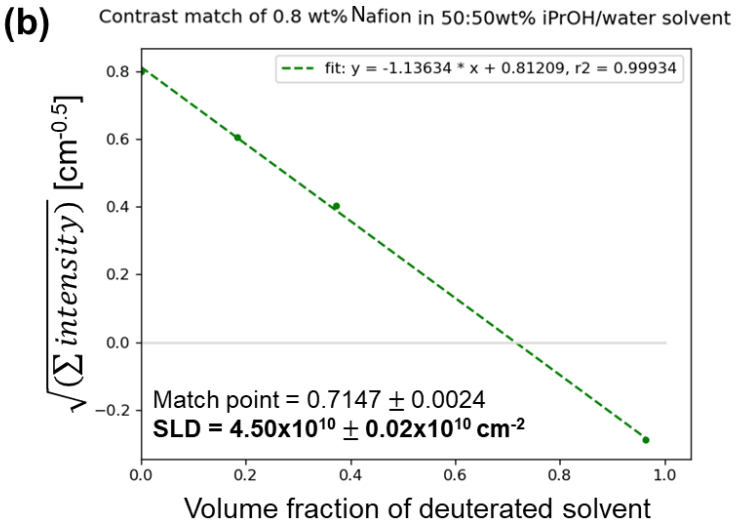


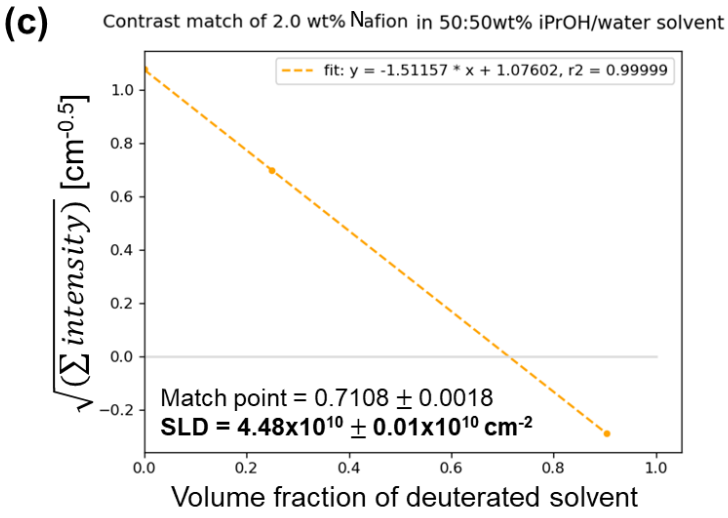

(b)
SANS data of 2 wt% Nafion in 25:75 wt% iPrOH/water
Solvent deuteration [wt%]:
0
25
75
100
Intensity [cm^{-1}]
Q [Å^{-1}]
Contrast match of 2 wt% Nafion in 25:75 wt% iPrOH/water
2 wt% Nafion in 25:75 wt% iPrOH/water
fit: y = -1.80901 * x + 1.20734, r2 = 0.99984
$\sqrt{(\sum intensity)}$ [cm$^{-0.5}$]
Match point = 0.6674 ± 0.0030
SLD = 4.22x10^{10} ± 0.02x10^{10} cm^{-2}
Volume fraction of deuterated solvent
(c)
SANS data of 2 wt% Nafion in 50:50 wt% iPrOH/water
Solvent deuteration [wt%]:
0
25
75
90
Intensity [cm^{-1}]
Q [Å^{-1}]
Contrast match of 2 wt% Nafion in 50:50 wt% iPrOH/water
2 wt% nafion in 50:50 wt% iPrOH/water
fit: y = -1.51301 * x + 1.07556, r2 = 0.99993
$\sqrt{(\sum intensity)}$ [cm$^{-0.5}$]
Match point = 0.7108 ± 0.0018
SLD = 4.48x10^{10} cm^{-2} ± 0.01x10^{10} cm^{-2}
Volume fraction of deuterated solvent
(d)
SANS data of 2 wt% Nafion in 75:25 wt% iPrOH/water
Solvent deuteration [wt%]:
0
25
75
100
Intensity [cm^{-1}]
Q [Å^{-1}]
Contrast match of 2 wt% Nafion in 75:25 wt% iPrOH/water
fit: y = -8.63806 * x + 6.24764, r2 = 0.99826
$\sqrt{(\sum intensity)}$ [cm$^{-0.5}$]
Match point = 0.7233 ± 0.0018
SLD = 4.53x10^{10} ± 0.01x10^{10} cm^{-2}
Volume fraction of deuterated solvent

15. **(a)** SANS measurements of 0.8 and 2 wt% Nafion dispersions in 50:50 wt% iPrOH/water solvent. Data has been shifted for visualization. Error bars in measurements corresponding to 75 wt% solvent deuteration have been removed. (**b)** contrast match of 0.8 wt% Nafion in 50:50 wt% iPrOH/water solvent. **(c)** contrast match of 2 wt% Nafion in 50:50 wt% iPrOH/water solvent.

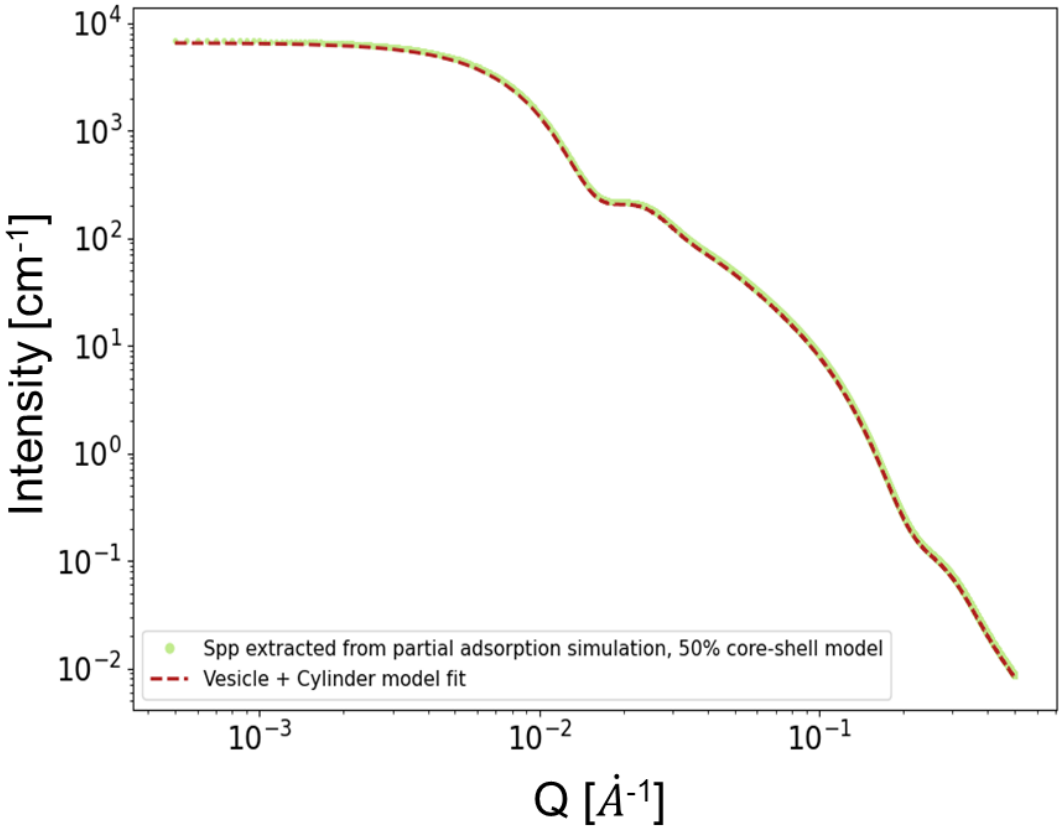


Solvent deuteration [wt%]	0.8 wt% Nafion	2 wt% Nafion
0		
25		
75		
100		



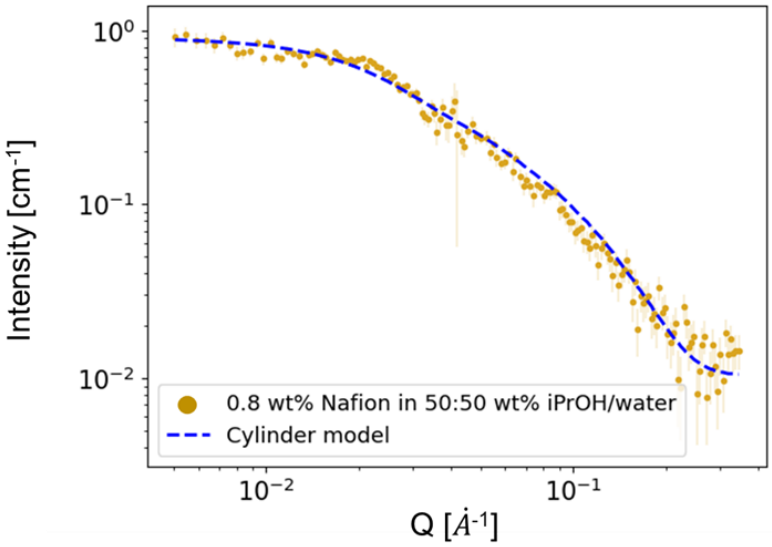


16. S_{pp} output extracted from a (50% core-shell) partial adsorption model based simulated dataset, fitted with the vesicle/cylinder combined model, using parameters that were used to generate the simulated data.



17. Fitting of 0.8 wt% Nafion in 50:50 wt% iPrOH/water scattering function using the cylinder model. 1.2 and 20 nm radius and length were estimated from the extracted parameters. Nevertheless, note an exact fit could not be achieved due to the presence of a structure factor.

(a)



(b)

Cylinder

Scale = 3.50e-03 ± 2.22e-04
Sld = 4.48x10^{10} cm^{-2}
Sld_solvent = -0.38x10^{10} cm^{-2}

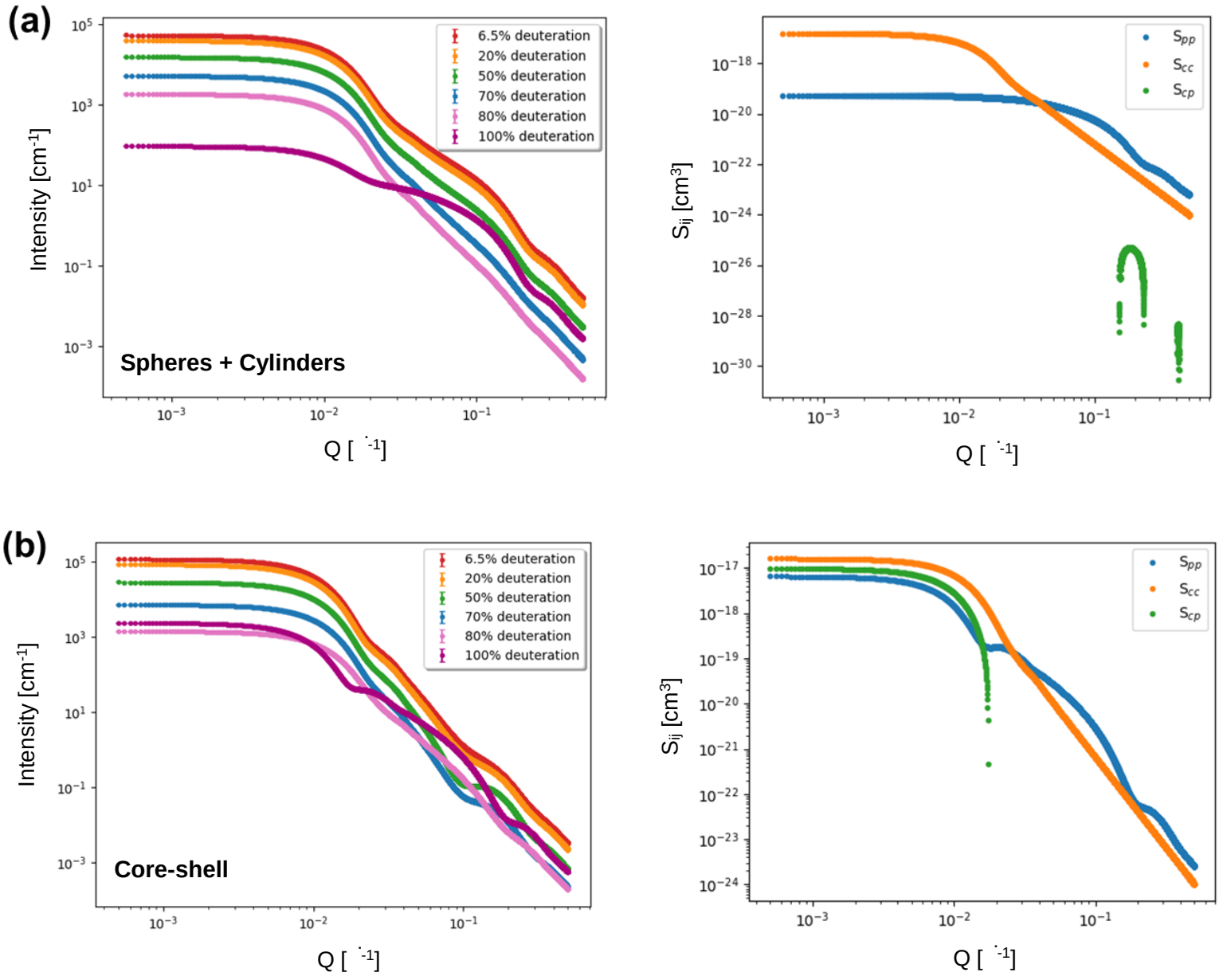
Radius = 11.59 ± 1.66e-05 Å
Length = 198.79 ± 2.21e-04 Å

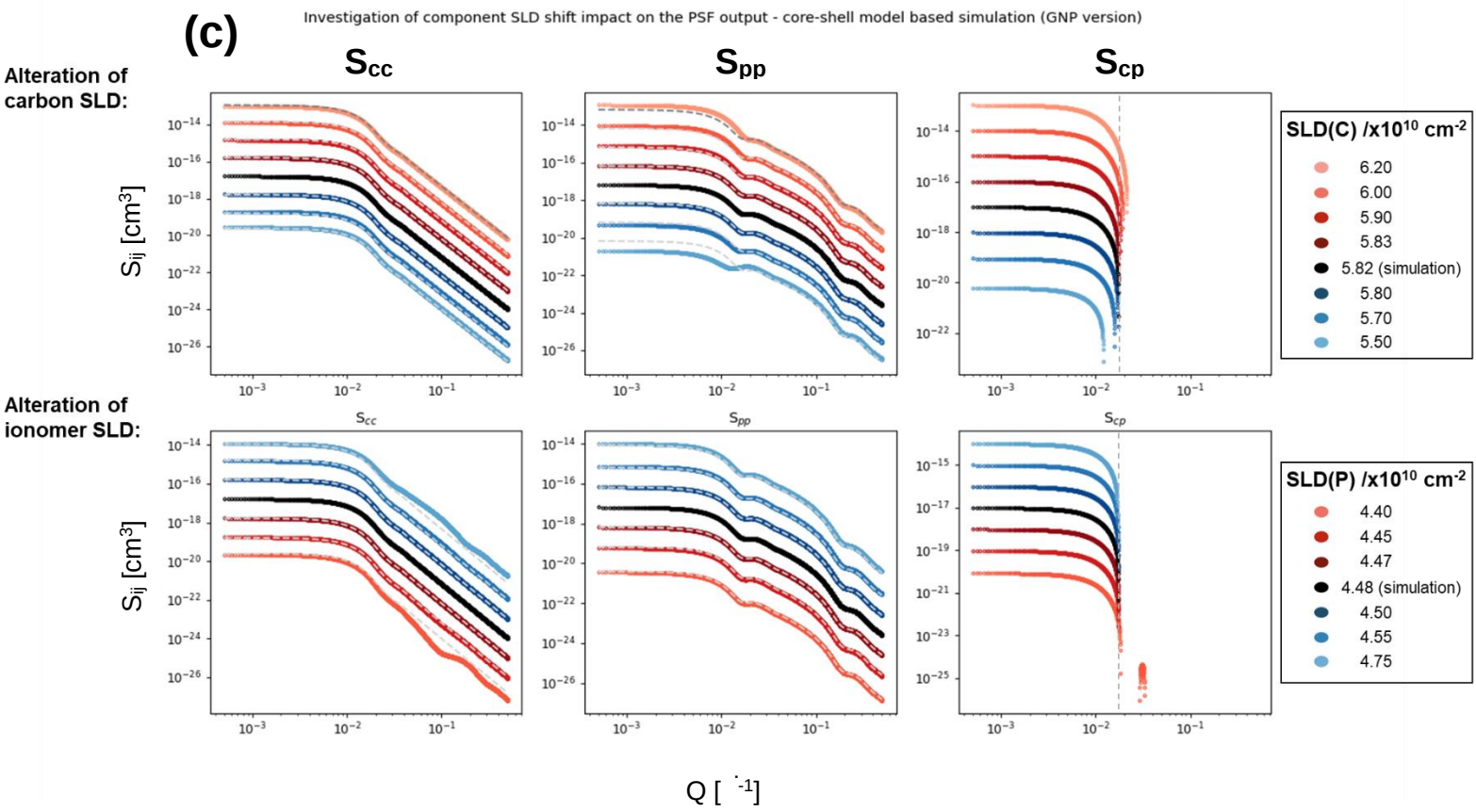
Distribution of radius = 0.20
Distribution of thickness = 0
(function:lognormal)

Chi^2/Npts = 1.92

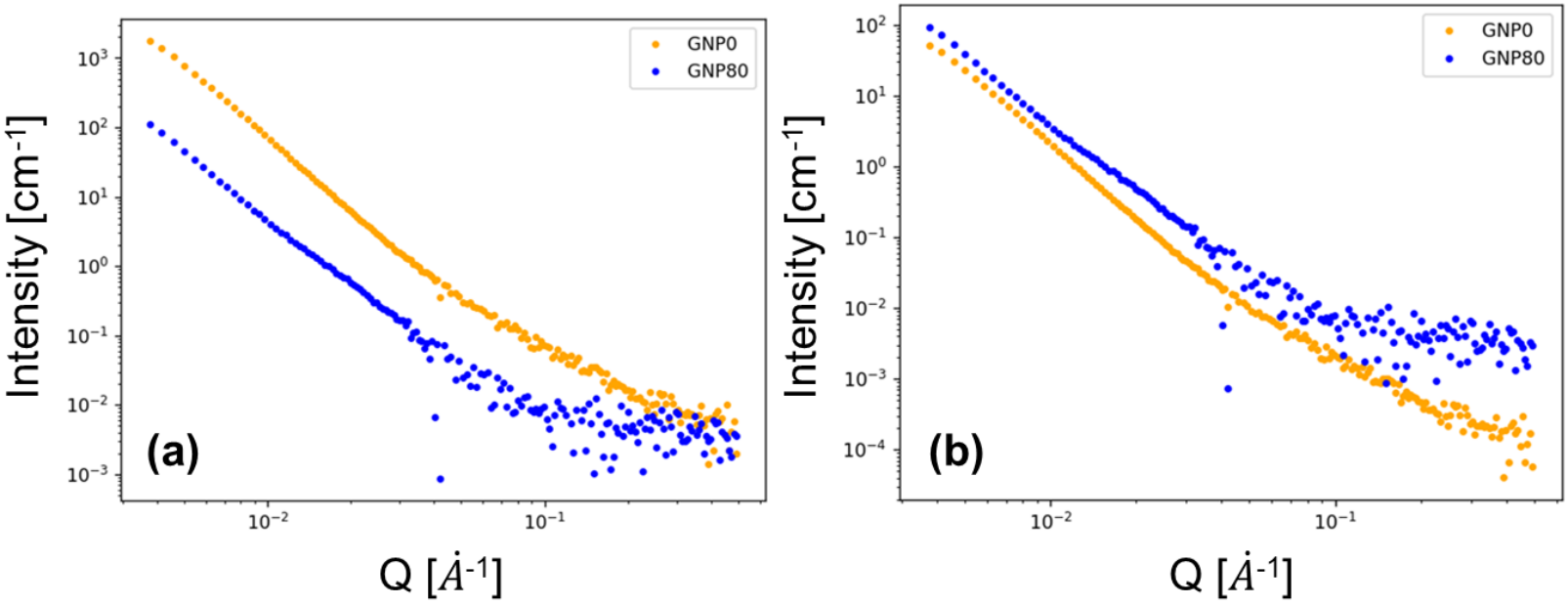
Fitting performed using SasView 5.0.6, SasModels version 1.0.7,
Fit optimizer DREAM

18. C+S **(a)** and core-shell **(b)** simulations based on experimental SLD values of the GNP ink series, as well as corresponding PSF outputs. Study of effect of SLD deviation on the PSF output for **(c)** core-shell model based simulated data.

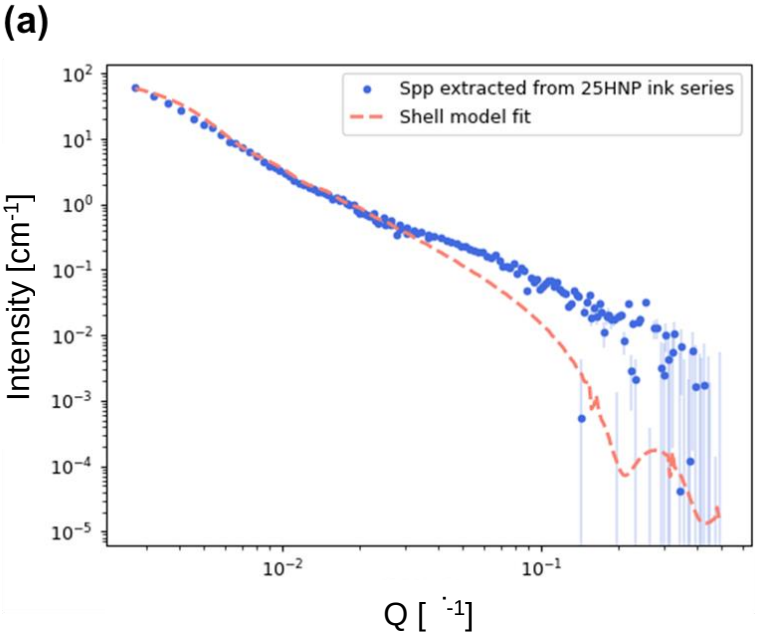



(c)
Investigation of component SLD shift impact on the PSF output - core-shell model based simulation (GNP version)
Alteration of carbon SLD:
Alteration of ionomer SLD:
Scc
Spp
Scp
Sij [cm3]
Q [Å-1]
SLD(C) /x10^10 cm-2
6.20
6.00
5.90
5.83
5.82 (simulation)
5.80
5.70
5.50
SLD(P) /x10^10 cm-2
4.40
4.45
4.47
4.48 (simulation)
4.50
4.55
4.75

19. Application of the scattering subtraction method to GNP ink series. GNP0 is a sample whose scattering function contains expression of the entire ink system. GNP80 is a sample whose scattering function contains information on the carbon structure only. (a) shows the two original scattering function for the two samples. (b) shows the scattering functions after scaling by $(\Delta\rho_c)^2$, SLD(C) = 5.82×10^{10} cm^{-2} as extracted from contrast match experiments. Note a significant gap in intensity is still present.



20. Fitting of the S_{pp} output extracted from the 25HNP ink series with a shell model. A very good fit is achieved in the low/mid Q regime, however, scattering at higher Q values remains unaccounted for.



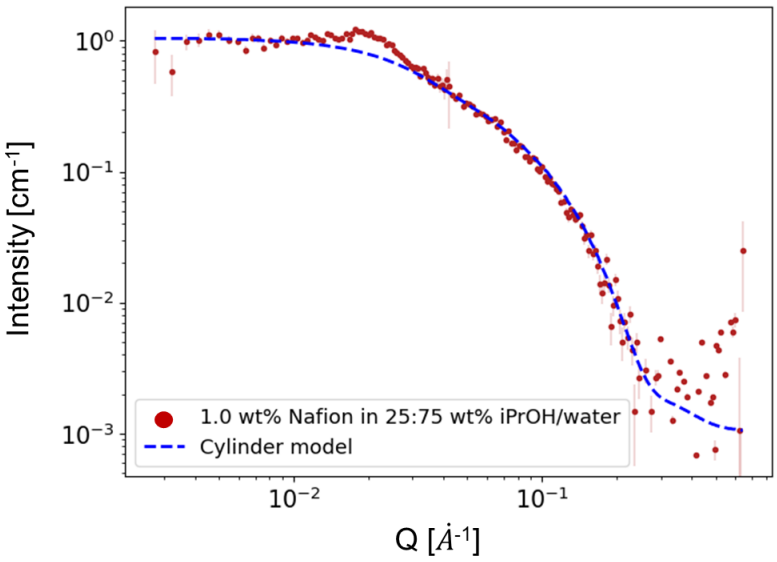
(b)

25HNP_517_v2_Spp_scaled.csv [02:24PM, September 04, 2024]

File name: 25HNP_517_v2_Spp_scaled.csv
SasView version: 6.0.0b1
SasModels version: 1.0.8
Fit optimizer used: DREAM
Model name: core_shell_sphere
Q Range: min = 0.0027156, max = 0.49909024
Chi2/Npts: 0.91733
scale = 0.004524 ± 0.0014227
background = 0.003 (fixed) cm^{-1}
core_shell_sphere = (fixed)
radius = 223.16 ± 5.1569 Å
thickness = 29.927 ± 4.8587 Å
sld_core = 0 (fixed) $10^{-6}/Å^2$
sld_shell = 4.22 (fixed) $10^{-6}/Å^2$
sld_solvent = 0 (fixed) $10^{-6}/Å^2$
Distribution of radius = 0.5 (fixed) Function: lognormal
Distribution of thickness = 0.2 (fixed) Function: lognormal

21. Estimation of radius and length of Nafion rod-like aggregates using 1.0 wt% Nafion in 25:75 wt% iPrOH/water scattering function. Due to the presence of a structure factor, fitting could not be performed, and parameters could only by gauged.

(a)



(b)

Cylinder

Scale = 0.0047 (fixed)
Sld = 4.22x10^{10} cm^{-2}
Sld_solvent = -0.49x10^{10} cm^{-2}

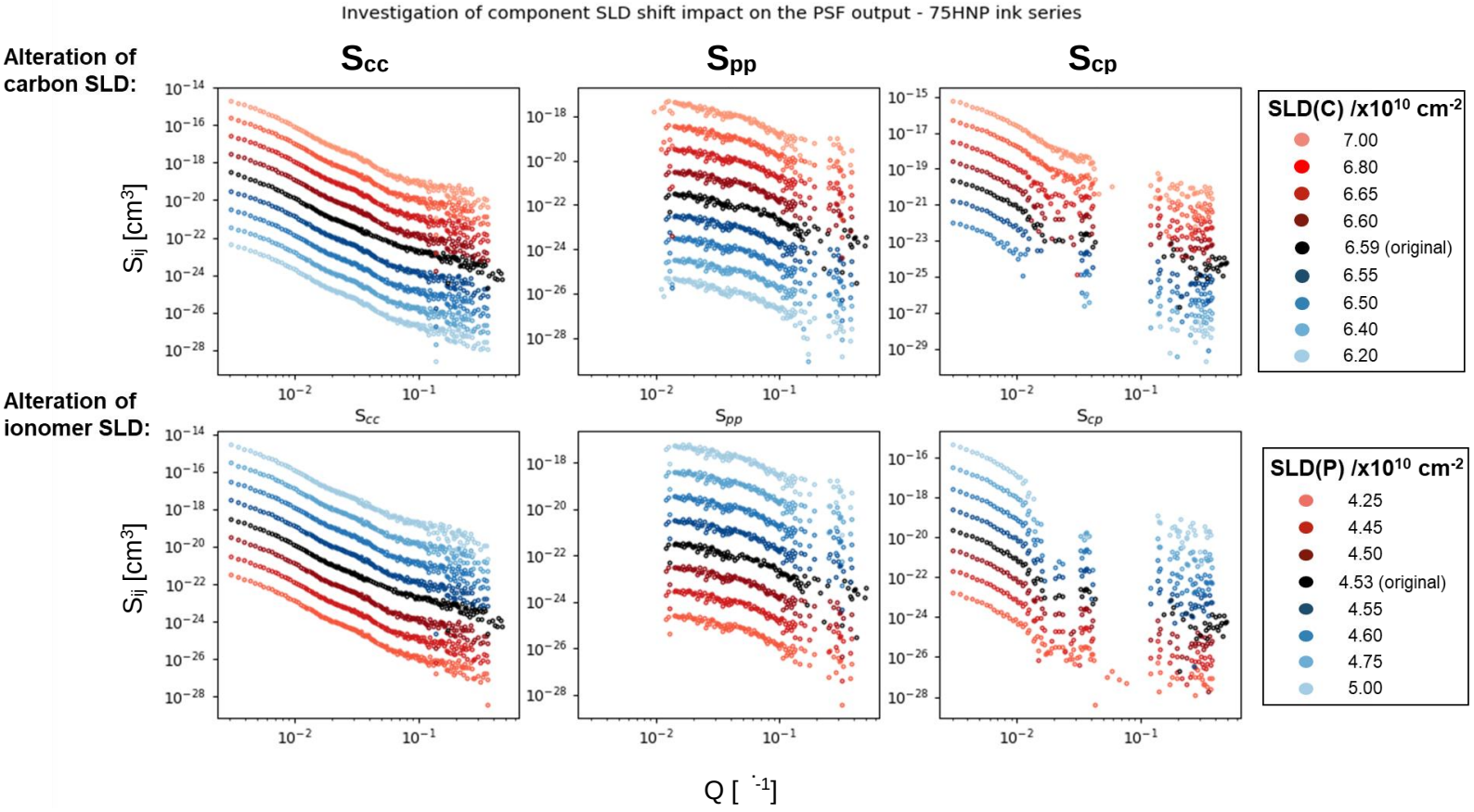
Radius = 13.0 $\dot{A}$
Length = 160.0 $\dot{A}$

Distribution of radius = 0.20
Distribution of thickness = 0
(function:lognormal)

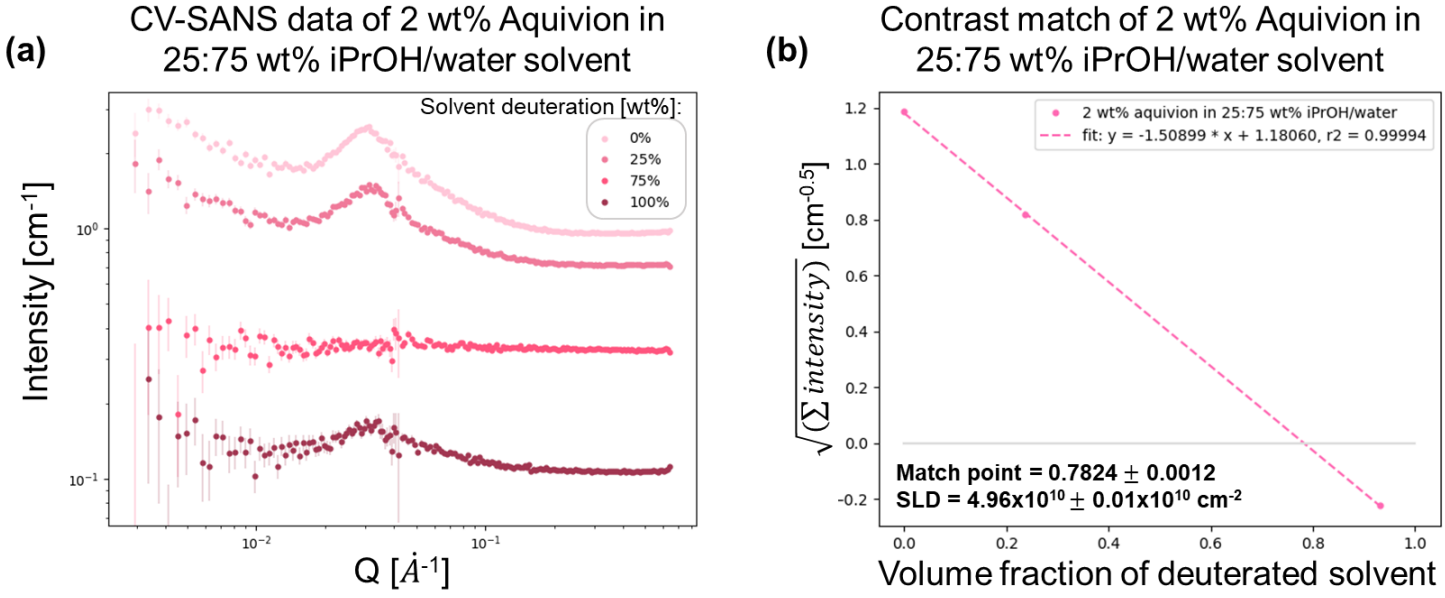
Chi^2/Npts = N/A

Modeled using SasView 5.0.6, SasModels version 1.0.7,

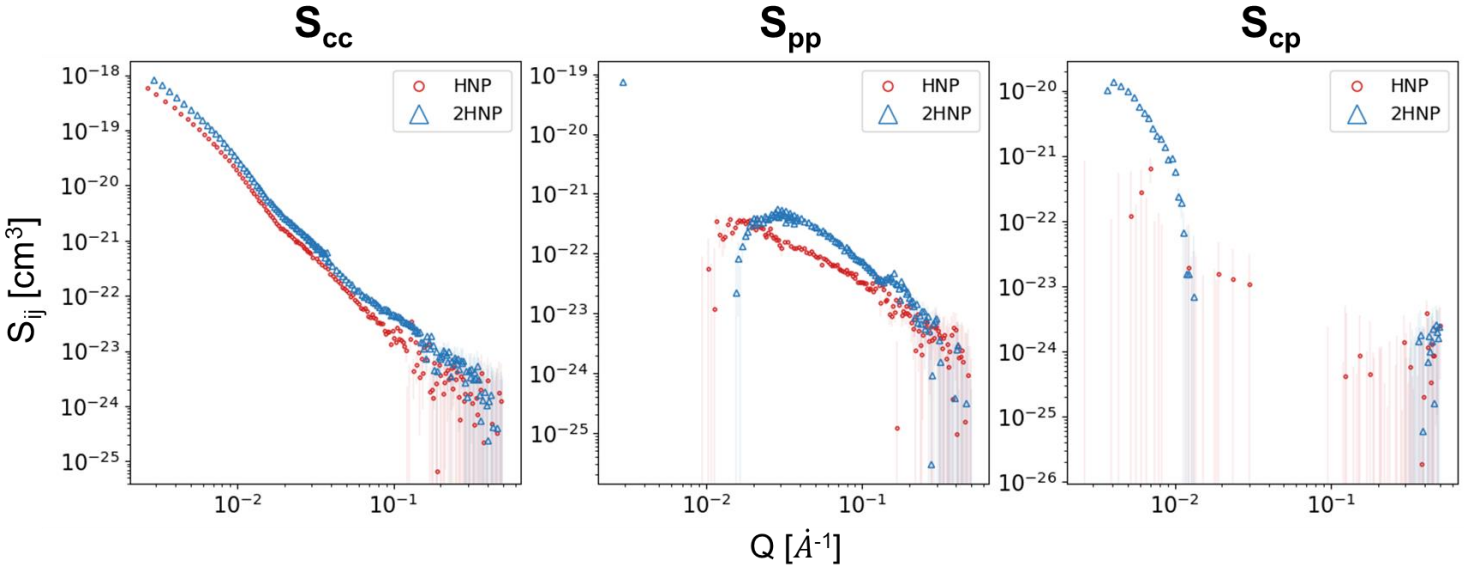
22. S_{cp} output extracted from 25HNP ink series, attempted to fit with a shell model with no polydispersity consideration. Parameters extracted in the S_{pp} fit (figure 69) were used to compute the plot. Unlike in the case of simulated data, no resemblance of the model to the data can be observed.



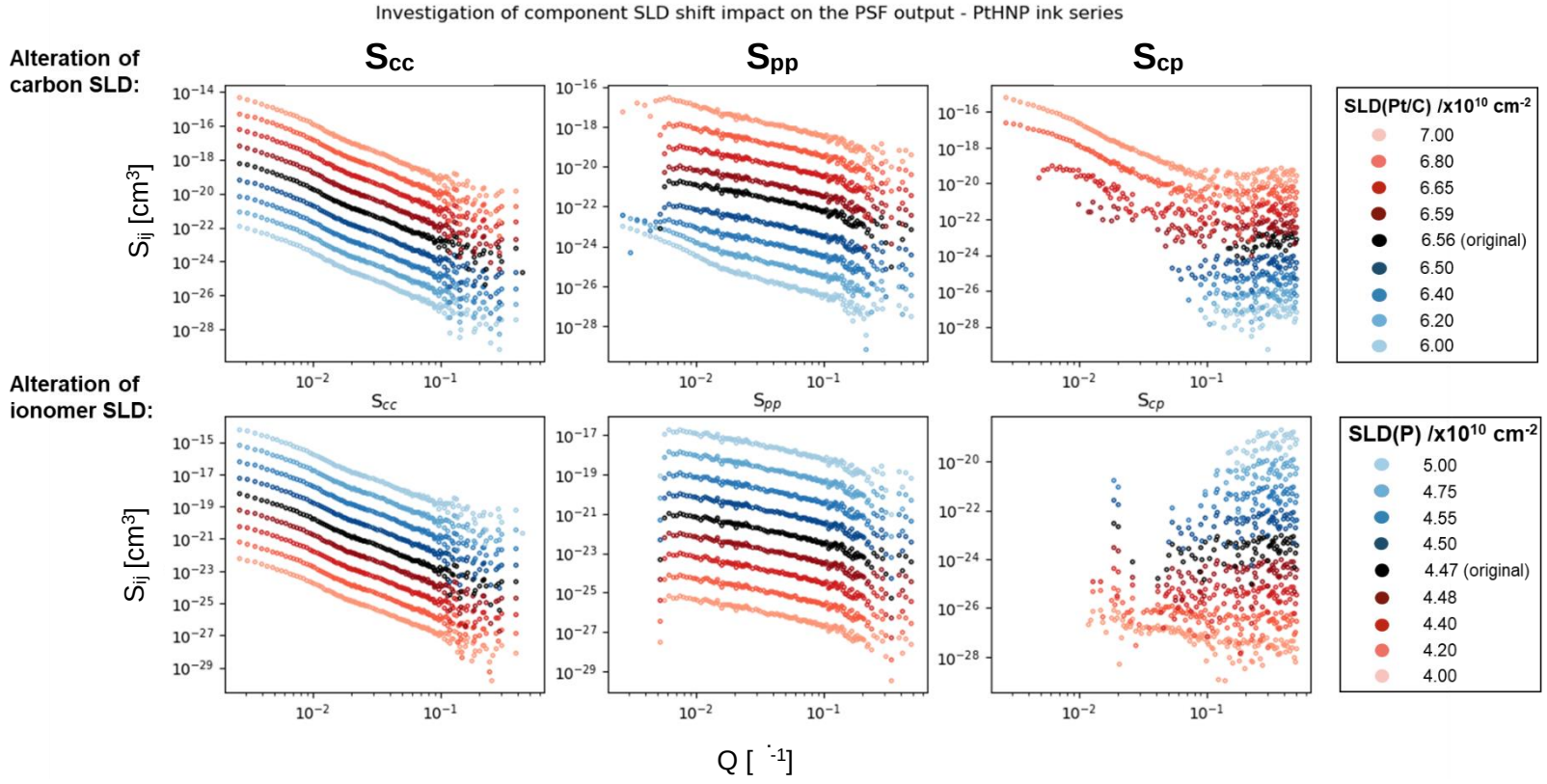
23. **(a)** CV-SANS data of 2 wt% Aquivion in 25:75 wt% iPrOH/water solvent. **(b)** contrast match evaluation, yielding an Aquivion SLD of 4.94×10^{10} cm^{-2}.



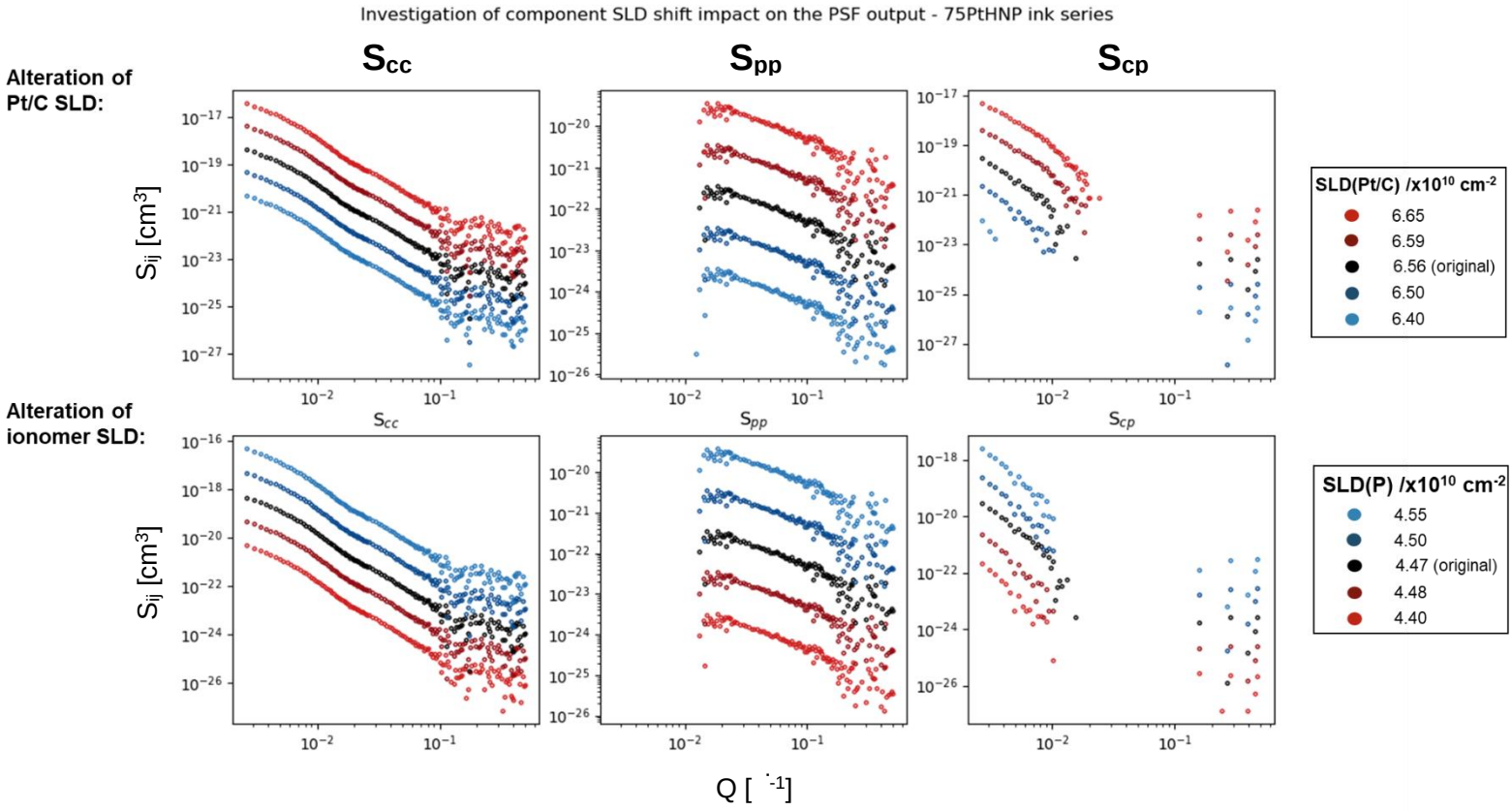
24. Comparison of PSF outputs extracted from ink compositions with different component concentrations. Slight deviation in intensity can be observed, which arises due to the component concentration differences.



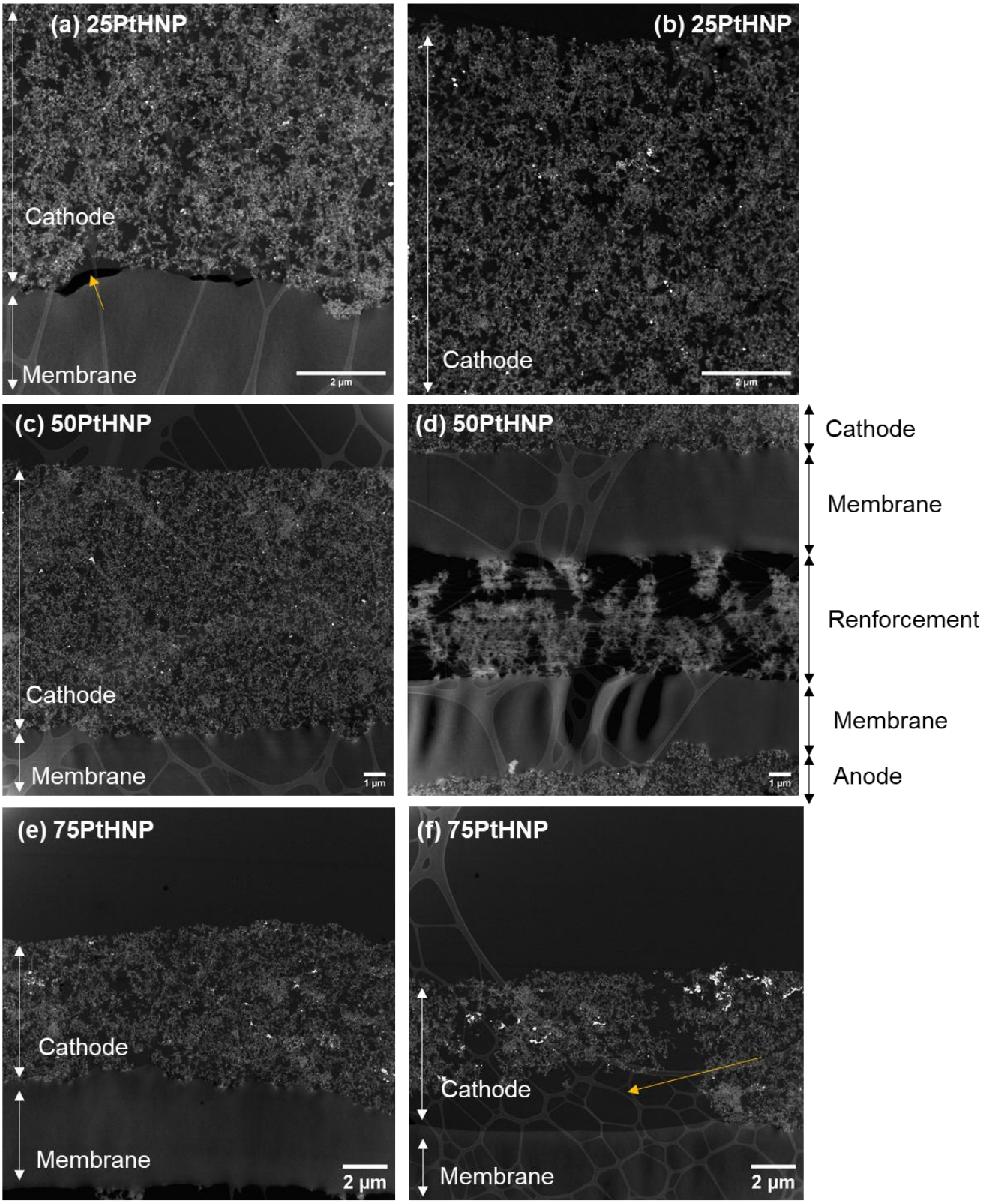
25. Investigation of component SLD shift on PSF outputs - PtHNP ink series. Error bars have not been included and data has been shifted on a logarithmic scale for visualization purposes.



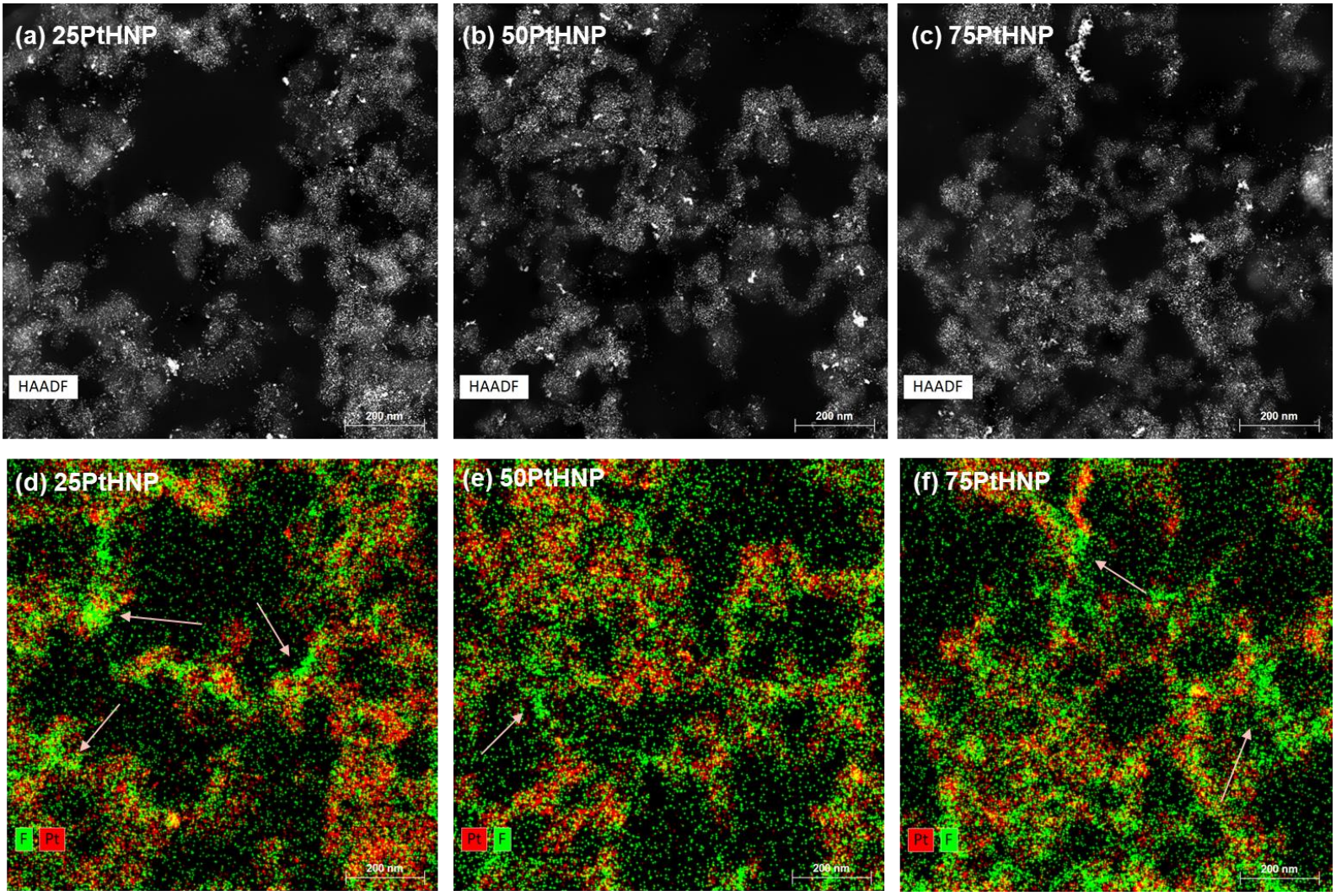
26. Investigation of component SLD shift on PSF outputs - 75PtHNP ink series. Error bars have not been included and data has been shifted on a logarithmic scale for visualization purposes.



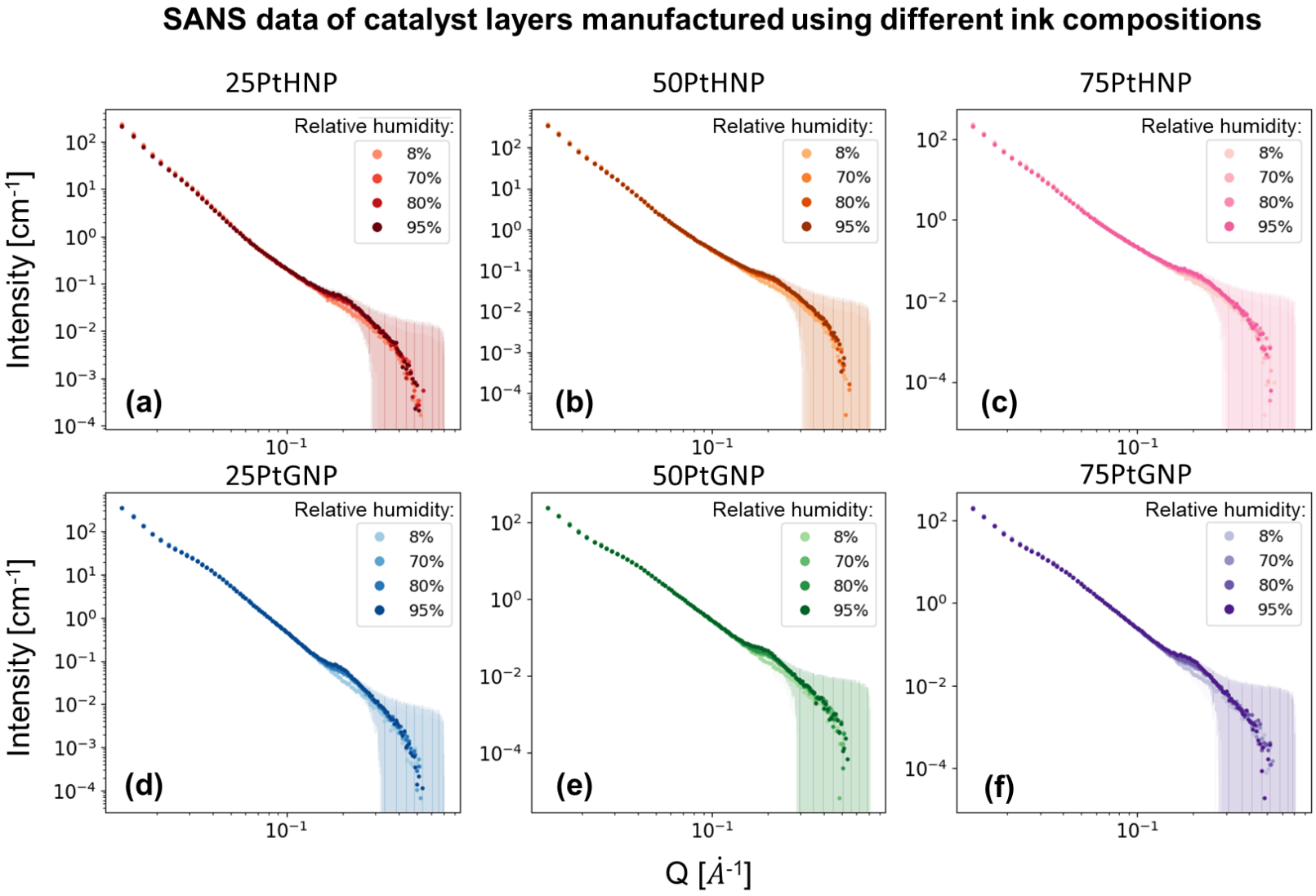
27. HAADF/STEM images of MEAs containing Pt/HSAC based CCLs, manufactured from inks with solvent containing 25 wt% (a, b), 50 wt% (c, d) and 75 wt% (e, f) iPrOH.



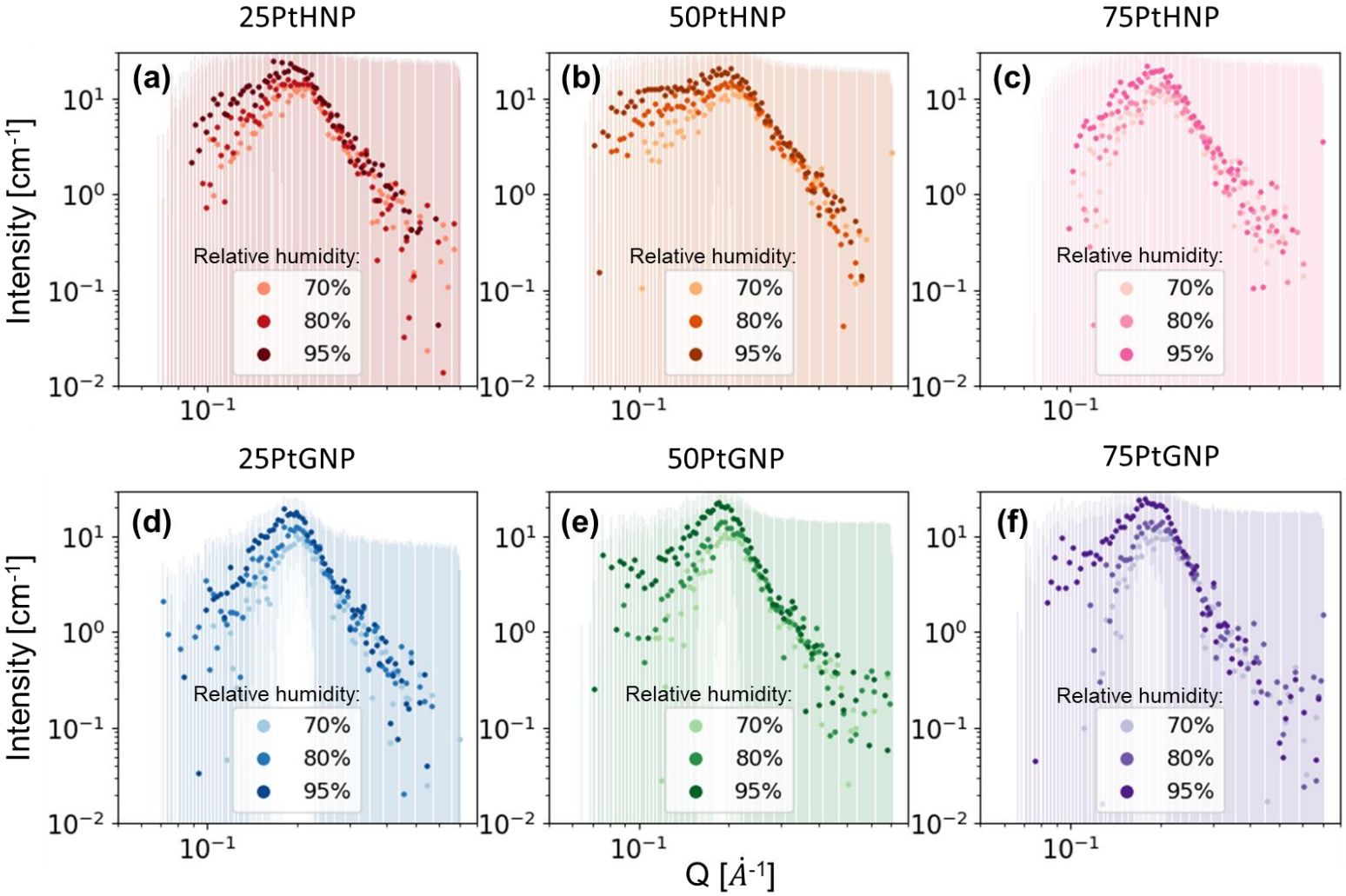
28. HAADF/STEM images of MEAs containing Pt/HSAC based CCLs, manufactured from inks with solvent containing 25 wt% (a), 50 wt% (b) and 75 wt% (c) iPrOH, with corresponding EDS elemental maps of Pt and F (d-f).



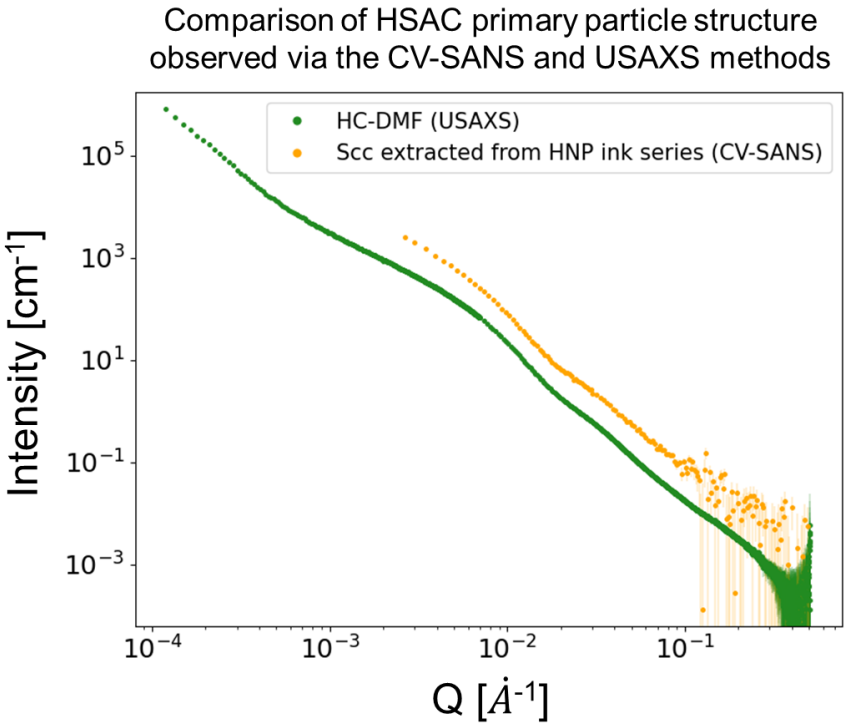
29. SANS data of catalyst layers (with incoherent scattering removed) manufactured using different ink compositions: **(a)** 25PtHNP, **(b)** 50PtHNP, **(c)** 75PtHNP, **(d)** 25PtGNP, **(e)** 50PtGNP, **(f)** 75PtGNP.



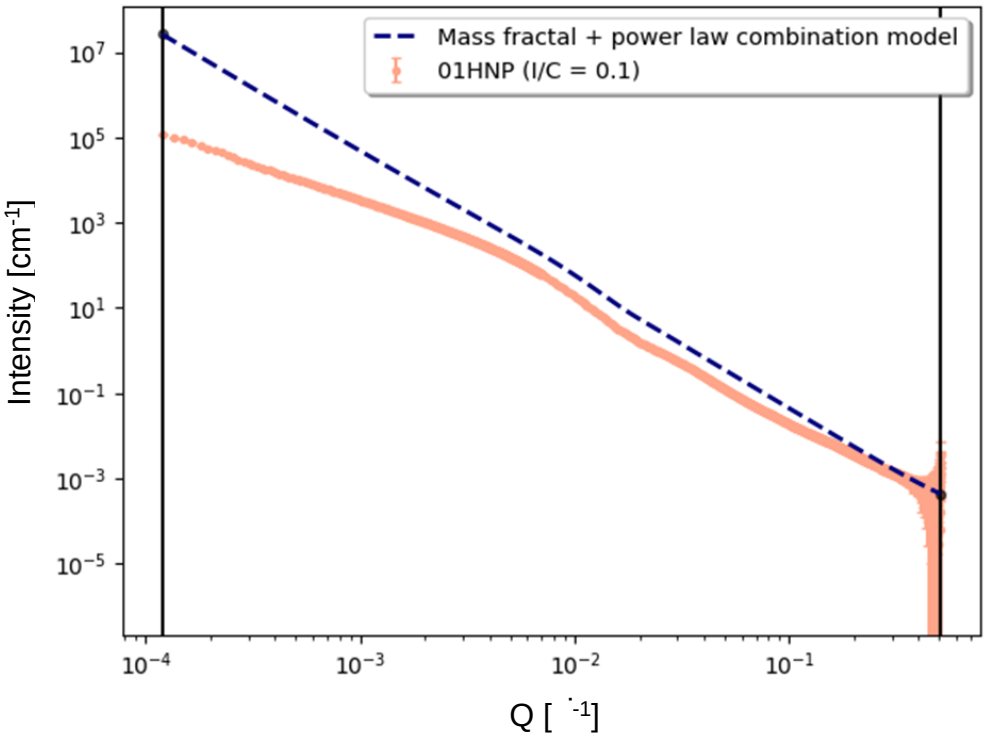
30. Scattering functions obtained at 70-95% RH, with scattering of the 'dry' reference sample removed, accentuating a peak-like feature related to the ionomer. **(a)** 25PtHNP, **(b)** 50PtHNP, **(c)** 75PtHNP, **(d)** 25PtGNP, **(e)** 50PtGNP, **(f)** 75PtGNP.



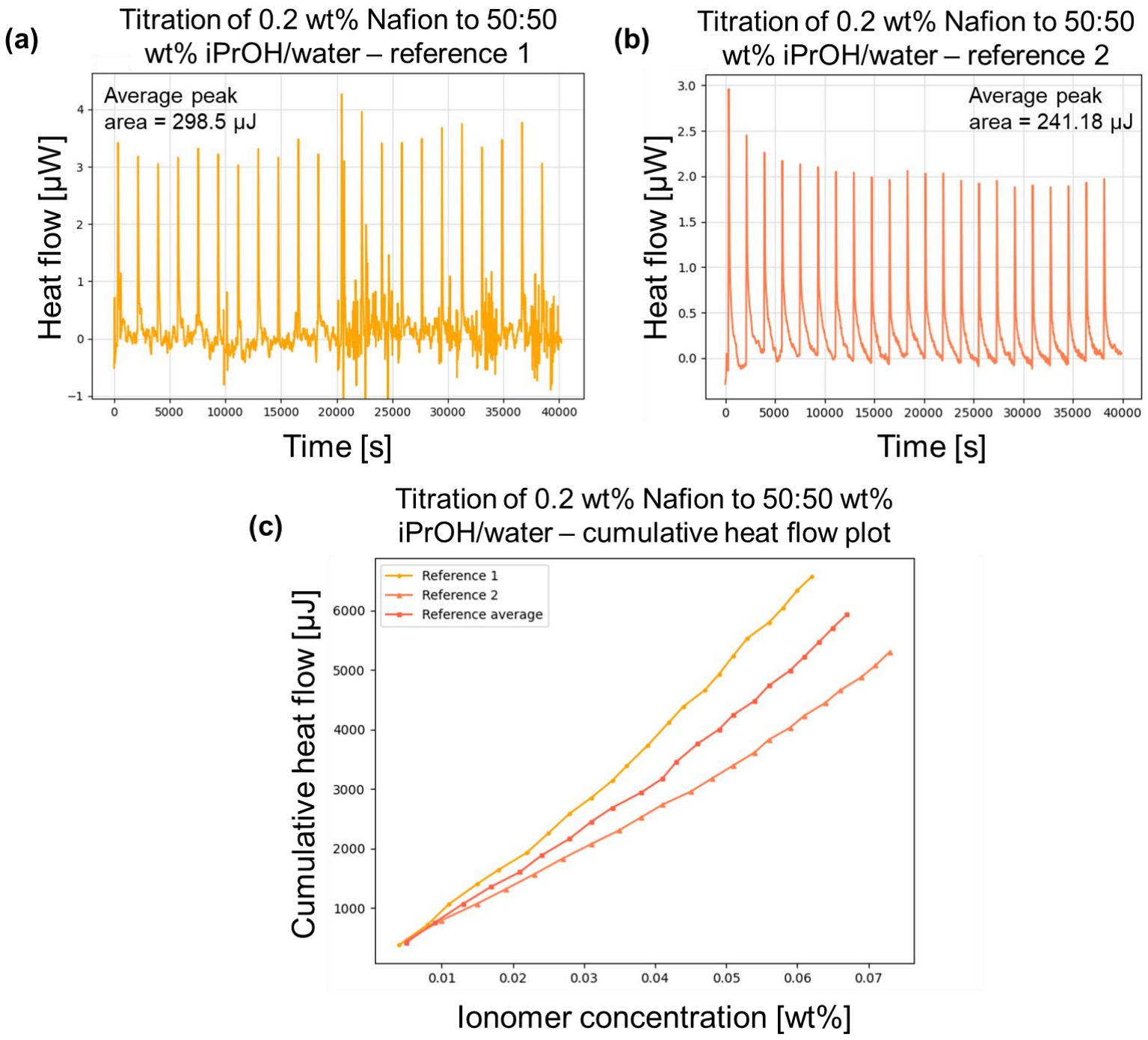
31. Comparison of carbon primary structure obtained from S_{cc} output of HNP ink series (CV-SANS method) and the USAXS scattering function obtained for the HC-DMF sample.



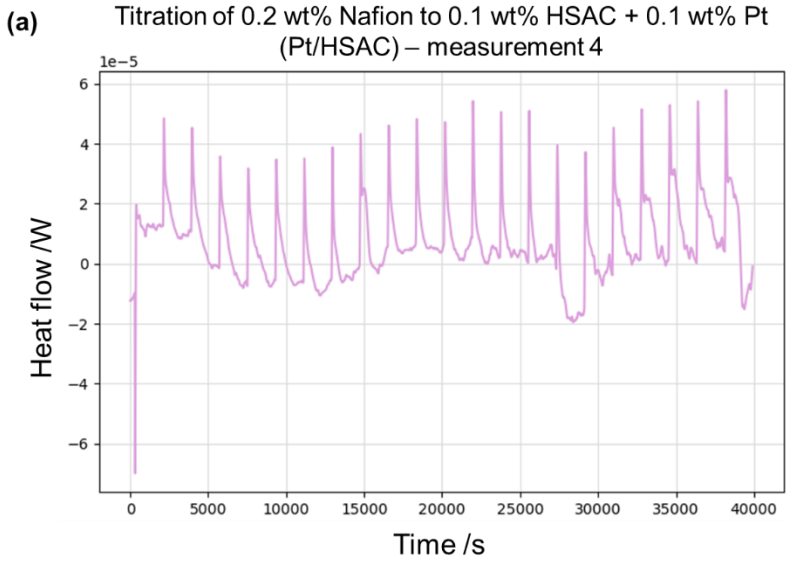
32. 0.1HNP fitted with a mass fractal + power law combination model. The proportions of each model were 99% and 1% respectively. The power was set to 3. The mass fractal model parameters set were the same as shown in figure 110(a).

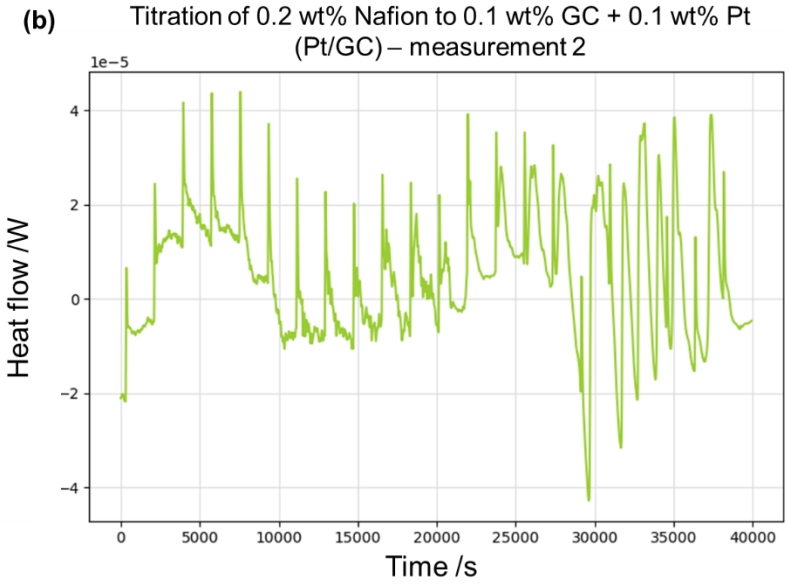


33. **(a)** ITC measurement arising from titration of 0.2 wt% nafion to 50:50 wt% iPrOH/water solvent – measurement reference 1, **(b)** ITC measurement arising from titration of 0.2 wt% nafion to 50:50 wt% iPrOH/water solvent – repeated measurement, reference 2, **(c)** cumulative heat flow calculated from integrated titration peak areas for reference 1 and reference 2 measurements, as well as the average of the two, plotted as a function of ionomer concentration.

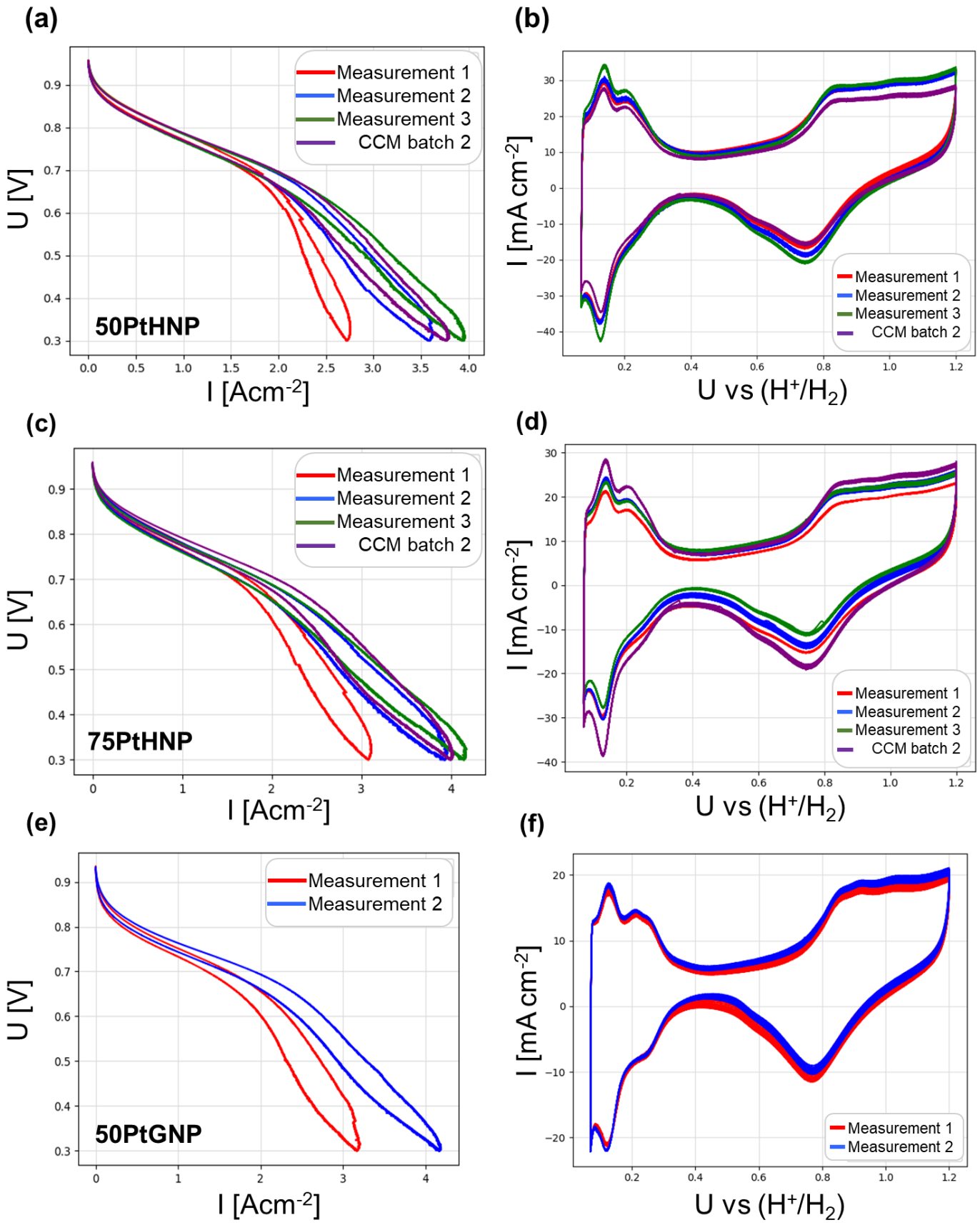


34. Repeated measurements of 0.2 wt% Nafion titration to (a) 0.1 wt% HSAC + 0.1 wt% Pt and (b) 0.1 wt% GC and 0.1 wt% Pt. No reproducible measurements were obtained.

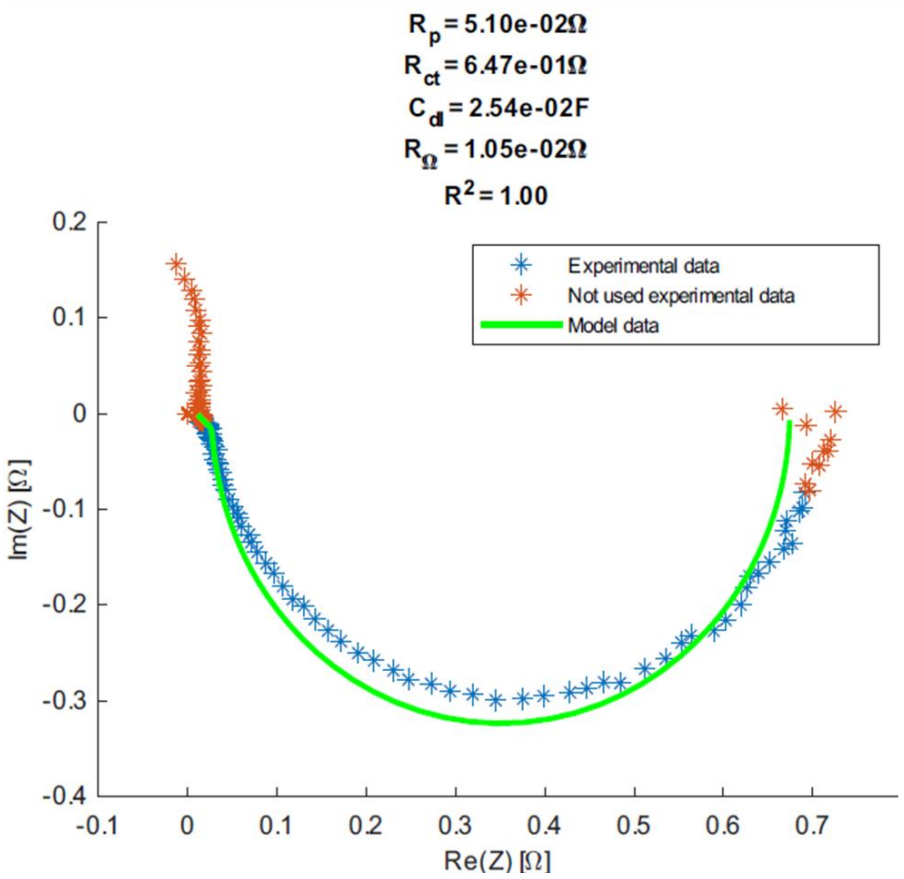




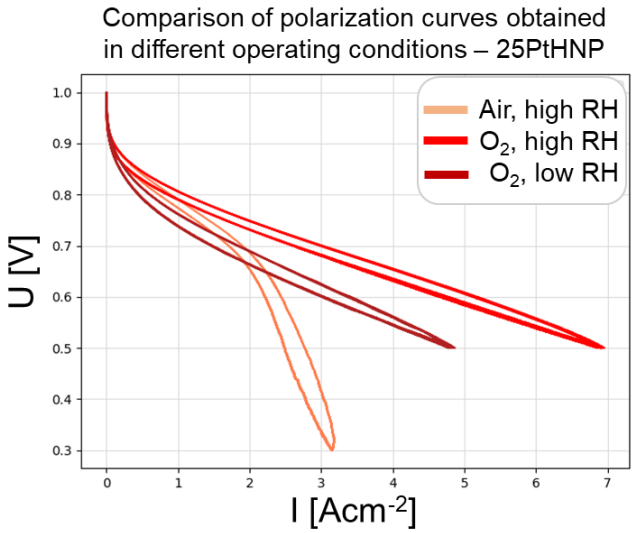
35. Electrochemical characterization reproducibility of results by inspection of (a) polarization curves and (b) cyclic voltammgoram, collected for a Pt/HSAC based cathode catalyst layer that was obtained from ink with 50:50 wt% iPrOH/water solvent composition, (c) polarization curves and (d) cyclic voltammgoram, collected for a Pt/HSAC based cathode catalyst layer that was obtained from ink with 75:25 wt% iPrOH/water solvent composition. (e) polarization curves and (f) cyclic voltammgoram, collected for a Pt/GC based cathode catalyst layer that was obtained from ink with 50:50 wt% iPrOH/water solvent composition. All polarization curves were measured in air, high RH operating conditions.

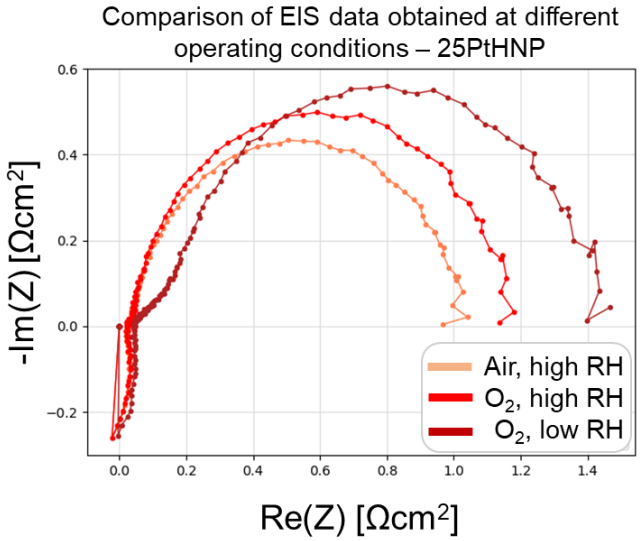

(a)
Measurement 1
Measurement 2
Measurement 3
CCM batch 2
50PtHNP
U [V]
I [Acm-2]
(b)
I [mA cm-2]
U vs (H+/H2)
(c)
75PtHNP
(d)
(e)
50PtGNP
(f)

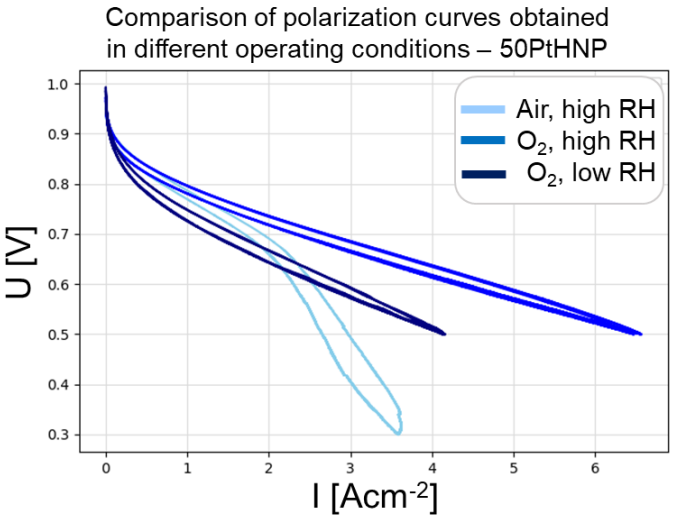
36. Example of fitting EIS data with model presented in equation (5.1.9). Note only data points in the frequency range of 1-3000 Hz were used for the fitting. Outside of the specified range artefacts arising from the potentiostat are present. The data points used for fitting are labelled as 'experimental data', while data points not used in the fitting are labelled as 'not used experimental data'. Unfortunately, a suitable fit could not be achieved when varying the parameters in question.

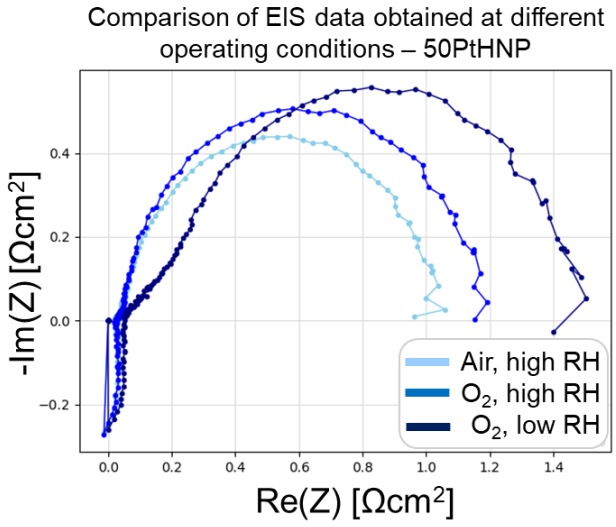


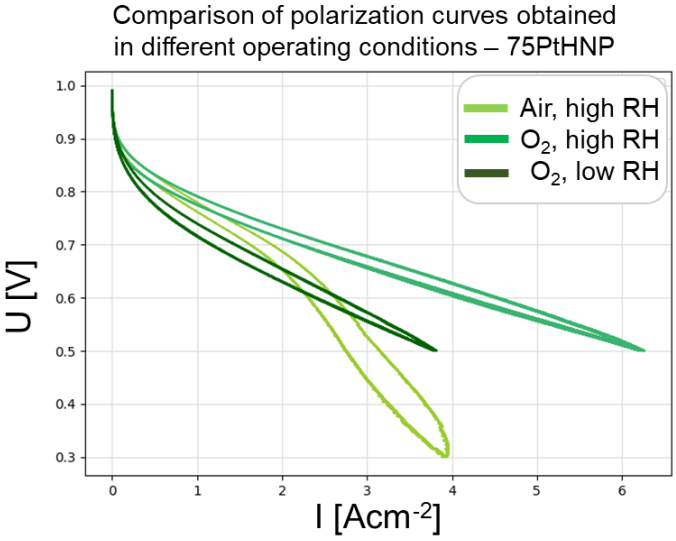
37. Comparison of polarization curves and EIS data obtained at different operating conditions for Pt/HSAC based CCMs.

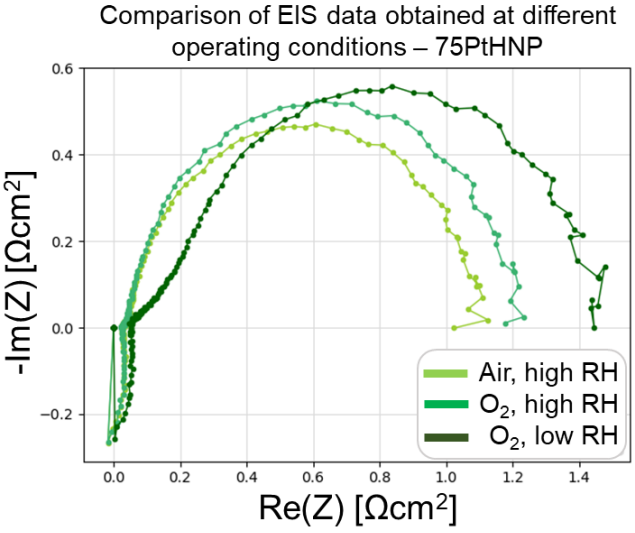






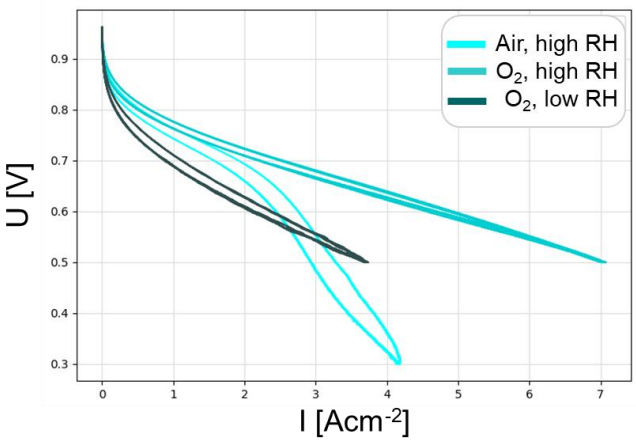




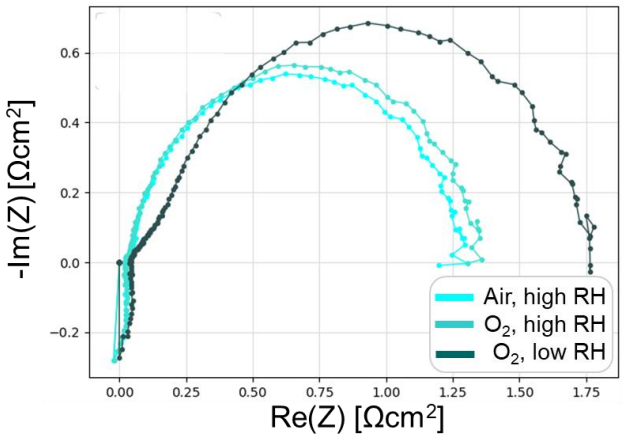


38. Comparison of polarization curves and EIS data obtained at different operating conditions for Pt/GC based CCMs.

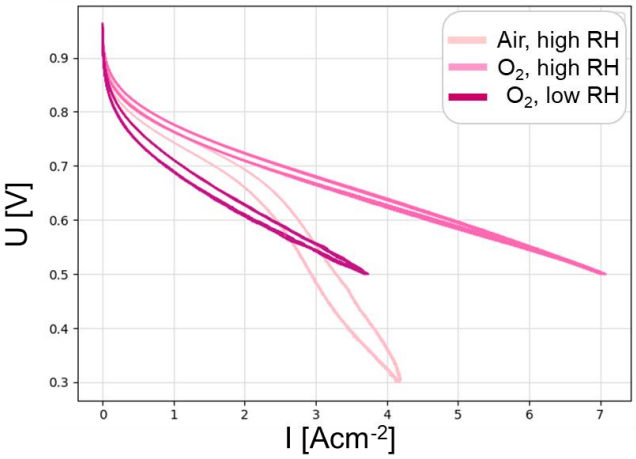
Comparison of polarization curves obtained in different operating conditions – 25PtGNP



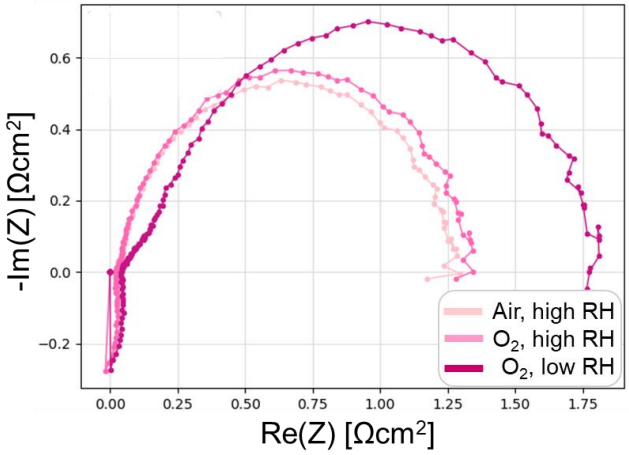
Comparison of EIS data obtained at different operating conditions – 25PtGNP



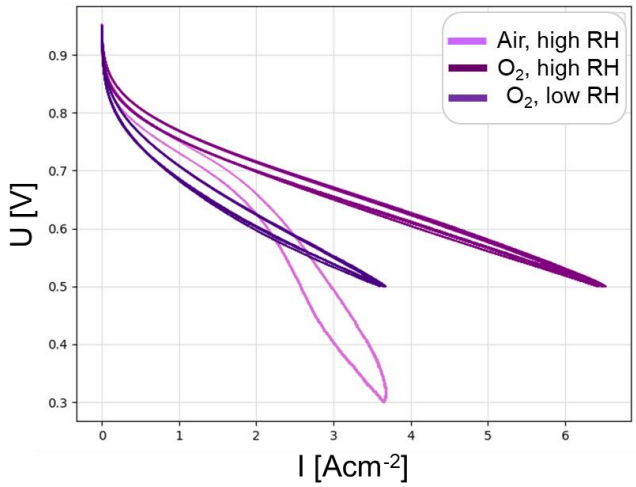
Comparison of polarization curves obtained in different operating conditions – 50PtGNP



Comparison of EIS data obtained at different operating conditions – 50PtGNP



Comparison of polarization curves obtained in different operating conditions – 75PtGNP



Comparison of EIS data obtained at different operating conditions – 75PtGNP

